

Dissertation  
submitted to the  
Combined Faculties for the Natural Sciences and for Mathematics  
of the Ruperto-Carola University of Heidelberg, Germany  
for the degree of  
Doctor of Natural Sciences

put forward by  
Dipl.-Phys. Christoph Hörmann  
born in Calw, Germany

Oral examination: 06.02.2013



# Space-based Monitoring of Volcanic Emissions Using the GOME-2 Instrument

Referees: Prof. Dr. Ulrich Platt  
Prof. Dr. Bernd Jähne



## Zusammenfassung

Die satellitengestützte Beobachtung der Erdatmosphäre ermöglicht es heutzutage, Vulkanemissionen, insbesondere auch während großer Eruptionen, global und aus sicherer Entfernung zu quantifizieren. Im Rahmen dieser Doktorarbeit wurden Daten des Satelliteninstruments GOME-2 mit Hilfe der differentiellen optischen Absorptionsspektroskopie (DOAS) systematisch auf das Vorkommen vulkanischer Emissionen von Schwefeldioxid ( $\text{SO}_2$ ) und Brommonoxid (BrO) untersucht. Neben einer Verbesserung des  $\text{SO}_2$  Auswertalgorithmus, der nun die deutlich genauere Ermittlung von Säulendichten im Fall sehr hoher  $\text{SO}_2$  Konzentrationen ermöglicht, wurde ein neues Verfahren entwickelt, das die automatische Detektion von Vulkanfahnen aus globalen Satellitendaten erlaubt. Die Anwendung auf den GOME-2 Datensatz der Jahre 2007–2011 ermöglichte eine systematische Suche nach BrO in nahezu 800 extrahierten Vulkanfahnen, welches in 64 Fällen nachgewiesen werden konnte. In einer Vielzahl dieser Fälle wurden Unterschiede in den räumlichen Verteilungen von  $\text{SO}_2$  und BrO festgestellt. Die mittleren BrO/ $\text{SO}_2$  Verhältnisse entsprachen dabei weitgehend den Beobachtungen durch Bodenmessungen der letzten Jahren. Auf Grund der erzielten Ergebnisse konnte die Gesamtzahl der weltweit bekannten Vulkane mit signifikanten Bromemissionen von 12 auf 19 gesteigert werden. Darüber hinaus wurde erstmals das BrO-Vorkommen an einem passiv ausgasenden Vulkan durch jährlich gemittelte Satellitenmessungen nachgewiesen. Der neu gewonnene, umfangreiche Datensatz vulkanischer BrO-Emissionen erlaubt eine detaillierte Untersuchung der Halogenchemie in großflächigen Vulkanfahnen sowie eine Abschätzung der globalen Bromemissionen in die Atmosphäre.

## Abstract

Today's satellite observations of the earth's atmosphere allow to quantify global volcanic emissions from a safe distance, in particular during major eruptions. In this thesis, GOME-2 satellite data has been investigated for the occurrences of volcanic sulfur dioxide ( $\text{SO}_2$ ) and bromine monoxide (BrO) emissions using Differential Optical Absorption Spectroscopy (DOAS). An improved version of the  $\text{SO}_2$  evaluation scheme has been implemented, which is able to retrieve accurate column densities in the case of very high  $\text{SO}_2$  concentrations. Furthermore, the automatic detection of volcanic plumes from global satellite data can be achieved by a newly developed algorithm. Almost 800 volcanic plumes were extracted from the GOME-2 dataset for the years 2007–2011 and systematically investigated for potentially elevated BrO, which has been detected in 64 cases. A large number of the volcanic plumes showed differences in the spatial distributions of BrO and  $\text{SO}_2$ . The associated mean BrO/ $\text{SO}_2$  ratios were generally consistent with those from ground-based measurements in recent years. Based on the results of this thesis, the total number of volcanoes known for significantly high bromine emissions could be raised from 12 to 19. Moreover, BrO from a passively degassing volcano was successfully detected for the first time by using yearly averaged satellite data. The new and extensive dataset of volcanic BrO emissions offers the possibility to further investigate halogen chemistry in widespread volcanic plumes, as well as to provide an estimate of the atmospheric bromine input from global volcanic emissions.



# Contents

## I. Motivation and Scientific Background

<b>1. Introduction</b>	<b>3</b>
<b>2. Volcanic emissions and their influence on atmospheric chemistry</b>	<b>7</b>
2.1. General volcanic gas composition . . . . .	7
2.2. Volcanic sulfur compounds . . . . .	8
2.2.1. SO <sub>2</sub> from volcanic emissions . . . . .	9
2.2.2. Other volcanic sulfur species . . . . .	12
2.3. Halogen compounds in volcanic plumes . . . . .	12
2.3.1. Bromine monoxide in volcanic plumes . . . . .	13
2.3.2. Formation of volcanic BrO . . . . .	14
<b>3. Optical remote sensing of volcanic emissions: State of the art</b>	<b>17</b>
3.1. Ground-based measurements . . . . .	17
3.1.1. COSPEC . . . . .	17
3.1.2. Fourier transform infrared spectroscopy (FTIR) . . . . .	20
3.1.3. Ground-based DOAS measurements . . . . .	21
3.2. Satellite-borne measurements . . . . .	23
3.2.1. SCIAMACHY . . . . .	24
3.2.2. OMI . . . . .	26
3.2.3. GOME-2 . . . . .	28
3.2.4. ASTER . . . . .	29
3.2.5. AIRS . . . . .	31
3.2.6. IASI . . . . .	32

## II. Methods and Instruments

<b>4. Differential Optical Absorption Spectroscopy</b>	<b>37</b>
4.1. Absorption spectroscopy . . . . .	37
4.2. The principle of DOAS . . . . .	38
4.3. Passive DOAS . . . . .	41
4.4. The Ring effect . . . . .	43
4.5. Satellite viewing geometry and geometrical AMF . . . . .	44
4.6. Radiative transfer calculations . . . . .	46

<b>5. Instruments</b>	<b>47</b>
5.1. The GOME-2 instrument . . . . .	47
5.2. DOAS instruments on CARIBIC . . . . .	50
<b>6. Satellite retrieval of SO<sub>2</sub> and BrO</b>	<b>53</b>
6.1. Instrument calibration . . . . .	53
6.2. SO <sub>2</sub> standard retrieval (312.1–324 nm) . . . . .	54
6.2.1. Sources of SO <sub>2</sub> in global daily maps . . . . .	54
6.2.2. Global mean maps of SO <sub>2</sub> . . . . .	57
6.3. Alternative SO <sub>2</sub> evaluation schemes at larger wavelengths . . . . .	60
6.3.1. SO <sub>2</sub> standard retrieval during major volcanic eruptions . . . . .	62
6.3.2. SO <sub>2</sub> alternative retrieval (326.5–335.3 nm) - AR <sub>1</sub> . . . . .	64
6.3.3. SO <sub>2</sub> alternative retrieval (360–390 nm) - AR <sub>2</sub> . . . . .	64
6.3.4. Implications of alternative SO <sub>2</sub> retrievals . . . . .	64
6.3.5. RTM comparison study for SO <sub>2</sub> SR and AR <sub>2</sub> . . . . .	68
6.4. BrO retrieval . . . . .	71
6.4.1. Daily and mean global maps of BrO . . . . .	73
<b>III. Applications and Results</b>	
<b>7. Global anthropogenic and volcanic SO<sub>2</sub> emission sources</b>	<b>79</b>
7.1. North and Middle America . . . . .	79
7.2. South America . . . . .	81
7.3. Europe . . . . .	81
7.4. Norilsk (Russia) . . . . .	84
7.5. Eastern China . . . . .	84
7.6. Malay Archipelago . . . . .	87
<b>8. Systematic detection of volcanic plumes</b>	<b>89</b>
8.1. Automatic identification of volcanic SO <sub>2</sub> plumes . . . . .	89
8.2. Global maps with two days coverage . . . . .	90
8.3. Volcanic plume extraction . . . . .	93
8.4. Non-volcanic background correction and plume pixel selection . . . . .	94
8.5. Combination of SO <sub>2</sub> SR and AR <sub>1</sub> for major eruptions . . . . .	97
8.6. Time series of volcanic SO <sub>2</sub> between January 2007 and June 2011 . . . . .	99
8.7. Discussion on the plume detection algorithm . . . . .	103
<b>9. Systematic investigation of BrO during volcanic events</b>	<b>107</b>
9.1. Satellite retrieval of volcanic BrO . . . . .	107
9.2. Correction for non-volcanic BrO . . . . .	108
9.3. Volcanic BrO within January 2007–June 2011 . . . . .	112
9.3.1. Etna (14 May 2008) . . . . .	114
9.3.2. Bezymianny/Kliuchevskoi (11/12 May 2007) . . . . .	114
9.3.3. Dalaffilla (4 November 2008) . . . . .	117

9.3.4.	Nabro (16 June 2011)	117
9.3.5.	Kasatochi (9 and 11 August 2008)	120
9.3.6.	Sarychev (15/16 June 2009)	123
9.4.	Systematic analysis of BrO events in volcanic plumes	125
9.4.1.	Category I: clear linear correlation	129
9.4.2.	Category II: weak linear correlation	132
9.4.3.	Category III: No linear BrO/SO <sub>2</sub> relationship	132
9.4.4.	Category IV: Volcanic plumes showing no enhanced BrO SCDs*	135
9.5.	Discussion on investigation of volcanic BrO during volcanic events	135
9.5.1.	Different BrO/SO <sub>2</sub> relationships	137
9.5.2.	Comparison to previous ground-based measurements	138
9.5.3.	Comparison to previous satellite studies	139
9.6.	Intercomparison of GOME-2 and CARIBIC data for Eyjafjallajökull	140
9.6.1.	GOME-2 SO <sub>2</sub> and BrO measurements on 16 May 2010	141
9.6.2.	CARIBIC SO <sub>2</sub> and BrO measurements on 16 May 2010	141
9.6.3.	GOME-2 and CARIBIC data comparison	145
<b>10.</b>	<b>BrO from a quiescent degassing volcano (Ambrym)</b>	<b>149</b>
10.1.	Previous BrO studies at Ambrym	149
10.2.	Straight forward averaged SO <sub>2</sub> and BrO over Vanuatu	150
10.3.	Background corrected annual mean maps	151
10.4.	Mean BrO/SO <sub>2</sub> ratio for Ambrym 2007–2011	157
10.5.	Discussion on volcanic BrO at Ambrym	161
<b>IV. Conclusions and Outlook</b>		
<b>11.</b>	<b>Conclusions</b>	<b>165</b>
<b>12.</b>	<b>Outlook</b>	<b>169</b>
<b>Appendix</b>		
<b>A.</b>	<b>Volcanic BrO events</b>	<b>175</b>
<b>B.</b>	<b>Extracted volcanic plumes January 2007–June 2011</b>	<b>241</b>
<b>Bibliography</b>		<b>253</b>



**parts of this thesis have been published in:**

Hörmann, C., Sihler, H., Bobrowski, N., Beirle, S., Penning de Vries, M., Platt, U., and Wagner, T.: Systematic investigation of bromine monoxide in volcanic plumes from space by using the GOME-2 instrument. *Atmos. Chem. Phys. Dis.*, **12**, 29325–29389, doi:10.5194/acpd-12-29325-2012, 2012.

Bobrowski, N., Kern, C., Platt, U., Hörmann, C., and Wagner, T.: Novel SO<sub>2</sub> spectral evaluation scheme using the 360–390 nm wavelength range. *Atmos. Meas. Tech.*, **3**, 879–891, doi:10.5194/amt-3-879-2010, 2010.

Heue, K.-P., Brenninkmeijer, C. A. M., Baker, A. K., Rauthe-Schöch, A., Walter, D., Wagner, T., Hörmann, C., Sihler, H., Dix, B., Frieß, U., Platt, U., Martinsson, B. G., van Velthoven, P. F. J., Zahn, A., and Ebinghaus, R.: SO<sub>2</sub> and BrO observation in the plume of the Eyjafjallajökull volcano 2010: CARIBIC and GOME-2 retrievals. *Atm. Chem. Phys.*, **11**(6), 2973–2989, 2011



**Part I.**

**Motivation and Scientific  
Background**



# 1. Introduction

Life on Earth has always been strongly influenced by volcanoes and their emissions. About 4.6 billion years ago the atmospheric composition consisted of water vapor ( $\text{H}_2\text{O}$ ), carbon dioxide ( $\text{CO}_2$ ), hydrogen sulfide ( $\text{H}_2\text{S}$ ), nitrogen ( $\text{N}_2$ ) and other species that had been mainly produced by volcanic degassing from the interior of Earth. Today, all of these species are still typically emitted by volcanoes (Seinfeld and Pandis, 1997).

In the meantime, the composition has significantly changed compared to the early state of the atmosphere. Nearly all water vapor has condensed out and formed the oceans, lakes and rivers. The  $\text{CO}_2$  was dissolved in the water and had subsequently built up carbonate sediments. Early bacterial life introduced oxygen to the atmosphere. It is believed that the first free oxygen was released through photosynthesis by cyanobacteria. The oxygen was initially soaked up by dissolved iron in the oceans and formed banded oxidised iron formations on the ground. Once the iron was used up, oxygen was able to start building up in the atmosphere about 2.4 billion years ago (Farquhar et al., 2000). As one of the remaining constants,  $\text{N}_2$  is today the most abundant constituent of Earth's atmosphere, mainly because it is chemically inert and shows a very low solubility in water.

Since the dawn of humanity, volcanoes have also significantly influenced human's life. Nowadays, it is known that major volcanic eruptions had disastrous consequences for life on Earth in the past, mainly due to their influence on the planet's climate. In 1783/84, the eruption of Laki (Iceland) caused the lowest average winter temperatures in the United States, with about  $4.8^\circ\text{C}$  below the 225-year average. At the same time, Europe suffered from a very hot summer in large parts of the western continent and the population was afterwards bothered by one of the most severe winters that has been ever recorded. The annual mean surface cooling on both continents was about  $-1.3^\circ\text{C}$  and lasted for 2–3 years (Thordarson and Self, 2003). Only 30 years later, the eruption of the Tambora volcano (Indonesia) in 1815 caused similar effects. The year 1816 became famous as the "year without a summer", implicating a very cold summer in western Europe and parts of North America at  $1\text{--}2.5^\circ\text{C}$  colder than normal (Rampino and Self, 1982). The eruption ranks as the largest known event in the past two millennia. About  $150\text{ km}^3$  of ash were injected into the stratosphere, probably up to altitudes of 44 km (Oppenheimer, 2003).

It was already suggested by Benjamin Franklin that the cold conditions after the Laki eruption in 1783 resulted from the blocking out of sunlight by dust and gases that were emitted by volcanoes (Franklin, 1784). Franklin's hypothesis is still consistent with modern scientific theory, which suggests that the injections of large sulfur dioxide ( $\text{SO}_2$ ) volumes and the subsequent formation of sulfuric acid ( $\text{H}_2\text{SO}_4$ ) aerosols are mainly responsible for global cooling after major volcanic eruptions (e.g. Robock,

2000). Initially it had been thought that volcanic ash particles cause this cooling by partially reflecting solar radiation back to space at high altitudes.

While the destructive power of violent volcanic eruptions has been regularly responsible for the devastation of large populated areas, the benefits of volcanism and related processes have always caused people to repopulate volcanic surroundings. Some of the earliest civilizations (for example, Greek, Etruscan, and Roman) settled on the rich, fertile volcanic soils in the Mediterranean-Aegean region and the best rice-growing areas of Indonesia are found at volcanic areas (Kious et al., 1996). It is estimated that about 500 million people live on or close to active volcanoes today (Tilling and Lipman, 1993).

Given this large number of people potentially threatened by volcanoes, there is a reasonable interest to investigate volcanic systems. As modern volcanology is a relatively young branch of science, large parts of the basic processes deep inside the Earth are not well known. Although volcanic eruptions cannot be predicted accurately yet, there has been significant progress during the last decades. Instruments that can monitor seismic activity, ground deformation or changes in the groundwater level due to increasing subsurface gas pressure near a volcano are successfully used to predict eruptions, like it has been the case for Mount St. Helens in 1980 (Tilling, 1984) or Popocatepetl (Mexico) in 1994 and 2001 (Martin-Del Pozzo, 2012).

Direct sampling and especially remote sensing of gaseous volcanic emissions can yield further important information about a volcano's state of activity. It is important to note that volcanic gases are first dissolved in the magma and that they are the driving force that causes an eruption when magma is rising towards the surface. In order to understand why, when and how a volcano will erupt, it is an unavoidable necessity to understand the interaction of the dissolved species. An often cited example where a volcanic eruption had been successfully predicted is Mt. Pinatubo in 1991. About four weeks prior to the main eruption on June 15, a continuously increasing  $\text{SO}_2$  flux was noticed, indicating the upcoming eruption (Daag et al., 1996b). Although it had been the second largest eruption of the whole 20th century, the early warnings allowed the evacuation of large parts of the population and many deaths could be prevented (Punongbayan and Newhall, 1999).

Since then, monitoring of gaseous volcanic emissions on a regular basis has become more and more important. Ratios of  $\text{SO}_2$  to other species like  $\text{CO}_2$  or halogens are typically used to monitor the volcano's activity. Although the total fluxes of halogen species like HCl, HF or HBr are large (Pyle and Mather, 2009), it had been thought that these gases are relative chemical inert and therefore have no significant influence on atmospheric chemistry. This view changed, after Bobrowski et al. (2003) detected very large mixing ratios of the bromine monoxide radical (BrO) in the plume of the Soufrière Hills volcano. Reactive bromine species are known to play an important role in the halogen-catalysed depletion of ozone ( $\text{O}_3$ ) in both, the tropo- and stratosphere (e.g. McConnell et al., 1992; Platt and Lehrer, 1996; Solomon, 1999; Wennberg, 1999; von Glasow and Crutzen, 2003; Simpson et al., 2007; Sihler et al., 2012).

In recent years, the abundance of volcanic BrO has been validated by ground-based measurements at several quiescent degassing volcanoes worldwide. Still, little is known about the globally released quantities and their potential to substantially affect at-

---

ospheric chemistry. Furthermore, literature about the injection of reactive bromine during major volcanic eruptions is sparse. However, it has been recently shown that giant volcanic eruptions in Nicaragua over the past 70,000 years could have injected enough bromine into the atmosphere to temporarily thin the stratospheric ozone layer (Krueger et al., 2012).

This thesis investigates volcanic emissions by satellite measurements that have been conducted during the years 2007–2011. As modern satellite instruments provide a global view on the Earth’s atmosphere, especially plumes that were caused by major volcanic eruptions can be detected with their full extend. Data from the second generation of the Global Ozone Monitoring Experiment (GOME-2) has been evaluated for SO<sub>2</sub> and BrO of volcanic origin applying the Differential Optical Absorption Spectroscopy (DOAS) technique (Platt and Stutz, 2008).

In a first step, a new SO<sub>2</sub> evaluation scheme has been developed that is capable to retrieve accurate slant column densities (SCDs) of SO<sub>2</sub> in case of high SO<sub>2</sub> concentrations, as usually found during major volcanic eruptions. Subsequently, the results have been used in the scope of a newly developed algorithm that allows to automatically detect volcanic plumes in the satellite dataset by conspicuously high SO<sub>2</sub> column densities. The large number of almost 800 SO<sub>2</sub> plumes that had been extracted from the GOME-2 data was in the following systematically analyzed for a simultaneous enhancement of BrO and checked for a possible spatial correlation between both species. Additionally, mean BrO/SO<sub>2</sub> ratios for all volcanic plumes have been calculated. Furthermore, averaged satellite measurements have been used to check into the potential of GOME-2 to detect the BrO abundance of a quiescent degassing volcano from space.

The thesis is presented in four main parts. While the first part focuses on the scientific background of volcanic emissions, their influence on the Earth’s atmosphere and how they can be detected from ground-based and spaceborne measurements (Chapters 2 and 3), the second part describes the DOAS technique (Chapter 4), the instruments used in this thesis (Chapter 5) and the satellite retrieval for SO<sub>2</sub> and BrO (Chapter 6). The third part presents applications and results from the SO<sub>2</sub> and BrO DOAS retrieval of GOME-2 data regarding volcanic emissions (Chapter 7–10), before conclusions and an outlook are formulated in the final part (Chapters 11 and 12).



## 2. Volcanic emissions and their influence on atmospheric chemistry

In this chapter, the main gaseous species that are emitted by volcanoes during active phases of quiescent degassing and eruptions will be introduced and their influence on the atmosphere are discussed. While this thesis focuses on the satellite retrieval on  $\text{SO}_2$  and BrO in volcanic plumes, the main chemical processes of both species will be described in more detail.

First, the typical gas composition of volcanoes will be discussed in Section 2.1, before the main volcanic sulfur species, including  $\text{SO}_2$ , are introduced in Section 2.2. As  $\text{SO}_2$  can have a significant influence on the Earth's climate when it is injected into the stratosphere during major volcanic eruptions, its specific role in this context will be discussed in more detail. Finally, volcanic halogen species are introduced and especially the formation process of BrO will be highlighted in Section 2.3.<sup>1</sup>

### 2.1. General volcanic gas composition

The composition of volcanic gas emissions depends on the type of magma that is found at a certain volcano. The magma is a complex mixture of molten rocks, crystals and bubbles that might form due to changes in the surrounding pressure and the solubility of present gaseous species. The different types of magma are usually defined by various factors, such as their fractions of silicon dioxide ( $\text{SiO}_2$ ), iron (Fe), magnesium (Mg), potassium (K) and calcium (Ca) as well as their temperature. As the solubility of volatile species dissolved in the magma predominantly depends on pressure respectively temperature of the melt, the composition of gaseous volcanic emissions may vary with changes in the distance of the magma to the surface and therefore with the volcano's state of activity (Schmincke, 2005).

Typically, the main emitted compounds are water vapor ( $\text{H}_2\text{O}$ ), carbon dioxide ( $\text{CO}_2$ ), sulfur dioxide ( $\text{SO}_2$ ), hydrogen sulfide ( $\text{H}_2\text{S}$ ), carbonyl sulfide (COS) and its precursor carbon disulfide ( $\text{CS}_2$ ) and different halogen species, such as hydrogen chloride (HCl), hydrogen fluoride (HF) and hydrogen bromide (HBr). Table 2.1 summarizes the characteristic composition of gaseous emissions at a volcano and their estimated total global budget according to Textor et al. (2004). Although  $\text{H}_2\text{O}$  and  $\text{CO}_2$  are the two most abundant species in a volcanic plume, their contribution to the atmosphere is negligible in comparison to other emission sources. Most of all water vapor in the atmosphere originates from the evaporation of the oceans and lakes. The global estimation of volcanic  $\text{CO}_2$  emissions (75 Tg/yr) is only about 2‰ of

---

<sup>1</sup>Parts of this chapter have been published in Hörmann et al. (2012).

**Table 2.1.:** *Characteristic composition of gaseous emissions at a volcano and their estimated total global budget according to Textor et al. (2004)*

species	H <sub>2</sub> O	CO <sub>2</sub>	SO <sub>2</sub>	H <sub>2</sub> S	COS	CS <sub>2</sub>	HCl	HBr	HF
%/vol	50 – 90	1–40	1–25	1–10	10 <sup>-4</sup> – 10 <sup>-2</sup>	10 <sup>-4</sup> – 10 <sup>-2</sup>	1–10	?	<10 <sup>-3</sup>
Tg/yr	?	75	1.5 – 50	1 – 2.8	0.006 – 0.1	0.007 – 0.096	0.4 – 11	0.0078 – 0.1	0.06 – 6

the anthropogenic CO<sub>2</sub> emissions of 35 Gt in 2010 (e.g. Friedlingstein et al., 2010; Gerlach, 2012). The sulfur species SO<sub>2</sub>, H<sub>2</sub>S, COS and CS<sub>2</sub> contribute with up to 35% to the total volume of gaseous volcanic species. SO<sub>2</sub> is only the third most abundant gaseous species from a volcano. It is normally easy to detect in the UV due to its strong differential absorption features and low background levels from other sources. Therefore, it also represents the most regular monitored gaseous volcanic compound. Due to its relatively long life time of ~1–3 days in the troposphere and up to several weeks in the stratosphere (Lee et al., 2011), it is often used as a relatively chemical inert tracer for the spatial extent of a volcanic plume (cf. Chapters 8 and 9). Thus, it can additionally be used as a reference for monitoring the abundance and evolution of other highly reactive volatile compounds in volcanic plumes.

Ratios of CO<sub>2</sub> and halogen species (e.g. HCl) to sulfur, respectively SO<sub>2</sub>, are typically used to monitor the volcano’s activity. Furthermore, the potential of BrO/SO<sub>2</sub> ratios as an additional indicator for magmatic movement inside volcanoes have been recently discussed by Bobrowski and Giuffrida (2012).

In the following, the abundance of sulfur and halogen species of volcanic origin and their influence to the atmosphere will be further described. As the focus of this thesis lies on satellite measurements of volcanic SO<sub>2</sub> and BrO, a more detailed compendium about the implications of both species to atmospheric chemistry (and in case of SO<sub>2</sub>, climate) will be given. For an extended review on other volcanic species, the reader is referred to Oppenheimer et al. (2003), Textor et al. (2004) and Pyle and Mather (2009).

## 2.2. Volcanic sulfur compounds

Sulfur species in the atmosphere originate from both, natural and anthropogenic emissions. While the anthropogenic sulfur emissions are responsible for the larger part of sulfur in the atmosphere (~ 70 Tg S yr<sup>-1</sup>), volcanic emissions are estimated to contribute with ~ 7.5–10.5 Tg S yr<sup>-1</sup> to the global sulfur budget of ~ 100 Tg yr<sup>-1</sup> (Halmer et al., 2002). The latter includes also non-volcanic natural sources like biomass burning and Dimethylsulfide (DMS) emissions from the oceans. However, the reported estimations of global volcanic sulfur emissions during the last three decades

range from 5 Tg S yr<sup>-1</sup> (Le Guern, 1982) to 25 Tg S yr<sup>-1</sup> (Lambert et al., 1988), depending on the database and extrapolation techniques that have been used by the authors.

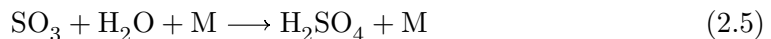
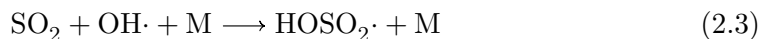
As volcanoes are typically located in inaccessible and therefore sparse populated areas, only a small number of active volcanoes are investigated for their contribution to the global volcanic emission budget. Only in recent years, the continuously SO<sub>2</sub> flux measurements at about 24 volcanoes worldwide have been made possible by establishing a global measurement network of remote sensing instruments (the Network for Observation of Volcanic and Atmospheric Change - NOVAC), that are able to investigate volcanic emissions from a safe distance and at low maintenance (Galle et al., 2010, 2011). As the injection height of volcanic emissions can widely range from the planetary boundary layer (PBL) in case of quiescent degassing volcanoes (e.g. Masaya, Nicaragua) up to the lower and upper stratosphere for major volcanic eruptions (e.g. Mt. Pinatubo in 1991 with an estimated maximum plume height of 39 km; Holasek et al., 1996), the influence to the regional or global atmosphere and climate may also vary significantly from case to case.

### 2.2.1. SO<sub>2</sub> from volcanic emissions

The most dominant directly emitted sulfur species by volcanoes is often SO<sub>2</sub>, with an estimated total amount of 1.5–50 Tg yr<sup>-1</sup> (see also Tab. 2.1). SO<sub>2</sub> is a toxic, colorless gas that can strongly effect flora and fauna due to its dry or wet deposition. It can also be converted into sulfuric acid (H<sub>2</sub>SO<sub>4</sub>), either by hydrolysis in water droplets:



or by oxidation with the OH radical and the subsequent formation of H<sub>2</sub>SO<sub>4</sub>:



The wet deposition of H<sub>2</sub>SO<sub>4</sub> via precipitation is also known as so-called "acid rain", which was widely discussed in the 1980s in Germany as one of the reasons for possible forest dieback (Schäfer and Metzger, 2009). However, the influence of acid deposition on the ecosystems in close proximity to active volcanoes is rarely documented (for more details see e.g. Delmelle et al., 2001; Delmelle, 2003; Pyle and Mather, 2005; Martin et al., 2009; Calabrese et al., 2011; D'Alessandro et al., 2011, and references therein).

If SO<sub>2</sub> (respectively H<sub>2</sub>SO<sub>4</sub>) is not removed from the atmosphere by wet/dry depo-

## 2. Volcanic emissions and their influence on atmospheric chemistry

**Table 2.2.:** *Global annual mean sulfur budget in  $Tg S yr^{-1}$  and top-of-atmosphere (TOA) radiative forcing in [%] of total. The efficiency is the relative burden divided by the relative source strength. Adopted from Graf et al. (1997).*

Source	Sulfur emissions [%]	SO <sub>2</sub> burden [%]	SO <sub>4</sub> <sup>2-</sup> burden [%]	Efficiency	Direct TOA forcing [%]
Anthropogenic	65.6	46.1	37.1	0.56	40
Biomass burning	2.5	1.2	1.6	0.64	2
DMS	18.2	17.8	25.3	1.39	26
Volcanoes	13.7	34.9	36.0	2.63	33

sition, it can be taken up by cloud droplets or other aerosol particles and form sulfate aerosols. In comparison to anthropogenic SO<sub>2</sub> emissions, volcanic SO<sub>2</sub> is usually emitted into the middle/upper troposphere during degassing phases and minor eruptions or even into the stratosphere during major eruptions, so that the removal processes are less effective and the atmospheric residence time increases. In Tab. 2.2, the global annual sulfur budget of the most important sulfur sources is given according to Graf et al. (1997). While the highest sulfur emissions come from anthropogenic sources (65.6%), the SO<sub>2</sub> burden is quite comparable to the one from volcanic emissions and the total sulfate burden is of similar size (36%). Because of their higher elevation and therewith associated increased lifetime, volcanic SO<sub>2</sub> emissions have a much higher relative impact on Earth's climate (Robock, 2000; Textor et al., 2004).

If SO<sub>2</sub> is injected into the stratosphere due to very strong explosive volcanic eruptions, H<sub>2</sub>SO<sub>4</sub> aerosols form within a few weeks and are distributed around the whole globe due to the very strong stratospheric winds, where they can remain for years. The sulfate aerosols have direct and indirect effects that influence the solar radiation in the atmosphere. Figure 2.1 shows a scheme of volcanic inputs and their influence on the atmosphere according to Robock (2000). Since sulfate aerosols reflect visible sunlight very effectively due to their single scattering albedo close to unity and typical effective diameters of  $\sim 500\text{nm}$ , the Earth's albedo is increased. More sunlight is reflected back into space and less direct radiation reaches the ground, which leads to a direct net cooling effect on the Earth surface temperature. However, some parts of the sunlight are also scattered forward and compensate the reduced light flux to a certain extent, increasing the fraction of diffuse radiation on Earth's surface (Robock, 2000).

Additionally to the direct cooling effect, sulfate aerosols may also cause indirect effects, which are mainly due to their influence on cloud formation and properties. As a first indirect effect, the aerosols serve as cloud condensation nuclei (CCN), which lead to an increased formation of clouds that consist out of more and smaller water droplets (Twomey, 1977). These clouds are therefore capable to reflect much more sunlight back into space or at least into the stratosphere, which in turn supports the

direct cooling effect. As a second indirect effect, such clouds have typically an enhanced lifetime, as the smaller cloud droplets need more time to increase to the size of rain drops and finally rain out (Andreae et al., 1991).

While sulfate aerosols lead to a net cooling effect in the troposphere respectively at the Earth's surface, they also enhance the absorption of IR radiation that is emitted by the Sun and also due to terrestrial radiation (Pollack et al., 1976). This leads to stratospheric warming and additionally to a net warming of the aerosol cloud. Especially for major volcanic eruptions in the tropics during winter time in the northern hemisphere, this results in a strong temperature gradient between the Arctic and the equatorial regions, which in turn can lead to a stronger polar vortex. Thereby, the Arctic Oscillation is forced into a positive phase, which means that warm winds from the Northern Atlantic Ocean are transported into the mid-latitudes. Such "winter warming" is stronger than the net cooling effect of sulfate aerosols, which is usually more dominant during summertime and/or at lower latitudes Kodera (e.g. 1994); Perlwitz and Graf (e.g. 1995); Thompson and Wallace (e.g. 1998).

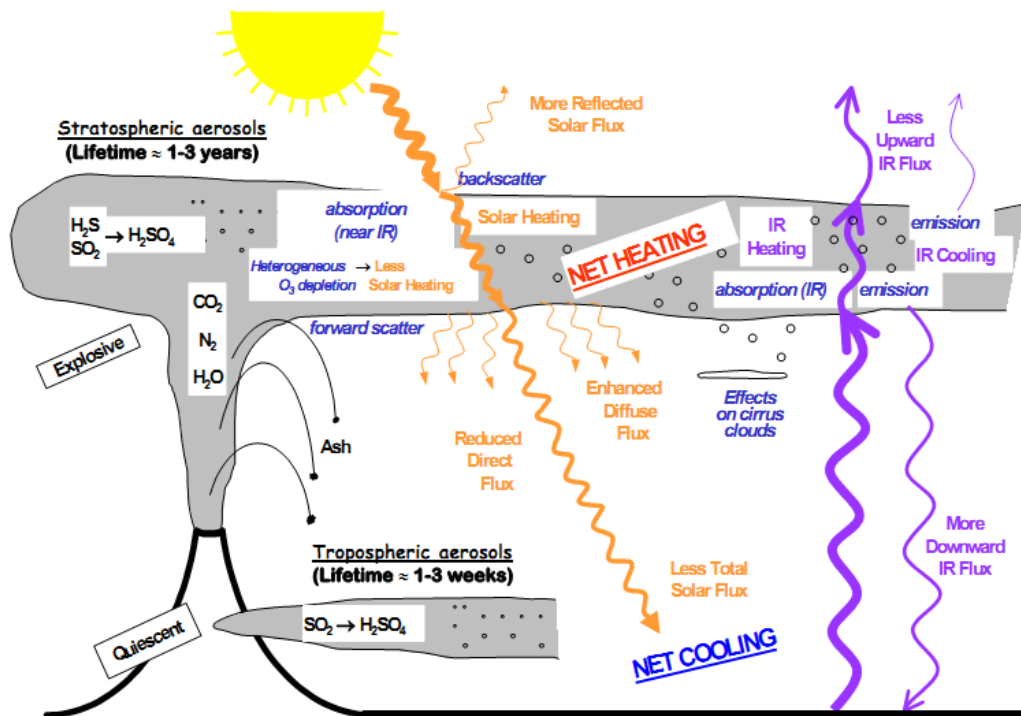


**Figure 2.1.:** Schematic diagram of volcanic inputs to the atmosphere and their effects. Adapted from Robock (2000), which is an extended version of Figures 1 and 2 of Simarski (1992), drawn by L. Walter and R. Turco.

### 2.2.2. Other volcanic sulfur species

The second largest fraction of gaseous sulfur species is released via  $\text{H}_2\text{S}$ . However, the absolute and relative quantities remain uncertain as measurements of the  $\text{SO}_2/\text{H}_2\text{S}$  ratio at different volcanoes have revealed very large variations of 1-125 (Gerlach, 2004). Additionally, the remote detection of volcanic  $\text{H}_2\text{S}$  is very difficult, so that the total number of observations is sparse. Aiuppa et al. (2007) found no decrease of the  $\text{SO}_2/\text{H}_2\text{S}$  ratio for the first 10 km of the volcanic plume of Mt. Etna from measurements with diffusive tubes, indicating that both species may have a comparable lifetime, at least during the first hours after their release from the crater.

Usually,  $\text{H}_2\text{S}$  is oxidized by the OH radical, which after several subsequent reactions leads to the formation of  $\text{SO}_2$ . Model simulations, however, revealed that this behavior could only be reproduced if halogen chemistry in the volcanic plume was not included, while the Etna emissions are known to be rather halogen rich compared to other volcanoes worldwide (e.g. Aiuppa et al., 2005; Bobrowski and Platt, 2007). If halogens were included, the  $\text{SO}_2/\text{H}_2\text{S}$  ratios increased significantly already after a few seconds after the plume's release, which could be explained by the rapid oxidation of  $\text{H}_2\text{S}$  with Cl molecules.

$\text{CS}_2$  and COS contribute to much lower parts to the total sulfur species emissions. While  $\text{CS}_2$  is mainly oxidized by OH radicals within a few days to COS or  $\text{SO}_2$ , COS is chemically very unreactive and can therefore reach the stratosphere, where it is oxidized into sulfuric acid which in turn has an important impact on Earth's climate (cf. Section 2.2.1).

### 2.3. Halogen compounds in volcanic plumes

As it has been already shown in Tab. 2.1, also halogen species like HCl, HBr and HF are typically emitted by volcanoes. Additionally, iodine compounds (e.g. HI) are released from volcanoes, but at much lower quantities than the other halogen species.

Although HCl is the most abundant halogen species in volcanic plumes with up to 1-10 %/vol (Symonds et al., 1988) and therefore comparable to anthropogenic emissions, the main part of the global chlorine emissions comes from the oceanic release of sea-salt (e.g. Keene et al., 1999). HCl is rapidly washed out of the atmosphere due to its high solubility and thus thought to have no significant influence on atmospheric chemistry when it is released in regular quantities by a volcano. Nevertheless, chlorine oxides in form of ClO and OClO have been measured in the volcanic plumes of the Sakurajima volcano in Japan (Lee et al., 2005) and Mt. Etna (Bobrowski et al., 2007). However, the very high ClO columns at Mt. Etna ( $\text{SO}_2/\text{ClO} \sim 20$ ) could not be reproduced by model studies in Bobrowski et al. (2007), which indicated that either the initial conditions and/or the chemical reactions that were included into the used model were not appropriate. Later measurements at both, Mt. Etna and the Masaya volcano (Nicaragua), were below the ClO and OClO detection limit and could therefore not reproduce the findings (Kern, 2009).

During the recent eruption of the Eyjafjallajökull volcano in 2010 (Iceland), Baker et al. (2011a) were able to estimate the chlorine radical concentration in a volcanic

plume for the first time at  $1.3\text{--}6.6\times 10^4$  Cl cm<sup>-3</sup>, since they found non-methane hydrocarbons (NMHCs) to be depleted in the plume during special research flights of the CARIBIC observatory aircraft, which indicates chemical reactions that are dominated by chlorine. Finally, (Zelenski and Taran, 2012) reported the first direct measurements of atom and molecular volcanic chlorine (Cl<sub>2</sub>, Cl) at the New Tolbachik scoria cones in Central Kamchatka. The highest measured concentration of Cl<sub>2</sub> of 60 ppmv was found in a small fumarole vent, representing also the highest concentrations of Cl<sub>2</sub> ever measured in a natural marine boundary layer environment overall.

Compared to HCl, HF as the second most abundant gaseous halogen species in a volcanic plume is quite unreactive and therefore eventually taken up by cloud droplets or deposited in the close surrounding of a volcano. As the total fraction in volcanic emissions is less than 1ppm (see also Tab. 2.1), its annual global volcanic flux was estimated at 0.06–6 Tg by Symonds et al. (1988).

Finally, the release of HBr was also thought to have no significant indications for atmospheric chemistry until considerable high slant column densities of bromine monoxide (BrO) were detected in ground-based measurements at the Soufrière Hills volcano in 2003 (Bobrowski et al., 2003). As a main part of this thesis is on the satellite detection of volcanic BrO, a brief summary of previous volcanic BrO observations will be given in the following as well as about the initial formation process in a volcanic plume.

### 2.3.1. Bromine monoxide in volcanic plumes

BrO is an important catalyst in the depletion of ozone (O<sub>3</sub>) in the stratosphere and troposphere, especially during springtime in polar regions (see Barrie et al., 1988; Simpson et al., 2007, and references therein). In addition to sources like the surfaces of salt lakes, polar sea ice or sea-salt aerosol in the mid-latitude marine boundary layer (von Glasow and Crutzen, 2003), volcanic emissions turned out to be a further natural source of bromine compounds and the subsequent formation of BrO (Bobrowski et al., 2003). The injection of BrO that has formed in volcanic plumes is, therefore, very likely to have a significant impact on atmospheric chemistry (von Glasow, 2010).

BrO in a volcanic plume was detected for the first time by Bobrowski et al. (2003), using ground-based Multi-Axis Differential Optical Absorption Spectroscopy (MAX-DOAS) measurements at the Soufrière Hills volcano on Montserrat. The BrO slant column densities (SCDs) were found to be closely correlated to the measured SO<sub>2</sub> SCDs, resulting in an average BrO/SO<sub>2</sub> molar ratio of  $\sim 8.2\times 10^{-4}$  (equal to a Br/S mass ratio of  $\sim 2\times 10^{-3}$ ). Based on this ratio, the authors estimated a global emission of 30,000 t Br yr<sup>-1</sup> using the estimation of the global volcanic SO<sub>2</sub>-source-strength of about  $14\pm 6$  Tg SO<sub>2</sub> yr<sup>-1</sup> by Graf et al. (1997).

Since then, similar ground-based observations were made at several volcanoes worldwide (e.g. Galle et al., 2005; Oppenheimer et al., 2006; Bobrowski and Platt, 2007; Boichu et al., 2011; Vogel, 2012, and references therein). All these measurements revealed an almost linear correlation between the two species and BrO/SO<sub>2</sub> molar ratios ranging from  $1\times 10^{-5}$  to  $8.2\times 10^{-4}$ , as it can be seen in Figure 2.2. In addition to the ground-based measurements, BrO has also been detected by airborne

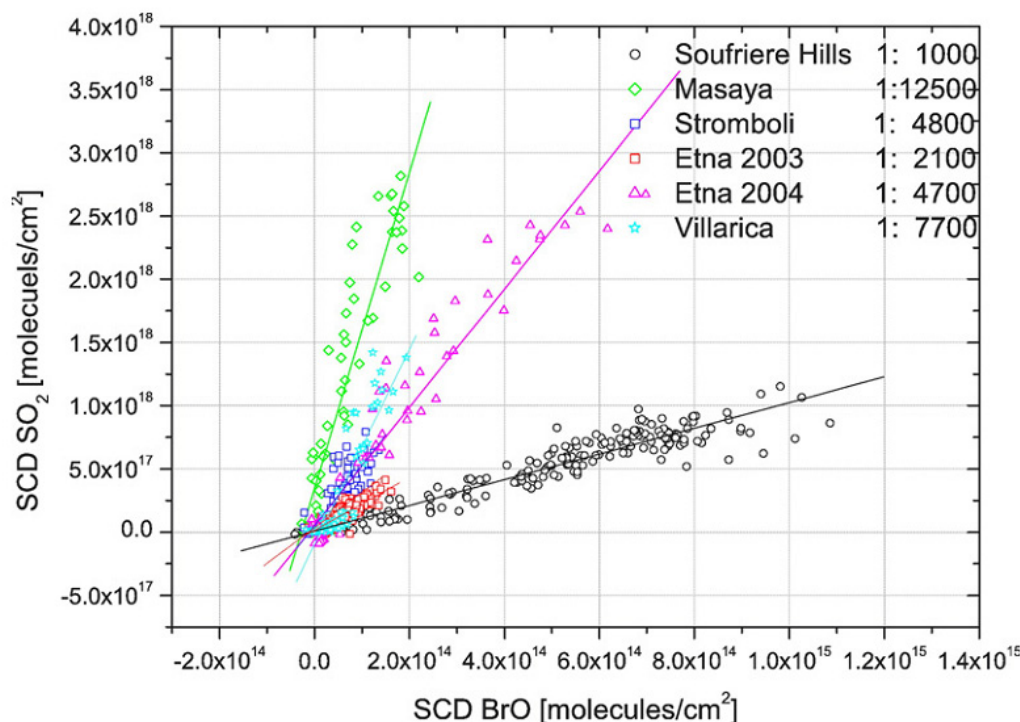


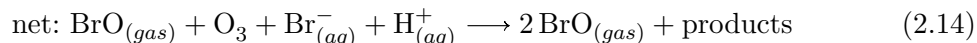
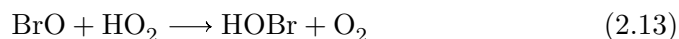
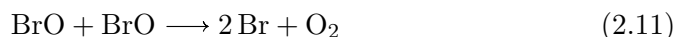
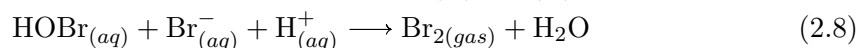
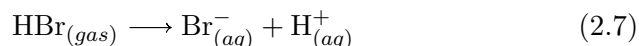
**Figure 2.2.:** *BrO and SO<sub>2</sub> correlation plot for ground-based MAX-DOAS measurements at five different volcanoes around the world (Soufrière Hills - Montserrat, Masaya - Nicaragua, Stromboli - Italy, Mt. Etna in 2003 and 2004 - Italy and Villarica - Chile). While a linear correlation can be seen for all measurements, the BrO/SO<sub>2</sub> ratios range from  $\sim 8 \times 10^{-5}$  to  $10^{-3}$ . Adapted from Bobrowski and Platt (2007).*

observations of volcanic plumes during the recent years (e.g. Bani et al., 2009; Heue et al., 2011; Kelly et al., 2012, cf. Section 9.6) , but also recently for the first time in satellite measurements from space (Theys et al., 2009).

### 2.3.2. Formation of volcanic BrO

First considerations about the origin of BrO in volcanic plumes in Bobrowski et al. (2003) and Gerlach (2004) suggested that BrO is probably not directly emitted by volcanoes, but formed as a secondary product from near-vent, high-temperature oxidation of magmatic gases and heterogeneous chemistry involving sulphate aerosols inside the plume. Motivated by that suggestion, Oppenheimer et al. (2006) and Bobrowski et al. (2007) investigated the daytime plume of Mt. Etna (Sicily) at different distances, directly at the summit crater, but also further away at a plume age of a few minutes. As BrO was only observed in the downwind plume (not in the crater measurements), these findings widely agreed with the former predictions. The rapid production of BrO inside the downwind plume could thus be explained by directly

emitted HBr, which is oxidized in an autocatalytic reaction cycle involving sulfate aerosols and solar radiation as well as the destruction of O<sub>3</sub>. The key steps in the BrO formation can be described as following (von Glasow et al., 2009):



Bromine in the gas phase (HBr and HOBr) is taken up by aerosol particles (Eq. 2.6 and 2.7). In the aqueous phase it is transformed in a acid catalysed reaction to H<sub>2</sub>O and Br<sub>2</sub> back into the gas phase (Eq. 2.8). The Br<sub>2</sub> is then rapidly photolysed into Br radicals (Eq. 2.9). In the following, the Br radicals lead to the formation of BrO under the destruction of an ozone molecule (Eq. 2.10). While ozone can be in principle regenerated by the reaction of O<sub>2</sub> and oxygen atoms that are released via the photolysis of BrO, the BrO is more effectively transformed via its self-reaction into O<sub>2</sub> and Br<sub>2</sub> (Eq. 2.11) or O<sub>2</sub> and Br (Eq. 2.12) leading back to Eq. 2.9. Additionally, the BrO is reconverted into HOBr by the reaction with HO<sub>2</sub> (Eq. 2.13).

An overview of all involved processes is also given in Figure 2.3. The effective reaction cycle can then be described as in Eq. 2.14: One BrO molecule is effectively converted into two BrO molecules by Br<sup>-</sup> that is oxidized at aerosol surfaces. Therefore, this results in an exponential growth of BrO in the gas phase. Please note that the auto-catalytic reaction is only possible as long as O<sub>3</sub> and sunlight is available to the volcanic plume. The mechanism is similar to the so-called "bromine explosion", a reaction cycle that is closely related to the formation of BrO from sea-salt bromine during polar spring and linked to tropospheric ozone depletion events (McConnell et al., 1992; Fan and Jacob, 1992; Platt and Lehrer, 1996; Wennberg, 1999; von Glasow and Crutzen, 2003; Simpson et al., 2007).

Other studies by Bobrowski et al. (2007) and Louban et al. (2009) showed both enhanced BrO slant column densities (SCDs) and BrO/SO<sub>2</sub> ratios toward the edges of the volcanic plume of Mt. Etna, in good agreement to model studies (Bobrowski et al., 2007; von Glasow, 2010), where the increase is caused by the entrainment of O<sub>3</sub>-rich ambient air into the plume devoid of O<sub>3</sub>. Additionally, a case study of day- and nighttime measurements at Masaya volcano by Kern et al. (2008), using Long Path Differential Optical Absorption Spectroscopy (LP-DOAS), showed no evidence

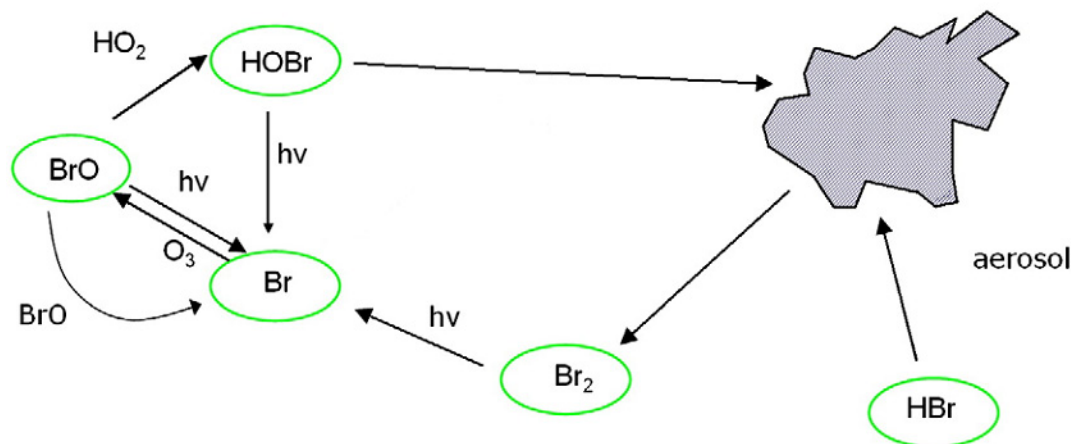


**Figure 2.3.:** *The auto-catalytic formation of BrO in the so-called "Bromine explosion". Adapted and modified from von Glasow et al. (2009).*

for BrO during nighttime, while a BrO/SO<sub>2</sub> ratio of up to  $6.4 \times 10^{-5}$  was observed during daytime. This confirmed the suggestion that the reaction cycle is photolytically driven.

For Mt. Etna, simultaneous measurements at several distances from the volcano by Vogel (2012) described the evolution of BrO and the BrO/SO<sub>2</sub> ratios were found in the range of  $0.4\text{--}1.2 \times 10^{-4}$ . From the comparison to chemical model calculations, it was shown that current model assumptions about the BrO formation processes are not capable to reproduce the actual measurements adequately.

## 3. Optical remote sensing of volcanic emissions: State of the art

Next to classical volcano observation techniques like seismicity, ground-deformation or geophysical measurements, optical remote sensing techniques are nowadays an important tool in order to persistently monitor the development of volcanic activity worldwide. As most measurements can be done at larger distances from a volcano, they provide a continuous recording of the volcanic emissions, even during eruptive phases. Especially remote ground-based techniques have been developed in recent decades and are partly organized in local and global networks of individual instruments, while the resulting data can be received from a safe distance by the national agencies (Galle et al., 2010).

Since first measurements with the still widely applied Correlation Spectrometer (COSPEC) in the 1970s (Stoiber and Jepsen, 1973), several kind of mobile application platforms using different techniques have been established, i.e. observations by traversing a volcanic plume by car, remote controlled model helicopters, boats, airplanes and satellites (e.g. Bluth et al., 1992; Bobrowski et al., 2003; Carn et al., 2005; Mori et al., 2007; McGonigle et al., 2008; Burton et al., 2009; Oppenheimer et al., 2010; Vogel et al., 2011).

In the following chapter, some of the most commonly used optical remote sensing techniques and instruments are shortly introduced for both, ground-based and satellite observations, in order to illustrate the state of the art in remote monitoring of volcanic emissions. For a more detailed introduction on ground-based applications, the reader is referred to McGonigle and Oppenheimer (2003). A comprehensive overview of different kinds of satellite monitoring instruments suited for the observation of active volcanoes is given in the review by Thomas and Watson (2009).

### 3.1. Ground-based measurements

#### 3.1.1. COSPEC

The most commonly used instrument for the ground-based observation of SO<sub>2</sub> from volcanoes is unchallengedly the COSPEC (McGonigle and Oppenheimer, 2003). The instrument is regularly used by volcanologists worldwide since it became first available in the 1970s. It can be either used at fixed positions at safe distances from a monitored volcano as well as while traversing a volcanic plume by feet, vehicles or airplanes.

In Figure 3.1, the configuration of the COSPEC instrument is shown. The COSPEC measures incident scattered sunlight typically between 300–315 nm, where relative strong SO<sub>2</sub> absorptions occur. The radiation is focused on plane mirrors by a telescope

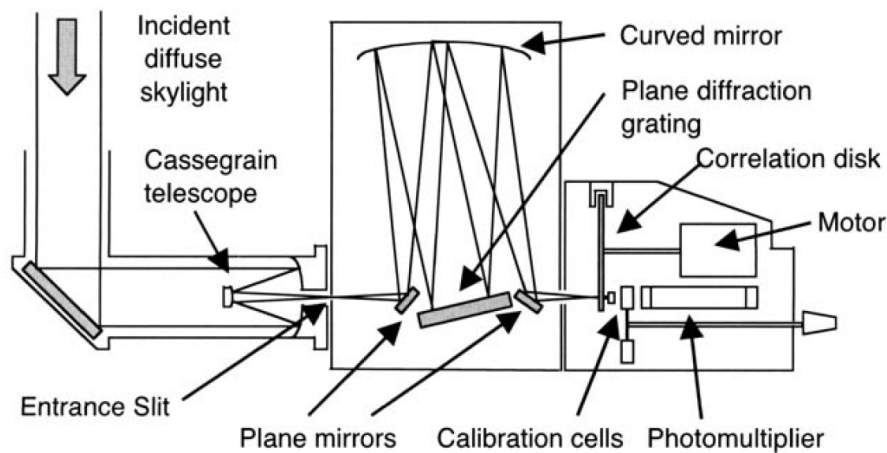


**Figure 3.1.:** Schematic view of a COSPEC instrument including the optical lighpath for one distinct wavelength. The incident scattered light is dispersed by a grating on to a spinning correlation disc, containing four slit etched masks. Since the slits are located at disc radii that correspond to wavelength of major and minor  $\text{SO}_2$  absorptions, the photomultiplier output is modulated according to the measured amount of  $\text{SO}_2$ . Adapted from McGonigle and Oppenheimer (2003).

and subsequently parallelized by a curved mirror. After the light has been dispersed by a diffraction grating, it is guided onto a motor-driven spinning correlation disc that contains four different masks, each of them corresponding to a quarter disc segment. The disc is etched with slits that are located at disc radii corresponding to individual wavelength of major and minor  $\text{SO}_2$  absorptions, so that distinct peaks and troughs of the  $\text{SO}_2$  absorption cross section are measured at the same time. The light intensities at the measured wavelengths are afterwards amplified by a photomultiplier, so that the electronic output is modulated by the total amount of  $\text{SO}_2$  that is present in a volcanic plume. As a result, the photomultiplier's signal is converted into a  $\text{SO}_2$  mixing ratio by using calibration cells that contain a known  $\text{SO}_2$  concentration. As the instrument detects exclusively scattered sunlight, volcanic monitoring is restricted to daytime.

Mean  $\text{SO}_2$  fluxes can be directly calculated if a volcanic plume is traversed perpendicular and the wind speed is known. Unfortunately, the wind speed is usually only estimated by the speed at the ground, while it often differs significantly for the summit region. Other possibilities for wind speed determination are e.g. the direct visual observation of the plume, if it is condensed. Especially the uncertainty of the wind measurements can lead to total flux errors of up to 40% (Tazieff and Sabroux, 1983).

Furthermore, COSPEC measurements don't account for the effects of radiative transfer (cf. Section 4.6 and 6.3). Some fractions of the measured radiation might be for example scattered in between the COSPEC and the volcanic plume without ever having penetrated the plume and therefore "dilute" the absorption signal (Fig-

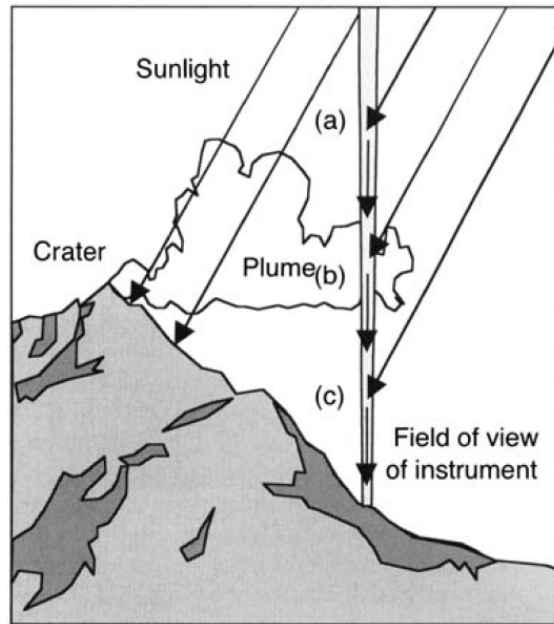


**Figure 3.2.:** Various lightpaths contribute to the measured scattered sunlight during a COSPEC measurement from **a)** above, **b)** within or **c)** below a volcanic plume. Thus, the total  $\text{SO}_2$  amount might be over- or underestimated. Adapted from McGonigle and Oppenheimer (2003).

ure 3.2). Other parts are scattered several times inside the plume and lead to an overestimation of the  $\text{SO}_2$  amount. Additionally, scattering inside a volcanic plume is influenced by aerosol respectively ash content in general (e.g. Millán, 1980; Kern et al., 2010).

However, the  $\text{SO}_2$  fluxes that have been provided by COSPEC measurements during the last four decades have significantly contributed to estimate the total volcanic  $\text{SO}_2$  amount that is released to the atmosphere, which is an important factor in climate model calculations and still not well known. Continuous  $\text{SO}_2$  flux measurements have been also successfully used as an indicator for upcoming eruptions of volcanoes, e.g. prior to the eruption of Mt. Pinatubo in 1991 (McCormick et al., 1995), where the measured  $\text{SO}_2$  fluxes increased significantly four weeks before the eruption (Hoff, 1992; Daag et al., 1996a). Nevertheless, an increased release of  $\text{SO}_2$  is not always a good indicator for a possible rising magma level (and therefore an imminent eruption), as scrubbing of magmatic gases due to ground- and surface water may prevent an increase of the  $\text{SO}_2$  fluxes until the pathway has dried out. In Symonds et al. (2001), the authors modeled the thermochemically reaction of magmatic gases with water and suggested that either  $\text{CO}_2$  or  $\text{H}_2\text{S}$  should be additionally used to monitor the volcanic activity if scrubbing occurs. In order to get a detailed understanding of the processes inside an active volcano from optical remote sensing of the emissions, it is preferable to measure not only  $\text{SO}_2$ , but also other gaseous species simultaneously.

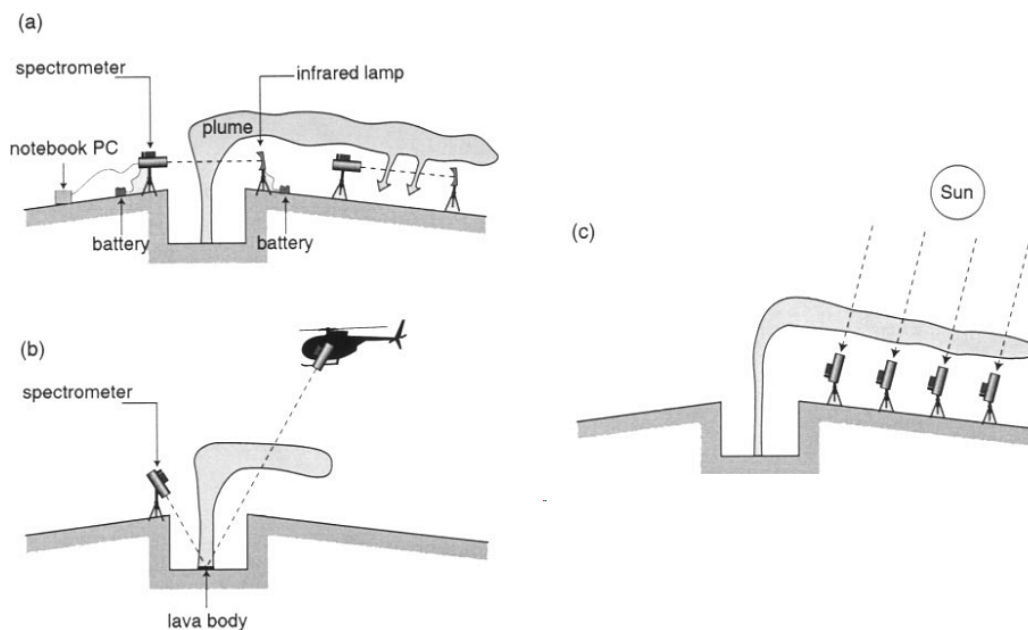


**Figure 3.3.:** *Different field configurations of volcanic FTIR measurements. a) active measurements at the crater rim or in the downwind plume, b) passive sensing using active lava bodies as IR source and c) passive solar occultation at various downwind positions. Adapted from Oppenheimer et al. (1998).*

#### 3.1.2. Fourier transform infrared spectroscopy (FTIR)

While COSPEC instruments are only able to monitor volcanic  $\text{SO}_2$  emissions, the Fourier transform infrared spectroscopy (FTIR) offers the possibility to measure also other volcanic gaseous species, such as  $\text{HCl}$ ,  $\text{HF}$ ,  $\text{CO}_2$ ,  $\text{H}_2\text{O}$ ,  $\text{SiF}_4$ ,  $\text{CO}$ , and  $\text{COS}$ , but still also  $\text{SO}_2$  (e.g. Francis et al., 1995; Mori and Notsu, 1997; Horrocks et al., 1999; Burton et al., 2000).

The technique is therefore suitable to determine  $\text{X}/\text{SO}_2$  ratios, which can provide a deeper understanding of the chemical processes inside a volcano (Oppenheimer et al., 1998).

The main component on which a FTIR instrument is based on is a Michelson interferometer, consisting of a beam-splitter, one static and one moving mirror. Light that is coupled into the optical path splits up into two individual beams that are reflected by both mirrors before they are recombined by the beam-splitter. By varying the position of the adjustable mirror, different optical pathlength are obtained for the light beams, leading to constructive or destructive interference after their recombination. The subsequent application of an inverse Fourier transformation reconverts the interferograms into absorption spectra and the concentrations of volcanic species may be determined by fitting high resolution absorption spectra of the regarded species, which are usually available from controlled measurements in laboratories.

Compared to spectroscopy techniques that use dispersive gratings, FTIR has mainly two advantages. The first one (called "Fellgett's advantage") is that all wavelengths are measured simultaneously, which leads to a significant increase of the signal-to-noise ratio. The second one ("Jacquinot advantage") results from the fact that the radiation throughput in an FTIR application is determined only by the diameter of the collimated beam, so that the complete light intensity from the source can be used in the measurements. For dispersion-based spectrometers, a narrow entrance slit is needed in order to reach a high spectral resolution, so that the initial intensity is significantly reduced.

Although FTIR measurements are in principle possible in the UV wavelength range, they are typically conducted in the infrared, since the moving mirror position has to be controlled very precisely for measurements at shorter wavelengths. The required positioning systems are additionally less suitable for observations in the field due to an increased size and weight (Cageao et al., 2001). For measurements in the IR, either natural or artificial light sources can be used as illustrated in Figure 3.3. For ideal conditions, even moonlight can be used as natural light source, when a volcanic plume is located in between the FTIR instrument and a full moon. Such measurements were i.e. conducted by Burton et al. (2001), who found increasing SO<sub>2</sub>/HCl ratios during nighttime measurements at the Masaya volcano (Nicaragua), which was supposed to be caused by the higher solubility of HCl compared to SO<sub>2</sub> in the volcanic plume that often condenses due to the cooler atmosphere at night.

### 3.1.3. Ground-based DOAS measurements

While COSPEC is exclusively capable to measure SO<sub>2</sub> and most FTIR applications are exclusively available for the observation of IR absorbing species, the Differential Optical Absorption Spectroscopy (DOAS - Platt and Stutz, 2008) has proven to be capable to detect several gaseous volcanic species in the UV wavelength range at volcanoes worldwide, including SO<sub>2</sub>, BrO, OClO and ClO (e.g. McGonigle et al., 2002; Bobrowski et al., 2003; Burton et al., 2009; Johansson et al., 2009; Galle et al., 2010; Boichu et al., 2011).

During recent years, the technique has been successfully applied for continuous monitoring of volcanic SO<sub>2</sub> emissions. Although the majority of such measurements is still conducted by using COSPEC, DOAS provides some important advantages to the volcanic monitoring community. As the main part of this thesis is on volcanic SO<sub>2</sub> and BrO from satellite measurements that had been retrieved by the application of DOAS, the technique will be later discussed in detail (cf. Chapter 4). At this point, only a short summary of the different DOAS applications in ground-based observations of volcanic emissions will be given.

DOAS uses the continuous wavelength information from the measured spectra of scattered sunlight instead of specific absorption peaks and troughs of the SO<sub>2</sub> cross-section and thus allows a comprehensive spectral analysis (Platt and Stutz, 2008). The application of this technique can therefore be used for the retrieval of different volcanic species that show absorption features in the regarded wavelength region at

### 3. Optical remote sensing of volcanic emissions: State of the art

---

the same time.

First DOAS measurements of volcanic emissions were conducted by Edner et al. (1994) and Weibring et al. (1998), who derived total SO<sub>2</sub> fluxes during three ship-borne field campaigns in 1992, 1994 and 1997 at Etna, Stromboli and Vulcano and compared their results to COSPEC and differential absorption lidar (DIAL) measurements. Since then, several applications have been continuously developed and more and more scientists are nowadays turn to DOAS from the still popular COSPEC technique. Especially during recent years, the development of commercially available compact instruments at low maintenance and price (e.g. the 'Mini-MAX-DOAS', produced by Fa. Hoffmann, Rauenberg, Germany) has led to a more regular use of DOAS instruments for volcanic monitoring.

Due to the ability of such instruments to be remotely operated and monitor volcanic emission fluxes continuously, they have been organized in global networks at several volcanoes worldwide. The hitherto largest DOAS network is the Network for Observation of Volcanic and Atmospheric Change (NOVAC), which was installed in the scope of a project of the European Union (EU) that began in 2005 and was funded until 2010 (Galle et al., 2010, 2011). The main aim of the project was to establish a network of automatically plume scanning ground-based DOAS instruments at different active volcanoes around the globe in order to monitor their total emissions and thus increase the knowledge of degassing volcanoes with a specific focus on implications on natural hazard risk assessment. By May 2011, a total of 64 instruments at 24 volcanoes worldwide had been installed, providing unprecedented amounts of data on the daily fluxes of volcanic degassing species (mainly SO<sub>2</sub>, but also others like e.g. BrO). Figure 3.4 shows the location of all volcanoes that were involved into the project as of April 2009. For most of these volcanoes, one or several NOVAC instruments had been installed during the project, other volcanoes had been investigated



**Figure 3.4.:** Location of all volcanoes that have been involved in the NOVAC project as of April 2009. Adapted from Galle et al. (2010).

in extended field campaigns (e.g. Kīlauea on Hawaii). The data (including all measured spectra and automatically evaluated near-real time data on wind speed, plume height and total fluxes) for all permanently installed instruments are stored in a central database, that is accessible via a webpage<sup>1</sup>.

Next to plume scanning instruments, also imaging DOAS applications (I-DOAS) have been developed that allow the examination of the trace gas distribution in volcanic plumes by using a 2-dimensional CCD detector. While one dimension of the CCD matrix is used to obtain the spectral information, the other one provides the spatial resolution. By the resulting differences in the spatial distribution for individual species, the chemistry inside the plume can be examined (Bobrowski et al., 2007; Louban et al., 2009).

Another DOAS application uses light from an artificial light source that is guided on a specific lightpath through a volcanic plume and is then reflected (typically by mirrors) back into the detector ('longpath-DOAS' or 'LP-DOAS'). Due to the topographical requirements, such measurements can only be conducted directly at the crater rim of volcanoes during quiescent degassing phases. However, a striking argument for LP-DOAS measurements is the ability to monitor a volcano during the nighttime in order to allow the investigation of the plume's chemistry in absence of sunlight. One example for such an application of LP-DOAS was reported by Kern et al. (2008), who detected significant amounts of volcanic BrO at the Masaya volcano during daytime measurements, while they were not able to detect any BrO over the instruments detection limit during the night. The measurements therefore proved the previously unverified supposition that the BrO formation in volcanic plumes is photolytically driven (Gerlach, 2004).

## 3.2. Satellite-borne measurements

The usage of satellite instruments in order to monitor volcanic emissions offers a unique perspective to the volcanic monitoring community. Especially during major volcanic eruptions, where measurements by ground-based instruments are associated with high risks for volcanologists, satellite observations are capable to detect the quantities of volcanic gaseous species or ash on a much wider spatial scale. The measurements therefore provide the potential to estimate also global emission budgets of volcanic emissions (such as SO<sub>2</sub>) that are still a widely unknown factor.

Generally, SO<sub>2</sub> is the most regular volcanic species that is observed from satellites, because of its quantity and significant absorption features in the UV and IR wavelength range (cf. Chapter 2). Furthermore, volcanic ash clouds can be identified and tracked after they have been injected into the atmosphere during major eruptions. This information is strongly needed by the aviation industry, as ash may endanger air traffic and can lead to massive financial implications like recently experienced during the eruption of Eyjafjallajökull (Iceland) in April/May 2010 (Prata and Prata, 2012).

In the following, a short overview of some currently operating satellite instruments

---

<sup>1</sup><http://novac.iup.uni-heidelberg.de/>

that can be used to monitor volcanic emissions will be given. The instruments can be basically divided into instruments sensitive to the UV or IR, although also the Microwave Limb Sounder (MLS) has been already used to detect SO<sub>2</sub> (Read et al., 1993) and HCl (Prata et al., 2007) during volcanic eruptions.

## UV-sensitive satellite instruments

At the present time, several UV-sensitive satellite instruments provide measurements that can be used to retrieve volcanic emissions. Most commonly, SO<sub>2</sub> is retrieved (e.g. Krotkov et al., 2006; Yang et al., 2007; Carn et al., 2008; Richter, 2009; Rix et al., 2012), but it has been recently demonstrated that also BrO from volcanic eruptions can be detected in this wavelength range (Theys et al., 2009; Heue et al., 2011; Hörmann et al., 2012). Other volcanic species that show absorption features in the UV (e.g. chlorine species) may generally also be detected by such instruments, but have been not successfully measured yet.

Volcanic ash respectively sulphate aerosols can be retrieved by the UV Aerosol Indices (UVAI), which are semi-quantitative indicators of aerosol absorption and scattering (e.g. Penning de Vries and Wagner, 2011; Kerminen et al., 2011). As light in the UV range is only available during the day, UV satellite measurements are restricted to daytime only.

### 3.2.1. SCIAMACHY

The Scanning Imaging Absorption Spectrometer for Atmospheric Cartography (SCIAMACHY) instrument on the Environmental Satellite (ENVISAT) was launched in 2002 (Gottwald and Bovensmann, 2010). However, after 10 years of continuous measurements, the contact to ENVISAT was lost permanently.

SCIAMACHY was capable to monitor the atmosphere basically in three different viewing geometry modes, so-called "nadir", "limb" and "occultation" geometry. The nadir and limb observation modes generally measure the sunlight that is scattered within the atmosphere. While the nadir geometry points approximately perpendicular to the Earth's surface (Figure 3.5 a), the limb geometry scans the upper troposphere respectively the stratosphere by pointing sideways at the edge of the atmosphere (Figure 3.5 b). For the occultation mode (Figure 3.5 c), the instrument points directly to the Sun or Moon in limb geometry, so that the atmosphere can be probed for a well-defined mean lightpath and very short integration times. However, the most regular used measurement geometry for satellite observations is nadir because of its sensitivity to the troposphere.

The instrument provided Earthshine spectra for a broad UV/Vis/NIR wavelength range from 240–2400 nm at a standard spatial resolution of 60×30 km<sup>2</sup>. Due to an alternating limb/nadir measurement routine (Figure 3.5 d), 3-dimensional information about the tracegases in the atmosphere could be obtained. However, the alternating modes led to a relative poor temporal resolution of the measurements. As global cover-

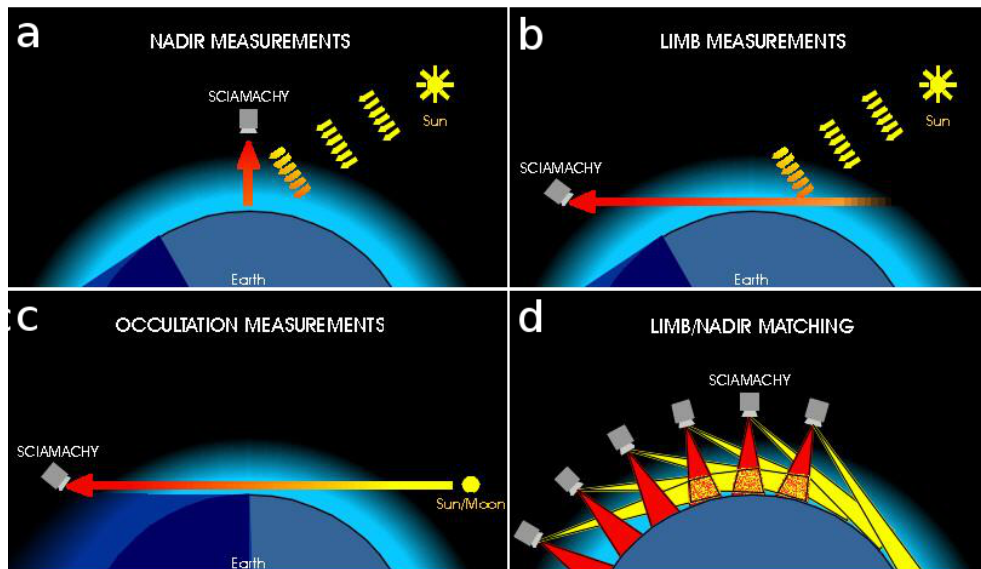


**Figure 3.5.:** SCIAMACHY viewing geometries and limb/nadir matching routine: (a) nadir, (b) limb and (c) occultation mode. By the alternating nadir/limb measurement routine (d), 3-dimensional information about the atmospheric composition can be obtained. Adapted from Gottwald and Bovensmann (2010).

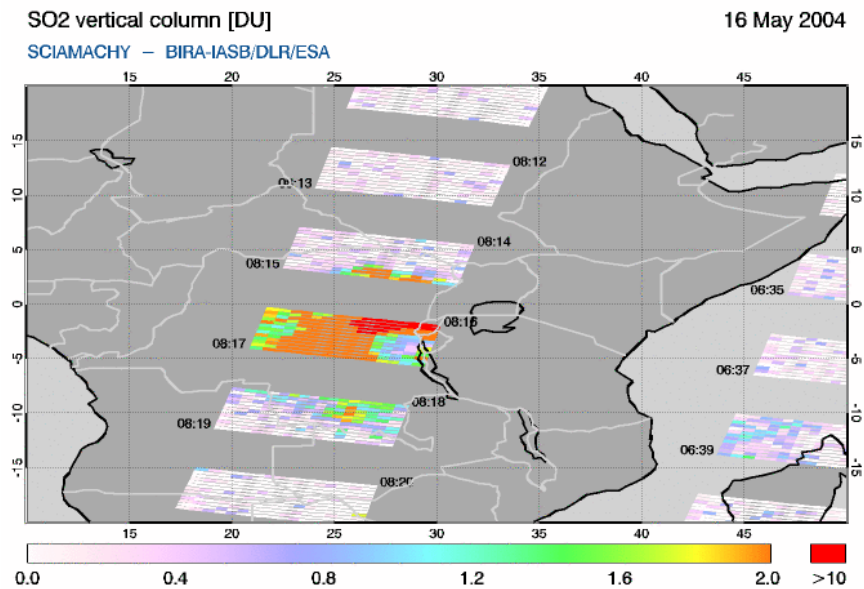


**Figure 3.6.:** SO<sub>2</sub> VCDs as seen by SCIAMACHY during the eruption of the Nyamuragira volcano on 16 May 2004. Besides the volcanic plume, the alternating limb/nadir measurement mode can be seen by the apparent data gaps. Adapted from SACS (2012).

### 3. Optical remote sensing of volcanic emissions: State of the art

---

age was only achieved from the nadir mode after 6 days at the equator, the instruments was not optimal suited for regular measurements of volcanic emissions. Nevertheless, SCIAMACHY data has been successfully used to detect volcanic SO<sub>2</sub> emissions by using the DOAS technique (e.g. Afe et al., 2004; Bramstedt et al., 2004; Richter et al., 2006; Khokhar, 2006; Lee et al., 2009).

Figure 3.6 shows an example for the SCIAMACHY SO<sub>2</sub> retrieval during an eruption of the Nyamuragira volcano (DR Congo) on 16 May 2004 SACS (2012). The SO<sub>2</sub> is clearly visible due to the strongly enhanced VCDs, but not entirely covered because of the alternating limb/nadir mode of the instrument.

#### 3.2.2. OMI

The Ozone Monitoring Instrument (OMI) was launched in 2004 on board of the NASA EOS Aura satellite into a near polar, sun-synchronous orbit with a period of approximately 100 minutes (Levelt et al., 2006). Aura is part of the so-called A-train, a satellite constellation of five currently active satellites (GCOM-W1, Aura, Cloudsat and Aqua). The constellation allows near-simultaneous observations of a wide variety of parameters for the atmospheric science community due to the multitude of different instruments.

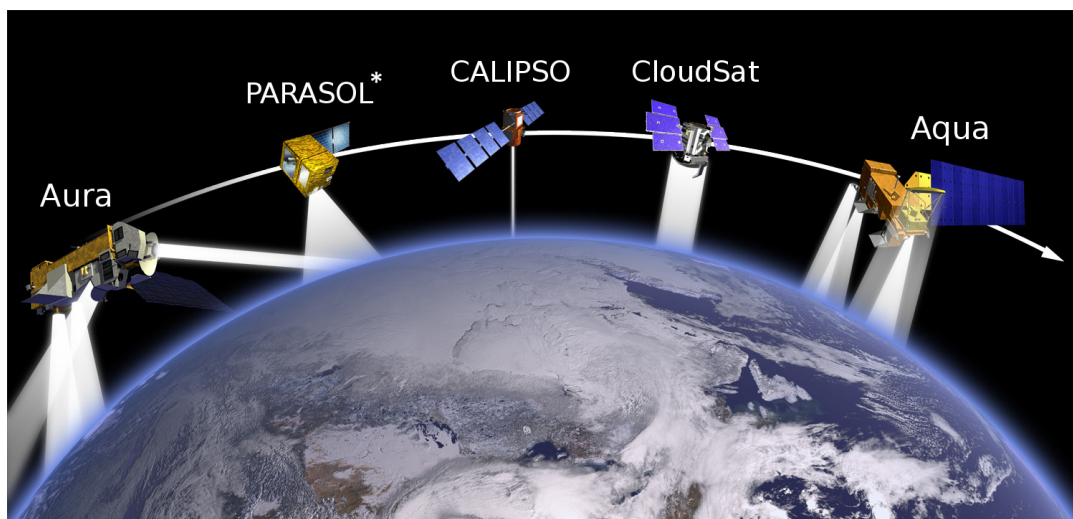


**Figure 3.7.:** *The NASA A-train consists currently of five satellite that follow closely one after another along the same orbital track. The different instruments on board of the individual satellites allow near-simultaneous observations of a wide variety of parameters for the atmospheric science community. Note that the PARASOL satellite has been moved to another orbit in 2009 and that a new spacecraft (GCOM-W1) has been become a new part of the A-train in 2012.<sup>2</sup>*

<sup>2</sup>[http://spacefellowship.com/wp-content/uploads/2009/08/380623main\\_atrain20090820-full.jpg](http://spacefellowship.com/wp-content/uploads/2009/08/380623main_atrain20090820-full.jpg)

OMI monitors the Earth's atmosphere in the UV/Vis wavelength range from 270–500 nm in nadir mode. With a typical ground pixel size of  $13 \times 25 \text{ km}^2$ , it provides a very high spatial resolution compared to other satellite instruments that are able to detect atmospheric components in the UV at the moment. In contrast to some other instruments, OMI is a non-scanning instrument with a very large field-of-view that yields a swath width of 2600 km perpendicular to flight direction. Scattered sunlight is detected via a 2-dimensional push-broom CCD detector, so that the ground pixels increase at the swath edges to  $13 \times 150 \text{ km}^2$ . Global coverage was achieved within 24 h, until a technical problem with one of the CCD rows occurred in 2007 that has further expanded in the meantime. Current measurements therefore achieve global coverage now within  $\sim 48 \text{ h}$  (van Hoek, 2010).

Volcanic  $\text{SO}_2$  emissions are regularly detected by the instrument during both quiescent degassing and major eruption events. The continuous spectra would generally make a  $\text{SO}_2$  DOAS retrieval possible. However, the widely used operational  $\text{SO}_2$  product of NASA is based on an advanced version of the algorithm that was already used for the Total Ozone Mapping Spectrometer (TOMS), one of OMI's predecessors, which was not designed for a wide spectral range. The so-called "Linear Fit Algorithm" (Yang et al., 2007) uses the measured radiances of OMI at 10 discrete wavelength in the UV to derive  $\text{SO}_2$ ,  $\text{O}_3$  and an effective reflectivity at the same time.

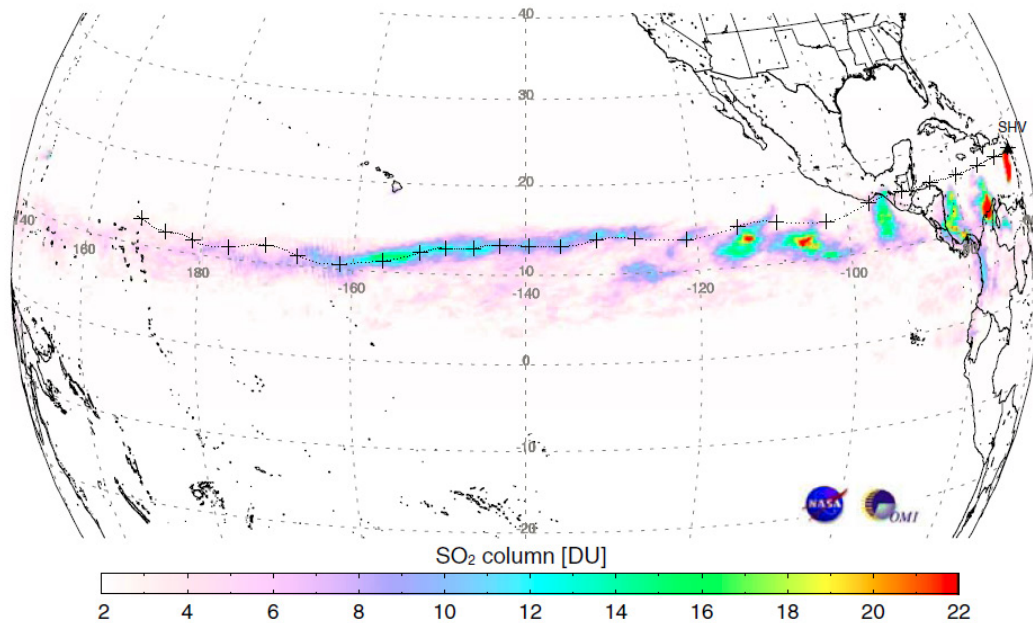


**Figure 3.8.:** Cumulative  $\text{SO}_2$  VCDs measured by OMI during an eruption of Soufrière Hills from May 20 to June 6, 2006. The dotted line indicates a forward trajectory for a cloud at 20 km altitude via the HYSPLIT trajectory model (Rolph, 2012; Draxler and Rolph, 2012). The trajectory covers 315 h (\*13 days) of cloud transport. Adapted from Carn et al. (2009a).

The used wavelength are centered at peaks and troughs of the SO<sub>2</sub> and O<sub>3</sub> absorption cross sections as well as at non absorbed spectral regions. The algorithm is therefore kind of similar to the COSPEC technique that is used in ground-based monitoring of volcanic SO<sub>2</sub> emissions (cf. Section 3.1.1). SO<sub>2</sub> total columns are derived by simulating top-of-atmosphere (TOA) radiances via a radiative transfer model as a function of a-priori SO<sub>2</sub> and O<sub>3</sub> vertical columns (respectively vertical profiles) and surface reflectivity. The a-priori assumptions are adjusted until the simulated TOA radiances match the actual measurements of the satellite instrument.

Figure 3.8 shows the cumulative SO<sub>2</sub> VCD measurements of OMI during an eruption of the Soufrière Hills volcano on Montserrat in May/June 2006 for a total of 18 consecutive days (Carn et al., 2009a). The SO<sub>2</sub> could be clearly tracked from the OMI measurements for almost one month and at least 26000 km distance from the volcano. The example therefore illustrates the huge advantage of OMI's ability to gain complete global coverage within one day compared to SCIAMACHY.

While the operational goal of the Aura spacecraft was intended for 6 years, OMI still provides valuable measurements after a current total operation time of 8.5 years. However, an advanced version of the instrument, the TROPospheric Monitoring Instrument (TROPOMI), is currently planned as payload for the ESA/GMES Sentinel 5 Precursor mission in 2015. TROPOMI will extent the measurements from OMI and SCIAMACHY, providing atmospheric measurements in the UV/Vis (270–500 nm), NIR (675–775 nm) and SWIR (2305–2385 nm) at an increased spatial resolution of 7×7 km<sup>2</sup> at nadir. The instrument is intended as a link between the current scientific missions and the Sentinel-4/-5 missions that are planed for 2019 and 2020.<sup>3</sup>

#### 3.2.3. GOME-2

The Global Ozone Monitoring Instrument-2 (GOME-2) was launched in 2006 on board the MetOp-A satellite and provides measurements in the UV/Vis wavelength range from 240–790 nm at a moderate groundpixel size of 40×80 km<sup>2</sup>. Global coverage is gained within 1.5 days. It is the first of three identical instruments. The second generation was recently launched in September 2012 and the third one is planned for 2018.

The instrument has been successful in monitoring volcanic SO<sub>2</sub> (e.g. Richter, 2009; Nowlan et al., 2011) and BrO emissions (Theys et al., 2009; Rix et al., 2012; Hörmann et al., 2012) by the application of the DOAS technique to the measured spectra in recent years. By the UV Aerosol Indices (UVAI), also volcanic ash can be retrieved from the data.

As the main focus of this thesis lies on the DOAS retrieval of volcanic emissions with GOME-2, a more detailed description of the instrument as well as the retrieval is given in Chapters 5 and 6.

---

<sup>3</sup><http://www.tropomi.eu>

## IR-sensitive satellite instruments

Satellite monitoring of volcanoes in the IR region provides measurements during day- and nighttime due to the Earth's thermal infrared (TIR) emissions. Typically, volcanic SO<sub>2</sub> (e.g. Urai, 2002; Prata et al., 2007; Clerbaux et al., 2008; Clarisse et al., 2008; Campion et al., 2010) and ash (e.g. Wen and Rose, 1994; Watson et al., 2004; Clarisse et al., 2010b; Thomas and Prata, 2011; Prata and Prata, 2012) are regularly retrieved, but it has been recently demonstrated that the detection of volcanic H<sub>2</sub>S (Clarisse et al., 2011) and CO (Martínez-Alonso et al., 2012) is also possible.

For the SO<sub>2</sub> retrieval, wavelengths between 7–12  $\mu\text{m}$  are used, as the molecule provides absorption bands in the IR, centered around 7.3  $\mu\text{m}$  and 8.6  $\mu\text{m}$ . While the SO<sub>2</sub> absorption at the 7.3  $\mu\text{m}$  band is stronger, this wavelength region is additionally affected by water vapor absorption, so that the SO<sub>2</sub> retrieval is critical for volcanic emissions in the lowest part of the atmosphere (0–5 km). For the 8.6  $\mu\text{m}$  band, the atmosphere is usually transparent during the absence of SO<sub>2</sub>, but the retrieval is very sensitive to surface temperature/emissivity and additionally strongly affected by volcanic ash (Clarisse et al., 2010a,b).

Usually, radiances at isothermal layers are simulated by the use of a radiative transfer model for atmospheric profiles of pressure, temperature, humidity and atmospheric constituents in order to estimate the ground and TOA brightness temperature for a SO<sub>2</sub>-free case (Realmuto et al., 1994). If a volcanic SO<sub>2</sub> plume is present, the measured brightness temperature difference (BTD) relative to the modelled cases is caused by SO<sub>2</sub> absorption. The apparent BTD is then a function of the SO<sub>2</sub> concentration in the atmosphere. In case of the 7.3  $\mu\text{m}$  band, it was shown that the BTD can be alternatively retrieved from a linear interpolation at two wavelength bands that show no SO<sub>2</sub> absorption (Prata et al., 2003; Doutriaux-Boucher and Dubuisson, 2009).

Volcanic ash is detected at wavelength between 11 and 12  $\mu\text{m}$ , where also ice and water shows strong scattering and absorption. However, while scattering and absorption for volcanic ash is stronger around 11  $\mu\text{m}$ , but at 12  $\mu\text{m}$  for ice and water, retrieved BTDs are negative when ash is present (Prata, 1989; Wen and Rose, 1994). From radiative transfer simulations, the optical depth and effective radius for the particles is estimated, so that the total ash mass may be calculated.

### 3.2.4. ASTER

The Advanced Spaceborne Thermal Emission and Reflection (ASTER) instrument on board the NASA EOS Terra satellite was launched in 1999 on a sun-synchronous orbit with a period of 90 minutes. Like Aura (cf. Section 3.2.2), Terra is part of the A-train constellation.

The instrument covers certain wavelength bands from the Vis to thermal IR region with a very high spatial resolution for the TIR measurements of 90 m at nadir position. Due to the B11 wavelength band that is centered around 8.6  $\mu\text{m}$ , ASTER is capable

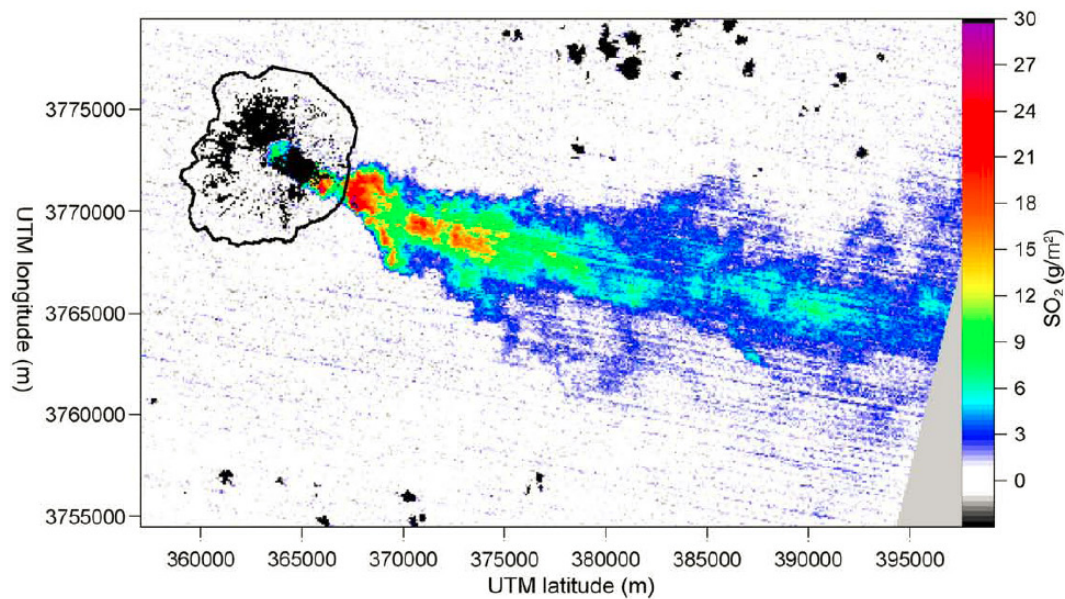


**Figure 3.9.:** *SO<sub>2</sub> column amounts as seen by ASTER at the Miyakejima volcano on 1 April 2001. Due to the instruments very high spatial resolution (90 m), even small SO<sub>2</sub> variations can be resolved near degassing volcanoes. Black spots represent cold respectively cloudy pixels. Adapted from Campion et al. (2010).*

of detecting volcanic SO<sub>2</sub> emissions. However, the instrument is not very well suited for continuous monitoring of volcanoes, since 16 days are needed for global coverage due to the narrow swath width of 60 km (Pieri and Abrams, 2004). A special feature of ASTER is that it can be pointed to specific targets (e.g. volcanoes) if requested, so that the time between two measurements over a specific volcano can be reduced to 7 days or better.

SO<sub>2</sub> emissions have been successfully detected at the Miyakejima volcano (Japan) by Urai (2002) and at Etna (Sicily) (Pugnaghi et al., 2006). Because of its high spatial resolution, results from both volcanoes were used for the validation by COSPEC and scanning DOAS ground-measurements (Campion et al., 2010). The determined SO<sub>2</sub> fluxes were in generally good agreement to the ground-based measurements, indicating ASTER's ability to monitor changes in emission fluxes for long-term evaluation. Figure shows one example of degassing SO<sub>2</sub> at the Miyakejima volcano on 1 April 2001 as seen by ASTER. Cold respectively cloudy pixels are shown as black spots. Within the volcanic plume, even small variations of the SO<sub>2</sub> amount can be seen due to the high spatial resolution of the instrument.

An advanced kind of similar instrument, the Hyperspectral Infrared Imager (HispIRI), is planned for the next years (2013–2016) and will allow more accurate and spatially higher resolved measurements as ASTER (60 m) at a regular revisit of five days due to a larger swath width of 600 km (Ramsey et al., 2012).

### 3.2.5. AIRS

The Atmospheric Infrared Sounder (AIRS) is a scanning spectrometer that was launched on the NASA EOS Aqua spacecraft in 2004 as part of the A-train constellation (cf. Section 3.2.2). The instrument has a swath width of 1650 km due to a scan angle of  $\pm 49^\circ$  off-nadir and provides global coverage twice a day. AIRS is sensitive to wavelengths in the range of 400–1000 nm and 3.7–15.4  $\mu\text{m}$  and therefore capable to detect  $\text{SO}_2$  as well as volcanic ash and aerosols. A high spatial resolution is provided by ground pixel sizes of  $15 \times 15 \text{ km}^2$  at nadir position and  $18 \times 40 \text{ km}^2$  at the swath's edge (Chahine and Center, 2000).

During recent years, AIRS has been regularly used to track volcanic  $\text{SO}_2$  and ash plumes, e.g. after eruptions of Mt. Etna (Carn et al., 2005), the Anatahan volcano (Northern Mariana Islands; Prata and Bernardo, 2007) or Chaitén (Chile; Carn et al., 2009b). For the latter eruption, a case study by Gangale et al. (2009) showed that the continuous high resolved spectra from AIRS can be used to discriminate volcanic ash from other particles by unique signatures in the 8–12  $\mu\text{m}$  range.

As an example, maps for the AIRS retrieval of  $\text{SO}_2$  and volcanic ash are shown in Figure 3.10 for the eruption of Mt. Etna on 30 October 2002 (Carn et al., 2005). While no major spatial separation between  $\text{SO}_2$  and ash are visible, the distance at which clearly enhanced ash amounts could be detected is shorter compared to those of enhanced  $\text{SO}_2$ , probably because of ash fallout.

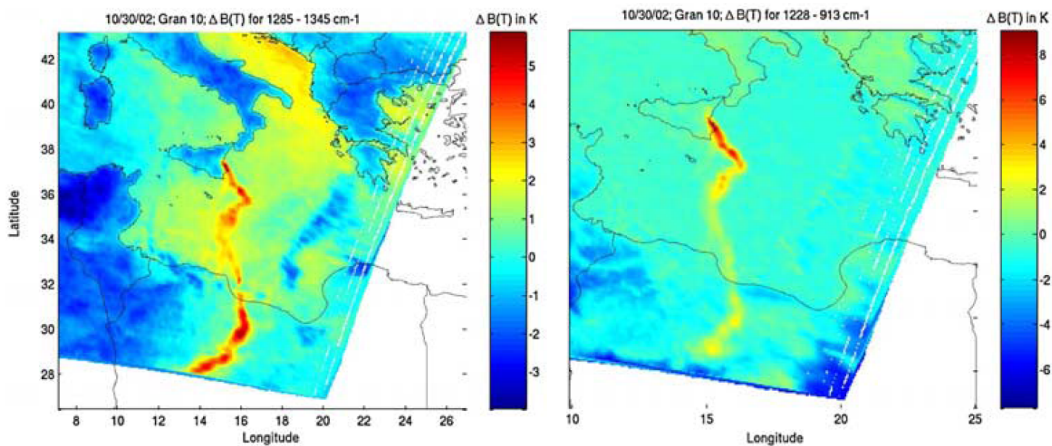


**Figure 3.10.:**  $\text{SO}_2$  and volcanic ash retrieval by the AIRS instrument during the eruption of Mt. Etna on 30 October 2002. The maps show the BT difference for the difference between the 7.7 and 7.4  $\mu\text{m}$  channels ( $\text{SO}_2$ , left) and the 8.1 and 10  $\mu\text{m}$  channels (volcanic ash, right). Adapted from Carn et al. (2005).

### 3.2.6. IASI

The Infrared Atmospheric Sounding Instrument (IASI) is a Fourier transform spectrometer (cf. Section 3.1.2) that was launched on the MetOp-A satellite in 2006. The instrument acts as a complementary sounder to the UV sensitive GOME-2 instrument that operates on the same platform (cf. Section 5.1). Like GOME-2, IASI is the first of three identical instruments (the second generation was recently launched on MetOp-B in September 2012, the third will be part of MetOp-C in 2016).

In contrast to GOME-2, global coverage is achieved twice a day due to possible day- and nighttime measurements. Furthermore, IASI provides a much higher spatial resolution (circular ground pixels at 12 km diameter) and a larger swath width of 2200 km. The spectrometer covers the entire wavelength region between 3.6–15.5  $\mu\text{m}$  and is therefore capable to detect volcanic  $\text{SO}_2$  at 7.3  $\mu\text{m}$  and 8.6  $\mu\text{m}$ , but also spectral features of volcanic ash and aerosols in the range between 7.6–12.5  $\mu\text{m}$ .

First  $\text{SO}_2$  retrievals had been reported by Clarisse et al. (2008), who investigated the  $\text{SO}_2$  emissions during the eruption of the Jebel at Tair volcano (Yemen) in 2007 and showed that an estimate of a plume's altitude can be obtained from BTDs in the 7.3  $\mu\text{m}$  absorption band (Figure 3.11). Additionally, the authors were able to detect volcanic ash and ice and retrieved particle sizes from IASI's very high resolved spectra. In a later publication, the same authors developed an algorithm that is not only capable of detecting volcanic ash from IASI, but can furthermore distinguish ash from other aerosols like water clouds or desert sand (Clarisse et al., 2010b). For this purpose, volcanic ash affected spectra from IASI during several detected eruptions were used to compile a reference database. It was demonstrated that these ash reference spectra may correlate well with spectra from other eruptions and can therefore be used to detect volcanic ash plumes of similar composition.

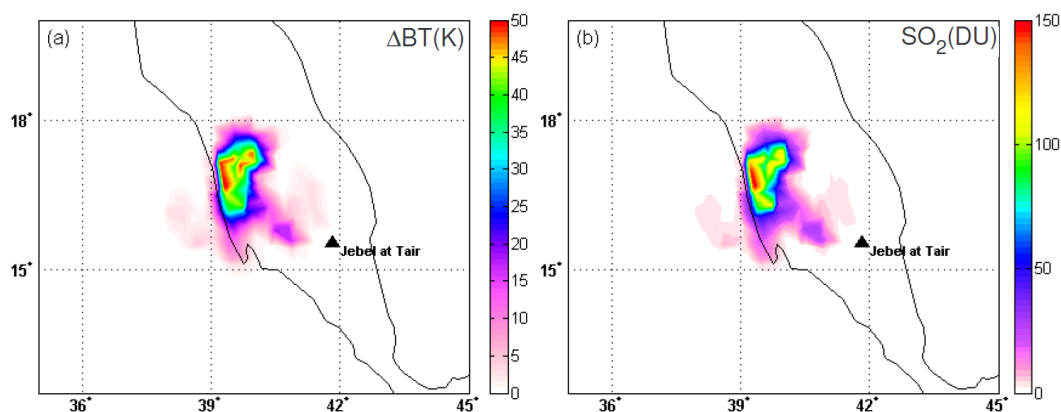


**Figure 3.11.:** Different views of the volcanic plume from the eruption at Jebel at Tair on 30 September 2007. (a) Brightness temperature differences in the 7.3  $\mu\text{m}$  band, (b) Retrieved  $\text{SO}_2$  concentrations in Dobson Unit ( $\hat{=} 2.69 \times 10^{16}$  molec/ $\text{cm}^2$ ). Adapted from Clarisse et al. (2008).

Recently, the instrument successfully observed the transformation of  $\text{SO}_2$  to liquid sulphuric acid ( $\text{H}_2\text{SO}_4$ ) particles during the eruption of Kasatochi in 2008, where the particles were detected for more than a month after the eruption (Karagulian et al., 2010). For the same eruption, Clarisse et al. (2011) reported the first observation of a large hydrogen sulfide ( $\text{H}_2\text{S}$ ) plume by a satellite instrument at all and developed a robust BTDs based retrieval approach at a narrow wavelength range between  $1234\text{--}1235\text{ cm}^{-1}$  ( $\cong 8.09\text{--}8.1\text{ }\mu\text{m}$ ).



**Part II.**

**Methods and Instruments**



## 4. Differential Optical Absorption Spectroscopy

The Differential Optical Absorption Spectroscopy (DOAS) is nowadays one of the most commonly used spectroscopic measurement techniques in order to measure a large number of gaseous atmospheric species. It was first introduced in the 1970s by Perner et al. (1976) and Platt et al. (1979), who detected OH radicals, respectively formaldehyde (CH<sub>2</sub>O), nitrogen dioxide (NO<sub>2</sub>) and ozone (O<sub>3</sub>) above Jülich (Germany) and for maritime air at the northern German coast.

Since then, many more atmospheric species have been detected by DOAS, e.g. SO<sub>2</sub>, HONO, HCNO and several halogen species like ClO, BrO, OClO, IO and OIO (e.g. Carroll et al., 1989; Winer and Biermann, 1994; Wagner and Platt, 1998; Bobrowski et al., 2003; Galle et al., 2003; Köhl et al., 2006; Bobrowski and Platt, 2007; Stutz et al., 2007; Lee et al., 2008; Seitz et al., 2010, and references therein). One of the main advantages of DOAS is that different tracegases can be measured at the same time without influencing their chemical behaviour. In the meanwhile, DOAS has been applied successfully to a large variety of different measurement geometries and platforms, such as cars, aircrafts, balloons, ships or even satellites.

In this thesis, volcanic emissions (SO<sub>2</sub> and BrO) have been evaluated from satellite-borne measurements by using the DOAS technique. Therefore a brief description of the main concept as well as the geometry for the satellite retrieval will be given in the following. For a detailed and comprehensive discussion of the past, present and future of DOAS, the reader is referred to Platt and Stutz (2008). For a special review on satellite-borne DOAS measurements, see also Richter and Wagner (2011).

### 4.1. Absorption spectroscopy

Absorption spectroscopy is based on Lambert-Beer's law, which describes the absorption of light at an initial intensity  $I_0(\lambda)$  at a certain wavelength  $\lambda$ , while it traverses a medium.

It can be written by:

$$I(\lambda) = I_0(\lambda) \cdot \exp[-\sigma(\lambda) \cdot c \cdot L] \quad (4.1)$$

where  $I(\lambda)$  is the measured light intensity after the radiation has traversed the medium,  $\sigma(\lambda)$  is the wavelength-dependent absorption cross-section,  $c$  is the concentration of the medium and  $L$  is the length of the lightpath. The absorption cross-section is a characteristic quantity for individual absorbers, as it shows specific absorp-

tion features e.g. for different atmospheric tracegases. Most absorption cross-sections for atmospheric species are well known due to laboratory measurements. The mean concentration  $c$  of an absorbing species can now be directly derived from:

$$c = \frac{\ln\left(\frac{I_0(\lambda)}{I(\lambda)}\right)}{\sigma(\lambda) \cdot L} = \frac{\tau}{\sigma(\lambda) \cdot L} \quad (4.2)$$

where  $\tau$  is the so-called *optical density* of a certain absorber.

### 4.2. The principle of DOAS

For spectroscopic measurements in the open atmosphere, also the light extinction due to scattering processes by aerosols, cloud droplets or molecules has to be considered.

Figure 4.1 shows a setup for measurements of light attenuation in the atmosphere. Like in Section 4.1, light with an initial intensity  $I_0$  is absorbed by the trace gas  $j$  with absorption cross-section  $\sigma_j(\lambda)$ , but also scattered by air molecules (Rayleigh scattering) and particles like cloud droplets or aerosols (Mie scattering). While the light extinction by Rayleigh scattering is proportional to  $\lambda^{-4}$  (Strutt, 1899), it is less wavelength dependent for Mie scattering ( $\lambda^{-n}$ ), where  $n$  depends on the particle's size and shape (Mie, 1908). Lambert-Beer's law (Eq. 4.1) can therefore be re-written for atmospheric measurements as:

$$I(\lambda) = I_0(\lambda) \cdot \exp\left[-L \cdot \sum_j \left(\sigma_j(\lambda) \cdot c_j\right) + \epsilon_R(\lambda) + \epsilon_M(\lambda)\right] \cdot A(\lambda) \quad (4.3)$$

where  $\epsilon_R(\lambda)$  and  $\epsilon_M(\lambda)$  are the extinction coefficients for Rayleigh and Mie scattering, respectively, and  $A(\lambda)$  accounts for possible instrumental effects and the influence of turbulence in the atmosphere.

Even if one would know the lightpath  $L$  of a photon at a certain wavelength  $\lambda$  on its way through the atmosphere, it is impossible to get detailed knowledge about the exact atmospheric composition that had influenced the measured light. The concentration of a certain trace gas in the atmosphere can therefore usually not be simply determined from Eq. 4.3 for a single wavelength.

The main principle of DOAS now solves this problem by using spectral informations and separating atmospheric influences that strongly depend on wavelength from those that are only weakly dependent on wavelength. While trace gases in the atmosphere typically cause characteristic narrow-band absorption features in the measured spectra, scattering as well as atmospheric turbulence generally affect the light in a broad-band way. Thus, DOAS separates the specific narrow-band absorption features of atmospheric species from the broad-band part. The absorption cross-section is therefore rewritten as:

$$\sigma_j(\lambda) = \sigma_{j,0}(\lambda) + \sigma'_j(\lambda) \quad (4.4)$$

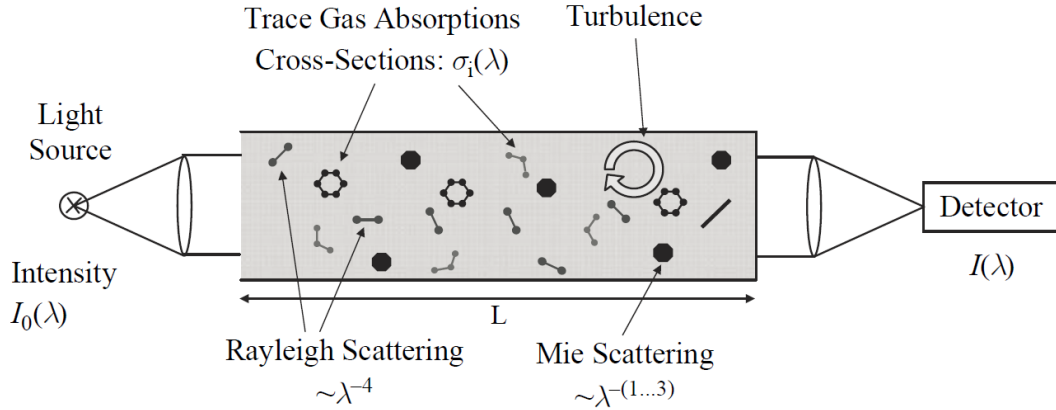


**Figure 4.1.:** Absorption and scattering in the open atmosphere. Light at an initial intensity  $I_0$  is attenuated due to absorption by atmospheric species as well as by Mie and Rayleigh Scattering. Adapted from Platt and Stutz (2008).

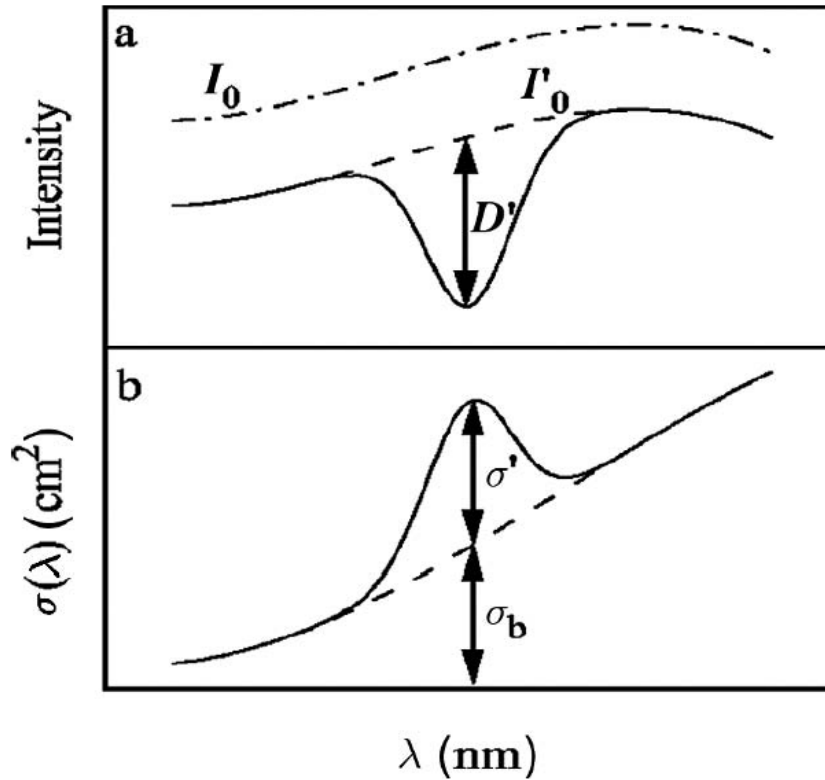
where  $\sigma_{j,0}(\lambda)$  is now the broad-band part of the absorption cross-section (mainly due to scattering processes) and  $\sigma'_j(\lambda)$  is the narrow-band ('differential') part due to light absorption by the atmospheric species  $j$ .

Figure 4.2 illustrates this separation of the absorption cross-section (respectively of the light intensity) for one absorption band. While the narrow-band absorption cross-section  $\sigma'_j(\lambda)$  varies on a small wavelength range, the broad-band part  $\sigma_{j,0}(\lambda)$  is only weakly dependent on wavelength and can be typically described by a polynomial function.

The combination of Eq. 4.4 and Eq. 4.3 leads to an extended version of Lambert-Beer's law:

$$I(\lambda) = I_0(\lambda) \cdot \exp \left[ -L \cdot \left( \sum_j \sigma'_j(\lambda) \cdot c_j \right) \right] \cdot \exp \left[ -L \cdot \left( \sum_j \left( \sigma_{j,0}(\lambda) \cdot c_j \right) + \epsilon_R(\lambda) + \epsilon_M(\lambda) \right) \right] \cdot A(\lambda) \quad (4.5)$$

The distribution of different trace gases and particles in the atmosphere is not homogeneous, so that the multiplication with the length of the lightpath  $L$  in Eq. 4.5 has to be replaced by an integral of space dependent  $c$ ,  $\epsilon_R$  and  $\epsilon_M$  over the whole lightpath. Furthermore, the absorption cross-sections may depend not only on wavelength, but additionally on the temperature and pressure.



**Figure 4.2.:** Principle of DOAS: The initial light intensity  $I_0$  and the absorption cross-section  $\sigma$  are separated into a narrow part that varies strongly with wavelength ( $D'$  and  $\sigma'$ ) and a broad-band part that is less dependent on  $\lambda$  ( $I'_0$  and  $\sigma_b$ ). Adapted from Platt and Stutz (2008).

The extended version of Lambert-Beer's law (Eq. 4.5) is then re-written as:

$$\begin{aligned}
 I(\lambda, l) = & I_0(\lambda) \cdot \exp \left[ - \int_0^L \left( \sum_j (\sigma'_j(\lambda, T, p) \cdot c_j(l)) \right) \cdot dl \right] \cdot \\
 & \exp \left[ - \int_0^L \left( \sum_j [\sigma_{j,0}(\lambda, T, p) \cdot c_j(l)] + \epsilon_R(\lambda, l) + \epsilon_M(\lambda, l) \right) \cdot dl \right] \cdot A(\lambda)
 \end{aligned} \tag{4.6}$$

The first exponent now comes up with the narrow-band variations from the absorption by atmospheric trace gases, while the second one describes all broad-band effects on the measured spectra.

The fraction of the light intensity that slowly varies with wavelength can therefore be defined as:

$$I'_0(\lambda) = I_0(\lambda) \cdot \exp \left[ - \int_0^L \left( \sum_j (\sigma_{j,0}(\lambda) \cdot c_j) + \epsilon_R(\lambda) + \epsilon_M(\lambda) \right) \cdot dl \right] \cdot A(\lambda) \quad (4.7)$$

so that Eq. 4.6 can now be re-written by using  $I'_0$  as "new" initial light intensity:

$$I(\lambda, l) = I'_0(\lambda) \cdot \exp \left[ - \int_0^L \left( \sum_j (\sigma'_j(\lambda, T, p) \cdot c_j(l)) \right) \cdot dl \right] \quad (4.8)$$

The differential optical density  $\tau'$  can now be defined analogue to Eq. 4.2 by:

$$\tau'(\lambda) = \ln \left( \frac{I'_0(\lambda)}{I(\lambda)} \right) = \int_0^L \left( \sum_j \sigma'_j(\lambda) \cdot c_j \right) \cdot dl \quad (4.9)$$

In practice, the broad-band part of a measured spectrum is approximated by a polynomial function  $P_x$  of order  $x$ . The differential cross-sections  $\sigma'_j$  can be determined by high resolution measurements in the laboratory. If the initial light intensity and the effective lightpath are known, the mean concentration of the individual absorbers can be directly determined by Eq. 4.9. Therefore, the measured spectra are fitted by the absorption spectra of tracegases that show narrow absorption features in the respective spectral range and the polynomial  $P_x$  via a non-linear least squares fitting algorithm. For a detailed description of this spectral fitting process, the reader is referred to the comprehensive review in Platt and Stutz (2008).

### 4.3. Passive DOAS

Some DOAS applications can be conducted by using artificial light sources (e.g. high pressure arc lamps or light-emitting diodes). The light at an initial intensity  $I_0$  traverses the atmosphere at the area of interest on a well-defined lightpath  $L$ , usually implemented by reflecting mirrors ('active' DOAS). However, for a lot of other DOAS applications, the implementation of such measurements is difficult due to the local topographic circumstances. Especially for field measurement at areas of volcanic activity or for satellite measurements in general, scattered sunlight is typically used as a natural light source ('passive' DOAS). As the wavelength dependent absorption and scattering at different atmospheric heights leads to very complex lightpaths,  $L$  is initially not known for passive DOAS measurements. Typically, the initial light intensity is unknown as well, since this would require measurements of a non-absorbing atmosphere (for satellite-borne DOAS, the latter is rather easy, as a satellite instrument can directly point at the sun without being influenced by Earth's atmosphere).

#### 4. Differential Optical Absorption Spectroscopy

---

Furthermore, the lightpaths also depend on the measurement geometry, i.e. the Sun's position as well as the viewing direction of the telescope. The total measured intensity is now the sum over the intensities of all photons that traversed the atmosphere on individual lightpaths.

Due to the unknown height profile of the absorbers and the total lightpath distribution, only the so-called *slant column density* (in the following SCD or S):

$$S_j = \int_0^{\infty} c_j(l) \cdot dl \quad (4.10)$$

can be calculated from Eq. 4.9 by the DOAS analysis. The slant column density is the concentration of an absorber integrated over the effective lightpath.

In order to make SCDs from different measurements comparable to each other, the SCDs need usually to be converted into so-called vertical column densities (VCD or V). The  $VCD_j$  is the vertically integrated concentration of a trace gas  $j$  from the ground to the top of the atmosphere (TOA):

$$V_j = \int_0^{TOA} c_j(z) \cdot dz \quad (4.11)$$

For the conversion of SCDs to VCDs, the concept of the air mass factor (AMF or A) is used. The AMF is defined as:

$$A_j = \frac{S_j}{V_j} \quad (4.12)$$

and generally depends on the measurement geometry as well as on the atmospheric conditions (i.e. the trace gas profiles, aerosol distribution or the presence of clouds).

For the specific case of volcanic eruptions, the knowledge about the height distribution of a volcanic plume is usually sparse and can only sometimes be estimated by eye witnesses, LIDAR or airborne profile measurements. Additionally, there is typically a multitude of single explosions at least during major volcanic eruptions, so that several resulting plumes might be located at different altitudes at the same time. Especially for such cases, it remains very difficult to obtain reliable VCDs. Furthermore, measurements of a volcanic  $SO_2$  plume are influenced by several other radiative transfer effects (Figure 4.3), e.g. by scattered sunlight that has traversed the plume several times and therefore increase the SCD. Other parts of the light may also have been scattered in between the instrument and the plume, without ever having penetrated it, thus decreasing the SCD (*dilution effect*). The SCD is additionally influenced by volcanic ash that is usually present during major volcanic eruptions. Due to the complex effects on the lightpaths by combined scattering and absorption processes, the SCD might be either in- or decreased (cf. also Chapter 6.3.5).

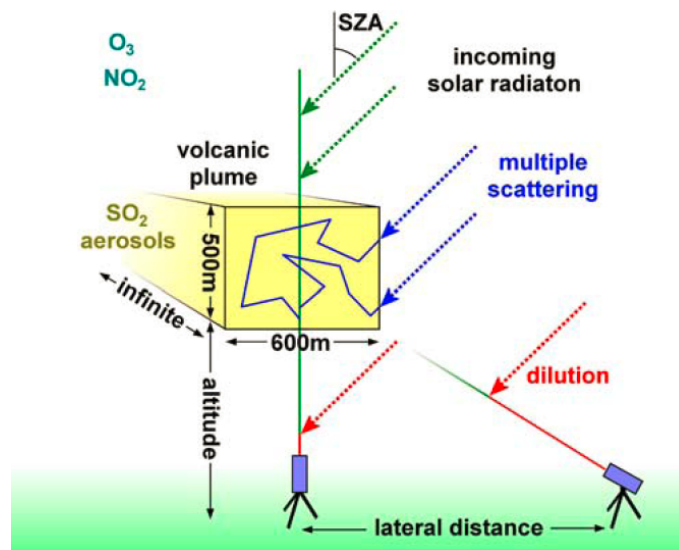


**Figure 4.3.:** Possible lightpaths for passive ground-based DOAS measurements at a volcano. While photons are ideally scattered above the volcanic plume and then pass straight through (green), they may also be scattered in between the plume and the instrument (red) and therefore reduce the effective measured SCD. Due to multiple scattering inside the plume, the lightpath can also increase and thus enhances the SCD. All of these effects affect also satellite-borne measurements. Adapted from Kern et al. (2010).

#### 4.4. The Ring effect

The general shape of the solar spectrum can be described in good approximation by a Planck spectrum for a black-body at  $\sim 5800^\circ\text{C}$  (cf. Figure 4.4). In reality, the Sun's spectrum exhibits a huge variety of absorption lines (so-called 'Fraunhofer lines') that are caused by several elements respectively molecules in the Sun's atmosphere. While Rayleigh- and Mie scattering influences the measured light intensity only in a broadband way (cf. Section 4.2), the depth of the Fraunhofer lines is not expected to be altered by the atmosphere. However, when the ratio between the measured spectrum  $I$  and the reference  $I_0$  is calculated for the DOAS evaluation (cf. Eq. 4.9), significant structures remain at the positions of the Fraunhofer lines, which are caused by the so-called 'Ring effect', named after one of its discoverer (Grainger and Ring, 1962).

The effect is caused by the 'filling-in' of the Fraunhofer lines by light at neighboring wavelengths due to inelastic rotational Raman scattering (e.g. Solomon et al., 1987; Chance and Spurr, 1997; Vountas et al., 1998; Beek et al., 2001; Wagner et al., 2009). While the probability of the Raman scattering at wavelength of the Fraunhofer lines is less than at the neighboring wavelength (the scattering is proportional to the light intensity), more light from neighboring wavelengths is scattered 'into' the lines than from the wavelength of the lines themselves. As this effect can contribute to some % to the optical density, an accurate correction is needed in the DOAS retrieval.

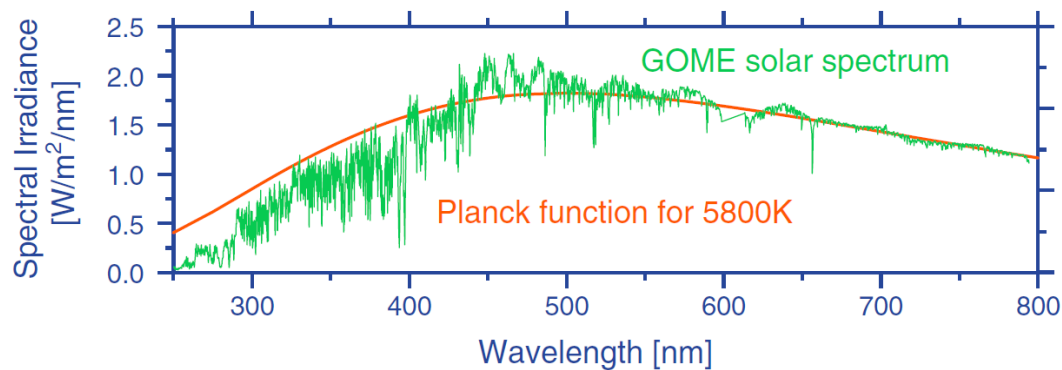


**Figure 4.4.:** Solar spectrum (green) measured by GOME instrument containing a variety of solar Fraunhofer lines. For comparison, the black-body radiation for 5,800 K is also shown (note that the sun is not a perfect black body; also the radiation in certain parts of the spectrum originates from layers at different temperatures). Adapted from Richter and Wagner (2011).

Therefore the Ring effect is usually simulated by radiative transfer model calculations (RTM - cf. Section 4.6) and included into the DOAS fit via a pseudo-absorber spectrum (so-called 'Ring spectrum'). Next to the Fraunhofer lines, also the absorption lines for atmospheric absorbers are filled-up by the ('telluric') Ring effect, but is of less significance for the DOAS retrieval and usually corrected in astronomical observations.

## 4.5. Satellite viewing geometry and geometrical AMF

In order to get a first approximation of the effective light path, the viewing geometry of the instrument needs to be considered. As the focus of this thesis lies on satellite-borne measurements, only the typical GOME-2 viewing geometry will be described in the following.

GOME-2 observes the Earth's atmosphere in *nadir* geometry, i.e. the instrument's telescope points directly to the center of Earth respectively orthogonal to the virtual plane at a specific location at the Earth's surface. The viewing geometry is then defined by three different angles between the satellite instrument and the position of the Sun (Figure 4.5):

1. The Solar Zenith Angle (SZA)  $\xi$ : This is the angle between the zenith position at a certain measurement location on Earth surface and the center position of the Sun.
2. The Line Of Sight (LOS)  $\theta$ : As most satellite instruments are not stationary pointing at only one specific location on Earth's surface, but scan the ground to a certain degree orthogonal to the actual nadir position (cf. also Chapter 5.1),

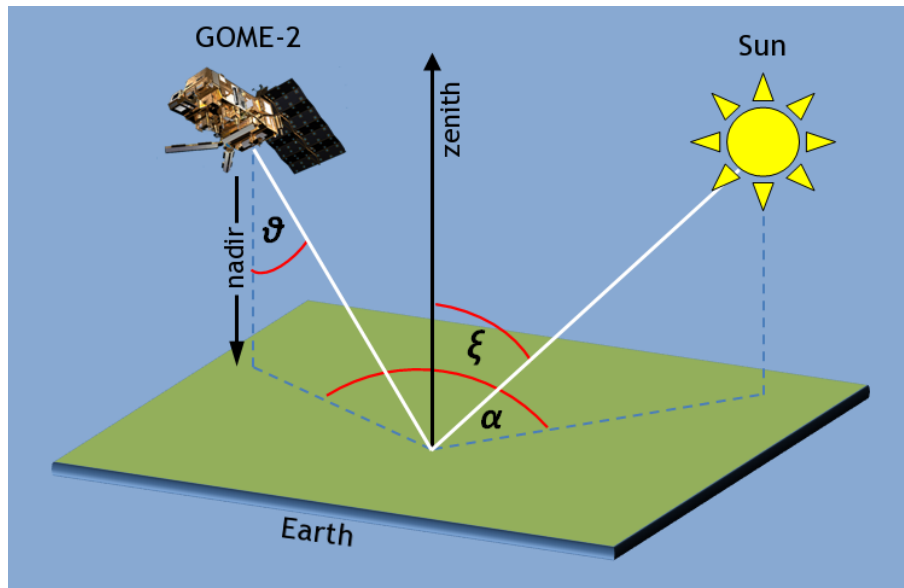


**Figure 4.5.:** The viewing geometry of the GOME-2 instrument is defined by three angles, the Solar Zenith Angle (SZA)  $\xi$ , the Line of Sight (LOS)  $\theta$  and the Solar Relative Azimuth Angle (SRAA)  $\alpha$ . By knowing the SZA and LOS, the geometrical light path can be determined in order to calculate a geometrical air mass factor  $AMF_{geo}$ .

the LOS is the angle of the true viewing direction relative to the actual nadir position.

3. The Solar Relative Azimuth Angle (SRAA)  $\alpha$ : This is the angle between the instrument's viewing direction and the Sun, projected in the orthogonal plane at the location of the measurement.

For  $SZA < 80^\circ$  and cloud-free conditions, the viewing geometry can be used for the calculation of a *geometrical* air mass factor  $A_{geo}$  in order to obtain a good approximation for VCDs of stratospheric absorbers:

$$A_{geo} = \frac{1}{\cos(\xi)} + \frac{1}{\cos(\theta)} \quad (4.13)$$

The scattering events for stratospheric absorbers take almost exclusively place in the subjacent troposphere, as the concentration of molecules and aerosols in the stratosphere is low and therefore doesn't significantly affect the simple geometrical light path.

For absorbers in the troposphere, the light paths may become much more complex. In particular the light paths can be significantly influenced by the presence of clouds and/or aerosols (and their specific properties), the Earth's surface albedo as well as the vertical profile of the regarded trace gases. For very high concentrations of a

trace gas (like SO<sub>2</sub> during a major volcanic eruption), the absorption may become so strong that almost no light can be anymore detected in the regarded wavelength region, so that the sensitivity to the trace gas is reduced ( $AMF \rightarrow 0$ ), although the absorptions become stronger (cf. Chapter 6.3). In such cases, the AMF needs usually to be calculated by radiative transfer models (RTM) that try to simulate the radiative transfer of the solar radiation on its way through the atmosphere.

### 4.6. Radiative transfer calculations

The influence of different trace gas profiles as well as multiple scattering on air molecules, aerosols and clouds on radiative transfer needs to be calculated by the use of numerical radiative transfer models (RTM).

Typically, RTMs are initialized by a state vector of the atmosphere including presumed profiles for temperature, pressure, humidity and tracegases that may influence the radiation at a regarded wavelength of interest. Additionally cloud and aerosol layers with specified properties (i.e. the cloud optical density or the single scattering albedo) can be included, as well as the surface albedo. Furthermore, the measurement geometry needs to be specified by the position and viewing direction of the detector relative to the Sun. The radiative transport is then simulated at a certain wavelength first for an atmosphere that includes a certain absorber of interest and afterwards for a 'clean' atmosphere, where the regarded absorber is excluded. The model may then calculate the apparent SCD from the simulations as well as the 'real' VCD from the initial state vector and the AMF is simply determined by the use of Eq. 4.12.

Next to several other implementations, some RTMs are based on the Monte Carlo method, which simulates the light paths of a huge number of individual photons on their way through the atmosphere. As a result, the radiance that is detected by a certain instrument can be obtained from the statistical analysis of the whole photon ensemble. Since such models have to simulate the light path for a sufficiently large number of single photons, they are rather time-consuming and have a high computational cost. However, Monte Carlo RTMs provide the most realistic simulations of the various effects on radiative transport in the atmosphere (Richter and Wagner, 2011). For a review on various RTMs, the reader is referred to Davis and Marshak (2010) and Wendisch and Yang (2012).

In this thesis, the Monte Carlo radiative transfer model *McArtim* (Deutschmann et al., 2011) has been used in the context of certain case studies in order to simulate the radiative transfer effects for large concentrations of SO<sub>2</sub> in volcanic plumes during major eruptions (cf. Chapter 6.3).

## 5. Instruments

In this chapter, the instruments that have been used within the scope of this thesis are introduced and described in detail. While the main focus of this thesis lies on the DOAS satellite retrieval of volcanic SO<sub>2</sub> and BrO column densities by the GOME-2 instrument, but also airborne DOAS measurements of SO<sub>2</sub> and BrO conducted by the CARIBIC project on board of a Lufthansa Airbus A340-600 aircraft are compared to the results from the GOME-2 data evaluation during the eruption of Eyjafjallajökull (Iceland) in April/May 2010 by Heue et al. (2011) (cf. Section 9.6).

In the following, the key features of the GOME-2 instrument will be introduced in Section 5.1, including the technical setup and the measurement routine according to the official GOME-2 product guide (EUMETSAT, 2005). Subsequently, the setup of the airborne DOAS instrument on CARIBIC will be shortly described in Section 5.2.

### 5.1. The GOME-2 instrument

The GOME-2 (Global Ozone Monitoring Experiment-2) is a 4 channel UV/Vis grating spectrometer that observes Earth's atmosphere in so-called 'nadir' viewing geometry, i.e. the measured spectra are obtained through a telescope that points to the Earth's center of gravity. It is the first of three identical instruments that are part of the MetOp satellite series operated by the European Organisation for the Exploitation of Meteorological Satellites (EUMETSAT).

MetOp-A was launched into a sun-synchronous polar orbit at 800 km altitude in October 2006 (Callies et al., 2000). The second GOME-2 instrument was recently launched on MetOp-B in September 2012 and the third one will be carried by MetOp-C in 2018, respectively. The satellite crosses the equator at 9:30 local time. Next to GOME-2, several other instruments are hosted by MetOp-A. This includes in particular the IASI (Infrared Atmospheric Sounding Interferometer) instrument, which is capable to monitor the atmosphere in the infrared region and therefore acts as a complementary instrument to GOME-2 (cf. Section 3.2.6).

Figure 5.1 shows the optical design of the instrument (EUMETSAT, 2005). Sunlight that is reflected from the Earth's surface or scattered within the atmosphere is directed into the telescope by a scanning mirror. The mirror can also be re-directed towards a sun diffuser for direct sunlight measurements or towards a calibration unit that allows regular calibration measurements once per day. Measured Earthshine spectra are subdivided into 4 different main channels, each one optimized for another wavelength region (channel 1: 240–315 nm, channel 2: 311–403 nm, channel 3: 401–600 nm and channel 4: 590–790 nm). The spectra are then focused onto linear silicon photodiode detector arrays of 1024 pixels each, which are actively cooled to -38° C in order to minimise the noise level due to dark current. Additionally, the instrument

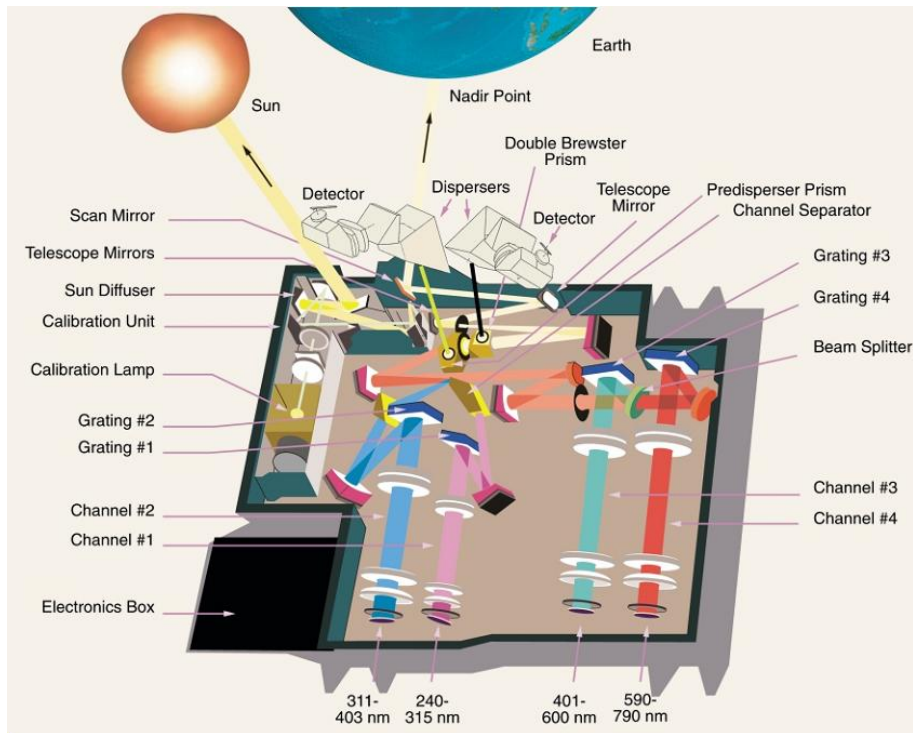


**Figure 5.1.:** *The optical layout of the GOME-2 instrument. The measured Earthshine spectra that enter the instrument are subdivided into 4 main channel detectors. Adapted from EUMETSAT (2005).*

has the capability to measure the linearly polarised intensity in two perpendicular directions by two Polarisation Measurement Devices (PMDs).

As the integration time depends on the light intensity, it can be separately set for each main channel. The first two channels are therefore further subdivided into two parts (Band 1A, 1B, 2A and 2B), as the intensity is typically lower for the UV wavelength region in comparison to the visible range. However, usually a default integration time of 187.5 ms is used in all channels, except Band 1A with a default integration time of 1.5 seconds, and at low solar elevations, where the integration time for all channels is enhanced in order to compensate for low light intensities (1.5 s for Band 1A/B, respectively 0.75 s for all others). The different channels come also with different spectral resolutions, ranging from 0.26–0.51 nm FWHM, and detector pixel sizes of 0.12 nm for channels 1 and 2, respectively 0.21 nm for channels 3 and 4. In this thesis, Band 2B in the spectral range of 300–412 nm is used for the evaluation of SO<sub>2</sub> and BrO, providing 953 single wavelength channels at a spectral resolution of 0.27 nm FWHM.

The scanning mirror allows across-track scanning of the Earth's surface with viewing angles up to 50° off-nadir with a total swath-width of 1920 km. Global coverage is therefore achieved within 1.5 days at the equator. A complete coverage of high latitude regions (> 45° N/S) can already be achieved within a single day, as individual

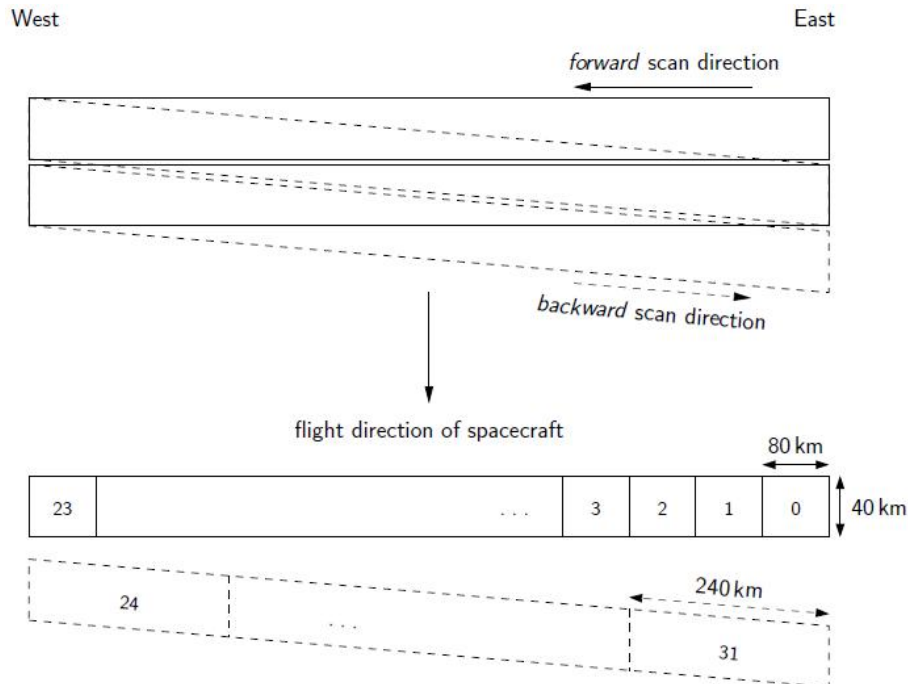


**Figure 5.2.:** GOME-2 scan pattern in default mode. During the forward scan, the scan mirror sweeps from negative to positive viewing angles (solid line), measuring ground pixels with a size of  $40 \times 80 \text{ km}^2$ . This is followed by the three times faster flyback of the scanning mirror, resulting in backscan ground pixels with a size of  $40 \times 240 \text{ km}^2$  (dashed line). Adapted from Sihler (2012).

scenes are measured even several times within 24 h due to the overlap of succeeding satellite orbits (EUMETSAT, 2005; Munro et al., 2006).

Figure 5.2 shows the default scan pattern of GOME-2. While the satellite circles the globe in North-South direction at daytime (South-North direction at the dark side of the Earth), the scanning mirror sweeps from negative to positive viewing angles (East to West) with a ground pixel size of  $40 \times 80 \text{ km}^2$ . The GOME-2 instrument therefore observes 4 times smaller ground pixels than its predecessor GOME on ERS-2. After 4.5s, the *forward-scan* is followed by a three times faster flyback of the mirror (West to East). This *back-scan* thus also provides only one third of the spatial resolution of a forward-scan ( $40 \times 240 \text{ km}^2$ ). In total, one complete scan of the mirror consists out of 24 measured forward-scan and 8 back-scan ground pixels. Typically, the back-scan ground pixels are not used for the evaluation of atmospheric tracegases, as the higher spatial resolution of the forward-scan measurements is preferred (cf. Section 9.6.3).

The spatial pattern of the daily orbits repeats after 29 days. During this time period, several special operation modes are performed, e.g. the swath is reduced to a sixth of the default swath (320 km) on day 15 of the timeline, resulting in ground pixels that have a six times increased spatial resolution perpendicular to the satellite's flight direction ( $\sim 40 \times 13 \text{ km}^2$ ). On the first day of the cycle, some instrumental calibration

measurements are additionally performed, e.g. to correct for the possibly varying wavelength calibration.

## 5.2. DOAS instruments on CARIBIC

The Civil Aircraft for the Regular Investigation of the atmosphere Based on an Instrument Container (CARIBIC) observatory is an instrument container that is usually carried by a Lufthansa Airbus A340-600 on a monthly basis during four consecutive regular passenger flights for 2–4 days (Brenninkmeijer et al., 2007). The container contains a large variety of instruments that can measure the atmosphere during a flight. Some species can even be measured in real time (CO, CO<sub>2</sub>, O<sub>3</sub>, NO, NO<sub>2</sub>, NO<sub>y</sub>, CH<sub>4</sub>, some organic compounds, total and gaseous water, mercury and aerosols). Additionally, aerosol samples as well as air samples can be collected for post-flight laboratory analysis of aerosol elemental composition (Nguyen et al., 2006) and several trace gases (Schuck et al., 2009; Baker et al., 2011b).

Next to other instruments, CARIBIC provides a compact DOAS system that consists of two main parts. While the main technical components (i.e. the spectrographs, a temperature stabilisation system and a computer that controls the measurement routine) are located in the container inside the aircraft, three miniature telescopes are mounted in the pylon of the inlet system at the belly of the aircraft that is also used for direct sampling of tracegases and/or aerosols (cf. Figure 5.3). The telescopes with an opening angle of 1.9° are adjusted to different elevation angles, two of them looking sideways at ±10° relative to the horizon and another one almost in nadir position (-82°). Every telescope is connected to an individual OMT CTF60 spectrometer via quartz fibre bundles, covering the spectral range between 300–400 nm with a spectral resolution of 0.5 nm FWHM. The temporal resolution of the system with the current setup is about 8s, which corresponds to a horizontal resolution of 2 km (Heue et al., 2011).

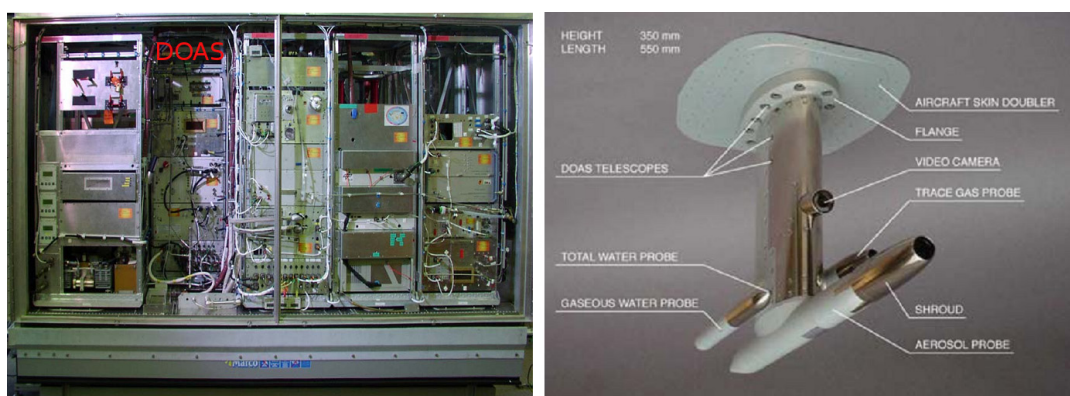


**Figure 5.3.:** left: CARIBIC container inside of the aircraft. The DOAS system is located in the upper left part, right: inlet system containing the three DOAS telescopes at the belly of the aircraft. Adapted from Brenninkmeijer et al. (2007).

For a more detailed description of the CARIBIC DOAS system, the reader is referred to Dix et al. (2009) and Heue et al. (2010).

The CARIBIC DOAS system has proven to be able to successfully detect several trace gases during recent years, including SO<sub>2</sub>, BrO, NO<sub>2</sub>, HONO, HCHO, O<sub>3</sub> and the oxygen dimer O<sub>4</sub>. In the context of emissions from volcanic eruptions, CARIBIC was able to probe a volcanic plume for the first time after the Kasatochi eruption in August 2008 and provided SO<sub>2</sub> VCDs from the DOAS measurements that were found to show a good agreement to satellite measurements by GOME-2 (Heue et al., 2010).

During the eruption of the Eyjafjallajökull volcano in April/May 2010, CARIBIC had the opportunity to investigate the corresponding volcanic plume during three special scientific research flights for the abundance of volcanic ash. Additional DOAS measurements were performed during one of these flights on May 16, where both SO<sub>2</sub> and BrO had been successfully detected within the volcanic plume. The data was later compared to GOME-2 measurements that had been evaluated within the scope of this thesis (cf. Section 9.6) and published in Heue et al. (2011).



## 6. Satellite retrieval of SO<sub>2</sub> and BrO

The following chapter describes the DOAS evaluation of SO<sub>2</sub> and BrO for the GOME-2 satellite data in detail. After a short description of the initial instrumental calibration process in Section 6.1, the standard DOAS retrieval for SO<sub>2</sub> is introduced (Section 6.2). As the SO<sub>2</sub> standard retrieval is conducted at wavelengths where the SO<sub>2</sub> absorptions are strongest, it generally provides the highest sensitivity to volcanic plumes and anthropogenic emissions. However, difficulties may occur during major volcanic eruptions, when very high SO<sub>2</sub> concentrations are present in a plume. In such cases, the SO<sub>2</sub> SCDs are usually strongly underestimated by the DOAS fit. To avoid this effect, 2 alternative evaluation schemes at longer wavelengths have been explored and optimized for an accurate retrieval of the SO<sub>2</sub> SCDs. Both novel SO<sub>2</sub> evaluation schemes will be introduced and compared to each other in Section 6.3. Finally, the BrO DOAS retrieval will be briefly discussed at the end of this chapter.<sup>1</sup>

### 6.1. Instrument calibration

The radiance spectra measured by the GOME-2 instrument were evaluated using the DOAS method (cf. Chapter 4). For the SO<sub>2</sub> and BrO retrievals, the GOME-2 spectral band 2B was used, covering the UV wavelength region from 300–412 nm and providing 953 channels at a spectral resolution of 0.27 nm FWHM (cf. Chapter 5.1). Before the DOAS algorithm was applied to the measured spectra, the spectral calibration of the 2B band has been conducted by the fit of a direct sun measurement of the instrument (*Sun Mean Reference Spectrum* - SMR) on 8 August 2008 to a high-resolution solar *Kurucz* spectrum (Kurucz et al., 1984). Additionally, a single O<sub>3</sub> cross-section at 241 K had been added to account for O<sub>3</sub> absorptions in the Kurucz spectrum. The calculations were performed by the *WINDOAS* 2.1 software, developed at the Belgian Institute for Space Aeronomy, Bruessels, Belgium (Fayt and Van Roozendaal, 2001). By the spectral calibration, a certain wavelength is assigned to each of the GOME-2 2B channels/pixels that cover the evaluation fit range (*wavelength-pixel-mapping*). The wavelength-pixel-mapping is usually non-linear due to limitations in the manufacturing process of a detector, but can be well described by a polynomial function. Furthermore, the wavelength dependent width of the slit function is determined in this process. The absorption cross-sections that are needed for the DOAS evaluation were calculated from high-resolution laboratory reference cross-sections by convolution with the slit function.

---

<sup>1</sup>Parts of this chapter have been published in Hörmann et al. (2012) and Bobrowski et al. (2010).

## 6.2. SO<sub>2</sub> standard retrieval (312.1–324 nm)

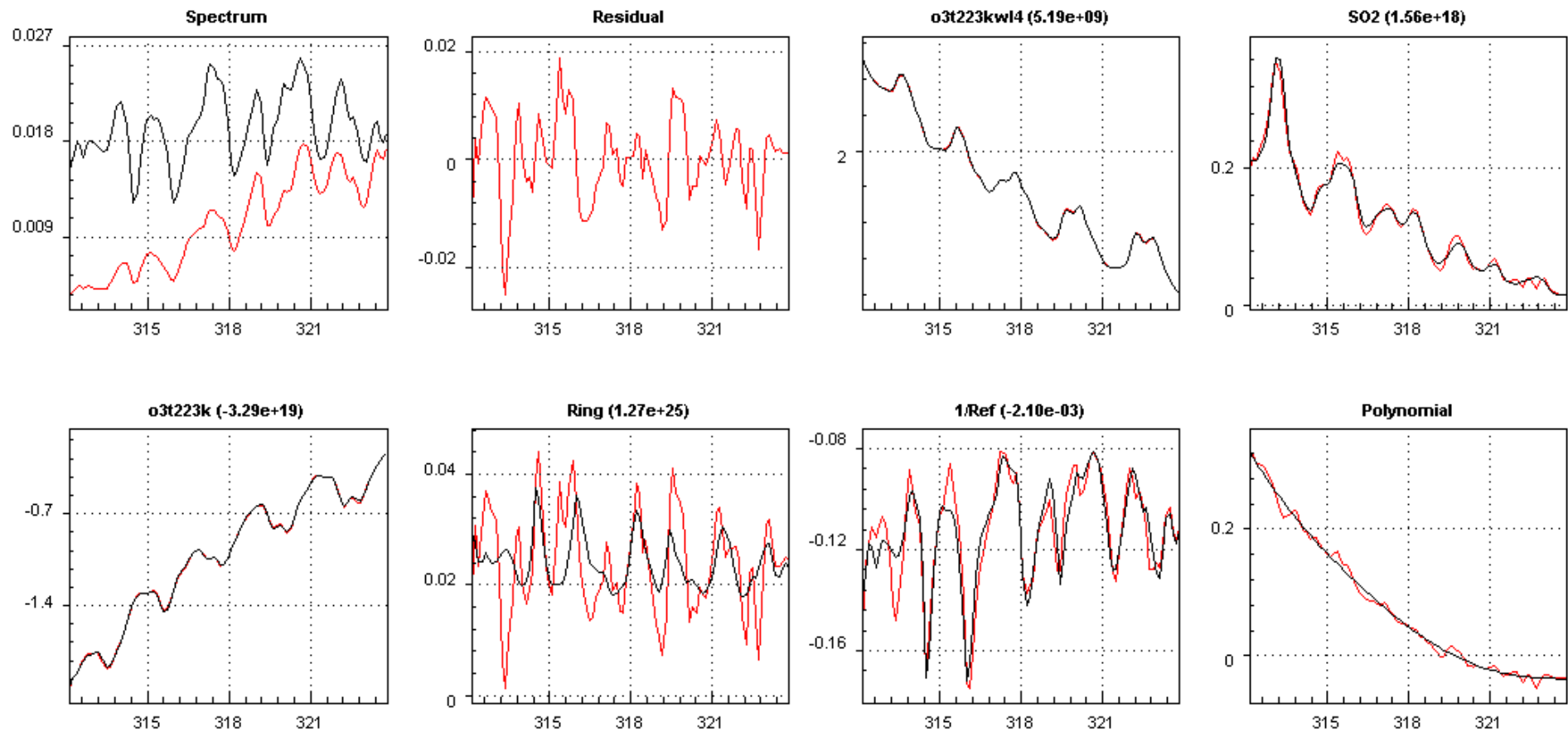
For the regular SO<sub>2</sub> DOAS retrieval, the wavelength range between 312.1–324 nm was used. Apart from a cross-section for SO<sub>2</sub> (Bogumil et al., 2003, 273 K), an O<sub>3</sub> cross section (Gür et al., 2005, 223 K), the individual SMR from GOME-2 for each day, a Ring spectrum (Wagner et al., 2009) and the inverse SMR spectrum were included into the fitting process (the inverse SMR spectrum is a first-order correction for possible spectrographic stray light). Since the length of the atmospheric light paths depends on wavelength (e.g. Van Roozendaal et al., 2006a; Puçite et al., 2010), not only the original O<sub>3</sub> absorption cross section, but also a second one (the original cross section scaled with a fourth order polynomial in wavelength) was included. A 5th order polynomial was applied to account for the broad-band structures. A small wavelength shift was allowed for the measured spectra in order to correct for changes in the wavelength-pixel mapping due to temperature variations of the detector or the Doppler shift.

Figure 6.1 shows example fit results for the SO<sub>2</sub> standard evaluation scheme during an eruption of Mt. Etna (Sicily) on 11 May 2008. The fit clearly identifies the SO<sub>2</sub> absorption features in the measured spectra (top right panel in Figure 6.1), yielding a SO<sub>2</sub> SCD of  $(1.56 \pm 0.04) \times 10^{18}$  molec/cm<sup>2</sup>. The residual (second panel in the top row of Figure 6.1), however, shows still some significant peaks ( $8.14 \times 10^{-3}$  RMS) that are not randomly distributed (as would be expected of white noise from a 'perfect' fit). Most of these structures originate from an imperfectly modelled Ring spectrum in this wavelength region. Nevertheless, the SO<sub>2</sub> standard evaluation fit range (SO<sub>2</sub> SR) is well suited for most observations of anthropogenic and minor volcanic SO<sub>2</sub> emissions in the GOME-2 data. This behaviour changes significantly if very high concentrations of SO<sub>2</sub> are present, e.g. during a major volcanic eruption. In Section 6.3, such cases will be investigated and discussed in more detail.

### 6.2.1. Sources of SO<sub>2</sub> in global daily maps

The DOAS evaluation yields SCDs for each satellite ground-pixel, representing the mean SCD in the area covered by a single measurement. For GOME-2, this area has usually an extent of  $40 \times 80$  km<sup>2</sup>. The corresponding VCDs are typically illustrated colorcoded on global maps, so that the global distribution of a specific trace gas becomes immediately visible. As the calculation of AMFs typically needs detailed informations on the atmospheric state (e.g. the vertical tracegas profile), geometrical VCDs (cf. Section 4.5) will be used in the following.

Commonly used projections of satellite data are just a 2-dimensional projection of the 3-dimensional surface of the geoid. The coordinates of the satellite pixel corners are converted into a orthogonal system, where the longitude is represented in x-direction and the latitude corresponds to the y-axis. Furthermore, all parallels and meridians are equidistant and orthogonal to each other, so that the distance for 1° in latitudinal direction equals the distance for 1° in longitude. However, such global maps provide neither equal-area properties nor are conformal.



**Figure 6.1.:** Example fit results for the GOME-2 SO<sub>2</sub> standard retrieval scheme in the fit range between 312.1–324 nm for one pixel in the volcanic plume during an eruption of Mt. Etna on 11 May 2008. The SO<sub>2</sub> absorption features are clearly visible from the DOAS fit (top right panel) and yield a SO<sub>2</sub> SCD of  $(1.56 \pm 0.04) \times 10^{18}$  molec/cm<sup>2</sup>. The structures in the residual spectrum show that the Ring effect (bottom second left spectrum) is not perfectly modelled by the fit.

# SO<sub>2</sub> VCD (geo.) 31.5.2008 [molec/cm<sup>2</sup>]

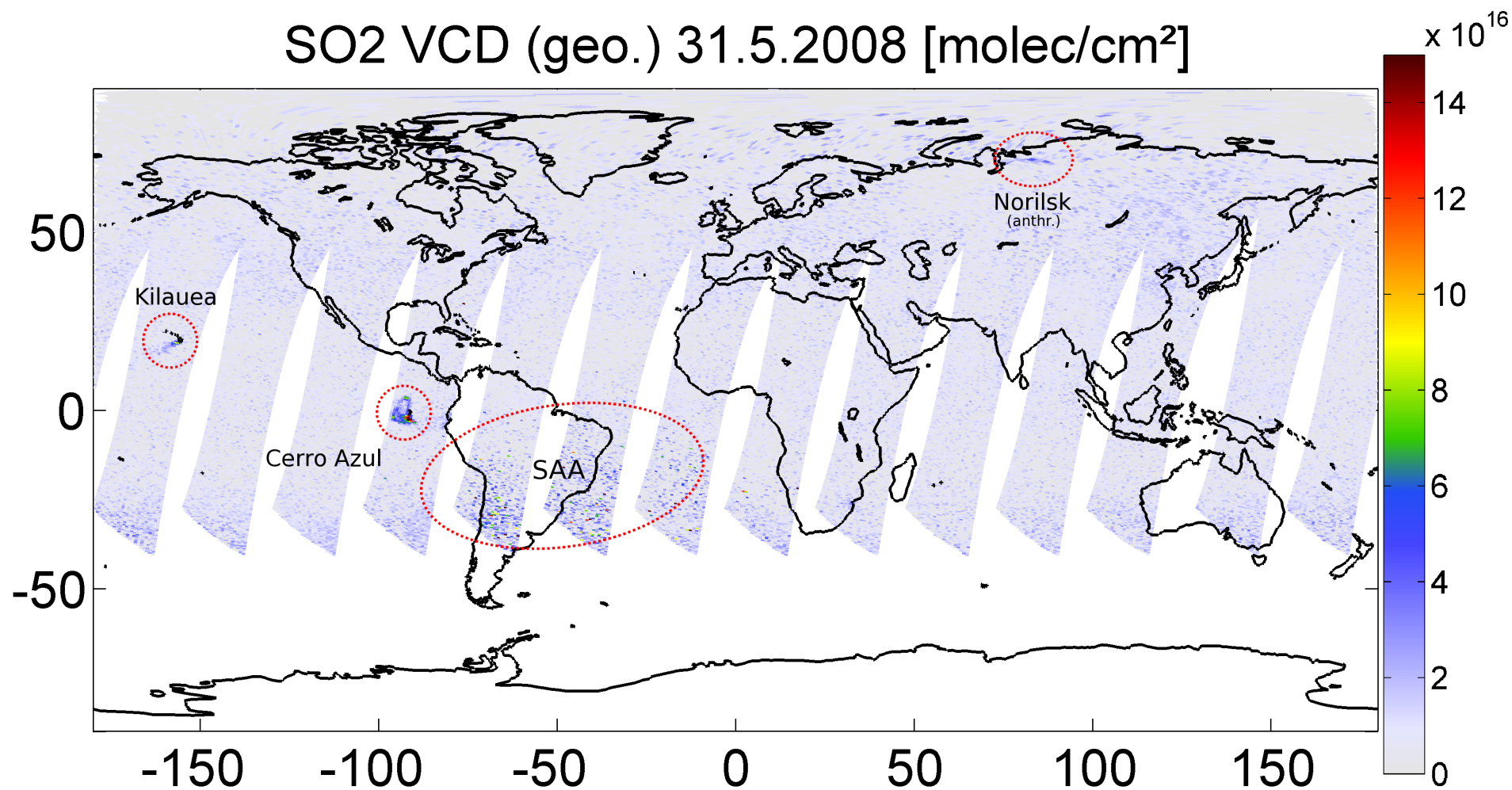


**Figure 6.2.:** Color-coded global projection of SO<sub>2</sub> VCDs retrieved from GOME-2 for 31 May 2008. Besides the volcanic SO<sub>2</sub> emissions of Kilauea (Hawaii) and Cerro Azul (Galapagos Islands), the influence of the South Atlantic Anomaly (SAA, see text) can be seen over large parts of the South American continent. Less clearly visible are anthropogenic emissions from copper smelters in Norilsk (Russia).

In Figure 6.2, an example for such a daily map is shown for the geometrical SO<sub>2</sub> VCDs that were calculated for the GOME-2 measurements on 31 May 2008. From the color-coded VCDs, the volcanic SO<sub>2</sub> plumes from the strongly degassing Kīlauea (Hawaii) as well as from an eruption of Cerro Azul (Galapagos Islands) can be clearly seen in the Western Hemisphere. Furthermore, some signs of anthropogenic SO<sub>2</sub> emissions can be identified over Norilsk in Northern Siberia (Russia), one of the world’s most polluted areas. The pollution originates from a huge industrial complex of the MMC Norilsk Nickel company, the world’s leading producer of nickel and palladium (Walter et al., 2012).

Although anthropogenic SO<sub>2</sub> emissions are the largest contribution to the global SO<sub>2</sub> budget (cf. Chapter 2.2.1), they can be seldomly detected from daily satellite measurements. Compared to volcanic emissions that are typically found at higher altitudes (due to the natural elevation of volcanoes in general or especially during explosive eruptions), the sensitivity to anthropogenic SO<sub>2</sub> located at the ground is lower. Furthermore, SO<sub>2</sub> emissions in the lower troposphere are more often shielded by clouds.

The example daily map (Figure 6.2) shows also the influence of the *South Atlantic Anomaly* (SAA) over large parts of the South American continent and the Atlantic Ocean. The SAA is caused by the inner *Van Allen* radiation belt of the Earth that approaches Earth’s surface down to a minimum altitude of  $\sim 200$  km in this area. Therefore, the GOME-2 instrument (as well as other satellites) is exposed to an increased amount of high-energy particles that can lead to erroneously signals if they hit the detector.

### 6.2.2. Global mean maps of SO<sub>2</sub>

Weak SO<sub>2</sub> emitters can often only be clearly identified from the GOME-2 data if all satellite measurements for a certain time period (several weeks, month or even years) are averaged in time. For this purpose, the individual satellite pixels from the daily measurements are projected on a regular grid (typically with a grid resolution of  $0.1^\circ \times 0.1^\circ$ ). While the background noise usually cancels out, constantly emitting sources of SO<sub>2</sub> may become visible from the averaged data. This includes in particular quiescent degassing volcanoes, but also huge industrial complexes consisting of coal plants as well as heavy metal smelters or emissions from oil refineries and even platforms.

However, some artefacts remain in such global mean maps, mostly because of the spectral interference between the SO<sub>2</sub> and ozone cross-sections. As both species show similarities in their absorption features, the presence of increased SCDs of O<sub>3</sub> in the mid-latitudes during the winter months leads to apparently increased SO<sub>2</sub> column densities in the DOAS analysis and therefore to an strong latitudinal-dependent positive offset. In Figure 6.3, the mean global SO<sub>2</sub> map for the data during the years 2007 and 2008 is shown, where this offset is clearly visible. Additionally, several SO<sub>2</sub> emitters that were not visible in the daily map (Figure 6.2) can now be identified (note the different scaling of the colorbar compared to Figure 6.2). Besides the anthropogenic emissions (e.g. over China, Norilsk, the South African Highveld or the Persian Gulf region), several small areas of clearly enhanced SO<sub>2</sub> VCDs indicate the

# SO<sub>2</sub> VCD 2007-2008 uncorrected [molec/cm<sup>2</sup>]

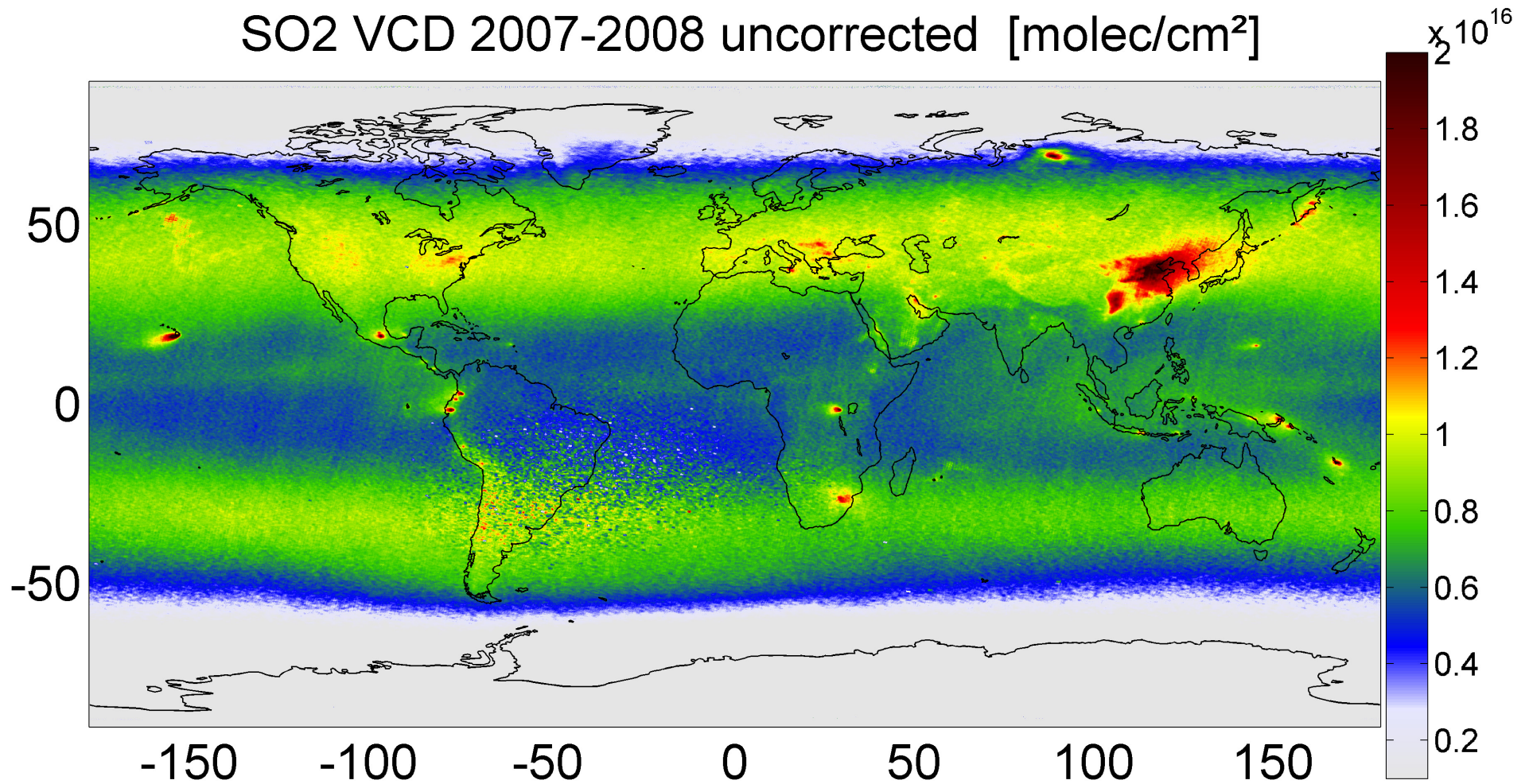


**Figure 6.3.:** Global mean map of the SO<sub>2</sub> VCD during the time period 2007 and 2008 without offset correction. Several anthropogenic and volcanic SO<sub>2</sub> sources are clearly visible. The data also shows a strong latitudinally varying offset due to the spectral interference with stratospheric ozone.

## SO<sub>2</sub> VCD 2007-2008 [molec/cm<sup>2</sup>]

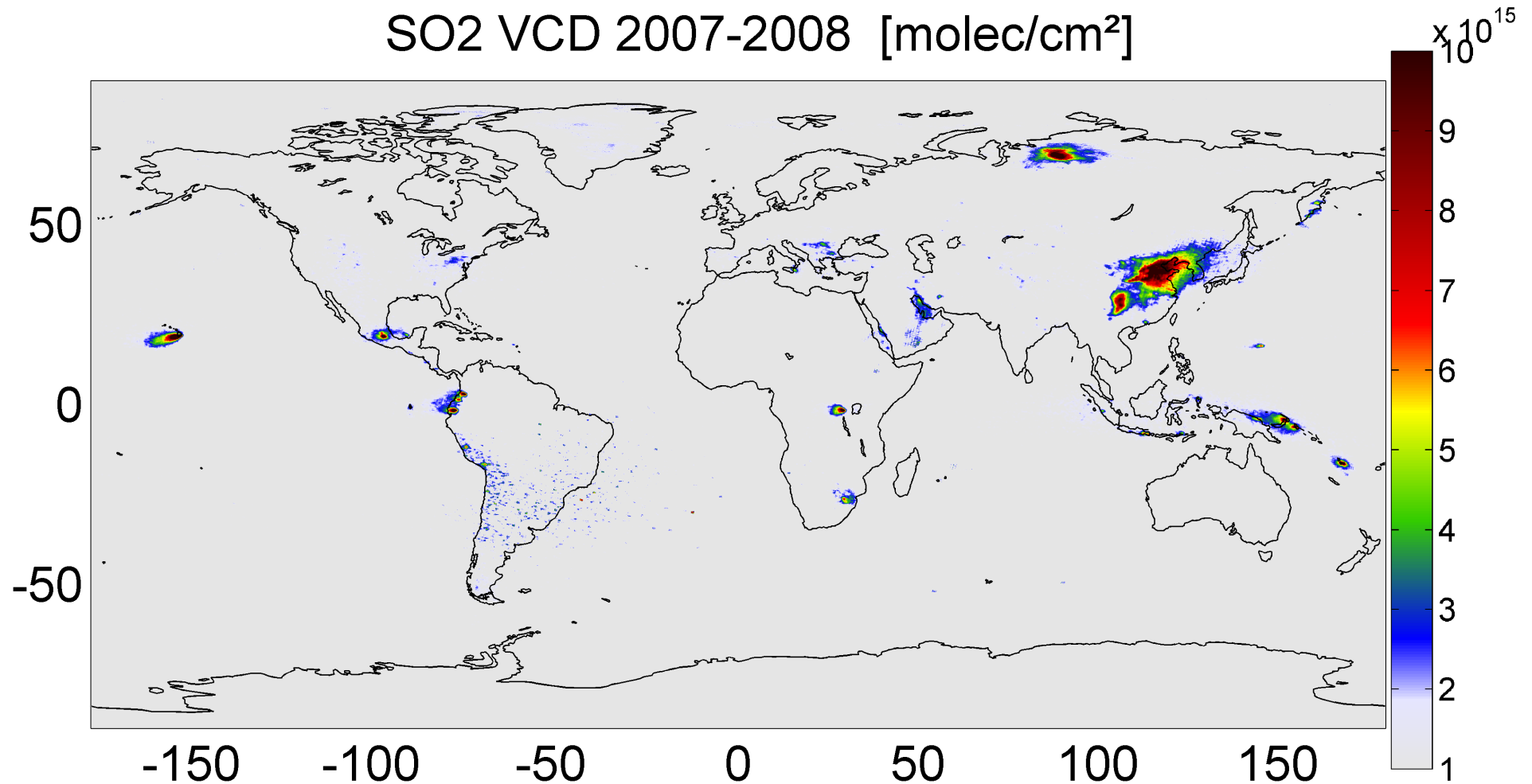


**Figure 6.4.:** Same as Figure 6.3 after applying the offset correction. The daily data has been corrected for interferences with ozone by subtracting the SO<sub>2</sub> VCD median for each gridrow (see text). Only very weak residual structures remain, mainly because of the imperfect treatment of the Ring effect over high and bright regions (e.g. Greenland). Note that the data during the Kasatochi eruption in August 2008 has been left out.

locations of highly active degassing volcanoes (e.g. on the Kamchatka Peninsula or the archipelago of Indonesia). In order to correct the satellite data for the offset that is mainly caused by spectral interference with ozone, the daily median for each latitudinal grid row ( $0.1^\circ$ ) was calculated and subsequently subtracted from each grid pixel. The offset corrected daily data was then averaged just in the same way as before. The corresponding offset corrected global map (Figure 6.4) shows that the artifacts in the mid-latitudes have been massively reduced. Nevertheless, some weak artefacts can be still seen over high and bright surfaces, probably due to the imperfect consideration of the Ring effect. The main SO<sub>2</sub> emitters are still clearly noticeable (please note, that the upper limit for the colorbar has been decreased to  $1 \times 10^{16}$  in comparison to the uncorrected map in Figure 6.3).

### 6.3. Alternative SO<sub>2</sub> evaluation schemes at larger wavelengths

The DOAS method is usually applied to weak absorbers with optical densities below about 0.05. However, for the evaluation of SO<sub>2</sub> in volcanic plumes in the standard wavelength region (cf. Section 6.2), optical densities can exceed unity when extraordinary SO<sub>2</sub> concentrations are present. Generally, the accuracy of passive DOAS measurements of volcanic SO<sub>2</sub> in this wavelength region is often largely dependent on the knowledge of the radiative transfer in and around the measured volcanic plume (Kern et al., 2010, 2012). The apparent SO<sub>2</sub> SCDs are therefore influenced due to the following reasons:

- Radiation is scattered in the atmosphere both, by air molecules (mostly Rayleigh scattering) and by aerosol particles. While aerosol scattering is only weakly dependent on the wavelength  $\lambda$  (approximately proportional to  $\lambda^{-1.3}$ ), Rayleigh scattering is proportional to  $\lambda^{-4}$ . This fact leads to a wavelength dependent mean free photon path in the atmosphere. Photons of shorter wavelengths travel significantly shorter mean paths between scattering events than photons of longer wavelengths (cf. Section 4.5). Thus, radiation of shorter wavelengths is more likely to be scattered between instrument and plume than radiation of longer wavelengths. Especially for long distances between instrument and plume (as it is the case for satellite instruments), evaluations at shorter wavelengths yield lower SO<sub>2</sub> SCDs than those performed at longer wavelengths. This effect has frequently been discussed in the satellite community since about a decade (e.g. Palmer et al., 2001; Richter and Burrows, 2002; Eskes and Boersma, 2003) and appropriate suggestions how to correct it have been made.
- Aside from the reduction of the apparent SO<sub>2</sub> SCD due to radiation dilution, multiple scattering inside the plume can also enhance the SO<sub>2</sub> SCD. Depending on the amount and properties of aerosols in the plume, the enhancement of the effective photon path due to multiple scattering can be of the same order of magnitude as the above described dilution. Therefore, the measured SCD can be either over- or underestimated in any particular measurement.

- In cases of strong absorption, the observed scattered light has only penetrated the outermost layers of the SO<sub>2</sub> plume. In extreme cases, the sensitivity for the whole plume can become essentially zero (AMF  $\sim 0$ ) leading to a strong underestimation of the true SCD, because at the wavelength where the SO<sub>2</sub> absorptions are observed the plume is completely dark. In reality, this effect is, however, typically reduced due to the presence of aerosols, and a small fraction of the observed light is scattered by aerosols inside the plume. Then the SO<sub>2</sub> absorption signal is still weak, but not zero.

Previous attempts have been made to correct for the non-linearity of SO<sub>2</sub> absorptions as a function of wavelength (e.g. Yang et al., 2007), especially in the case of rather high SO<sub>2</sub> concentrations. The AMF in the standard fit range ( $< 320$  nm) strongly depends on wavelength. In order to account for these effects, an iterative model approach can be applied (cf. Yang et al., 2009; Richter et al., 2009). As such iterative model calculations are rather time intensive, we follow a different approach by switching to a fit window at longer wavelength where the response of the measured SO<sub>2</sub> absorption to enhanced SO<sub>2</sub> concentrations is more linear. As demonstrated below, this is a sufficient and particularly fast method to correct for the occurring non-linear effects (e.g. Yang et al., 2007).

In the following we will focus on two alternative wavelength regions that have been investigated for the SO<sub>2</sub> evaluation in the scope of this thesis and have not been used by all hitherto reported UV-spectroscopic SO<sub>2</sub> measurements, as the absorptions are quite low in this fit range:

1. The wavelength region between 326.5–335.3 nm, where the absorption lines are caused due to the  $A^1B_1 \leftarrow X^1A_1$  transition.
2. The wavelength region between 360–390 nm, where the relatively weak system of absorption lines are caused by the spin-forbidden  $a^3B_2 \leftarrow X^1A_1$  transition of the SO<sub>2</sub> molecule.

Figure 6.5 shows the absolute SO<sub>2</sub> cross-section from Bogumil et al. (2003) and the evaluation wavelength ranges that have been used within this thesis. The absorption cross-section of SO<sub>2</sub> for the alternative wavelength regions is up to more than two orders of magnitude lower than for the SR, so that the above mentioned problems of non-linearity are avoided. While the weaker absorptions also lead to a lower SO<sub>2</sub> sensitivity, this effect is partly compensated by less Rayleigh scattering (dilution effect) and a stronger light intensity at longer wavelengths, which leads to considerably better signal/noise ratios. However, it should be once more emphasized that the SO<sub>2</sub> SR is usually the best suited evaluation scheme for most satellite observations in the UV due to its high sensitivity for low SO<sub>2</sub> concentrations like they are present during passive volcanic degassing, minor eruptions or from anthropogenic emissions.

In order to demonstrate the advantages for the alternative retrievals during major volcanic eruptions, we will compare the standard fit range (312.1–324 nm; in the following referred to as *SO<sub>2</sub> SR*) to both alternative evaluation fit ranges (326.5–335.3 nm and 360–390 nm, in the following referred to as *SO<sub>2</sub> AR<sub>1</sub>* and *SO<sub>2</sub> AR<sub>2</sub>*) in

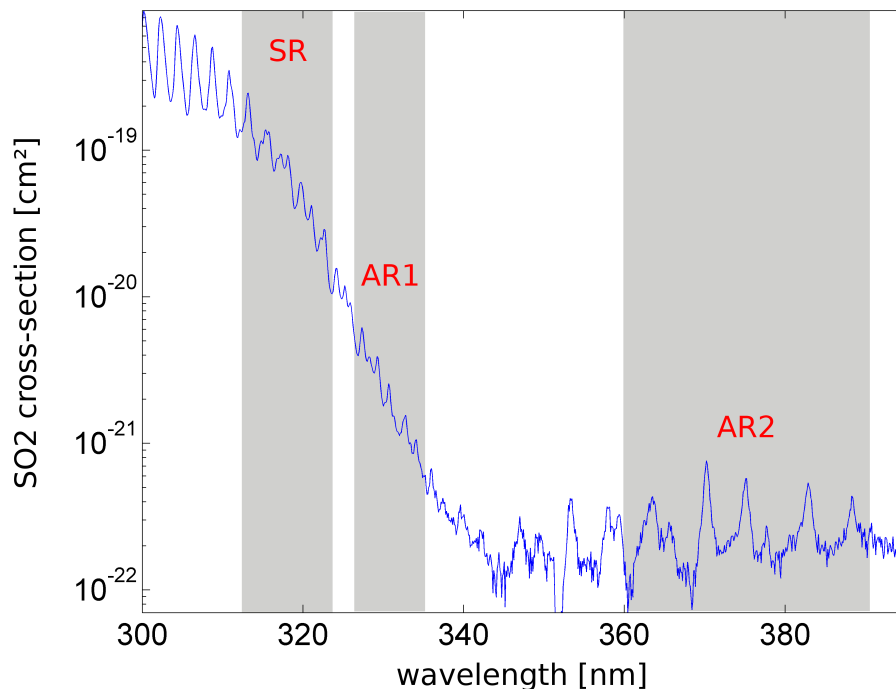


**Figure 6.5.:** Absolute SO<sub>2</sub> cross-section in the wavelength range from 300–395 nm for 273K from Bogumil et al. (2003). Please note the logarithmic scale. The highlighted intervals indicate the evaluation wavelength ranges that have been used for the SO<sub>2</sub> SR (312.1–324 nm), AR<sub>1</sub> (326.5–335.3 nm) and AR<sub>2</sub> (360–390 nm).

the next two sections by an example of GOME-2 measurements during the Kasatochi eruption on 8 August 2008. The comparison of the SR to the AR<sub>2</sub> was already published in Bobrowski et al. (2010), where additionally ground-based DOAS measurements have been investigated for this evaluation scheme.

### 6.3.1. SO<sub>2</sub> standard retrieval during major volcanic eruptions

In order to demonstrate the non-linear effects that may occur in the case of major volcanic eruptions where very high SO<sub>2</sub> concentrations are present, Figure 6.6 shows example fit results for the SO<sub>2</sub> standard evaluation scheme during the volcanic eruption of the Kasatochi volcano (Aleutian Islands, Alaska) on 8 August 2008. The SO<sub>2</sub> absorption features are well identified in the measured spectra by the fit (top right box in Fig. 6.1) and yield a SO<sub>2</sub> SCD of  $(2.03 \pm 0.07) \times 10^{18}$  molec/cm<sup>2</sup>, but compared to the previous shown example for Mt. Etna (cf. Figure 6.1), the fit is not accurately matching the single absorption peaks. Although the Ring spectrum is captured this time much better, the residual (second box in the top row of Fig. 6.1) shows strong and regular structures ( $4.98 \times 10^{-2}$  RMS) that are clearly caused by the SO<sub>2</sub> discrepancies, i.e. by the wavelength dependence of the SO<sub>2</sub> AMF (cf. Figure 6.12).

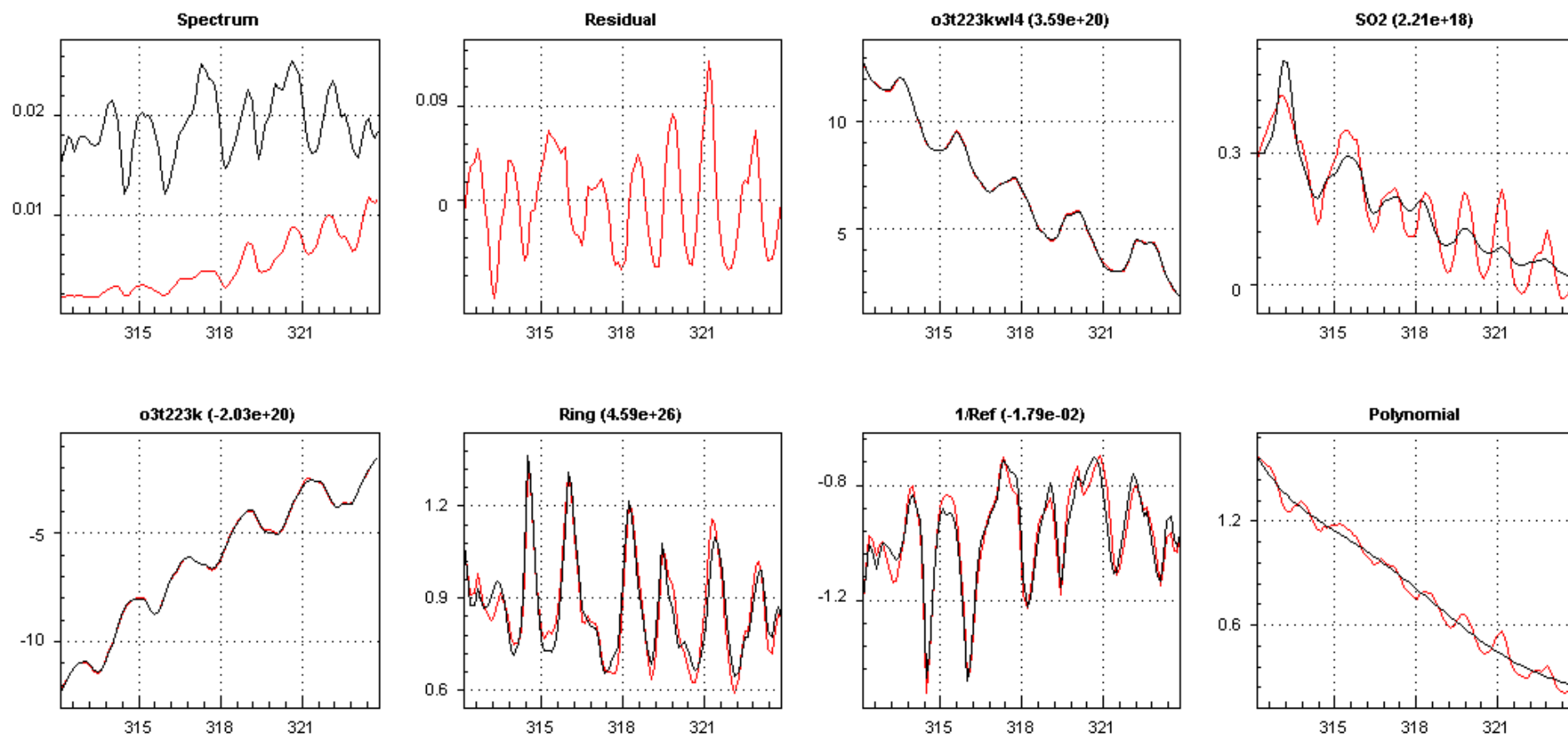


**Figure 6.6.:** Example fit results for the GOME-2 SO<sub>2</sub> standard retrieval scheme in the evaluation fit range between 312.1–324 nm for one pixel in the volcanic plume during the Kasatochi eruption on 8 August 2008. The SO<sub>2</sub> absorption features are clearly visible from the DOAS fit (top right) and yield a SO<sub>2</sub> SCD of  $(2.21 \pm 0.28) \times 10^{18}$  molec/cm<sup>2</sup>.

### 6.3.2. SO<sub>2</sub> alternative retrieval (326.5–335.3 nm) - AR<sub>1</sub>

For the SO<sub>2</sub> alternative retrieval in the wavelength region from 326.5–335.3 nm (SO<sub>2</sub> AR<sub>1</sub>), two O<sub>3</sub> cross sections (Gür et al., 2005, 223 K and 243 K) were used, as well as SO<sub>2</sub> (Bogumil et al., 2003, 273 K), the SMR, two Ring spectra (following the suggestions in Wagner et al. (2009) and both calculated and normalized using the DOASIS software version 3.2 by Kraus (2004)), an inverse spectrum (calculated from the SMR) and a 5th order polynomial.

Figure 6.7 shows the fit results for the same satellite measurement in the volcanic plume of Kasatochi as in Figure 6.6 for the SO<sub>2</sub> SR. The results show a significantly higher SO<sub>2</sub> SCD of  $(2.38 \pm 0.07) \times 10^{19}$  molec/cm<sup>2</sup> and are thus exceeding the value of the standard fit range by a factor of about 11. Additionally, in contrast to Figure 6.1, the SO<sub>2</sub> absorption features are much better reproduced by the DOAS fit, indicating that the non-linear effects that were caused by the very strong SO<sub>2</sub> absorptions have been significantly reduced in the alternative fit window. The now quite random looking residual structures are up to 30 times smaller than those obtained in the short wavelength range ( $1.69 \times 10^{-3}$  RMS).

### 6.3.3. SO<sub>2</sub> alternative retrieval (360–390 nm) - AR<sub>2</sub>

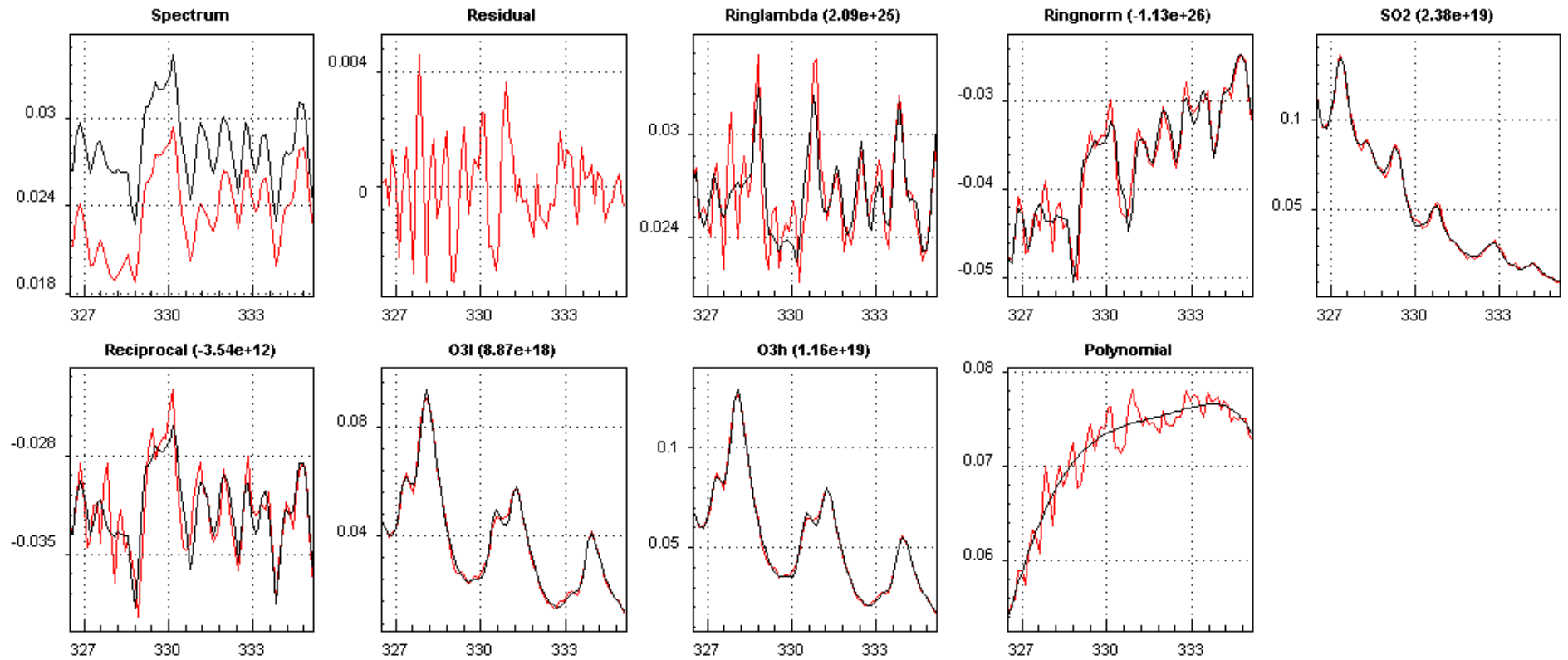
For the SO<sub>2</sub> retrieval in the second alternative wavelength region from 360–390 nm (SO<sub>2</sub> AR<sub>2</sub>) a cross-section for SO<sub>2</sub> (Bogumil et al., 2003, 273 K), an O<sub>3</sub> cross section (Gür et al., 2005, 223 K), O<sub>4</sub> (Greenblatt et al., 1997, 298 K), NO<sub>2</sub> (Vandaele et al., 1998, 294 K), the individual SMR from GOME-2 for each day (containing no atmospheric absorptions), a Ring spectrum and again the inverse SMR spectrum were included into the fitting process.

Figure 6.8 shows the associated fit results for the Kasatochi measurement on the 8 August 2008 (cf. Figure 6.6 and 6.7). The SO<sub>2</sub> SCD is slightly higher than the one from the SO<sub>2</sub> AR<sub>1</sub> with  $(2.81 \pm 0.11) \times 10^{19}$  molec/cm<sup>2</sup> and therefore differs from the SO<sub>2</sub> AR<sub>1</sub> value just by 18%, but still exceeding the SO<sub>2</sub> SR value by a factor of almost 13. The even more random looking residual structures are almost 35 times smaller than those obtained in the short wavelength range ( $1.43 \times 10^{-3}$  RMS). Overall, the SO<sub>2</sub> AR<sub>2</sub> seems to be capable to clearly detect SO<sub>2</sub> during major volcanic eruptions, but without being influenced by strong absorptions.

Please note, that the SO<sub>2</sub> AR<sub>2</sub> covers an almost 3 times larger wavelength range than the SO<sub>2</sub> SR and AR<sub>1</sub>, which might have an influence on the visual interpretation of the results (e.g. the residuum of the AR<sub>2</sub> seems to be somewhat smoother than the one from the AR<sub>1</sub>, although they are of similar magnitude).

### 6.3.4. Implications of alternative SO<sub>2</sub> retrievals

The evaluation of GOME-2 spectra via the two alternative fit ranges AR<sub>1</sub> and AR<sub>2</sub> leads to significantly enhanced SO<sub>2</sub> SCDs in comparison to the SR during major volcanic eruptions with very high SO<sub>2</sub> concentrations. Due to the weaker absorptions,



**Figure 6.7.:** Example fit results for the GOME-2 SO<sub>2</sub> alternative retrieval scheme in the evaluation fit range between 326.5–335.3 nm (SO<sub>2</sub> AR<sub>1</sub>) for one pixel in the volcanic plume during the Kasatochi eruption on 8 August 2008 (cf. Figure 6.6). The SO<sub>2</sub> SCD is significantly higher than for the SO<sub>2</sub> SR and yield a 11 times higher SO<sub>2</sub> SCD of  $(2.38 \pm 0.07) \times 10^{19}$  molec/cm<sup>2</sup> due to prevention of non-linearities effects.

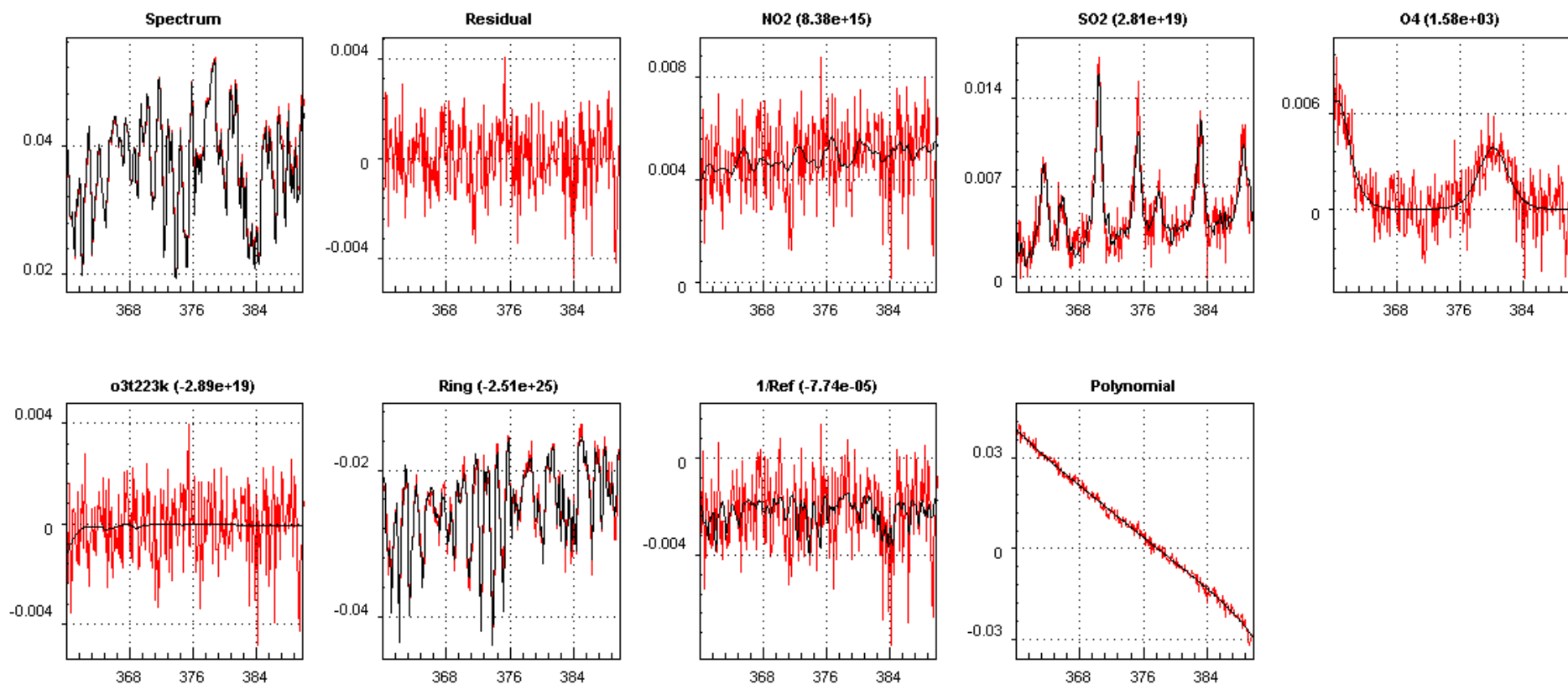


**Figure 6.8.:** Example fit results for the GOME-2  $\text{SO}_2$  alternative retrieval scheme in the evaluation fit range between 360–390 nm ( $\text{SO}_2$   $\text{AR}_2$ ) for one pixel in the volcanic plume during the Kasatochi eruption on 8 August 2008 (cf. Figure 6.6 and 6.7). Like for the  $\text{AR}_1$ , the  $\text{SO}_2$  SCD is significantly higher than for the  $\text{SO}_2$  SR and yield a 13 times higher  $\text{SO}_2$  SCD of  $(2.81 \pm 0.11) \times 10^{19}$  molec/ $\text{cm}^2$  due to prevention of non-linearities effects.

the non-linear saturation effects that are caused by strong absorption in the SO<sub>2</sub> SR can be prevented. This has extensive consequences to the general view on a volcanic plume during such violent eruptions:

Figure 6.9 shows the GOME-2 measurements of the Kasatochi plume on the 8 August 2008 for all three previously discussed SO<sub>2</sub> fit ranges. For all evaluation schemes, the plume can be clearly identified from the measurements. As it was already indicated by the previous fit example, the AR<sub>1</sub> and AR<sub>2</sub> (Figure 6.9 b and c) lead to SO<sub>2</sub> VCDs that are more than one magnitude higher than for the SR (Figure 6.9 a). However, some further interesting discrepancies remain. While the highest SO<sub>2</sub> columns are measured in the north-east and south-west regions of the plume when using the SR, the maximum SO<sub>2</sub> column is found in the south-east when using one of the SO<sub>2</sub> AR (the maximum VCDs are indicated by white stars inside Figure 6.9 a-c). This effect is likely to be a result of the decreased sensitivity for high SO<sub>2</sub> columns that occurs in the SR when the SO<sub>2</sub> absorption becomes so strong that radiation can no longer penetrate the volcanic plume. In the following, we will have a closer look to the influence of the radiative transport on the Kasatochi plume by simulating the situation in the full spherical Monte Carlo radiative transfer model McArtim (cf. Section 4.6).

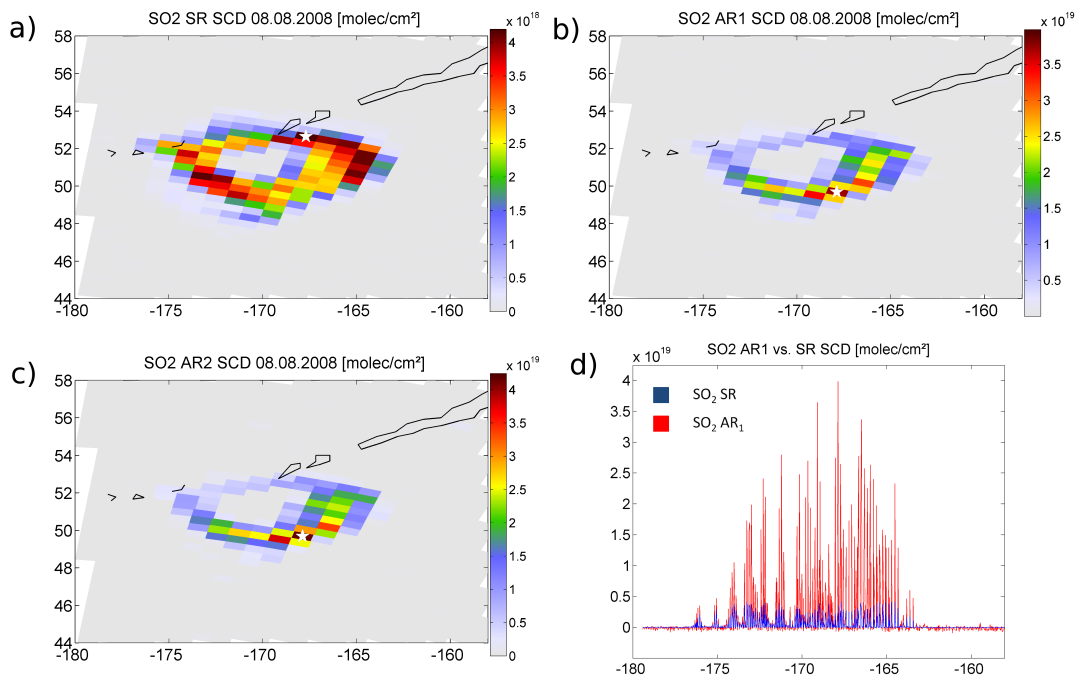


**Figure 6.9.:** SO<sub>2</sub> plume after the Kasatochi eruption on 8 August 2008 as seen by GOME-2. The pixels with the maximum SCDs are indicated by a white star: a) While the SO<sub>2</sub> SR (312.1–324 nm) shows the maximum SCD at the north-eastern part of the plume, the b) AR<sub>1</sub> and c) AR<sub>2</sub> show comparable high SO<sub>2</sub> SCDs, but about one magnitude larger than the SR. Furthermore, the location of the maximum has shifted to the southern plume region. The differences between the SR and AR<sub>1</sub> can also be clearly seen in d).

### 6.3.5. RTM comparison study for SO<sub>2</sub> SR and AR<sub>2</sub>

The SO<sub>2</sub> SCDs for the SR and both alternative retrievals strongly differ in magnitude. While for relatively low SCDs ( $< 1 \times 10^{18}$  molec/cm<sup>2</sup>) an almost linear relationship is found for the SR in comparison to the AR<sub>1</sub> and AR<sub>2</sub> (cf. Figure 6.10 a and b), large differences occur for high SCDs (derived from the alternative retrievals). For very large SCDs in the AR<sub>1</sub> and AR<sub>2</sub> ( $> 1.5 \times 10^{19}$  molec/cm<sup>2</sup>), the SR SCDs even seem to decrease. As indicated by the scattering around zero, the AR<sub>1</sub> seems to be capable to retrieve the SO<sub>2</sub> SCDs at a lower noise level than the AR<sub>2</sub>, probably because of the stronger absorptions in this wavelength region. Additionally, the AR<sub>2</sub> SCDs suffer from a small negative offset. However, when the SCDs for both alternative retrievals are compared to each other (Figure 6.10 c), only weak differences show up.

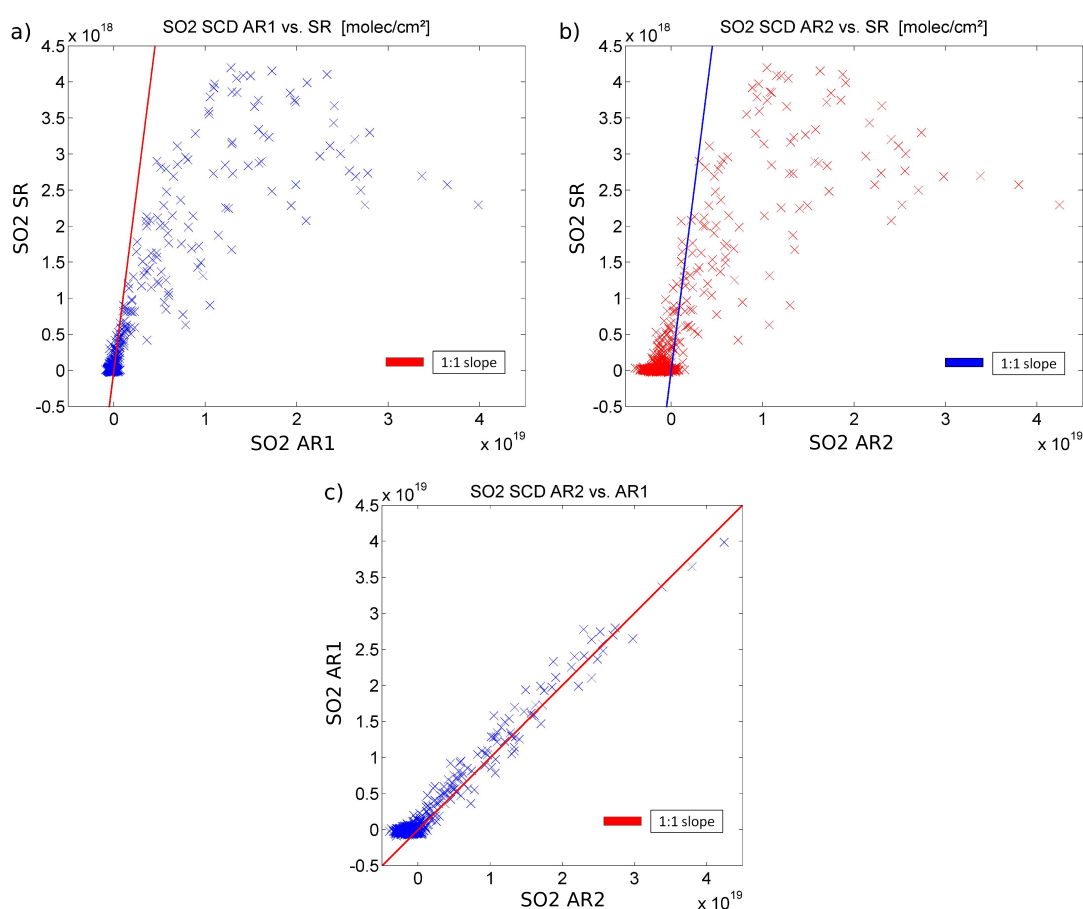


**Figure 6.10.:** Intercomparison of the SO<sub>2</sub> SCDs for the Kasatochi plume on 8 August 2008 for a) the SR vs. the AR<sub>1</sub>, b) the SR vs. the AR<sub>2</sub> and c) the AR<sub>1</sub> vs. the AR<sub>2</sub>. Large differences occur for the alternative retrievals in comparison to the SR. For very large SO<sub>2</sub> SCDs ( $> 1.5 \times 10^{19}$  molec/cm<sup>2</sup>), the SR SCD even decrease. For low SCDs ( $< 1 \times 10^{18}$  molec/cm<sup>2</sup>) a linear relationship is found between SR and the AR<sub>1,2</sub> (a,b). In contrast, the SCDs for AR<sub>1</sub> and AR<sub>2</sub> show no large differences (c).

In order to further investigate this behaviour, the satellite measurements were simulated by the use of the radiative transfer model McArtim (Deutschmann et al., 2011). For the sake of simplicity, only the SO<sub>2</sub> SR and AR<sub>2</sub> were simulated, as the results for the AR<sub>1</sub> seem to indicate no substantial differences compared to the ones from the AR<sub>2</sub>. The simulations were conducted with representative parameters for the GOME-2 measurements with a SZA of 50° and a nadir viewing angle of -90°. The layer of enhanced SO<sub>2</sub> concentrations was assumed to be between 10 and 11 km as suggested by Theys et al. (2009), with constant SO<sub>2</sub> concentration within this layer. Below the SO<sub>2</sub> layer, a cloud layer extending from 5 to 6 km (optical density: 20, single scattering albedo: 1, asymmetry parameter: 0.85) was included in the simulations.

Two basic model runs were performed:

1. Without the presence of volcanic aerosols
2. Including aerosols within the SO<sub>2</sub> layer (aerosol optical depth: 3, asymmetry parameter: 0.68, single scattering albedo: 0.9)

For both runs, the SO<sub>2</sub> concentration was varied from zero to  $5 \times 10^{14}$  molec/cm<sup>3</sup> and the corresponding SO<sub>2</sub> SCDs were calculated for two wavelength that are representative for both retrievals (315 nm and 375 nm). The results are presented in Figure 6.11, where the modelled SO<sub>2</sub> SCDs for 315 nm are plotted versus those at 375 nm. In addition to the modelled SO<sub>2</sub> SCDs, also the measurements for 8 August 2008 are included in Figure 6.11. Like in the measured data, a linear relationship between the

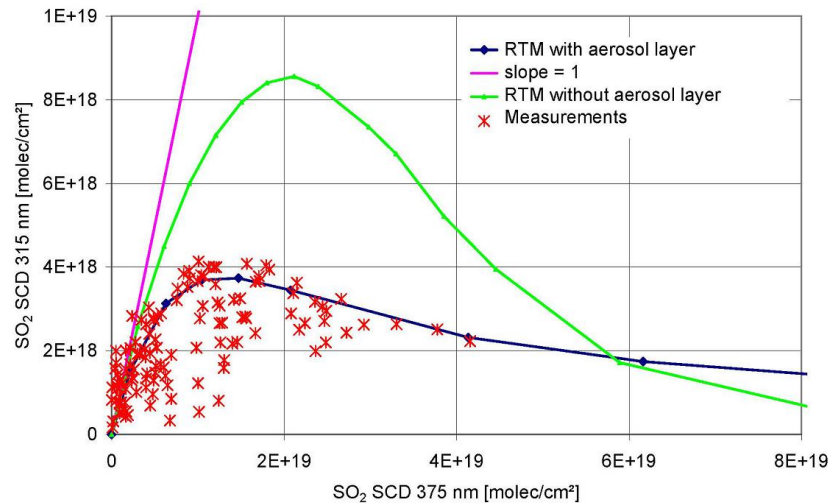


**Figure 6.11.:** Simulated SO<sub>2</sub> SCDs for 315 nm versus SO<sub>2</sub> SCDs at 375 nm for satellite remote sensing of the Kasatochi SO<sub>2</sub> plume on 8 August 2008 for two cases: without aerosols or with aerosol inside the plume (optical depth of 3). In addition to the modelled SO<sub>2</sub> SCDs, also the GOME-2 measurements are included in the figure. Only if aerosols are present in the plume, simulations and measurements are in agreement.

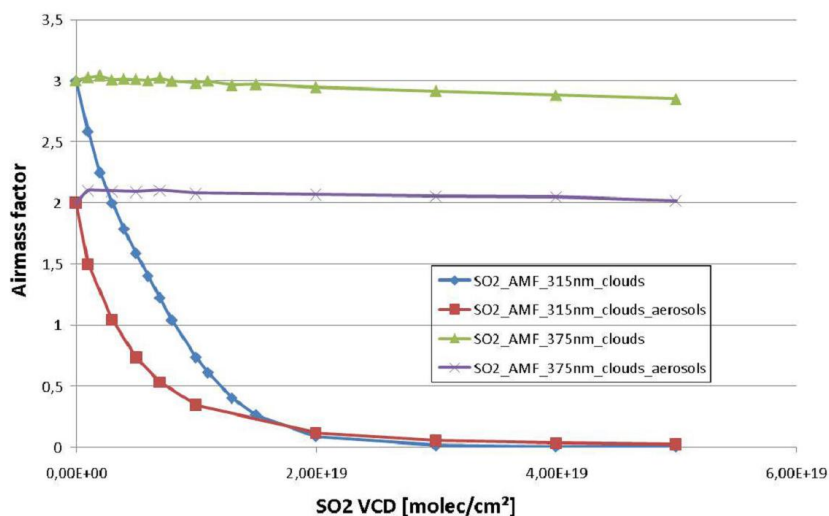


**Figure 6.12.:** AMF dependency on the SO<sub>2</sub> VCD, wavelength and aerosols. While the AMF for the SO<sub>2</sub> SR rapidly decrease for large SO<sub>2</sub> VCDs, it almost remains constant for the long wave UV range. In the presence of aerosols, the reduced sensitivity is less pronounced for very high SO<sub>2</sub> loads ( $> 2 \times 10^{19}$  molec/cm<sup>2</sup>), because more light is scattered back by the aerosol particles to the satellite instrument from the layer of enhanced SO<sub>2</sub>.

SO<sub>2</sub> SCDs for both wavelengths is only found for rather small SO<sub>2</sub> concentrations (about  $< 1 \times 10^{13}$  molec/cm<sup>3</sup> in both model runs, corresponding to a SCD of about  $2.5 \times 10^{18}$  molec/cm<sup>2</sup>). For higher concentrations, the SO<sub>2</sub> SCDs for 315 nm increase much slower compared to those for 375 nm and eventually decrease if the SO<sub>2</sub> concentration is further increased. This is a result of the very strong light absorption caused by SO<sub>2</sub> inside the volcanic plume. If aerosols are present, this effect is less pronounced (and for very high SO<sub>2</sub> concentrations even higher SO<sub>2</sub> SCDs for 315 nm are found compared to the non-aerosol case), because more light is scattered back by the aerosol particles to the satellite instrument from the layer of enhanced SO<sub>2</sub>.

The comparison with the measured SO<sub>2</sub> SCDs clearly indicates that it is not possible to describe the satellite observations from 8 August 2008 without aerosols present in the volcanic plume. Good agreement for the upper bound of measured SO<sub>2</sub> SCDs for 315 nm is found for an assumed aerosol optical depth of about 3. The scatter of the measured data indicates that the aerosol load was different (and mostly higher than 3) in different parts of the observed plume.

Additionally, Figure 6.12 shows the strong dependency of the AMF on the SO<sub>2</sub> VCD for the different wavelengths. While the AMF for the SO<sub>2</sub> SR range rapidly decrease for large SO<sub>2</sub> VCDs, it almost remains constant for the SO<sub>2</sub> AR<sub>2</sub>. The SO<sub>2</sub> SR has the general advantage of a much higher sensitivity for weakly enhanced SO<sub>2</sub> SCDs in volcanic plumes during degassing phases or minor eruptions. However, for major eruptions, where very high SO<sub>2</sub> concentrations are likely to be present in a volcanic plume, the non-linearities in the DOAS retrieval can be clearly overcome by the SO<sub>2</sub> AR<sub>1</sub> and AR<sub>2</sub>. To combine the advantages of different retrievals, the results from the

SR and  $AR_1$  were used for a *combined*  $SO_2$  product in the scope of the systematic extraction of volcanic plumes from the GOME-2 dataset in the time period between January 2007–June 2011 (cf. Chapter 8).

## 6.4. BrO retrieval

The BrO retrieval that is used in the scope of this thesis was developed by H. Sihler from MPIC Mainz. It is usually used to investigate the abundance of BrO during the Arctic/Antarctic spring. Enhanced BrO amounts are observed in connection with *ozone depletion events* (ODE), since the BrO formation mechanism leads to extensive destruction of  $O_3$  (McConnell et al., 1992; Platt and Lehrer, 1996; Simpson et al., 2007). The related chemistry is similar to the formation process of BrO in volcanic plumes (cf. Section 2.3).

For the DOAS retrieval, the wavelength range from 336–360 nm was used, which contains 4 adjacent absorption bands (Sihler et al., 2012). In addition to the BrO cross section from Wilmouth et al. (1999, 228 K), ozone cross sections at 223 and 243 K Gür et al. (2005),  $O_4$  (Greenblatt et al., 1997),  $NO_2$  (Vandaele et al., 2002, 220 K), OClO (Bogumil et al., 2003, 293 K) and  $SO_2$  (Bogumil et al., 2003, 273 K) were included in the retrieval. As in the case of the  $SO_2$  fit, the SMR, a Ring spectrum, an inverse spectrum (calculated from the SMR) and a 5th order polynomial were included.

Figure 6.13 and 6.14 show the fit results for the BrO fit for the same measurement during the Kasatochi eruption as for the previous introduced  $SO_2$  fits in Section 6.3 (cf. Figure 6.6, 6.7 and 6.8). The strongly enhanced BrO abundance in the volcanic plume can be clearly identified by the DOAS fit with a BrO SCD of  $(3.27 \pm 0.29) \times 10^{14}$  molec/cm<sup>2</sup>. Even the strong  $SO_2$  absorptions are still visible in this wavelength

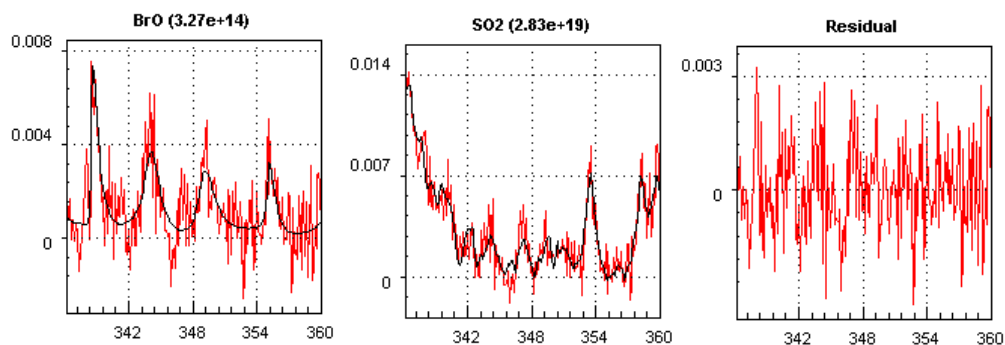


**Figure 6.13.:** Part 1 of an example fit results for the BrO retrieval in the fit range between 336–360 nm for one pixel in the volcanic plume of Kasatochi on 8 August 2008 (cf. Figure 6.6, 6.7 and 6.8). Enhanced BrO concentrations are clearly detected by the DOAS fit with a SCD of  $(3.27 \pm 0.29) \times 10^{14}$  molec/cm<sup>2</sup>. Interestingly, also  $SO_2$  can be detected in this fit range with comparable results as for the  $SO_2$   $AR_1$  and  $AR_2$  (cf. Figure 6.7 and 6.8)

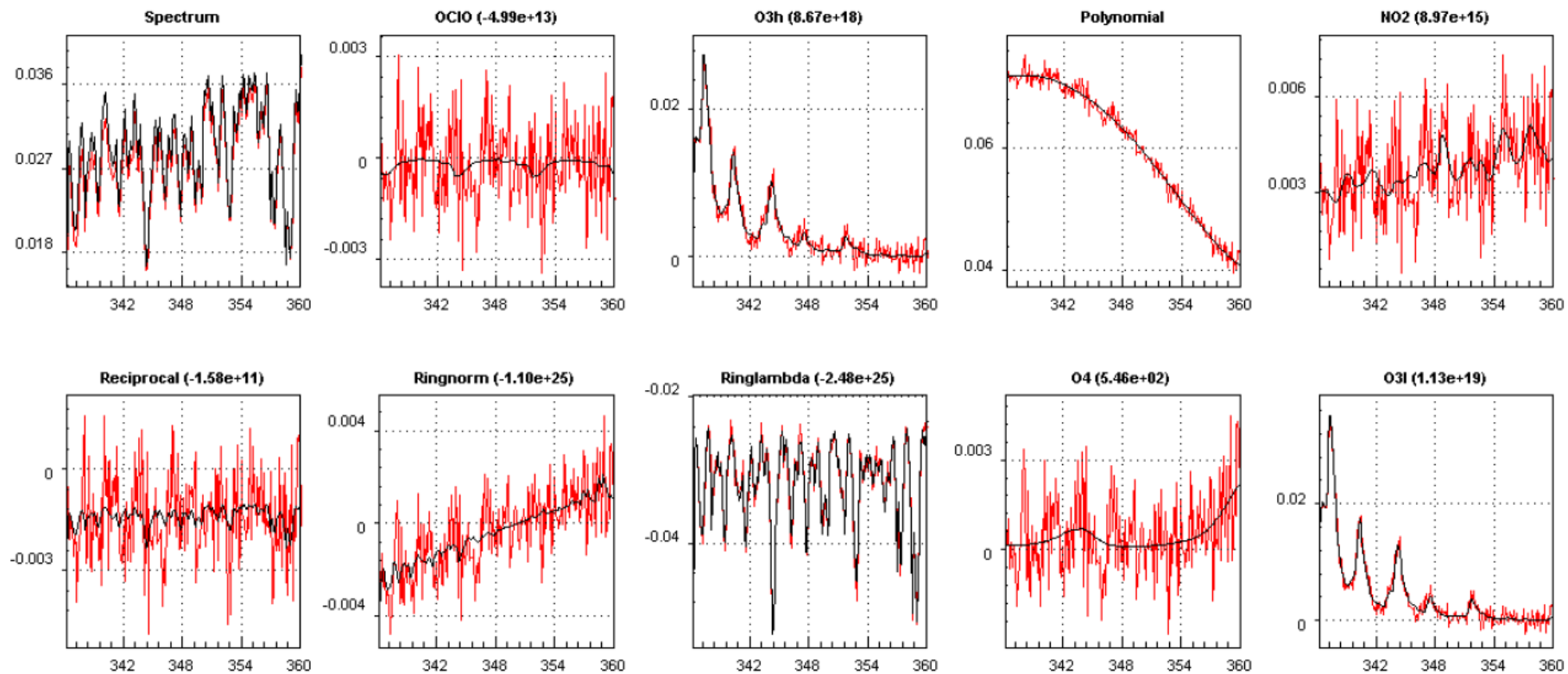


**Figure 6.14.:** Part 2 for the GOME-2 BrO retrieval scheme in the evaluation fit range between 336–360 nm for one pixel in the volcanic plume during the Kasatochi eruption on 8 August 2008.

region and in good agreement with the results from the alternative  $\text{SO}_2$  retrievals  $\text{AR}_1$  and  $\text{AR}_2$  with  $(2.83 \pm 0.22) \times 10^{19}$  molec/cm<sup>2</sup>, although the absorption features are not as incisive as for the other wavelength regions. The mostly random residual ( $1.28 \times 10^{-3}$  RMS) further indicates the quality of the fit.

In Chapter 9 and 10, the BrO fit results will be used for a systematic investigation of the GOME-2 dataset for the abundance of volcanic BrO.

#### 6.4.1. Daily and mean global maps of BrO

If the daily BrO VCDs (geo.) are projected on a global map (cf. Section 6.2.1), usually no distinct sources can be seen. Figure 6.15 shows the BrO VCDs for the 31 May in 2008 (cf. Figure 6.2 for the  $\text{SO}_2$  data of the same day). The enhanced BrO VCDs that result from the *bromine explosion* (cf. Section 2.3.2) can be seen over the Arctic region. For the northern mid-latitudes, some patches of enhanced BrO VCDs are mostly caused by an imperfect fit of the Ring spectra over clouded scenes, but also from spectral interference with formaldehyde over strongly polluted areas (Theys et al., 2011). As the measured sunlight has traversed also the stratosphere, the measurements contain also the absorptions from stratospheric BrO, whose distribution depends systematically on latitude but to a smaller degree also on longitude.

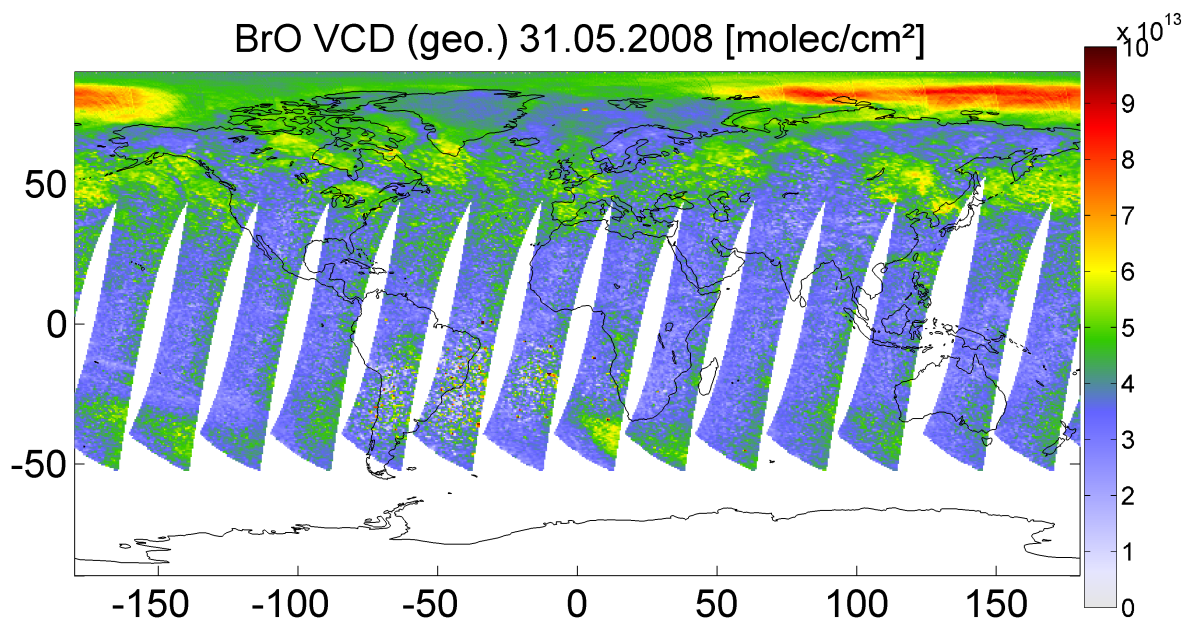


**Figure 6.15.:** Daily global map of the GOME-2 BrO geometrical VCDs on 31 May 2008. Enhanced BrO VCDs can be clearly seen in arctic regions, where the bromine activation during Arctic spring is taking place. Further structures of enhanced VCDs over the northern mid-latitudes are mostly due to imperfect correction for the ring effect over cloudy scenes or due to spectral interference with formaldehyde (data by courtesy of H. Sihler from MPIC Mainz).

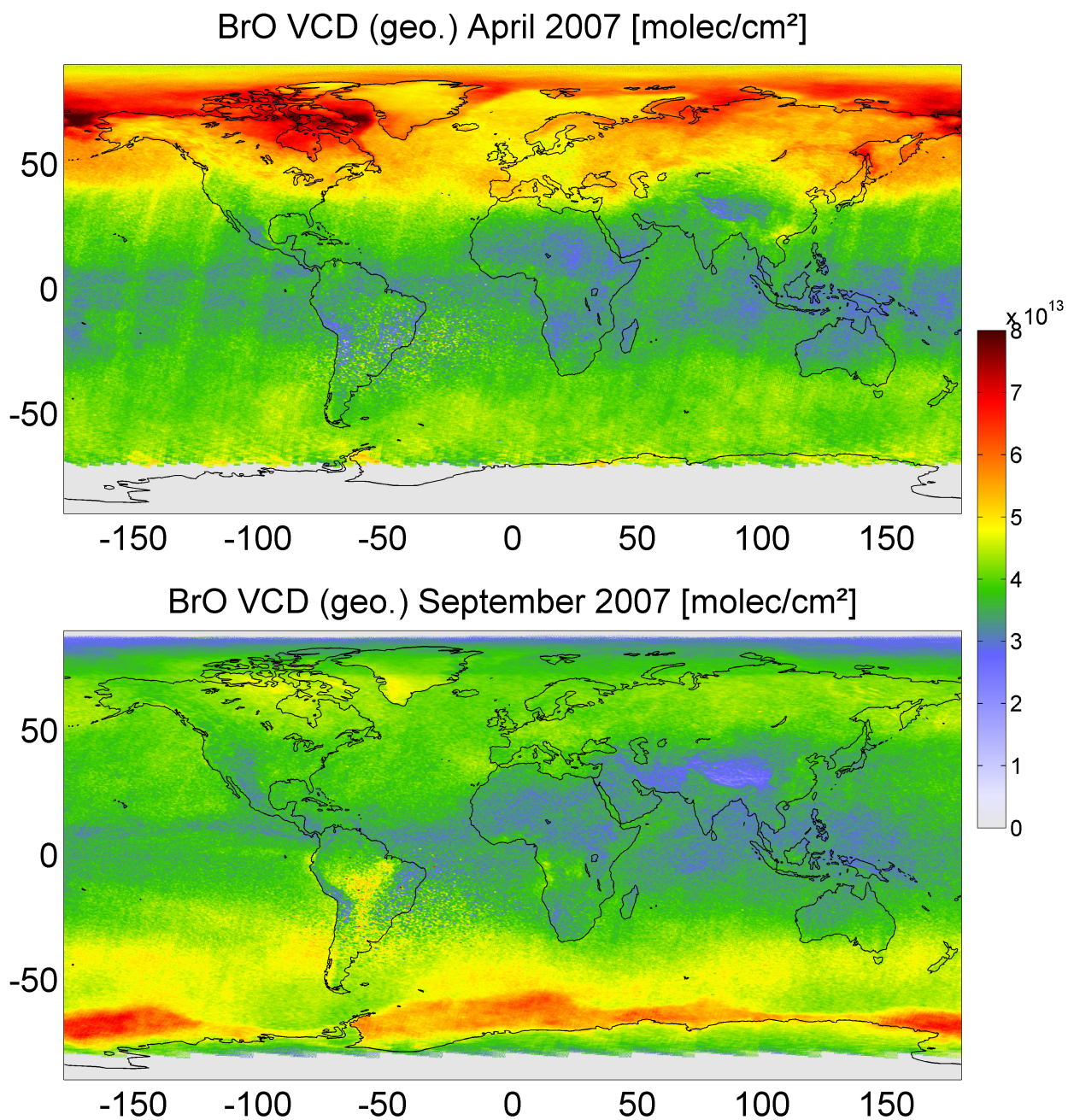


**Figure 6.16.:** GOME-2 monthly mean maps for April and September 2007, i.e. months of Arctic respectively Antarctic spring. Increased abundance of BrO in polar regions caused by bromine explosion events are visible in the averaged satellite data (data by courtesy of H. Sihler from MPIC Mainz).

Figure 6.16 shows the global mean maps of the geometrical BrO VCD during 2 months within the Arctic respectively Antarctic spring in April/September 2007. Again, the bromine activation during polar spring can be clearly seen for both, the Arctic and Antarctic. The latitudinal dependency of the BrO distribution can be mostly explained by the changing mean tropopause height from the equator to the poles, but also the chemical partitioning depends slightly on latitude. Most stratospheric BrO is located in the lower part of the stratosphere, so that a changing tropopause height significantly influences the measured BrO column densities (Wagner, 1999; Richter et al., 2002).



**Part III.**

# **Applications and Results**



## 7. Global anthropogenic and volcanic SO<sub>2</sub> emission sources

In this chapter, some of the most prominent SO<sub>2</sub> emission sources that can be seen in maps of averaged GOME-2 data will be presented (cf. Figure 6.4 on page 59). The main part of the global SO<sub>2</sub> abundance in the atmosphere is released by anthropogenic and volcanic emissions as discussed in Chapter 2 (Table 2.2 on page 10).

In order to distinguish the emissions from volcanic hot spots and anthropogenic sources, similar GOME-2 maps of the tropospheric nitrogen dioxide (NO<sub>2</sub>) SCD product (TSCD - by courtesy of S. Beirle from MPIC Mainz) will be shown for the same areas. Due to its formation in internal combustion engines and thermal power stations, NO<sub>2</sub> is generally well suited as tracer for anthropogenic pollution (Beirle et al., 2011). As the strongest NO<sub>2</sub> absorption bands (as well as the typical DOAS fit window) are found in between 425–450 nm, satellite instruments are usually more sensitive for the presence of tropospheric NO<sub>2</sub> than for SO<sub>2</sub>, because the measured sunlight is less affected by Rayleigh-scattering. Furthermore, the absorption cross-section of NO<sub>2</sub> is much stronger in this wavelength region compared to the one for SO<sub>2</sub> in the UV. The NO<sub>2</sub> mean maps are therefore capable to make even relative low VCDs visible that correspond to weak anthropogenic emission sources.

It should be noted that the colorbar for both, the SO<sub>2</sub> and NO<sub>2</sub> maps slightly differs from case to case in order to gain a maximum contrast of the sources compared to the background signal.

### 7.1. North and Middle America

While most SO<sub>2</sub> emissions over Northern America are of anthropogenic origin, volcanic emissions can be typically found for certain eruptions of the volcanoes in Alaska and especially for the volcanoes in the Aleutian Arc (e.g. Kasatochi, Mt. Cleveland, Okmok; USGS, 2012). However, strongly degassing volcanoes can not be identified from the GOME-2 data for this region (Figure 7.1, upper map), but a widely distributed pattern indicates general enhanced SO<sub>2</sub> emissions. Additionally, some remaining artefacts from the spectral interference with ozone in the Mid Latitudes and the Ring spectrum over the Rocky Mountains are clearly present. Only for some uncertain spots and especially at the region near the Great Lakes, the comparison with the NO<sub>2</sub> map (Figure 7.1, lower map) indicates coincident enhancement of NO<sub>2</sub> and SO<sub>2</sub> caused by emissions from industrial complexes in major cities. The most prominent but weak SO<sub>2</sub> spot here is probably caused by the huge steel industry around Pittsburgh (Fioletov et al., 2011b). Due to strict environmental laws, most anthro-

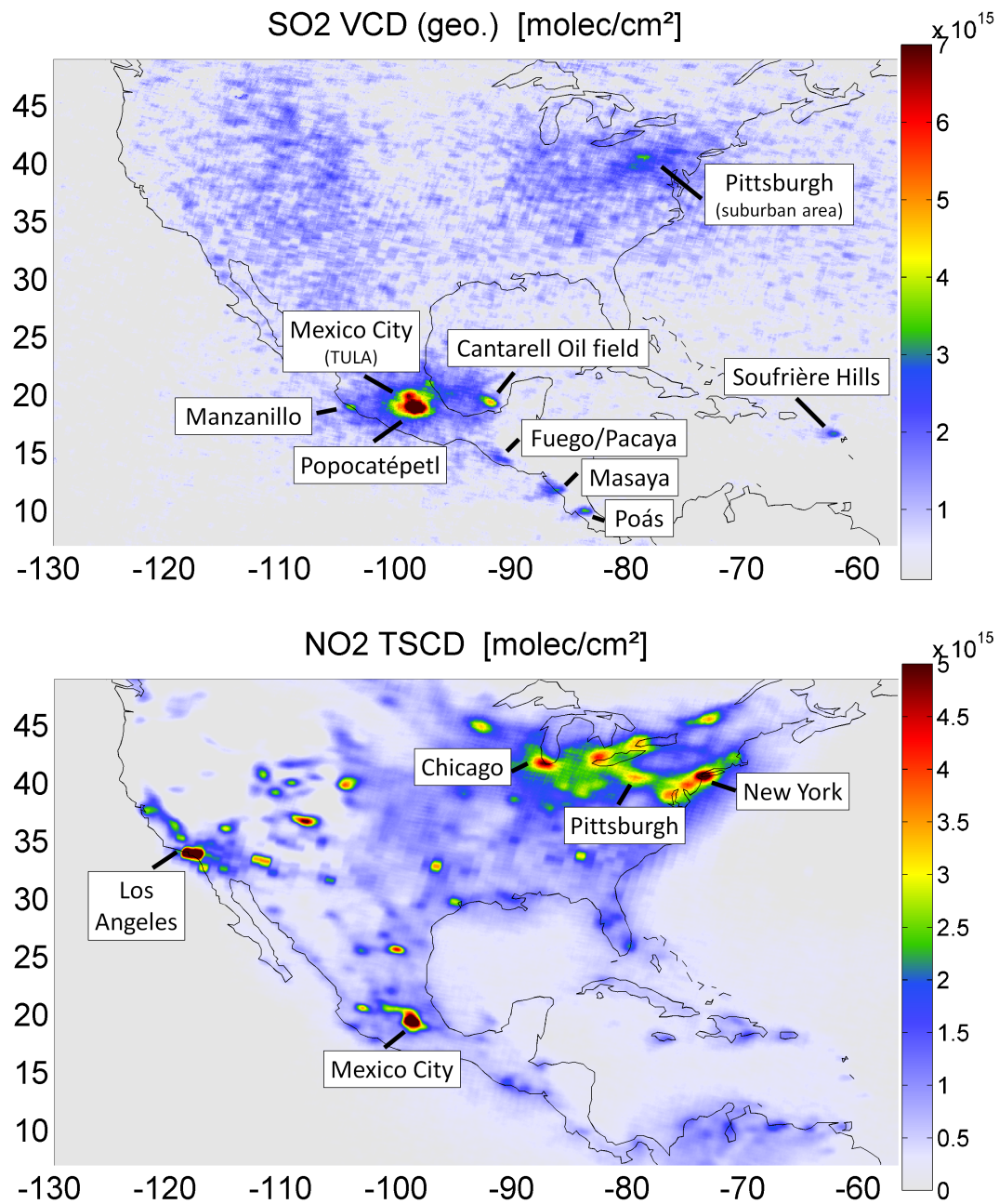


**Figure 7.1.:** Mean SO<sub>2</sub> and NO<sub>2</sub> emissions over North and Middle America as seen by the GOME-2 instrument in 2007 and 2008. Besides some anthropogenic SO<sub>2</sub> and NO<sub>2</sub> emissions at the region near the Great Lakes, volcanic SO<sub>2</sub> can be clearly identified from Popocatépetl (Mexico) and in Guatemala (Fuego/Pacaya), Nicaragua (Masaya), Costa Rica (Poás) and from Soufrière Hills (Montserrat).

pogenic SO<sub>2</sub> emissions are removed from exhaust flue gases of fossil-fuel power plants in the US, most of them by the application of flue-gas desulfurization techniques like e.g. wet scrubbing (Biondo and Marten, 1977).

For Middle America (especially for Mexico), the SO<sub>2</sub> emission sources are much clearer visible in the maps. However, while the area around Mexico City shows the most prominent SO<sub>2</sub> and NO<sub>2</sub> emissions, only a small fraction of the SO<sub>2</sub> emissions can be attributed to anthropogenic emissions in the northern part of Mexico City, where the *TULA* industrial complex is located (Rivera et al., 2009).

The major part of SO<sub>2</sub> originates from the volcanic emissions of Popocatépetl, one of the world's highest and most active volcanoes (Grutter et al., 2008). Furthermore, anthropogenic SO<sub>2</sub> emissions from the Manzanillo power plant at the western Mexican coast can be seen (Fioletov et al., 2011a) as well as from the Cantarell Oilfield Complex in the southern part of the Gulf of Mexico (Villasenor et al., 2003). Additionally, degassing volcanoes in Guatemala (Fuego/Pacaya), Nicaragua (Massaya), Costa Rica (Poás) and from Montserrat (Soufrière Hills) can be identified.

## 7.2. South America

The SO<sub>2</sub> map of the South American continent (Figure 7.2) is dominated by the volcanic emissions from Colombia (Nevado del Huila) and especially Ecuador (Galeras and Tungurahua), where about 18 active volcanoes are located. Several erroneously signals can be seen over large parts of the continent that are caused by the SAA due to high energy particles that hit the detector (cf. Section 6.2.1). Thus, the observation of volcanoes in the southern part of the continent (especially Chile) is difficult and normally restricted to major eruptions. Like it can already be seen from the corresponding NO<sub>2</sub> map in Figure 7.2, anthropogenic emissions are less than for the North American continent due to the widely unpopulated area of the Amazonas Basin. Nevertheless, some weak SO<sub>2</sub> and NO<sub>2</sub> emissions are found along the coasts. While most NO<sub>2</sub> emissions are caused by anthropogenic fossil fuel burning in cities (e.g. Lima), the enhanced SO<sub>2</sub> VCDs are mainly caused by Peruvian copper smelters (Carn et al., 2007; Khokhar et al., 2008) at La Oroya (11.53° S, 75.9° W) and Ilo (17.63° S, 71.33° W).

## 7.3. Europe

Like for the North American continent, little similarities to the anthropogenic NO<sub>2</sub> emissions can be seen over parts of the Balkan Peninsula. These are mainly caused by the emissions from the *Maritsa Iztok Complex*<sup>1</sup>, the largest energy complex in South Eastern Europe in the Stara Zagora Province, Bulgaria, with three huge thermal power stations, burning brown coal. Furthermore, some minor similarities can

---

<sup>1</sup>[http://en.wikipedia.org/wiki/Maritsa\\_Iztok\\_Complex](http://en.wikipedia.org/wiki/Maritsa_Iztok_Complex)

## 7. Global anthropogenic and volcanic SO<sub>2</sub> emission sources

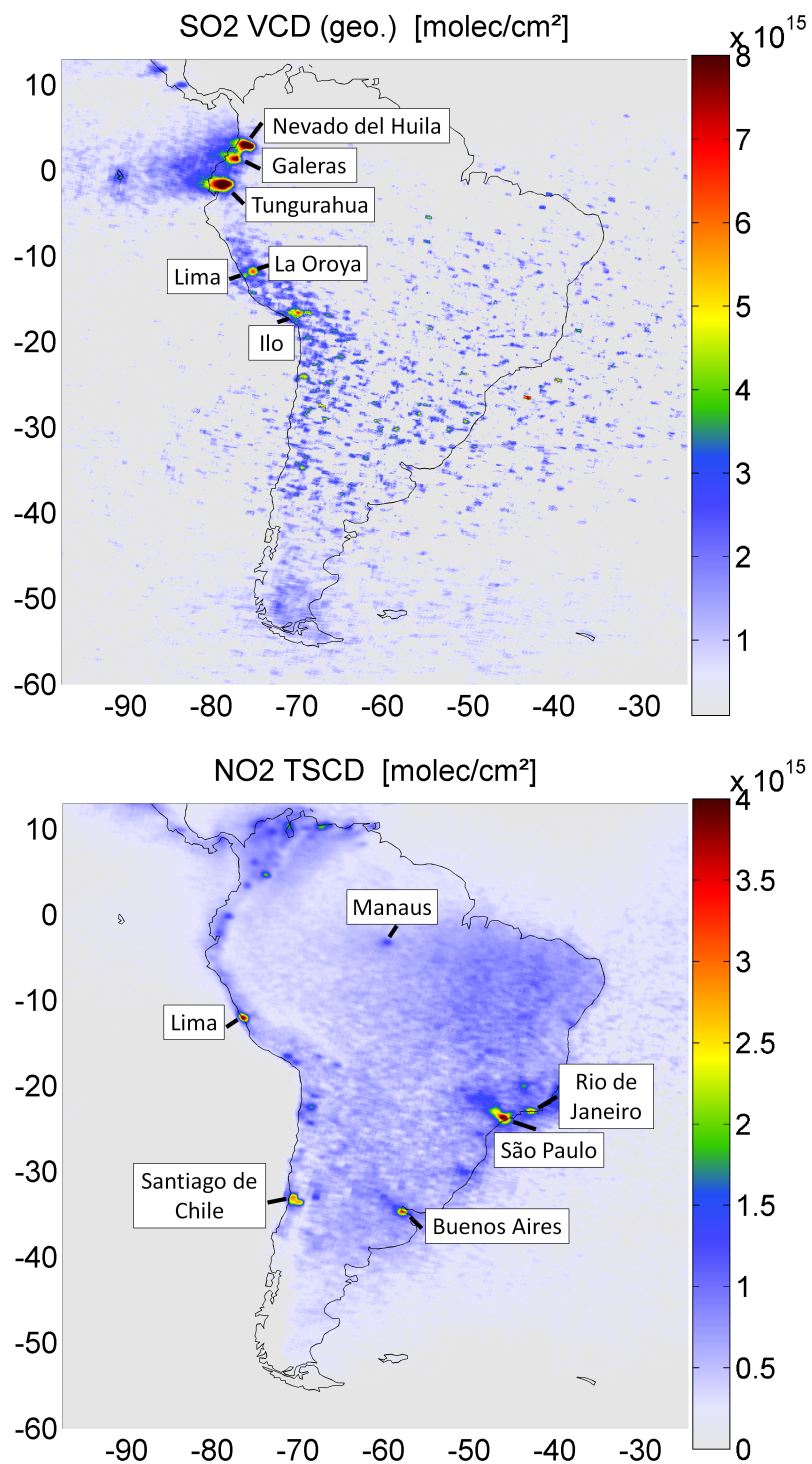


**Figure 7.2.:** Mean SO<sub>2</sub> and NO<sub>2</sub> emissions over South America as seen by the GOME-2 instrument in 2007 and 2008. Natural and anthropogenic SO<sub>2</sub> and NO<sub>2</sub> emissions can be identified in regions at the western coast. Most prominent are the volcanic SO<sub>2</sub> emissions from Nevado del Huila (Colombia), Galeras and Tungurahua (Ecuador). The measurements are distorted by the SAA.

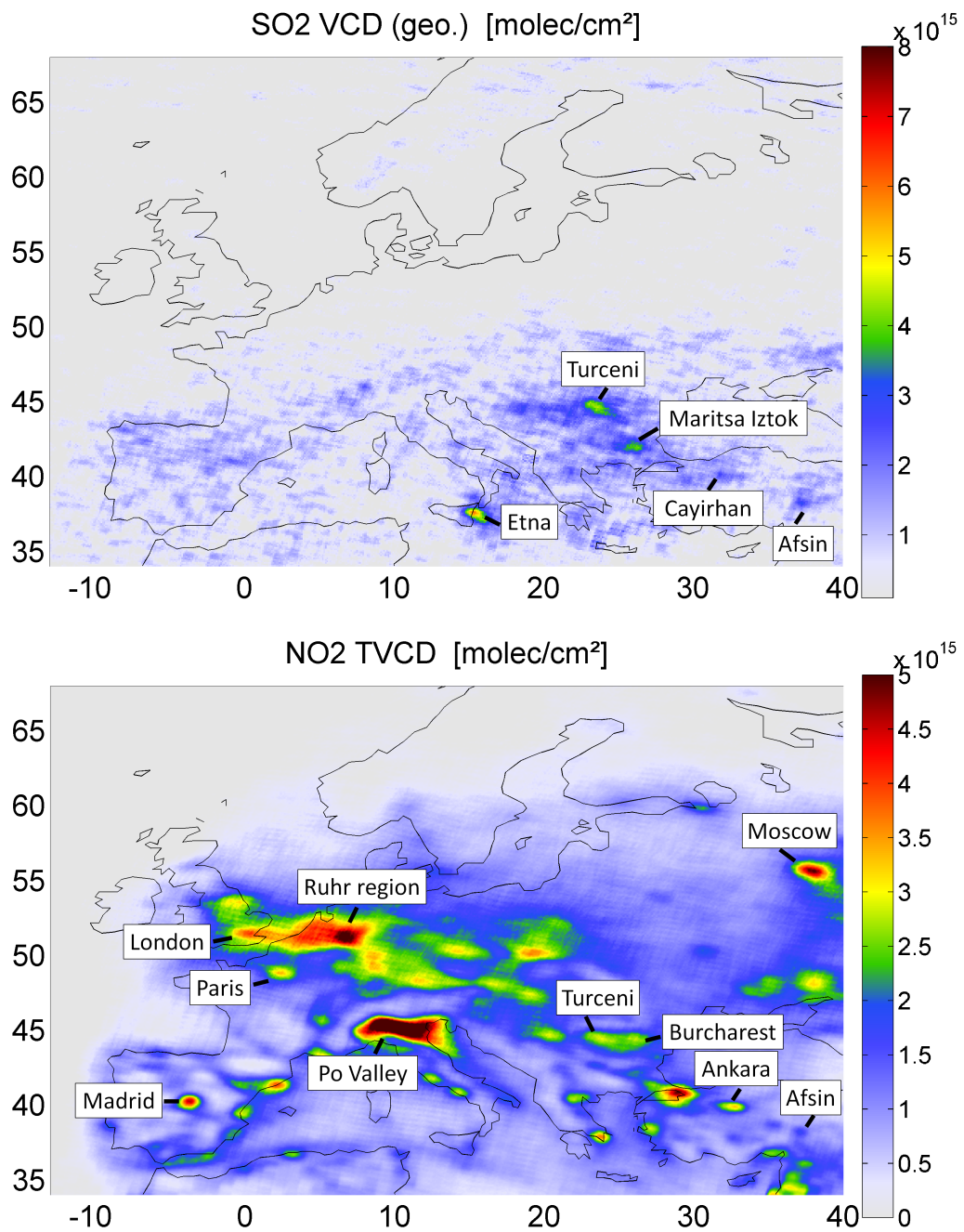


**Figure 7.3.:** Mean SO<sub>2</sub> (upper panel) and NO<sub>2</sub> (lower panel) emissions over Europe as seen by the GOME-2 instrument in 2007 and 2008. The Etna volcano (Sicily) is the only visible volcanic source of SO<sub>2</sub>. Furthermore, anthropogenic emissions (mostly from thermal power stations) can be identified over Eastern Europe and Turkey.

be identified in the region of Cayirhan/Ankara and Afsin (Turkey), also mainly because of emissions from brown coal burning in power plants and industrial complexes (Fioletov et al., 2011a). Being one of the most active volcanoes in the world, the volcanic SO<sub>2</sub> emissions of Mt. Etna (Sicily) cause the highest VCDs in Figure 7.3. The volcano shows an almost constant state of activity, with some minor eruptions during the last years. Some of these eruptions have been also detected in the daily GOME-2 measurements in 2007, 2008 and 2011, producing SO<sub>2</sub> clouds that were transported for several thousands of kilometers (cf. Chapter 8).

### 7.4. Norilsk (Russia)

The enormous SO<sub>2</sub> emissions from the area of Norilsk are one of the most prominent features that can be observed in global SO<sub>2</sub> mean maps (cf. Figure 6.4). The activities of the *MMC Norilsk Nickel*<sup>2</sup> company lead to very high SO<sub>2</sub> emissions that are the highest from a single polluter worldwide. The emissions cause environmental problems like acid rain and smog, but also strongly influences population's health. The area around Norilsk was therefore assigned to be one of the 10 most polluted areas in the world by the *Blacksmith Institute* in 2006 and 2007, an international non-profit organization "dedicated to solving pollution problems in low and middle income countries, where human health is at risk"<sup>3</sup>.

Figure 7.4 shows the SO<sub>2</sub> and NO<sub>2</sub> distribution around Norilsk. Interestingly, the NO<sub>2</sub> map shows only a very weak abundance of NO<sub>2</sub> compared to the SO<sub>2</sub> signal (note the aligned colorbar), emphasizing that a huge part of the pollution from heavy metal smelters is directly due to the smelting process, where the sulfur in the ores have to be oxidized and is then finally emitted (Walter et al., 2012). Most of the NO<sub>2</sub> results from a power plant in Surgut and the natural gas industry in Novy Urengoy.

### 7.5. Eastern China

The largest anthropogenic emissions of both, SO<sub>2</sub> and NO<sub>2</sub> can be observed over Eastern China, as can be seen in Figure 7.5. By comparing the maps for both species, a similar distribution shows up, even for small details. Most of these emissions are located over the greater region around Beijing and caused by coal-fired thermal power plants, as about three-quarters of China's primary energy is coal-burning driven (Xu et al., 2000). On the other hand, for some regions the air pollution seems to be only dominated by SO<sub>2</sub> emissions. This is in particular the case for the Sichuan area (103–108° E, 25–32° N), where iron, titanium, vanadium and cobalt are exploited and smeltered. In contrast, the pollution in the Pearl River Delta region (112–115° E, 22–24° N), China's most economically dynamic region (Zhang et al., 2012), is dom-

---

<sup>2</sup>[http://en.wikipedia.org/wiki/Norilsk\\_Nickel](http://en.wikipedia.org/wiki/Norilsk_Nickel)

<sup>3</sup><http://www.blacksmithinstitute.org>

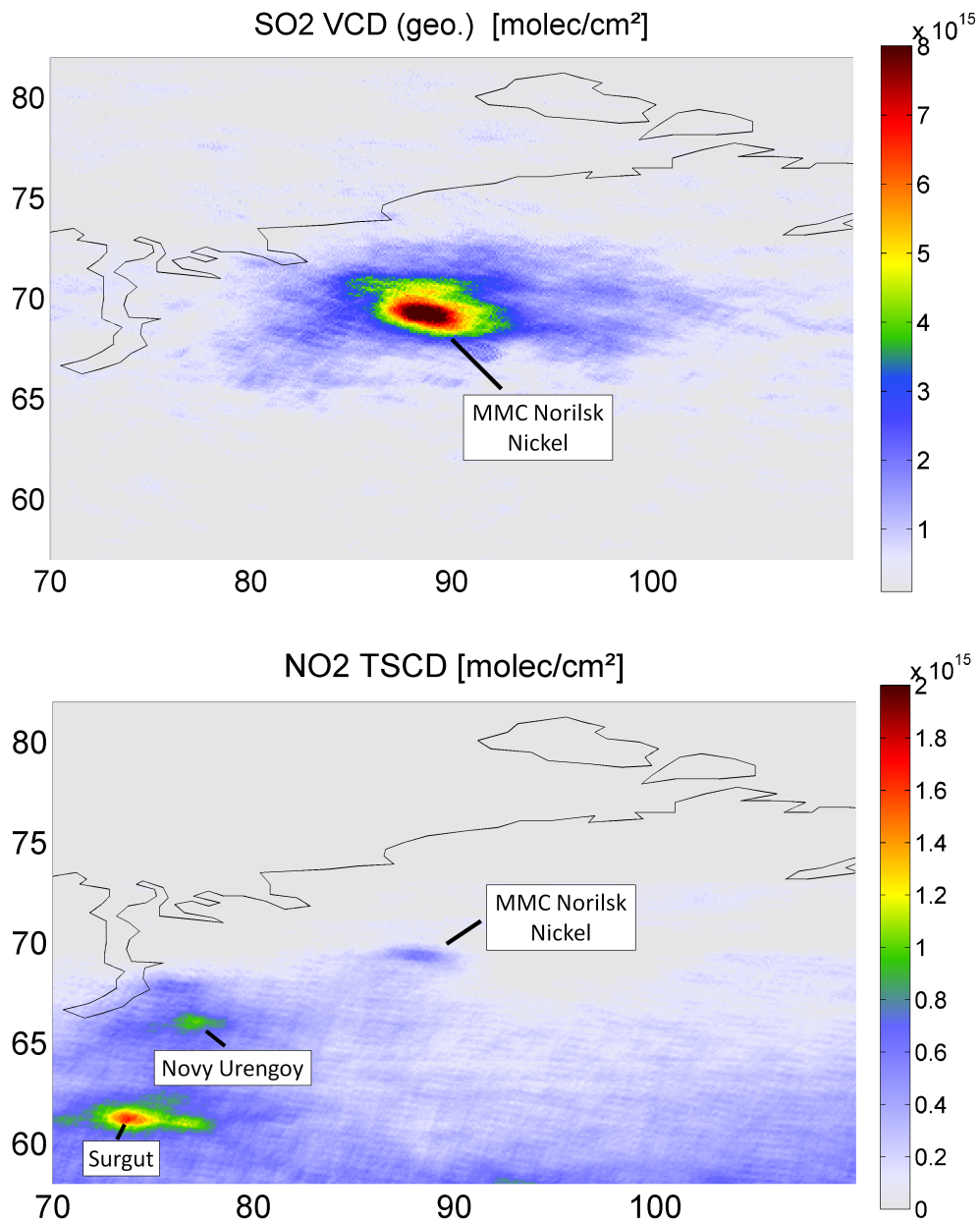


**Figure 7.4.:** Mean  $\text{SO}_2$  and  $\text{NO}_2$  emissions over Norilsk as seen by the GOME-2 instrument in 2007 and 2008. The area around Norilsk, which is one of the most polluted areas of the world, is dominated by  $\text{SO}_2$  emissions from the heavy metal smelters of the MMC Norilsk Nickel company.  $\text{NO}_2$  at Norilsk are relatively weak.

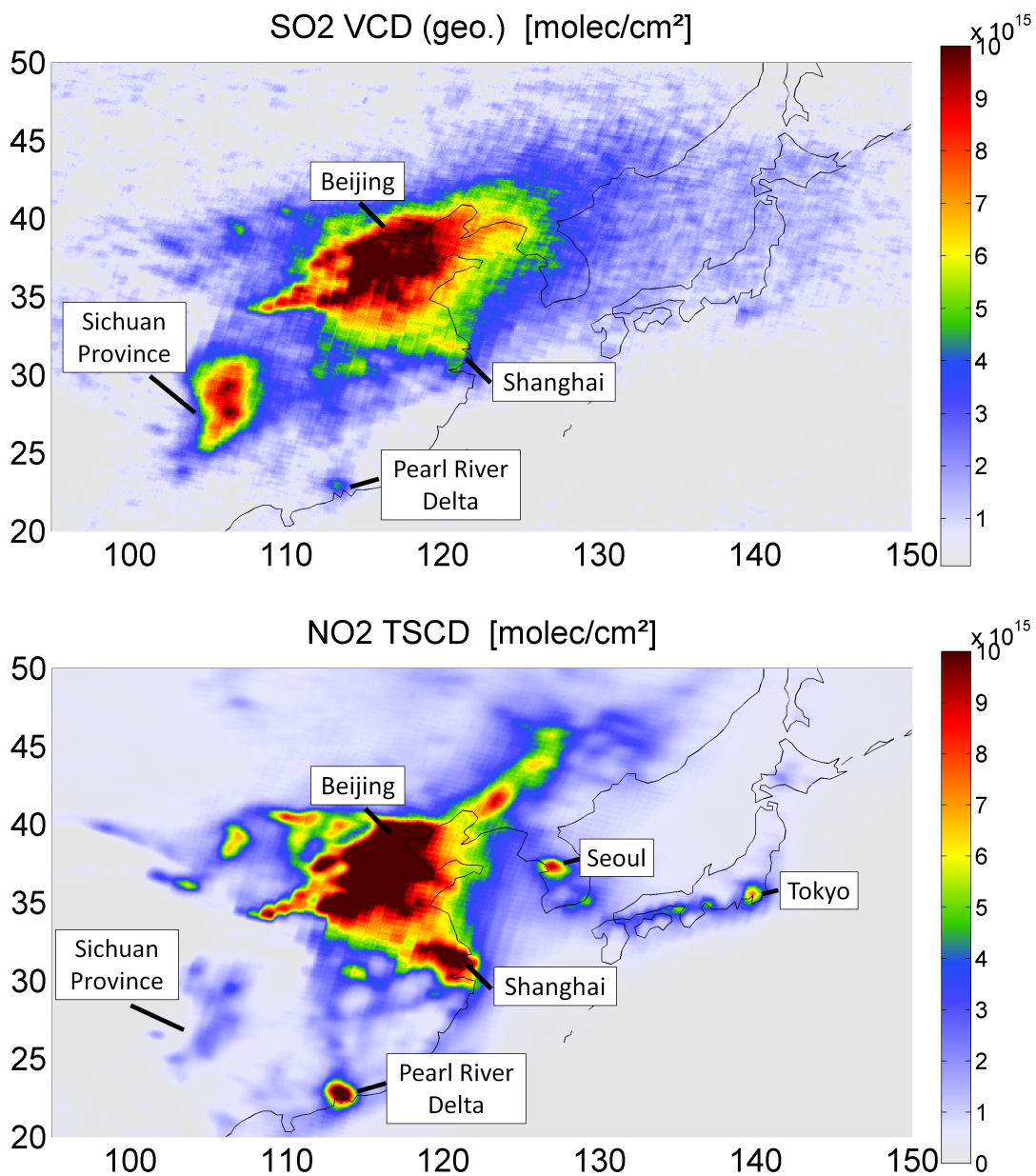


**Figure 7.5.:** SO<sub>2</sub> and NO<sub>2</sub> emissions over China as seen by the GOME-2 instrument. Large parts of the SO<sub>2</sub> and NO<sub>2</sub> distribution are similar. Most of the emissions result from coal-fired thermal power plants, as about three-quarters of China's primary energy is coal-burning driven. Some regions are more dominated by SO<sub>2</sub> emissions from heavy metal smelters.

inated by  $\text{NO}_2$ , as well as over large cities like Shanghai (China), Seoul (South Korea) or Tokyo (Japan). The total emissions of  $\text{SO}_2$  and  $\text{NO}_x$  in 1995 (25.2 Tg/yr respectively 12 Tg/yr) have been predicted to further increase to 30.6 Tg/yr respectively 26.6–29.7 Tg/yr, even if emission controls will be implemented (Streets and Waldhoff, 2000).

However, recently, a dramatic reduction in the  $\text{SO}_2$  emissions has been reported by (Li et al., 2010), which started as a part of Chinas anti-pollution program in the course of the Olympic Games in Beijing and is supposed to show first signs of the successful installation of flue-gas desulfurization devices that remove sulfur emissions via water scrubbing.

## 7.6. Malay Archipelago

The Malay Archipelago is dominated by volcanic landscapes, with Indonesia hosting most of the world's active volcanoes ( $\sim 150$ ). According to Siebert et al. (2011), four-fifths of all Indonesian volcanoes with dated eruptions have erupted during the 20th century. Figure 7.6 shows the  $\text{SO}_2$  emissions from several significantly active volcanoes during the years 2007–2008.

Besides some minor eruptions that were monitored by the GOME-2 instrument in this time period (e.g. Anatahan, which belongs to the Northern Mariana Islands), the whole region around the Archipelago is affected by the emissions from a huge number of quiescent degassing volcanoes in this part of the world. This includes the Indonesian volcanoes Kerinchi, Semeru, Raung, Batu Tara and Dukono, Mayon on the Philippines and Manam, Rabaul and Bagana in Papua–New Guinea. The  $\text{SO}_2$  map further shows the  $\text{SO}_2$  emissions from the Ambrym volcano (Vanuatu), which has been almost constantly active since 1996 (cf. Figure 7.6, lower right corner). Due to its strong degassing activity and isolated location, the Ambrym volcano has also been investigated for the detection of BrO from averaged daily measurements in this thesis (cf. Chapter 10).

The  $\text{NO}_2$  distribution (Figure 7.6, below) shows no similarities to the  $\text{SO}_2$  distribution, as most emissions originate from combustion processes in major cities like Bangkok, Singapore or Jakarta. Furthermore, some streaky  $\text{NO}_2$  patterns show up on the ocean at the Strait of Malacca between the Malay Peninsula and the Indonesian island of Sumatra, which are caused by ship emissions (Beirle et al., 2004). Although also significant  $\text{SO}_2$  emissions are released by ships (e.g. Berg et al., 2012), current satellite instruments (including GOME-2) are not sensitive enough to resolve similar  $\text{SO}_2$  patterns.

## 7. Global anthropogenic and volcanic SO<sub>2</sub> emission sources

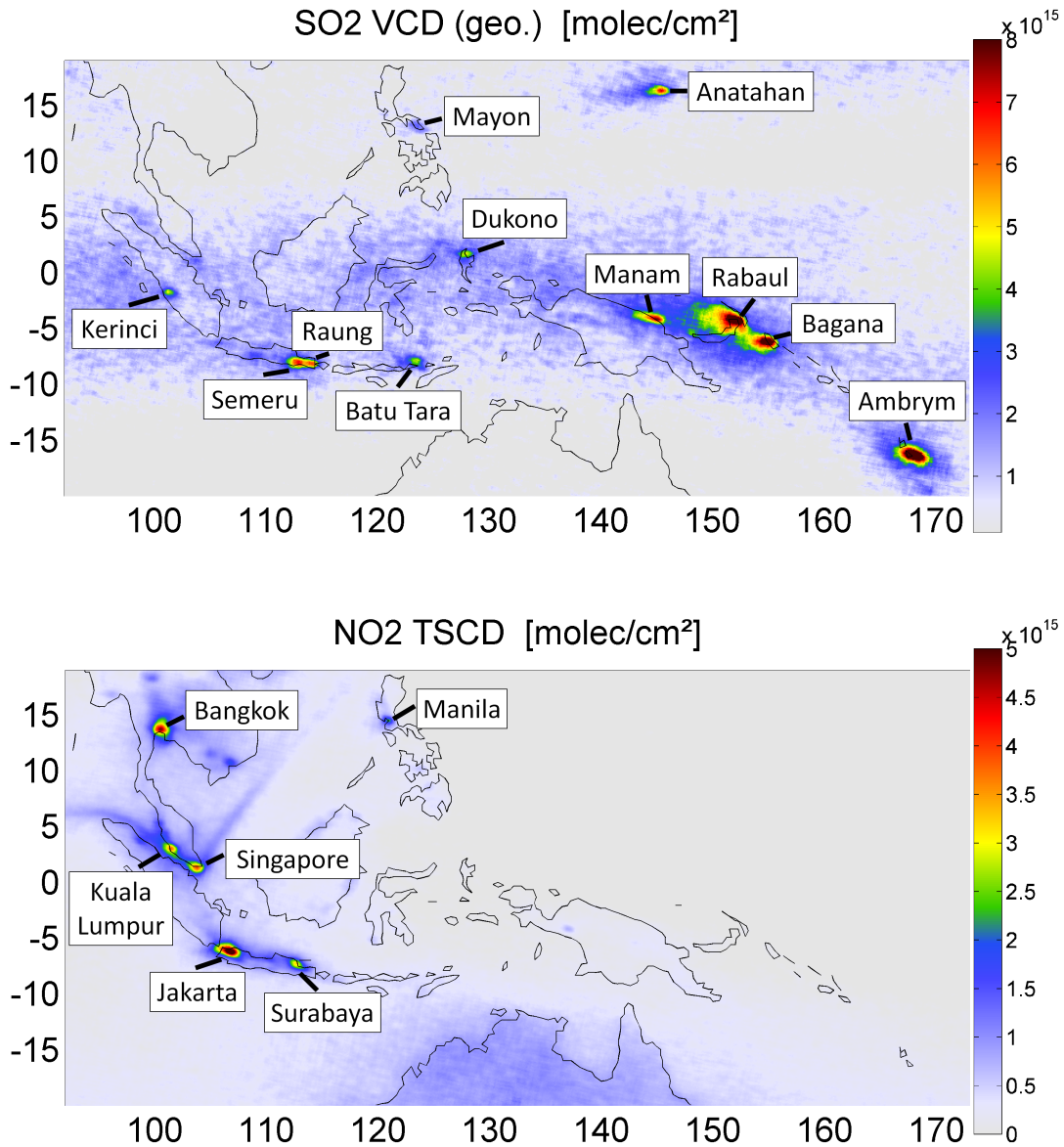


**Figure 7.6.:** SO<sub>2</sub> and NO<sub>2</sub> emissions over the Malay Archipelago as seen by the GOME-2 instrument. Hosting most of the world's active volcanoes, the map is dominated by volcanic SO<sub>2</sub> emissions. For NO<sub>2</sub>, some streaky patterns can be additionally seen that are caused by ship tracks.

## 8. Systematic detection of volcanic plumes

The GOME-2 dataset provides a great number of volcanic SO<sub>2</sub> plume observations from both strong degassing and minor/major eruption events. In order to analyze these volcanic emissions, individual plumes have to be identified in the satellite data. For this purpose, a new algorithm has been developed to automatically detect volcanic plume events. While SO<sub>2</sub> is the third most abundant gaseous species that is emitted by a volcano (see Chapter 2), the levels in the free troposphere are typically low. Conspicuously high SO<sub>2</sub> column densities were therefore used as an indicator for areas that were affected by volcanic emissions in the daily satellite measurements.

The chapter is organized as followed: After a short motivation in Section 8.1, the initial preparation of the GOME-2 data is discussed. This includes the correction for temporal discontinuities (Section 8.2), a first rough identification of volcanic plumes (Section 8.3) and the accurate correction for a non-volcanic SO<sub>2</sub> background signal, which is strongly linked to the final detection of satellite measurements that had been affected by volcanic SO<sub>2</sub> emissions (Section 8.4). For major volcanic eruptions, the extracted data has to be further corrected for non-linear effects of the DOAS retrieval due to high SO<sub>2</sub> concentrations (Section 8.5). Finally, the detected SO<sub>2</sub> plumes are presented in Section 8.6 in the form of a time series for January 2007 until June 2011 and subsequently discussed (Section 8.7).<sup>1</sup>

### 8.1. Automatic identification of volcanic SO<sub>2</sub> plumes

To detect volcanic SO<sub>2</sub> plumes from the GOME-2 measurements, the dataset from January 2007 until June 2011 was analyzed by a newly developed detection algorithm that searches the data for contiguous areas of conspicuously elevated SO<sub>2</sub> columns. Similar approaches have been developed during the last years in the course of operational early-warning systems for volcanic ash (e.g. Richter, 2009; SACS, 2012). Such systems provide rapid information to the aviation community about the location of a volcanic plume, which might compromise the safety of airplanes if they contain ash, but can also cause damages to windows, airframe or the engine due to the exposure to SO<sub>2</sub> or sulfuric acid (Vogel et al., 2011).

The early-warning system projects focus on near-real time early-warnings for volcanic ash plumes. In contrast to that, the focus of the algorithm described here is aimed at the offline identification of volcanic plumes and especially the accurate extraction of satellite pixels contaminated by SO<sub>2</sub>. These are used in a later step to

---

<sup>1</sup>Parts of this chapter have been published in Hörmann et al. (2012).

compare the associated SO<sub>2</sub> SCDs with those of BrO in the GOME-2 dataset (see Chapter 9).

## 8.2. Global maps with two days coverage

In a first step, the geometrical SO<sub>2</sub> vertical column densities (VCDs) for all GOME-2 pixels were calculated from the SCDs applying a geometrical AMF (cf. Section 4.3):

$$\bar{V}_{S,i,geo.} = \frac{S_{S,i}}{A_{i,geo.}} \quad (8.1)$$

$$A_{i,geo.} = \frac{1}{\cos(\xi_i)} + \frac{1}{\cos(\theta_i)} \quad (8.2)$$

where  $\xi_i$  is the solar zenith angle (SZA) and  $\theta_i$  is the line of sight zenith angle (LOS; nadir=0°) of satellite pixel  $i$ .

Subsequently, the day containing the data plus the following day (i.e. two consecutive days) were projected on gridded global maps, covering both days at a grid resolution of 0.5°×0.5°. These two days global maps (*TDGM*) differ from the layout for operational GOME-2 DOAS products commonly used, where all measurements of satellite orbits that had started within the regarded day (start time 00:00:00-23:59:59 UTC) are projected on a single global map (-90°N to +90°N and -180°E to +180°E). By using the TDGMs, we overcome a serious disadvantage of single day maps which is due to a temporal discontinuity occurring at the borders of these maps with data from satellites operating in sun-synchronous orbits. The most important advantages of the TDGMs are:

- To be able to identify volcanic plumes close to the first or the last orbit recorded on one day by satellites in sun-synchronous orbits
- The ability to capture the complete plume, even if it extends beyond the common map boundaries in westerly direction (<-180°E)

Figure 8.1a shows the GOME-2 satellite orbits for two consecutive days next to each other (day 1 on the right, day 2 on the left side). As the first and the last orbit of a single day are typically located at more than +105°E and extend up to +180°E and beyond, adjacent and/or overlapping pixels exhibit a time shift of up to 24 hours (area between the light blue and green satellite orbits during day 1 and the green and dark red orbits during day 2 in Figure 8.1a). Additionally, the orbits overlap towards polar regions, so that also here time shifts of up to 10 hours may occur between individual neighboring satellite pixels.

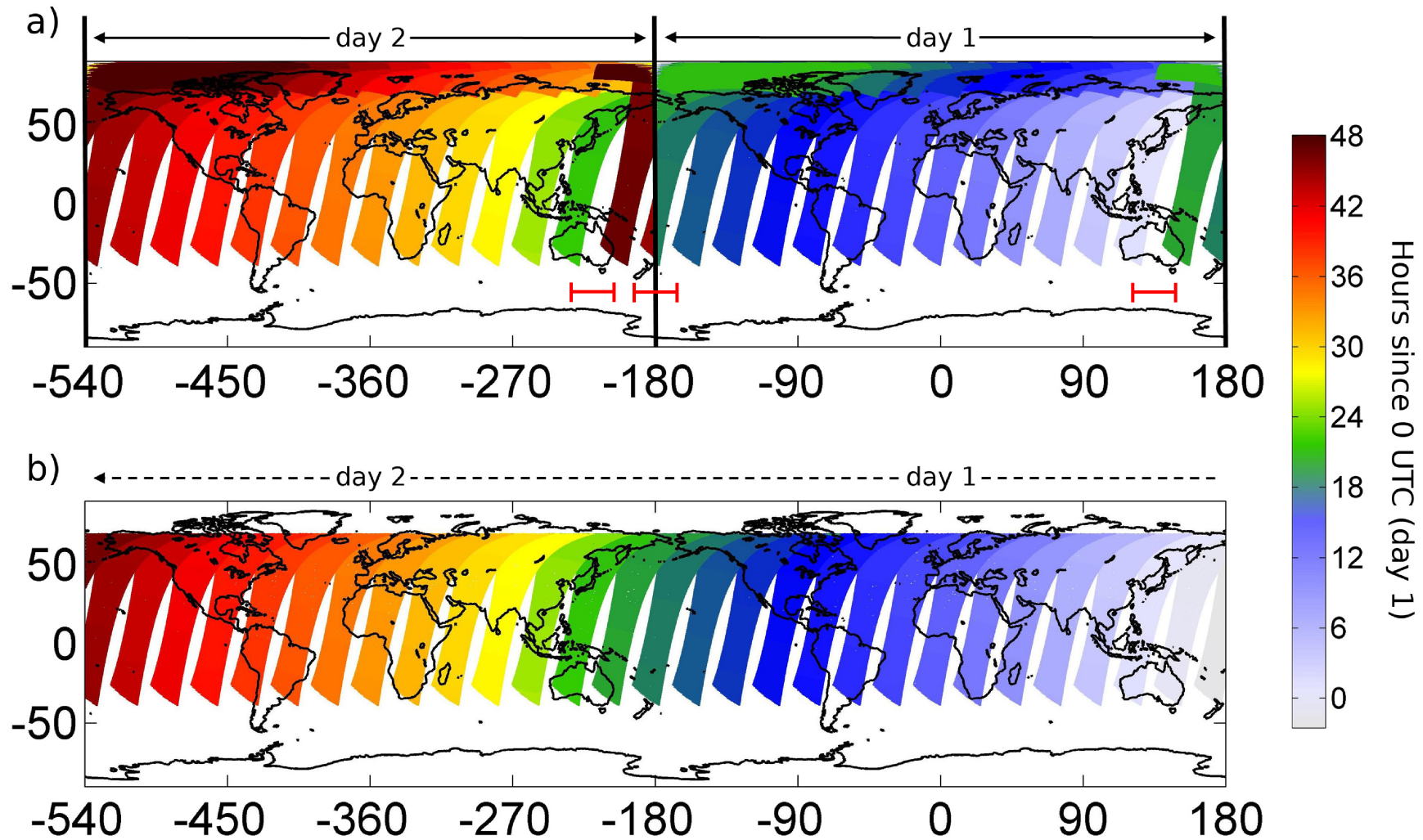


**Figure 8.1.:** a) Two consecutive daily maps of GOME-2 satellite orbits as widely used in the scientific community (right: day 1, left: day 2). Due to an overlap of the first and the last orbit during the day of interest, a temporal discontinuity of up to (or even more than) 24 h occurs (indicated by red bars) as well as other discontinuities due to overlapping pixels at high latitudes. b) Alternative TDGM layout for the maps with two days coverage at latitudes below/above  $\pm 70^\circ$ . The chronology of satellite orbits in direct succession is now monotonous in westerly direction.

## 8. Systematic detection of volcanic plumes

---

For the analysis of volcanic plumes located at the edge of single day maps, the associated data can not be illustrated properly by simply putting the maps of two consecutive days beside each other, as another time shift of  $\sim 24$  h occurs at the intersecting region between day 1 and 2 (mid red bar in Figure 8.1 a). Therefore, the data in the TDGM was rearranged in such a way that the chronology of the satellite orbits in direct succession is conserved in western direction (Figure 8.1b). As the data has also been restricted to latitudes from  $-70^\circ\text{N}$  to  $+70^\circ\text{N}$  and  $\text{SZA} < 70^\circ$  for this study, most overlapping pixels at high latitudes are skipped. In addition, remaining overlapping pixels with a measurement time difference of more than  $\sim 3.5$  h (13000 s) were discarded.

By using the chronologically correct projection on the TDGM (that now extends from  $-540^\circ\text{E}$  to  $+180^\circ\text{E}$  in longitudinal direction), the temporal discontinuity is eliminated. The thus filtered satellite data within  $-180^\circ\text{E}$  to  $+180^\circ\text{E}$  consequently contain all  $\text{SO}_2$  fit results observed during the first regarded day (parts of the first 2 orbits at the eastern boundary of day 1 usually belong to the previous day), while most of the data within  $-540^\circ\text{E}$  to  $-180^\circ\text{E}$  contains the  $\text{SO}_2$  columns for the following day.

In order to prevent the detection of  $\text{SO}_2$  events that are caused by non-volcanic emissions and/or measurement errors, the data for several areas with contamination by anthropogenic  $\text{SO}_2$  are masked out (Table 8.1). These include, in particular, the greater area of Eastern China, Norilsk (Siberia, Russia) and the Highveld plateau (South Africa), where anthropogenic  $\text{SO}_2$  emissions can be regularly detected (caused e.g. by huge industrial coal plant and/or heavy metal smelter complexes). Additionally, large parts of South America are skipped, because the GOME-2 measurements are here strongly influenced by the South Atlantic Anomaly (SAA) of the radiation belt (cf. Section 6.2.2).

**Table 8.1.:** Areas where the GOME-2 data were excluded for the automatic detection of volcanic  $\text{SO}_2$  plumes.

name	reason	excluded area
Highveld plateau	anthropogenic emissions	$[20^\circ - 35^\circ\text{S}, 20^\circ - 35^\circ\text{E}]$
China	anthropogenic emissions	$[20^\circ - 45^\circ\text{N}, 100^\circ - 135^\circ\text{E}]$ $[30^\circ - 50^\circ\text{N}, 130^\circ - 140^\circ\text{E}]$
Norilsk	anthropogenic emissions	$[50^\circ - 70^\circ\text{N}, 70^\circ - 110^\circ\text{E}]$ $[60^\circ - 70^\circ\text{N}, 65^\circ - 70^\circ\text{E}]$
SAA	cosmic particles	$[10^\circ - 70^\circ\text{S}, 10^\circ - 85^\circ\text{W}]$ $[0^\circ - 10^\circ\text{S}, 10^\circ - 75^\circ\text{W}]$ $[20^\circ - 35^\circ\text{S}, 0^\circ - 10^\circ\text{W}]$

### 8.3. Volcanic plume extraction

After the data were projected on the TDGM, the SO<sub>2</sub> VCDs were corrected for a non-volcanic offset. The offset is mainly caused by interferences with the O<sub>3</sub> absorption cross section and/or an imperfect fitting of the Ring effect. For the offset correction, the median in longitudinal direction for each grid pixel row (0.5°) was subtracted from the data. The offset corrected data were then subdivided into boxes of 5°×5° (10×10 grid pixels; cf. Figure 8.2). All boxes were investigated for a maximum SO<sub>2</sub> VCD of at least 5×10<sup>16</sup> molec/cm<sup>2</sup>, indicating that a box might contain a volcanic plume. This threshold was found to be well above the detection limit of the instrument and is consistent with typical SO<sub>2</sub> VCDs that are measured during strong degassing episodes and minor volcanic eruptions. However, the algorithm is not sensitive to the majority of weaker plumes from volcanic degassing.

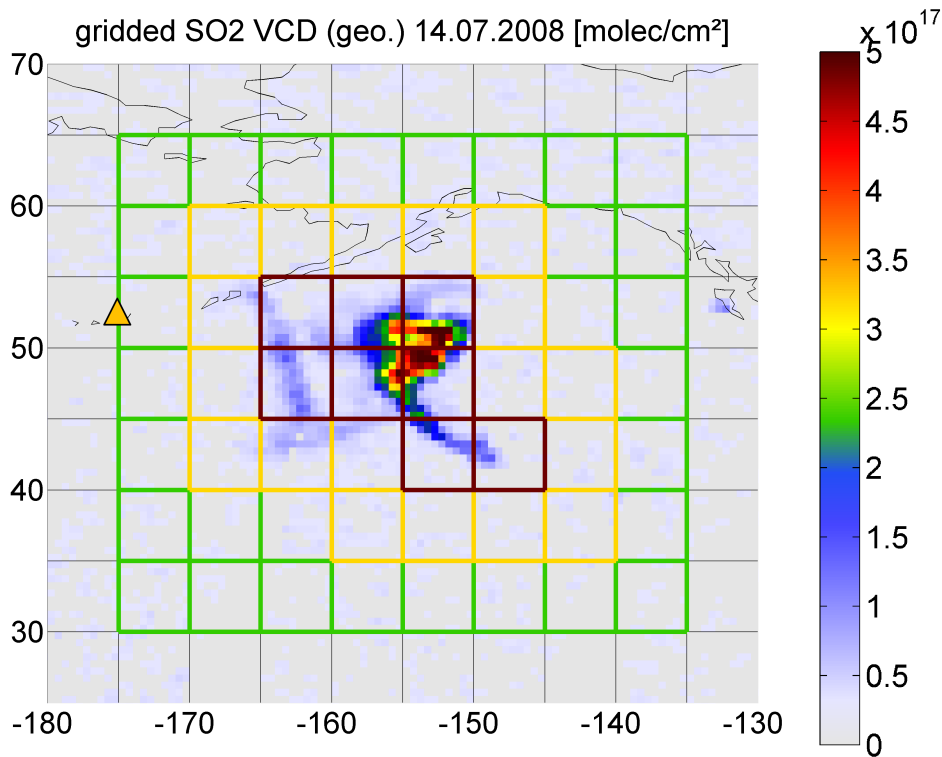


**Figure 8.2.:** Automatic detection of the volcanic SO<sub>2</sub> plume after the eruption of the Okmok volcano (location marked by the orange triangle) on 14 July 2008. The red frames in the centre region highlight the detected SO<sub>2</sub> plume event boxes (PEBs) that were identified to contain parts of the volcanic plume. Neighbouring boxes are assigned to each specific PEB in order to capture also parts of the volcanic plume where the VCDs were not sufficiently high to be identified as an individual PEB (yellow boxes). To get a reference area next to the captured SO<sub>2</sub> plume events, all non-SO<sub>2</sub> PEBs within a second surrounding box exceeding from ±5° from the max/min lat/long grid pixel position of the SO<sub>2</sub> PEB cluster were registered (green boxes).

It is further noted that, according to the resulting data, the SO<sub>2</sub> detection limit has increased from approximately  $1 \times 10^{16}$  molec/cm<sup>2</sup> in 2007 to more than  $2 \times 10^{16}$  molec/cm<sup>2</sup> in June 2011 due to instrument degradation. For a detailed analysis of the impacts of the GOME-2 degradation on Level 2 products the reader is referred to Dikty and Richter (2011). Since single erroneous measurements cause SO<sub>2</sub> VCD that are comparable to those from volcanic emissions, all directly neighbouring grid pixels were additionally investigated using a second, lower SO<sub>2</sub> VCD threshold of  $3 \times 10^{16}$  molec/cm<sup>2</sup>, to ensure the actual presence of an enhanced SO<sub>2</sub> VCD cluster inside the box area. Whenever at least 4 neighbouring grid pixels exceeded the second threshold, the box was assumed to contain at least parts of a volcanic SO<sub>2</sub> plume (see dark red boxes in Figure 8.2). For each identified "SO<sub>2</sub> plume event box" (in the following abbreviated as *SO<sub>2</sub> PEB*), all directly neighbouring boxes were also assigned to this specific event in order to prevent losing parts of the volcanic plume where the VCDs were not sufficiently high to be identified as an independent SO<sub>2</sub> PEB (yellow boxes in Figure 8.2). After all plume affected boxes had been determined, resulting clusters of SO<sub>2</sub> PEBs (red and yellow boxes) represent individual SO<sub>2</sub> plumes for the regarded days. In order to obtain a reference area next to the captured SO<sub>2</sub> plume events, all non-SO<sub>2</sub> PEBs within another surrounding box (that extends from  $\pm 5^\circ$  from the maximum/minimum latitudinal/longitudinal grid pixel position of the SO<sub>2</sub> PEB cluster) were registered (green boxes in Figure 8.2).

To prevent the algorithm from capturing the same plume twice (as it always considers the data of two consecutive days), only SO<sub>2</sub> events that consist completely of satellite pixels recorded during the first regarded day or on the first *and* the following day were accepted for further investigation. Therefore, a SO<sub>2</sub> event that consists exclusively of measurements from the second of the two regarded days during an iteration of the algorithm was not captured until the subsequent iteration. This also means that the detection of a possible (but unlikely) case of a volcanic plume that encompasses the whole globe cannot be captured in its full extent using this approach. For the time period between January 2007 and June 2011, such an event has not occurred.

### 8.4. Non-volcanic background correction and plume pixel selection

Gridded satellite data are much easier to handle by the plume detection algorithm (cf. Section 8.3), because of the grid's regular geometry. Additionally, it has the advantage that background noise partly averages out during the gridding process, so that the misidentification of satellite measurements outside of a volcanic plume is prevented. However, for the further analysis of the volcanic plume events, the original GOME-2 ground-pixels associated with the registered grid boxes were regarded, as they represent the actual satellite measurements. In particular, individual satellite pixels are used for the correlation analysis between SO<sub>2</sub> and BrO (Chapter 9), because the spatial patterns of both species are generally different.

The SCDs for SO<sub>2</sub> from the GOME-2 measurements need to be corrected for a

non-volcanic offset. In contrast to the previous background correction process for gridded satellite data (cf. Section 6.2.2 and Section 8.3), the lat-/longitudinal offset was now corrected in a more sophisticated way in order to consider local effects around the individual volcanic plumes, such as the latitudinal dependent concentration of stratospheric ozone and the influence of the topography to the fitting of the Ring spectrum.

In a first step, the geometrical AMF was used to convert SCDs to VCDs (see also Section 8.3). This is a reasonable approach, as we are mainly interested in correcting the influence of stratospheric O<sub>3</sub> to the resulting SO<sub>2</sub> SCDs (cf. Section 4.3). For the determination of the lat-/longitudinal dependent SO<sub>2</sub> offset, a 2-dimensional spatial polynomial fit of 3rd degree was applied to the pixels from the reference area of the SO<sub>2</sub> PEB cluster (Figure 8.2) and those pixels from the PEB cluster itself, whose SO<sub>2</sub> VCDs lay within 3σ of the reference area (and were therefore supposed to be located outside the volcanic plume):

$$V_{i,\text{offset}} = \sum_{m,n=0}^3 a_{mn} \times x_i^m \times y_i^n \quad (8.3)$$

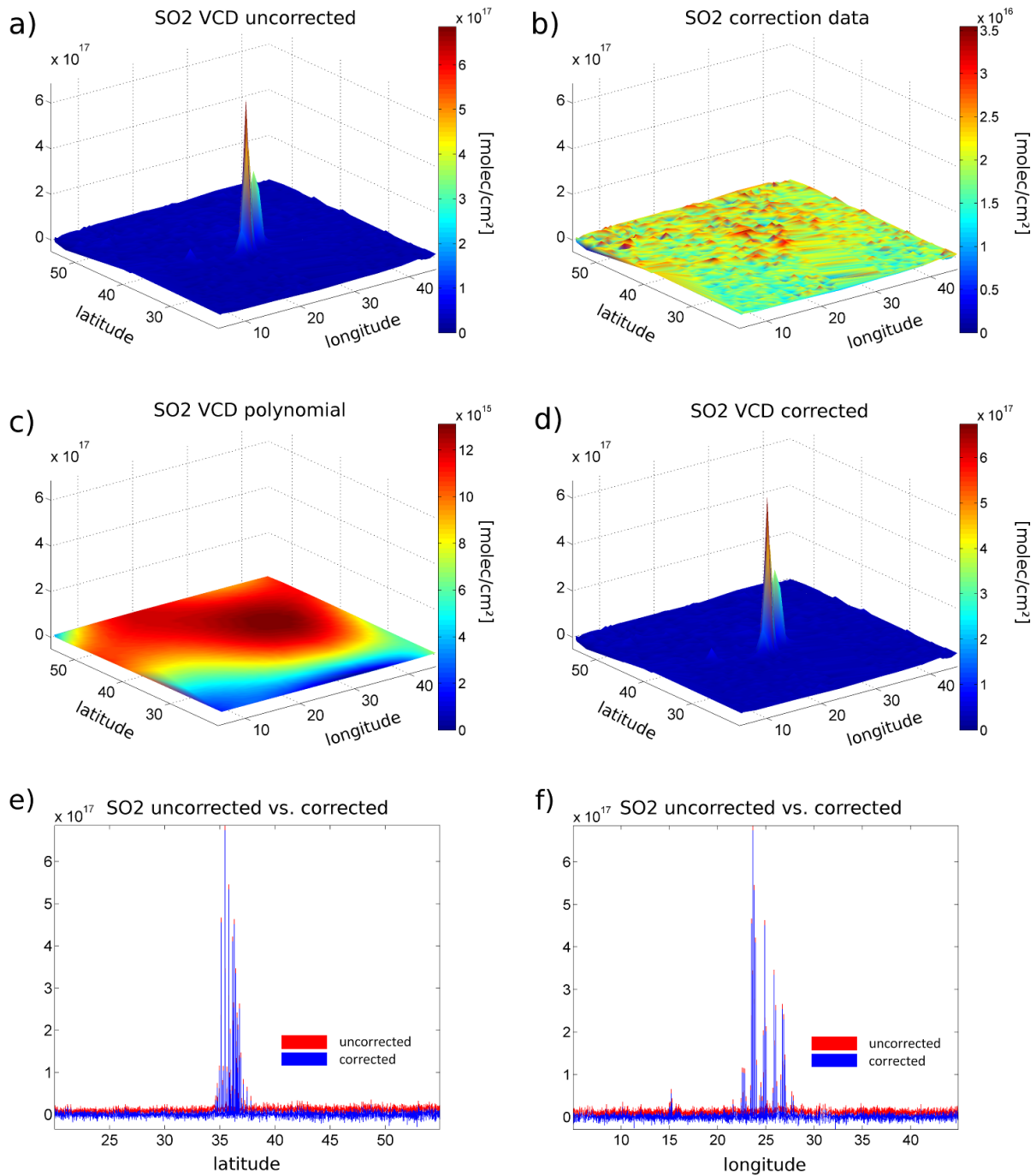
where  $a_{mn}$  are the fitted SO<sub>2</sub> offset VCDs at the centre coordinates  $x$  and  $y$  [°] of the satellite pixel  $i$ . All other satellite pixels within the PEB cluster (SO<sub>2</sub> VCD > 3σ of the combined reference area) were initially assumed to be part of the volcanic plume. By subtracting the fitted polynomial from all SO<sub>2</sub> VCDs (including the VCDs from the presumed volcanic plume pixels), we obtained the offset corrected geometrical SO<sub>2</sub> vertical column densities  $V_i^*$ :

$$V_i^* = V_{i,\text{geo.}} - V_{i,\text{offset}} \quad (8.4)$$

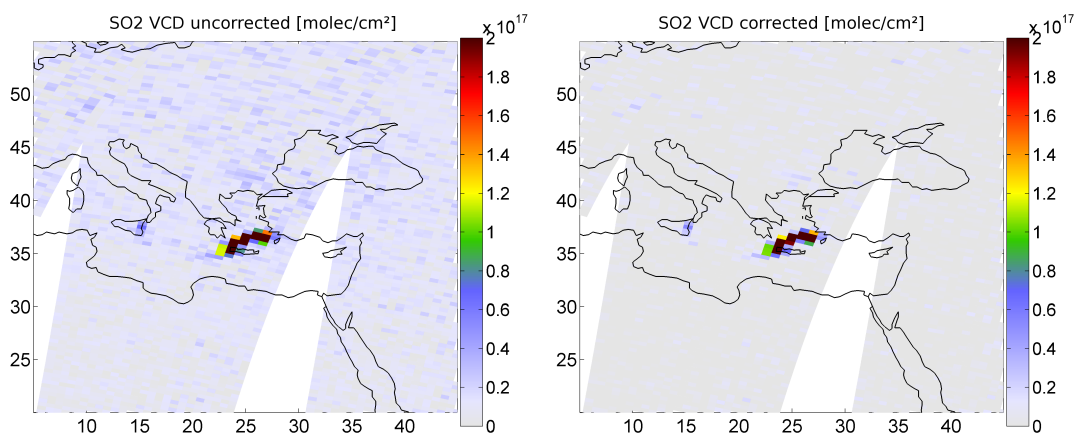
All offset/background corrected pixels within the SO<sub>2</sub> PEB cluster were once again checked for pixels whose  $V_i^*$  exceeded 3σ of the offset-corrected combined reference area. These pixels finally represent the identified volcanic plume.

Figure 8.3 shows an example for the volcanic plume of Mt. Etna on 11 May 2008. While the offset is in principle low compared to the maximum SO<sub>2</sub> VCD in the plume, an accurate correction can indeed have an influence on the specific plume pixel extraction, where only GOME-2 pixels are taken into account that exceed the 3σ threshold of the offset corrected reference area. In Figure 8.3 a, all extracted data including the SO<sub>2</sub> PEBs and the reference area are shown. By excluding all satellite measurements that fulfill the 3σ criterion and therefore are supposed to be a part of the volcanic plume (Figure 8.3 b), the 2D-polynomial may be calculated (Figure 8.3 c). The peak maximum of the polynomial in Figure 8.3 c mainly corrects for weak anthropogenic SO<sub>2</sub> emission signals that are caused by coal burning power plants over Bulgaria (cf. Section 7.3) in addition to the offset that is caused by the ozone interference. After the polynomial has been subtracted from the data, the SO<sub>2</sub> VCDs outside the plume are equally scattered around zero (Figure 8.3 d) for both, lat- and longitudinal direction (Figure 8.3 e and f).

## 8. Systematic detection of volcanic plumes



**Figure 8.3.:** SO<sub>2</sub> offset correction example of the volcanic plume of Mt. Etna on 11 May 2008. By excluding GOME-2 pixels that show SO<sub>2</sub> VCDs\* > 3σ of the reference area from all measurements (Figure 8.3a), the correction data (Figure 8.3b) can be used to calculate an offset polynomial (Figure 8.3c) that accounts for the ozone interferences and anthropogenic emissions. By subtracting the polynomial from all measurements, the SO<sub>2</sub> VCDs outside the plume are equally scattered around zero (Figure 8.3d) for both, lat- and longitudinal direction (Figure 8.3e and f).



**Figure 8.4.:** SO<sub>2</sub> maps for the Mt. Etna plume on 11 May 2008, before (left) and after (right) the offset correction. The offset is dominated by interferences with ozone increasing with latitude, but also due to anthropogenic emissions over the Balkans. Note that the colorbar has not been scaled to the maximum to make the offset more clearly visible.

Figure 8.4 shows the associated SO<sub>2</sub> maps of the uncorrected plume (Figure 8.4, left) and the plume after offset correction (Figure 8.4 right). Note that the colorbar has not been scaled to the maximum range of the SO<sub>2</sub> VCDs, in order to make the offset more clearly visible. The non-volcanic offset seems to be dominated by the spectral interference with ozone, as it increases with latitude, which is typical for mid-latitude regions during this time of the year (cf. 6.3 in Chapter 6), but also detects the anthropogenic emissions over the Balkans.

## 8.5. Combination of SO<sub>2</sub> SR and AR<sub>1</sub> for major eruptions

For major volcanic events, we sometimes have to account for non-linearities in the SO<sub>2</sub> retrieval, while for minor events, the standard retrieval is more appropriate (cf. Section 6.3). Thus, for the automatic plume extraction algorithm, both retrievals had to be combined. For all detected volcanic plumes where the maximum SO<sub>2</sub> SCD exceeded  $1 \times 10^{18}$  molec/cm<sup>2</sup>, the results from the SO<sub>2</sub> AR<sub>1</sub> at 326.5–335.3 nm (cf. Section 6.3.2) were investigated for the same PEB clusters and associated reference areas as for the standard retrieval. The geometrical SO<sub>2</sub> VCDs from the AR<sub>1</sub> were offset corrected in the same way as the VCDs from the SR (cf. Section 8.4). Again, all satellite pixels within the PEB cluster with a SO<sub>2</sub> VCD  $> 3\sigma$  of the offset corrected reference area were assumed to be part of the volcanic plume.

Maps of the SO<sub>2</sub> plume were subsequently created by using the initial plume pixels from the SR, but all pixels with a SO<sub>2</sub> SCD  $> 1 \times 10^{18}$  molec/cm<sup>2</sup> were replaced by the results from the AR<sub>1</sub>, if the corresponding pixels were also found to be part of the plume after the background correction process. In Figure 8.5, the SO<sub>2</sub> plume from the Kasatochi eruption is shown on 9 August 2008 (note the logarithmic scale in Figure 8.5a, b and d). The effects of the non-linearities due to the strong SO<sub>2</sub> absorptions are similar to the already presented example from the previous day (cf. Section 6.3.4).

## 8. Systematic detection of volcanic plumes

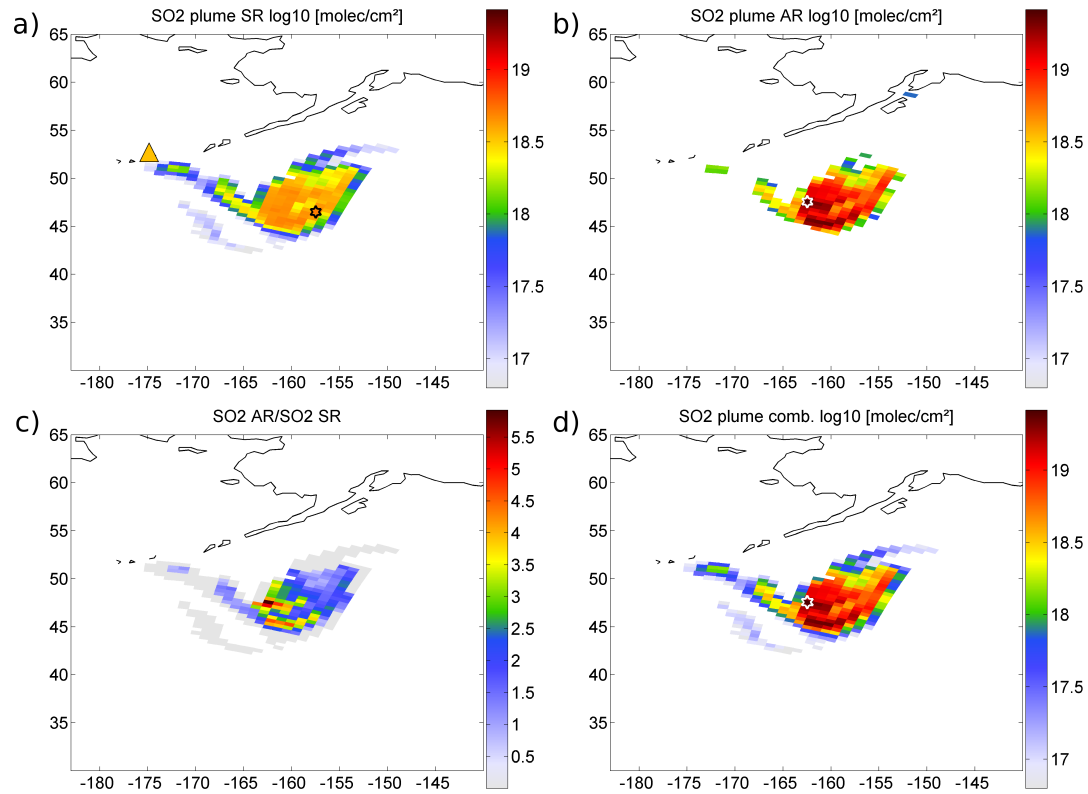


**Figure 8.5.:** Volcanic  $\text{SO}_2$  plume as seen by GOME-2 on 9 August 2008 during the eruption of Kasatochi volcano. **a)**  $\text{SO}_2$  SCDs from the standard retrieval (312.1–324 nm), **b)**  $\text{SO}_2$  SCDs from the  $\text{AR}_1$  (326.5–335.3 nm). While the maximum  $\text{SO}_2$  SCD for the SR ( $5.2 \times 10^{18}$  molec/cm<sup>2</sup>) is located in the south-eastern part of the plume (indicated by a black hexagon), it is now found to be shifted towards the west with a 5 times higher SCD ( $2.7 \times 10^{19}$  molec/cm<sup>2</sup>) in the  $\text{AR}_1$  (white hexagon). **c)** Ratios between the  $\text{SO}_2$  SCDs from the alternative and standard retrieval **d)** The new  $\text{SO}_2$  SCD product combines the results from both retrievals. Note the logarithmic scale in a), b) and d).

While the maximum  $\text{SO}_2$  SCD for the SR (Figure 8.5a) is located in the south-eastern part of plume (indicated by the small black star), it is shifted towards west for the  $\text{AR}_1$  (Figure 8.5b). Additionally, the resulting  $\text{SO}_2$  SCDs for the  $\text{AR}_1$  are now up to 5 times higher than for the SR, as can be seen in Figure 8.5c, where the ratios of the resulting  $\text{SO}_2$  columns from the different retrievals are shown for all pixels that were identified to be part of the plume in both evaluation wavelength regions. Results from both retrievals are finally combined in Figure 8.5d. The plume's centre looks much more structured than for the SR, where the central part of the plume mainly consists of a large homogeneous area, as most of the  $\text{SO}_2$  SCDs seem to be scattered around  $5 \times 10^{18}$  molec/cm<sup>2</sup> due to the saturation effect.

## 8.6. Time series of volcanic SO<sub>2</sub> between January 2007 and June 2011

The analysis of the GOME-2 measurements during the time period between January 2007 and June 2011 resulted in 772 individual SO<sub>2</sub> PEB clusters on 553 days. Therefore, 33.7% of all considered days (1642 days in total) showed evidence for enhanced volcanic activity and/or eruptions in the satellite data. Each PEB cluster represents an individual or at least completely isolated part of a volcanic plumes.

By the careful inspection of all captured volcanic events, it became clear that a general problem remains in identifying the source of some volcanic plumes in areas where several highly active volcanoes are located in close proximity. This is especially the case for the Kamchatka peninsula, where approximately 30 active volcanoes are located. Whenever the origin of a volcanic plume could not clearly be identified, the most likely volcano is named. For that purpose, the data was cross-checked with online reports on the Global Volcanism Program (GVP) website of the Smithsonian Institution (available under <http://www.volcano.si.edu/reports/usgs/>) and additionally with daily SO<sub>2</sub> maps from the Ozone Monitoring Instrument (OMI, <http://so2.gsfc.nasa.gov/>), the latter providing a more detailed spatial resolution of up to 13×25 km<sup>2</sup> (compared to 40×80 km<sup>2</sup> for GOME-2) and also daily global coverage. In total, the identified SO<sub>2</sub> plumes were caused at least 36 different volcanoes worldwide.

Figure 8.6 shows the time series of the maximum SO<sub>2</sub> VCDs\* that were present in the 772 plumes within the investigated time period in order to get an overview of the frequency and magnitude of the automatically extracted volcanic plumes. Besides a large number of volcanic plumes during strong degassing phases and minor eruptions that caused moderate SO<sub>2</sub> VCDs\*, several major eruptions can be directly identified by VCDs\* of up to 7×10<sup>18</sup> molec/cm<sup>2</sup> (eruption of Mt. Kasatochi, August 2008). It is noted that the SO<sub>2</sub> VCDs\* for the major eruptions (SCDs\*>1×10<sup>18</sup>) were obtained using the results from the plume combination process (cf. Section 8.5) and that the y-axis was set to a logarithmic scale. In addition, the most prominent volcanic events in Figure 8.6 are indicated by the highlighted time periods:

1. Piton de la Fournaise (La Réunion) on the 4 April 2007. The volcano is currently one of the most active volcanoes worldwide.
2. Jebel at Tair (Yemen), that erupted on 30 September 2007 after 124 years of dormancy.
3. Mt. Etna (Sicily) on 11 May 2008, one of the world's most active volcanoes. Due to its accessibility, Etna is frequently monitored by various kinds of instruments.
4. Okmok (Aleutian Islands, Alaska) on 13 July 2008, the strongest eruption by far of the volcano since at least 700 years.
5. Kasatochi (Aleutian Islands, Alaska) on 8 August 2008, probably the eruption that was richest in sulphur since the eruption of Pinatubo in 1991 (and therefore

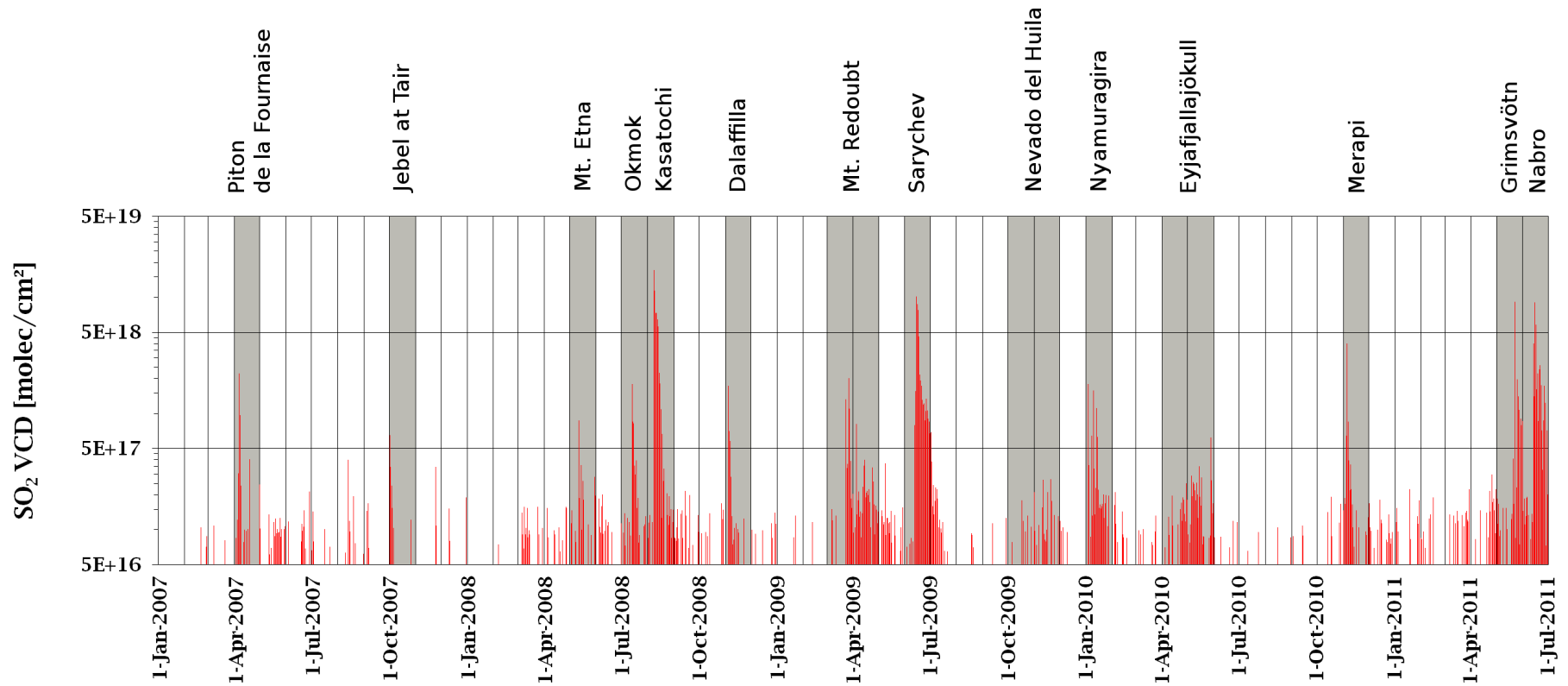


**Figure 8.6.:** Time series of maximum GOME-2  $\text{SO}_2$  VCDs\* within all volcanic plumes captured by the automatic plume detection algorithm between January 2007 - June 2011. Several major eruptions can be directly identified by VCDs\* of up to  $7 \times 10^{18}$  molec/cm<sup>2</sup> (eruption of Mt. Kasatochi, August 2008). The time periods highlighted in gray denote the most prominent volcanic events (logarithmic scale for  $\text{SO}_2$ ).

also in the here regarded time period). The injected SO<sub>2</sub> could be monitored by GOME-2 for more than 6 weeks.

6. Dalaffilla (Ethiopia) on 4 November 2008, the first recorded eruption of the volcano in history.
7. Mt. Redoubt (Alaska) on 22 March 2009, after several month of seismic unrest. SO<sub>2</sub> plumes could be monitored by GOME-2 until mid-June.
8. Sarychev (Kuril Islands, Russia), the largest eruption for SO<sub>2</sub> in 2009. The SO<sub>2</sub> encircled the globe within 4 weeks after the eruption had started.
9. Nevado del Huila (Colombia), with several minor eruptions within the end of October until mid-December 2009.
10. Nyamuragira (Democratic Republic of the Congo) on 2 January 2010, with extensive lava flows that reached a maximum distance of about 11 km away from the main eruptive site until the activity stop at the end of January.
11. Eyjafjallajökull (Iceland) on 14 April 2010. Large amounts of ash were injected into the atmosphere especially during the initial phase of the eruption due to lava-ice-interaction. Enhanced SO<sub>2</sub> SCDs were only measured during the later phase after 22 April for about 1 month.
12. Merapi (Indonesia) on 4 November 2010, after several smaller eruptions had already taken place for one week. The eruption was the most violent one in 2010, with about 350,000 people that had to be evacuated from their homes.
13. Grimsvötn (Iceland) on 21 May 2011, the second icelandic eruption that caused flight cancelations in parts of Europe due to increased amounts of volcanic ash, although the total impact on the aviation industry was low compared to the Eyjafjallajökull eruption.
14. Nabro (Eritrea) on 13 June 2011, the first historically reported eruption of the volcano. The eruption was clearly the richest in sulphur in whole 2011, injecting continously large amounts of SO<sub>2</sub> in the atmosphere for about 1 month.

### **Exemplary retrieval: The eruption of Dalaffilla (Ethiopia)**

In order to illustrate the algorithm's ability to extract GOME-2 measurements of a volcanic SO<sub>2</sub> plume, Figure 8.7 shows the captured plume pixels for the first four days after the start of the Dalaffilla eruption on 4 November 2008. Gaps within the captured plume are caused by areas, where the GOME-2 measurements did not cover the volcanic emissions in between two neighboring satellite orbits. The plume was rapidly transported eastwards, while the SO<sub>2</sub> SCDs decreased due to the plume's dispersion and the decay of SO<sub>2</sub>. As shown, the algorithm is clearly capable to identify main parts of A volcanic plume during an eruption and detects also smaller filaments that are formed due to wind shear and differences in the initial release altitude of the emissions.

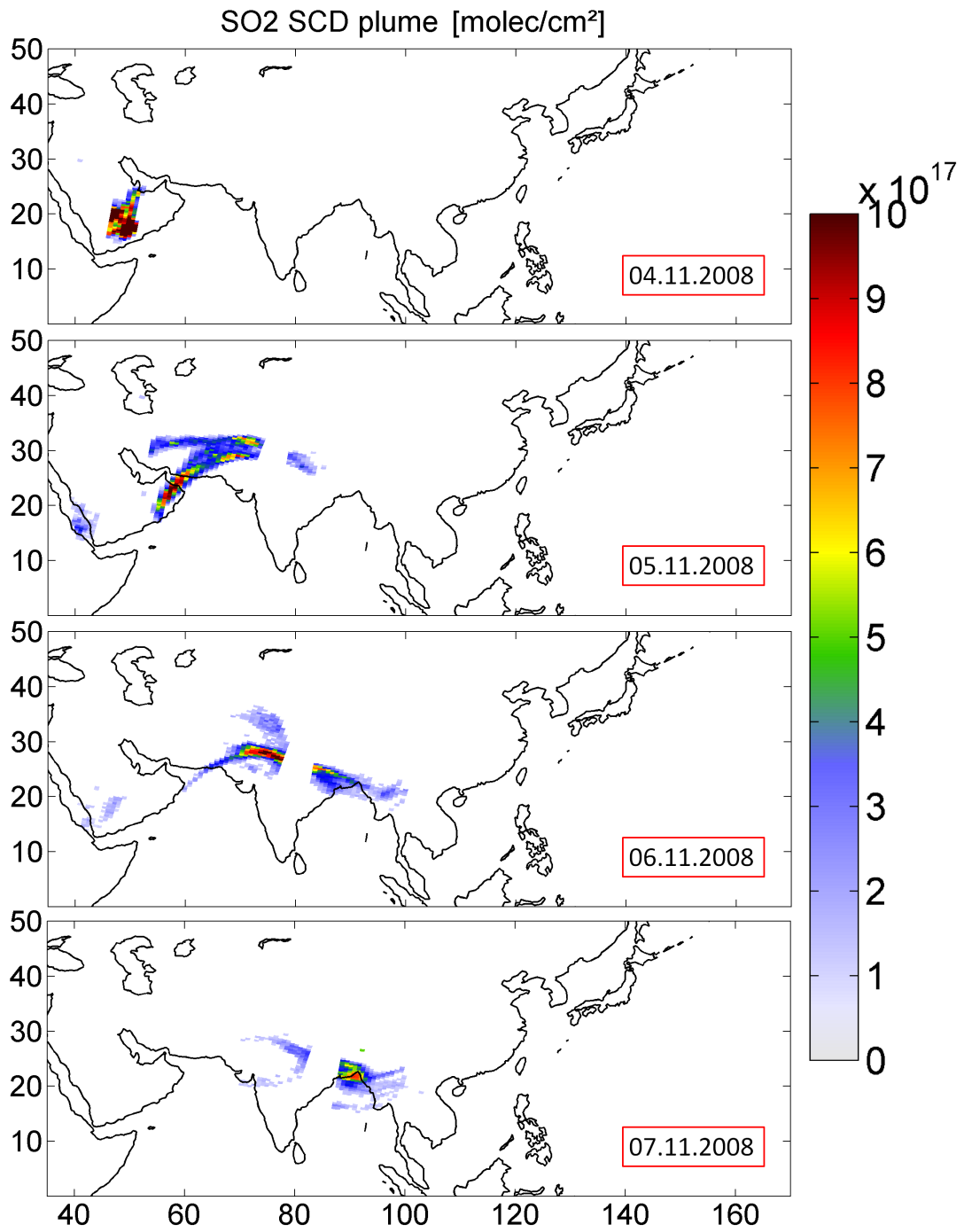


**Figure 8.7.:** Automatically extracted GOME-2 pixels of the  $\text{SO}_2$  plume during the first four days of the Dalaffilla eruption that started on 4 November 2008. While the plume is rapidly transported eastwards, the  $\text{SO}_2$  SCDs decrease due to the plume's dispersion and the decay of  $\text{SO}_2$ .

## 8.7. Discussion on the plume detection algorithm

Table 8.2 lists all 36 individual volcanoes that were associated with the 772 SO<sub>2</sub> events and the individual annual number of detected events. Most SO<sub>2</sub> plume events were detected during the years 2008 and 2009.

In 2008, the total number of plume events (199) is clearly dominated by events from the extensive degassing phase of Kilauea (82) and the major eruption of Kasatochi (57), together contributing almost 70% to all detected plumes in this year. The year 2009 revealed even more SO<sub>2</sub> plumes (212) due to the eruptions of Redoubt (62) and Sarychev (83), again contributing about 70% of all detected plumes in this year. Together, about 26% (202) of all extracted plume events are associated with the eruptions of Kasatochi, Redoubt and Sarychev, while these volcanoes showed no increased column densities in the years before or after their eruptions.

Since the detection algorithm attempts to identify contiguous parts of a volcanic plume, spatially separated parts of a SO<sub>2</sub> plume from a single eruption are detected as individual plume events. Thus, a volcanic plume that has been caused by a major eruption (e.g. Kasatochi) is identified as several individual plumes, if it consists out of several fractions that are spatially widely separated with distances larger than 5° away from the associated reference areas (cf. Figure 8.2). The total number of 772 single SO<sub>2</sub> plume events therefore consists of a large number of individual plume events from the major eruptions, while strong degassing phases are usually detected only once per regarded day.

Interestingly, the two volcanoes that showed no considerable eruption, but strong degassing phases for the regarded time period contribute with nearly the same number of events (197):

1. Ambrym (Vanuatu) with the largest number of events (104), almost half of them in 2010 (59)
2. Kilauea (Hawaii), providing the second largest number of events (93), with by far most of them during the very strong degassing phase in 2008 (82)

It should be noted that besides Ambrym, only the Tungurahua volcano (Ecuador) caused SO<sub>2</sub> plume events that were detected by the algorithm for all years during the whole time period (for Kilauea, however, plume events for all years except 2007 were found). While for some volcanoes this may result from a stop of enhanced activity after an eruption, other emissions were probably just too low to be detected on a daily basis by the satellite instrument. This is also indicated in maps showing mean SO<sub>2</sub> levels, in which several degassing volcanoes can be clearly identified although they were not or only occasionally detected by the algorithm (cf. Section 7). Some minor plumes (e.g. from quiescent degassing volcanoes) are not detected by the algorithm due to the relatively large initial SO<sub>2</sub> VCD threshold of  $5 \times 10^{16}$  molec/cm<sup>2</sup> (cf. Section 8.3). The threshold was chosen to focus on volcanic plumes of a certain minimum extent and furthermore to reduce the number of misidentifications caused by erroneous results of the DOAS fit in case of low SO<sub>2</sub> SCDs.

**Table 8.2.:** *Extracted volcanic SO<sub>2</sub> events between January 2007–June 2011. Whenever the origin of the SO<sub>2</sub> plumes could not be clearly assigned to a certain volcano, it is indicated by \*. If at least some of the plumes could be assigned to the volcano, it is indicated by †.*

volcano	2007	2008	2009	2010	2011	total number
Ambrym	8	5	13	59	19	104
Anatahan	2	4	-	-	-	6
Bagana	3	-	-	-	-	3
Bezymianny*	2	-	-	2	-	4
Chikurachki†	8	-	-	-	-	8
Dalaffilla	-	11	-	-	-	11
Etna	6	3	-	-	3	12
Eyjafjallajökull	-	-	-	30	-	30
Ferndina	-	-	18	-	-	18
Fuego	1	-	-	-	-	1
Galeras	-	1	1	-	-	2
Gorely*	-	-	-	1	-	1
Grímsvötn	-	-	-	-	31	31
Karymsky	-	4	1	3	-	8
Kasatochi	-	57	-	-	-	57
Kilauea	-	82	4	6	1	93
Kizimen†	-	-	-	-	5	5
Kliuchevskoi†	21	-	-	3	2	26
Koryaksky	-	-	5	-	-	5
Langila	-	-	1	-	-	1
Manda Hararo	2	-	1	-	-	3
Merapi	-	-	-	11	-	11
Mt. Redoubt	-	-	62	-	-	62
Nabro	-	-	-	-	25	25
Nevado del Huila	1	4	21	-	-	26
Nyamuragira	-	-	-	21	-	21
Nyiragongo	1	-	-	-	-	1
Okmok	-	14	-	-	-	14
Pacaya†	-	-	-	6	-	6
Piton de la Fournaise	6	-	-	-	-	6
Popocatépetl	1	2	-	-	-	3
Rabaul	-	-	1	1	-	2
Sakurajima*	-	-	-	-	1	1
Sarychev	-	-	83	-	-	83
Shiveluch†	-	-	-	4	25	29
Soufrière Hills	-	-	-	3	-	3
Soputan	2	1	-	-	-	3
Tengger Caldera	-	-	-	4	8	12
Tungurahua	2	4	1	7	7	21
Turrialba*	-	-	-	1	-	1
total	72	199	212	159	130	772

Generally, the algorithm is capable of detecting also very small plumes with low SO<sub>2</sub> column densities by the implementation of a lower threshold. However, the number of misidentifications can only be confined to an acceptable level for such weak emissions by restricting the detection algorithm to certain regions close to an active volcano. A first trial of the algorithm for a lowered SO<sub>2</sub> VCD threshold of  $1 \times 10^{16}$  molec/cm<sup>2</sup> close to Ambrym and Kilauea resulted in significantly more detected volcanic plumes for all years. In total 740 plumes for Ambrym and 562 plumes for Kilauea were found for the years 2007-2011, after some still misidentified plumes had been removed manually. In the future, more strictly criterias will be needed to provide the accurate detection of such weaker SO<sub>2</sub> plumes from degassing volcanoes by the algorithm.



## 9. Systematic investigation of BrO during volcanic events

The abundance of bromine monoxide (BrO) in volcanic emissions has been frequently measured via ground-based DOAS measurements at volcanoes worldwide since its first detection by Bobrowski et al. (2003) (cf. Section 2.3.1). In contrast, the first observation of volcanic BrO by a satellite instrument has been only recently reported during the Kasatochi eruption in 2008 (Theys et al., 2009). In this chapter, the extracted volcanic SO<sub>2</sub> plumes from the automatic plume extraction algorithm (Chapter 8) will be further analyzed for a coincident enhancement of BrO that might have been formed after the plume's release.

The chapter is structured as follows: After a short introduction on the detection of volcanic BrO by satellite instruments in general (Section 9.1), the extracted volcanic plumes are background corrected for non-volcanic BrO (Section 9.2). In the following, each plume will be examined for enhanced BrO SCDs and the general BrO/SO<sub>2</sub> behaviour will be investigated. Subsequently, several examples for different BrO/SO<sub>2</sub> relationships from the identified volcanic plumes will be shown (Section 9.3). In Section 9.4, all extracted volcanic plumes are systematically analyzed and categorized according to their BrO/SO<sub>2</sub> relationship. The results are finally discussed in Section 9.5.<sup>1</sup>

### 9.1. Satellite retrieval of volcanic BrO

Given the numerous spectroscopic ground-based measurements of BrO in volcanic plumes (cf. Section 2.3) and the general ability of satellite instruments to monitor BrO globally (e.g. Wagner and Platt, 1998; Richter et al., 2002; Theys et al., 2011), it appears like an obvious idea to use satellite data for the investigation of volcanic BrO during eruptive events. However, a first attempt to detect volcanic BrO from space, using data from the GOME and the SCIAMACHY (cf. Section 3.2.1) instruments, failed (Afe et al., 2004): No correlation between enhanced columns of SO<sub>2</sub> and the corresponding BrO columns was found in the plumes of selected eruptions at Mt. Etna (Sicily), Popocatepetl (Mexico), the Soufrière Hills volcano (Montserrat) and Nyamuragira (Democratic Republic of the Congo). The authors named several reasons for the lack of enhanced BrO observations in this first study, including the reduced sensitivity of the satellite instruments and the absence of high BrO concentrations during these eruptions. As the size of a GOME ground-pixel is 40×320 km<sup>2</sup>, a volcanic BrO plume might be invisible to satellite instruments, because the plume

---

<sup>1</sup>Parts of this chapter have been published in Hörmann et al. (2012).

often only covers a small fraction of the satellite ground-pixel. Thus the signal from the plume is "diluted" by the radiation originating from the remaining (much larger) part of the pixel, which is not affected by the plume. Although the SCIAMACHY instrument provides a much higher spatial resolution ( $30 \times 60 \text{ km}^2$ ) compared to GOME, it has the disadvantage of a rather sparse daily coverage of the troposphere due to the instrument's alternating limb/nadir observation sequence (Bovensmann et al., 1999). In addition, the signal-to-noise ratio in the UV range of SCIAMACHY is reduced due to an anomalously low grating efficiency (De Smedt et al., 2004).

The first detection of a volcanic BrO plume by a satellite instrument was eventually reported after the eruption of the Kasatochi volcano on 7 August 2008 by Theys et al. (2009). The GOME-2 instrument (with an improved spatial resolution of  $40 \times 80 \text{ km}^2$  compared to its precursor GOME) was able to track the BrO plume for several days during its transport eastwards across the whole North American continent. Additionally, the authors reported that similar BrO SCDs were now also observed by SCIAMACHY and a significant enhancement of BrO after the Mt. Etna eruption on 13 May 2008 was furthermore mentioned.

Motivated by these findings, the whole dataset of GOME-2 from the beginning of the regular measurements in January 2007 until the end of June 2011 was examined for further volcanic events with detectable amounts of BrO. For that purpose, the volcanic plumes that were automatically extracted from the plume extraction algorithm in Chapter 8 were further investigated. Since  $\text{SO}_2$  is the third most abundant gaseous species emitted by volcanoes (Textor et al., 2004) and is normally easy to detect in the UV due to its strong differential absorption features, it is well-suited as a proxy for the existence and extent of a volcanic plume, regardless the gaseous species of interest.

In the next sections, a detailed description of the BrO analysis for the previously extracted  $\text{SO}_2$  plumes will be given. The area covered by each captured  $\text{SO}_2$  plume was first examined for a simultaneous enhancement of BrO. Afterwards, the data were checked for the degree of spatial correlation between the two species and the BrO/ $\text{SO}_2$  ratios were calculated.

### 9.2. Correction for non-volcanic BrO

The GOME-2 measurements for volcanic BrO are generally superimposed by the stratospheric BrO distribution, which systematically depends on latitude, but to a smaller degree also on longitude (cf. Chapter 6.4.1). Additionally, extended areas in high latitudes are occasionally affected by tropospheric BrO plumes that are formed e.g. at the sea ice surface during Arctic spring in polar regions and can sometimes extend to latitudes of  $\pm 70^\circ\text{N}$  (Wagner and Platt, 1998).

Usually, a volcanic BrO plume is not instantaneously visible in daily global satellite maps, because the fraction of bromine species in volcanic plumes is small compared to  $\text{SO}_2$  and the BrO absorptions are less strong. Instead, the signal from non-volcanic BrO dominates the global distribution. Consequently, the extracted  $\text{SO}_2$  pixels from the plume detection algorithm (cf. Chapter 8) were used for the correction of the non-

volcanic BrO signal. In principle, the same offset correction procedure as for SO<sub>2</sub> was used, i.e. a 2D-polynomial was spatially fitted to all GOME-2 pixels that were found not to be a part of the volcanic plume (SO<sub>2</sub> VCD < 3σ of the preselected reference area). However, where a 3rd grade polynomial was sufficient for the SO<sub>2</sub> correction, a polynomial of 4th degree (m, n = 0,...,4) was required in order to account for the generally stronger spatial gradients of the BrO VCDs:

$$V_{i,\text{offset}} \sim \sum_{m,n=0}^4 a_{mn} \times x_i^m \times y_i^n \quad (9.1)$$

where  $a_{mn}$  are the fitted BrO offset VCDs at the centre coordinates  $x$  and  $y$  [°] of the satellite pixel  $i$ . By subtracting the fitted polynomial from all BrO VCDs (including the VCDs from the presumed volcanic plume pixels), we obtained the offset corrected geometrical BrO vertical column densities  $V_i^*$ :

$$V_i^* = V_{i,\text{geo}} - V_{i,\text{offset}} \quad (9.2)$$

In Figure 9.1, the BrO background correction process is illustrated analogous to that for SO<sub>2</sub> in Section 8.4 for the eruption of Mt. Etna on 11 May 2008. From the uncorrected data (Figure 9.1 a), the strong non-volcanic BrO VCD offset (mainly caused by stratospheric BrO) is clearly visible at about  $5 \times 10^{13}$  molec/cm<sup>2</sup>. The exclusion of satellite measurements that showed strongly enhanced SO<sub>2</sub> VCDs (> 3σ out of the corresponding reference area) yields the data for the BrO offset correction (Figure 9.1 b), which already indicates the lat-/longitudinal dependence of the stratospheric BrO distribution. The correction data is then described by the 2D-polynomial (Figure 9.1 c) and subsequently subtracted from the initial data. Compared to the result of the background correction for non-volcanic SO<sub>2</sub> (cf. Figure 8.3), the effects of the correction on BrO data (Figure 9.1 d) are clearly stronger. Although dominated by the spatially homogeneous offset of  $\sim 5 \times 10^{13}$  molec/cm<sup>2</sup>, some lat-/longitudinal variations are also clearly compensated as illustrated in Figure 9.1 e+f, where the VCDs are shown before and after the correction in latitudinal and longitudinal direction, respectively.

The corresponding data can be also seen projected on daily maps in Figure 9.2, where the differences between the BrO VCDs before and after the background correction process are more clearly visible. On the left side of Figure 9.2, the uncorrected VCDs are shown. Apart from the volcanic BrO plume over the Greek island Crete that is visible even in the uncorrected data, the large, mostly latitude-dependent stratospheric BrO offset can be clearly seen. Additionally, some scattered slightly enhanced BrO VCDs are found for the north-eastern part of the map, probably caused by imperfect fitting of the Ring effect over clouded or highly elevated scenes. However, as the right panel in Figure 9.2 shows, the non-volcanic signal is widely corrected for the whole area, yielding a much more prominent volcanic signal. By comparing the BrO and SO<sub>2</sub> maps for this specific volcanic plume (Figure 9.2 respectively Figure 8.3), it is clearly seen that the plumes are collocated to a high degree.

## 9. Systematic investigation of BrO during volcanic events

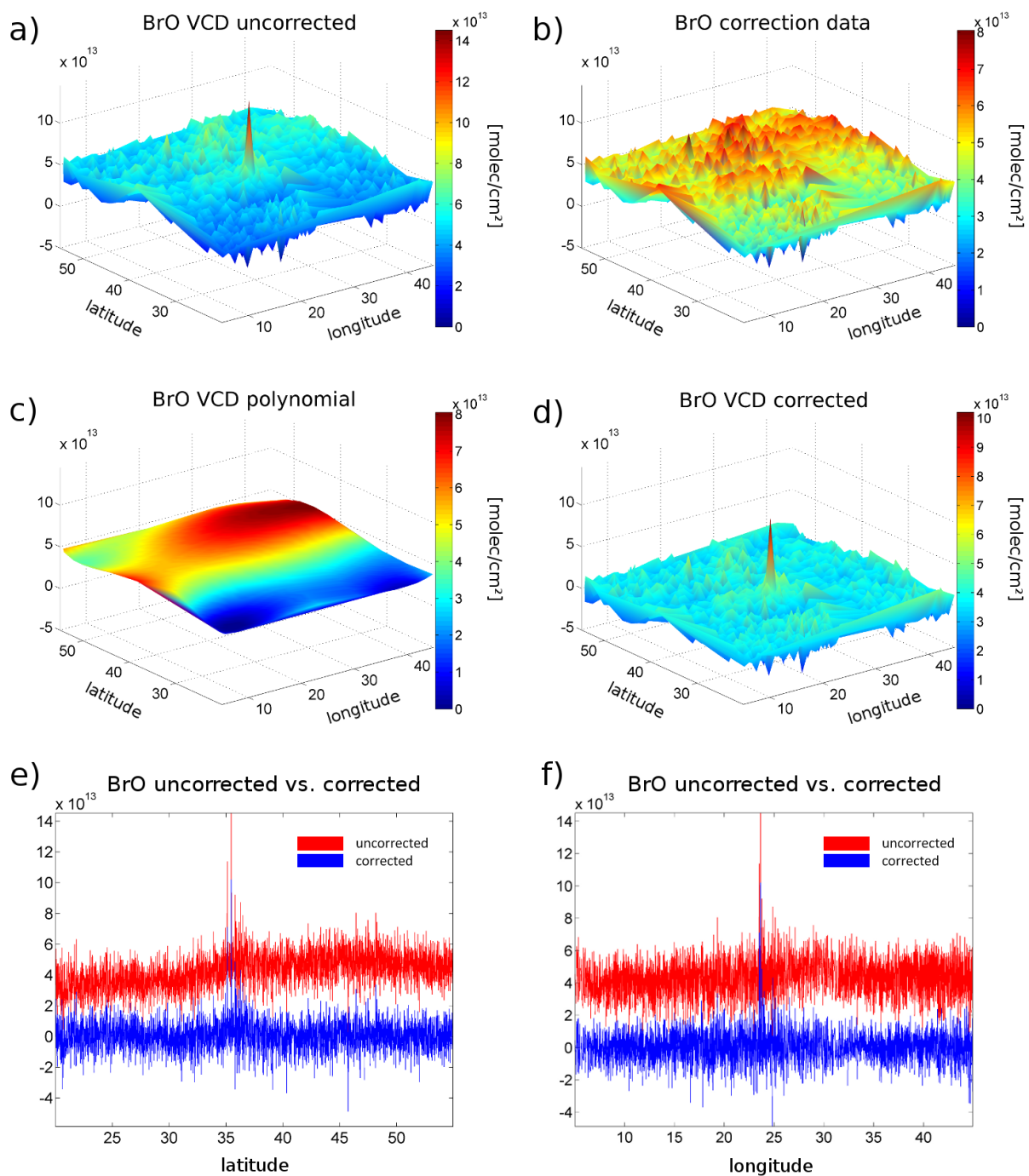


**Figure 9.1.:** BrO offset correction by an example of the volcanic plume of Mt. Etna on 11 May 2008. By excluding GOME-2 pixels that show  $\text{SO}_2$  VCDs\*  $> 3\sigma$  of the reference area (cf. Figure 8.3 in Section 8) from all measurements (Figure 9.1a), the correction data (Figure 9.1b) can be used to calculate an offset polynomial (Figure 9.1c) that accounts for the non-volcanic, mostly stratospheric BrO signal. By subtracting the polynomial from all measurements, the BrO VCDs outside the plume are equally scattered around zero (Figure 9.1d) for both, lat- and longitudinal direction (Figure 9.1e and f).

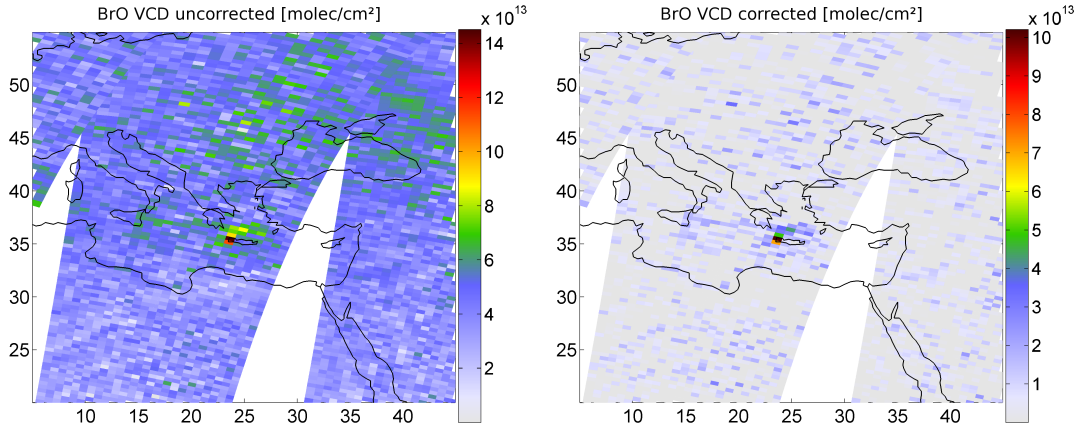


**Figure 9.2.:** *Uncorrected (left) and non-volcanic BrO corrected (right) maps of the GOME-2 BrO VCDs for the volcanic plume after the Mt. Etna eruption on 11 May 2008. The BrO plume seems to form a continuous trail from the volcano to the location of the SO<sub>2</sub> plume at the time of the measurements, probably caused by spectral interference of clouds.*

Interestingly, the BrO plume forms a continuous trail from the volcano to the location of the SO<sub>2</sub> plume at the time of the measurements, which is not found for the SO<sub>2</sub> data. Most probably, this weak trail also results from interferences of the Ring spectrum with clouds that were present at that time.

Despite the different evaluation wavelength ranges, the AMF of SO<sub>2</sub> and BrO should be very similar and depend only slightly on the altitude of the volcanic plume during most detected SO<sub>2</sub> events, with typical plume heights between 7 and 13 km (cf. Afe et al., 2004). The influence of non-linearities in the SO<sub>2</sub> retrieval for volcanic plumes with an exceptionally high SO<sub>2</sub> concentration have been prevented by using the SO<sub>2</sub> data from the combined product as described in Section 8.5. However, the presence of volcanic ash might have an important influence on radiative transfer and therefore further information (e.g. about plume height and ash content) is necessary for a precise VCD calculation (cf. Section 4.6), but normally not available. As the focus of this study lies in the general ability of the GOME-2 instrument to detect BrO in addition to SO<sub>2</sub> during increased activity/eruptive phases of volcanoes and the possible correlation between them, we simply reconverted the background corrected VCD<sub>i</sub><sup>\*</sup> into slant column densities SCD<sub>i</sub><sup>\*</sup> for the following investigations by multiplication with their AMF<sub>i,geo</sub>:

$$S_i^* = V_{i,geo}^* \times A_{i,geo} \quad (9.3)$$

In the future, detailed radiative transform calculations will be needed to further investigate the influence of ash on the retrieved slant column densities.

### 9.3. Volcanic BrO within January 2007–June 2011

As a result from the BrO analysis for all 772 extracted volcanic SO<sub>2</sub> plumes (cf. Section 8.6), the maximum BrO VCDs in the regarded plume areas are presented in Figure 9.3 in comparison to the maximum SO<sub>2</sub> VCDs. While the maximum BrO VCD\* for most of the volcanic events is around  $2.5 \times 10^{13}$  molec/cm<sup>2</sup>, the VCDs\* during several eruptions show much higher values. Interestingly, this is not the case for some of the major SO<sub>2</sub> eruptions, e.g. Okmok in July 2008, Merapi in November 2010 or Grimsvötn in May 2011.

In the following, several volcanic eruptions will be presented and discussed in more detail in order to investigate the different SO<sub>2</sub> to BrO relationships that have been observed. The focus will be on some of those volcanic plumes where the BrO VCD\*<sub>max</sub> was clearly enhanced ( $> 5 \times 10^{13}$  molec/cm<sup>2</sup>) and therefore indicate the presence of volcanic BrO. This includes the eruptions of BZ - Bezymianny (Kamchatka Peninsula) in May 2007, ET - Mt. Etna in May 2008, KS - Kasatochi volcano in August 2008, DL - Dalaffilla (Ethiopia) in November 2008, RD - Mt. Redoubt (Alaska) in March/April 2009, SA - Sarychev (Kuril Islands) in June 2009, EY - Eyjafjallajökull (Iceland) in April/May 2010 and NB - Nabro volcano in June 2011 (see labelled time periods in Figure 9.3 and Table 9.1, respectively).

The sequence of selected examples starts with volcanic plumes showing a high correlation and continues with examples of decreasing degree of correlation. All examples are examined for linear correlation between the two species by applying a bivariate linear fit (Cantrell, 2008) to the SO<sub>2</sub> and BrO SCDs\* of the identified plume pixels.

**Table 9.1.:** *Examples for the abundance of volcanic BrO that are presented in Section 9.3.1–9.3.6*

label	volcano	date	section	figure
ET	Etna	14 May 2008	Section 9.3.1	Figure 9.4
BZ	Bezymianny	11/12 May 2007	Section 9.3.2	Figure 9.5
DL	Dalaffilla	4 November 2007	Section 9.3.3	Figure 9.6
NB	Nabro	16 June 2011	Section 9.3.4	Figure 9.7
KS	Kasatochi	9 August 2008	Section 9.3.5	Figure 9.8
		11 August 2008	Section 9.3.5	Figure 9.9
SR	Sarychev	15/16 June 2009	Section 9.3.6	Figure 9.10

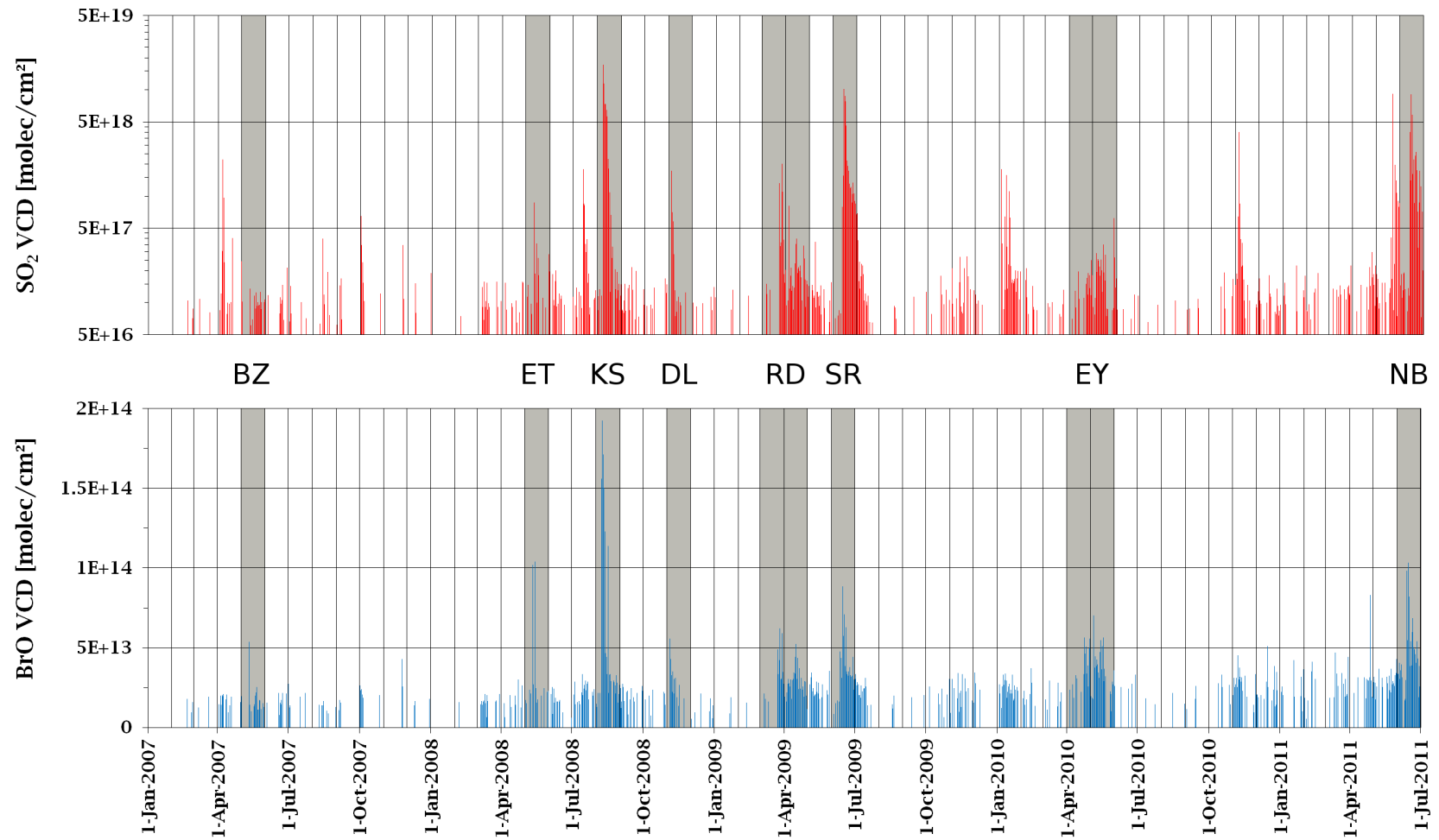


**Figure 9.3.:** Time series of maximum GOME-2 SO<sub>2</sub> and BrO VCDs\* within all volcanic plumes that were captured between January 2007–June 2011. The highlighted time periods indicate volcanic events where clearly enhanced were present, including eruptions of BZ - Bezymianny (Kamchatka Peninsula) in May 2007, ET - Mt. Etna in May 2008, KS - Kasatochi volcano in August 2008, DL - Dalaffilla (Ethiopia) in November 2008, RD - Mt. Redoubt (Alaska) in March/April 2009, SA - Sarychev (Kuril Islands) in June 2009, EY - Eyjafjallajökull (Iceland) in April/May 2010 and NB - Nabro volcano in June 2011.

### 9.3.1. Etna (14 May 2008)

Being one of the most active volcanoes in the world and easily accessible, Etna is one of the most frequently monitored volcanoes. According to reports from the Istituto Nazionale di Geofisica e Vulcanologia, sezione di Catania (INGV-CT), a new eruptive fissure opened on Etna's upper east side on May 13, after several months of seismic unrest (Smithsonian, 2007-2011).

Figure 9.4 shows the volcanic plume during the eruption on 14 May 2008 (labeled ET in Figure 9.3). The SO<sub>2</sub> and BrO SCDs\* of the whole regarded area (including the plume and reference area) can be seen in Figure 9.4 a and 9.4 c, respectively. Figure 9.4 b and 9.4 d show only the satellite pixels where the SO<sub>2</sub> VCDs\* were larger than 3 $\sigma^*$  (with  $\sigma^*$  the standard deviation of the reference area). The corresponding correlation plot (Figure 9.4 e) shows a clear linear correlation between the two species with  $r^2=0.7$  and a fitted mean BrO/SO<sub>2</sub> ratio of  $\sim 2.5 \times 10^{-4}$ . It is interesting to mention, that the location of the SO<sub>2</sub> SCD\*<sub>max</sub> corresponds to the location of the BrO SCD\*<sub>max</sub>. Another eruption at the Southeast Crater of Mt. Etna on 10 May 2008 (Bonaccorso et al., 2011) showed similar behaviour, with a linear correlation between the two species and BrO/SO<sub>2</sub> ratios of some  $10^{-4}$ .

### 9.3.2. Bezymianny/Kliuchevskoi (11/12 May 2007)

The Bezymianny volcano is one of 29 active volcanoes on the Kamchatka Peninsula. The volcano was moderately active throughout 2007, interrupted by some small explosions in May and October-December.

Figure 9.5 shows the trace gas distribution after such an explosion on 11/12 May 2007 (labelled BZ in Figure 9.3). In Figure 9.5 a, the background corrected volcanic SO<sub>2</sub> plume from Bezymianny (indicated by the orange triangle) can be seen over the Kamchatka Peninsula. Below (Fig. 9.5 c), the BrO SCDs\* are shown for the same area, indicating the presence of enhanced BrO columns in the same area as the enhanced SO<sub>2</sub> SCDs\*. Like for the previous example of Mt. Etna, Fig. 9.5 b and d show only the satellite pixels containing the volcanic plume (SO<sub>2</sub> VCDs\* > 3 $\sigma^*$ ). These pixels were used for the correlation plot (Figure 9.5 e), with a correlation coefficient  $r^2=0.62$  and a resulting mean BrO/SO<sub>2</sub> ratio of  $\sim 4.4 \times 10^{-4}$ .

Due to the close proximity of Bezymianny to the Kliuchevskoi volcano ( $\sim 10$  km), we can not be entirely sure that the observed volcanic plume came from Bezymianny alone, as Kliuchevskoi also showed increased activity at the time of the measurements according to reports of the Kamchatka Volcanic Eruption Response Team (KVERT). However, as seismic data suggested an explosive eruption of Bezymianny shortly before the satellite measurements (Smithsonian, 2007-2011), it seems most likely that the major part of the visible plume originated from that volcano with minor parts from Kliuchevskoi (see also the KVERT webpage for detailed activity reports on <http://www.kscnet.ru/ivs/kvert/updates/>).

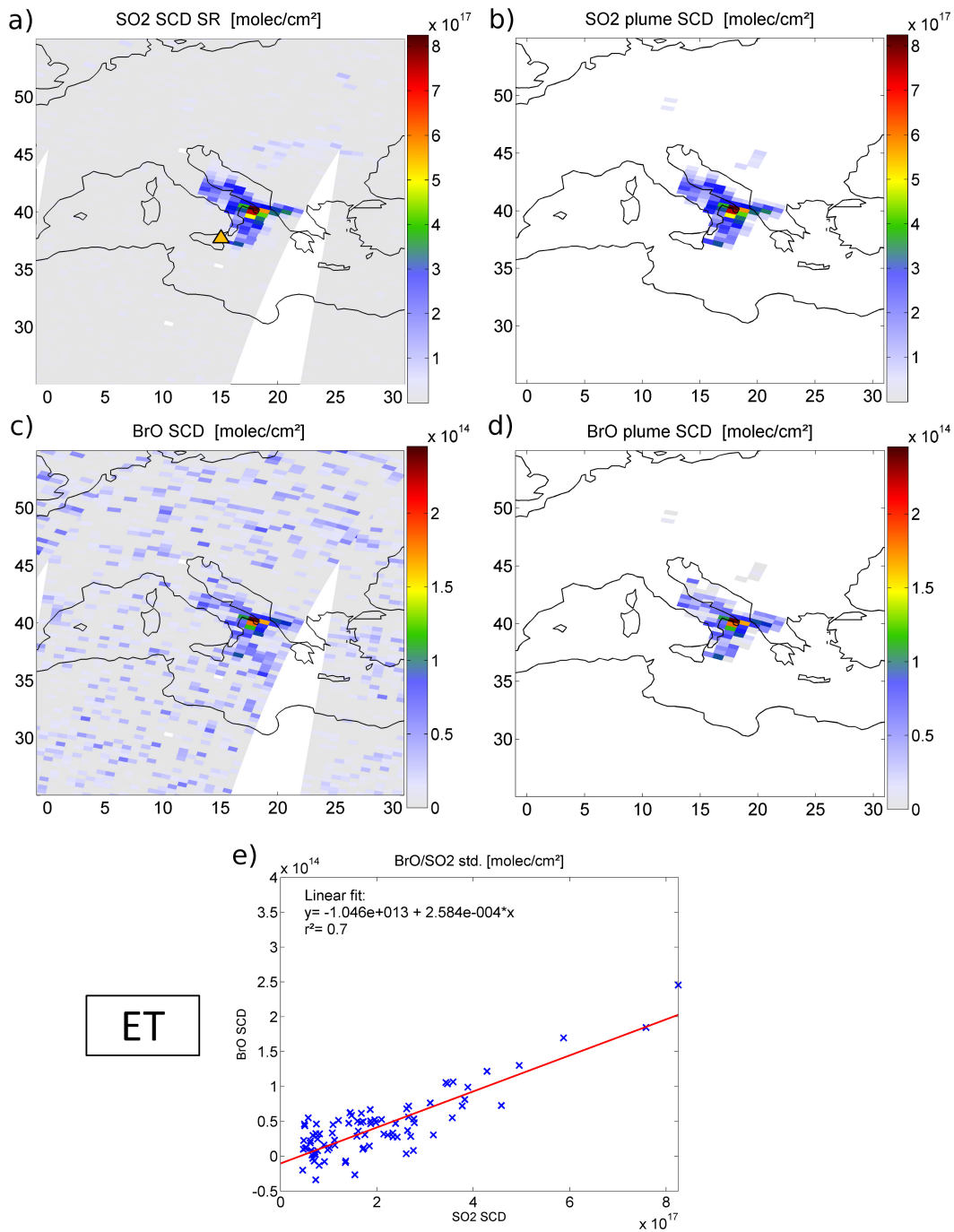


**Figure 9.4.:** SO<sub>2</sub> and BrO SCDs during an eruptive phase of Mt. Etna on 14 May 2008. The SCDs for SO<sub>2</sub> and BrO (9.4a and 9.4c) show that the BrO SCDs were clearly enhanced in the SO<sub>2</sub> plume and have a similar distribution. 9.4b and 9.4d show only those satellite pixels, that belong to the volcanic plume (SO<sub>2</sub> VCD\* > 3σ\*). The correlation plot for the identified plume pixels (9.4e) shows a linear relationship between the two species ( $r^2 = 0.7$ ) and a fitted mean BrO/SO<sub>2</sub> ratio of  $\sim 2.5 \times 10^{-4}$ .

## 9. Systematic investigation of BrO during volcanic events

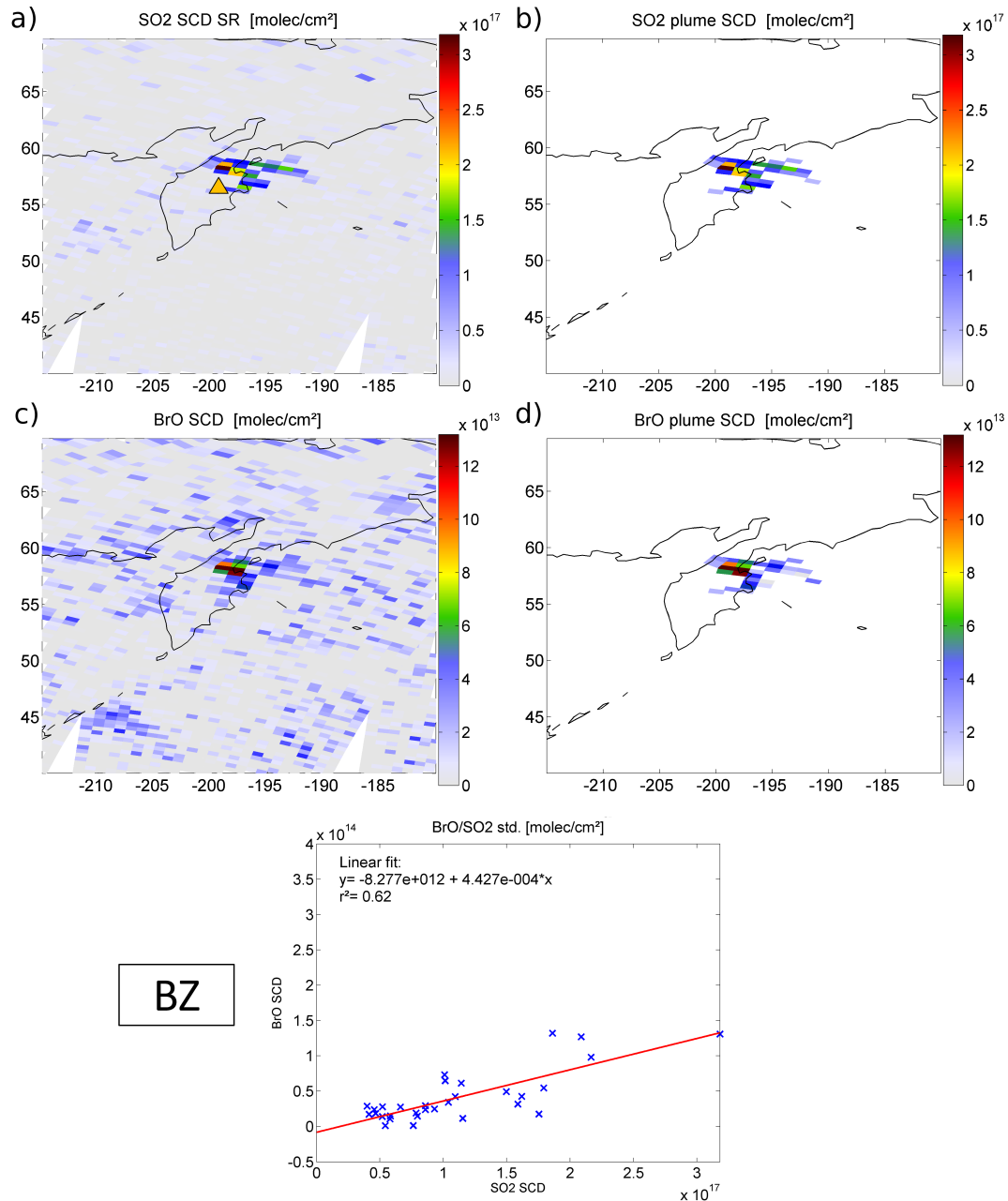


**Figure 9.5.:** SO<sub>2</sub> and BrO SCDs during an eruptive phase of Bezymianny volcano (Kamchatka Peninsula) on 11/12 May 2007. Next to the SO<sub>2</sub> plume (9.5 a), volcanic BrO was present, as the BrO SCDs are clearly enhanced in the vicinity of the SO<sub>2</sub> plume (9.5 c). The satellite pixel with SO<sub>2</sub> SCDs >3 $\sigma$  of the reference area are shown in 9.5 b and 9.5 d for both species. The correlation plot for the identified plume pixels (9.5 e) shows a linear relationship between the two species ( $r^2=0.62$ ) and a fitted mean BrO/SO<sub>2</sub> ratio of  $\sim 4.4 \times 10^{-4}$ .

### 9.3.3. Dalaffilla (4 November 2008)

On 3 November 2008, an eruption of the Dalaffilla volcano in Ethiopia's Afar region produced an extensive plume of SO<sub>2</sub> which was rapidly transported in north-eastern direction towards the Arabian Peninsula and reached the western part of China after two days (cf. Figure 9.6). While the GOME-2 instrument was able to track the SO<sub>2</sub> plume for about 10 days, BrO was only clearly detected on the first day after the eruption on November 4, when the plume was also seen for the first time by the satellite instrument (labelled DL in Figure 9.3).

Figure 9.6 a shows that the SO<sub>2</sub> plume can be separated into two main parts, one with rather high SO<sub>2</sub> SCDs\* over the south-eastern side of the Arabian Peninsula, the other one with lower SO<sub>2</sub> SCDs\* further in the north west. In contrast to these findings, the BrO SCDs\* (Figure 9.6 c) were only significantly enhanced in the north-western part of the extracted SO<sub>2</sub> plume (Figure 9.6 b) and in a long band towards the Persian Gulf. The consideration of all identified SO<sub>2</sub> plume pixels therefore leads to no clear linear correlation between the two species, but already indicates that such a correlation might be present in some parts of the plume. If we limit the focus to the plume pixels around the region with the enhanced BrO SCDs\* (indicated by the red polygon in Fig. 9.6 b and d), a linear correlation between the SO<sub>2</sub> and BrO SCDs\* is found, with  $r^2=0.54$  and a mean fitted BrO/SO<sub>2</sub> ratio of  $\sim 6.3 \times 10^{-5}$ .

It seems remarkable that no enhanced BrO SCDs\* can be found in the south-eastern part of the plume, while the maximum SCDs\* of SO<sub>2</sub> were observed within this area. Possible reasons for this non-uniform distribution of the enhanced BrO SCDs\* will be discussed in Section 9.5.

### 9.3.4. Nabro (16 June 2011)

Announced by an earthquake swarm on 12 June 2011, the first recorded eruption of the Nabro volcano (Eritrea, Africa) started one day later in the early morning of June 13 (labelled NB in Figure 9.3). As the Afar Triangle area in Southern Eritrea is barely populated, first observations of the eruption by eye witnesses did not occur until the late evening (Smithsonian, 2007-2011), while several satellite instruments (namely GOME-2, SCIAMACHY, OMI, the Atmospheric Infrared Sounder - AIRS - and the Infrared Atmospheric Sounding Interferometer - IASI) were already monitoring the plume's propagation towards Northern Egypt during the whole day (SACS, 2012).

On the 16th June, the GOME-2 SO<sub>2</sub> measurements (Figure 9.7 a) show that while the plume front had been transported to Western China, the volcano continued to emit significant amounts of SO<sub>2</sub>. From the BrO retrieval (Figure 9.7 c), enhanced SCDs\* can only be seen clearly within the area of the highest SO<sub>2</sub> SCDs\* that occur about 600–700 km from the volcano. Whenever the volcanic plume was captured by the GOME-2 measurements in the course of the eruption, similar behaviour was found. Taking all SO<sub>2</sub> plume pixels into account (Figure 9.7 b and d) yields a poor correlation coefficient ( $r^2=0.29$ ) of the linear fit, which results mainly from the majority of pixels where the SO<sub>2</sub> SCDs\* were significantly enhanced while the BrO SCD\* were not, causing a strong scattering around zero at low SO<sub>2</sub> slant column densities (Figure

## 9. Systematic investigation of BrO during volcanic events

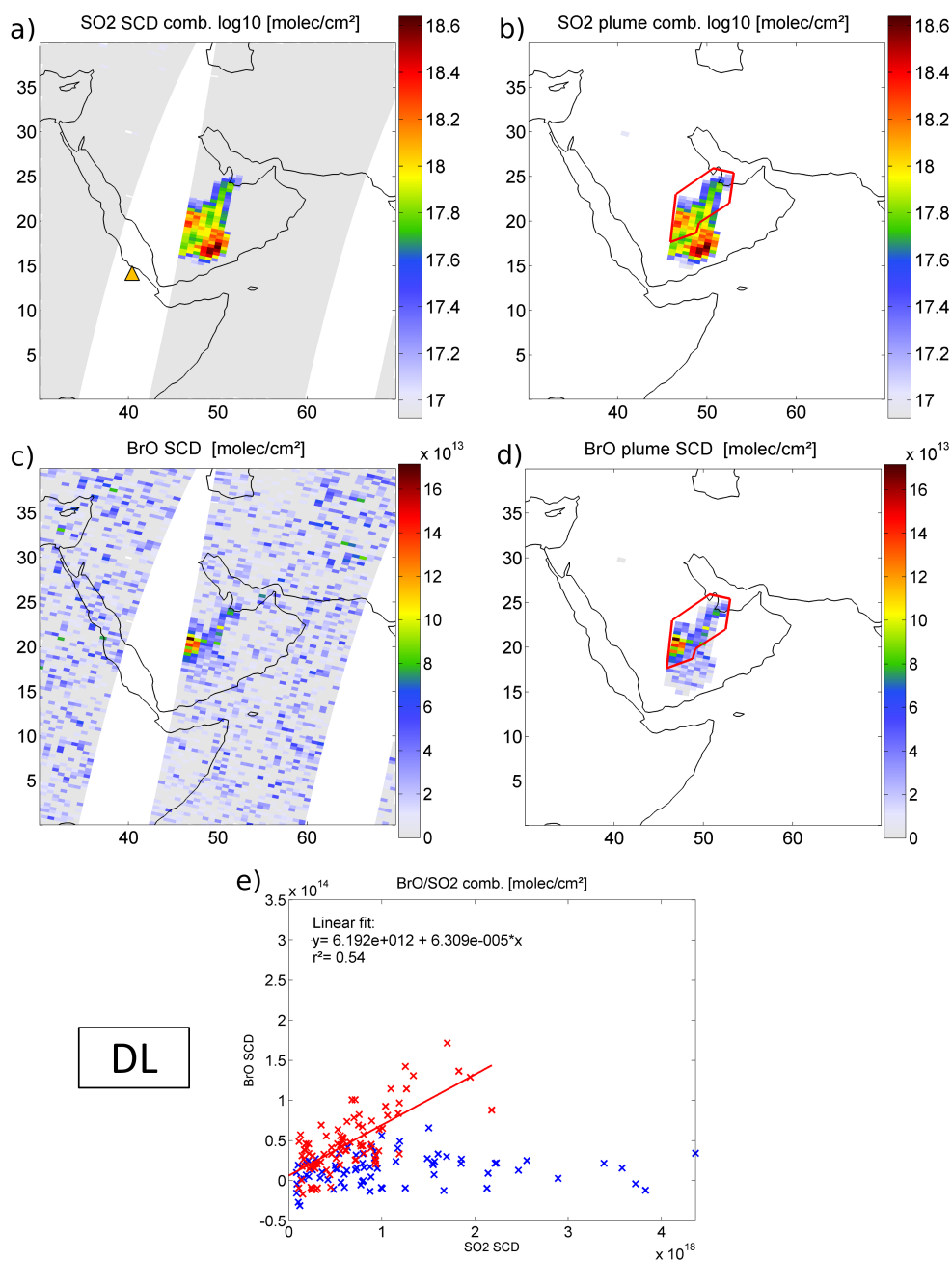


**Figure 9.6.:** GOME-2 measurements of SO<sub>2</sub> and BrO SCDs after the eruption of the Dalaffila volcano on 4 November 2008. The SO<sub>2</sub> plume is separated into two main parts and can be clearly seen in 9.6a the combined SO<sub>2</sub> retrieval (please note the logarithmic scale). In 9.6b, only the significantly enhanced SO<sub>2</sub> SCDs\* > 3σ\* are shown. Enhanced BrO SCDs\* are only located in the north-western part (9.6c and d). A linear correlation can only be seen for a restriction to this area, which is indicated by the red polygon in the maps and the red crosses in the correlation plot (9.6e). Blue crosses represent measurements outside the restriction area. The r<sup>2</sup> is then 0.54 with a fitted mean BrO/SO<sub>2</sub> ratio  $\sim 6.3 \times 10^{-5}$ .

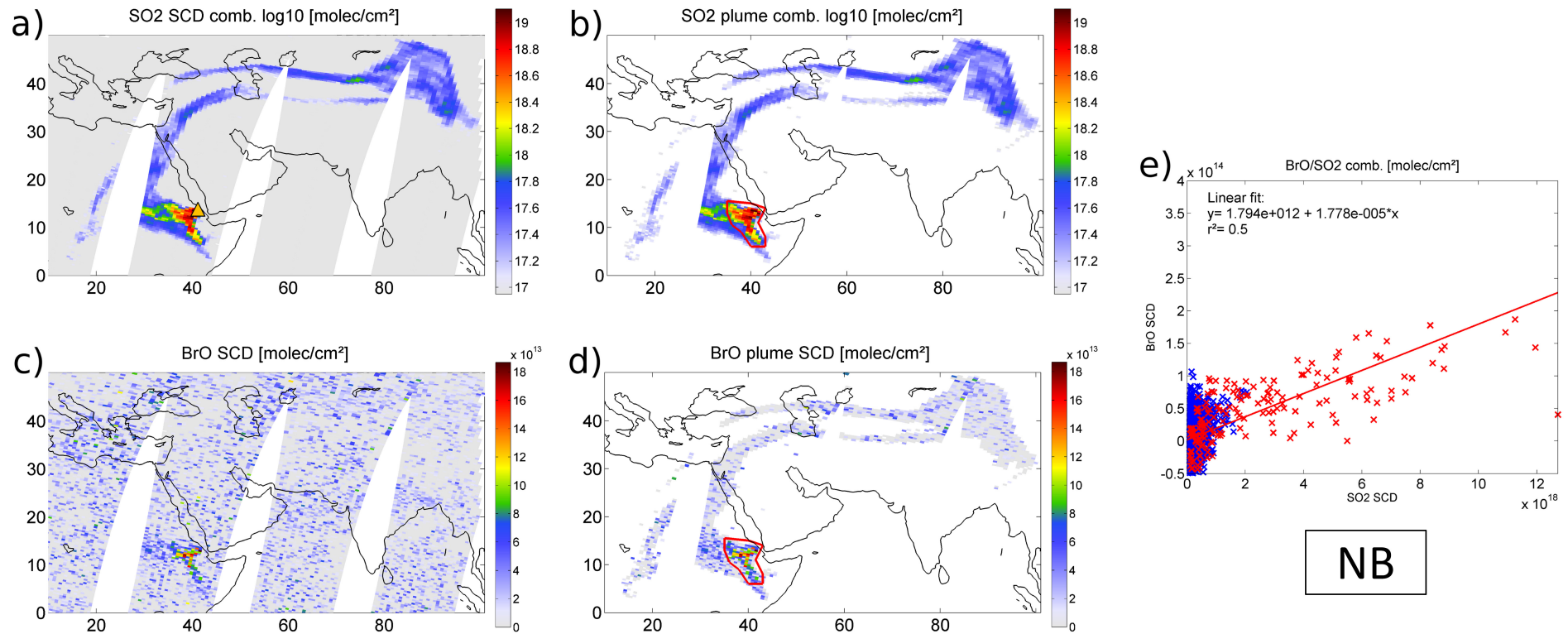


**Figure 9.7.:**  $SO_2$  and BrO SCDs during the eruption of the Nabro volcano (Eritrea) on 16 June 2011. The  $SO_2$  plume extends over several thousands of kilometres from the volcano towards East Asia (9.7a and b). The enhanced BrO SCDs\* appear only relatively close to the volcano (in the same area where the highest SCDs\* of  $SO_2$  are detected) and show a similar distribution (9.7b and d). While the  $r^2$  from the linear fit for all identified plume pixels (blue and red crosses) is rather low (0.29), the restriction to the area with clearly enhanced BrO SCDs\* results in  $r^2 = 0.5$  (area is indicated by the red polygon in 9.7c and e; corresponding SCDs\* by red crosses in the correlation plot 9.7e). The fitted mean BrO/ $SO_2$  ratio is low compared to other eruptions with  $\sim 1.8 \times 10^{-5}$ .

9.7 e - blue crosses). By restricting the data to the area with clearly enhanced BrO SCDs (indicated by the red shape in Figure 9.7 b and d), the  $r^2$  value increases to 0.5 (Fig. 9.7 e - red crosses). The rather low fitted mean BrO/SO<sub>2</sub> ratio of  $1.8 \times 10^{-5}$  suggests that the main reason for the apparent absence of BrO in the aged plume might be that the BrO SCDs no longer exceeded the instruments' detection limit. The conversion of BrO into other bromine species might also play a role.

### 9.3.5. Kasatochi (9 and 11 August 2008)

After an increase in the seismic activity during the first days of August 2008, at least five distinct explosions occurred at the Kasatochi volcano in the afternoon of the 7th August. While the first two explosions produced large ash-poor gas-charged plumes, the third one was relatively ash-rich and emitted massive amounts of SO<sub>2</sub>, which reached the lower stratosphere at about 18 km. The two remaining explosions were of minor intensity and only detected by seismic stations (Neal et al., 2011).

The SO<sub>2</sub> plume was detected the first time on 8 August by several satellite instruments (including GOME-2, SCIAMACHY and OMI) and further tracked for at least one month while the plume encircled the globe (labeled KS in Figure 9.3). The observation of an extensive BrO cloud in the vicinity of the SO<sub>2</sub> plume by GOME-2 was reported by Theys et al. (2009). In contrast to the SO<sub>2</sub> plume, the BrO could only be clearly tracked for about one week. Yet, the GOME-2 observations of the Kasatochi plume provide so far the longest continuous measurements of a single volcanic BrO plume since the first ground-based measurements of volcanic BrO (Bobrowski et al., 2003). The absolute BrO VCDs\* during the first days of the eruption ( $\sim 2 \times 10^{14}$  molec/cm<sup>2</sup>) were about a factor of 2–3 larger than for the cases discussed in Section 9.3.1 - 9.3.4.

While all previously presented eruptions of Mt. Etna, Bezymianny, Dalaffilla and Nabro showed similar spatial distributions for BrO and SO<sub>2</sub> and a linear correlation (at least in parts of the plume), the eruption of Kasatochi showed only a roughly similar spatial pattern for the two observed species, with growing differences in the distribution of the two species during the plume's eastward transport. Figure 9.8 shows the volcanic plume on the second day of the GOME-2 observations (9 August 2008). While the enhanced BrO SCDs\* (Figure 9.8 c and d) are located in the same area as the captured SO<sub>2</sub> plume pixels (Figure 9.8 a and b), the spatial distribution for BrO appears more circular in shape than that of SO<sub>2</sub>. The location of the maximum SCDs\* also differs for both species. The maximum SO<sub>2</sub> SCDs\* are located in the southern region of the plume, while the maximum BrO SCDs\* can be found in the western and eastern part. The correlation plot (Figure 9.8 e) shows a positive correlation between the species ( $r^2=0.24$ ), but also a large scatter in the BrO SCDs\* with increasing SO<sub>2</sub> SCDs\*.

In Figure 9.9, the plume is shown on 11 August 2008. Whereas the main plume has moved towards the Canadian west coast, several branches reach out from the plume centre in south-western and north-eastern direction (Figure 9.9 a). The clearly enhanced BrO SCDs\* are located around the centre region of the SO<sub>2</sub> plume, but the detailed distribution of the trace gases within this area is different (Figure 9.9 c).

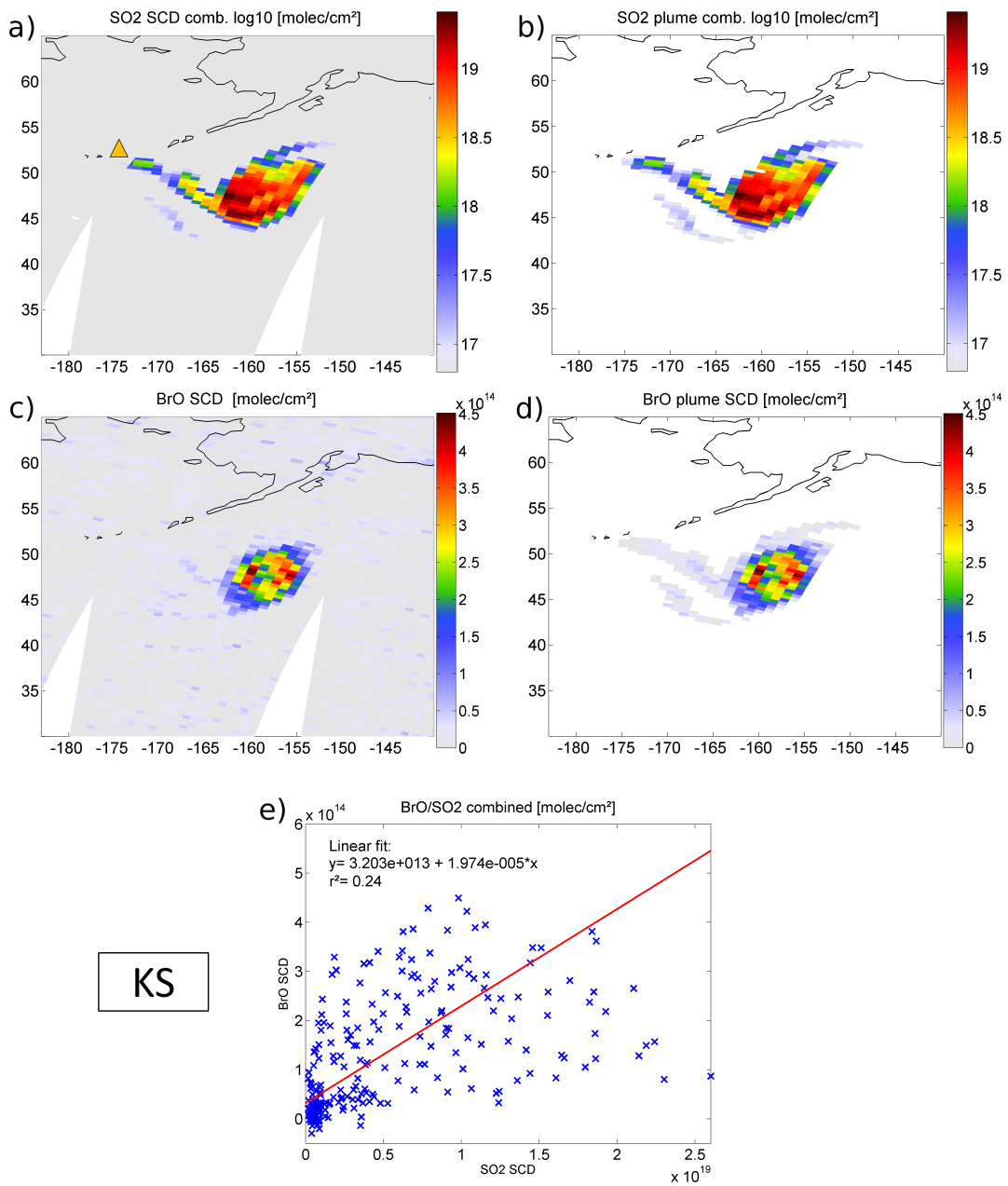


**Figure 9.8.:** SO<sub>2</sub> and BrO SCDs during the second day of the Kasatochi eruption (9 August 2008). While the SO<sub>2</sub> plume (9.8a and b) and the enhanced BrO (9.8c and d) are in principle located at the same area, the spatial distribution for BrO appears more circular than for the SO<sub>2</sub>. The correlation plot (9.8e) shows a positive correlation between the species ( $r^2=0.24$ ), but also a large scatter in the BrO SCDs\* with increasing SO<sub>2</sub> SCDs\*.

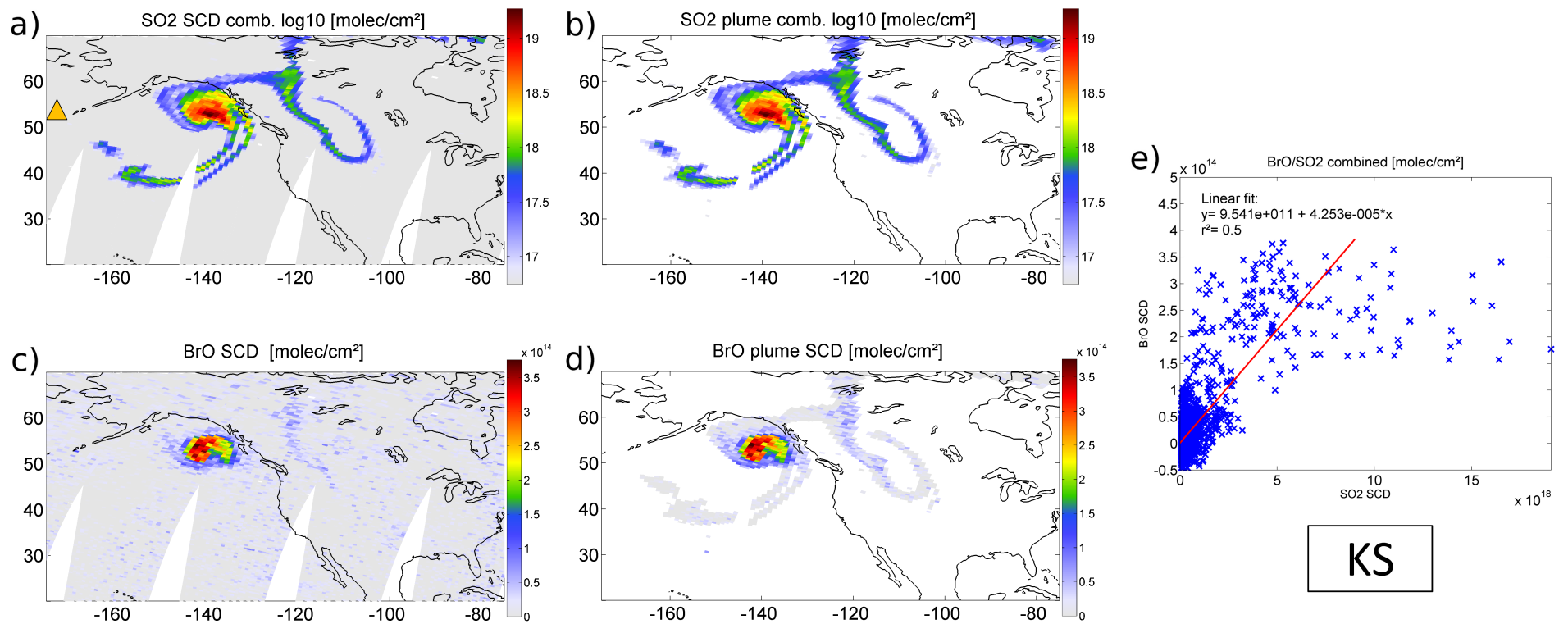


**Figure 9.9.:** GOME-2 maps for SO<sub>2</sub> and BrO for the volcanic plume of Kasatochi on 11 August 2008. The centre part of the plume has further travelled in eastern direction, several branches now extend from the plume centre in south western and north eastern direction (9.9a and b). The enhanced BrO SCDs\* are located around the centre region, but the distribution inside this area remains different compared to the one for SO<sub>2</sub> (9.9c and d), as the highest SO<sub>2</sub> SCDs\* appear directly in the plume centre, while the BrO seems to be twisted around it. This can also be seen in the correlation plot (9.9e), where the BrO columns are independently scattered around  $2.5 \times 10^{14}$  for SO<sub>2</sub> SCDs\*  $> 5 \times 10^{18}$  molec/cm<sup>2</sup>.

The map of the extracted plume pixels for BrO (Figure 9.9 d) in comparison to those for SO<sub>2</sub> (Figure 9.9 b) indicates that most of the BrO seems to be twisted around the plume centre containing the highest SO<sub>2</sub> SCDs\*. Especially the BrO SCDs\* at the location of the highest SO<sub>2</sub> SCDs\* are not as high as for the surrounding area. This can also be seen in the correlation plot (Figure 9.9 e), where the BrO SCDs\* are linearly correlated up to SO<sub>2</sub> SCDs\*  $5 \times 10^{18}$ . For higher SO<sub>2</sub> SCDs\*, the BrO columns level out at around  $2.5 \times 10^{14}$  molec/cm<sup>2</sup>. One reason for such a behaviour might be that the plume centre was not yet entirely mixed with ambient ozone-rich air after sunrise at the time of the GOME-2 measurements.

### 9.3.6. Sarychev (15/16 June 2009)

The eruption of the Sarychev volcano (Kuril Islands, Russia) in June 2009 is another example of a complex BrO/SO<sub>2</sub> relationship (labelled SR in Figure 9.3). According to the Sakhalin Volcanic Eruption Response Team (SVERT), the first signs of an eruption were found in satellite observations acquired on 11th June (Smithsonian, 2007-2011). After the main phase ended on the 16th June, several weaker eruptions occurred in the following 2 weeks.

In Figure 9.10 a, the plume for the combined SO<sub>2</sub> retrieval can be clearly seen for the 15th/16th of June. The volcano (indicated by the orange triangle in Figure 9.10 a) is located on the island Matua (48° 5' 30" N, 153° 12' 0" E). Surprisingly, the SO<sub>2</sub> plume spreads in opposing directions, westward and eastward from the volcano (Figure 9.10 a and b). Enhanced BrO SCDs\* were only detected in a relatively small region in the western part of the plume for that day (Figure 9.10 c and d). Correspondingly, the correlation plot (Figure 9.10 e) leads to an  $r^2$  value close to zero from the bivariate linear fit ( $r^2=0.005$ ). Although a linear branch seems to be present in the plot at lower SO<sub>2</sub> SCDs\* (like for the Dalaffilla eruption described in Section 9.3.3), a restriction to the area of the satellite pixels with elevated BrO SCDs\* did not lead to a clearer result regarding a linear correlation between both species.

To investigate the influence of volcanic ash, the GOME-2 UV Absorbing Aerosol Index (AAI) for the regarded day is shown in Figure 9.11a (Penning de Vries et al., 2009). The AAI is a semi-quantitative measure of aerosols that absorb UV radiation. It is most sensitive to elevated layers of absorbing particles such as smoke, mineral dust and volcanic ash and depends mainly on aerosol optical thickness, single-scattering albedo and altitude of the aerosol layer (e.g. Herman et al., 1997; Torres et al., 1998; Graaf et al., 2005). As seen in the map, volcanic ash was present almost throughout the entire volcanic SO<sub>2</sub> plume, while the most enhanced AAI values occur in western direction from the volcano. This suggests that there was an ash-rich explosion shortly before the GOME-2 measurements, of which the plume was mainly transported westwards.

In a case study, the volcanic plume's propagation was simulated by trajectories from the Hybrid Single Particle Lagrangian Integrated Trajectory Model (HYSPLIT - see Draxler and Rolph, 2012; Rolph, 2012). For the simulation of the plume's spreading, we used the starting times for individual explosions, as reported by Levin et al. (2010), who used satellite images of the geostationary Multi-functional Transport Satellites

## 9. Systematic investigation of BrO during volcanic events

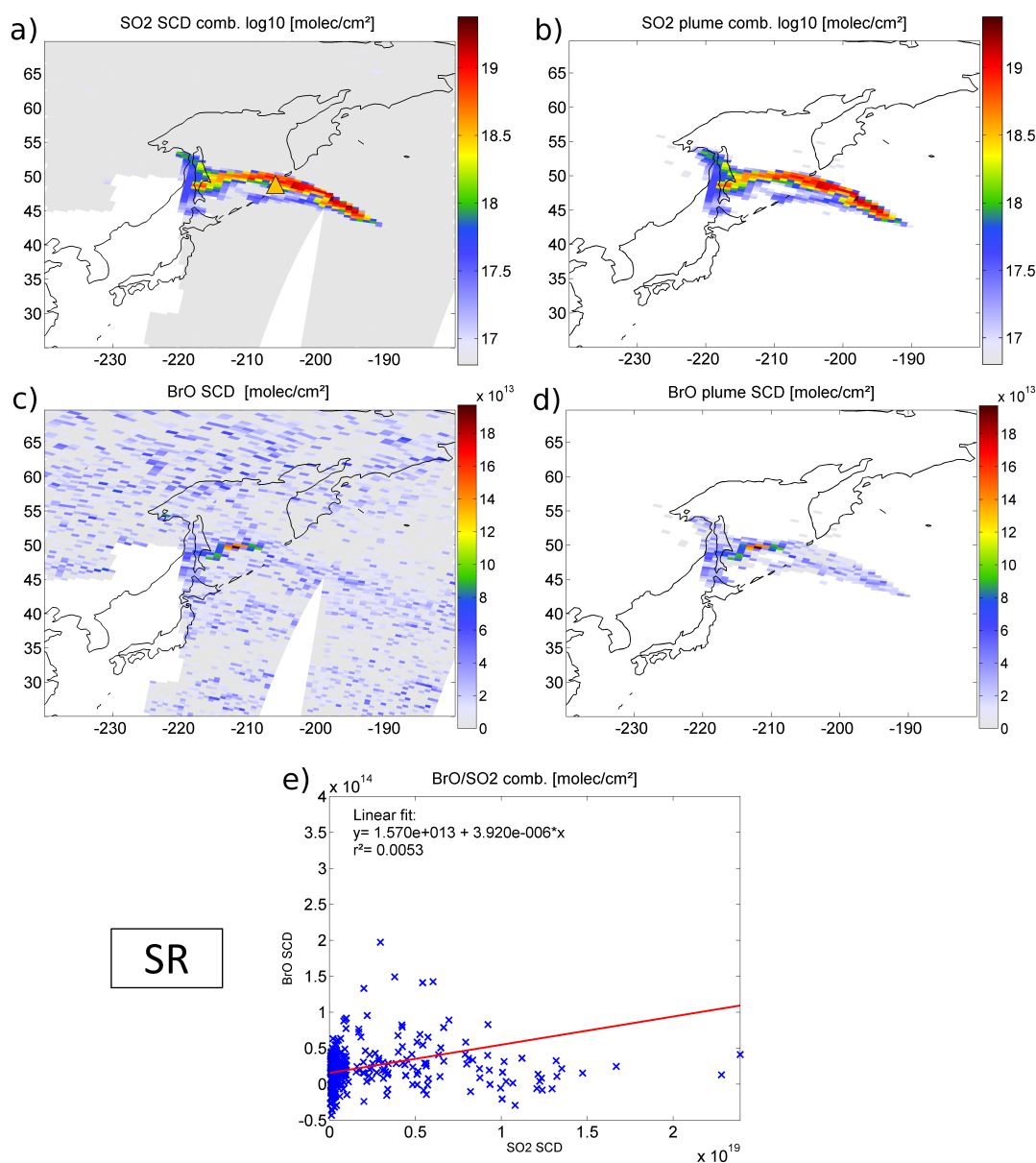


**Figure 9.10.:** The volcanic  $\text{SO}_2$  and BrO plume during the eruption of Sarychev on 15/16 June 2009. The  $\text{SO}_2$  plume (9.10 a and b) is transported in western and eastern direction from the volcano (indicated by the orange triangle in 9.10 a; the white area in the lower left corner is due to data restrictions in order to prevent the detection of anthropogenic  $\text{SO}_2$  over China). Surprisingly, enhanced BrO columns are only observed in a fraction of the western part (9.10 c and d). The correlation plot for both species therefore lead to an  $r^2$  value close to zero from the bivariate linear fit (9.10 e).

(MTSAT) during the eruptive phase of the volcano in order to reconstruct the main explosion events. In total, 23 individual explosions were found between the 13th and the 22nd June, with 13 of them being powerful enough to reach more than 6 km altitude. For the calculation of the forward trajectories, the starting times of the five strongest explosions within the two days prior to the satellite measurements (19 UTC on June 14; 1 and 9–11 UTC on June 15) were used, all of them with reported top heights of more than 10 km. The trajectories for all explosions were calculated for injection heights between 5–20 km, starting at the volcano and ending at the time of the overpass of GOME-2, around 00:00 UTC on June 16.

The resulting trajectory endpoints can be seen in Figure 9.11 b and agree very well with the overall extent of the detected volcanic plume. Apparently, the plume's transport in opposite directions from the volcano results from different injection heights and a change in the wind direction from westerly to easterly between 11–13 km height. In Figure 9.12 a and b, the trajectory endpoints are additionally shown in comparison with the SCDs\* of the combined SO<sub>2</sub> product as well as for BrO. A closer look to the trajectory endpoints reveals that the enhanced BrO SCDs\* were most probably caused by the 3 explosions between 9–11 UTC on the 15th June at plume heights of 6–8 km. This indicates that meteorological parameters such as temperature and relative humidity might have a crucial influence on the formation of BrO in different layers of a volcanic plume in addition to plume conditions such as the individual amount of reactive bromine species and the presence of aerosol particles. The multitude of explosions points out the difficulties of the determination of a mean BrO/SO<sub>2</sub> ratio for such major eruptions, as several overlapping plumes at different altitudes (and therefore different ambient conditions) are usually present, whereas the satellite data only represent a 2-dimensional projection of the plumes at different altitudes. Additionally, the plume's chemical composition may also change significantly in the course of an eruption.

## 9.4. Systematic analysis of BrO events in volcanic plumes

In order to quantify the abundance of BrO in a more systematic way, the results from all captured volcanic plumes were further analyzed and divided into different categories, each one representing a different class of BrO to SO<sub>2</sub> relationship:

Category I: The volcanic plume shows a **clear linear** BrO/SO<sub>2</sub> correlation.

Category II: The volcanic plume shows a **weak linear** BrO/SO<sub>2</sub> correlation.

Category III: Clearly enhanced BrO SCDs, but **no linear** correlation.

Category IV: No enhanced BrO SCDs are found in the SO<sub>2</sub> plume's area.

The members of each category were determined by several parameters, including  $r^2$ , the maximum BrO VCD\*, the presence of BrO clusters with enhanced BrO VCDs\*

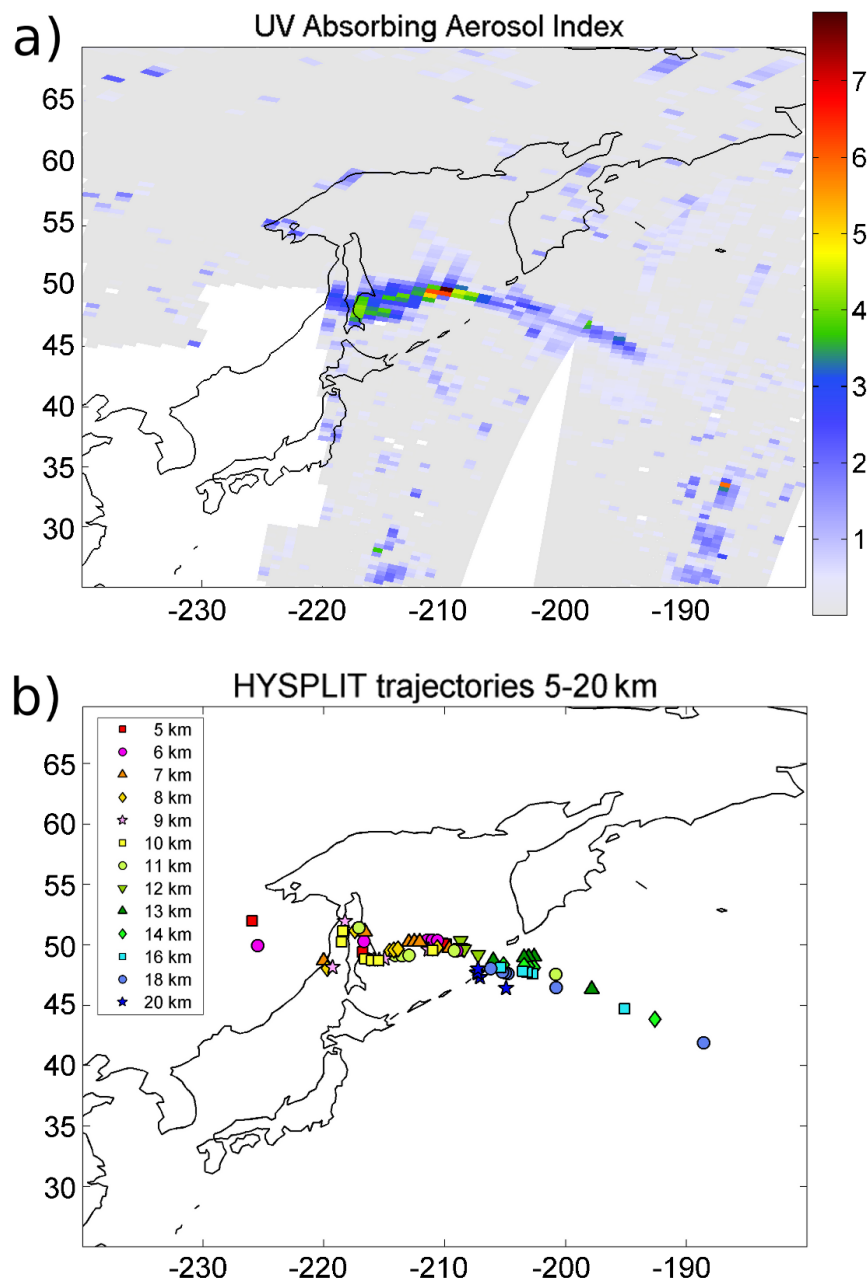


**Figure 9.11.:** a) UV Absorbing Aerosol Index (AAI) for the Sarychev eruption on 15/16 June 2009. Like for BrO, the highest values occur in the western part of the plume, indicating an ash-rich explosion in temporal proximity to the satellite measurements. b) HYSPLIT trajectory endpoints for starting heights between 5 and 20 km of the last 5 major explosions during the two days before the GOME-2 measurements. The trajectory simulations point out, that the wind changed from western to eastern direction between 11 and 13 km with increasing height.

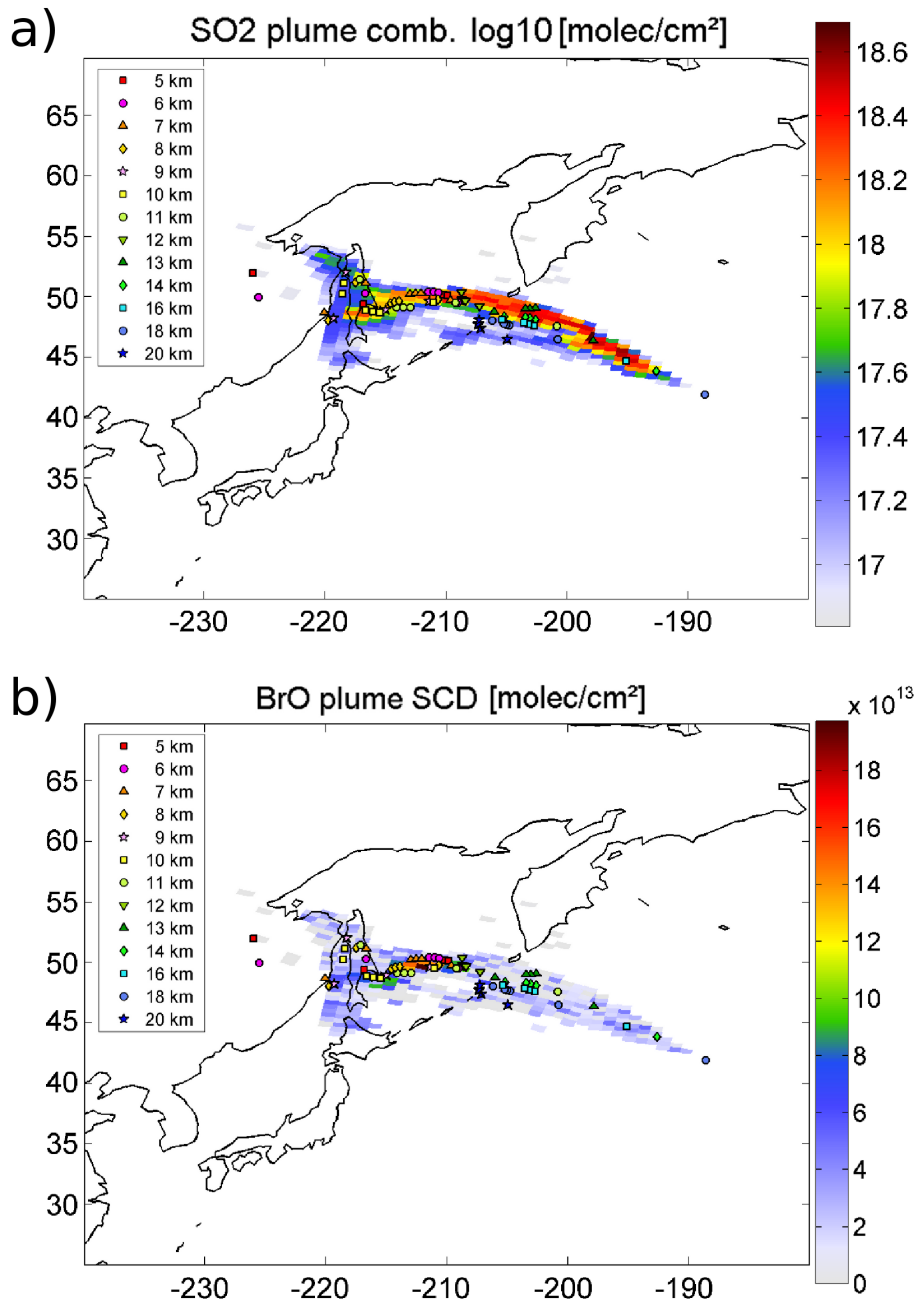


**Figure 9.12.:** a) *Overlap of the volcanic SO<sub>2</sub> plume from the combined retrieval with the trajectory endpoints.* b) *Overlap of the BrO<sub>2</sub> SCDs\* in the area of the captured SO<sub>2</sub> plume with the trajectory endpoints.*

## 9. Systematic investigation of BrO during volcanic events

---

and the p-value. The p-value "is associated with a test statistic. It is the probability, if the test statistic really were distributed as it would be under the null hypothesis, of observing a test statistic (as extreme as, or more extreme than) the one actually observed" (Davidson and MacKinnon, 1993). The smaller the p-value, the more strongly the test rejects the null hypothesis, that is, the hypothesis being tested. The criteria for sorting volcanic plume events into one of the defined categories as well as the total number of plumes in each category are summarized in Table 9.2.

In total, 64 individual volcanic plumes were found with indications for the presence of volcanic BrO of which all corresponding maps can be found in Appendix A. By looking at the results, it again becomes clear that each volcanic eruption/degassing event has its own specific circumstances (see also Sect. 9.3.1 - 9.3.6). For a more detailed analysis of the individual plumes, it will be necessary to perform several case studies, taking into account the influence of volcanic ash, the age of the plume and the plume's height distribution with the corresponding meteorological parameters, such as the ambient air temperature and relative humidity. In the following, only a brief overview of the results is given.

**Table 9.2.:** *Parameterized categories that were used for the BrO/SO<sub>2</sub> analysis of all detected volcanic plumes. Additionally, the resulting total plume number for each category is given.*

category	$r^2$	p-value	BrO VCD* <sub>max</sub>	BrO cluster	number of events
I	>0.5	$<5 \times 10^{-3}$	$>2\sigma^*$	3-pixel cluster with VCD* $>2\sigma^*$	17
II	$\geq 0.25$	$<1 \times 10^{-3}$	$>2\sigma^*$	3-pixel cluster with VCD* $>2\sigma^*$	23
III	$\leq 0.25$	-	$>4\sigma^*$	6-pixel cluster with VCD* $>2\sigma^*$	24
IV	-	-	-	-	708

### 9.4.1. Category I: clear linear correlation

All captured volcanic plumes that showed signs for a clear linear BrO to SO<sub>2</sub> correlation by a correlation coefficient  $r^2 > 0.5$  and a corresponding p-value  $< 5 \times 10^{-3}$  were collected in category I. Additionally, the results were restricted to plume events that contained a cluster of at least 3 neighbouring satellite pixels with BrO VCDs\*  $> 2\sigma^*$ . Table 9.3 lists the 17 volcanic events that were identified as part of category I, containing individual plumes from 6-8 different volcanoes.

Apart from the eruptions discussed in Sect. 9.3 (Bezymianny, Etna and Kasatochi), plumes from eruptions of Mt. Redoubt and Eyjafjallajökull were identified. Additionally, another plume from an eruption of Etna at the end of November 2007 and two further eruptions on Kamchatka were detected. Like for the already discussed case of the Bezymianny volcano (event No.22 in Table 9.3 - see Section 9.3.2), we cannot be completely sure if the named volcanoes were really responsible for the detected volcanic plumes. In case of the Kliuchevskoi eruption on 29th/30th March 2011 (event No.675 in Table 9.3), the volcanic plume extended over an area of approximately 250 km in latitudinal direction of Kamchatka's eastern coast (encompassing the Kliuchevskoi, Kizimen and Shiveluch volcanoes). While Bezymianny showed no increased activity, the Kizimen volcano (about 100 km south) and the Shiveluch volcano (approximately 80 km north-east) had periods of significant unrest, as reported by KVERT. The location of the maximum SO<sub>2</sub> SCDs\* and an additional report from the Volcanic Ash Advisory Center Tokyo (VAAC Tokyo) about a possible eruption from Kliuchevskoi on the 30th March indicate that the major part of the volcanic plume most probably came from Kliuchevskoi (Smithsonian, 2007-2011). For the volcanic plume events over Kamchatka on 8th/9th May 2011 (event No.700 in Table 9.3) and 7 June 2011 (event No.740 in Table 9.3), none of the activity reports from the KVERT can give a clear preference regarding the responsible volcano, but the location of the main parts of the plumes as seen by the OMI instrument indicate that the corresponding eruptions were more likely to have occurred at Kizimen than at the Shiveluch volcano, which also showed increased activity at the same time. For almost all of the category I cases, it is obvious that BrO of volcanic origin was present in the plume, as the BrO SCDs\* were clearly enhanced in the area of enhanced SO<sub>2</sub>.

For most cases, the BrO columns even showed a quite similar spatial pattern compared to the SO<sub>2</sub> SCDs\*, indicating a direct one-to-one correlation between the two species. However, it should be pointed out that the presence of enhanced BrO is not that clear for the volcanic plumes of the Ambrym volcano (event No.535 and No.563 in Table 9.3) in comparison to the other events in this category. Figure 9.13 a shows the SO<sub>2</sub> plume from a strong degassing event of Ambrym on 8 April 2010. While the captured SO<sub>2</sub> plume consists only of a few satellite pixels (but can be clearly seen in the map), the BrO map shows no increased values at first sight, since all BrO SCDs\* appear randomly scattered in the whole regarded area (Figure 9.13 c). This point of view changes by looking only at the area of captured SO<sub>2</sub> plume pixels (Figure 9.13 b and d). Although the BrO SCDs\* in the plume's area are not well above the SCDs\* in the reference area, a similar pattern can be seen in the distribution of the two species. The correlation plot (Figure 9.13 e) yields a surprisingly clear linear correlation, with

**Table 9.3.: Category I (clear linear correlation)**

*BrO/SO<sub>2</sub>-analysis of all detected volcanic plumes of Category I. Columns contain: event number, volcano, measurement date, max. BrO SCD, max. SO<sub>2</sub> SCD, coincidence of max. SO<sub>2</sub> and BrO SCD, BrO/SO<sub>2</sub> slope, ratio of max. SO<sub>2</sub> and BrO SCD and coordinates of regarded area.*

#	volcano	date	BrO SCD <sub>max</sub> [molec/cm <sup>2</sup> ]	SO <sub>2</sub> SCD <sub>max</sub> [molec/cm <sup>2</sup> ]	⊕	r <sup>2</sup>	BrO/SO <sub>2</sub> slope	BrO <sub>max</sub> /SO <sub>2</sub> max	coordinates
22	Bezymianny*	11./12.05.2007	1.3×10 <sup>14</sup>	3.1×10 <sup>17</sup>	no	0.62	4.4×10 <sup>-4</sup>	4.1×10 <sup>-4</sup>	[40 - 70°N, 145 - 180°E]
68 <sup>‡</sup>	Etna	24.11.2007	1.4×10 <sup>14</sup>	1.1×10 <sup>18</sup>	yes	0.61	1.0×10 <sup>-4</sup>	1.2×10 <sup>-4</sup>	[20 - 49°N, 0 - 35°E]
94 <sup>†</sup>	Etna	11.05.2008	2.3×10 <sup>14</sup>	1.5×10 <sup>18</sup>	yes	0.60	9.8×10 <sup>-5</sup>	1.4×10 <sup>-4</sup>	[20 - 55°N, 5 - 45°E]
97	Etna	14.05.2008	2.4×10 <sup>14</sup>	8.2×10 <sup>17</sup>	yes	0.70	2.5×10 <sup>-4</sup>	2.9×10 <sup>-4</sup>	[20 - 60°N, -5 - 35°E]
164 <sup>†</sup>	Kasatochi	11.08.2008	3.7×10 <sup>14</sup>	1.9×10 <sup>19</sup>	no	0.50	4.2×10 <sup>-5</sup>	1.9×10 <sup>-5</sup>	[20 - 70°N, 60 - 180°W]
282 <sup>†</sup>	Mt. Redoubt	26.03.2009	1.9×10 <sup>14</sup>	5.8×10 <sup>18</sup>	yes	0.90	3.5×10 <sup>-5</sup>	3.3×10 <sup>-5</sup>	[40 - 70°N, 135 - 170°W]
322	Mt. Redoubt	18.04.2009	1.1×10 <sup>14</sup>	4.8×10 <sup>17</sup>	no	0.62	2.2×10 <sup>-4</sup>	2.4×10 <sup>-4</sup>	[35 - 70°N, 135 - 170°W]
363	Mt. Redoubt	29.05.2009	9.1×10 <sup>13</sup>	3.8×10 <sup>17</sup>	yes	0.56	2.4×10 <sup>-4</sup>	2.4×10 <sup>-4</sup>	[45 - 70°N, 135 - 170°W]
535	Ambrym	08.04.2010	6.7×10 <sup>13</sup>	3.0×10 <sup>17</sup>	no	0.70	3.3×10 <sup>-4</sup>	2.2×10 <sup>-4</sup>	[0 - 35°S, 150 - 185°E]
541	Eyjafjallajökull	23.04.2010	1.6×10 <sup>14</sup>	3.7×10 <sup>17</sup>	yes	0.65	5.1×10 <sup>-4</sup>	4.3×10 <sup>-4</sup>	[45 - 70°N, 0 - 35°W]
545	Eyjafjallajökull	25.04.2010	1.3×10 <sup>14</sup>	4.6×10 <sup>17</sup>	no	0.75	3.3×10 <sup>-4</sup>	2.9×10 <sup>-4</sup>	[45 - 70°N, 0 - 35°W]
546	Eyjafjallajökull	26.04.2010	8.8×10 <sup>13</sup>	4.2×10 <sup>17</sup>	yes	0.58	2.5×10 <sup>-4</sup>	2.0×10 <sup>-4</sup>	[45 - 70°N, 0 - 35°W]
550	Eyjafjallajökull	29.04.2010	1.3×10 <sup>14</sup>	6.1×10 <sup>17</sup>	yes	0.54	1.9×10 <sup>-4</sup>	2.1×10 <sup>-4</sup>	[40 - 70°N, 0 - 45°W]
563	Ambrym	11.05.2010	8.6×10 <sup>13</sup>	6.4×10 <sup>17</sup>	yes	0.59	1.6×10 <sup>-4</sup>	1.3×10 <sup>-4</sup>	[0 - 35°S, 150 - 190°E]
675	Kliuchevskoi*	29./30.03.2011	1.3×10 <sup>14</sup>	6.0×10 <sup>17</sup>	yes	0.79	2.6×10 <sup>-4</sup>	2.1×10 <sup>-4</sup>	[40 - 70°N, 145 - 180°E]
700	Kizimen*	08./09.05.2011	8.8×10 <sup>13</sup>	3.3×10 <sup>17</sup>	no	0.56	3.0×10 <sup>-4</sup>	2.6×10 <sup>-4</sup>	[40 - 70°N, 140 - 180°E]
740	Kizimen*	07.06.2011	6.8×10 <sup>13</sup>	1.6×10 <sup>17</sup>	yes	0.63	4.7×10 <sup>-4</sup>	4.0×10 <sup>-4</sup>	[40 - 70°N, 145 - 180°E]

<sup>†</sup> combined SO<sub>2</sub> product in case of high SO<sub>2</sub> SCDs ≥1×10<sup>18</sup> [molec/cm<sup>2</sup>]

<sup>‡</sup> SO<sub>2</sub> SCDs ≥1×10<sup>18</sup> [molec/cm<sup>2</sup>], but no plume pixels found in the SO<sub>2</sub> AR

\* corresponding volcano cannot be clearly identified

⊕ location of SO<sub>2</sub> SCD<sub>max</sub> is the same as for BrO SCD<sub>max</sub>

#### 9.4. Systematic analysis of BrO events in volcanic plumes

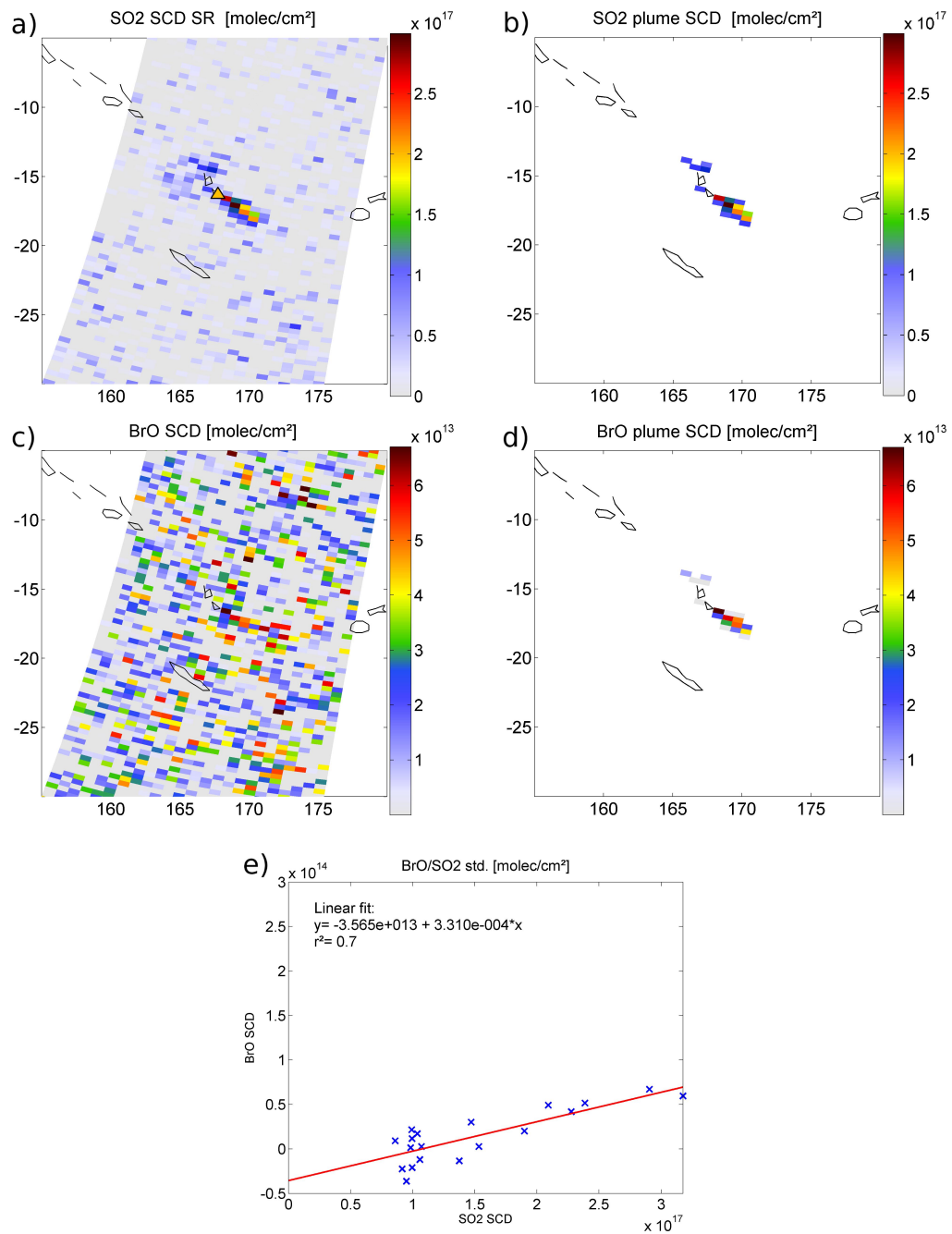


**Figure 9.13.:** SO<sub>2</sub> and BrO SCDs during a phase of enhanced passively degassing from the Ambrym volcano on 8 April 2010. While the SO<sub>2</sub> plume can be clearly seen in the satellite data (9.13 a), enhanced BrO columns are not observed at first sight, since the large scatter indicates values around the instrument's detection limit (9.13 c). By focusing on the area of extracted SO<sub>2</sub> plume pixels (9.13 b and d), the correlation plot for both species shows a surprisingly clear linear correlation with a resulting  $r^2 = 0.7$  and a relatively high mean BrO/SO<sub>2</sub> ratio of  $3.3 \times 10^{-4}$  from the bivariate linear fit (9.13 e).

$r^2 = 0.7$  and a relatively high mean BrO/SO<sub>2</sub> ratio of  $3.3 \times 10^{-4}$ . While the  $r^2$  in this example is one of the highest of all events in category I, it is worth noting that it is also the event with the lowest measured maximum BrO SCD\*.

### 9.4.2. Category II: weak linear correlation

In category II, volcanic plumes that showed a weak linear BrO to SO<sub>2</sub> correlation were collected (cf. Table 9.4). The events in this category were characterized by a correlation coefficient  $0.25 \geq r^2 < 0.5$  and a corresponding p-value  $< 1 \times 10^{-3}$  (80% lower than in category I). Like for the first category, the results were restricted to plume events that showed a cluster of at least 3 neighbouring satellite pixels with BrO VCDs\*  $> 2\sigma^*$ . For category II, in total 23 different volcanic events from 8–9 different volcanoes were identified. Some of the plume events originated from the volcanoes highlighted in Figure 9.3 (Kasatochi, Mt. Redoubt, Eyjafjallajökull and Nabro), and some were attributed to eruptions on Kamchatka (Kliuchevskoi, Kizimen and Karymsky). In contrast to several plume events from category I, the corresponding volcanoes for all plumes could easily be identified due to reports about specific explosion events shortly before the satellite measurements. In addition to several days during the eruptions of Mt. Redoubt and Eyjafjallajökull, the third day after the eruption of Kasatochi was also sorted into category II. Like in the examples in Section 9.3.5, the patterns of the enhanced BrO slant column densities look similar compared to those of SO<sub>2</sub> but only a weak linear correlation is found.

### 9.4.3. Category III: No linear BrO/SO<sub>2</sub> relationship

For the third category, the captured volcanic events were also screened for plumes without signs of a linear correlation between SO<sub>2</sub> and BrO, but for which significantly enhanced BrO SCDs\* were detected (correlation coefficient  $r^2 \leq 0.25$ ). As no clear linear relationship is found for these cases, the threshold for the maximum BrO VCD\* was increased to  $4\sigma^*$ , in order to assure an unambiguous detection of enhanced BrO in volcanic plumes. Additionally, the cluster size of neighbouring satellite pixels with BrO VCDs\*  $> 2\sigma^*$  (which is the criterion to identify a possible volcanic BrO plume) was raised from 3 to 6.

The identified plumes of category III can be seen in Table 9.5. In total 24 different volcanic events from 6 volcanoes were identified. For this category, only volcanic events were detected that showed conspicuously high maximum BrO VCDs\*<sub>max</sub> at the same time as the SO<sub>2</sub> in Figure 9.3 (Kasatochi, Dalaffilla, Mt. Redoubt, Sarychev, Eyjafjallajökull and Nabro). As already pointed out for the examples in Section 9.3.3–9.3.6 (Figures 9.6–9.10), most of these events only showed a roughly similar spatial pattern for both of the observed volcanic species. Especially for the eruptions of Kasatochi, Sarychev and Nabro, BrO could only be detected in some parts of the SO<sub>2</sub> plume for these volcanic events, resulting in low  $r^2$  values from the linear fit. Apart from the different plume ages and ambient conditions in the different parts of the plume, this might also be caused by the significant ash content that was present during these eruptions and the associated heterogeneous chemical processes in the

**Table 9.4.: Category II (weak linear correlation)**

*BrO/SO<sub>2</sub>-analysis of all detected volcanic plumes of Category II. Columns contain: event number, volcano, measurement date, max. BrO SCD, max. SO<sub>2</sub> SCD, coincidence of max. SO<sub>2</sub> and BrO SCD, BrO/SO<sub>2</sub> slope, ratio of max. SO<sub>2</sub> and BrO SCD and coordinates of regarded area.*

#	volcano	date	BrO SCD <sub>max</sub> [molec/cm <sup>2</sup> ]	SO <sub>2</sub> SCD <sub>max</sub> [molec/cm <sup>2</sup> ]	⊕	r <sup>2</sup>	BrO/SO <sub>2</sub> slope	BrO <sub>max</sub> /SO <sub>2</sub> max	coordinates
28	Kliuchevskoi	20./21.05.2007	5.1×10 <sup>13</sup>	1.9×10 <sup>17</sup>	no	0.40	2.7×10 <sup>-4</sup>	2.6×10 <sup>-4</sup>	[40 - 70°N, 145 - 180°E]
48	Ambrym	16.07.2007	5.3×10 <sup>13</sup>	2.6×10 <sup>17</sup>	yes	0.38	2.1×10 <sup>-4</sup>	2.0×10 <sup>-4</sup>	[0 - 35°S, 150 - 181°E]
163 <sup>†</sup>	Kasatochi	10.08.2008	4.3×10 <sup>14</sup>	1.9×10 <sup>19</sup>	no	0.41	2.4×10 <sup>-5</sup>	2.2×10 <sup>-5</sup>	[25 - 70°N, 110 - 185°W]
186	Kasatochi	20.08.2008	5.0×10 <sup>13</sup>	2.8×10 <sup>17</sup>	no	0.28	1.6×10 <sup>-4</sup>	1.7×10 <sup>-4</sup>	[35 - 70°N, 160 - 180°W]
278 <sup>†</sup>	Mt. Redoubt	23.03.2009	1.7×10 <sup>14</sup>	4.4×10 <sup>18</sup>	no	0.47	4.4×10 <sup>-5</sup>	3.8×10 <sup>-5</sup>	[45 - 70°N, 115 - 170°W]
279	Mt. Redoubt	24.03.2009	1.1×10 <sup>14</sup>	1.0×10 <sup>18</sup>	no	0.50	1.0×10 <sup>-4</sup>	1.0×10 <sup>-4</sup>	[45 - 70°N, 115 - 142°W]
281	Mt. Redoubt	26.03.2009	9.3×10 <sup>13</sup>	7.2×10 <sup>17</sup>	no	0.31	1.4×10 <sup>-4</sup>	1.2×10 <sup>-4</sup>	[20 - 70°N, 85 - 130°W]
306	Mt. Redoubt	09.04.2009	8.5×10 <sup>13</sup>	3.3×10 <sup>17</sup>	no	0.41	3.0×10 <sup>-4</sup>	2.5×10 <sup>-4</sup>	[40 - 70°N, 115 - 170°W]
312	Mt. Redoubt	13.04.2009	9.2×10 <sup>13</sup>	3.0×10 <sup>17</sup>	no	0.33	2.7×10 <sup>-4</sup>	3.0×10 <sup>-4</sup>	[45 - 70°N, 135 - 170°W]
317	Mt. Redoubt	16.04.2009	1.4×10 <sup>14</sup>	5.1×10 <sup>17</sup>	yes	0.49	2.6×10 <sup>-4</sup>	2.7×10 <sup>-4</sup>	[35 - 70°N, 140 - 180°W]
324	Mt. Redoubt	19.04.2009	6.7×10 <sup>13</sup>	3.3×10 <sup>17</sup>	no	0.33	2.1×10 <sup>-4</sup>	2.0×10 <sup>-4</sup>	[50 - 70°N, 140 - 175°W]
344	Mt. Redoubt	05.05.2009	8.2×10 <sup>13</sup>	3.0×10 <sup>17</sup>	no	0.37	2.6×10 <sup>-4</sup>	2.7×10 <sup>-4</sup>	[35 - 70°N, 140 - 175°W]
551	Eyjafjalla, jökull	30.04.2010	1.4×10 <sup>14</sup>	4.2×10 <sup>17</sup>	yes	0.50	2.9×10 <sup>-4</sup>	3.3×10 <sup>-4</sup>	[40 - 70°N, -40 - 5°E]
555	Eyjafjalla, jökull	05.05.2010	1.7×10 <sup>14</sup>	7.2×10 <sup>17</sup>	no	0.34	1.3×10 <sup>-4</sup>	2.4×10 <sup>-4</sup>	[35 - 70°N, -35 - 15°E]
557	Eyjafjalla, jökull	07.05.2010	1.0×10 <sup>14</sup>	5.5×10 <sup>17</sup>	no	0.29	1.5×10 <sup>-4</sup>	1.9×10 <sup>-4</sup>	[20 - 70°N, -45 - 10°E]
558	Eyjafjalla, jökull	08.05.2010	9.5×10 <sup>13</sup>	5.7×10 <sup>17</sup>	no	0.26	1.5×10 <sup>-4</sup>	1.6×10 <sup>-4</sup>	[25 - 70°N, 0 - 50°W]
568	Eyjafjalla, jökull	14.05.2010	1.3×10 <sup>14</sup>	8.4×10 <sup>17</sup>	no	0.42	1.4×10 <sup>-4</sup>	1.6×10 <sup>-4</sup>	[35 - 70°N, -50 - 15°E]
570	Eyjafjalla, jökull	16.05.2010	1.2×10 <sup>14</sup>	3.5×10 <sup>17</sup>	no	0.32	3.1×10 <sup>-4</sup>	3.5×10 <sup>-4</sup>	[35 - 70°N, -35 - 20°E]
572	Eyjafjalla, jökull	17.05.2010	1.5×10 <sup>14</sup>	7.3×10 <sup>17</sup>	no	0.42	2.6×10 <sup>-4</sup>	2.0×10 <sup>-4</sup>	[35 - 70°N, -55 - 20°E]
696	Kizimen	03.05.2011	6.6×10 <sup>13</sup>	3.7×10 <sup>17</sup>	yes	0.46	2.1×10 <sup>-4</sup>	1.7×10 <sup>-4</sup>	[40 - 70°N, 140 - 175°E]
706	Karymsky	21./22.05.2011	8.0×10 <sup>13</sup>	3.7×10 <sup>17</sup>	no	0.44	2.1×10 <sup>-4</sup>	2.1×10 <sup>-4</sup>	[35 - 70°N, 140 - 175°E]
748 <sup>†</sup>	Nabro	15.06.2011	2.6×10 <sup>14</sup>	2.2×10 <sup>19</sup>	no	0.27	1.8×10 <sup>-5</sup>	1.1×10 <sup>-5</sup>	[-10 - 65°N, 5 - 95°E]
749 <sup>†</sup>	Nabro	16.06.2011	1.8×10 <sup>14</sup>	1.2×10 <sup>19</sup>	no	0.29	2.0×10 <sup>-5</sup>	1.4×10 <sup>-5</sup>	[-15 - 60°N, 0 - 110°E]

<sup>†</sup> combined SO<sub>2</sub> product in case of high SO<sub>2</sub> SCDs ≥1×10<sup>18</sup> [molec/cm<sup>2</sup>]

⊕ location of SO<sub>2</sub> SCD<sub>max</sub> is the same as for BrO SCD<sub>max</sub>

**Table 9.5.: Category III (eruptions with enhanced BrO cluster, but no linear correlation)**

BrO/SO<sub>2</sub>-analysis of all detected volcanic plumes of Category III. Columns contain: event number, volcano, measurement date, max. BrO SCD, max. SO<sub>2</sub> SCD, coincidence of max. SO<sub>2</sub> and BrO SCD, BrO/SO<sub>2</sub> slope, ratio of max. SO<sub>2</sub> and BrO SCD and coordinates of regarded area.

#	volcano	date	BrO SCD <sub>max</sub> [molec/cm <sup>2</sup> ]	SO <sub>2</sub> SCD <sub>max</sub> [molec/cm <sup>2</sup> ]	⊕	r <sup>2</sup>	BrO/SO <sub>2</sub> slope	BrO <sub>max</sub> /SO <sub>2</sub> max	coordinates
160 <sup>†</sup>	Kasatochi	08.08.2008	3.6×10 <sup>14</sup>	3.9×10 <sup>19</sup>	no	0.22	8.6×10 <sup>-6</sup>	9.2×10 <sup>-6</sup>	[30 - 70°N, 145 - 195°W]
162 <sup>†</sup>	Kasatochi	09.08.2008	4.5×10 <sup>14</sup>	2.6×10 <sup>19</sup>	no	0.24	1.9×10 <sup>-5</sup>	1.7×10 <sup>-5</sup>	[25 - 70°N, 135 - 190°W]
165 <sup>†</sup>	Kasatochi	12.08.2008	3.0×10 <sup>14</sup>	1.6×10 <sup>19</sup>	no	0.21	2.4×10 <sup>-5</sup>	1.9×10 <sup>-5</sup>	[20 - 70°N, 50 - 175°W]
167 <sup>†</sup>	Kasatochi	13.08.2008	1.3×10 <sup>14</sup>	1.5×10 <sup>19</sup>	no	0.14	1.2×10 <sup>-5</sup>	9.0×10 <sup>-6</sup>	[25 - 70°N, 20 - 175°W]
169 <sup>†</sup>	Kasatochi	14.08.2008	1.1×10 <sup>14</sup>	6.9×10 <sup>18</sup>	no	0.00	1.8×10 <sup>-6</sup>	1.7×10 <sup>-5</sup>	[20 - 70°N, -200 - 15°E]
249 <sup>†</sup>	Dalaffilla	04.11.2008	1.7×10 <sup>14</sup>	4.3×10 <sup>18</sup>	no	0.01	1.4×10 <sup>-5</sup>	3.9×10 <sup>-5</sup>	[0 - 40°N, 30 - 70°E]
250 <sup>†</sup>	Dalaffilla	05.11.2008	1.2×10 <sup>14</sup>	1.6×10 <sup>18</sup>	no	0.05	3.1×10 <sup>-5</sup>	7.4×10 <sup>-5</sup>	[-5 - 50°N, 25 - 100°E]
280	Mt. Redoubt	25.03.2009	1.2×10 <sup>14</sup>	1.0×10 <sup>18</sup>	no	0.25	8.2×10 <sup>-5</sup>	1.2×10 <sup>-4</sup>	[30 - 70°N, 100 - 140°W]
326	Mt. Redoubt	20.04.2009	9.1×10 <sup>13</sup>	4.2×10 <sup>17</sup>	no	0.17	2.2×10 <sup>-4</sup>	2.1×10 <sup>-4</sup>	[40 - 70°N, 135 - 170°W]
369 <sup>†</sup>	Sarychev	12./13.06.2009	1.2×10 <sup>14</sup>	1.7×10 <sup>18</sup>	no	0.02	2.2×10 <sup>-5</sup>	7.0×10 <sup>-5</sup>	[30 - 65°N, 130 - 175°E]
370 <sup>†</sup>	Sarychev	13./14.06.2009	1.0×10 <sup>14</sup>	3.9×10 <sup>18</sup>	no	0.01	4.6×10 <sup>-6</sup>	2.7×10 <sup>-5</sup>	[25 - 70°N, 115 - 235°W]
375 <sup>†</sup>	Sarychev	15./16.06.2009	1.9×10 <sup>14</sup>	2.3×10 <sup>19</sup>	no	0.01	3.9×10 <sup>-6</sup>	8.2×10 <sup>-6</sup>	[25 - 70°N, 120 - 180°E]
377 <sup>†</sup>	Sarychev	16./17.06.2009	1.4×10 <sup>14</sup>	1.6×10 <sup>19</sup>	no	0.01	4.0×10 <sup>-6</sup>	8.7×10 <sup>-6</sup>	[20 - 70°N, 135 - 250°W]
378 <sup>†</sup>	Sarychev	17./18.06.2009	1.6×10 <sup>14</sup>	1.1×10 <sup>19</sup>	no	0.01	5.8×10 <sup>-6</sup>	1.4×10 <sup>-5</sup>	[20 - 70°N, 115 - 250°W]
380 <sup>†</sup>	Sarychev	19.06.2009	1.4×10 <sup>14</sup>	2.3×10 <sup>18</sup>	no	0.02	8.7×10 <sup>-6</sup>	6.3×10 <sup>-5</sup>	[45 - 70°N, 110 - 135°E]
548	Eyjafjallajökull	27.04.2010	1.1×10 <sup>14</sup>	3.1×10 <sup>17</sup>	no	0.07	9.4×10 <sup>-5</sup>	3.5×10 <sup>-4</sup>	[45 - 70°N, 0 - 40°W]
559	Eyjafjallajökull	09.05.2010	1.0×10 <sup>14</sup>	5.0×10 <sup>17</sup>	no	0.14	1.3×10 <sup>-4</sup>	2.1×10 <sup>-4</sup>	[25 - 70°N, -55 - 5°E]
560	Eyjafjallajökull	10.05.2010	9.8×10 <sup>13</sup>	3.8×10 <sup>17</sup>	no	0.12	1.1×10 <sup>-4</sup>	2.5×10 <sup>-4</sup>	[20 - 70°N, -50 - 5°E]
569	Eyjafjallajökull	15.05.2010	8.8×10 <sup>13</sup>	4.4×10 <sup>17</sup>	no	0.02	4.6×10 <sup>-5</sup>	2.0×10 <sup>-4</sup>	[40 - 70°N, 0 - 60°W]
745 <sup>†</sup>	Nabro	13.06.2011	2.6×10 <sup>14</sup>	1.0×10 <sup>19</sup>	no	0.00	3.0×10 <sup>-6</sup>	2.4×10 <sup>-5</sup>	[-5 - 35°N, 10 - 60°E]
755 <sup>†</sup>	Nabro	20.06.2011	1.4×10 <sup>14</sup>	5.6×10 <sup>18</sup>	no	0.12	3.2×10 <sup>-5</sup>	2.6×10 <sup>-5</sup>	[-20 - 55°N, -13 - 130°E]
758 <sup>†</sup>	Nabro	21.06.2011	1.5×10 <sup>14</sup>	5.2×10 <sup>18</sup>	no	0.08	2.7×10 <sup>-5</sup>	2.9×10 <sup>-5</sup>	[-25 - 55°N, -15 - 90°E]
760 <sup>†</sup>	Nabro	22.06.2011	1.1×10 <sup>14</sup>	3.8×10 <sup>18</sup>	yes	0.11	3.6×10 <sup>-5</sup>	3.0×10 <sup>-5</sup>	[-20 - 50°N, -20 - 100°E]
767 <sup>†</sup>	Nabro	26.06.2011	1.2×10 <sup>14</sup>	3.6×10 <sup>18</sup>	yes	0.27	4.2×10 <sup>-5</sup>	3.3×10 <sup>-5</sup>	[-10 - 55°N, -4 - 75°E]

<sup>†</sup> combined SO<sub>2</sub> product in case of high SO<sub>2</sub> SCDs  $\geq 1 \times 10^{18}$  [molec/cm<sup>2</sup>]

⊕ location of SO<sub>2</sub> SCD<sub>max</sub> is the same as for BrO SCD<sub>max</sub>

plume. For some of the detected events, the BrO SCDs\* showed a large scatter, although the 6-neighbouring pixels criterion was fulfilled in parts of the plume. This is especially true for the second day after the Dalaffilla eruption (event No.250 in Table 9.5), one day of the Mt. Redoubt eruption (event No.326) and some days during the eruption of Eyjafjallajökull (event No.559, No.560 and No.569). In case of the Nabro eruption, the BrO SCDs\* in the area of the captured SO<sub>2</sub> plume were well above the SCDs\* in the corresponding reference area, but in contrast to all other major eruptions, they could only be observed in the area close to the volcano for all detected days, where also the largest SO<sub>2</sub> SCDs\* were detected (see Sect. 9.3.4). For the last 2 detected days of the Nabro eruption in June 2011, the location of the maximum SO<sub>2</sub> SCDs\* from the combined SO<sub>2</sub> product (see also Sect. 8.5) matches the one for the maximum BrO SCDs\*, which was not the case when using the SO<sub>2</sub> SR.

#### 9.4.4. Category IV: Volcanic plumes showing no enhanced BrO SCDs\*

The majority of all captured plumes (92%) showed no signs for the presence of volcanic BrO in the data, i.e. the retrieved BrO SCDs\* were not enhanced with respect to the slant columns in the associated reference areas. This resulted in a correlation coefficient  $r^2$  and a BrO/SO<sub>2</sub> ratio close to zero in such cases (the ratio was here typically on the order of  $<10^{-5}$ ).

Figure 9.14 shows such an example for the eruption of the Fernandina volcano (Galapagos Island, Ecuador) on 13 April 2009. In Figure 9.14 a and c, the background corrected SCDs\* for SO<sub>2</sub> and BrO are shown, including all pixels of the PEB cluster and the surrounding reference area. Accordingly, Figure 9.14 b and d show only the identified plume pixels for both species. The resulting correlation plot for the captured plume pixels (Figure 9.14 e) indicates no enhancement of BrO inside the plume.

## 9.5. Discussion on investigation of volcanic BrO during volcanic events

The analysis of BrO SCDs within the SO<sub>2</sub> plumes that were extracted from the GOME-2 dataset (cf. Chapter 8) demonstrates the capability of the instrument to monitor the abundance of volcanic BrO during moderate and major eruptions (or even very strong degassing events, whenever the BrO SCD is sufficiently high to exceed the instrument's detection limit).

Overall, 64 volcanic plumes from 11-12 different volcanoes showed clear evidence for BrO of volcanic origin, representing 8% of all captured plumes and about 30% of all volcanoes which emitted detectable SO<sub>2</sub> plumes (772) within the observed time period. For at least 6 volcanoes (Dalaffilla, Karymsky, Kizimen, Kliuchevskoi, Nabro and Sarychev) these are the first reported measurements of BrO to the authors' knowledge. Another detected BrO plume can most probably be assigned to the Bezymianny volcano on Kamchatka (event #22; see Section 9.3.2), and three more identified volcanic BrO plumes (events #675, #700 and #740) might have been caused by explosions at

## 9. Systematic investigation of BrO during volcanic events

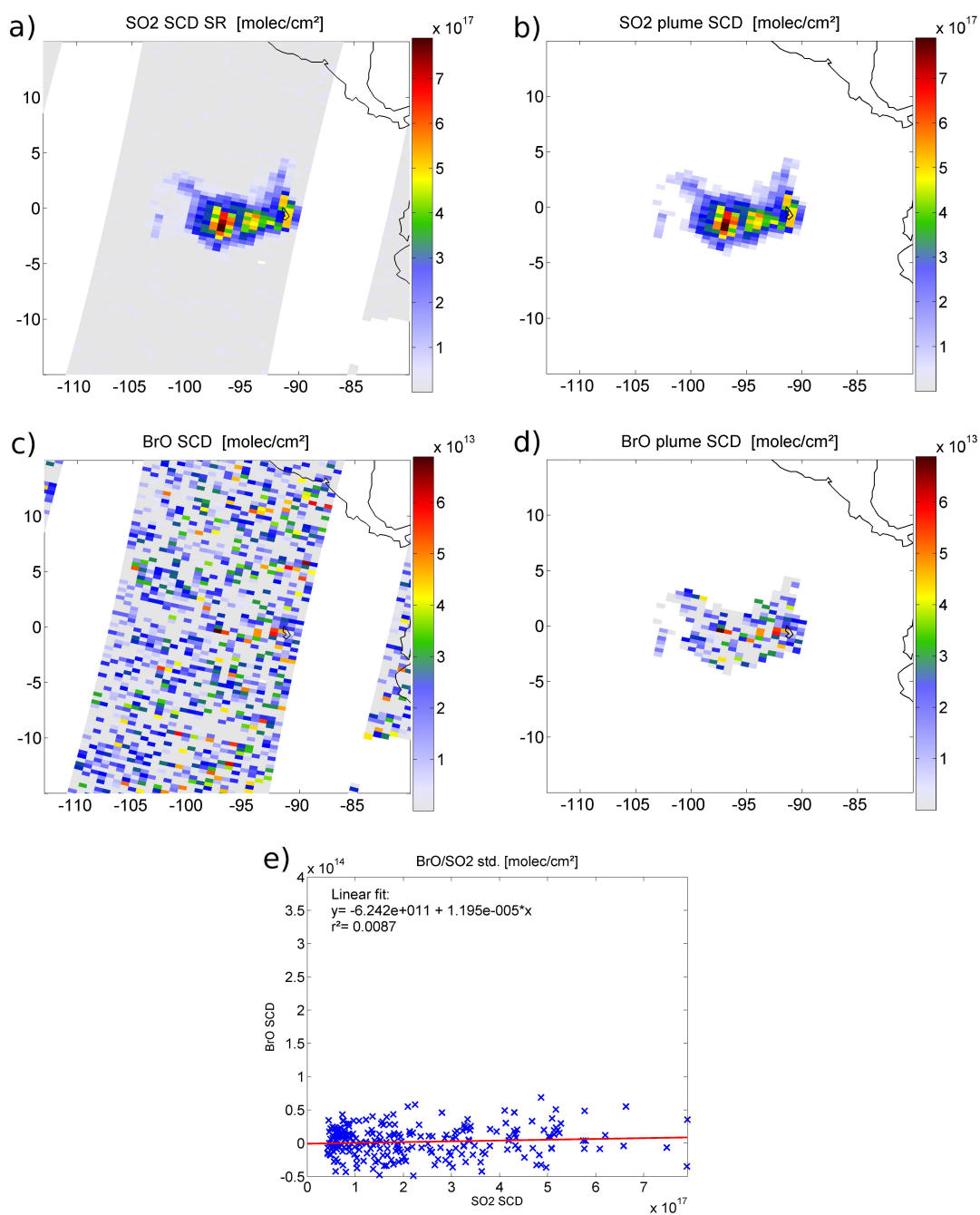


**Figure 9.14.:** SO<sub>2</sub> and BrO SCDs for the eruption of the Fernandina volcano (Galapagos Islands, Ecuador) on 13 April 2009. The background corrected SCDs\* for SO<sub>2</sub> and BrO are shown (Figure 9.14 a and c), including the pixels of the PEB and the reference area. The extracted plume pixels are shown in Figure 9.14 b and d. The resulting correlation plot (Figure 9.14 e) shows no correlation between the two species. The BrO SCDs\* are statistically distributed over the whole area of the volcanic SO<sub>2</sub> plume, resulting in a vanishing correlation and a BrO/SO<sub>2</sub> ratio close to zero.

the Shiveluch volcano (Kamchatka), although reports from KVERT in combination with OMI data suggest that Kliuchevskoi and Kizimen were most probably the origin of the detected plumes. This demonstrates clearly the advantage of satellite observations to monitor volcanic events in sparsely populated areas, where ground-based measurements are often difficult to realize (e.g. for Dalaffilla in Ethiopia or Nabro in Eritrea).

For all other detected BrO plumes, the results confirm the general abundance of BrO at the corresponding volcanoes (Ambrym, Eyjafjallajökull, Kasatochi, Mt. Redoubt) as it has been found from former ground-based, airborne and satellite observations. The total number of volcanoes where BrO has been detected by UV-DOAS measurements, can therefore be raised from 12 to 19 (for a survey of all former BrO observations see Kelly et al., 2012, and references therein).

Two different reasons may explain those cases where no significantly enhanced BrO SCDs were found:

1. The emissions of quiescent degassing volcanoes and/or during minor eruptions are too low. In such cases, even if moderate or high BrO/SO<sub>2</sub> ratios are present in the plume, the BrO SCDs will be below the detection limit.
2. The BrO/SO<sub>2</sub> ratio is too low. This might be even the case for moderate or strong eruptions with high SO<sub>2</sub> SCDs. Regarding the top five of all 772 volcanic plumes with the largest SO<sub>2</sub> SCDs\* in this study, two of them showed no evidence for the presence of volcanic BrO (Merapi on 5 November 2010 with a maximum SO<sub>2</sub> SCDs\* of  $8.9 \times 10^{18}$ , and Grímsvötn on 22 May 2011 with a maximum SO<sub>2</sub> SCDs\* of  $2.2 \times 10^{19}$  molec/cm<sup>2</sup>). However, from such cases, upper limits for the BrO/SO<sub>2</sub> ratio can be estimated by the ratio of the maximum BrO and SO<sub>2</sub> SCDs\* or the resulting slope of the linear fit (both ratios can be found in Appendix B for all investigated plumes). For the above mentioned cases of Merapi and Grímsvötn, the upper limits for the BrO/SO<sub>2</sub> ratios were found to be  $8 \times 10^{-6}$  and  $2.5 \times 10^{-6}$ , respectively.

Since satellite instruments usually have a relatively large footprint ( $40 \times 80$  km<sup>2</sup> for GOME-2), they are not able to resolve small scale variations in the trace gas distribution. All measured columns of SO<sub>2</sub> and BrO need therefore to be interpreted as mean values within the area of a satellite pixel. This also implies that significantly higher BrO and SO<sub>2</sub> SCDs and probably also BrO/SO<sub>2</sub> ratios might have been present locally in the highlighted volcanic plumes, which may be investigated by applying the algorithm to data from satellite instruments with higher spatial resolution in the future (e.g. OMI).

### 9.5.1. Different BrO/SO<sub>2</sub> relationships

The collected examples of volcanic plumes show large variations of the BrO/SO<sub>2</sub> behaviour. For some of the identified plumes, the extent and shape of the BrO plume is roughly comparable to that of SO<sub>2</sub> and is accompanied by a similar distribution of

the two species within the plume. This results in high values for the correlation coefficient ( $r^2 > 0.5$ ) for the respective SCDs of the extracted plume pixels and allows us to determine the mean BrO/SO<sub>2</sub> ratio. Most of these cases were observed for moderate eruptions, where a well-defined, compact plume was visible in the satellite data less than 24 hours after the start of the associated eruption.

For other cases, only a weak linear correlation between BrO and SO<sub>2</sub> columns was observed that on the one hand may be caused by BrO SCDs that were only slightly above the instrument's detection limit, and on the other hand by the gradual chemical processing of aged volcanic plumes. For instance, in parts of the plume of the Dalaffilla eruption (Section 9.3.3), BrO was well correlated with SO<sub>2</sub>, whereas in other parts no BrO was found. One explanation for this behaviour might be that not only the local composition of the volcanic plume (such as ash and/or other plume contents) have a crucial influence on the formation of BrO, but that the ambient meteorological conditions (temperature, humidity and plume height) also play an important role. This is also suggested by the results for the Sarychev eruption (cf. Section 9.3.6), where enhanced BrO SCDs were only observed in relatively small plume heights of 6–8 km, but not at higher altitudes (>10 km), despite the fact that the largest SO<sub>2</sub> SCDs occurred there.

The HYSPLIT trajectory analysis of the Sarychev case points out another problem that may show up especially during major eruptions. Passive DOAS instruments, such as GOME-2, SCIAMACHY and OMI often can not distinguish individual volcanic plumes at different altitude, if they overlap in the x-y-plane of observation. To investigate the influence of different ambient conditions on the formation of BrO in individual parts of the detected volcanic plumes, further trajectory calculations along with chemical model simulations will be necessary. Such simulations might also be used to analyse the temporal development of the BrO/SO<sub>2</sub> ratio and determine the lifetime for both species. This will be essential for the calculation of total SO<sub>2</sub> and BrO budgets in the future.

### 9.5.2. Comparison to previous ground-based measurements

It should be emphasized that comparisons of satellite observations with ground-based measurements have to be interpreted with care: whereas satellites almost exclusively detect plumes from explosive eruptions, ground-based observations usually investigate stable conditions at degassing volcanoes. Ground-based observations of volcanic plumes are ideal for the investigation of the initial development of the BrO/SO<sub>2</sub> behaviour during the first minutes after the plume's release at quiescent degassing volcanoes.

The advantage of satellite instruments like GOME-2, SCIAMACHY and OMI lies in the ability to investigate this behavior in entire volcanic plumes from moderate/major eruptions or strong degassing events on a much larger spatial and temporal scale. Nevertheless, our results indicate that the BrO/SO<sub>2</sub> ratios during eruptions and periods of quiet degassing are not significantly different, as the BrO/SO<sub>2</sub> ratios for all identified volcanic BrO events were found to be similar to the ones from worldwide ground-based measurements with some  $10^{-5}$  to several  $10^{-4}$  (for a survey of former

BrO observations the reader is again referred to Kelly et al., 2012, and references therein).

### 9.5.3. Comparison to previous satellite studies

An attempt to investigate the abundance of volcanic BrO using GOME and SCIAMACHY data by Afe et al. (2004) failed. As the spatial resolution of SCIAMACHY is better than for the GOME-2 instrument ( $30 \times 60 \text{ km}^2$  compared to  $40 \times 80 \text{ km}^2$ ), this result appears surprising. Meanwhile, the SCIAMACHY instrument has proven to be able to detect enhanced BrO SCDs of volcanic origin as well, as the BrO plume from Kasatochi was clearly visible in the data (Theys et al., 2009).

In order to further investigate the potential of SCIAMACHY to detect BrO during volcanic events, we looked at BrO Level-2 data from the Belgian Institute for Space Aeronomy (Van Roozendael et al., 2006b) for all volcanic plumes with enhanced BrO SCDs that we had found in the GOME-2 data within this study (see Tables 9.3, 9.4 and 9.5). A considerable fraction of the identified plumes with enhanced BrO SCDs (36%) was not covered by the SCIAMACHY instrument. Especially for the major eruptions of Sarychev and Nabro, the instrument missed the affected plume regions for almost all days, as the enhanced BrO columns occurred only in a relatively small area of about  $10^\circ \times 10^\circ$ , while the gaps in SCIAMACHY observations are typically  $4^\circ \times 15^\circ$  in latitude and longitude, respectively. For all other volcanic plumes, the SCIAMACHY data indeed showed similar enhancements of the BrO SCDs in 90% of these cases. Only for about 10% of these events, the enhanced BrO columns were not clearly visible in the SCIAMACHY data, even though the instrument provided a sufficient coverage of the volcanic plume. However, in those cases the BrO SCDs were also close to the detection limit of the GOME-2 measurements.

The poor daily coverage of the instrument in combination with the comparatively short time period of about 18 months of SCIAMACHY data (33 scenes of volcanic  $\text{SO}_2$  emissions from August 2002 - January 2004) that were analyzed in Afe et al. (2004) might be the main reason why their attempt failed. However, some of the proposed explanations for the lack of correlation between  $\text{SO}_2$  and BrO columns in Afe et al. (2004) remain plausible and important, particularly because for the majority of GOME-2 measurements in the here presented study, no evidence for volcanic BrO was found either. The most important reasons are:

1. Current satellite instruments are usually not sensitive enough for the detection of BrO from steadily degassing volcanoes, especially not on daily basis. This is, for a large part, due to the coarse spatial resolution of these instruments, as a single ground pixel may cover an area that is much larger than the plume, causing the already small BrO SCDs to decrease. In most cases, only larger BrO plumes from moderate to major eruptions are detected. Furthermore, the sensitivity of satellite measurements decreases towards lower altitudes.
2. The formation rate and lifetime of BrO is influenced by several factors, like the plume height and the associated ambient meteorological conditions, the plume's composition and probably the abundance of volcanic ash, which both have an

important influence on heterogeneous chemistry. While clearly enhanced BrO SCDs from Kasatochi were, for example, detected for several days after the eruption and thousands of kilometres from the volcano, this was only possible for a few hundred kilometres and an estimated plume age of 24 hours after the eruption of the Nabro volcano.

3. The amount of reactive halogen compounds in volcanic plumes may vary for individual volcanoes, so that the reactive bromine content for some of the space monitored eruptions is insufficient to form detectable amounts of BrO. Furthermore, the geophysical processes inside a volcano, such as the varying solubility of bromine and sulphur (which alters with raising magma), might also play an important role for the initial BrO/SO<sub>2</sub> ratio during an eruption, as it was recently suggested by Bobrowski and Giuffrida (2012). Examples for very low BrO/SO<sub>2</sub> ratios are the major eruptions of Okmok (July 2008), Merapi (October/November 2010) and Grímsvötn (May 2011), with estimated upper limits in the range of 10<sup>-6</sup> to 10<sup>-5</sup>).

In the future, a detailed analysis of higher spatially resolved OMI data (available since October 2004 up to now with full daily global coverage) and the re-analysis of the entire SCIAMACHY data of the past 10 years will probably increase the total number of volcanic BrO observations. In addition, the GOME-2 series will be completed by two additional instruments during the next 5-10 years (GOME-2B was successfully launched in September 2012), improving spatial coverage and temporal resolution of volcanic monitoring from space. Furthermore, the Sentinel satellite series of the European Space Agency (ESA) will provide instruments with much higher spatial and temporal resolution for atmospheric monitoring (Sentinel-5 and Sentinel-5 precursor) and even one high resolution instrument on a geostationary satellite (Sentinel-4).

### 9.6. Intercomparison of GOME-2 and CARIBIC data during the eruption of Eyjafjallajökull

The systematical analysis of volcanic BrO in Section 6.4 revealed GOME-2 measurements and different kinds of BrO/SO<sub>2</sub> relationships in volcanic plumes from several days during the eruption of Eyjafjallajökull on Iceland in April and May 2010 (cf. Tables 9.3–9.5). Due to the large amount of fine ash particles that were probably caused by the interaction of magma with the glacier on the top of the volcano (especially during the first week after the start of the main eruption on 14 April 2010), the eruption led to a prolonged closure of airspace over large parts of Europe.

In order to analyze the main properties and general location of the ash plume, several research flights were conducted during the eruption (e.g. by the FALCON aircraft of the German Aerospace Center (DLR) - cf. Schumann et al., 2011). The CARIBIC aircraft laboratory (cf. Section 5.2 and Brenninkmeijer et al., 2007) also performed flights during 3 different days. Unfortunately, reliable DOAS measurements of the tracegases inside the volcanic plume could only be performed during the flight on May 16. In the following, the GOME-2 measurements for that day will be presented

first, showing a weak but noticeable linear relationship between BrO and SO<sub>2</sub> (cf. Table 9.5). Afterwards, the CARIBIC SO<sub>2</sub> and BrO evaluation will be described and results are presented and compared to the satellite data. All CARIBIC data, including measurements of ash, SO<sub>2</sub>, BrO, O<sub>3</sub> and the comparison with satellite data have been published in Heue et al. (2011).

### 9.6.1. GOME-2 SO<sub>2</sub> and BrO measurements on 16 May 2010

The volcanic plume of Eyjafjallajökull on 16 May 2010 has been automatically extracted by the plume extraction algorithm as described in Chapter 5. Furthermore, enhanced SCDs of BrO have been detected in the scope of the systematic BrO analysis in the area of the SO<sub>2</sub> plume and a weak linear correlation between the two species was found (as listed in Table 9.5).

Figure 9.15 shows the corresponding maps for both species. The SO<sub>2</sub> plume can be clearly identified from the satellite data, extending from the volcano towards Great Britain (Figure 9.15 a and b). The BrO SCDs are weak compared to the background signal, but still clearly enhanced in the main area of the SO<sub>2</sub> plume (Figure 9.15 c and d). The linear fit for both species leads to an  $r^2$  value of 0.32 and a mean BrO/SO<sub>2</sub> ratio of  $3.1 \times 10^{-4}$  (Figure 9.15 e). However, it can be seen from the maps that the highest BrO SCDs\* were found close to the volcano, while the SO<sub>2</sub> SCDs\* remained at a similar level in downwind direction for the initial part of the plume.

Considering the whole time period from the beginning of the main eruption on 14 April until the end on 18 May 2010, almost all days during the eruption identified by the extraction algorithm showed a relatively clear enhancement of BrO SCDs. Because the SO<sub>2</sub> SCDs were low compared to other eruptions with BrO abundance, the highest BrO/SO<sub>2</sub> ratios of up to  $5.1 \times 10^{-4}$  of all investigated plumes were found for this eruption.

### 9.6.2. CARIBIC SO<sub>2</sub> and BrO measurements on 16 May 2010

As described in Section 3.3, the CARIBIC container provides a DOAS system that is able to measure scattered sunlight via three small telescopes at the belly of the Lufthansa Airbus A340-600 at different elevation angles. Two of the telescopes point sideways at  $-10^\circ$  relative to the horizon and the third has a near-nadir geometry ( $-82^\circ$ ). For the measurements on 16 May 2010, only one of the sideways looking telescopes ( $-10^\circ$ ) and the one at  $-82^\circ$  were available.

For the DOAS evaluation of SO<sub>2</sub> at 311.6–333 nm, cross-sections of SO<sub>2</sub> (Bogumil et al., 2003, 273 K), O<sub>3</sub> (Bogumil et al., 2003, 223 and 243 K), BrO (Wilmouth et al., 1999, 228 K) and OCIO (Kromminga et al., 2003) were included in the fit scenario, as well as a 4th degree polynomial. For the BrO retrieval at 324–354 nm, cross-sections for NO<sub>2</sub> (Vandaele et al., 1998, 220 K), O<sub>4</sub> (Greenblatt et al., 1997) and HCHO (Meller and Moortgat, 2000) were included in addition to the cross-sections that had been already used in the SO<sub>2</sub> retrieval. Unlike for satellite retrievals, a reference spectrum can not be directly measured by simply pointing the telescopes in the Sun's direction, because it would be still affected by the absorptions in the atmosphere.

## 9. Systematic investigation of BrO during volcanic events

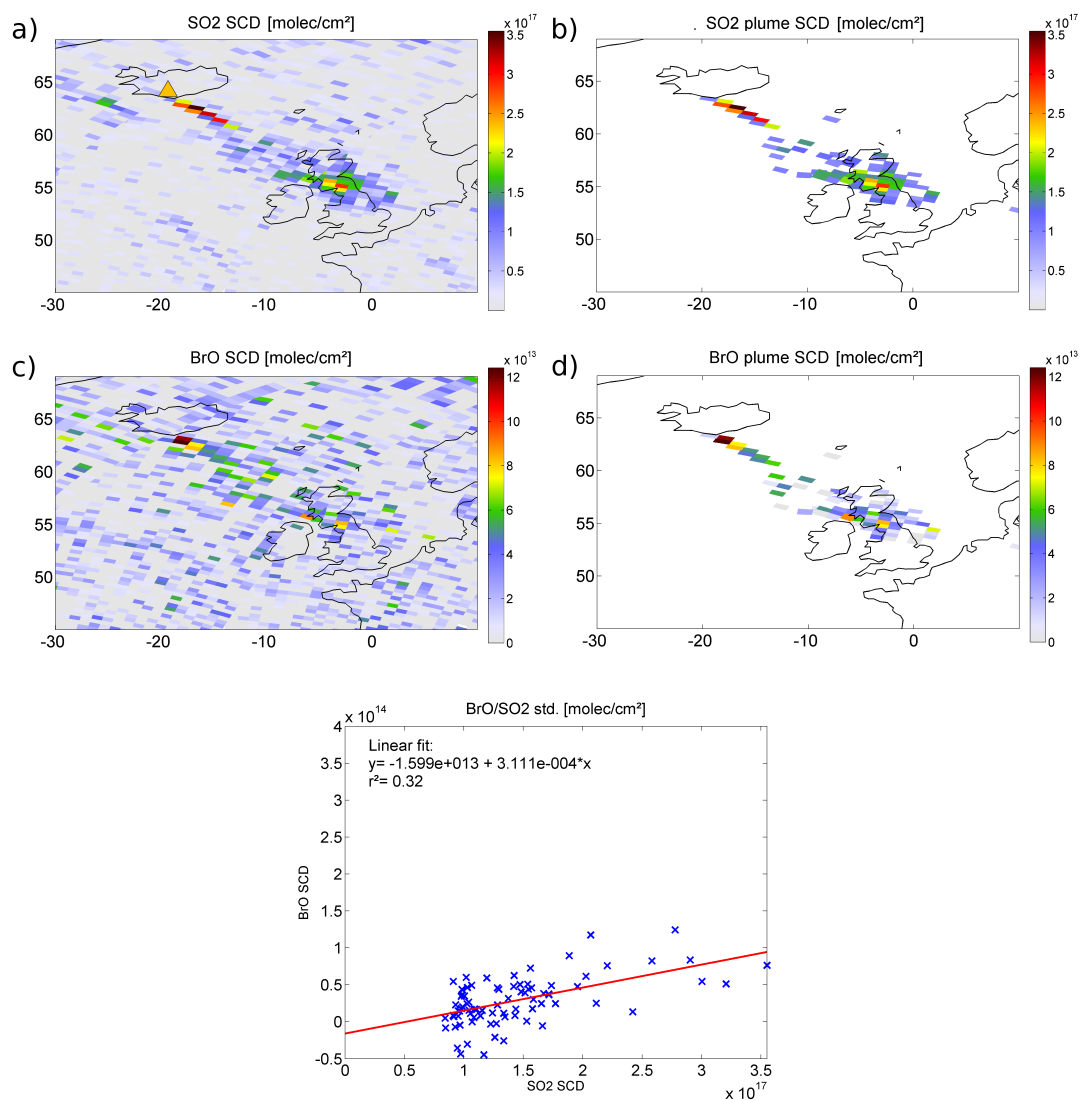


**Figure 9.15.:** The volcanic SO<sub>2</sub> and BrO plume during the eruption of the Eyjafjallajökull volcano on 16 May 2010 as observed by GOME-2. The SO<sub>2</sub> plume (Figure 9.15 a and b) is transported in south-eastern direction from the volcano (indicated by the orange triangle). The BrO columns are only slightly enhanced compared to the background signal (9.15 c and d), but clearly collocated with the SO<sub>2</sub> plume. The correlation plot for both species leads to an  $r^2$  value of 0.32 and a mean BrO/SO<sub>2</sub> ratio of  $3.1 \times 10^{-4}$  (Figure 9.15 e).

Thus, usually a scattered sunlight spectrum that is assumed to be not affected by the absorptions of interest (in this case outside the volcanic plume) is used as reference, so that the resulting SCDs are "differential SCD" (relative to the reference). For the measurements on 16 May 2010, the spectrum of a clouded scene was chosen that was recorded shortly after the aircraft crossed the Eyjafjallajökull plume. The reference spectrum was subsequently used to calculate a Ring spectrum which was also included in both the SO<sub>2</sub> and BrO retrieval.

In order to make a comparison between the measured CARIBIC and GOME-2 data possible, AMFs were calculated with the radiative transfer model McArtim (cf. Section 4.6), which were used to convert SCDs from both datasets to VCDs. Apart from the measurement geometry and the volcanic plume (which was assumed to be homogeneously distributed between 3 and 6 km altitude), a cloud layer with a cloud optical thickness (COT) of 10, extending from 0.5–1.5 km altitude, was included in the simulations (a closed cloud deck was observed below the aircraft for most of the time during the measurements, of which the COT and vertical extent were estimated from video images taken in flight). Furthermore, the optical properties of volcanic ash were included with an aerosol extinction of 0.8 km<sup>-1</sup> and a single scattering albedo (SSA) of 0.95, as derived from measured O<sub>4</sub> SCDs (e.g. Wagner et al., 2004; Heue, 2005; Frieß et al., 2006). The evaluation of the CARIBIC data as well as the RTM simulations were conducted by Klaus-Peter Heue from MPIC Mainz and are described in more detail in Heue et al. (2011).

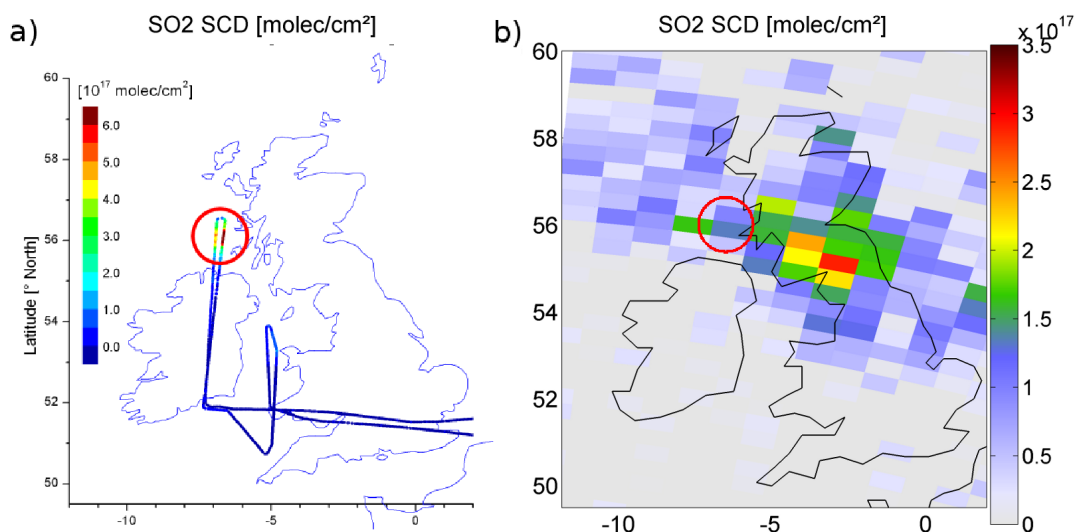


**Figure 9.16.:** CARIBIC and GOME-2 SO<sub>2</sub> measurements of the Eyjafjallajökull plume on 16 May 2010. Shortly before and after the aircraft reached the turning point, the enhanced SO<sub>2</sub> SCDs indicate the presence of the volcanic plume about 1° north of Ireland (Figure 9.16 a; adapted from Heue et al. (2011)). The location of the plume is confirmed by the satellite data, which shows enhanced SO<sub>2</sub> SCDs at the same location in Figure 9.16 b (indicated by the red circle).

## 9. Systematic investigation of BrO during volcanic events

Figure 9.16 a shows the flight track of the aircraft and the observed CARIBIC SO<sub>2</sub> SCDs from the near-nadir telescope. The aircraft was initially headed in northern direction across the island of Ireland. During the return flight, a second leg was probed over the Irish Sea. As the airspace north of the Isle of Man was closed due to a warning of high volcanic ash concentrations, the aircraft had to turn south at this point (about 54° N). During the flight, the altitude was varied between 2 and 7 km,

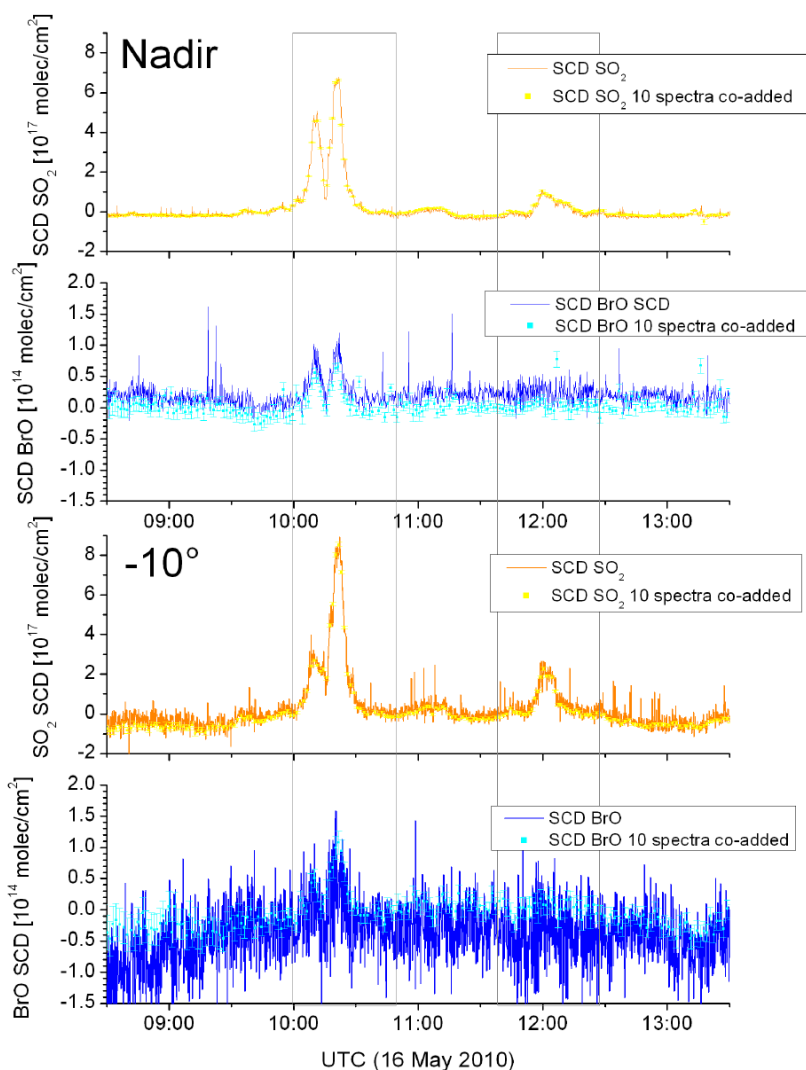


**Figure 9.17.:** Time series of CARIBIC SO<sub>2</sub> and BrO measurements for the nadir and -10° telescopes (single spectra and 10 spectra co-added). The volcanic plume shows up by three distinct peaks in the SO<sub>2</sub> data (orange/yellow), where the first and second peak can be attributed to the same plume before and after the turning point. Additionally, enhanced BrO SCDs show up at the location of the main plume for both flying directions. Adapted from Heue et al. (2011).

as model predictions yielded lower plume concentrations for higher altitudes that day. The volcanic SO<sub>2</sub> plume was clearly detected by CARIBIC shortly before and after the flight's turning point was reached about 1° north of Ireland, with maximum observed SO<sub>2</sub> SCDs of  $6 \times 10^{17}$  molec/cm<sup>2</sup>. In Figure 9.16 b, the GOME-2 SO<sub>2</sub> data is shown for the same area. The SO<sub>2</sub> distribution confirms the CARIBIC measurements in general, as the volcanic plume shows up at the same region in the satellite data, however with lower SO<sub>2</sub> SCDs due to the coarse spatial resolution of the instrument. The overpass time of GOME-2 was within less than 15 min of the time of the CARIBIC measurements, so it can be assumed that the same air masses were observed.

In Figure 9.17, the CARIBIC SO<sub>2</sub> and BrO measurements for both available telescopes are shown for the entire length of the research flight. Again, the enhanced SO<sub>2</sub> SCDs can be identified at a first glance, as three distinct peaks appear for both telescopes in the time series. While the first two peaks (10:05–10:25 UTC) are associated with the strongly enhanced SCDs north of Ireland during the first leg, the third, weaker peak in the SO<sub>2</sub> SCDs (11:50–12:20 UTC) was probably caused by the edge of another part of the plume over Great Britain (cf. Figure 9.16 b) that was probed during the second leg over the Irish Sea. The differences in the measured SCDs for the different telescopes (especially for SO<sub>2</sub> during the first and second intersection of the volcanic plume north of Ireland) can be mainly explained by a change of the flight altitude from 8 km to 4 km. The aircraft was probably flying above the plume during the first intersection, so that the sideways looking telescope probably only probed the outermost layer of the volcanic plume. During the second intersection, the aircraft was directly flying inside the plume, so that both telescopes showed comparable SO<sub>2</sub> SCDs (the sideways looking telescope showed indeed higher SCDs, probably because the plume was more horizontally extended than in vertical direction).

### 9.6.3. GOME-2 and CARIBIC data comparison

The validation of satellite data by using results from ground-based or airborne instruments is generally difficult due to the differences in spatial and temporal resolution. GOME-2 forward scan pixels cover an area of  $40 \times 80$  km<sup>2</sup> (respectively  $40 \times 240$  km<sup>2</sup> for the backward scan pixels; cf. Section 5.1) and usually provide only one measurement per day for a specific location (depending on latitude). CARIBIC provides nearly continuous measurements during a flight at a horizontal spatial resolution of about 2 km in flight direction (according to a flight speed of 900 km/h), and at a horizontal resolution of some hundreds of meters (depending on flight altitude). In contrast to the satellite instrument, CARIBIC has the opportunity to probe a certain location for several times. Differences in the local trace gas distribution might, therefore, not be visible in the satellite measurements. Furthermore, data from different platforms for a specific volcanic event are rare. In order to compare both datasets to each other, the VCDs have been calculated for both instruments as described in Section 9.6.2.

Figure 9.18 a shows the SO<sub>2</sub> VCDs from the CARIBIC nadir measurements in comparison with those that were detected at almost the same time by GOME-2. While the two peaks from the CARIBIC measurements (orange) result from the intersection

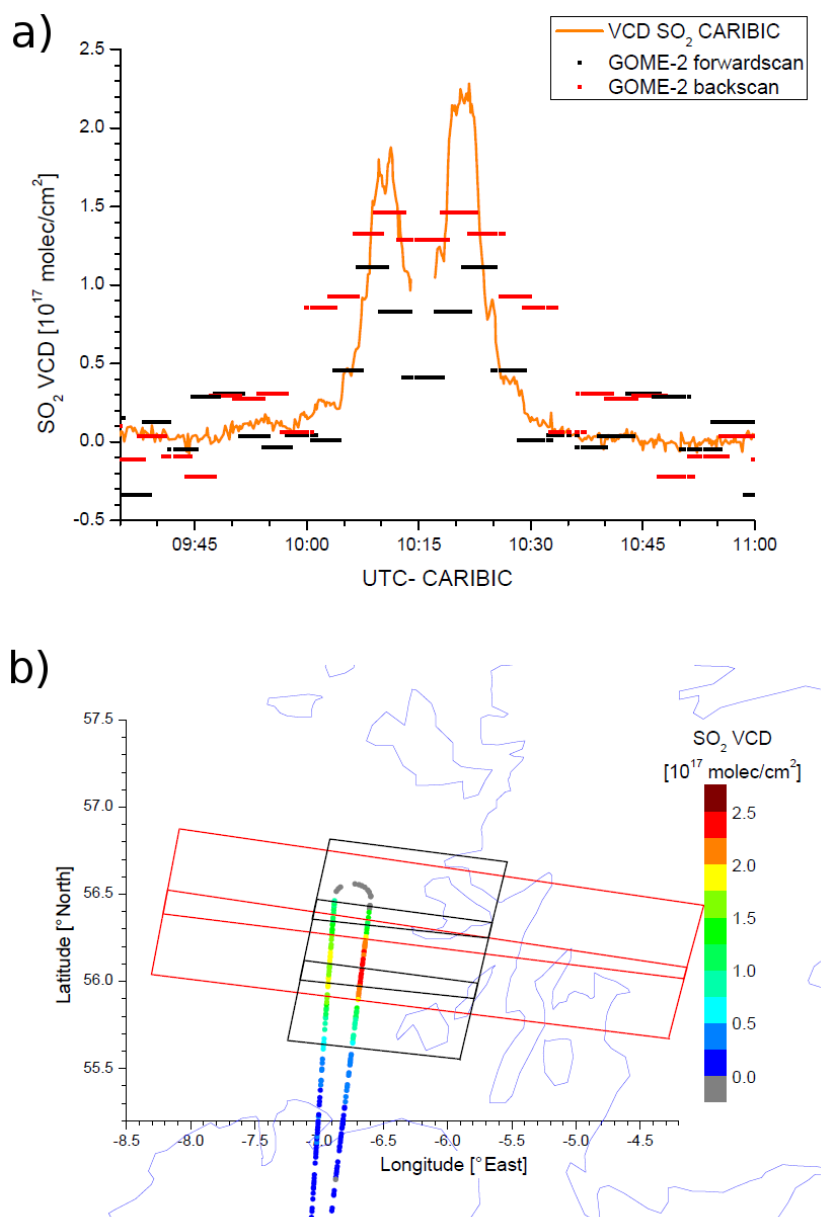


**Figure 9.18.:** Comparison of CARIBIC and GOME-2 SO<sub>2</sub> measurements. While the two peaks from the CARIBIC nadir measurements (orange) result from the intersection of the plume before and after the turning point, the GOME-2 data appear symmetrical, as the whole scene was only probed once by the satellite instrument (Figure 9.18 a). The CARIBIC measurements were covered by three GOME-2 forward scan and two backward scan pixels (Figure 9.18 b). While the maximum CARIBIC SO<sub>2</sub> VCDs are found in between two forwardscan pixels, they are perfectly covered by a backscan pixel, which might explain the better quantitative agreement between the GOME-2 backscans and the CARIBIC data to a certain degree. Adapted from Heue et al. (2011).

of the plume before and after the turning point, the GOME-2 data are symmetrical, as the whole scene was only probed once by the satellite instrument and therefore the VCDs for both CARIBIC intersections are the same. Unlike for other studies in this thesis, not only the results from the satellite instrument's forwardscan are shown (black), but also the  $\text{SO}_2$  VCDs from the backscan measurements (red). To indicate the time period where the aircraft was flying inside an area that was covered by a satellite measurement, the GOME-2 VCDs are illustrated as horizontal lines.

While the general location of the plume and the resulting  $\text{SO}_2$  VCDs agree well for all measurements, the VCDs from the GOME-2 backscans are, surprisingly, in even better agreement with the CARIBIC measurements than those from the forwardscans. The reason for this effect can be explained partly by taking the orientation of the GOME-2 pixels is taken into account. As illustrated in Figure 9.18 b, the location of the maximum CARIBIC VCDs was only covered in between two GOME-2 forwardscan pixels, while it had been perfectly covered by one of the backscan pixels. Additionally, the  $\text{SO}_2$  distribution in Figure 9.16 b indicates that the plume was mostly extended parallel to the backscan pixels at that time, so that they had covered a larger fraction of the plume, especially some parts of the much higher  $\text{SO}_2$  VCDs that were detected over Scotland.

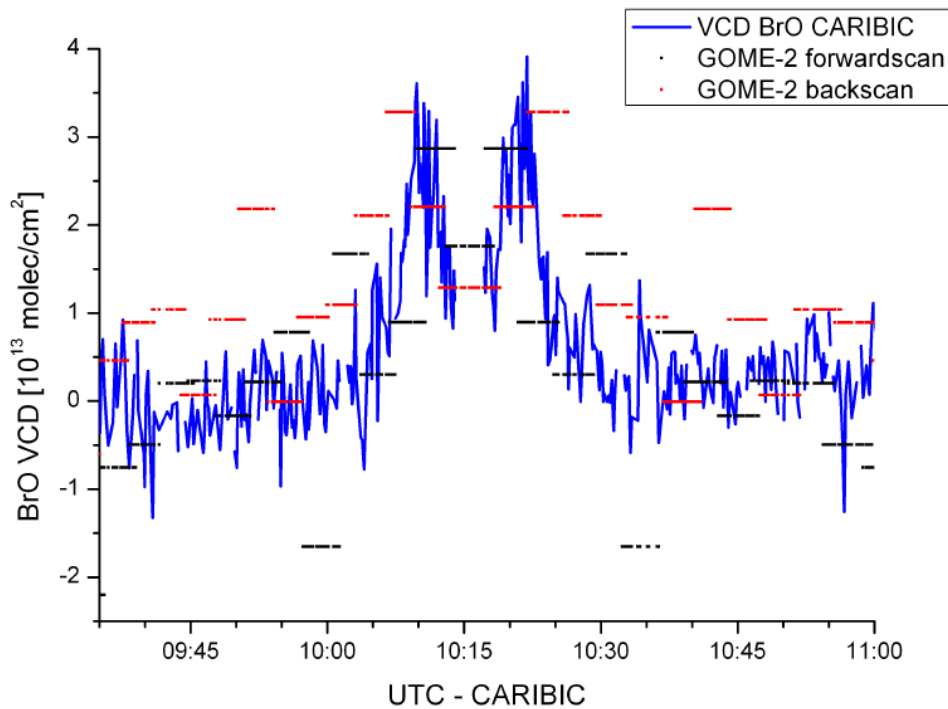


**Figure 9.19.:** Comparison of CARIBIC and GOME-2 BrO measurements. Adapted from Heue et al. (2011).

However, the GOME-2 VCDs for both the forward- and backscans pixels need to be interpreted as mean values for much larger areas than the CARIBIC measurements had covered. The better agreement between backscan measurements and the airborne data has therefore to be assigned as coincidence. In general, the GOME-2 measurements (as well as measurements from other satellite instruments) usually yield smaller tracegas column densities for local enhanced concentrations, because also areas with lower concentrations are probed at the same time.

For the BrO measurements, both datasets are again in good agreement, despite the fact that the BrO VCDs from the GOME-2 measurements were only slightly higher than the detection limit as indicated in Figure 9.15 c. Figure 9.19 shows the direct comparison of both datasets analogous to the SO<sub>2</sub> comparison in Figure 9.18 a. The maximum VCDs are very well captured by GOME-2, but in contrast to SO<sub>2</sub>, the forwardscan pixels seem to agree best with CARIBIC measurements this time, especially outside the plume. As the location of the SO<sub>2</sub> and BrO maxima agreed in the CARIBIC measurements and the GOME-2 data indicated a weak linear relationship between both species during the eruption (cf. Figure 9.15 e respectively Table 9.4), the BrO/SO<sub>2</sub> ratios have been calculated for the CARIBIC measurements inside the plume (i.e. the second intersection). The ratio was  $(1.32 \pm 0.16 \times 10^{-4}; r^2=0.57)$  for the first and  $(1.18 \pm 0.09 \times 10^{-4}; r^2=0.78)$  for the second intersection of the plume. For the GOME-2 measurements, a linear fit for the satellite pixels that were probed by CARIBIC led only to a poor correlation coefficient of  $r^2=0.16$  and a BrO/SO<sub>2</sub> ratio of  $(1.3 \pm 0.6 \times 10^{-4})$ . However, as most of the satellite measurements in the regarded area were close to the detection limit, the measurements might be not well suited for such a comparison. The linear fit of all satellite plume pixels for that day showed a larger ratio of  $3.1 \pm \times 10^{-4}$  and an  $r^2$  of 0.32, but these should be interpreted as mean values that were especially influenced by larger SO<sub>2</sub> and BrO VCDs in close proximity to the volcano (cf. Figure 9.15 e).

## 10. BrO from a quiescent degassing volcano (Ambrym)

The systematic investigation of volcanic plumes in Chapter 9 revealed that volcanic BrO can be regularly detected during minor and major eruptions by the GOME-2 instrument. These findings can improve our knowledge on halogen chemistry inside large volcanic plumes and the potential of such emissions to affect atmospheric chemistry on local and global scales during major eruptions.

Two weak plumes from the Ambrym volcano (Vanuatu) were found to show evidence for a BrO enhancement during a very strong quiescent degassing phase in Section 9.4 and a linear relationship between the SO<sub>2</sub> and BrO SCDs\* (cf. Figure 9.13 and Table 9.3) showed up. However, the resulting BrO SCDs\* were close to the detection limit.

In general, even if a relative high BrO/SO<sub>2</sub> ratio of some 10<sup>-4</sup> might be present in a volcanic plume during quiescent degassing, the corresponding BrO SCDs will not be visible to the satellite instrument from daily measurements, because they are below the detection limit. The SO<sub>2</sub> VCDs for such events are typically smaller than the threshold of 5×10<sup>16</sup> that was applied for the volcanic detection algorithm in Chapter 8). Therefore, ground-based DOAS instruments close to a volcano are usually best suited for long-term measurements of BrO and SO<sub>2</sub> and the investigation of the bromine chemistry in the initial phase after the plume's release.

In this chapter the potential of GOME-2 to detect BrO at passive degassing volcanoes from averaged data will be investigated. The analysis will be restricted to the Ambrym volcano (Vanuatu), as it showed strong SO<sub>2</sub> degassing throughout the whole time period of the analysed GOME-2 dataset from 2007–2011.

### 10.1. Previous BrO studies at Ambrym

The volcanic emissions of Ambrym have been already investigated in recent years by airborne and satellite measurements. Bani et al. (2009) reported the first measurements of SO<sub>2</sub> and BrO emission rates for Ambrym from airborne measurements in 2005 and 2007. Both species were detected within distances of 4–40 km away from the Marum and Benbow craters, yielding extraordinary SO<sub>2</sub> emission rates within a range of 180–270 kg s<sup>-1</sup> and BrO fluxes of 62–113 g s<sup>-1</sup> in January 2005. From these findings, a mean BrO/SO<sub>2</sub> ratio of ~3×10<sup>-4</sup> had been determined. After even higher fluxes for SO<sub>2</sub> (382 kg s<sup>-1</sup>), but significantly smaller ones for BrO (8 g s<sup>-1</sup>) in March 2005, the total emissions were found to be at a much lower level of 39–59 kg s<sup>-1</sup> respectively 34–41 g s<sup>-1</sup> in August 2007, illustrating the high variability of the BrO/SO<sub>2</sub> ratios (0.1–7×10<sup>-4</sup>). Nevertheless, the BrO fluxes in January 2005 were

## 10. BrO from a quiescent degassing volcano (Ambrym)

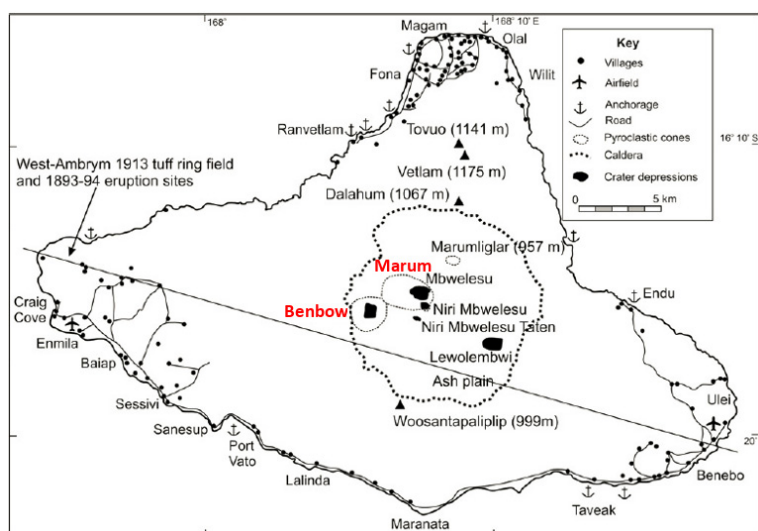


**Figure 10.1.:** Map of the regional settings and topography for the Ambrym volcano. The triangle shaped volcanic island is rather flat (peak altitude  $\sim 1334$  m) and hosts a 12 km wide summit caldera with the two main active craters Marum and Benbow. During recent years, a lava lake has been present for most of the time in Benbow.

about 5–8 times greater than those observed by Bobrowski et al. (2003) at Soufrière Hills or Oppenheimer et al. (2006) at Mt. Etna. This makes Ambrym one of the largest known emitters for both volcanic species worldwide.

A first preliminary report on the satellite observation of BrO from Ambrym with the OMI instrument was presented by Kurosu et al. (2006) during a scientific conference, but was never published in a peer-review journal.

### 10.2. Straight forward averaged $\text{SO}_2$ and BrO over Vanuatu

In order to investigate the potential of GOME-2 to detect BrO from degassing volcanoes, the satellite data in the vicinity of Ambrym were first simply projected on a grid at a spatial resolution of  $0.1^\circ \times 0.1^\circ$  (cf. Chapter 6) without either correcting the  $\text{SO}_2$  signal for the spectral interference with  $\text{O}_3$  nor the BrO signal for the contribution of stratospheric BrO.

In Figure 10.2, the resulting mean  $\text{SO}_2$  and BrO VCDs are shown for 2010. The mean  $\text{SO}_2$  plume (Figure 10.2, left) can be clearly identified, centered over the volcanic island. Please note that the island itself is not visible in the maps due to the coarse resolution of the coast lines, but is quite accurately located at the centre of the mean  $\text{SO}_2$  plume. In contrast, the averaged BrO data show a strong latitudinal dependent signal, caused by the predominating stratospheric BrO (cf. also Figure 6.16). Nevertheless, a slightly enhanced BrO signal can already be seen at the location of the  $\text{SO}_2$  maximum, but almost at the same magnitude as the stratospheric background further south.

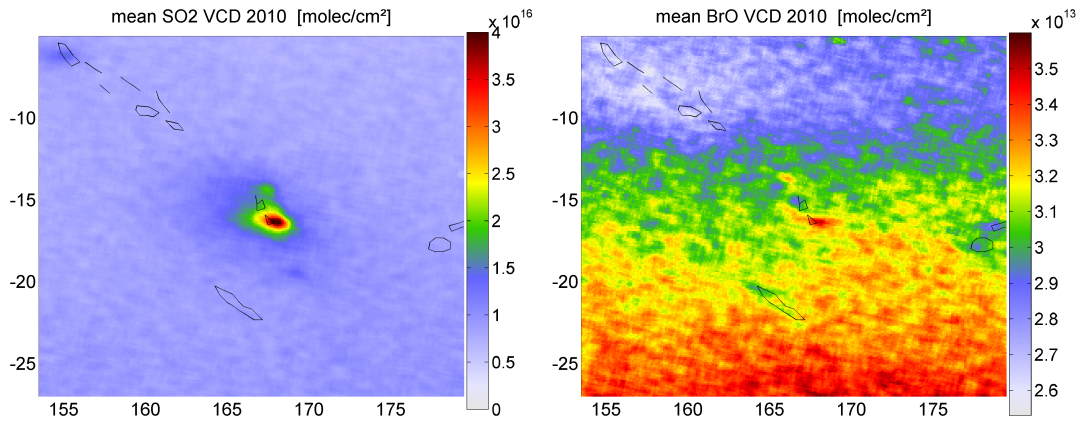


**Figure 10.2.:** Mean  $\text{SO}_2$  and BrO VCDs (geo.) over Vanuatu as seen from GOME-2 in 2010 without correcting for the non-volcanic background. While the location of the volcano is clearly visible by strongly enhanced  $\text{SO}_2$  VCDs (left), the mean BrO distribution is dominated by the stratospherical signal (right). Nevertheless, slightly enhanced values can be noticed at the same area as the maximum  $\text{SO}_2$  columns appears. Please note that the BrO colorbar was scaled to provide maximum contrast.

### 10.3. Background corrected annual mean maps

In order to correct for non-volcanic  $\text{SO}_2$  and especially the stratospheric BrO background, the data was treated in a similar way as for the volcanic  $\text{SO}_2$  plume extraction algorithm (cf. Section 8.4) and the inherent study on BrO from daily events (cf. Section 9.2). The daily satellite data in a preselected area around the volcano ( $150\text{--}180^\circ \text{ E}$ ,  $0\text{--}35^\circ \text{ S}$ ) was fitted by a 2D-polynomial of 3rd respectively 4th degree for both species.

In case of the  $\text{SO}_2$  measurements, all satellite pixels that showed a  $\text{SO}_2$  VCD  $> 2\sigma$  were excluded for the fit to prevent the influence of probable high  $\text{SO}_2$  VCDs during days with strong enhanced volcanic activity. For BrO, however, no satellite measurements had been excluded from the polynomial fit. Furthermore, there had been no attempts to prevent a possible influence of clouds on the VCDs, but the operational GOME-2 cloud fraction data (Fast Retrieval Scheme for Cloud Observables - FRESCO - more details in Wang and van der A, 2011) were additionally gridded for the according years.

The yearly averaged  $\text{SO}_2$  and BrO VCD maps for Ambrym are presented in Figures 10.3–10.5. Additionally, maps of the mean cloud fractions are shown. Please note, that the colorbars for  $\text{SO}_2$  and BrO have been scaled to the maximum values within the 5 years period, i.e. all  $\text{SO}_2$  maps were scaled to the maximum mean  $\text{SO}_2$  VCD of  $3.1 \times 10^{16}$  in 2011, while the BrO maps were scaled to the maximum mean BrO VCD of  $2.9 \times 10^{12}$  in 2010. As the mean cloud fraction showed no significant variation (except for 2011), the associated maps were all scaled to 0.55.

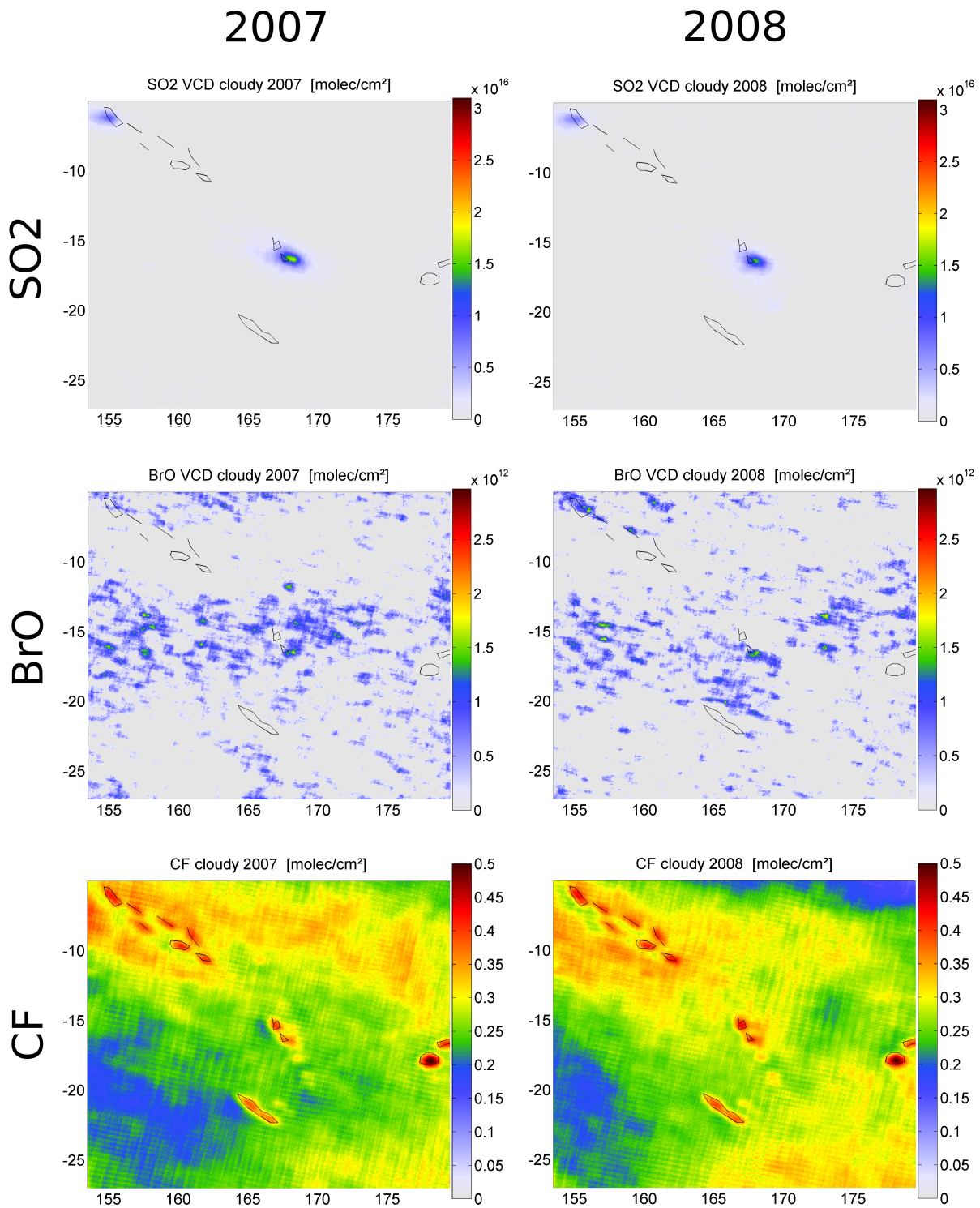


**Figure 10.3.:** GOME-2 mean maps for the SO<sub>2</sub> and BrO VCDs (geo.) as well as the cloud fraction (CF) over Vanuatu in 2007–2008. Both SO<sub>2</sub> and BrO have been corrected for a non-volcanic signal. While a relative weak SO<sub>2</sub> plume shows up at the location of the volcano (upper row), the mean BrO maps shows only a large scatter of the data (mid row). The mean CFs for both years appear similar with increased values over the islands due to convection and/or orographic effects (bottom row).

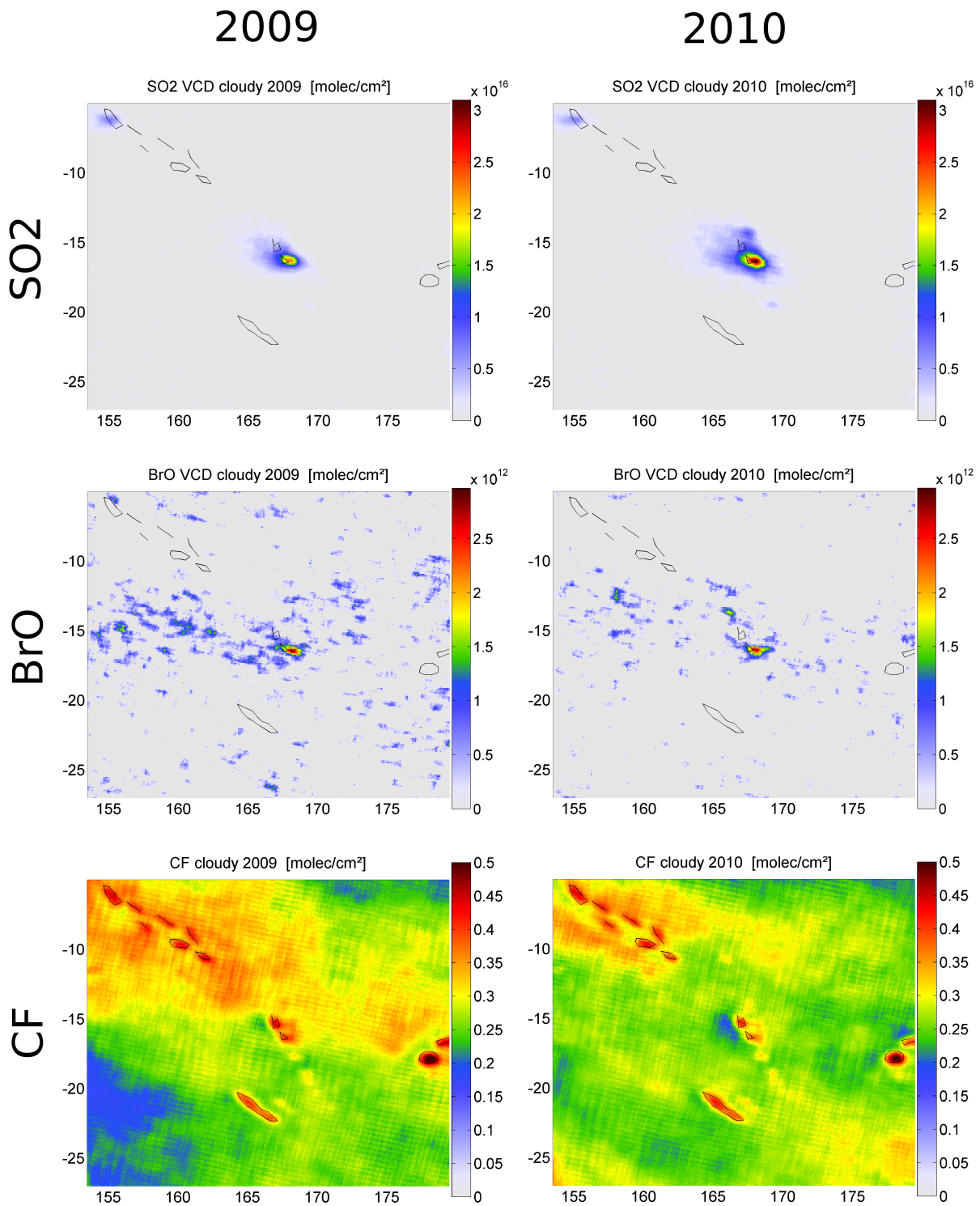


**Figure 10.4.:** GOME-2 mean maps for the  $\text{SO}_2$  and BrO VCDs (geo.) as well as CFs over Vanuatu in 2009–2010. With increasing  $\text{SO}_2$  VCDs (upper row), also clearly enhanced BrO VCDs can be identified in the vicinity of the  $\text{SO}_2$  plume (mid row). The mean CF (bottom row) is similar to previous years (cf. Figure 10.3).

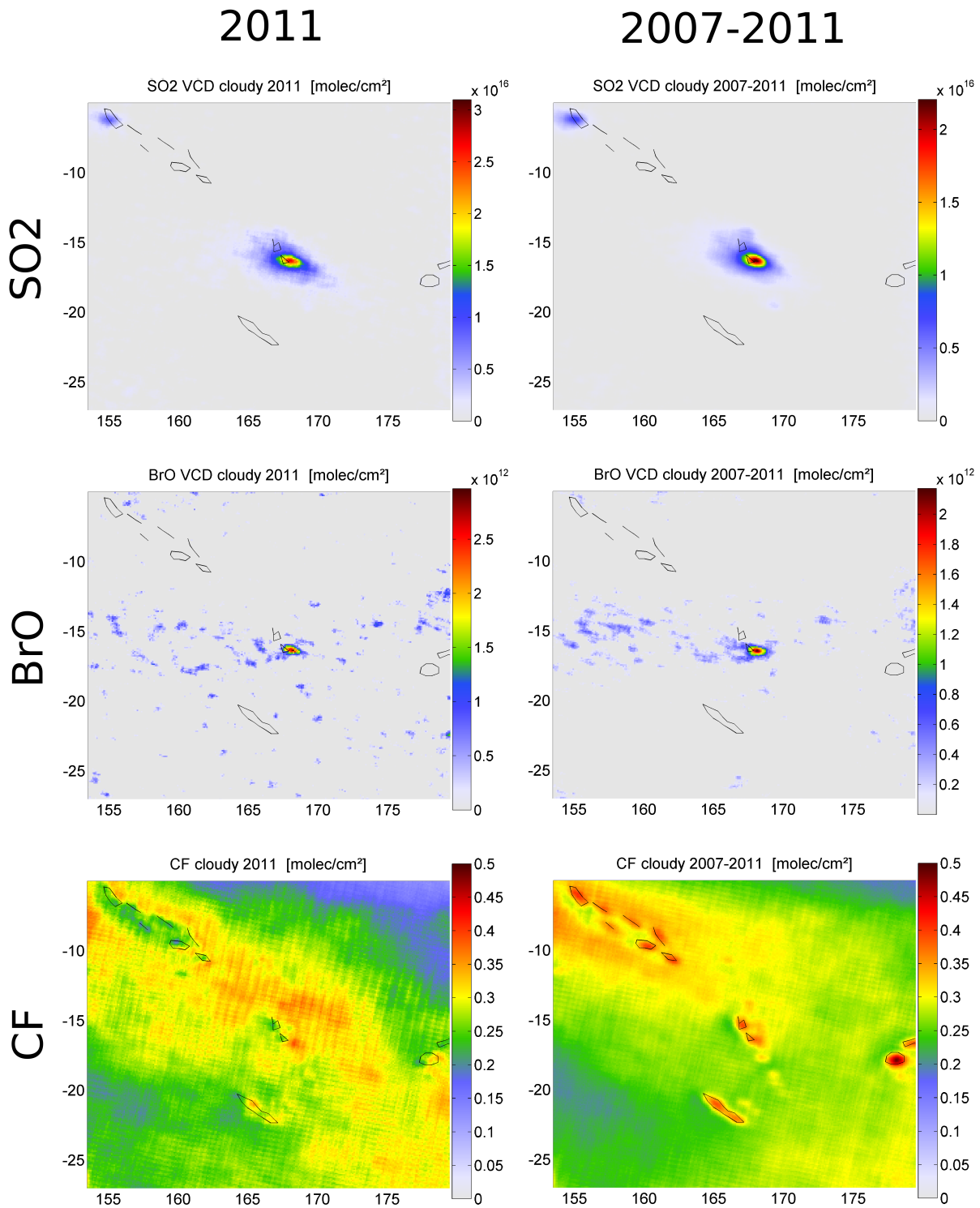


**Figure 10.5.:** GOME-2 mean maps for SO<sub>2</sub> and BrO VCDs (geo.) as well as the CFs over Vanuatu in 2011 and for the whole investigated time period 2007–2011. Both, the maps for 2011 and the mean maps for all five years yield a clear spatial correlation between enhanced SO<sub>2</sub> and BrO VCDs at the location of the volcano. For 2011, the CF distribution appears different from former years, probably caused by an extensive La Niña event during the year.

While the  $\text{SO}_2$  plume showed up during all years, the mean  $\text{SO}_2$  VCDs increased significantly after 2008 before they slightly decreased for 2011 (Figures 10.3–10.5, top row). At the same time, the mean BrO VCDs at the volcano showed a similar behaviour, although the maximum BrO VCDs were registered in 2010 (Figures 10.3–10.5, mid row). During the weaker  $\text{SO}_2$  emissions in 2007/2008, only a very weak BrO signal is noticeable in the corresponding maps at the location of the  $\text{SO}_2$  plume, even though the remaining signal in the background is of comparable magnitude. After 2008, enhanced BrO VCDs are much clearer visible and found in the same area as the largest  $\text{SO}_2$  VCDs. This behaviour illustrates that even for constantly high BrO/ $\text{SO}_2$  ratios, the BrO plume will only show up if the volcano’s activity provides emissions that are large enough to exceed the BrO detection limit. The increased non-volcanic BrO scatter in 2007–2009 compared to 2010–2011 is probably caused by a spurious slant column viewing angle dependency in the satellite data (Theys et al., 2011). An estimate of the detection limit can be retrieved from the  $2\sigma$  value in a reference area outside the plume and was found at  $\sim 1 \times 10^{15}$  respectively  $\sim 1.1 \times 10^{12}$  molec/cm<sup>2</sup> for  $\text{SO}_2$  and BrO during all years.

While the maximum mean cloud fractions (CF) showed up over the surrounding islands due to convection and/or orographical effects for 2007–2010, the distribution appears somewhat different in 2011, with overall lower values for the entire area. The main reason for this behaviour, however, remains unclear at this time. Possibly, the differences can be explained by the influence of a very strong La Niña episode in 2011 that was one of the strongest in the past 60 years according to the World Meteorological Organization (World Meteorological Organization, 2012).

In order to rule out a possible influence of clouds on the findings, the GOME-2 data was additionally analyzed after all daily satellite pixels with a cloud fraction of more than 30% were sorted out. Apart from some minor differences for individual

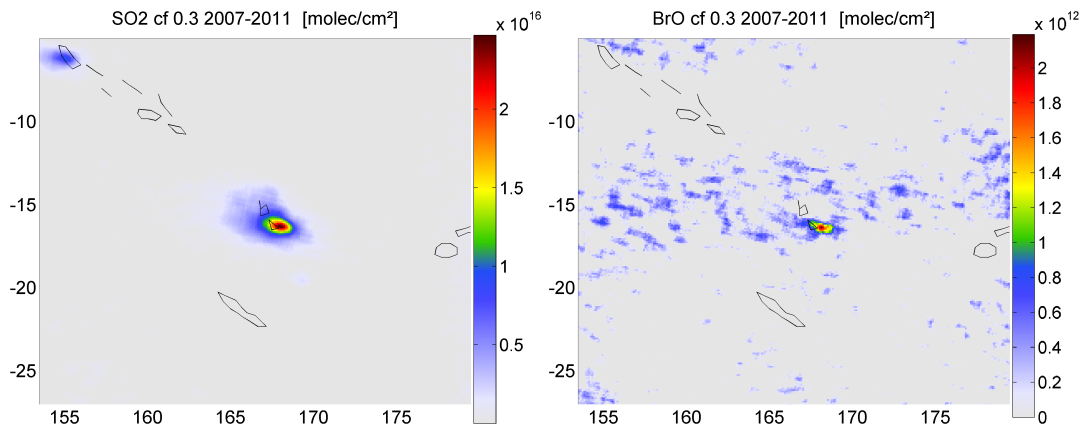


**Figure 10.6.:** Mean  $\text{SO}_2$  and BrO VCDs during 2007–2011 for all GOME-2 pixels that showed a effective cloud fraction  $< 0.3$  from the daily measurements. Although the BrO maps reveals a larger scatter, the findings are essentially the same as for the inclusion of all GOME-2 pixels (cf. Figure 10.5, right column).

## 10. BrO from a quiescent degassing volcano (Ambrym)

years, the resulting SO<sub>2</sub> and BrO enhancements for 2007–2011 revealed no significant discrepancies (Figure 10.6). While the maximum SO<sub>2</sub> and BrO VCDs were found at SO<sub>2</sub> VCD<sub>max</sub>= $2.47 \times 10^{16}$  molec/cm<sup>2</sup> ( $2.2 \times 10^{16}$  for cloudy conditions) and BrO VCD<sub>max</sub>= $2.19 \times 10^{12}$  molec/cm<sup>2</sup> ( $2.17 \times 10^{12}$ ), they are even slightly larger than without the cloudy pixel filter (cf. Figure 10.5). This might be explained by the exclusion of daily measurements, where clouds at higher altitudes had shielded the emissions from observation. The scattered background BrO signal was, however, found to be slightly larger than by taking all daily measurements into account, probably as a result of poorer statistics. A closer look on the distribution of the enhanced BrO VCDs

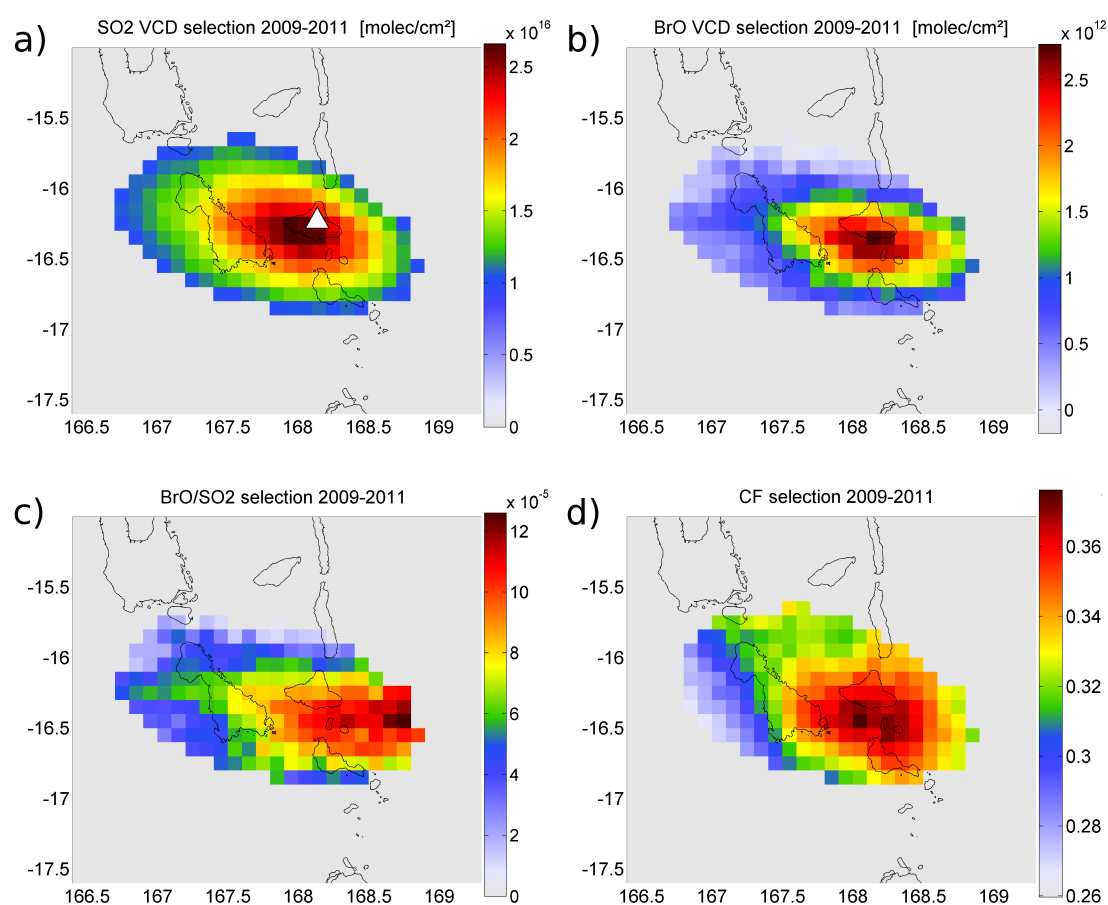


**Figure 10.7.:** Maps of the mean SO<sub>2</sub> and BrO VCDs, corresponding BrO/SO<sub>2</sub> ratios and mean CF for the time period 2009–2011 for all gridpixels that showed a SO<sub>2</sub> VCD  $> 1 \times 10^{16}$ . While the SO<sub>2</sub> plume (a) extends slightly more towards the north-west of the volcano (indicated by the white triangle), the BrO VCDs (b) are found to be almost symmetrical in longitude around the volcano. This leads to larger BrO/SO<sub>2</sub> ratios in the eastern part of the plume, while low ratios are found in the west (c). The effect partly correlates with the mean CFs (d).

during the years 2009–2011 reveals that the plume is only visible close to the volcano, while the enhanced SO<sub>2</sub> VCDs can still be identified further away in western direction. In order to illustrate this effect, the data for SO<sub>2</sub>, BrO and CFs are in the following restricted to those grid pixels that showed at least a mean SO<sub>2</sub> VCD of  $1 \times 10^{16}$  molec/cm<sup>2</sup>.

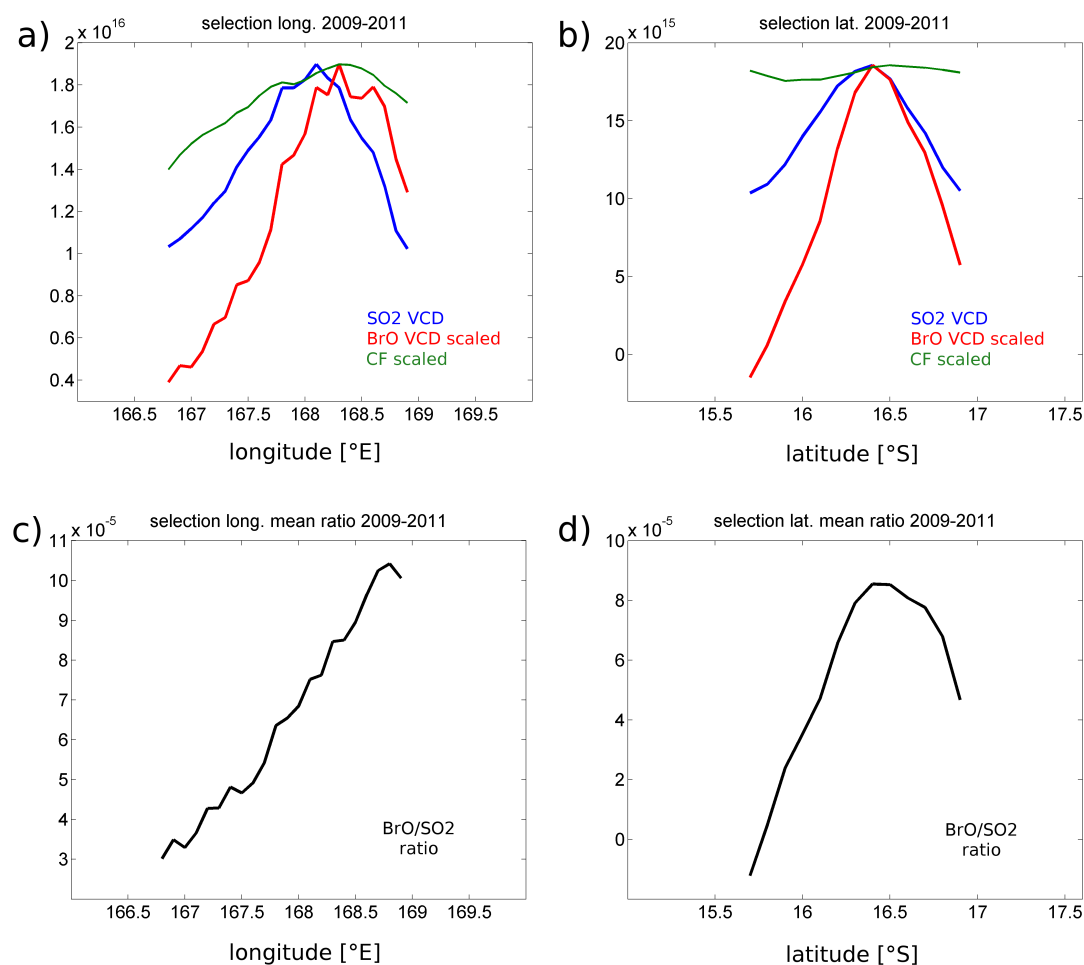
In Figure 10.7, the corresponding average maps for all three data products as well as for the BrO/SO<sub>2</sub> ratios are shown. The restriction of the SO<sub>2</sub> VCDs yields an oval-shaped SO<sub>2</sub> distribution with the maximum next to the volcano (Figure 10.7 a), while the plume is slightly more extended towards the north-west because of the prevailing south-eastern tradewinds. For BrO, the maximum VCDs are found close to the volcano as well (Figure 10.7 b), but the longitudinal extent appears more symmetrical. No enhanced BrO columns are found at the western SO<sub>2</sub> plume area ( $2\sigma \sim 8.1 \times 10^{11}$  molec/cm<sup>2</sup>). This can be additionally seen from the distribution of the BrO/SO<sub>2</sub> ratios (Figure 10.7 c). The largest ratios are found in the eastern part of the SO<sub>2</sub> plume, while they decrease towards the west due to a faster decrease of the BrO VCDs compared to the SO<sub>2</sub> VCDs. Figure 10.7 d shows that this effect seems to be partly correlated to the distribution of the mean CFs, although some of the largest CFs can be found in the south-eastern edge of the plume, where no significantly enhanced BrO VCDs are found.

Figure 10.8 finally shows the same data as for Figure 10.7, this time for the mean values integrated in long- and latitudinal direction (i.e. the mean values for each grid row respectively column had been calculated). To make the different quantities comparable, the maximum BrO VCD and CF have been scaled to the maximum SO<sub>2</sub> VCD. The different location of the maximum SO<sub>2</sub> and BrO VCDs can be seen from both longitudinal and latitudinal means (Figure 10.7 a and b), although the shift in longitude is much more prominent. Interestingly, the longitude of the maximum mean CF fits the location of the maximum BrO, while the mean CFs show no clear dependence on latitude at all. Like it has been suggested from Figure 10.7 c, the longitudinal mean BrO/SO<sub>2</sub> ratios increase continuously from  $3 \times 10^{-5}$  to about  $1 \times 10^{-4}$  towards the eastern part of the plume selection (Figure 10.7 c). The maximum latitudinal mean of  $8.5 \times 10^{-5}$  is, however, found for the latitude of the maximum mean SO<sub>2</sub> and BrO VCDs (Figure 10.7 d).

## 10.4. Mean BrO/SO<sub>2</sub> ratio for Ambrym 2007–2011

In order to calculate a representative BrO/SO<sub>2</sub> ratio for the time period of 2007–2011, the daily GOME-2 measurements from a small area around the volcano (167.5–169° E, 15.7–17° S) as well as outside the volcanic plume (175–176.5° E, 15.7–17° S) had been extracted from the satellite data. In total, 8843 individual measurements inside the plume area and a similar number of 8696 measurements in the reference area were found. Figure 10.9 shows the resulting SO<sub>2</sub> and BrO VCD distributions for both investigated areas. For the upper panel in Figure 10.9, the SO<sub>2</sub> VCDs from the reference area are found to be scattered around zero as expected (blue marked histogram bars). The SO<sub>2</sub> VCDs from the area covering the volcano (red marked

## 10. BrO from a quiescent degassing volcano (Ambrym)



**Figure 10.8.:** Lat-/longitudinal integrated mean SO<sub>2</sub> VCDs, BrO VCDs and CFs for the same data as in Figure 10.7, as well as the associated BrO/SO<sub>2</sub> ratios. The different locations of the maximum SO<sub>2</sub> and BrO VCDs can be seen clearly in latitudinal (a) and longitudinal (b) direction, while the location of the maximum CFs corresponds to that of BrO for the longitudinal mean. The resulting BrO/SO<sub>2</sub> ratios increase continuously from  $3 \times 10^{-5}$  to about  $1 \times 10^{-4}$  in longitudinal direction (c), while a ratio of  $8.5 \times 10^{-5}$  is found at the location of the maximum BrO and SO<sub>2</sub> VCDs in latitudinal direction (d).

bars) positively differ from normal and therefore clearly indicate the presence of the SO<sub>2</sub> plume. This is also pointed out by the mean value for the SO<sub>2</sub> VCDs inside the plume area ( $\mu_{\text{SO}_2, \text{in}} = 1.24 \times 10^{16}$  molec/cm<sup>2</sup>) and close to zero for the reference area with  $\mu_{\text{SO}_2, \text{out}} = -4.03 \times 10^{14}$  molec/cm<sup>2</sup>. For the BrO measurements (lower panel in Figure 10.9), again a random distribution around zero is found for the measurement from the area outside the SO<sub>2</sub> plume (blue marked histogram bars). While the distribution inside the plume area reveals no obvious deviation from the normal distribution outside the plume (not shown in Figure 10.9), a restriction to all measurements, where

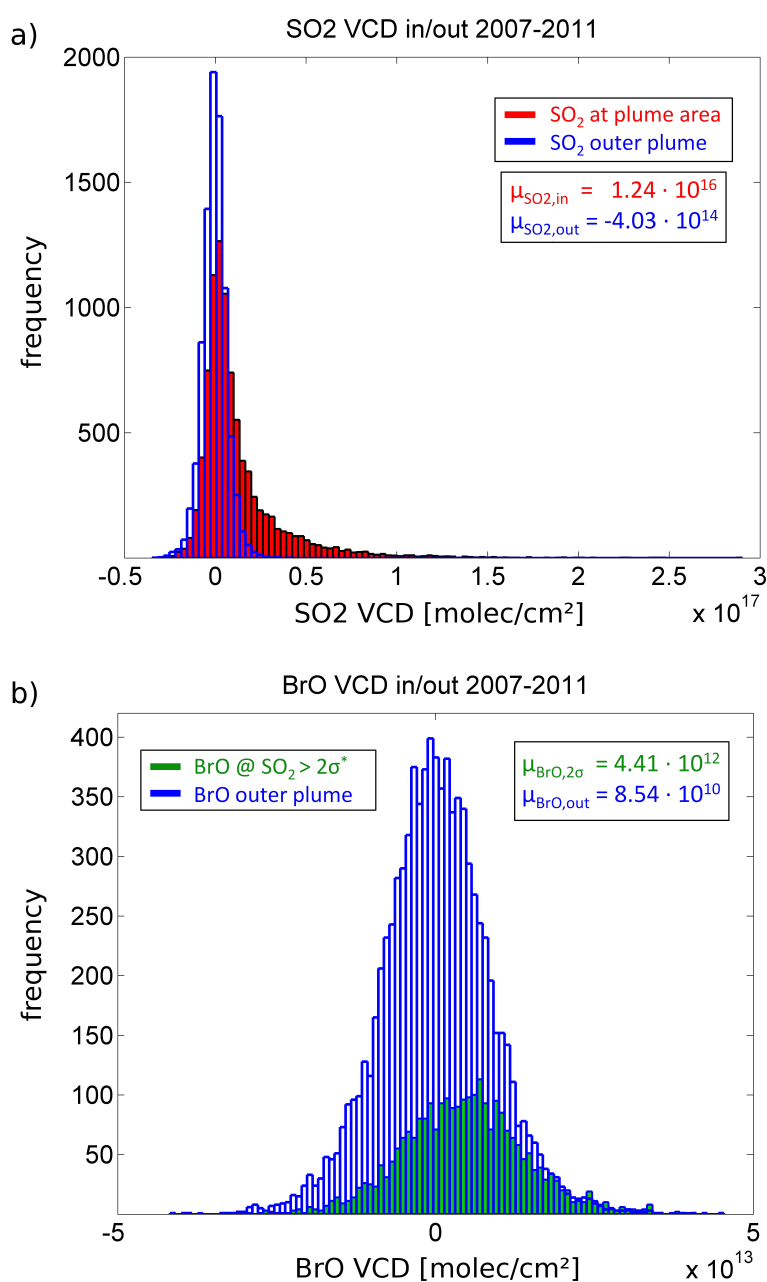


**Figure 10.9.:** Daily GOME-2 SO<sub>2</sub> and BrO VCDs 2007-2011 for preselected areas in- and outside the volcanic plume from Ambrym. The SO<sub>2</sub> distribution (a) inside the plume (red marked bars) differs positively from the normal distributed values for the reference area (blue marked bars), indicating the presence of the volcanic emissions (mean values  $\mu_{SO_2,in} = 1.24 \times 10^{16}$  and  $\mu_{SO_2,out} = -4.03 \times 10^{14}$  molec/cm<sup>2</sup>). A restriction to the BrO measurements (b) inside the plume area that showed a SO<sub>2</sub> VCD of more than  $2\sigma^*$  of the reference area at the same time (green marked bars) leads to a positive shifted maximum in comparison to the VCDs from the reference area (blue marked bars) with mean values  $\mu_{BrO,2\sigma} = 4.41 \times 10^{12}$  and  $\mu_{BrO,out} = 8.54 \times 10^{10}$  molec/cm<sup>2</sup>.

## 10. BrO from a quiescent degassing volcano (Ambrym)

the  $\text{SO}_2$  VCD exceeded  $2\sigma$  of the VCDs from the reference area ( $\sigma^* = 1.33 \times 10^{16}$  molec/cm<sup>2</sup>) leads to a positive shifted maximum of the BrO VCDs (green marked bars). The mean value for the plume pixel selection is therefore found at  $\mu_{\text{BrO}, 2\sigma} = 4.41 \times 10^{12}$  molec/cm<sup>2</sup>, while again a mean VCD close to zero is found for the reference area measurements with  $\mu_{\text{BrO}, \text{out}} = 8.54 \times 10^{10}$  molec/cm<sup>2</sup>.

From the mean values for the plume pixel selection ( $\text{SO}_2 > 2\sigma^*$ ), a BrO/ $\text{SO}_2$  ratio of  $1.15 \times 10^{-4}$  can be calculated. However, this ratio is probably still strongly influenced by daily satellite measurements, where very low BrO amounts or even no BrO was present at the volcano. This is also supported by the close to normal BrO VCD distribution. The same result can be derived from a linear fit for all measurements. Figure 10.10 shows the associated correlation plot and fit results. While the strong scatter in the BrO data is clearly visible, the fit yields a BrO/ $\text{SO}_2$  ratio of  $\sim 1.1 \times 10^{-4}$ , just like for the averaged distribution in Figure 10.9.

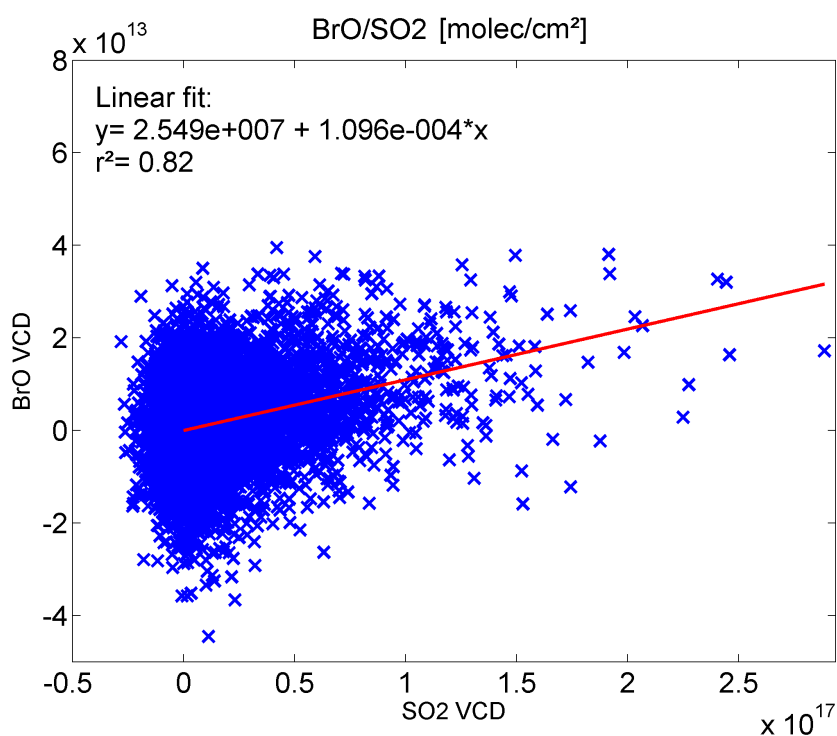


**Figure 10.10.:** BrO/ $\text{SO}_2$  correlation plot for the GOME-2 measurements with  $\text{SO}_2$  VCD  $> 2\sigma^*$  in the vicinity of Ambrym 2007–2011. From the linear fit for all measurements, a positive correlation ( $r^2 = 0.82$ ) and a mean BrO/ $\text{SO}_2$  ratio of  $1.1 \times 10^{-4}$  is found, but the large scatter for the BrO VCDs dominate the plot.

## 10.5. Discussion on volcanic BrO at Ambrym

The yearly averaged GOME-2 data at the Ambrym volcano revealed a clear enhancement of BrO in close correlation to the SO<sub>2</sub> plume for at least three out of five years of the measurements. This illustrates that the observation of volcanic BrO by satellite instruments is not generally limited to major eruption events (cf. Chapter 9), but also suited for long-term measurements at strong passively degassing volcanoes. To the author's knowledge, the findings for Ambrym are the first measurements of BrO at a degassing volcano from space at all (except the preliminary findings by Kurosu et al. (2006)). The data has the potential to improve the estimates of the total BrO release to the atmosphere from volcanic emissions. By including detailed radiative transfer calculations in the future, more representative total SO<sub>2</sub> and BrO budgets for Ambrym can be calculated.

The Ambrym study shows that the BrO enhancement at the volcano is about one order of magnitude lower than the predominating stratospheric background signal. The application of a 2-dimensional polynomial fit to correct for stratospheric BrO is a rather easy technique and might be also applied to other volcanoes. From the globally averaged GOME-2 SO<sub>2</sub> map for 2007/2008 (cf. Figure 6.4 in Section 6.2.2) several other prominent degassing volcanoes can be clearly detected by GOME-2, e.g. Nevado del Huila (Colombia), Popocatepetl (Mexico) or Nyiragongo/Nyamuragira (DR Congo). However, the Ambrym case study has been probably only possible, because of the unique circumstances that the volcano provides for satellite measurements.

While the mean SO<sub>2</sub> emissions from other volcanoes are similar to those from Ambrym, the retrieval of volcanic BrO can be difficult due to certain reasons:

1. The total amount of bromine species (and therefore detectable BrO/SO<sub>2</sub> ratios) from volcanic emissions may vary strongly for individual volcanoes as well as a volcano's state of activity. While ground-based measurements at different volcanoes worldwide showed BrO/SO<sub>2</sub> ratios from  $1 \times 10^{-5}$  to  $8.2 \times 10^{-4}$  (cf. Section 2.3.1), no clear evidence for significant amounts of BrO was for example found during the extensive degassing phase of Kilauea (Hawaii) in 2008 (Kern, 2009; Salerno et al., 2010; Kern, 2010). Even during major volcanic eruptions with very high SO<sub>2</sub> concentrations, BrO is often not detected, as it was pointed out in Chapter 9.
2. Generally, the emissions from a degassing volcano need to be of a certain amount and regularity to be detected from long-termed averaged data. As the sensitivity of spaceborne instruments usually decreases towards to the ground, low emissions from quiescent degassing volcanoes are even more difficult to detect than during eruptions. Being one of the world strongest known SO<sub>2</sub> degassing volcano with a significant deposit of bromine species (Bani et al., 2009), Ambrym is eminently suited for the BrO retrieval from continuous satellite observations.
3. Volcanoes are usually part of extended mountain ranges, which are strongly affected by the presence of orographic clouds. Furthermore, significant cloud

## 10. BrO from a quiescent degassing volcano (Ambrym)

---

amounts occur over extended land areas because of convection. These clouds may often shield the volcanic plume from the satellite instrument. Therefore more individual measurements at (near-) cloud-free conditions are needed to guarantee sufficient statistics in order to make the weak BrO signal visible. As Ambrym is an isolated, small and low elevated volcanic island, the influence of clouds to the satellite measurements are probably lower compared to volcanoes in mountain ranges (e.g. the volcanoes of the Andes).

4. The DOAS retrieval depends strongly on the correction of the Ring effect (cf. Section 4.4), in particular for very weak absorbers like BrO. Over mountain chains respectively elevated areas in general, the Ring effect is less strong due to a reduced probability for Raman scattering events. Additionally, the filling-in of the Fraunhofer lines is influenced by clouds, depending on the cloud top height (CTH) as well as the cloud optical thickness (COT) (Beek et al., 2001). This may lead to an inaccurate correction of the Ring effect and therefore also to an insufficient BrO retrieval.

Since regular ground-based measurements are still coupled to huge organizational efforts, future satellite instruments with an improved spatial, temporal and spectral resolution will allow a more detailed and regular monitoring of volcanic bromine emissions. Furthermore, the detailed analysis of existing datasets from other satellite instruments (e.g. OMI and SCIAMACHY) will help to increase the statistics for the emissions of Ambrym and other degassing volcanoes.

**Part IV.**

## **Conclusions and Outlook**



# 11. Conclusions

In this thesis, volcanic emissions have been investigated by the analysis of spaceborne measurements obtained from the second Global Ozone Monitoring Experiment instrument (GOME-2). The column densities of sulfur dioxide ( $\text{SO}_2$ ) and bromine monoxide (BrO) were derived by the application of the well established Differential Optical Absorption Spectroscopy (DOAS) that is capable to detect tracegases in the atmosphere by their unique narrow-band absorption features.

While ground-based optical measurement techniques have been applied for regular monitoring of volcanic emissions since the 1970s, the ability of satellite instruments to detect volcanic emissions has been continuously improved in recent years. The observation of the atmosphere by satellite instruments nowadays provides us a more comprehensive view of volcanic emissions on a global scale, especially during minor and major eruptions. In the following the main achievements of this thesis are summarized.

## **$\text{SO}_2$ retrieval during major volcanic eruptions**

Commonly applied  $\text{SO}_2$  DOAS retrievals suffer from non-linearity effects, which may appear if extraordinary high  $\text{SO}_2$  concentrations are present, like it is often the case for major volcanic eruptions. In such cases, the observed scattered light has often only penetrated the outermost layers of a  $\text{SO}_2$  plume and the sensitivity for the whole plume can become essentially zero. Light at wavelengths where the  $\text{SO}_2$  absorption cross-section is strongest is almost completely absorbed. As a result, the  $\text{SO}_2$  slant column densities (SCDs) for such volcanic plumes are strongly underestimated by the DOAS fit.

While previous attempts have been made to correct for these effects by applying iterative model approaches to measured spectra, the necessary calculations are rather time intensive. Therefore, alternative  $\text{SO}_2$  DOAS evaluation wavelength ranges have been investigated within the scope of this thesis that are capable to retrieve accurate  $\text{SO}_2$  SCDs also during volcanic eruptions. As the commonly used evaluation wavelength range still provides the highest sensitivity to lower  $\text{SO}_2$  concentrations, a new  $\text{SO}_2$  product has been developed that combines the advantages of analyses using different wavelength ranges.

The novel approach is a sufficient and fast method to correct for the occurring non-linear effects. It is in particular well-suited to make the near-real time evaluation of  $\text{SO}_2$  possible for future satellite instruments with improved spatial and temporal resolution, which at the same time will increase the total amount of data that has to be processed.

### Systematic detection of volcanic plumes

SO<sub>2</sub> is the third most abundant gaseous species that is emitted by volcanoes and relatively easy to detect due to its strong absorption features in the UV. Therefore, it is also the most regular monitored volcanic species in spectroscopical ground-based and spaceborne applications. Consequently, in this thesis, SO<sub>2</sub> has been used as a tracer for satellite measurements that were affected by volcanic emissions.

In order to identify volcanic plumes in the GOME-2 dataset, a new detection algorithm has been developed. The plume detection algorithm is able to extract volcanic SO<sub>2</sub> plumes automatically from the satellite measurements by conspicuous high SO<sub>2</sub> column densities exceeding a certain threshold. The algorithm subsequently investigates the affected areas for enhanced SO<sub>2</sub> VCD clusters.

From the application of the detection algorithm, a total number of 772 individual volcanic SO<sub>2</sub> plumes from 37 different volcanoes has been extracted from the GOME-2 dataset for January 2007 until the end of June in 2011. A detailed analysis of all plumes showed that the algorithm is capable to detect volcanic emissions from both, strong degassing and eruptive volcanoes. About one out of four plume events were caused by one of the major eruptions of Kasatochi, Redoubt and Sarychev (202) or strong phases of quiescent degassing from Ambrym (Vanuatu) and Kīlauea on Hawaii (197). Only Ambrym and the Tungurahua volcano (Ecuador) caused SO<sub>2</sub> plumes that were detected by the algorithm during the whole investigated time period. For Kīlauea, SO<sub>2</sub> plumes for all years except 2007 were found.

### Volcanic BrO during eruptions

Volcanic BrO was detected for the first time in the plume of Soufrière Hills (Montserrat) by Bobrowski et al. (2003). Since then, the species has been detected at several volcanoes worldwide by ground-based DOAS measurements. Commonly, SO<sub>2</sub> is used as a tracer for the plume and the BrO/SO<sub>2</sub> ratios are calculated in order to investigate bromine chemistry processes inside a plume.

A first attempt to detect volcanic BrO also from GOME and SCIAMACHY satellite measurements, however, failed (Afe et al., 2004). Only recently, volcanic BrO was detected for the first time from space by GOME-2 in the Kasatochi plume after the eruption in August 2008 (Theys et al., 2009).

In the scope of this thesis, the volcanic SO<sub>2</sub> plumes from the plume detection algorithm have been analyzed for an enhancement of BrO at the same time. As satellite measurements of the atmosphere are always affected by non-volcanic BrO in the stratosphere, the data had to be first corrected for this offset. The extracted SO<sub>2</sub> plumes from the automatical detection algorithm were again used as a tracer, but this time to identify measurements outside a volcanic plume in order to get a reference area for the non-volcanic offset correction.

The SO<sub>2</sub> and BrO column densities for all 772 volcanic plumes have been checked for a possible spatial correlation between the two species. Additionally, the mean

---

BrO/SO<sub>2</sub> ratios for the plumes were calculated by the application of a bivariate linear fit. In total, 64 volcanic plumes from 11–12 different volcanoes showed clear evidence for the formation of BrO after the plumes' release. For the volcanoes of Dalaffilla, Karymsky, Kizimen, Kliuchevskoi, Bezymianny, Nabro and Sarychev, these are the first reported measurements of BrO to the authors' knowledge and therefore raise the total number of volcanoes where BrO has been detected from 12 to 19.

Corresponding BrO/SO<sub>2</sub> ratios for all cases of enhanced BrO SCDs were found to be similar to worldwide ground-based measurements that usually investigate stable conditions at quiescent degassing volcanoes. Although the majority of the detected volcanic plumes originated from explosive eruptions, the BrO/SO<sub>2</sub> ratios were of the same order of magnitude, ranging from some 10<sup>-5</sup> to several 10<sup>-4</sup>. However, the majority of all investigated volcanic plumes (92%) showed no evidence for the abundance of BrO, even for eruptions with very high SO<sub>2</sub> SCDs like the ones of Merapi (Java) and Grímsvötn (Iceland). Here, the corresponding BrO/SO<sub>2</sub> ratios had been estimated to below 8×10<sup>-6</sup> and 2.5×10<sup>-6</sup>, respectively.

While some of the extracted volcanic plumes showed a good correlation of the SO<sub>2</sub> and BrO distribution patterns, others revealed only a similar enhancement of BrO in parts of the plume or even only a roughly similar spatial pattern. One explanation for this behaviour might be that not only the local composition of the volcanic plume (such as ash and/or other plume contents) has a crucial influence on the formation of BrO but that also the ambient meteorological conditions (e.g. temperature and relative humidity) play an important role.

### **BrO from a quiescent degassing volcano**

While the systematic investigation of volcanic SO<sub>2</sub> plumes revealed enhanced BrO column densities at the same time for several cases, nearly all of these volcanic plumes were caused by minor or major eruptions. For quiescent degassing volcanoes, only two weak plumes were found by the algorithm for Ambrym. Usually, satellite measurements for such cases are not able to detect enhanced BrO column densities on a daily basis, as the column densities are just too low to exceed the instrument's detection limit, even for very high BrO/SO<sub>2</sub> ratios ( $\gg 1 \times 10^{-4}$ ).

In the last part of this thesis, the ability of the GOME-2 measurements have been used in order to investigate the instruments ability to detect volcanic BrO from Ambrym by using yearly averaged data for 2007–2011 has been investigated. The daily BrO measurements were corrected for the stratospheric background in a similar way as for the eruptive events by the application of a simple 2-dimensional polynomial. This is a rather easy technique and might be also applied to other volcanoes.

A clear enhancement of BrO in close correlation to the SO<sub>2</sub> plume was found for at least three out of all five years (2009–2011). To the author's knowledge, the results for Ambrym are the first measurements of BrO at a quiescent degassing volcano from space at all. For 2007/2008, the volcanic emissions were probably too low to exceed the detection limit. From a linear fit to the daily SO<sub>2</sub> and BrO measurements in the

## 11. Conclusions

---

vicinity of the volcano, a mean BrO/SO<sub>2</sub> ratio of  $1.1 \times 10^{-4}$  was found for the entire time period 2007–2011.

The findings illustrate that observations of volcanic BrO by satellite instruments are not generally limited to major eruptions, but they're also suited for long-term measurements at quiescent degassing volcanoes. The data has the potential to improve the estimates of the total BrO release to the atmosphere from volcanic emissions.

## 12. Outlook

While all new developed algorithms in this thesis had been exclusively applied to data from GOME-2, they can be in general also used for datasets from similar UV sensitive satellite instruments like SCIAMACHY and OMI (cf. Section 3.2). Compared to GOME-2, these instruments provide spatially higher resolved measurements and might therefore be better suited to investigate especially emissions from quiescent degassing volcanoes. Both instruments provide measurements back to 2002 and 2004, respectively, and thus may largely extend the total number of volcanic plumes that can be analysed by the here proposed algorithms.

In the future, data from new UV/Vis satellite instruments will be additionally available. The third generation of the GOME instrument (GOME-2B) had been recently launched on board of the MetOp-B satellite (September 2012) and first regular measurements were announced for early 2013. For 2015, the launch of the Tropospheric Monitoring Instrument (TROPOMI) is planned. TROPOMI will provide a very high spatial resolution of  $7 \times 7 \text{ km}^2$  at nadir and a global coverage within one day and is therefore expected to substantially improve our ability to monitor atmospheric composition, including in particular volcanic emissions.

The findings from this thesis constitute a solid basis for further studies aimed at several tasks and open scientific questions. In the following, the most important ones will be briefly outlined:

1. The investigation of alternative  $\text{SO}_2$  evaluation schemes showed that accurate  $\text{SO}_2$  SCDs can be obtained during major volcanic eruptions, if the DOAS technique is applied to wavelength regions where the  $\text{SO}_2$  absorptions are less strong. As there had been previous attempts to correct for the non-linearity of  $\text{SO}_2$  absorptions in case of high concentrations by iterative model approaches, the results should be validated against each other for selected case studies (e.g. the eruptions of Kasatochi, Sarychev and Nabro). Furthermore, detailed radiative transfer simulations will be needed in order to avoid possible inconsistencies for the transition from the standard to the alternative retrieval. In addition, the possible influence of volcanic ash on the different  $\text{SO}_2$  retrievals during major volcanic eruptions needs to be investigated.
2. The contribution of  $\text{SO}_2$  to the atmosphere from both passively degassing and eruptive volcanoes is still highly uncertain. Space-based monitoring of volcanic eruptions is generally best suited to determine the total amount of  $\text{SO}_2$  released from such events. The quantities are highly requested by the climate modeling community in order to investigate the possible influence of volcanic emissions on climate change.

The SO<sub>2</sub> plumes that were detected within this thesis allow to give an estimate of the total emissions that are regularly injected into the atmosphere from volcanic eruptions. By the application of the SO<sub>2</sub> plume detection algorithm to datasets from other satellite instruments, the temporal and spatial coverage for this purpose will be significantly improved.

Moreover, a statistical analysis of SO<sub>2</sub> plumes that can be extracted from operating satellite instruments of the last decades offers the possibility to investigate the frequency distribution of SO<sub>2</sub> amounts that are injected into the Earth's atmosphere.

3. Clouds can have a significant influence on slant column densities that are retrieved from the DOAS evaluation. While thick clouds below a volcanic plume may increase the sensitivity of the measurements due to higher reflectivity, parts of a plume can also be shielded when clouds are found at higher altitudes. Multiple scattering inside both volcanic plumes and clouds strongly influences the effective path and therefore leads to an over- or underestimation of the "true" SCD. Additionally, the Ring effect is affected by the presence of clouds and may prevent an accurate DOAS fit, especially for weak absorbers like BrO. Detailed radiative transfer calculation studies will be necessary to determine the influence of such effects and correct the data.

4. The systematic investigation of volcanic plumes in the GOME-2 dataset revealed more than 60 individual plumes that showed clear evidence for BrO of volcanic origin. However, the ambient atmospheric conditions that are needed for a significant formation of volcanic BrO are hitherto hardly known. Furthermore, previously conducted studies on BrO chemistry in volcanic plumes focused on the initial formation processes from ground-based measurements close to quiescent degassing volcanoes.

The volcanic BrO plumes that were detected from GOME-2 measurements in this thesis will help to better understand the associated chemical formation processes during eruptions as well as the bromine behavior during magma differentiation at quiescent degassing volcanoes from chemistry model approaches. For this purpose, the data should be investigated for the ambient meteorological conditions that were present at the time of the eruptions. Additionally, a detailed analysis of the BrO/SO<sub>2</sub> ratios as a function of the plume age via trajectory model simulations may improve our understanding of bromine chemistry in volcanic plumes.

5. The Ambrym case study showed that the detection of volcanic BrO from quiescent degassing volcanoes from averaged GOME-2 data is generally possible. The dataset from other satellite instruments, especially OMI, should be well suited to reproduce the findings and improve the measurement statistics. Additionally, SCIAMACHY and OMI were in operation during a phases of extreme strongly passive degassing of Ambrym in 2005 where airborne DOAS measurements by Bani et al. (2009) showed high BrO/SO<sub>2</sub> ratios of up to  $4 \times 10^{-4}$ . By including radiative transfer calculations in the future, more representative

---

total SO<sub>2</sub> and BrO budgets for Ambrym and probably other volcanoes may be calculated. This will allow to estimate the total amount of BrO that is released from strongly degassing volcanoes.



# Appendix



## A. Volcanic BrO events

This appendix contains SO<sub>2</sub> and BrO maps of all volcanic plumes that were found to show evidence for enhanced BrO SCDs from the systematic investigation of the GOME-2 dataset in the time period from January 2007 until the end of June 2011 (cf. Chapter 9, Section 9.4). The findings were sorted into four categories:

Category I: The volcanic plume showed a **clear linear** BrO/SO<sub>2</sub> correlation.

Category II: The volcanic plume showed a **weak linear** BrO/SO<sub>2</sub> correlation.

Category III: Clearly enhanced BrO SCDs, but **no linear** correlation.

Category IV: No enhanced BrO SCDs were found in the SO<sub>2</sub> plume's area.

category	r <sup>2</sup>	p-value	BrO VCD* <sub>max</sub>	BrO cluster	number of events
I	>0.5	<5×10 <sup>-3</sup>	>2σ*	3-pixel cluster with VCD* >2σ*	17
II	≥0.25	<1×10 <sup>-3</sup>	>2σ*	3-pixel cluster with VCD* >2σ*	23
III	≤0.25	-	>4σ*	6-pixel cluster with VCD* >2σ*	24
IV	-	-	-	-	708

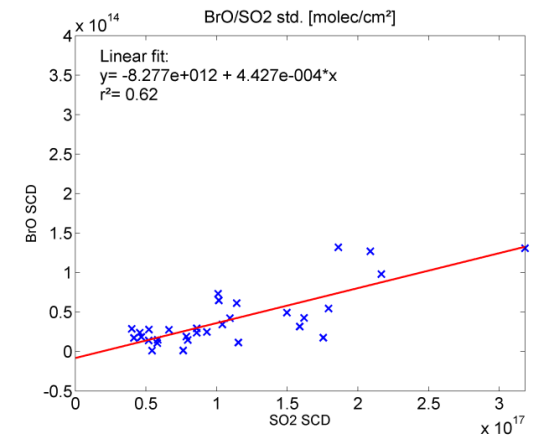
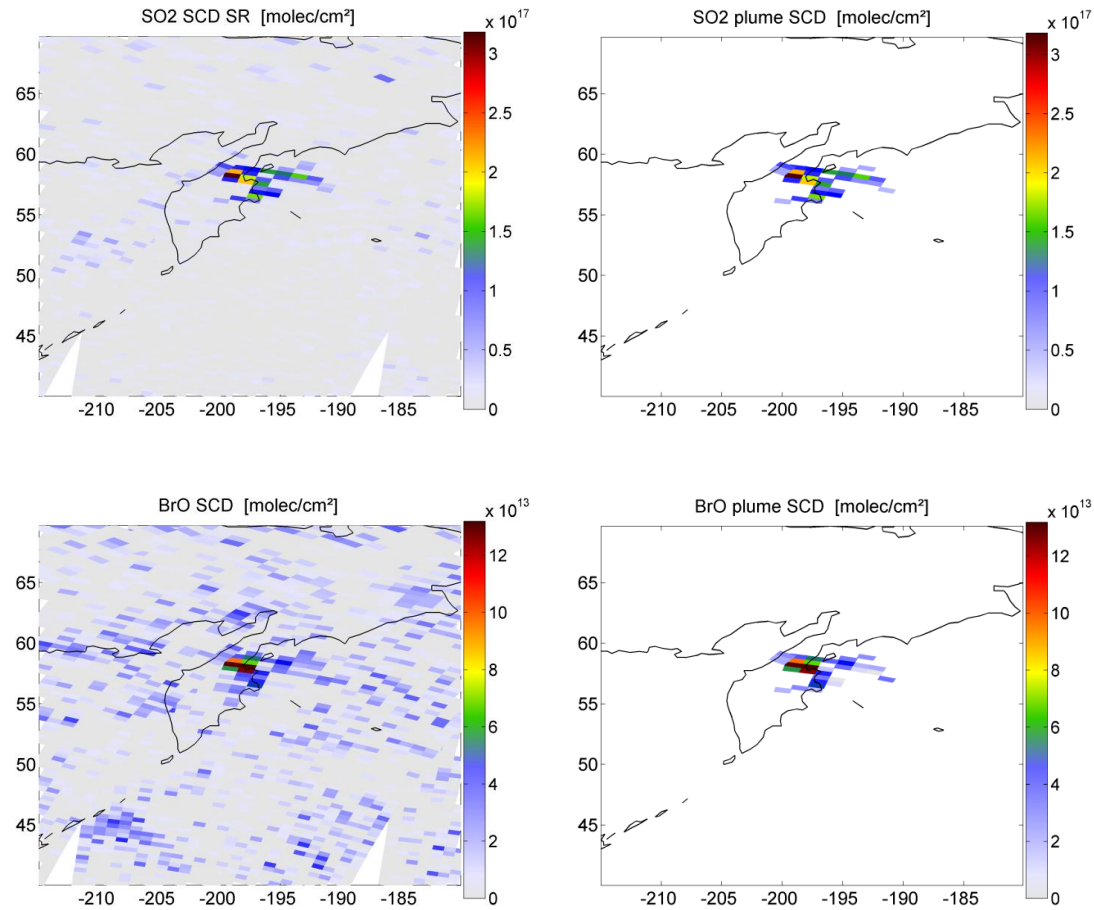
In the following, SO<sub>2</sub> and BrO maps for all regarded areas and extracted satellite groundpixels are presented. Furthermore, a BrO/SO<sub>2</sub> correlation plot is shown for each individual case, including the main results from a bivariate linear fit. The mean BrO/SO<sub>2</sub> ratio can be derived from the associated slope.

As the majority of volcanic plumes (92%) showed no indications for the abundance of BrO, only volcanic events from Categories I–III are presented.<sup>1</sup>

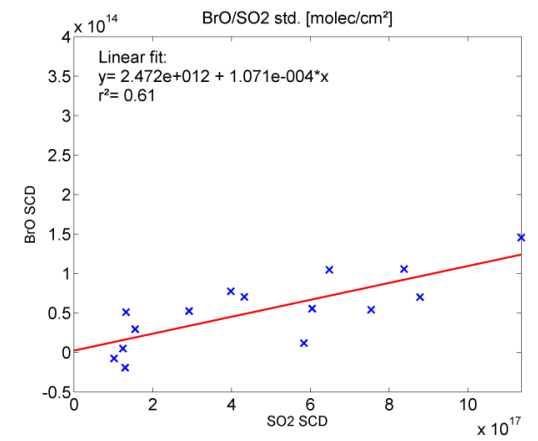
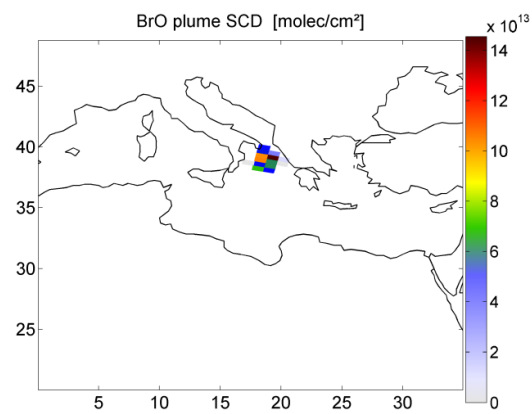
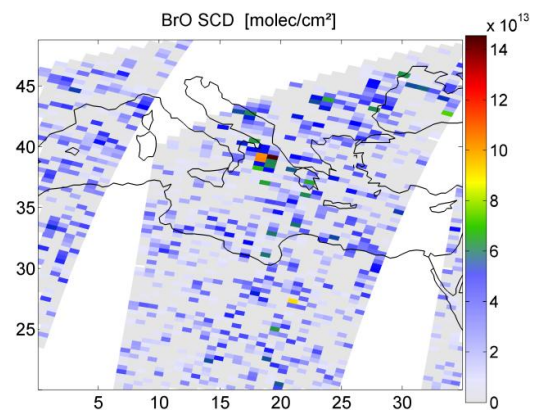
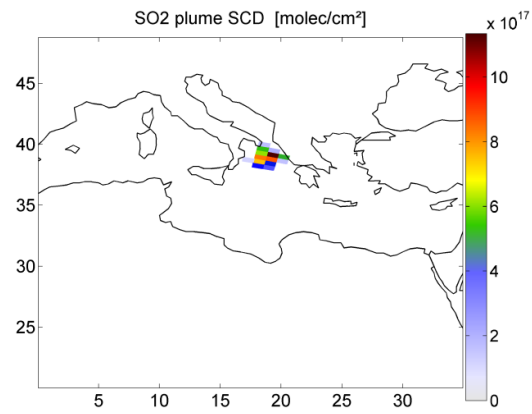
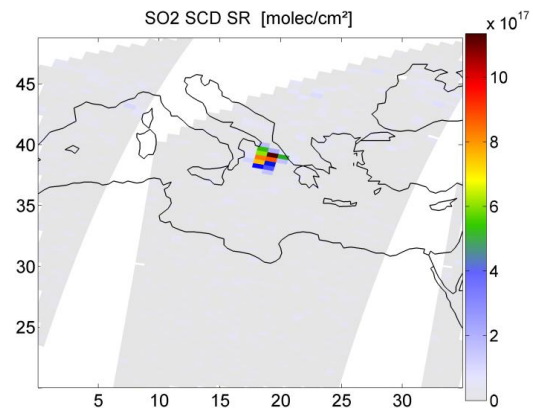
<sup>1</sup>This appendix has been accepted for publication as a supplementary part of Hörmann et al. (2012)

## Category I

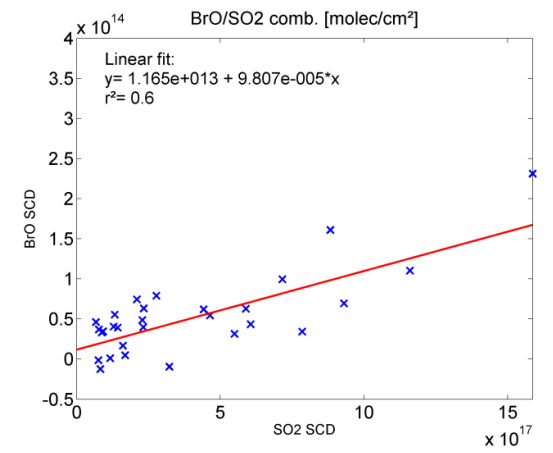
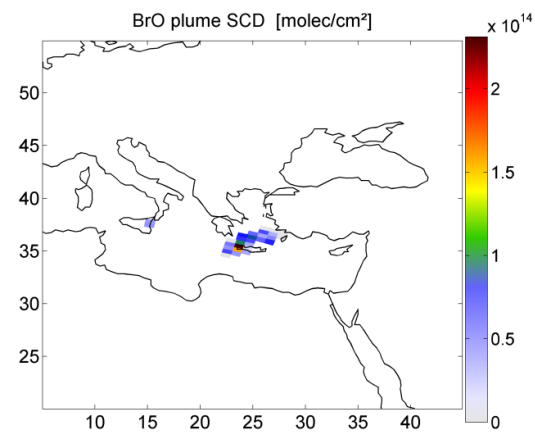
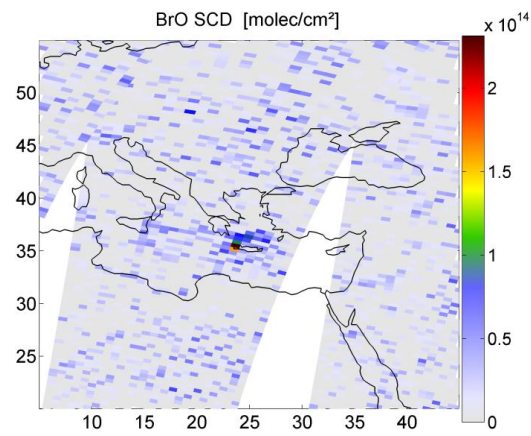
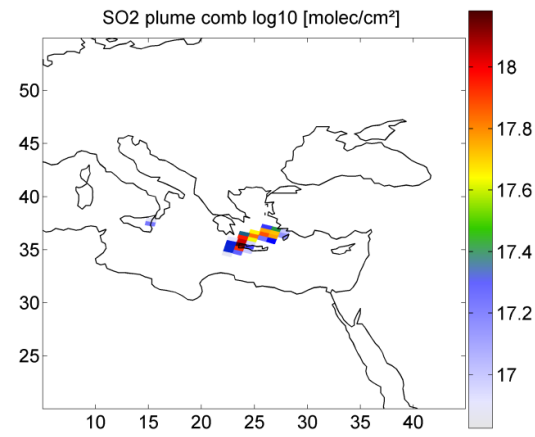
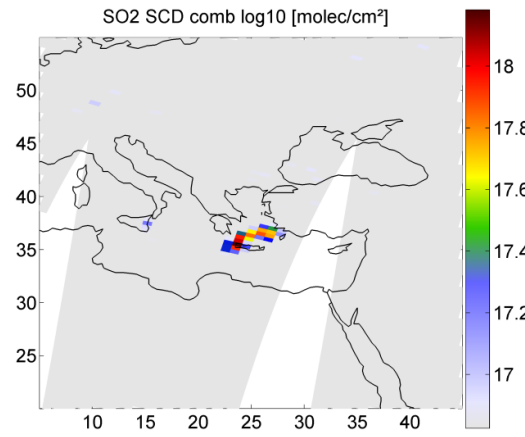
#22 Bezymianny 11./12.05.2007



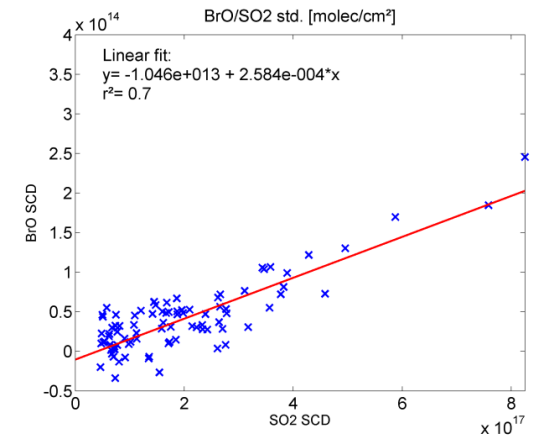
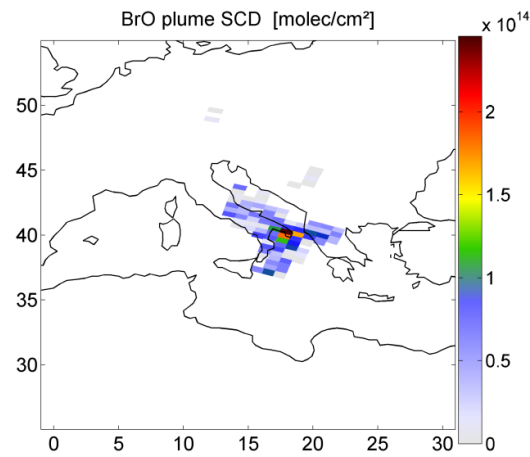
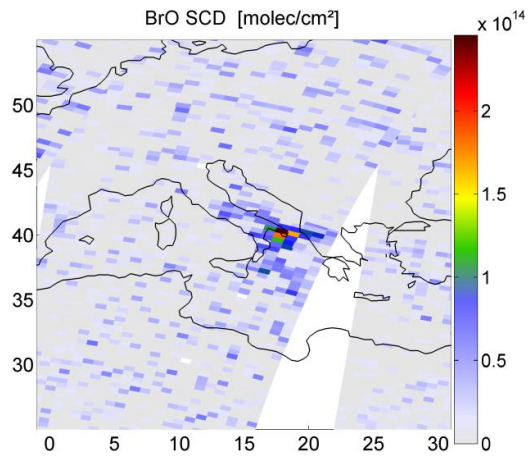
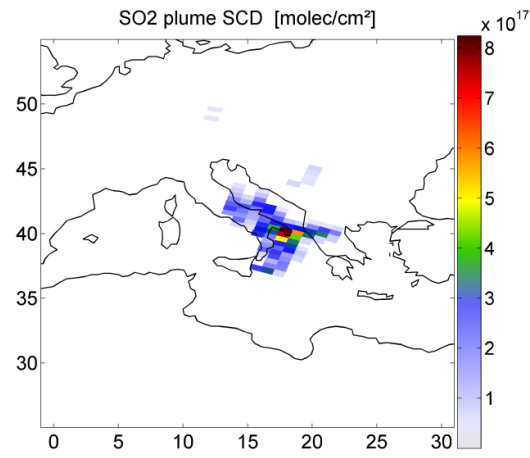
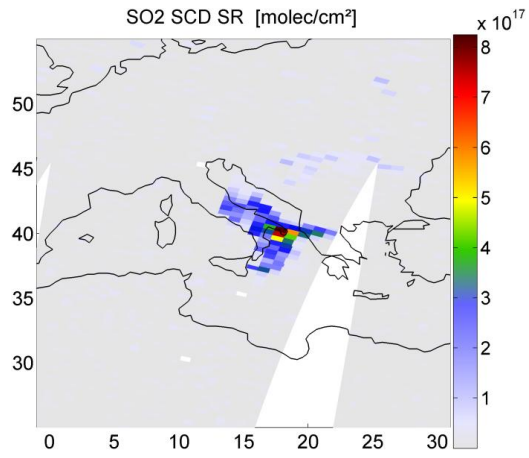
#68 Etna 24.11.2007



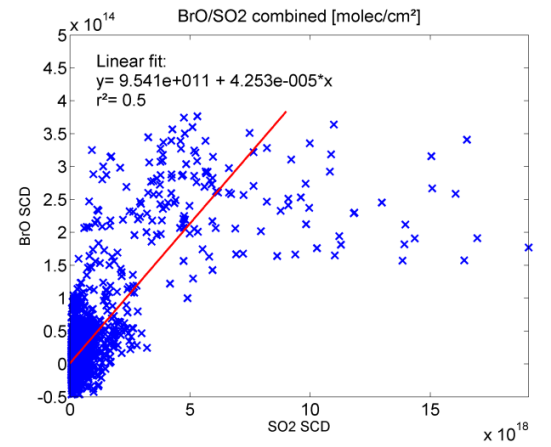
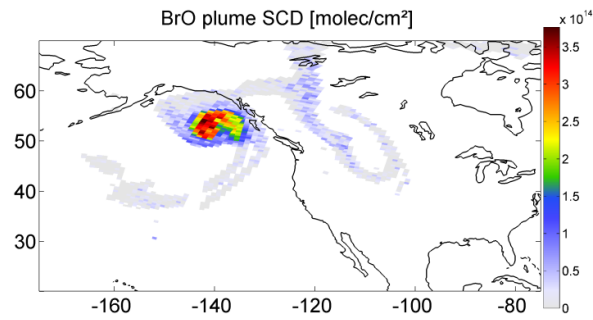
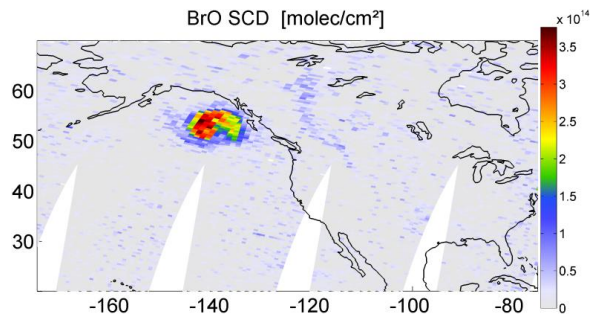
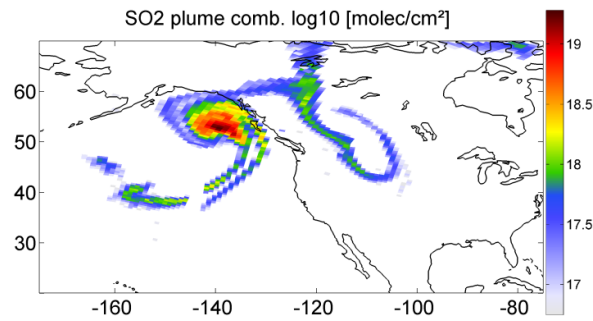
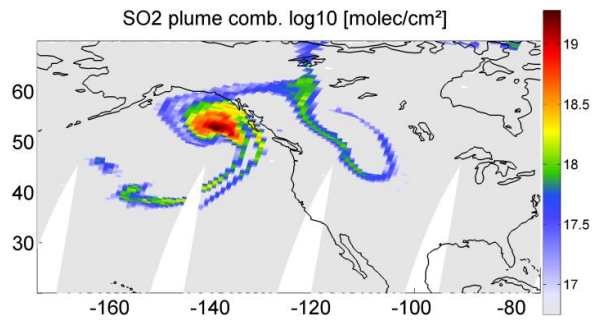
#94 Etna 11.05.2008



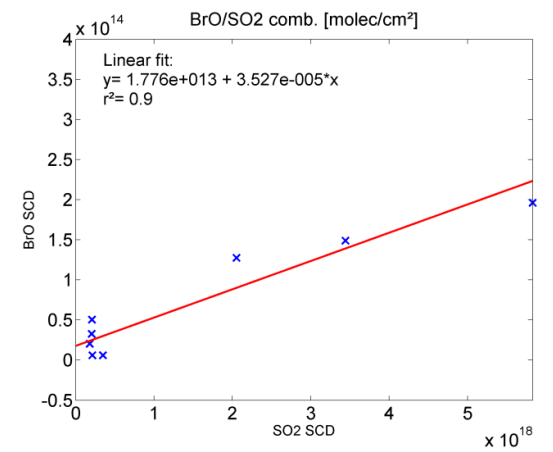
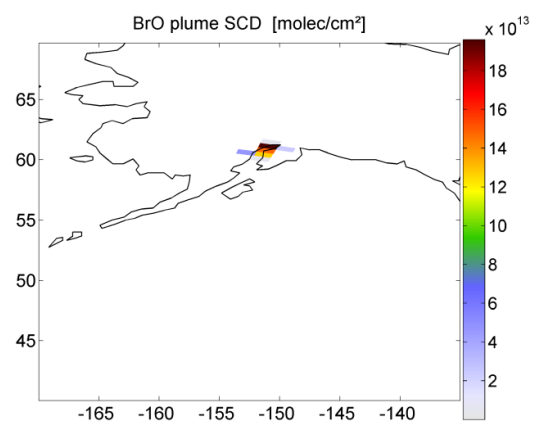
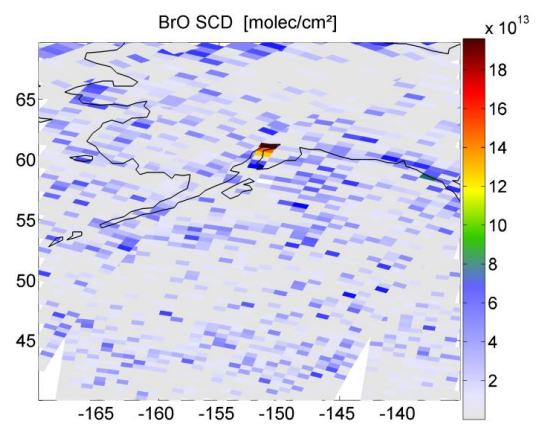
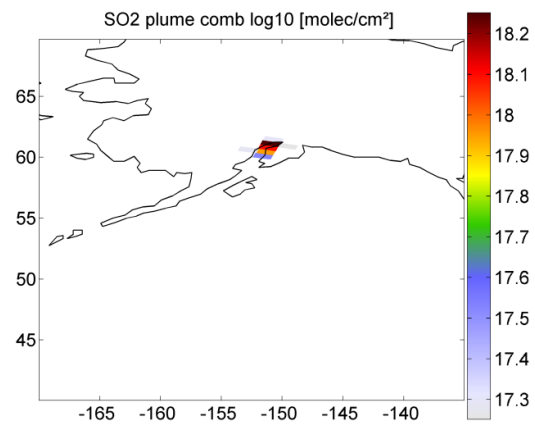
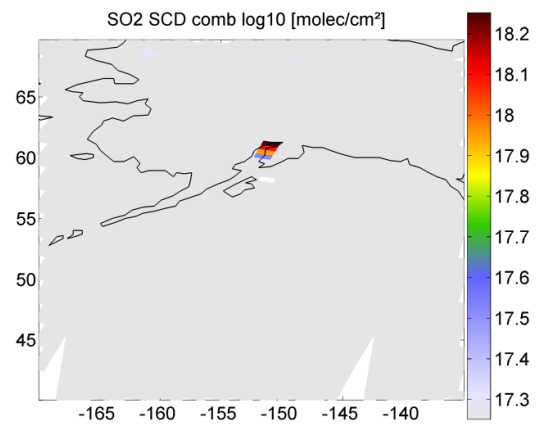
#97 Etna 14.05.2008



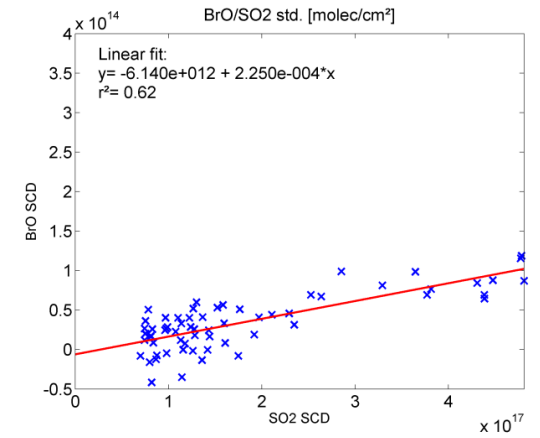
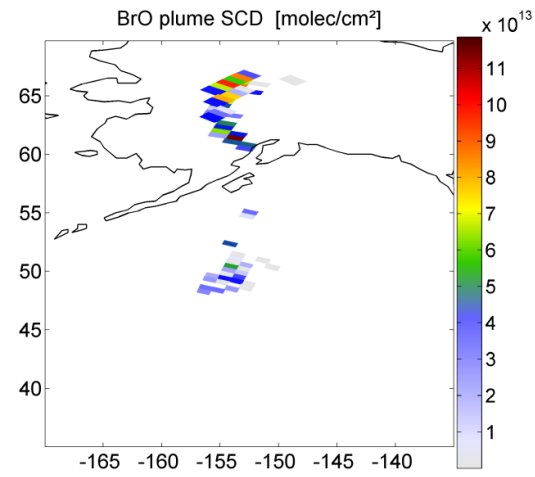
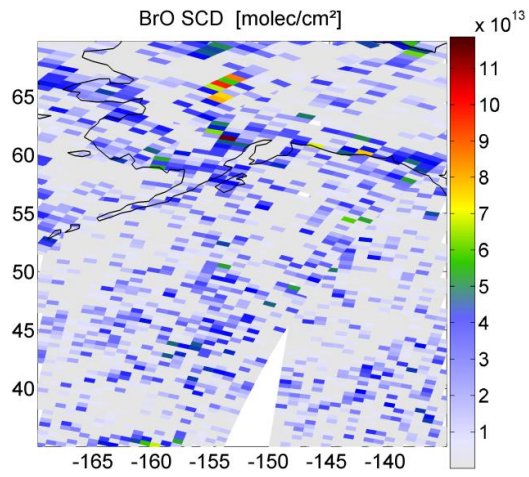
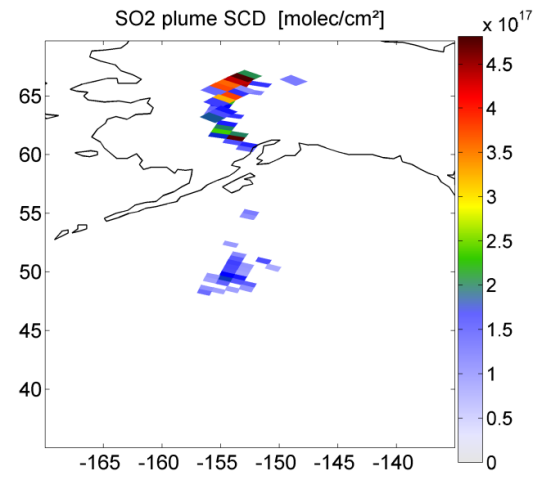
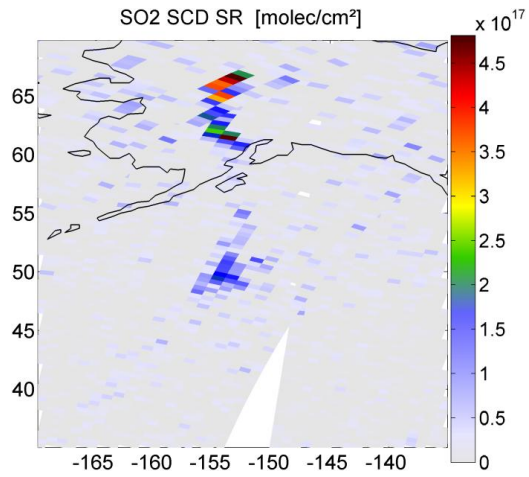
#164 Kasatochi 11.08.2008



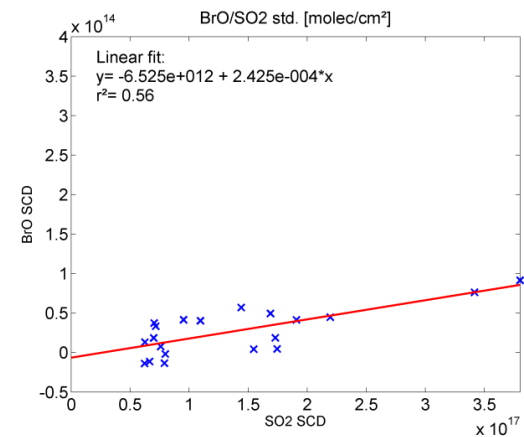
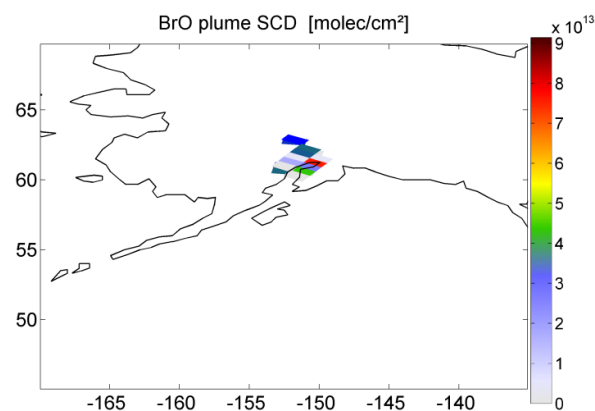
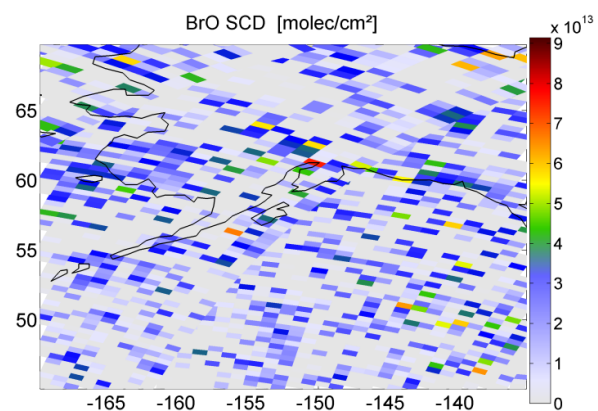
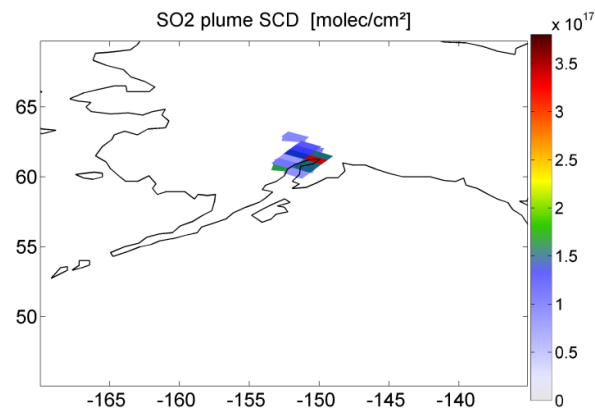
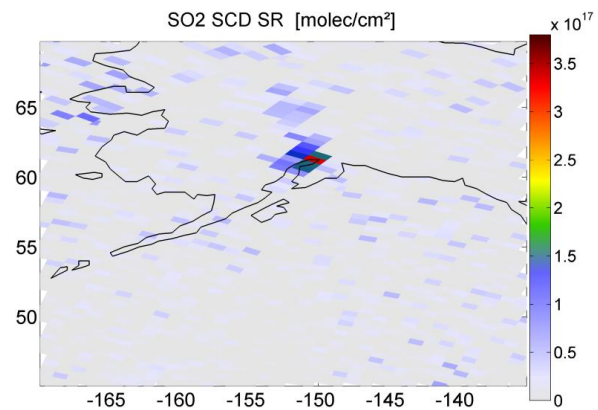
#282 Mt. Redoubt 26.03.2009



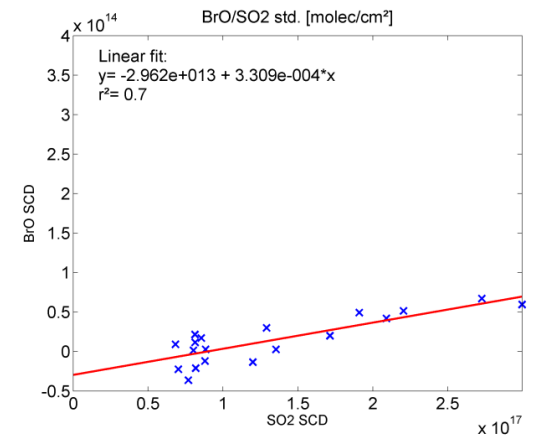
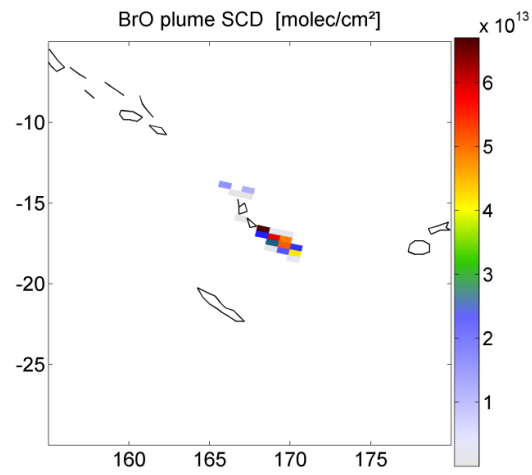
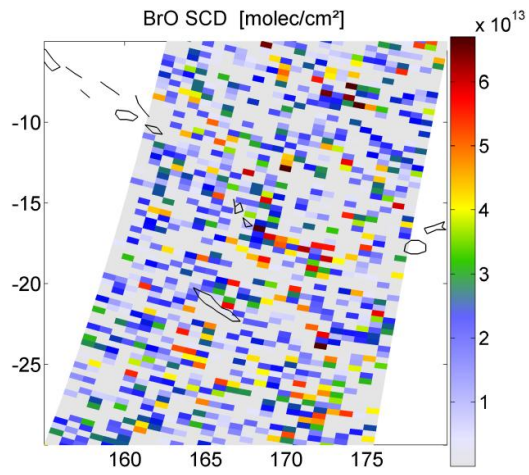
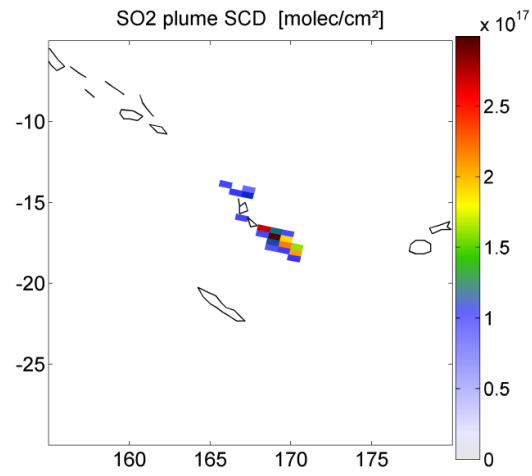
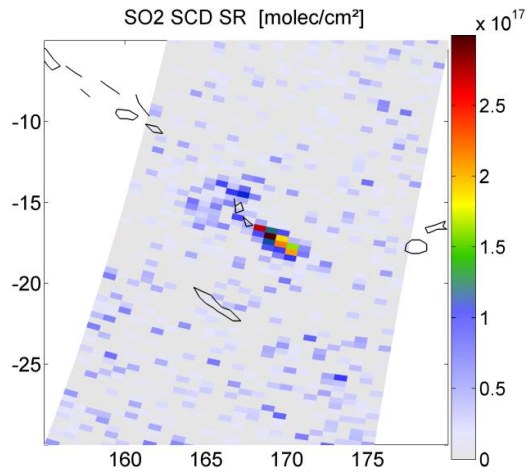
#322 Mt. Redoubt 18.04.2009



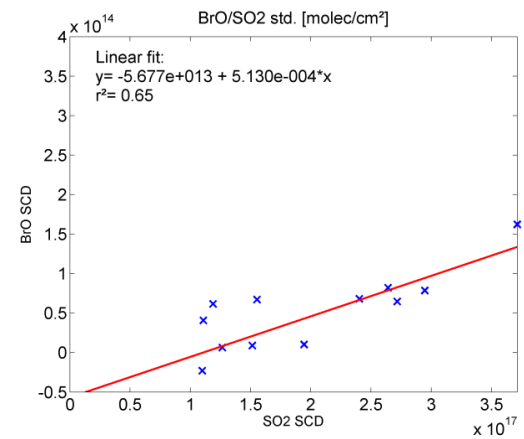
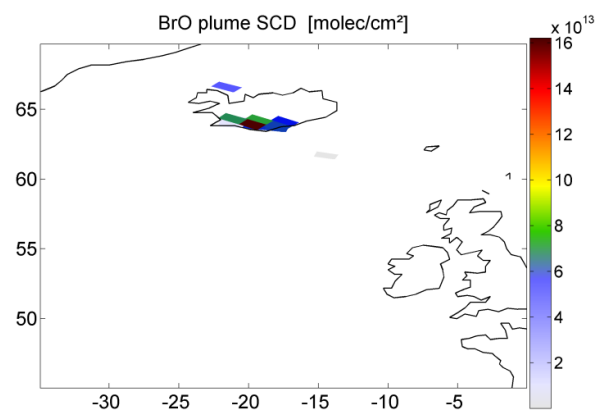
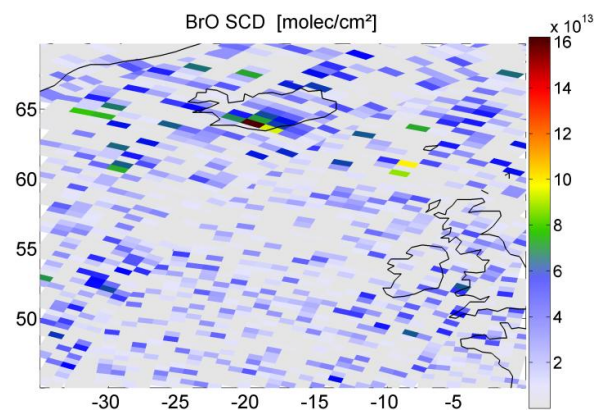
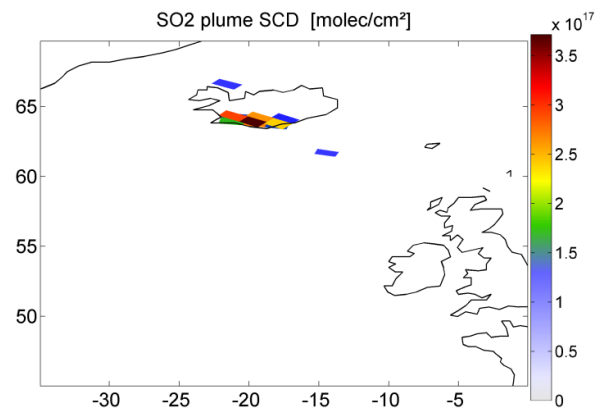
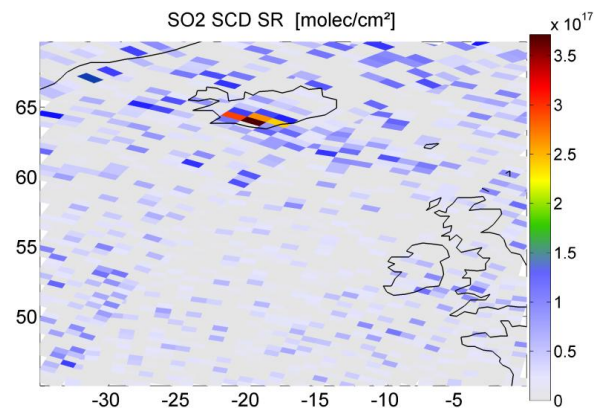
#363 Mt. Redoubt 29.05.2009



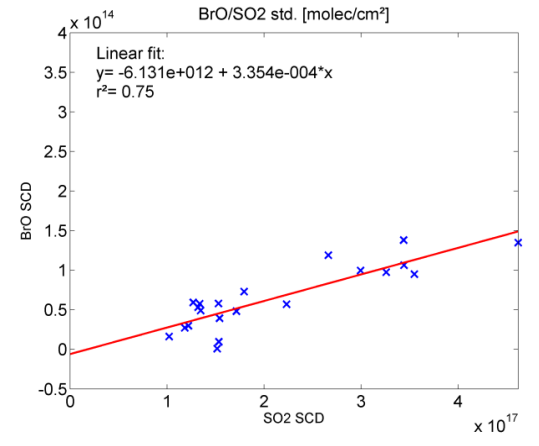
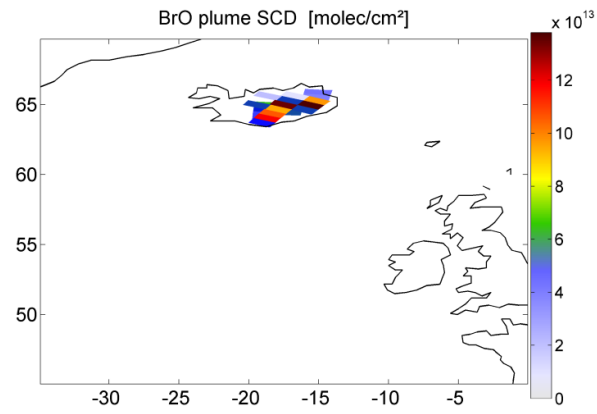
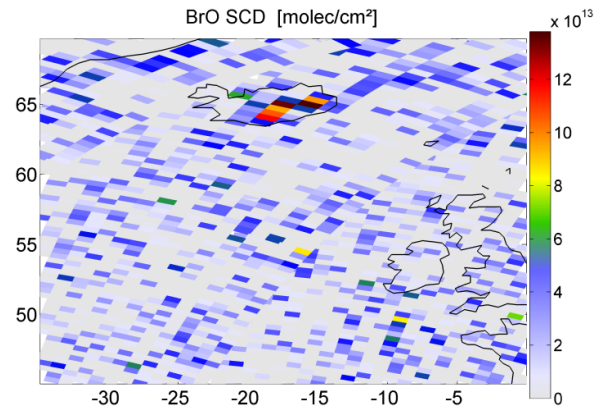
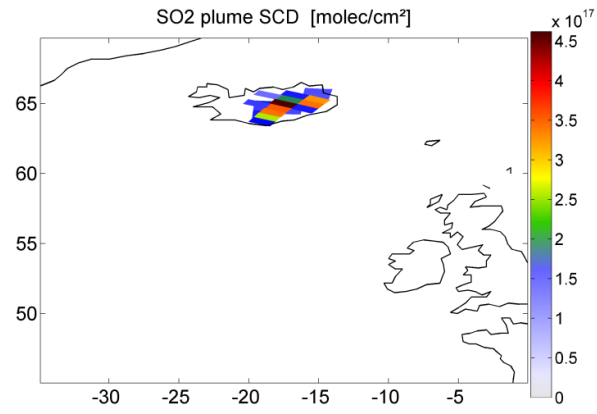
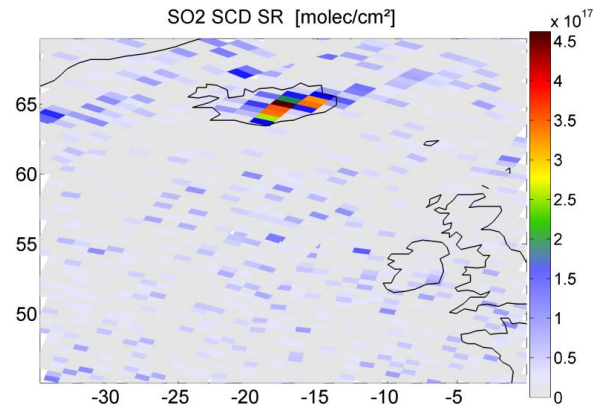
#535 Ambrym 08.04.2010



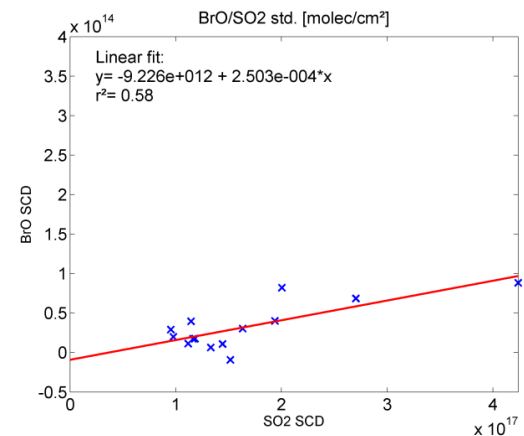
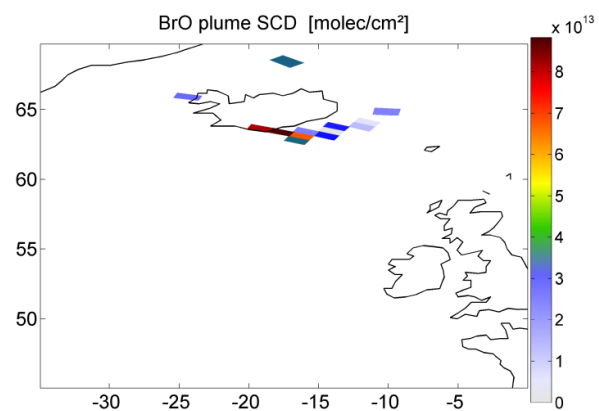
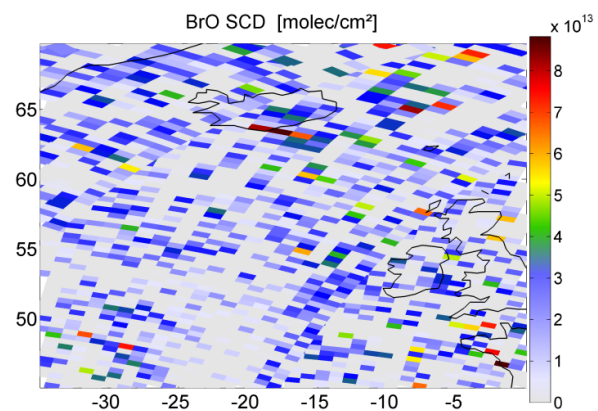
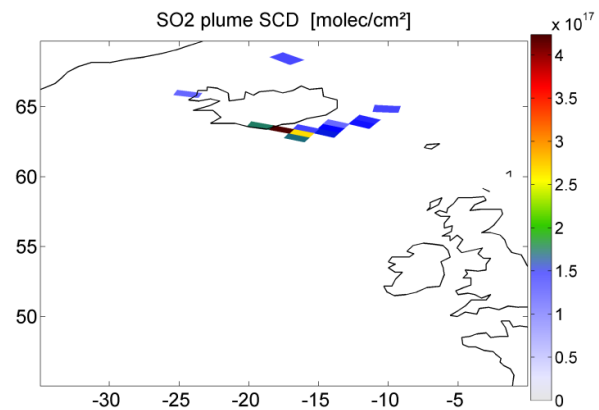
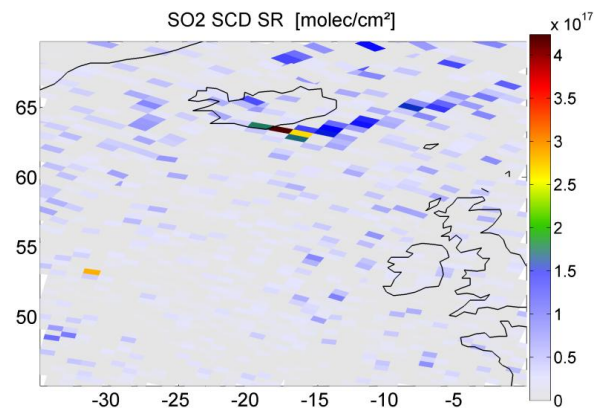
#541 Eyjafjallajökull 23.04.2010



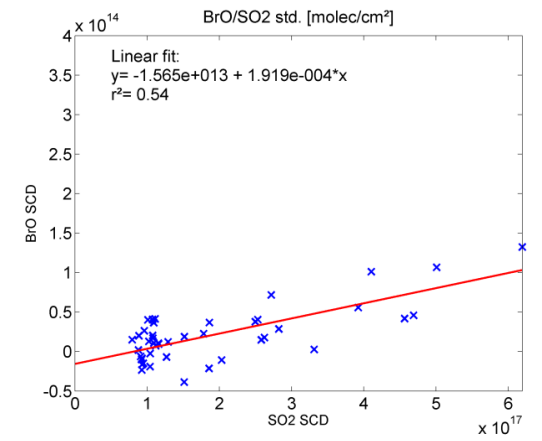
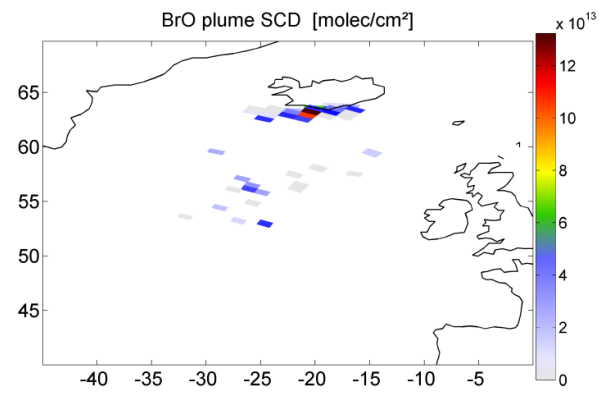
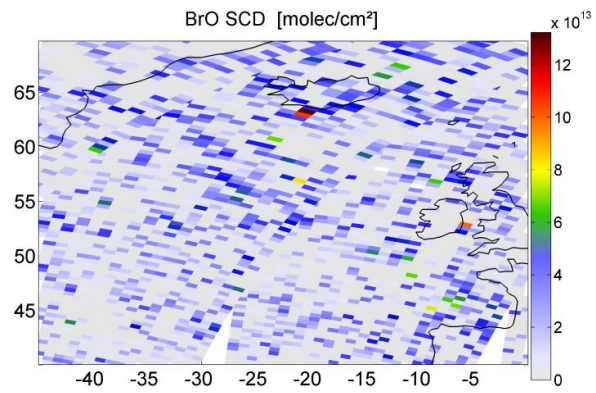
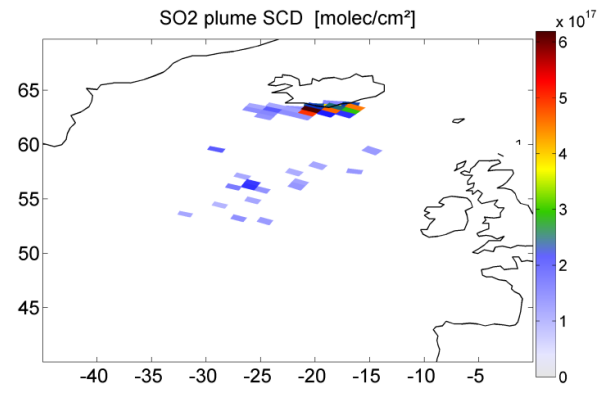
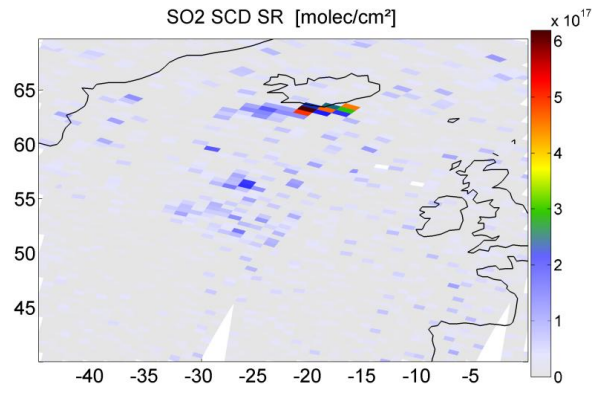
#545 Eyjafjallajökull 25.04.2010



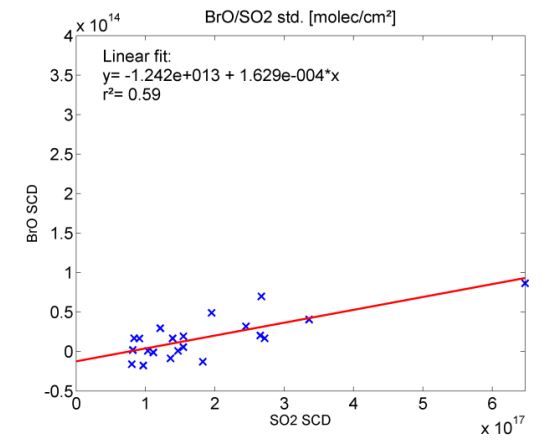
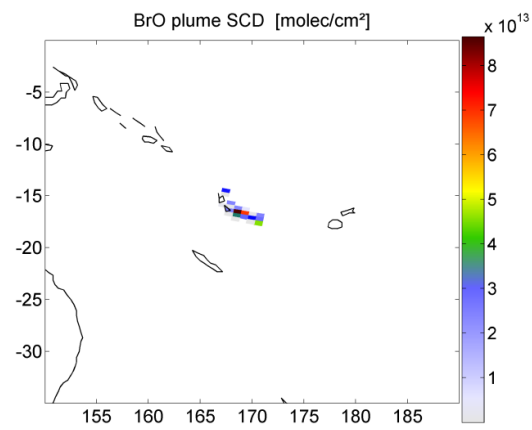
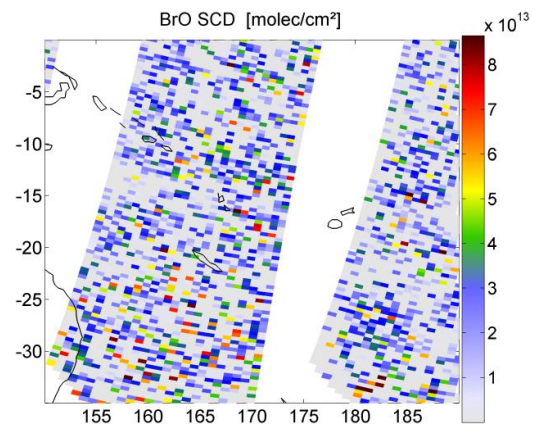
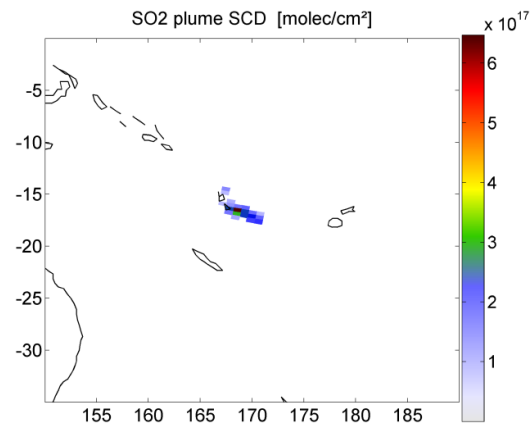
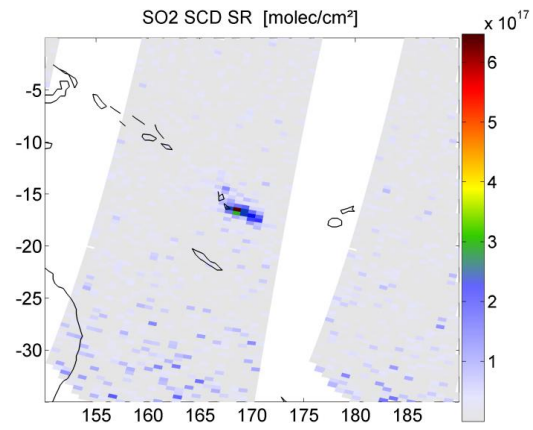
#546 Eyjafjallajökull 26.04.2010



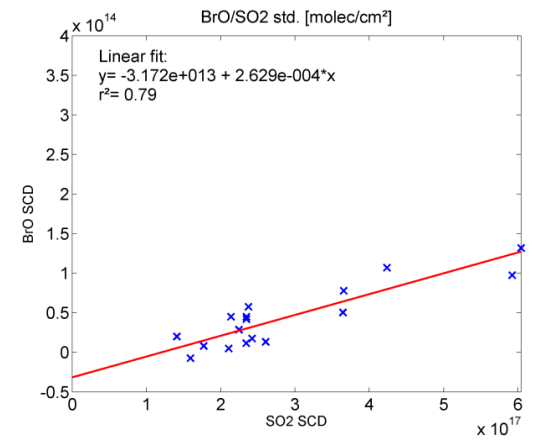
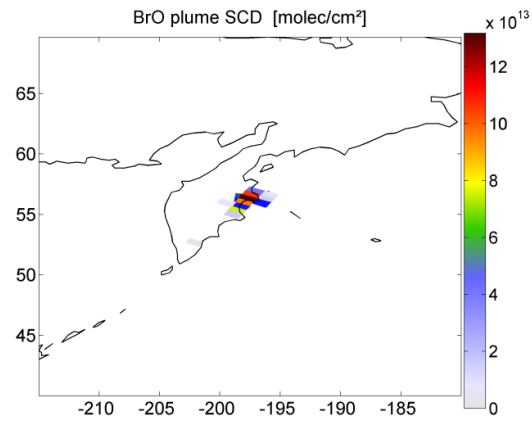
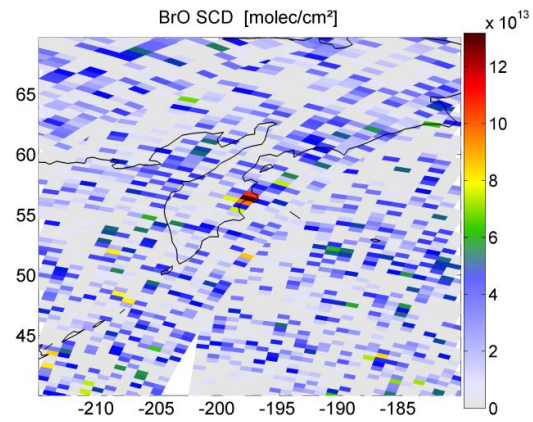
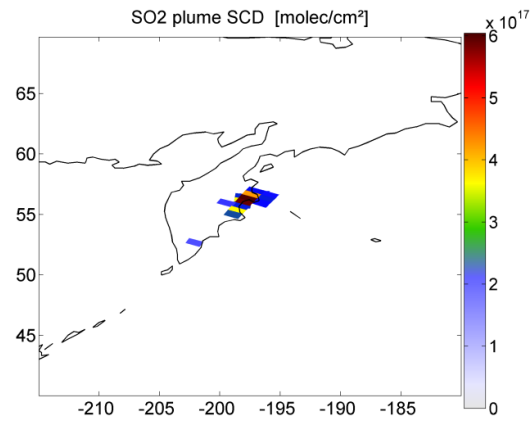
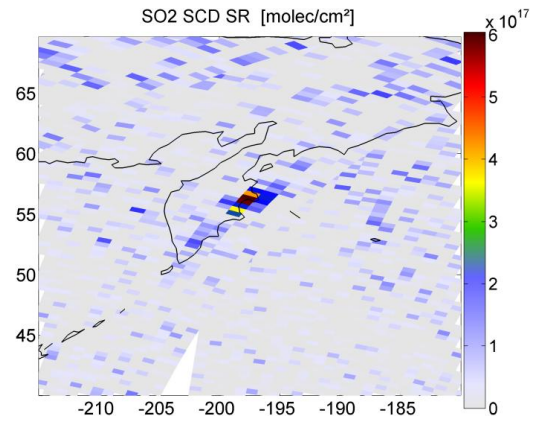
#550 Eyjafjallajökull 29.04.2010



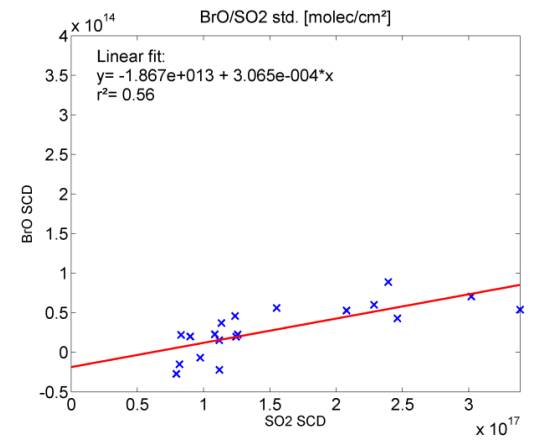
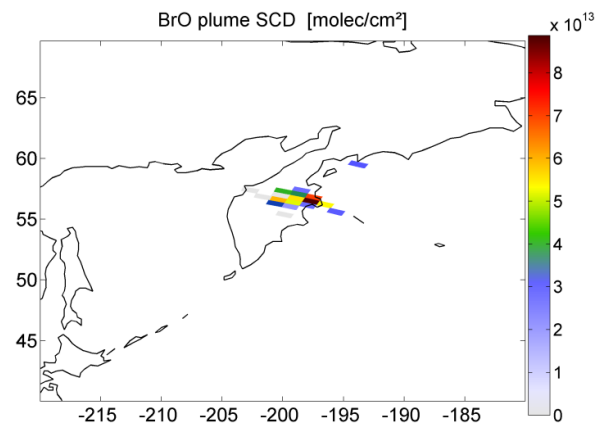
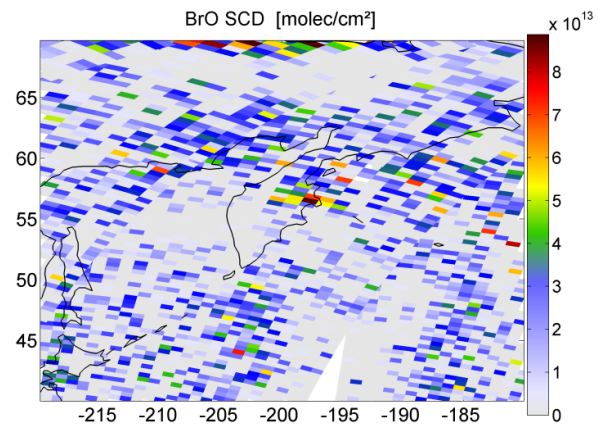
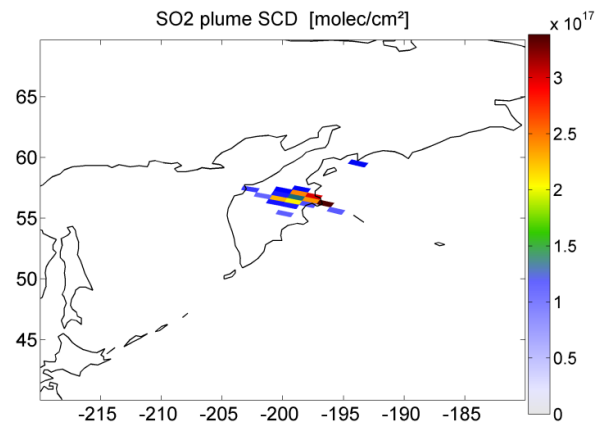
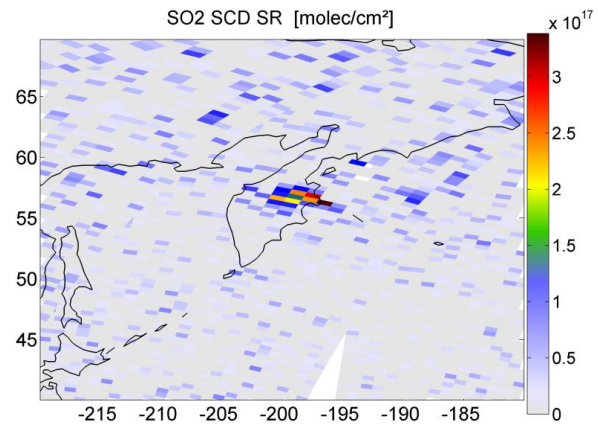
#563 Ambrym 11.05.2010



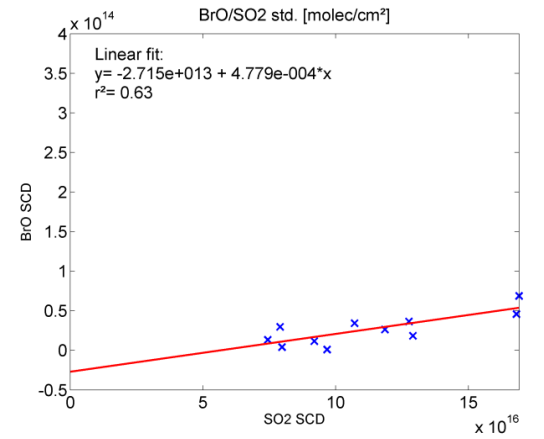
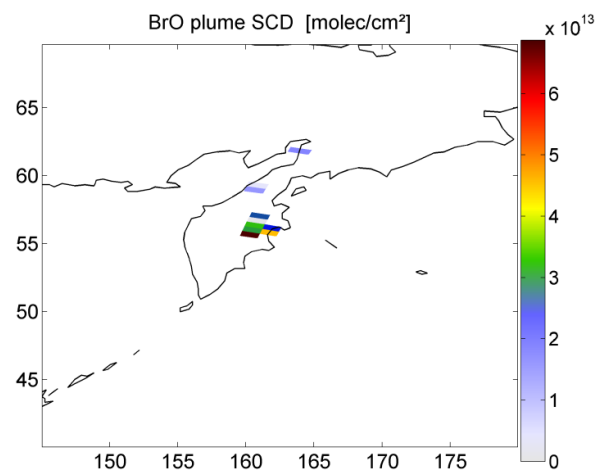
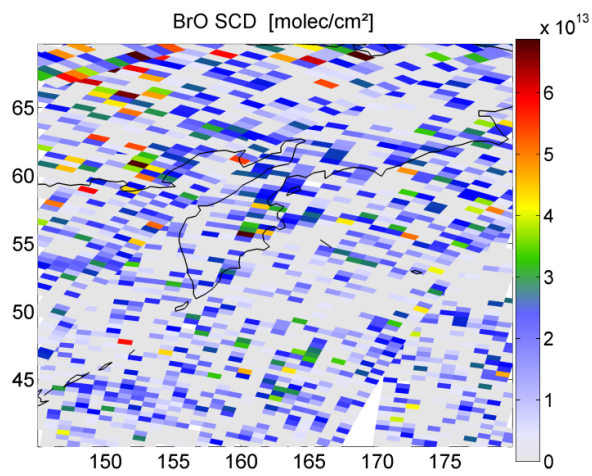
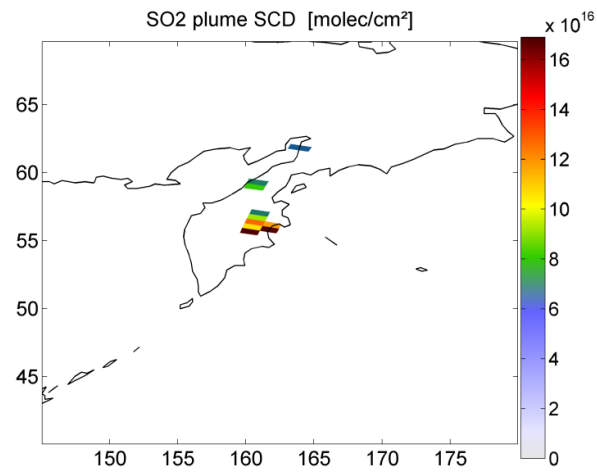
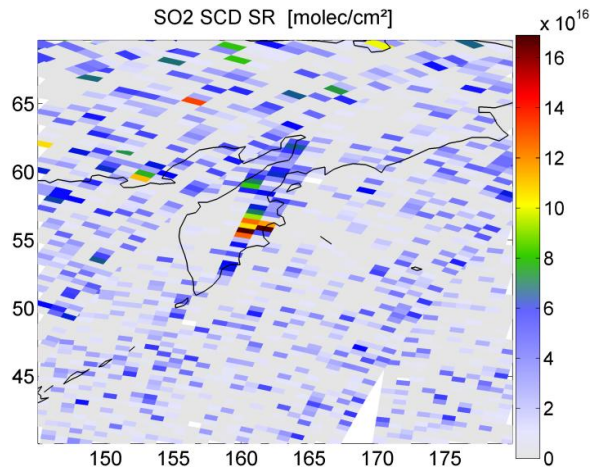
#675 Kliuchevskoi\* 29./30.03.2011



#700 Kizimen\* 08./09.05.2011

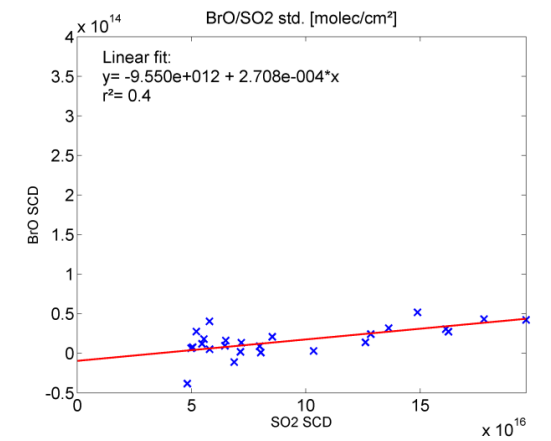
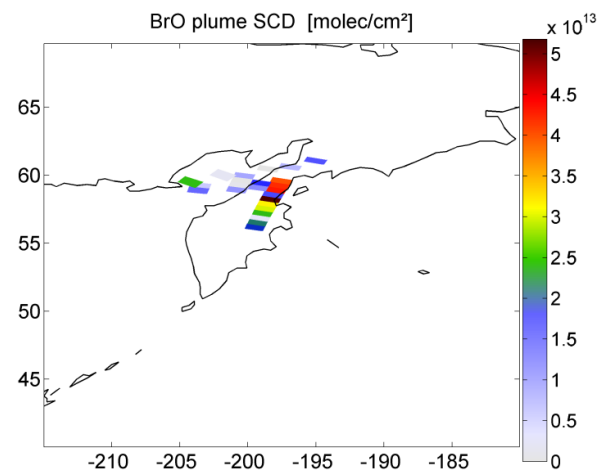
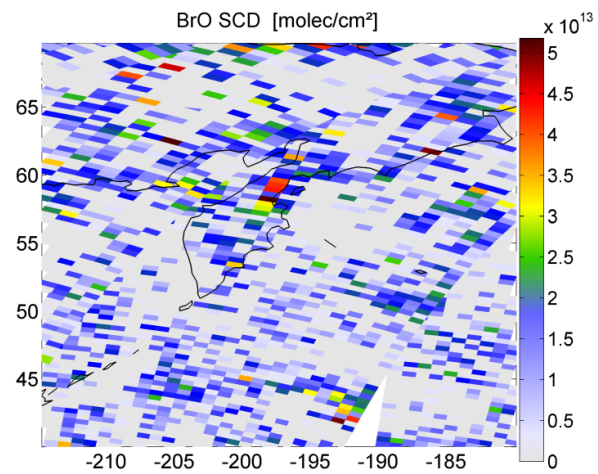
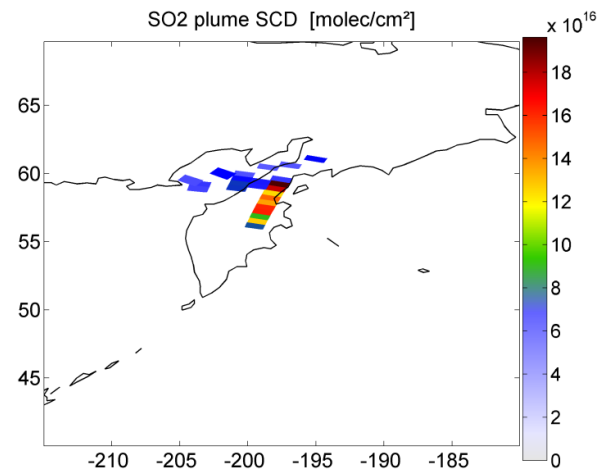
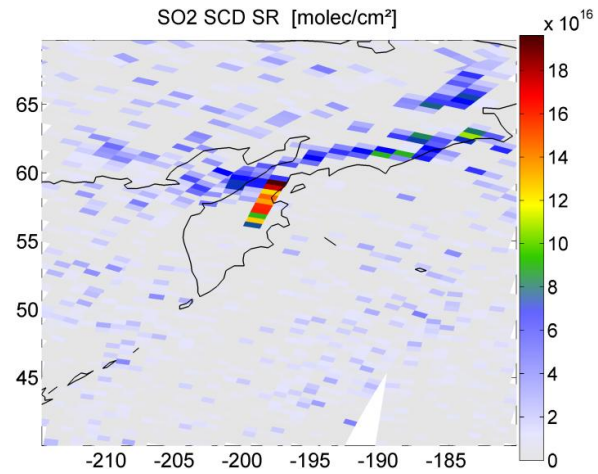


#740 Kizimen\* 07.06.2011

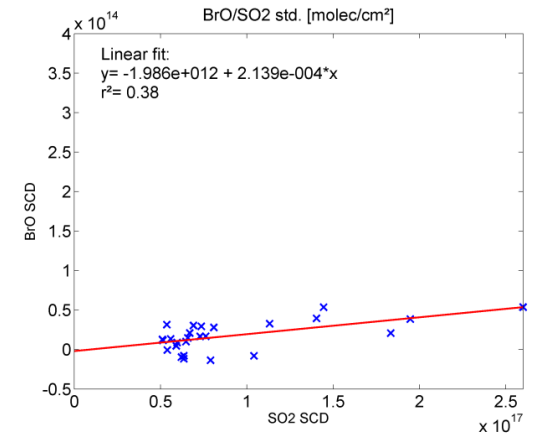
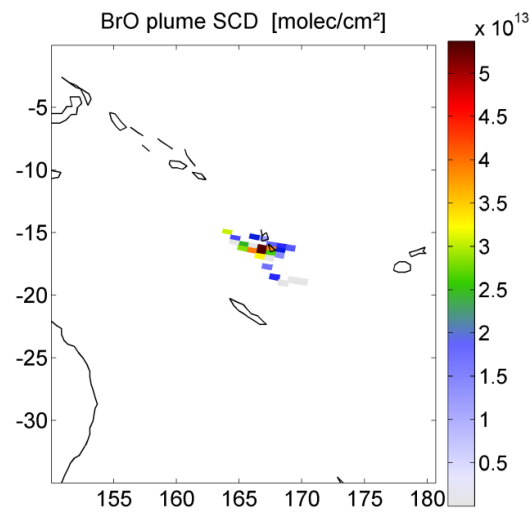
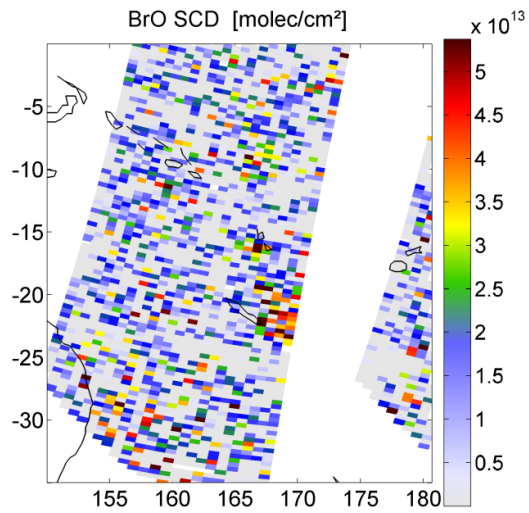
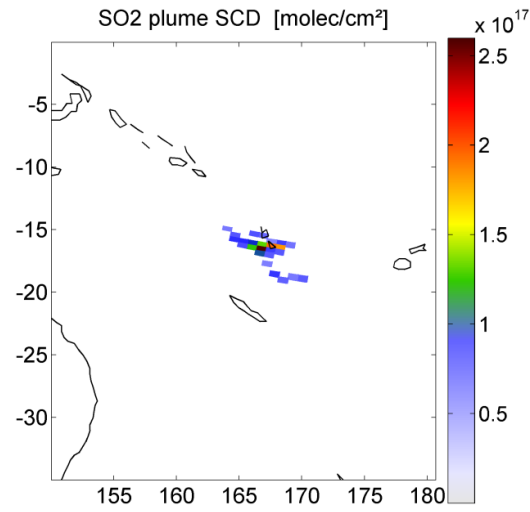
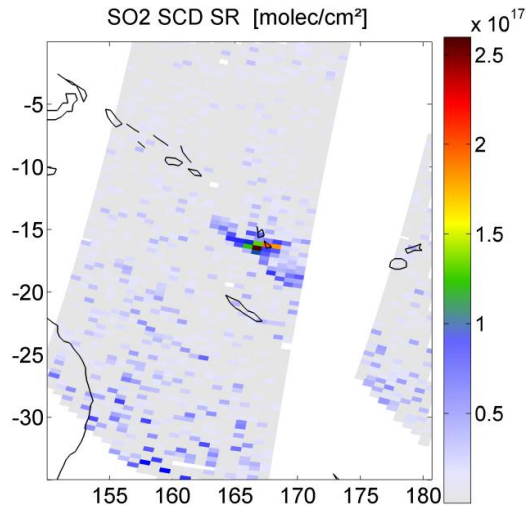


## Category II

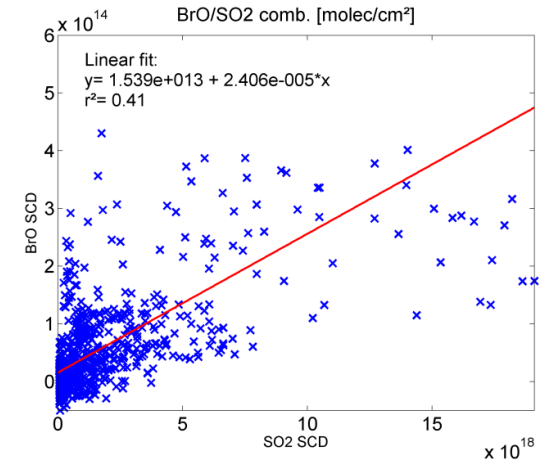
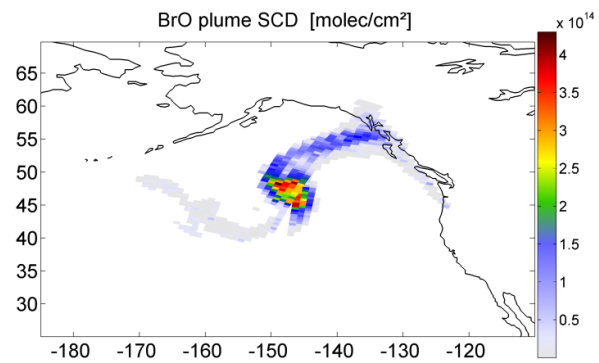
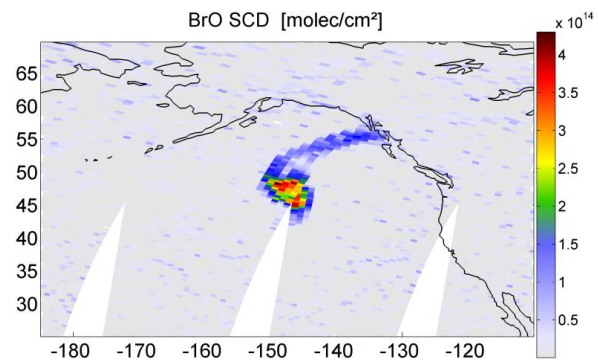
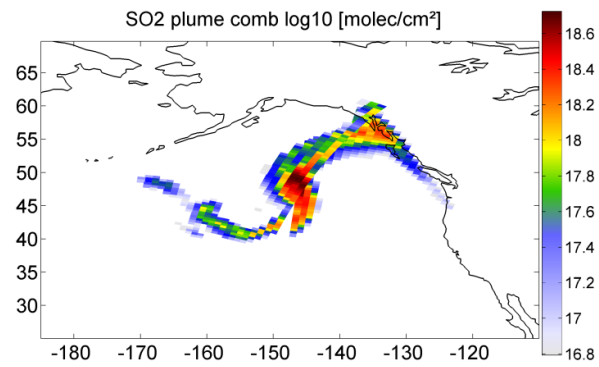
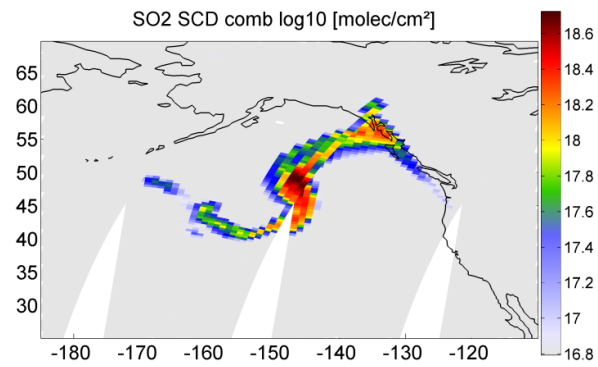
#28 Kliuchevskoi 20./21.05.2007



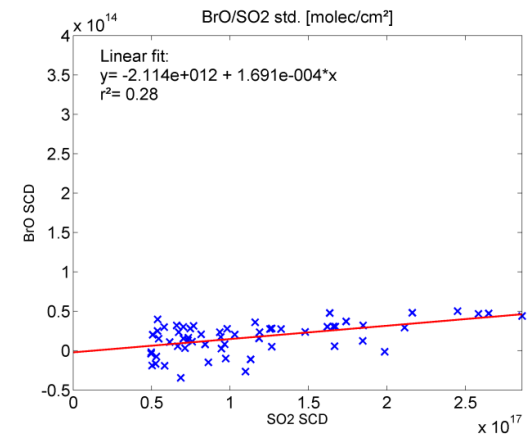
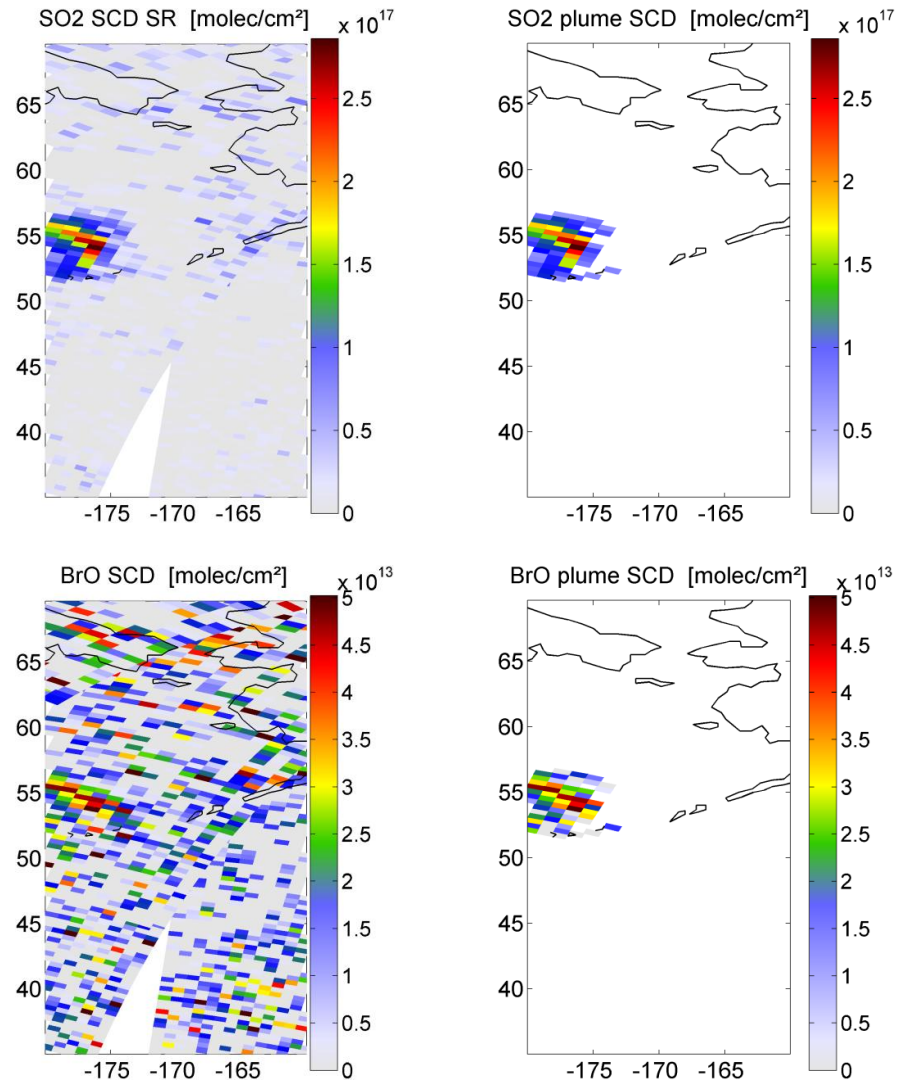
#48 Ambrym 16.07.2007



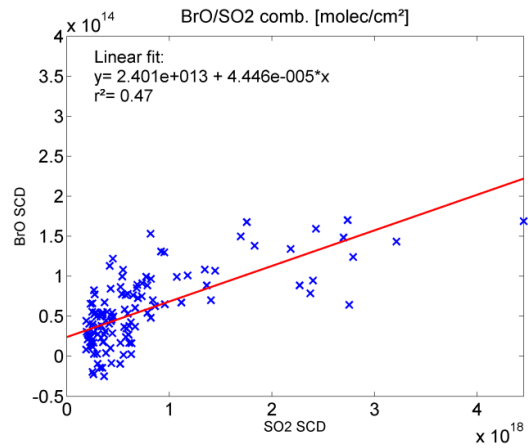
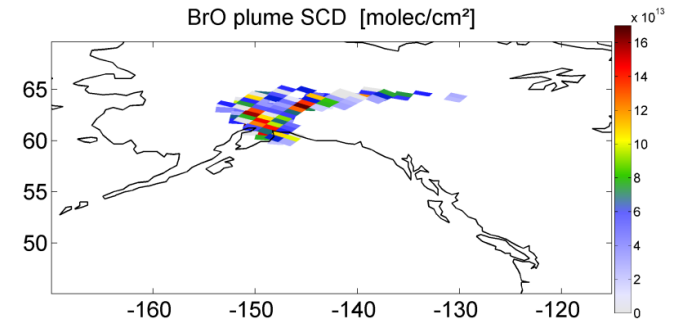
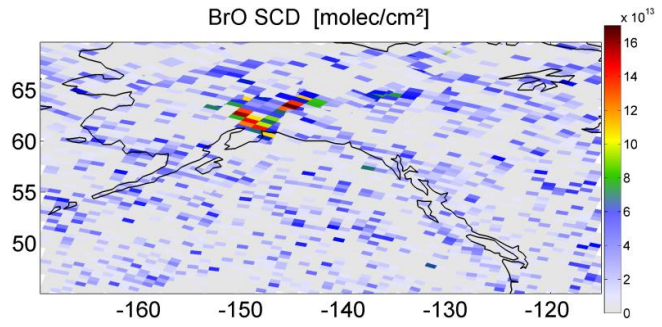
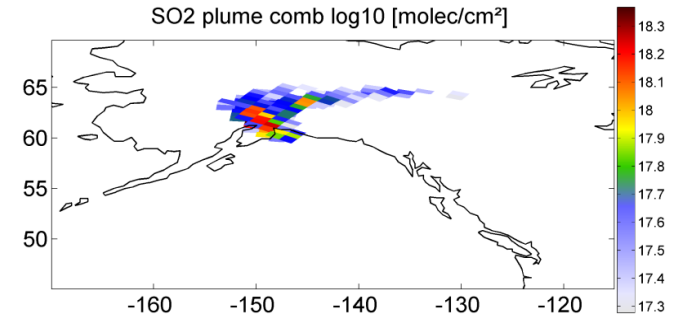
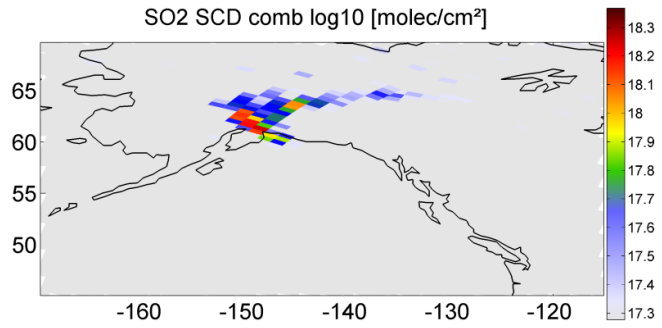
#163 Kasatochi 10.08.2008



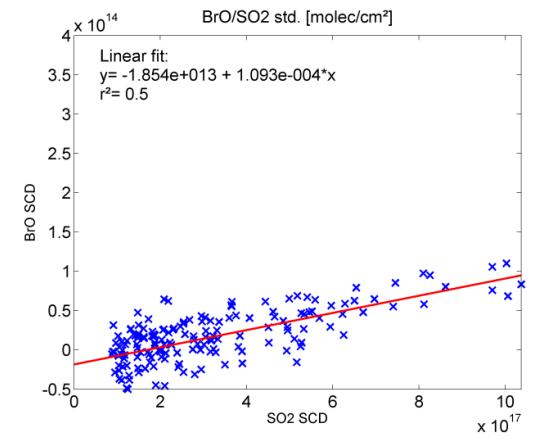
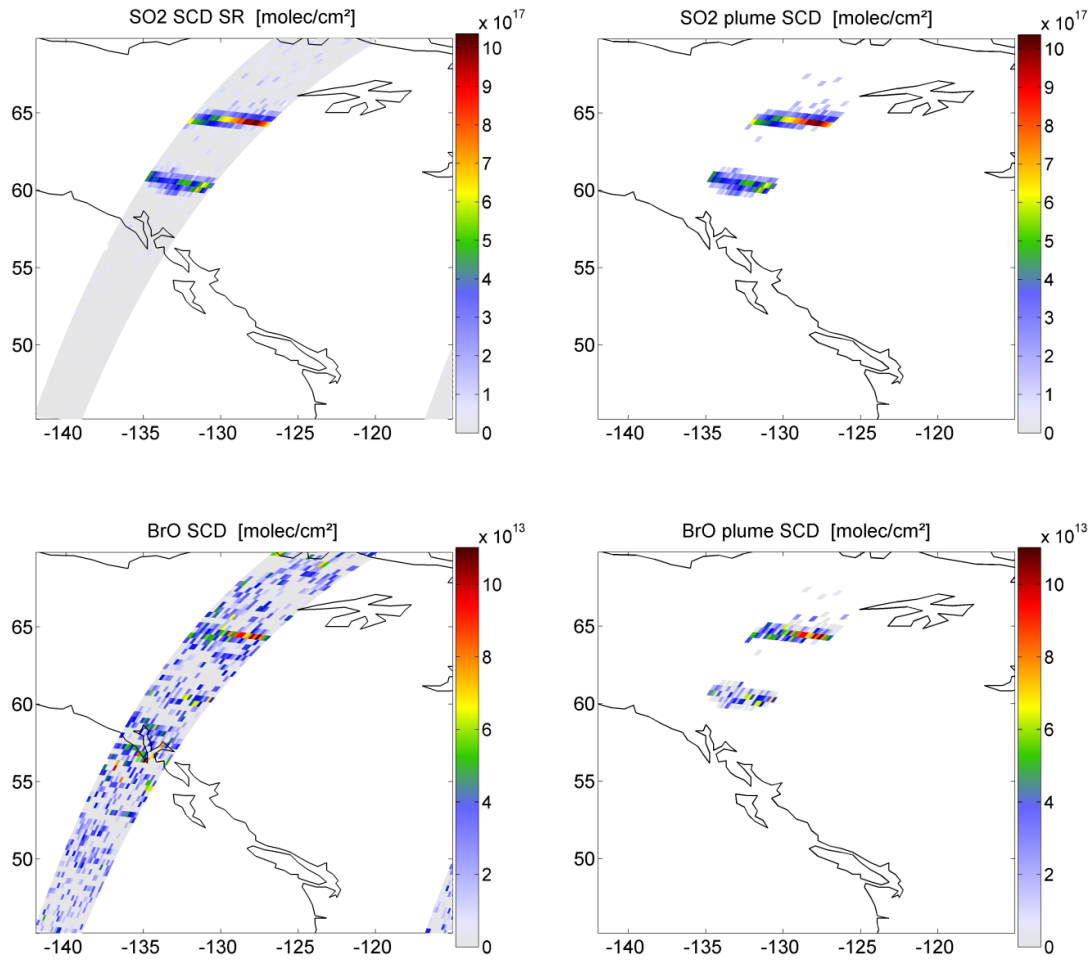
#186 Kasatochi 20.08.2008



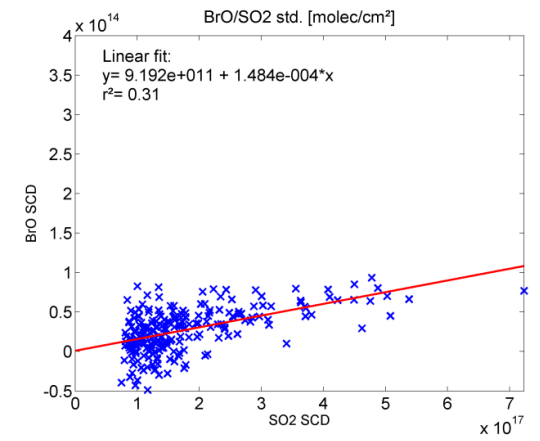
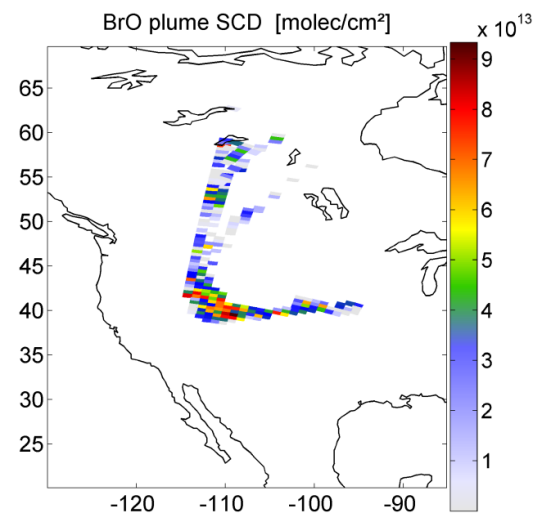
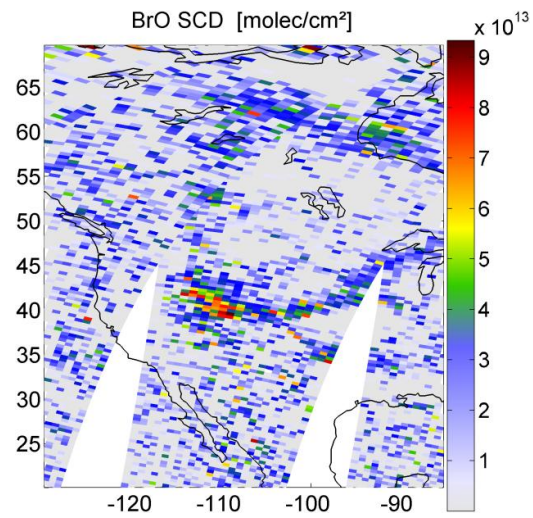
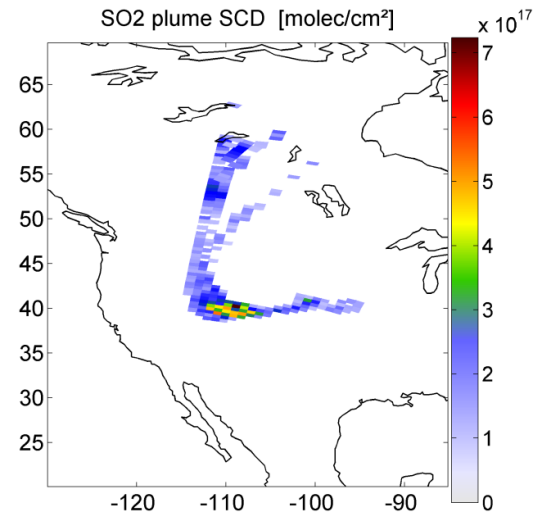
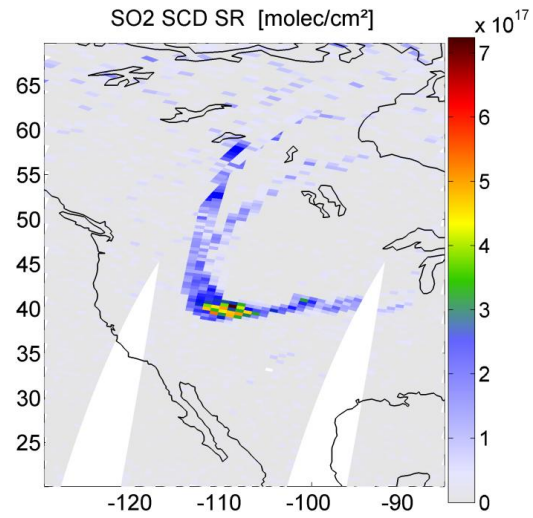
#278 Mt. Redoubt 11.03.2009



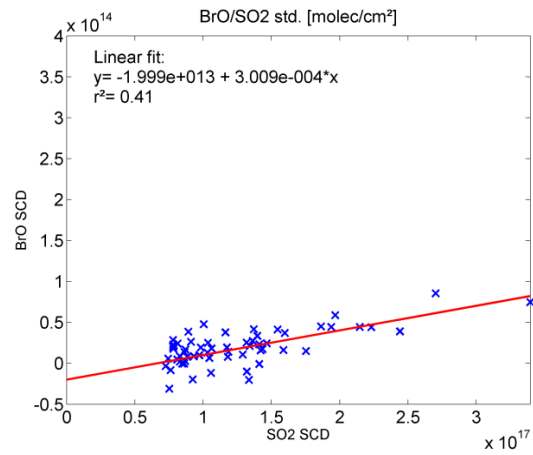
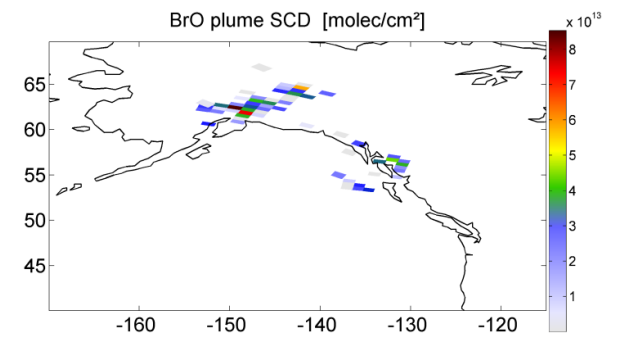
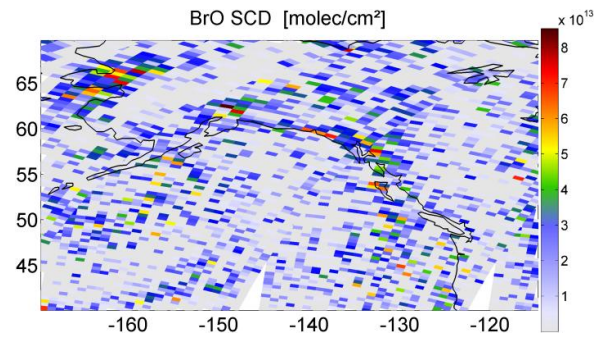
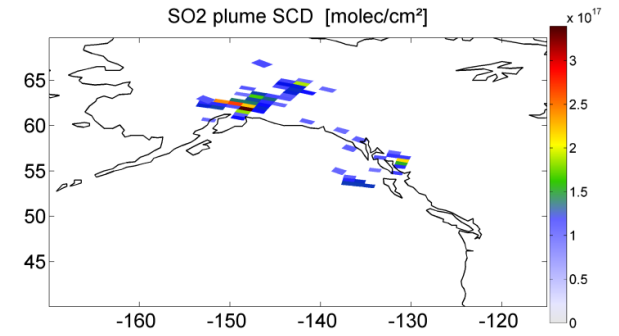
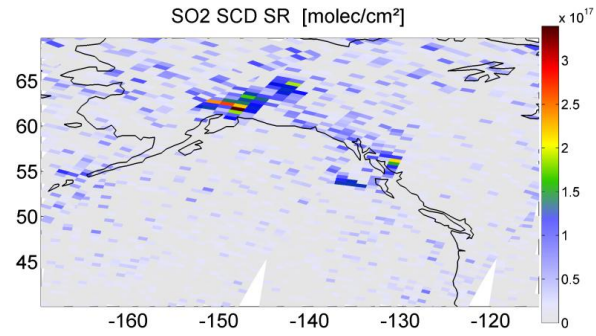
#279 Mt. Redoubt 24.03.2009



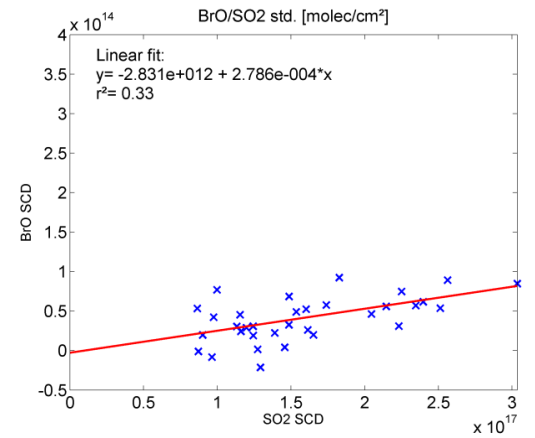
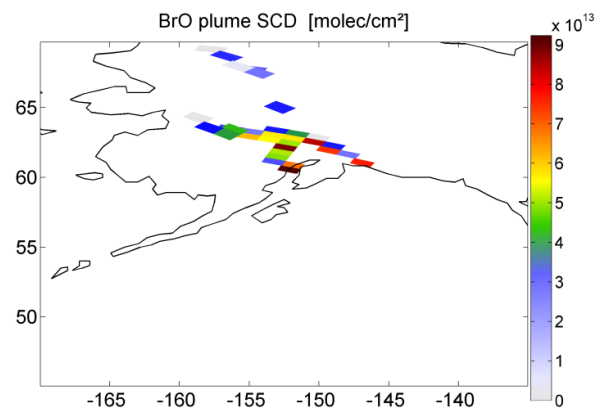
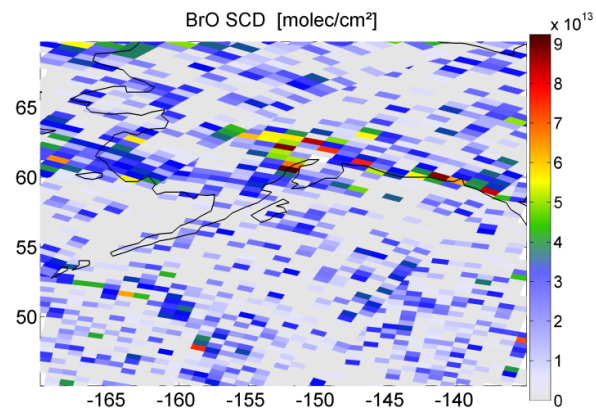
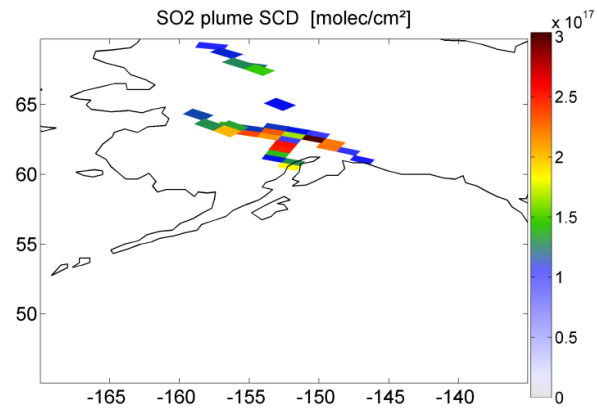
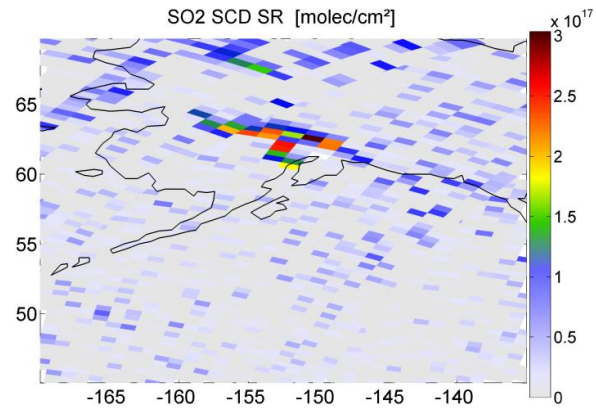
#281 Mt. Redoubt 26.03.2009



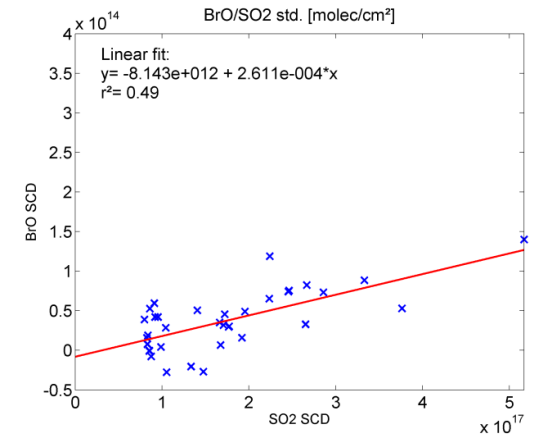
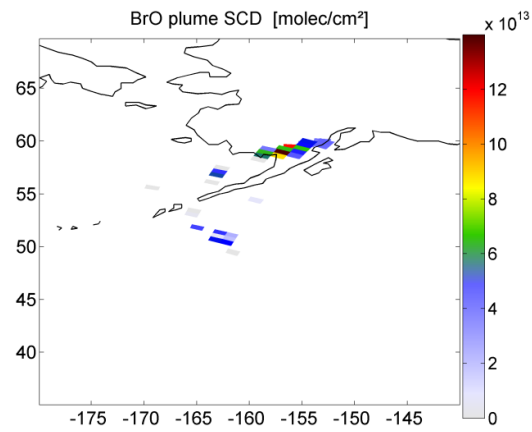
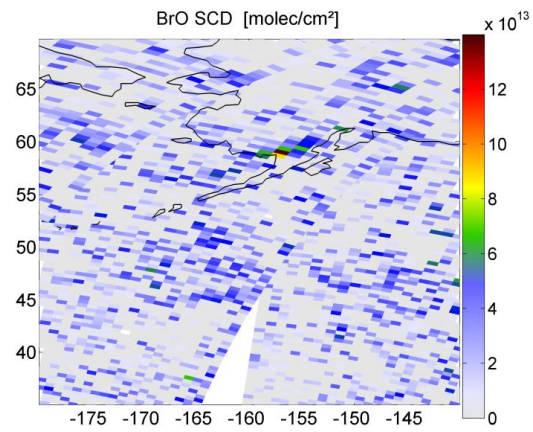
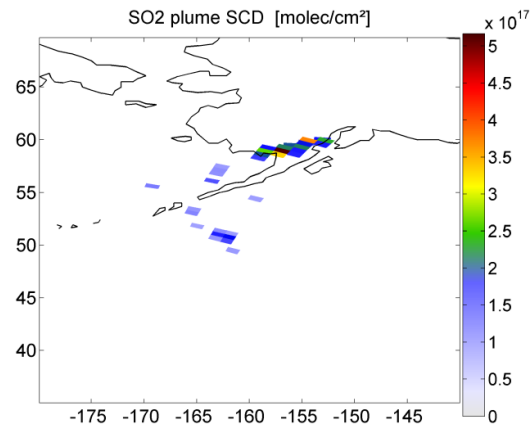
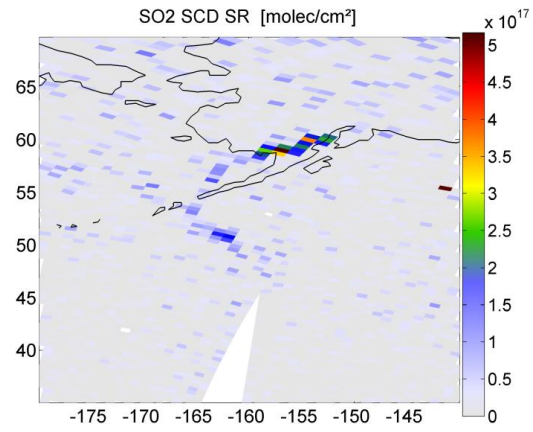
#306 Mt. Redoubt 09.04.2009



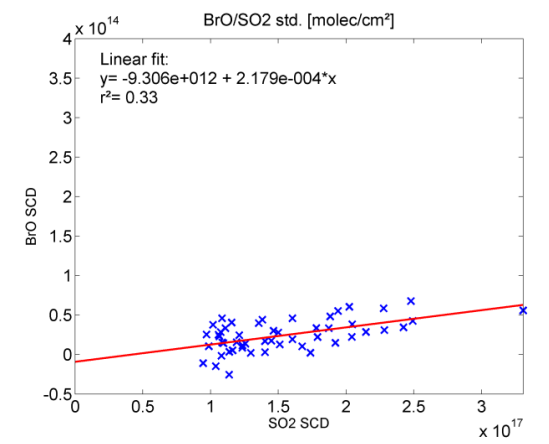
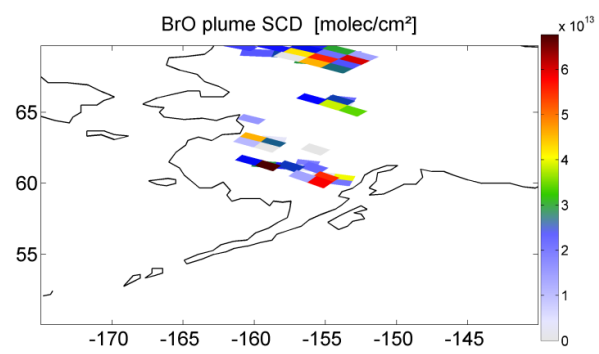
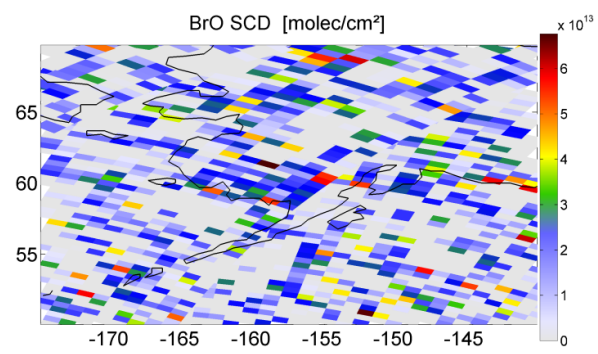
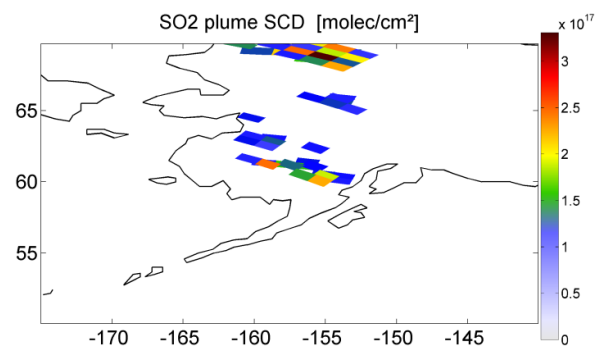
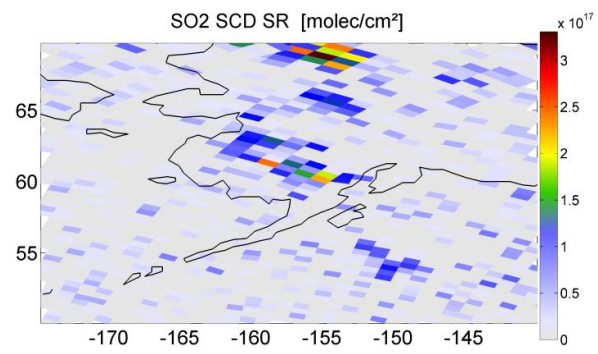
#312 Mt. Redoubt 13.04.2009



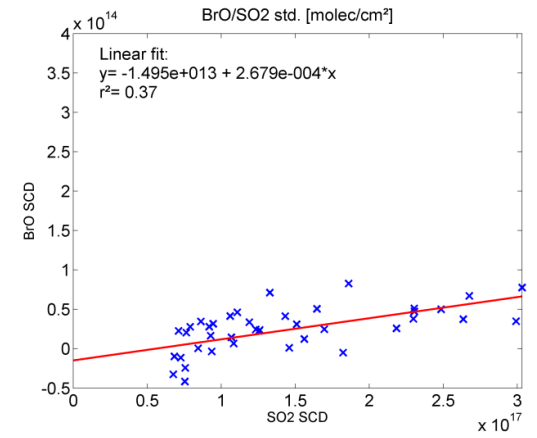
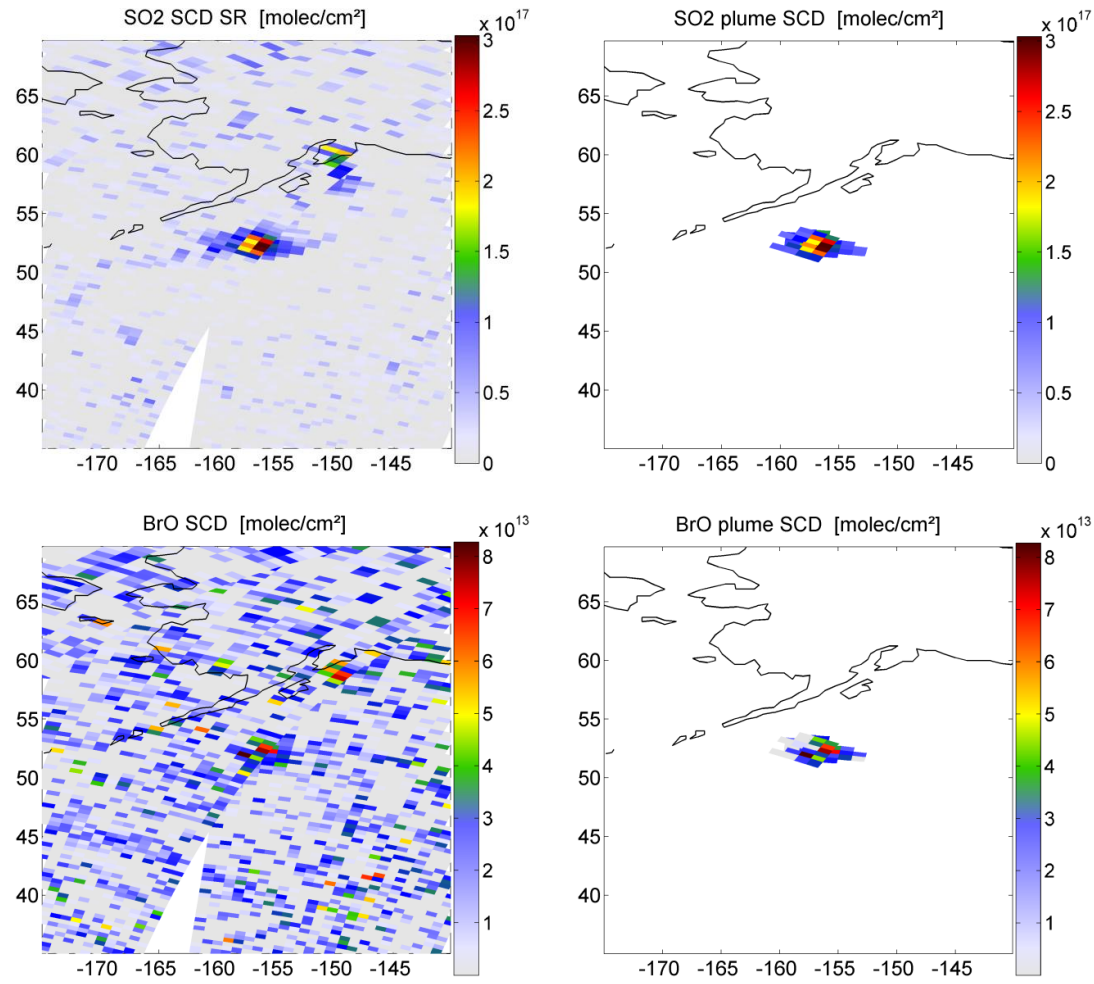
#317 Mt. Redoubt 16.04.2009



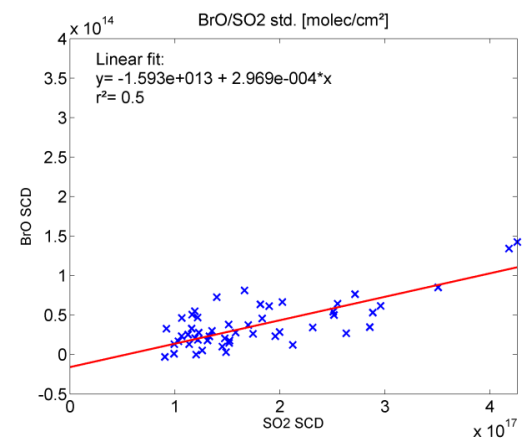
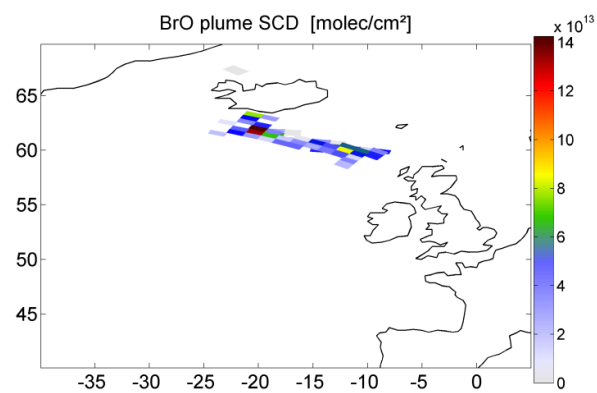
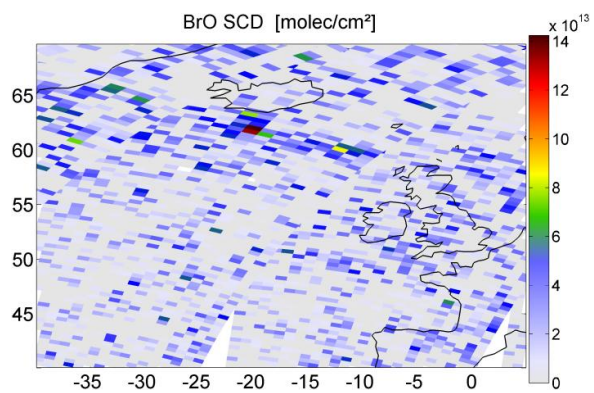
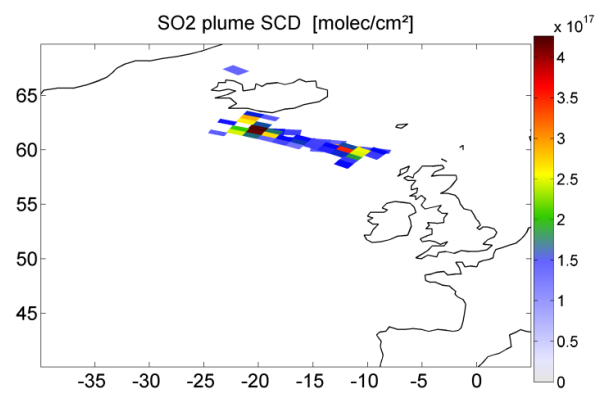
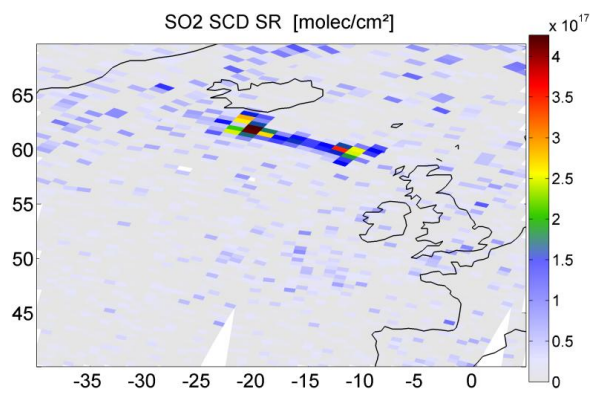
#324 Mt. Redoubt 19.04.2009



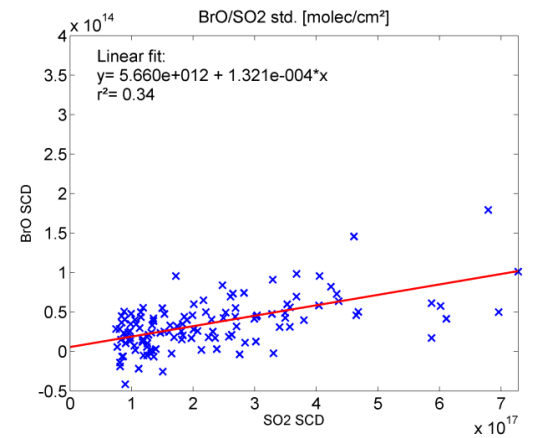
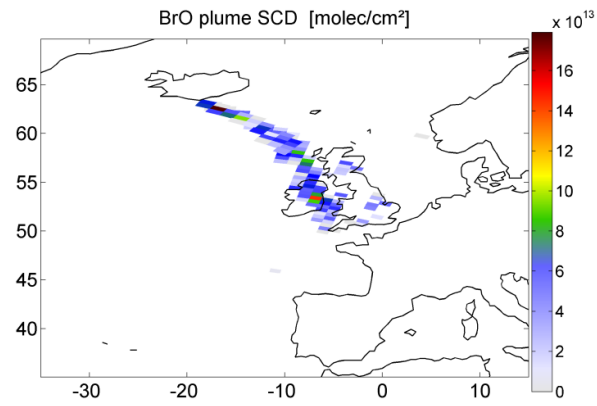
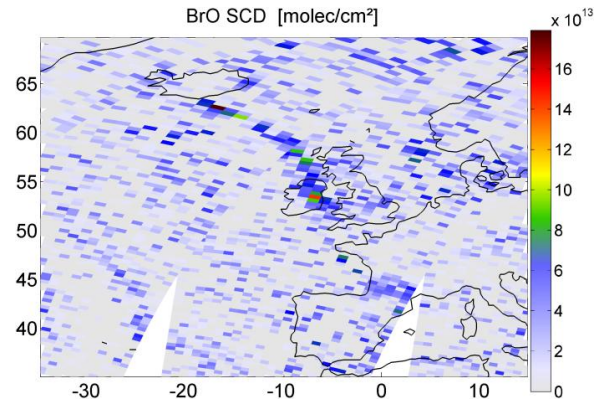
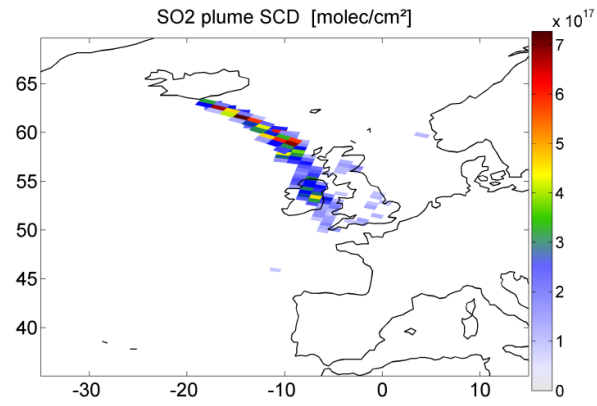
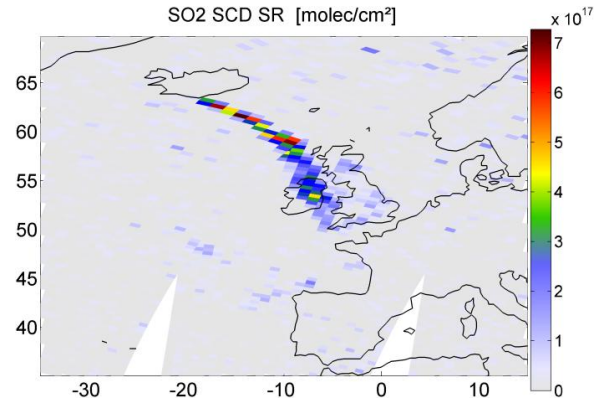
#344 Mt. Redoubt 05.05.2009



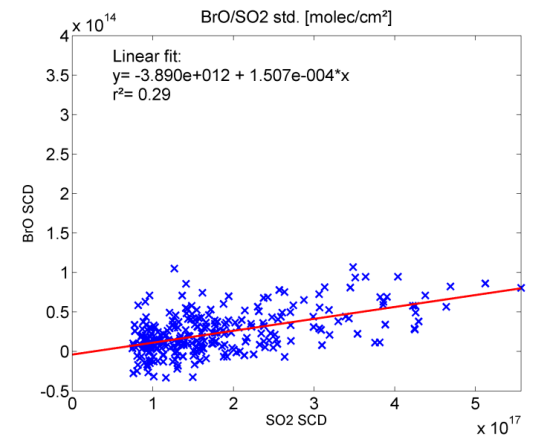
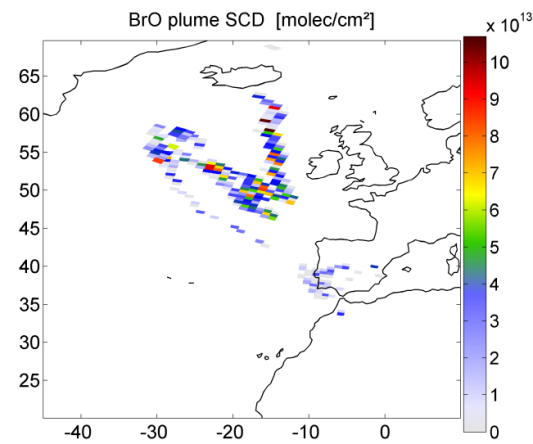
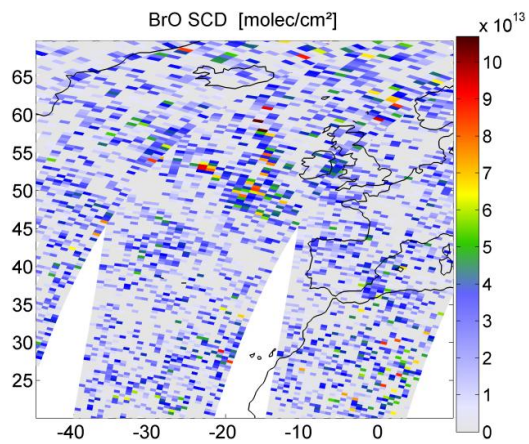
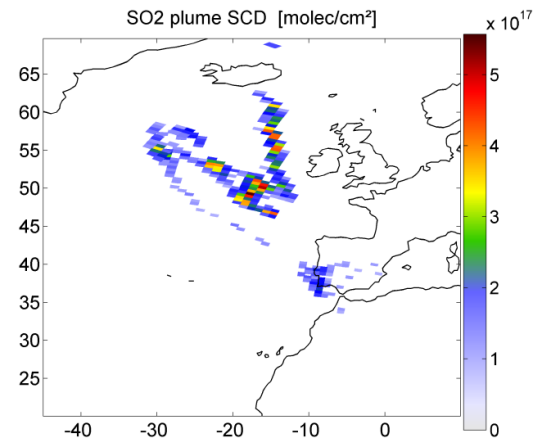
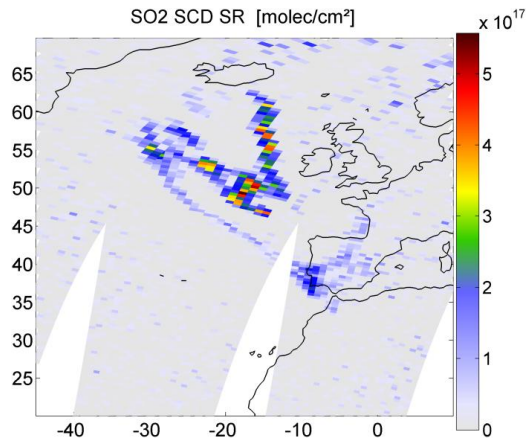
#551 Eyjafjallajökull 30.04.2010



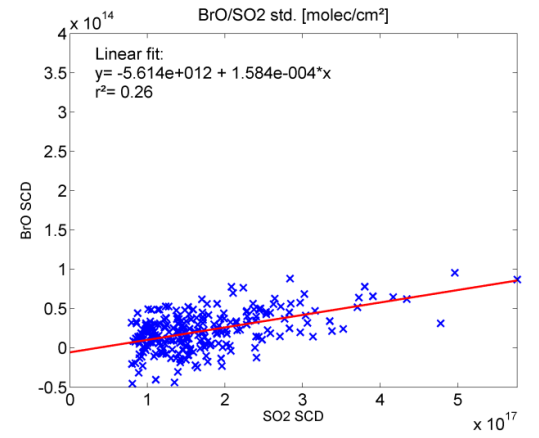
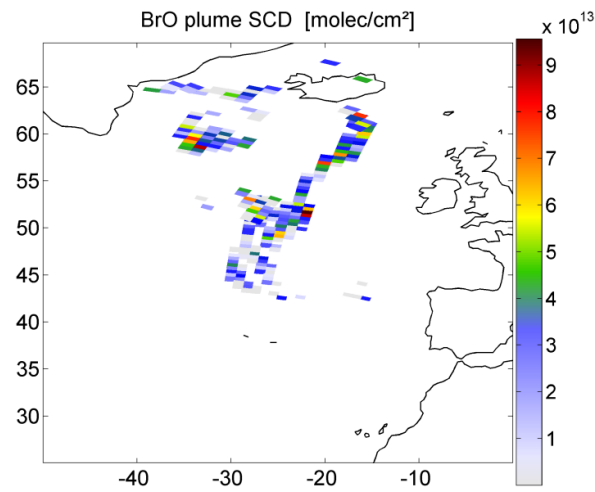
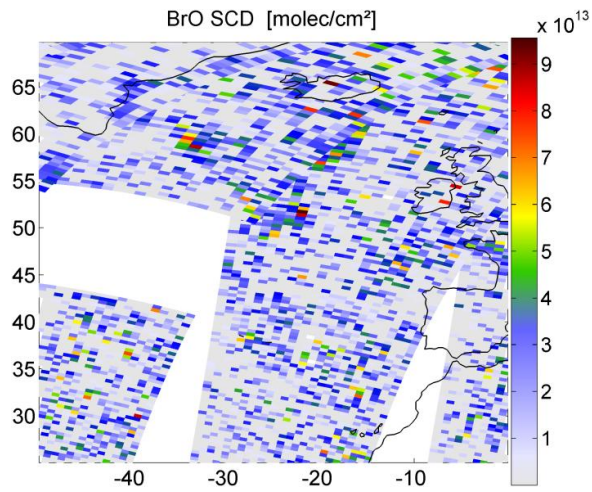
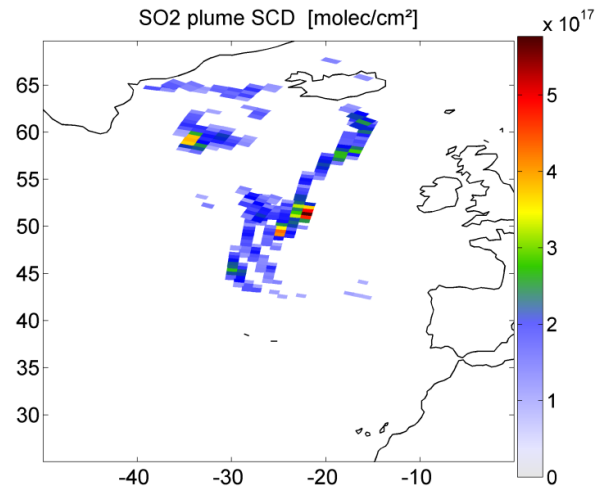
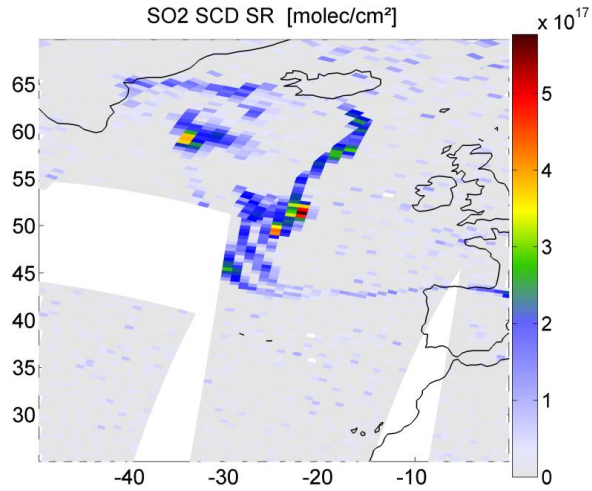
#555 Eyjafjallajökull 05.05.2010



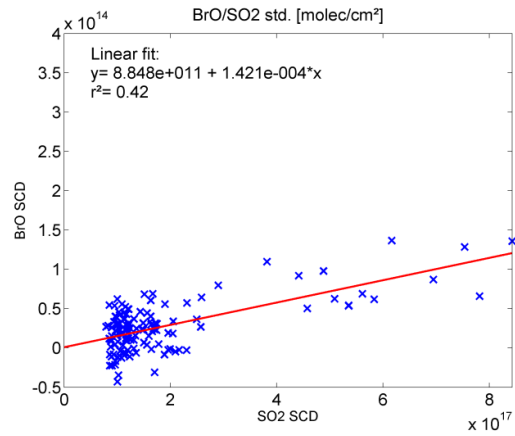
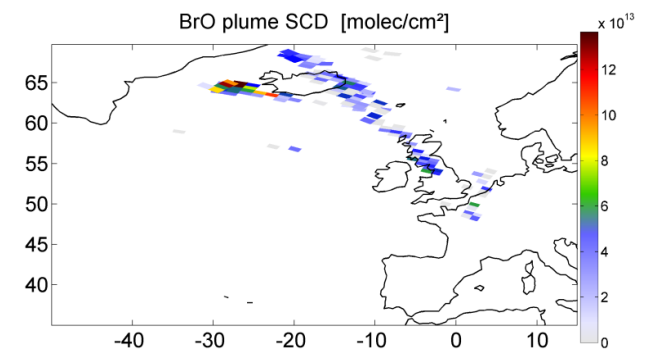
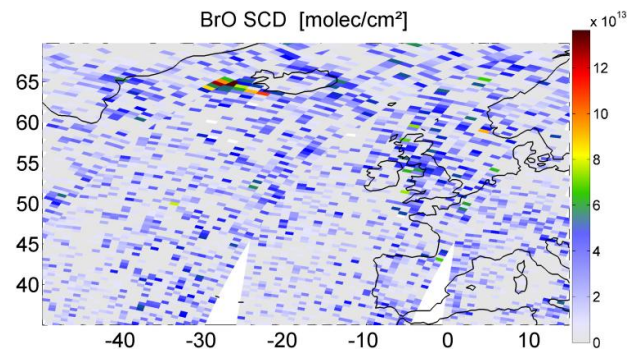
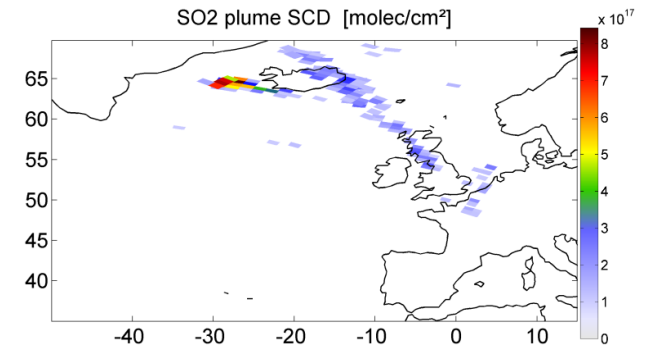
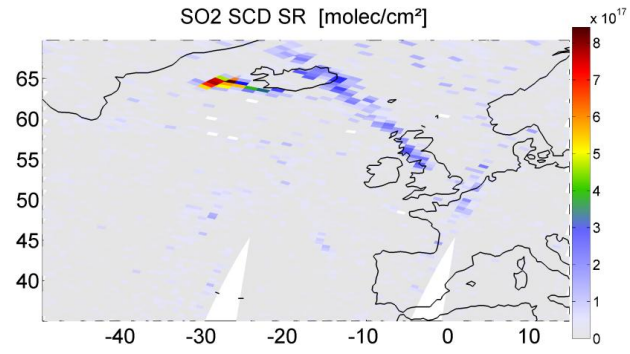
#557 Eyjafjallajökull 07.05.2010



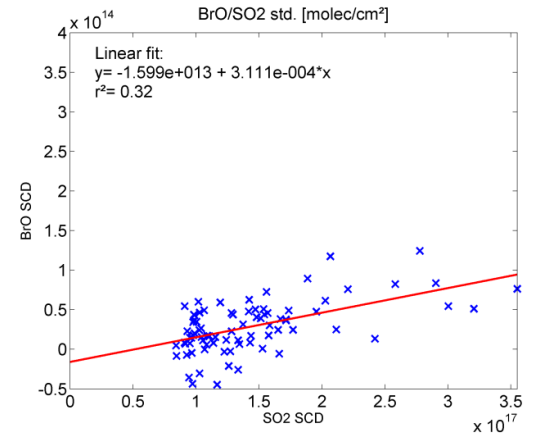
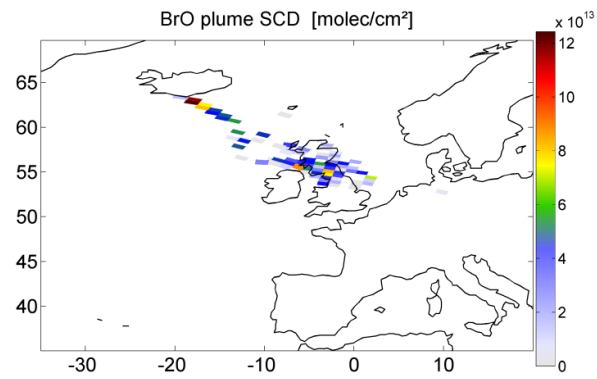
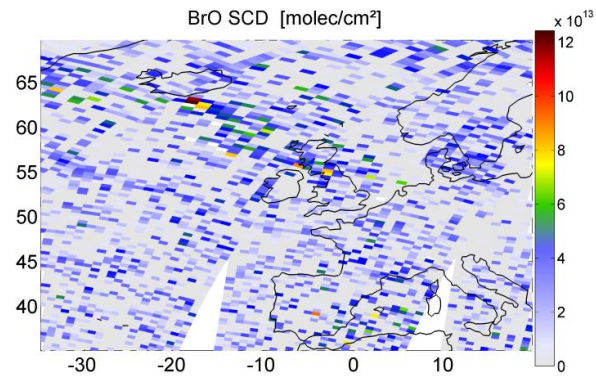
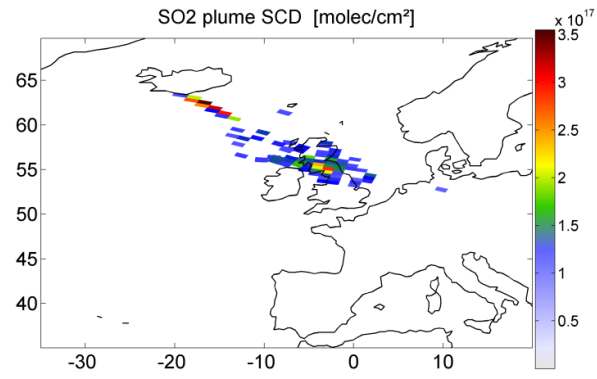
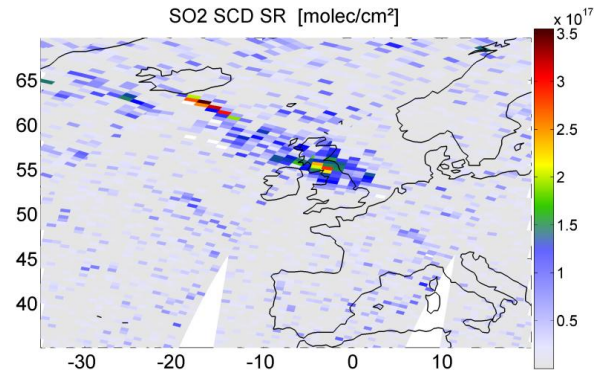
#558 Eyjafjallajökull 08.05.2010



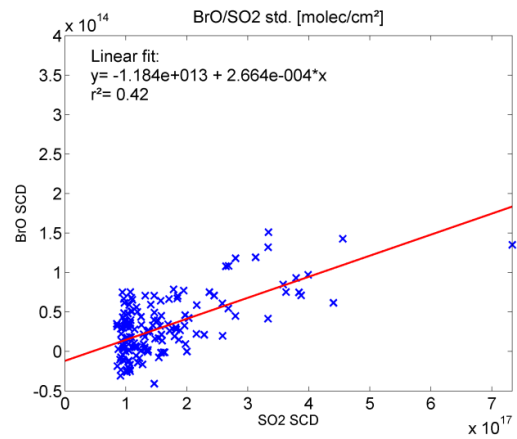
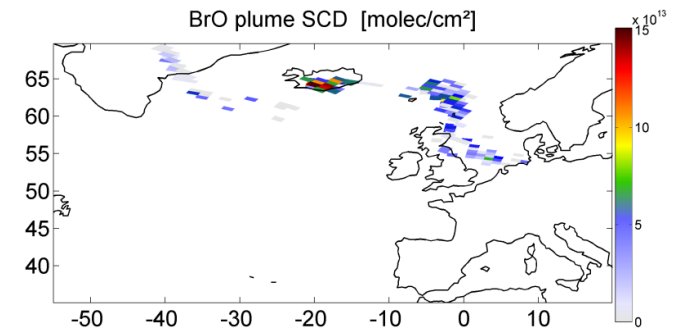
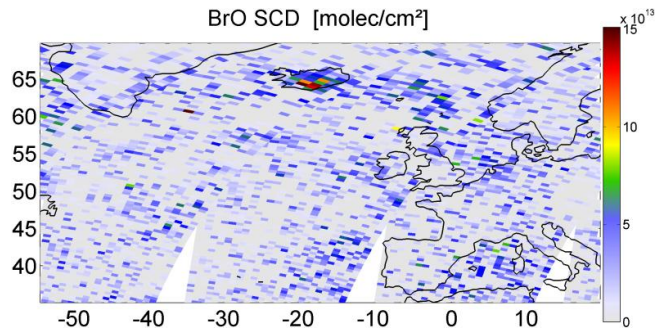
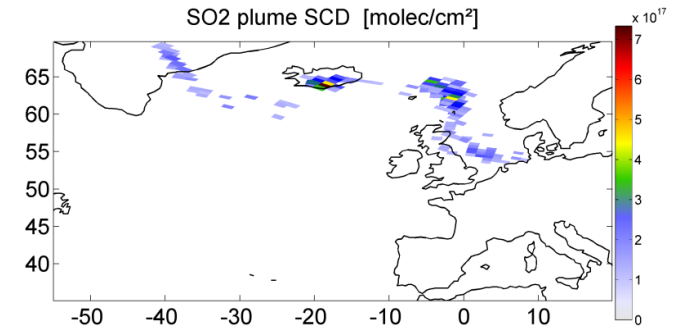
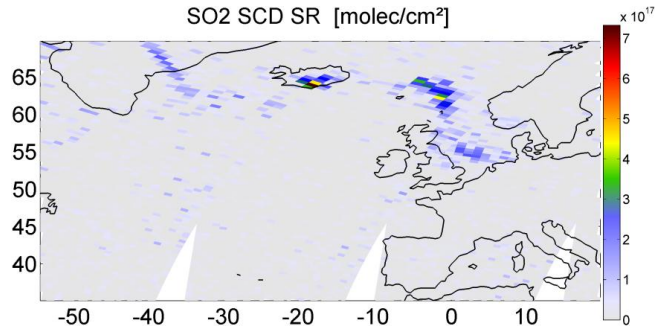
#568 Eyjafjallajökull 14.05.2010



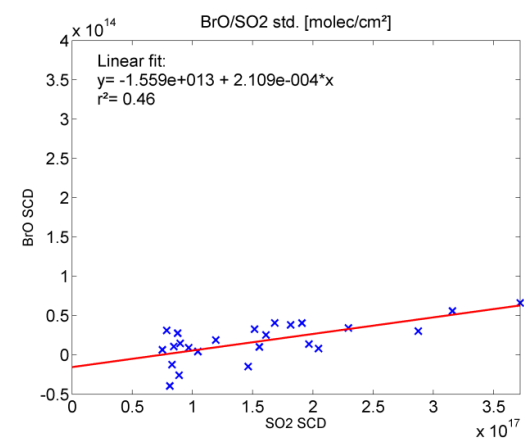
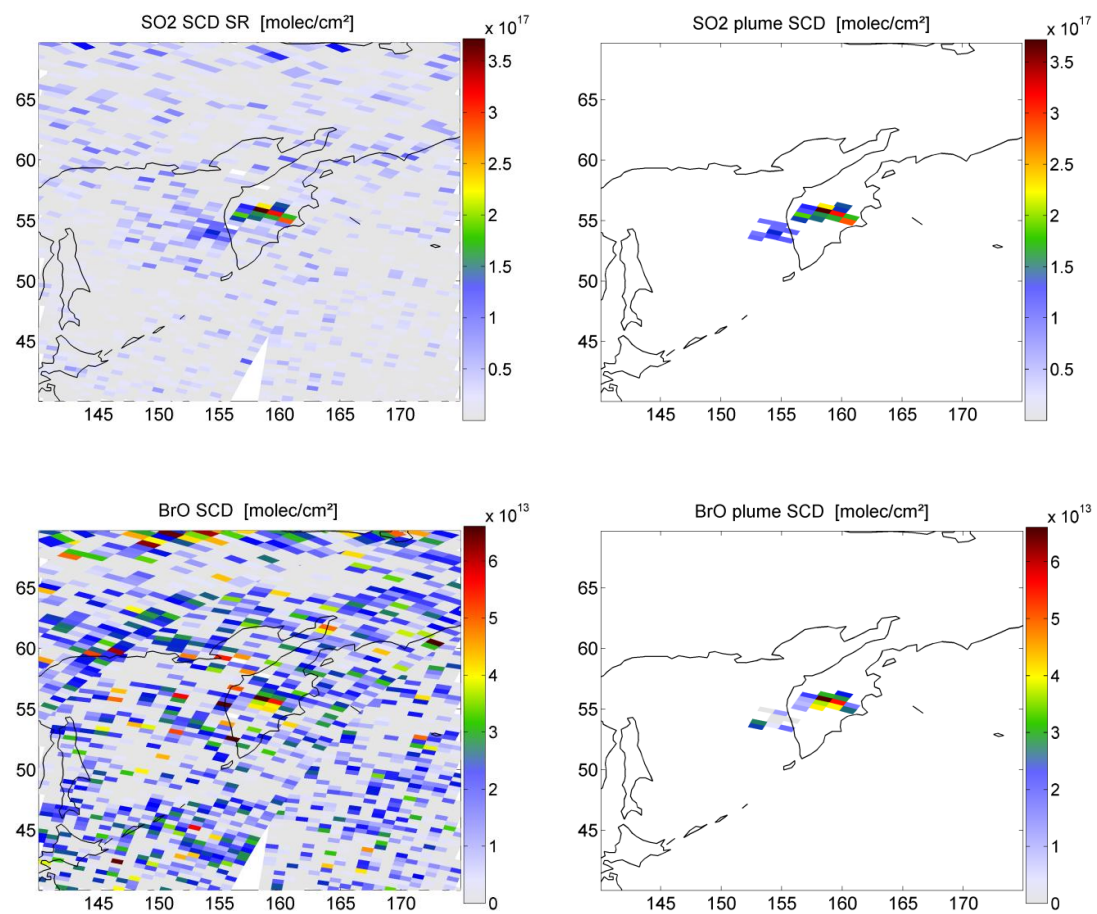
#570 Eyjafjallajökull 16.05.2010



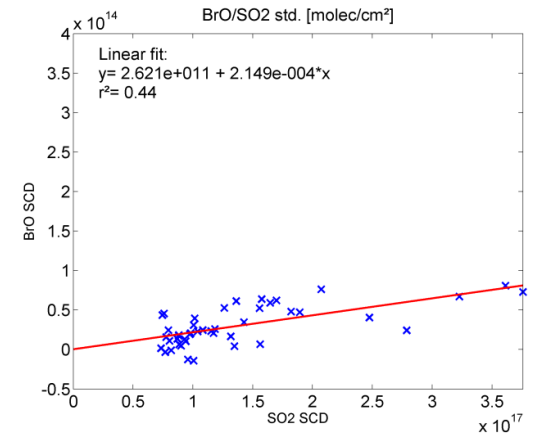
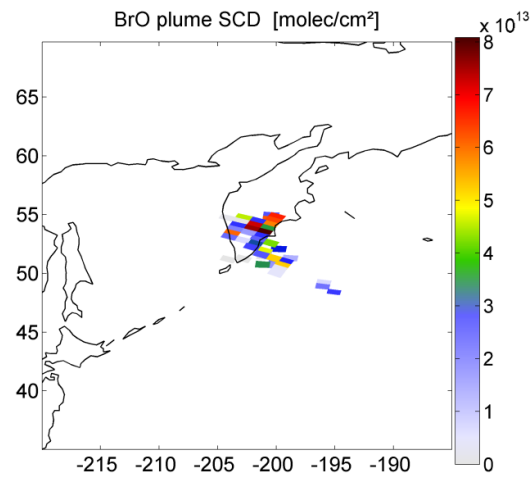
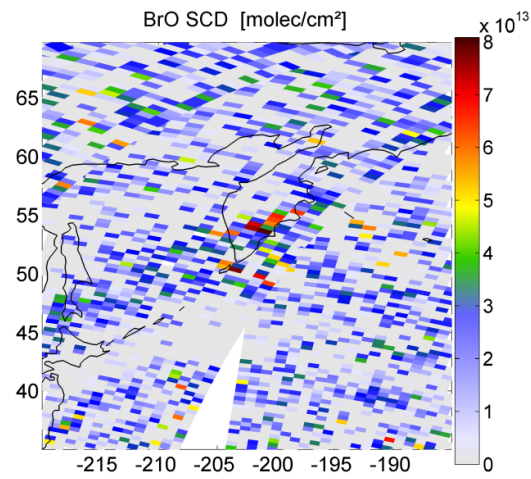
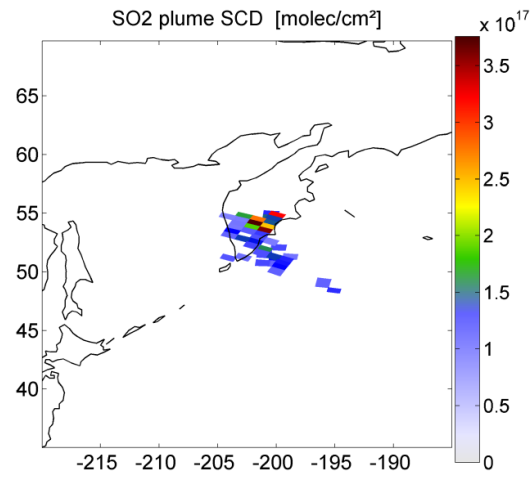
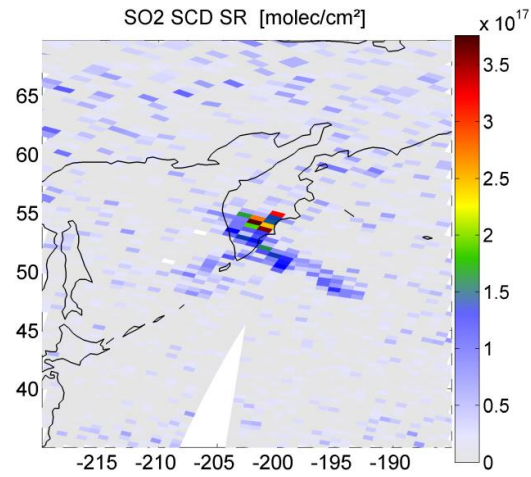
#572 Eyjafjallajökull 17.05.2010



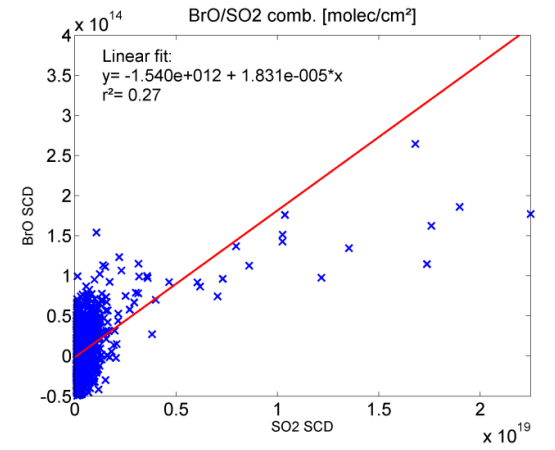
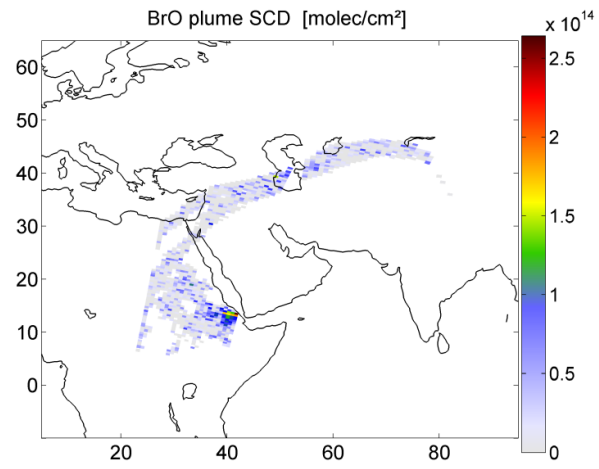
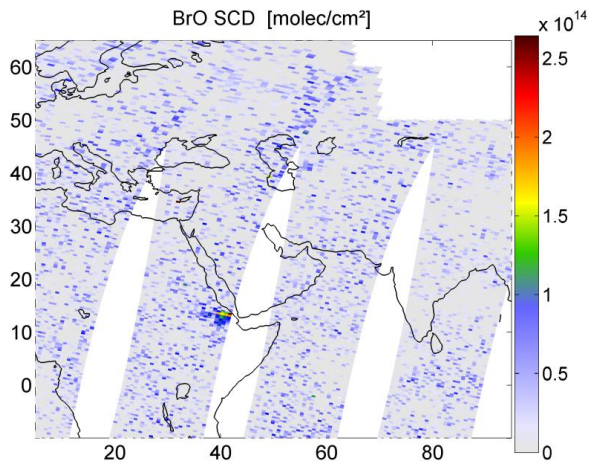
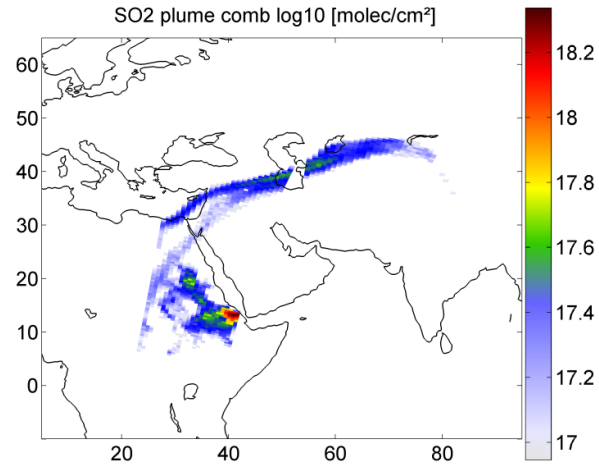
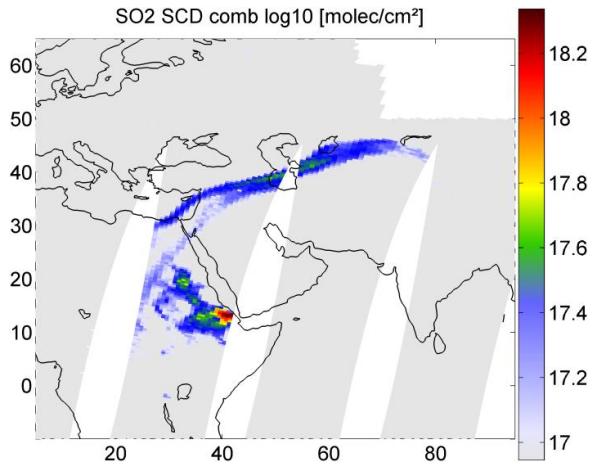
#696 Kizimen 03.05.2011



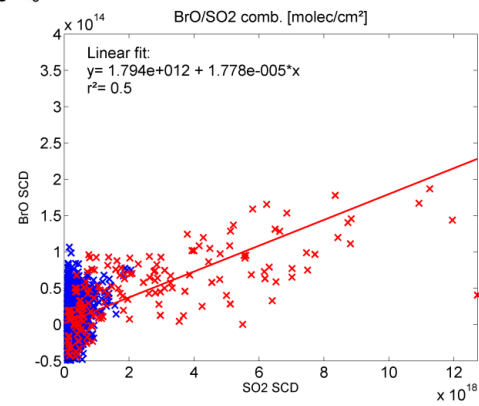
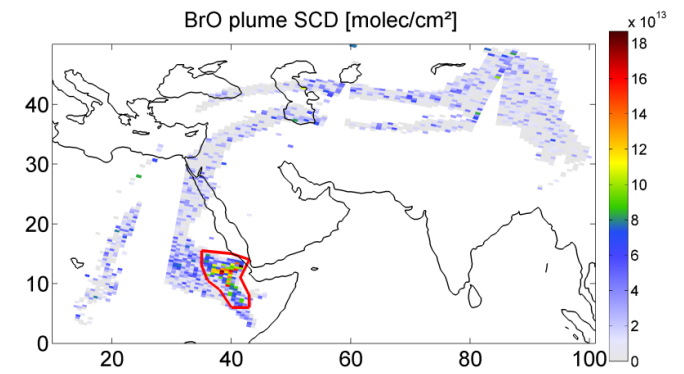
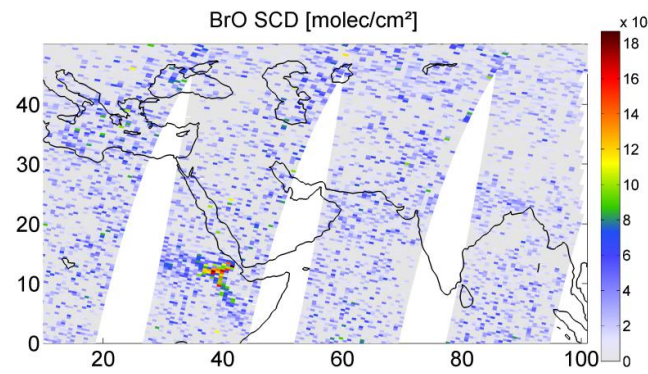
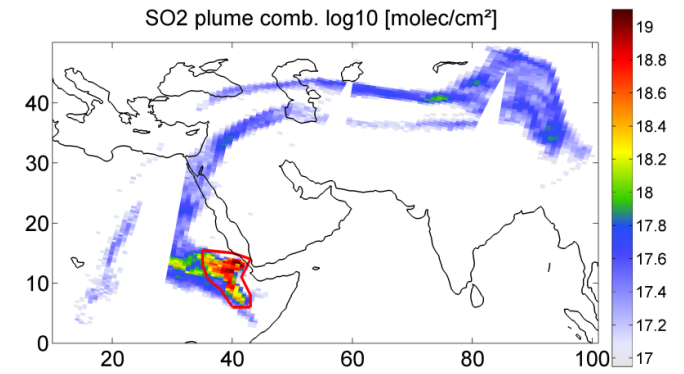
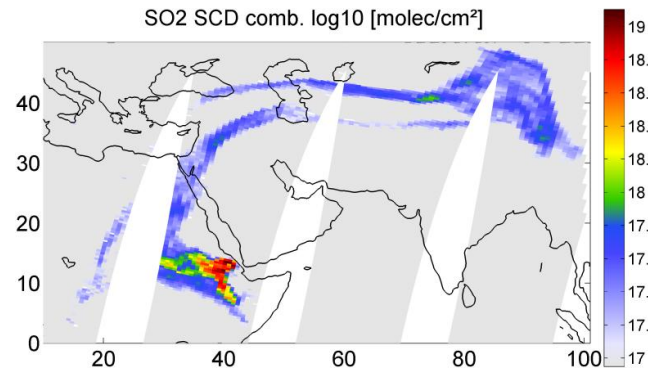
#706 Karymsky 21./22.05.2011



#748 Nabro 15.06.2011

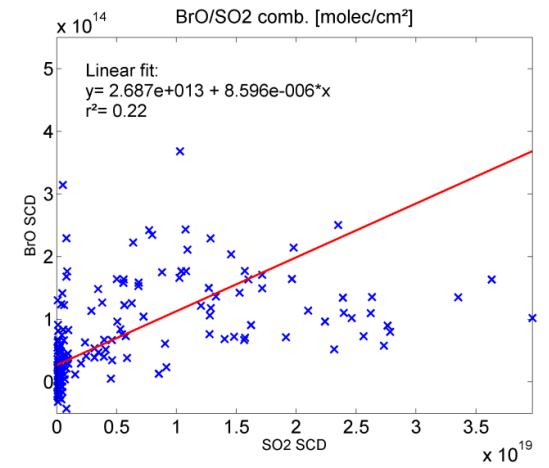
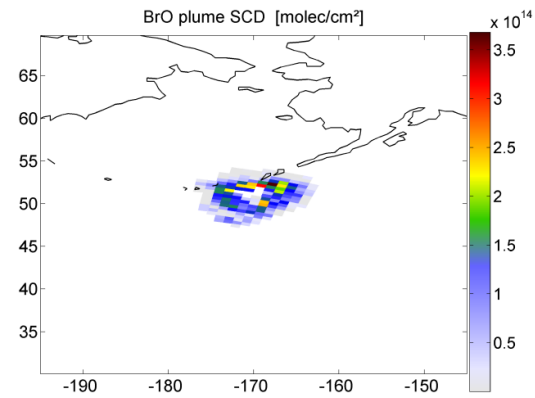
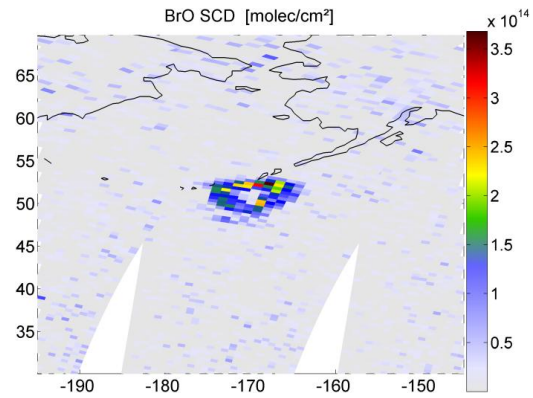
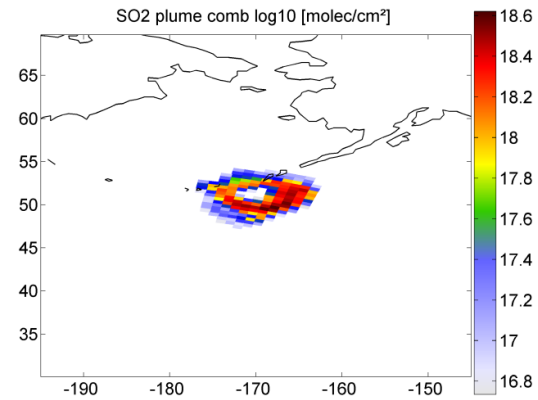
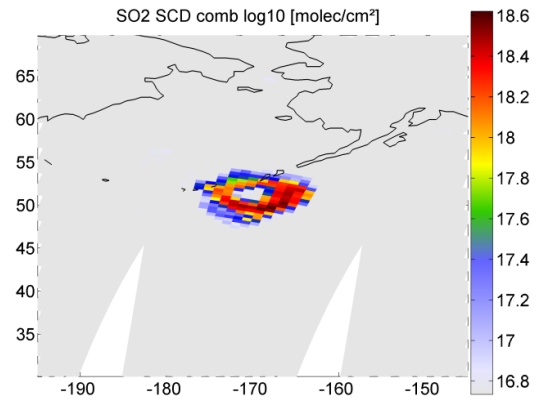


#749 Nabro 16.06.2011

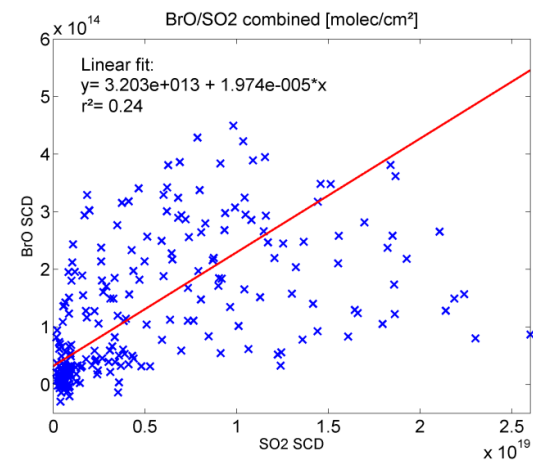
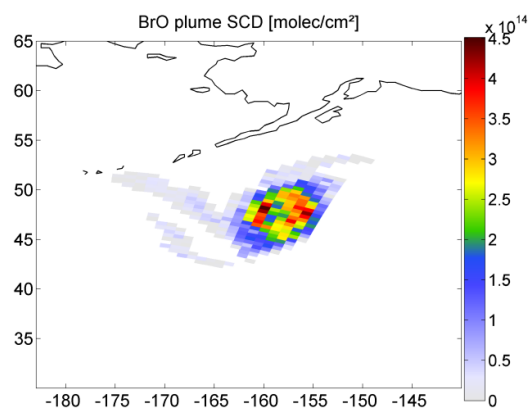
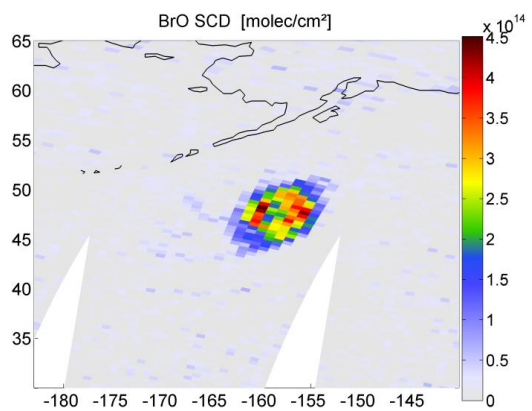
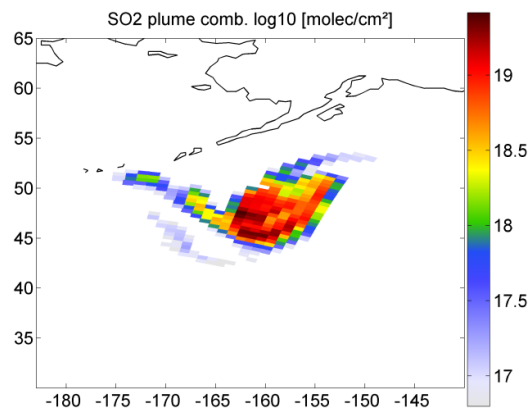
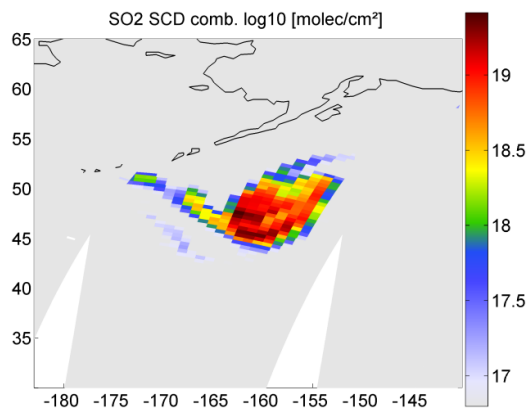


## Category III

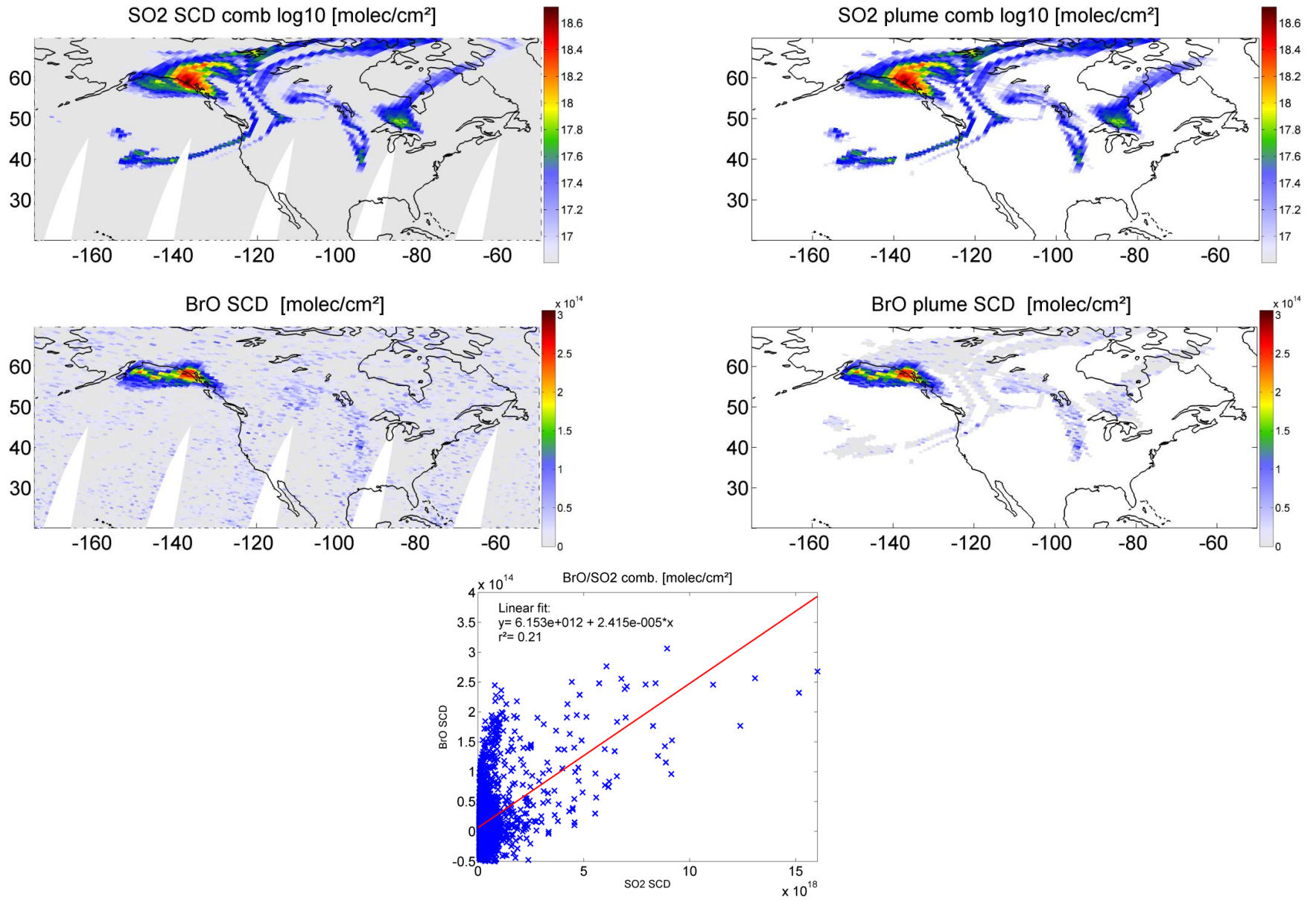
#160 Kasatochi 08.08.2008



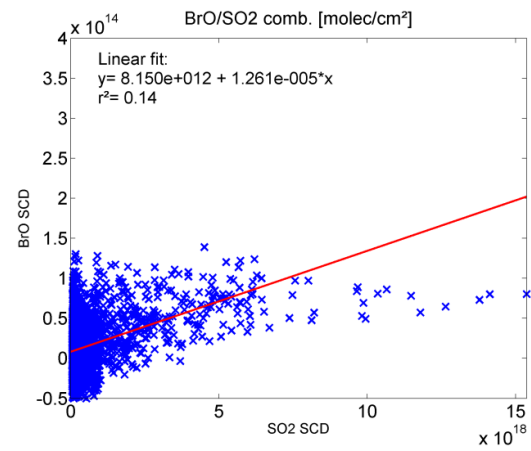
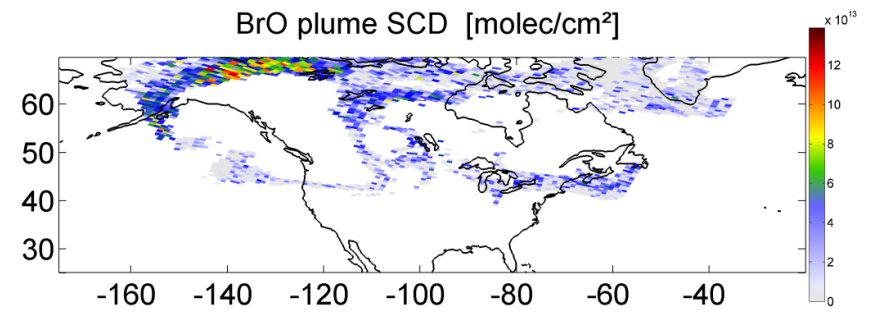
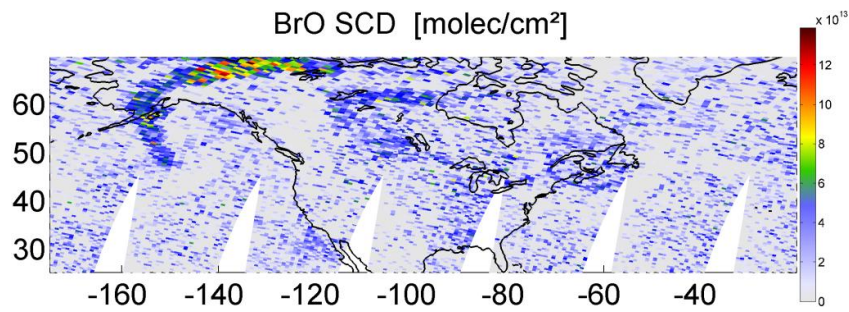
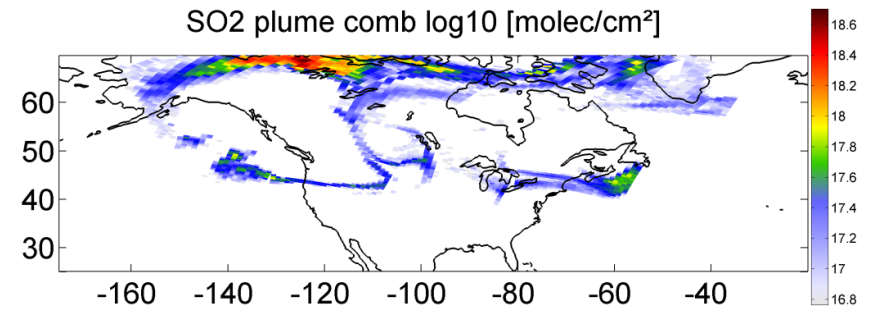
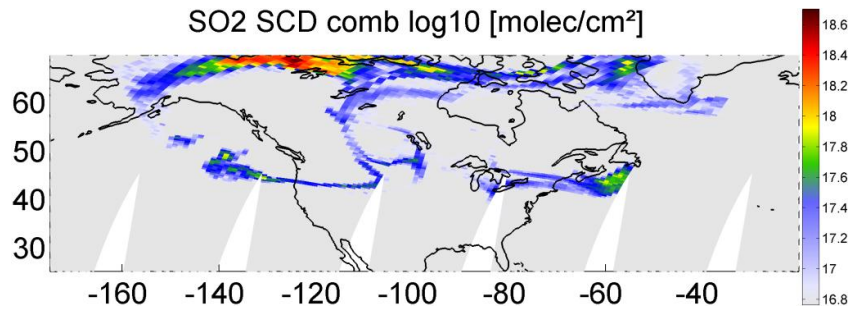
#162 Kasatochi 09.08.2008



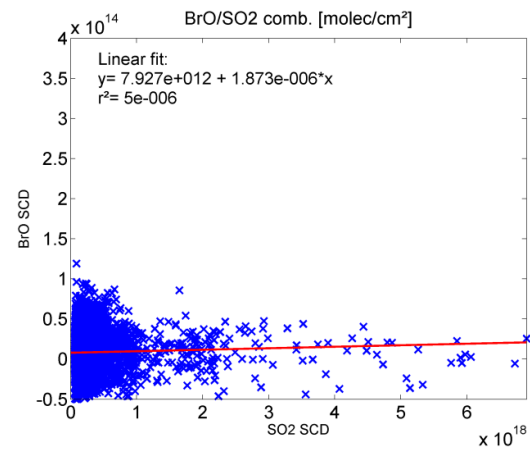
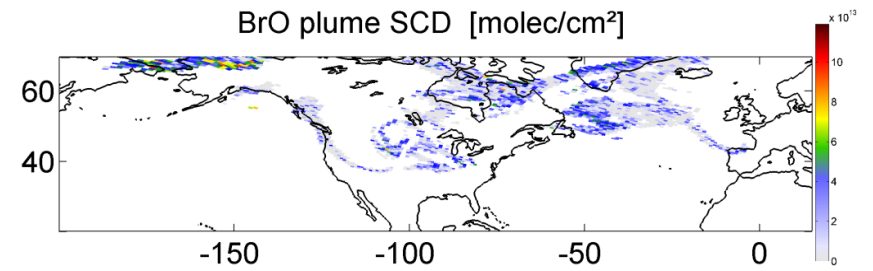
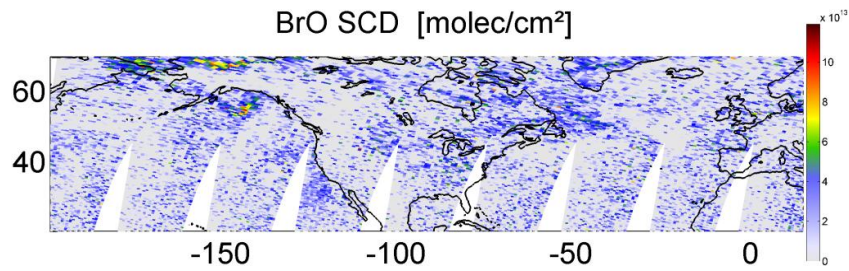
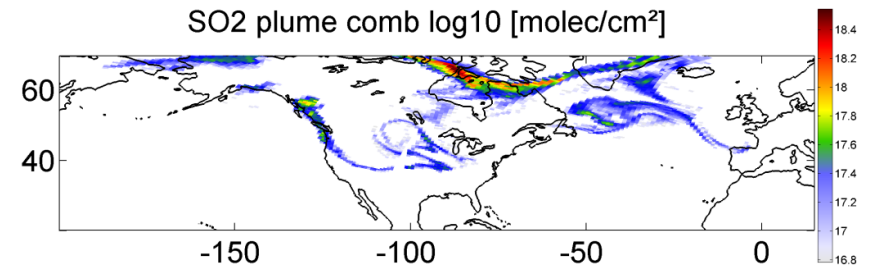
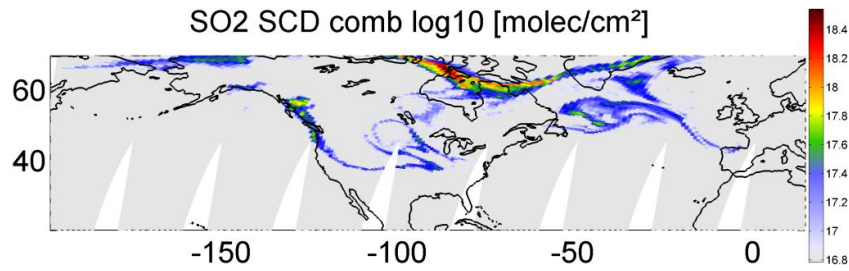
#165 Kasatochi 12.08.2008



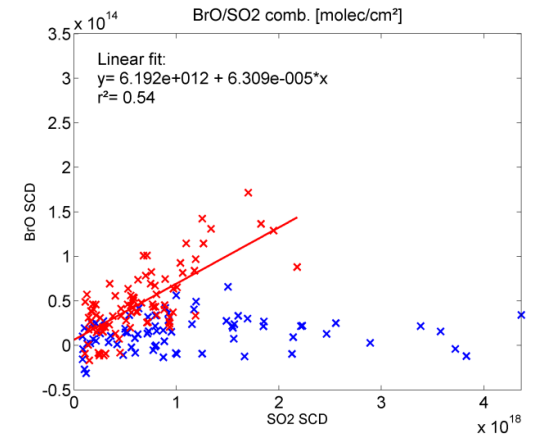
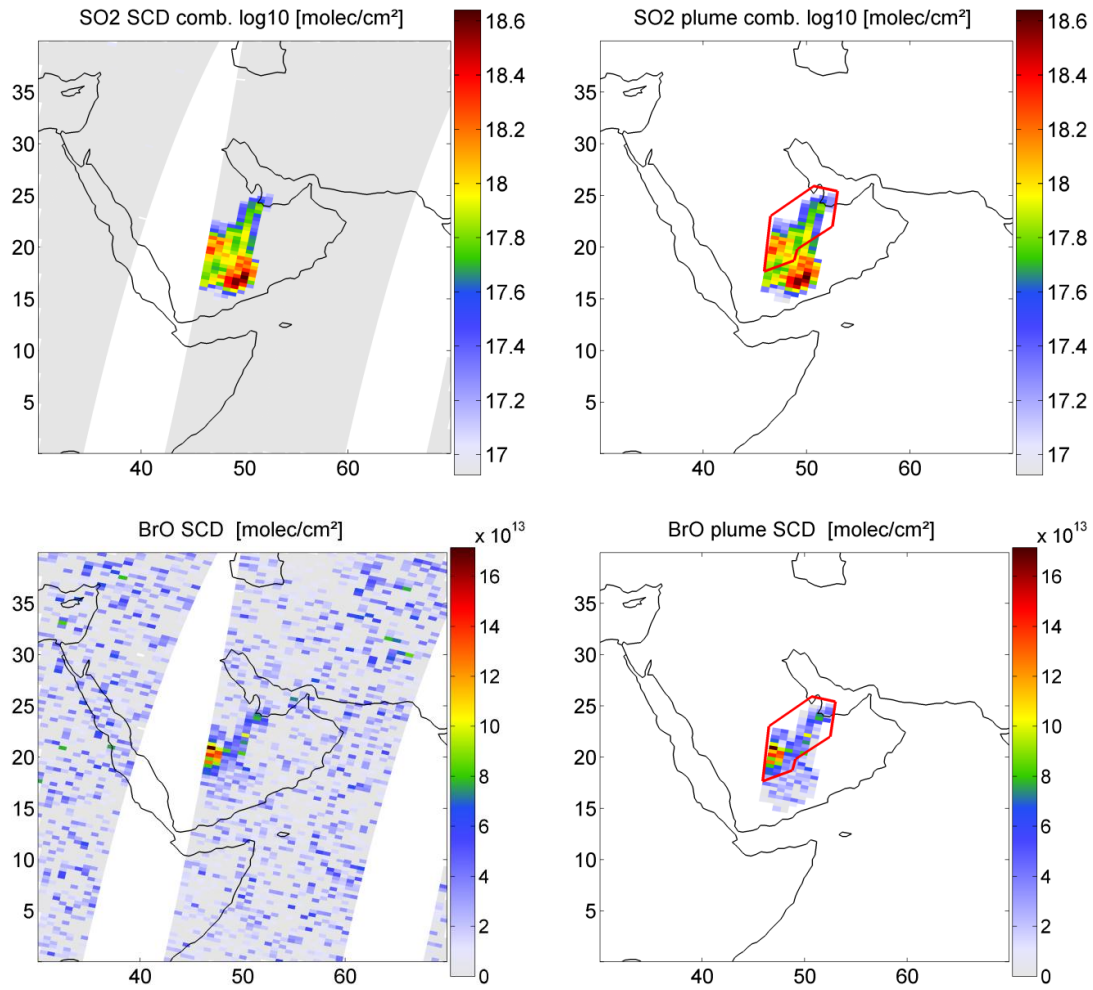
#167 Kasatochi 13.08.2008



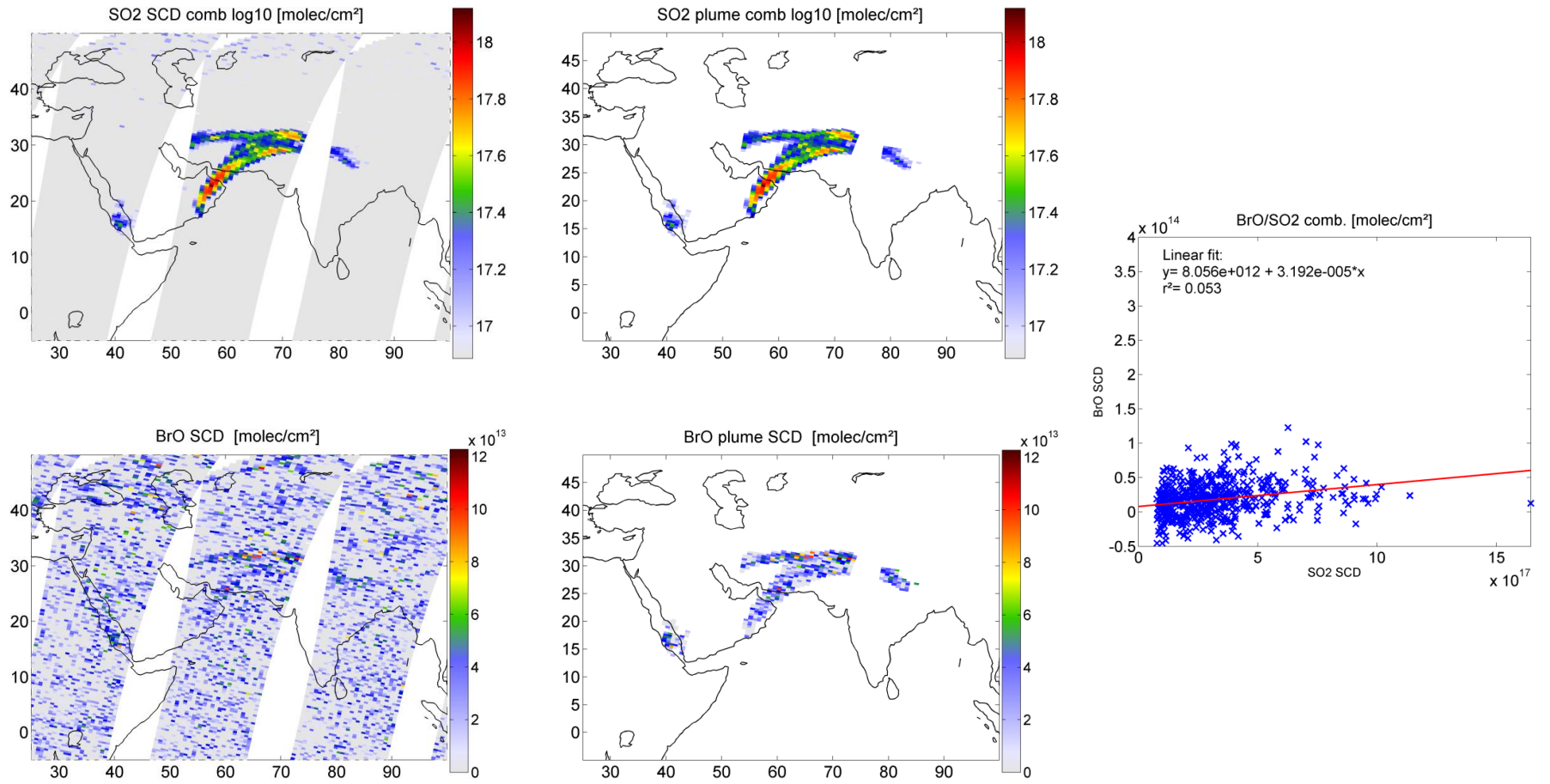
#169 Kasatochi 14.08.2008



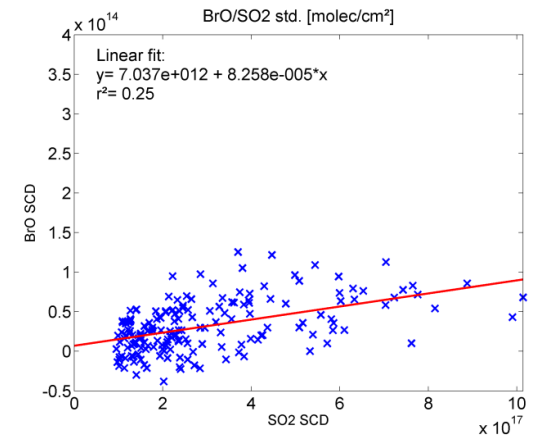
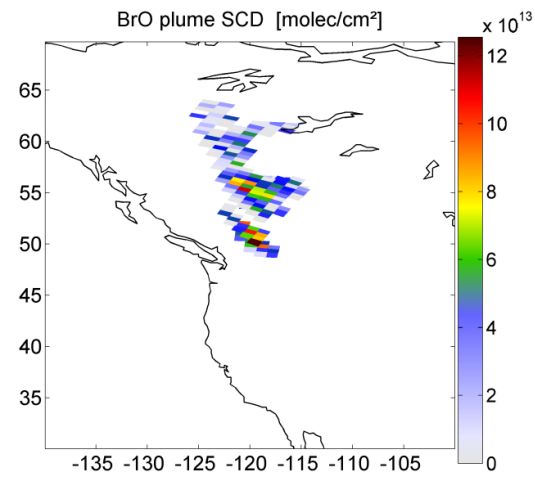
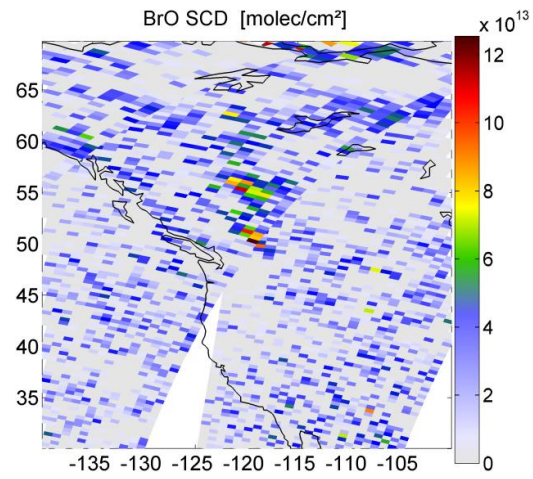
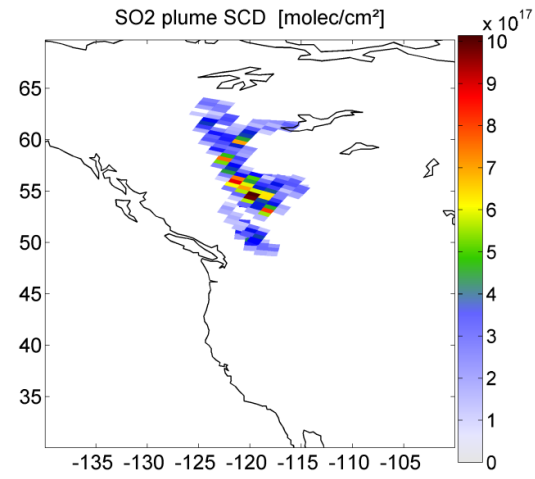
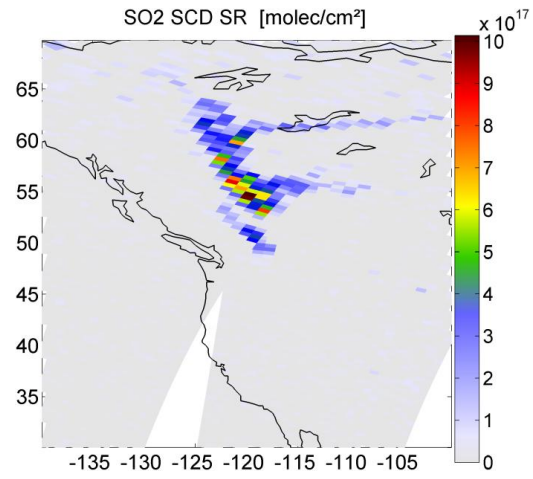
#249 Dalaffilla 04.11.2008



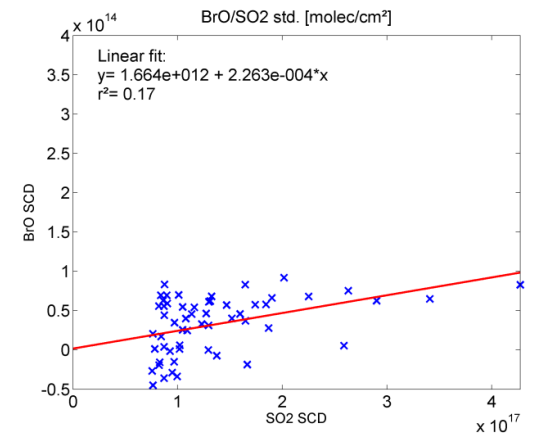
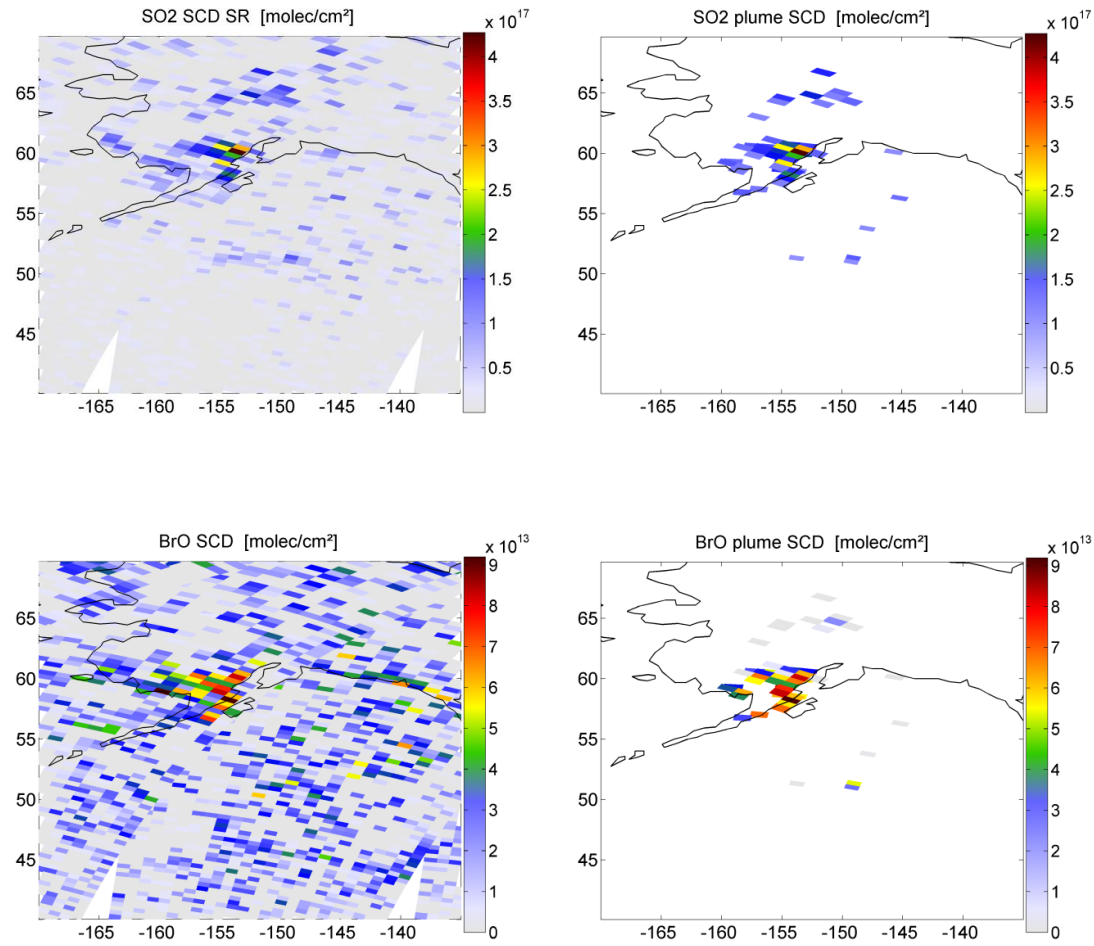
#250 Dalaffilla 05.11.2008



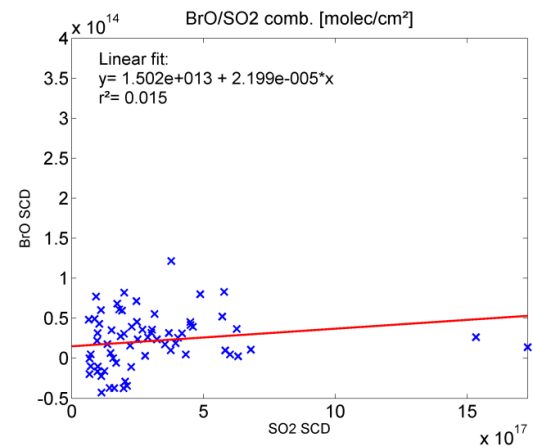
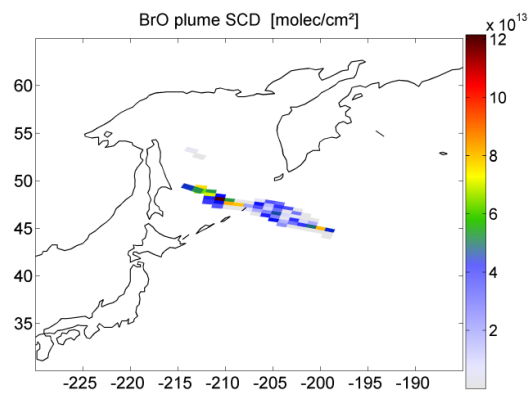
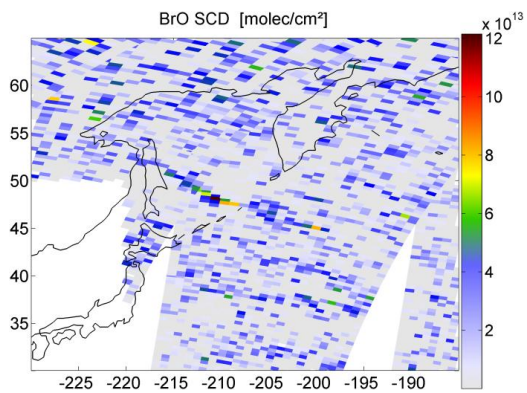
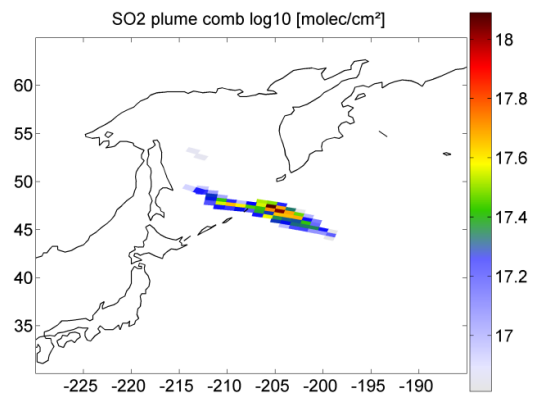
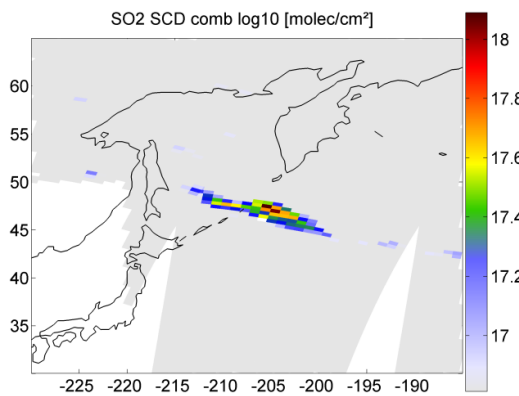
#280 Mt. Redoubt 25.03.2009



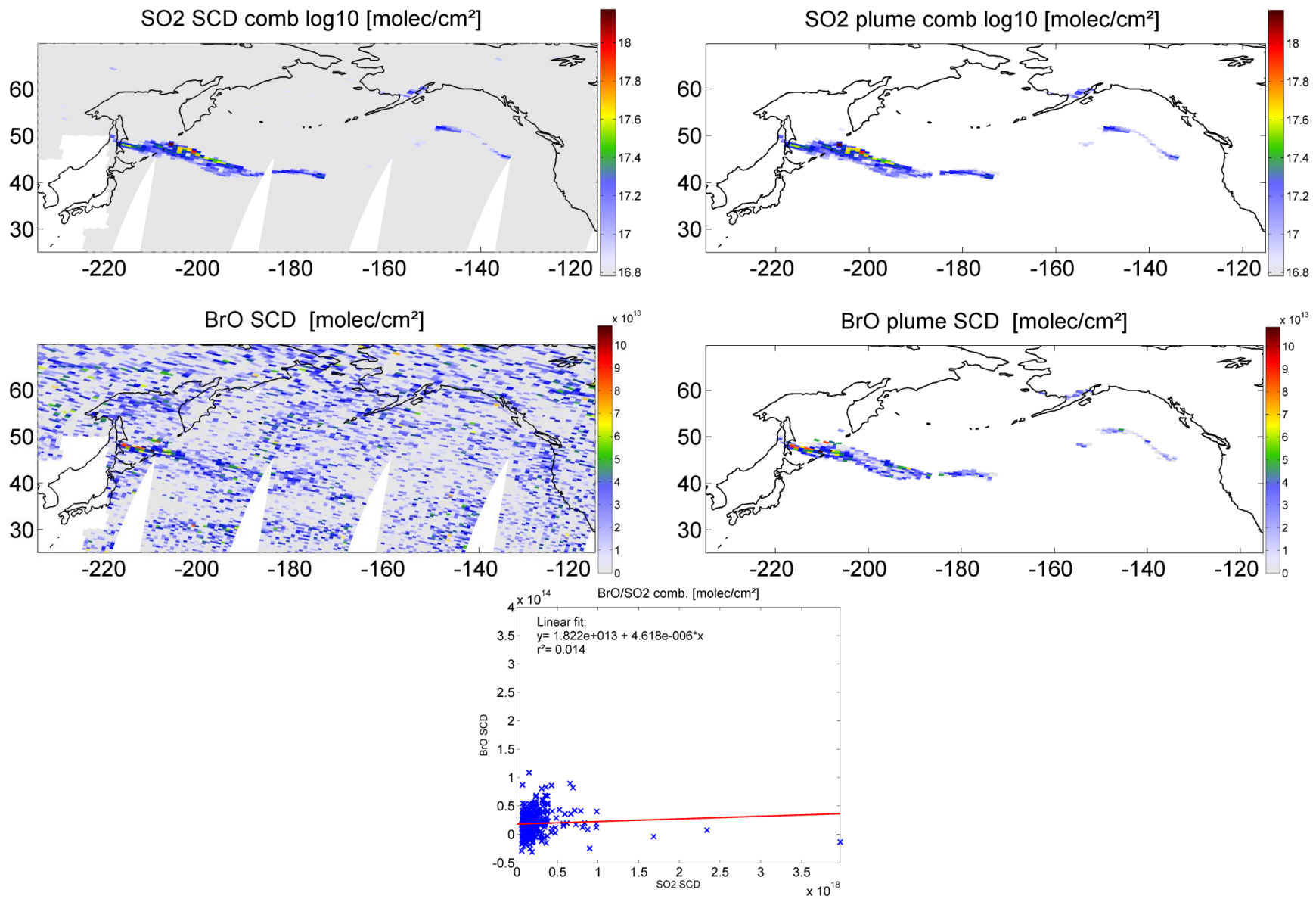
#326 Mt. Redoubt 20.04.2009



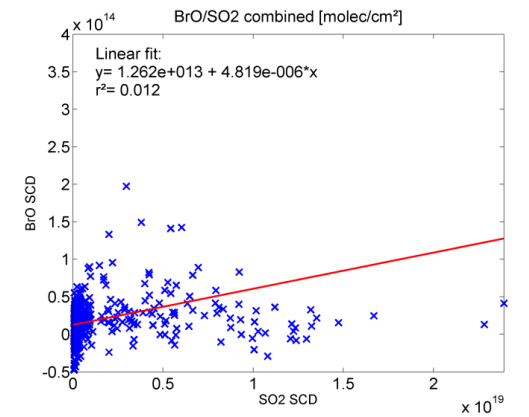
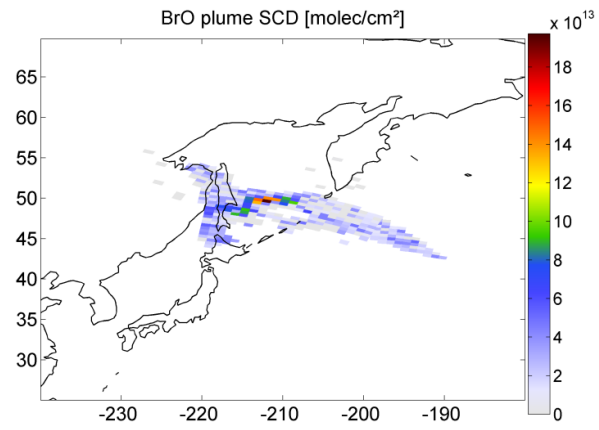
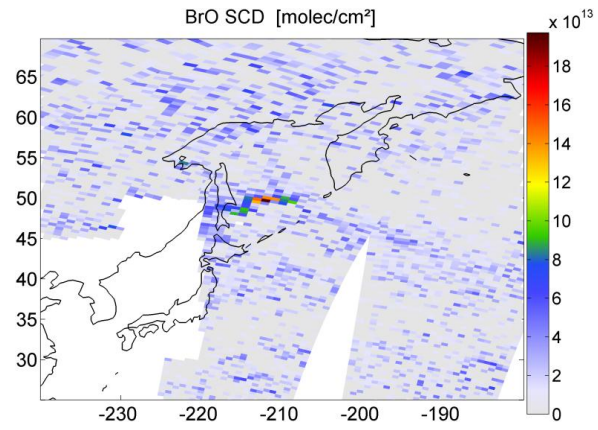
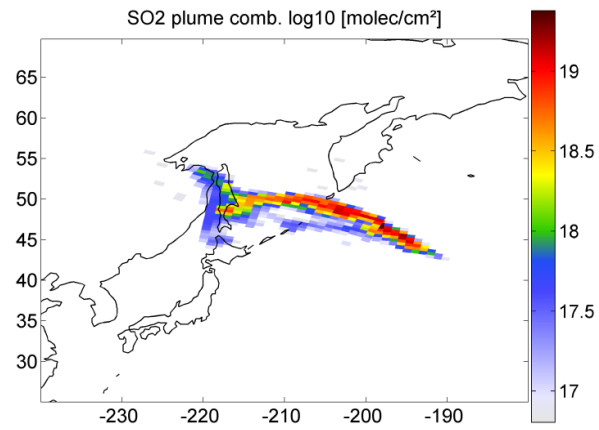
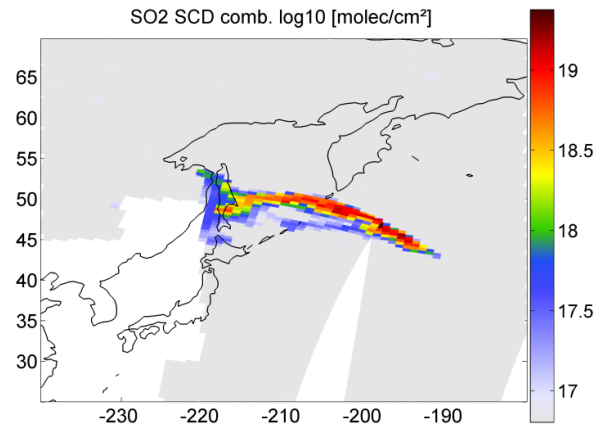
#369 Sarychev 12./13.06.2009



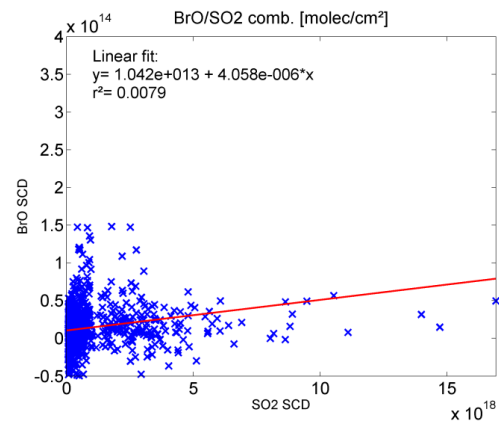
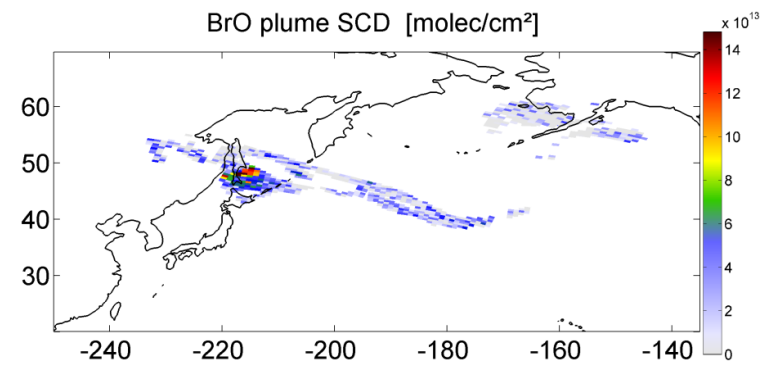
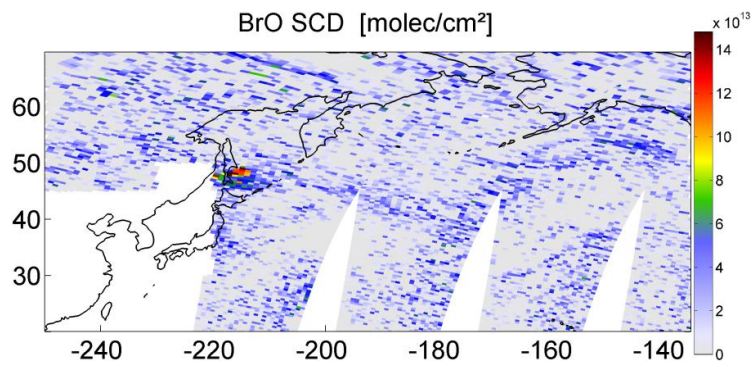
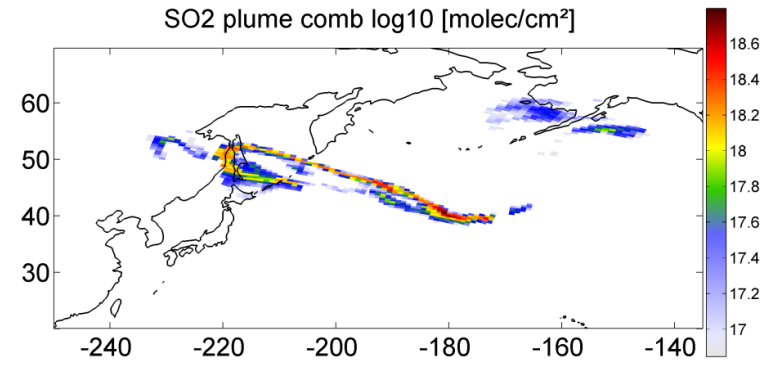
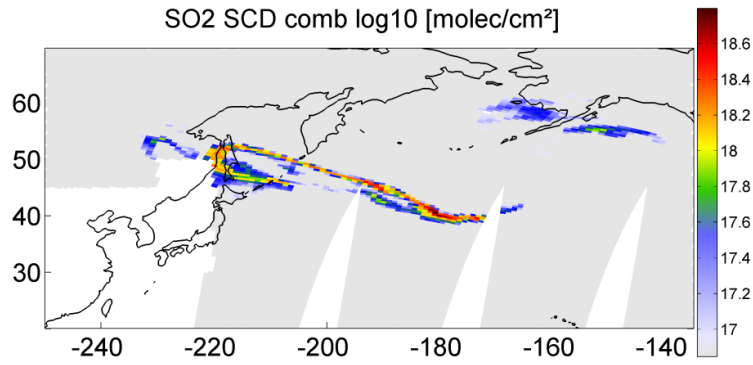
#370 Sarychev 13./14.06.2009



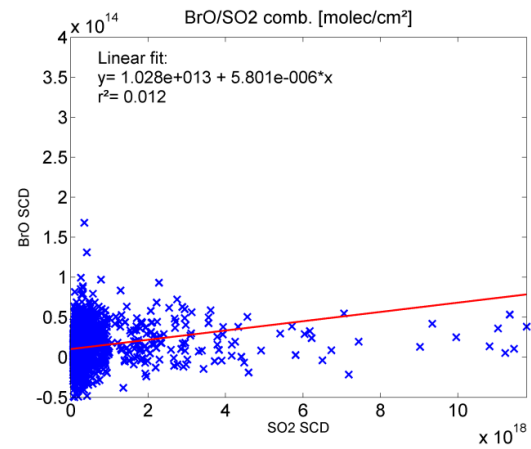
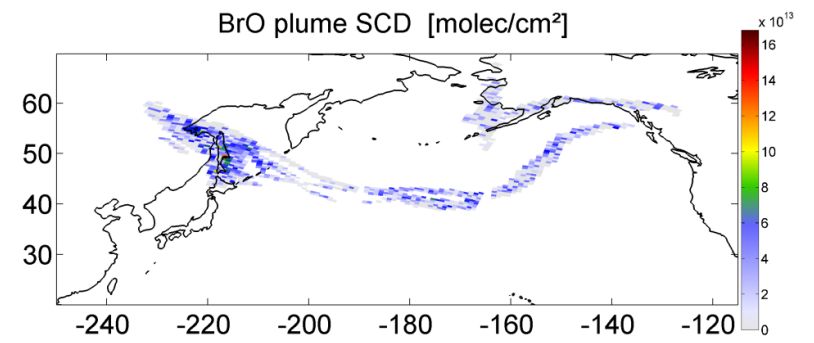
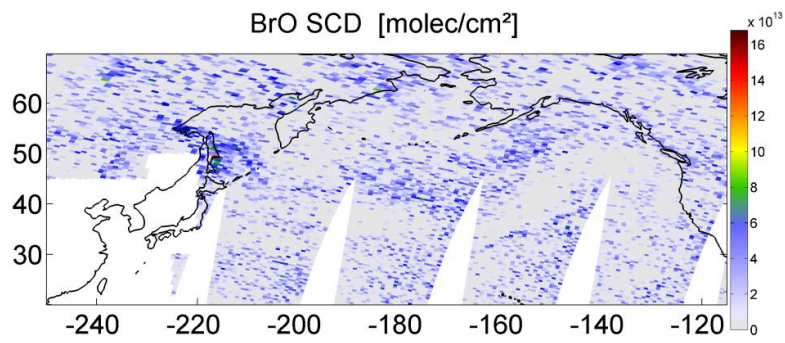
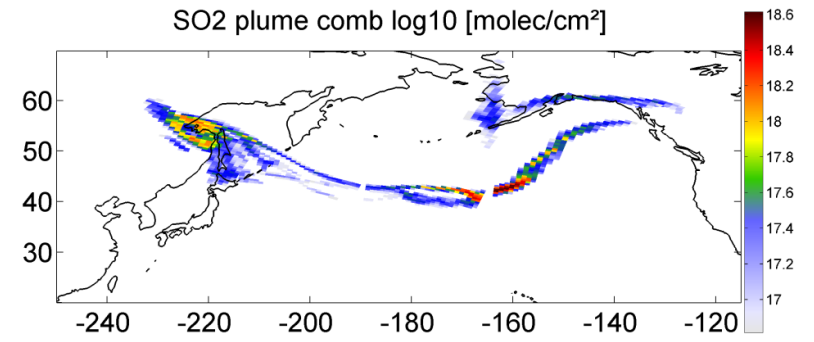
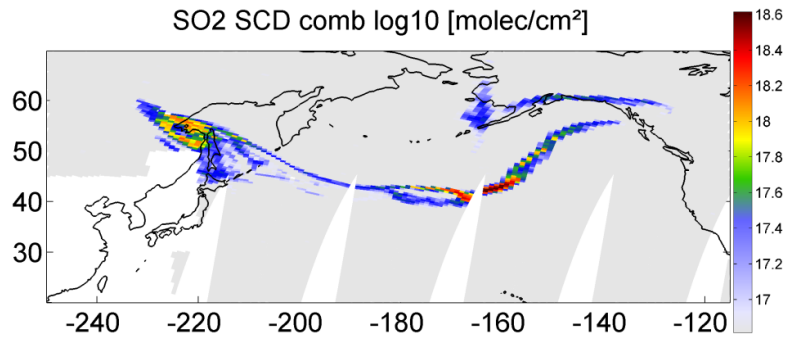
#375 Sarychev 15./16.06.2009



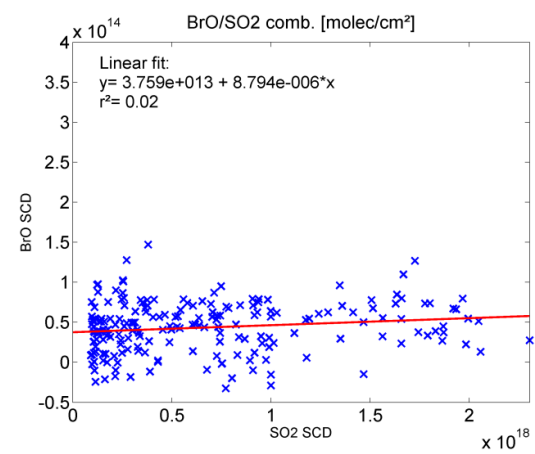
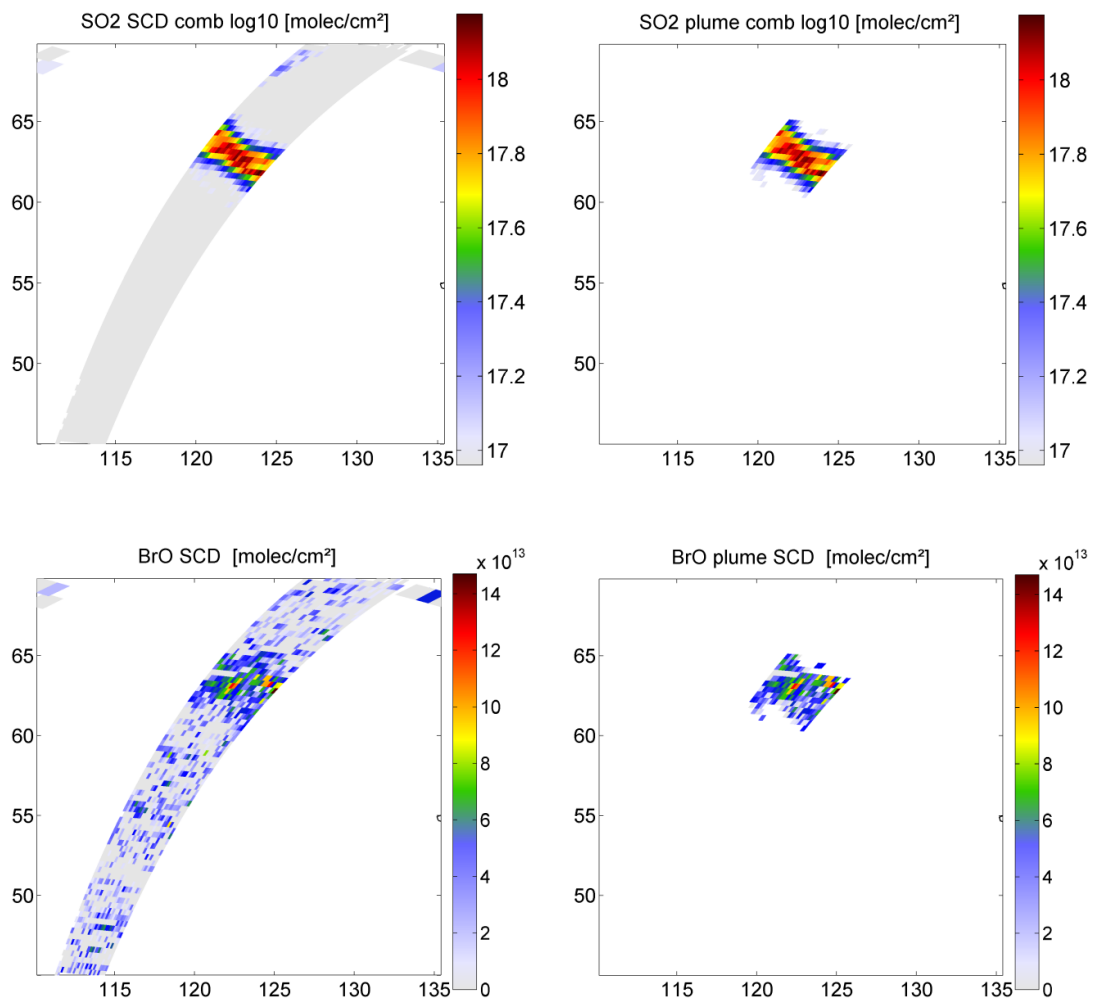
#377 Sarychev 16./17.06.2009



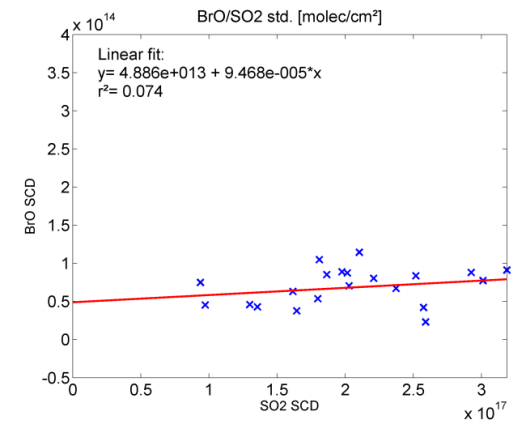
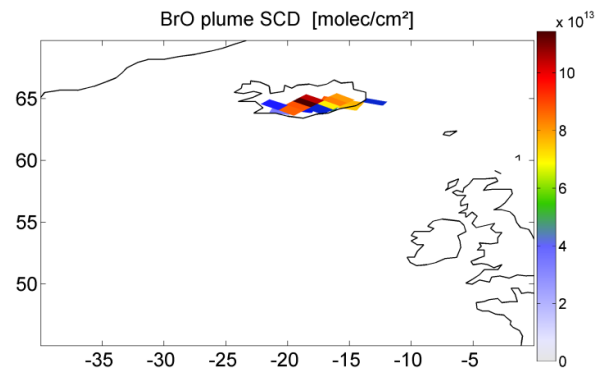
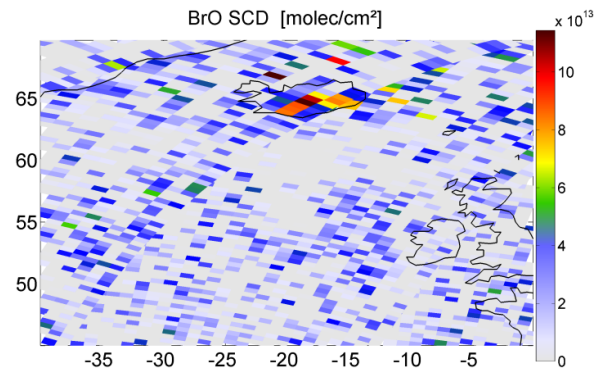
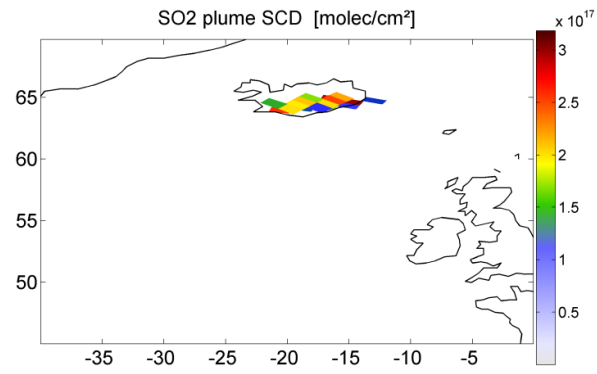
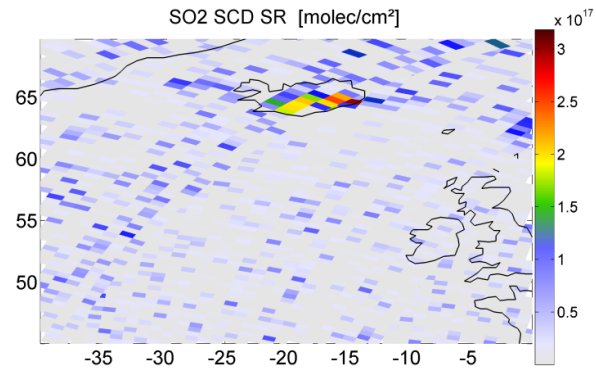
#378 Sarychev 17./18.06.2009



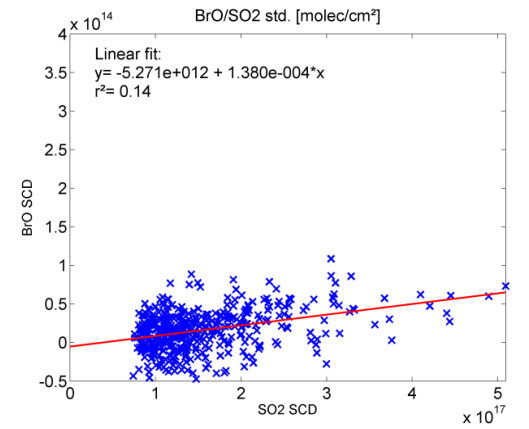
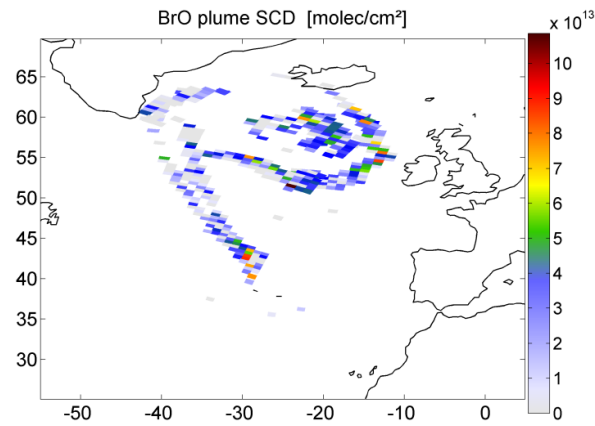
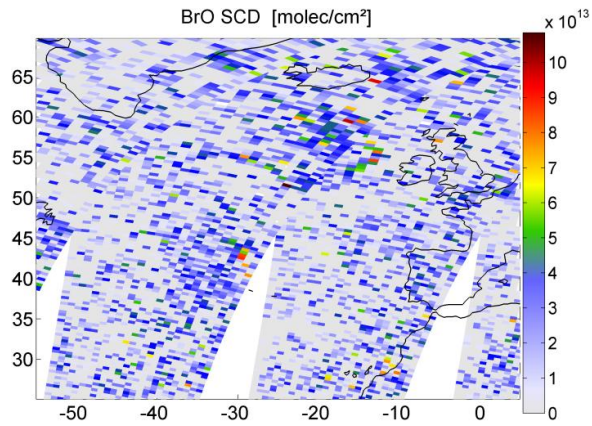
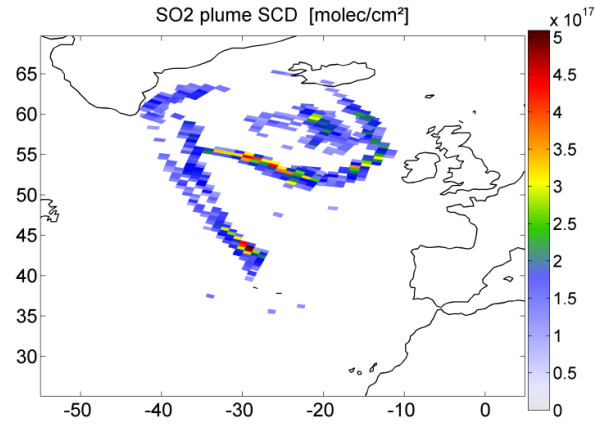
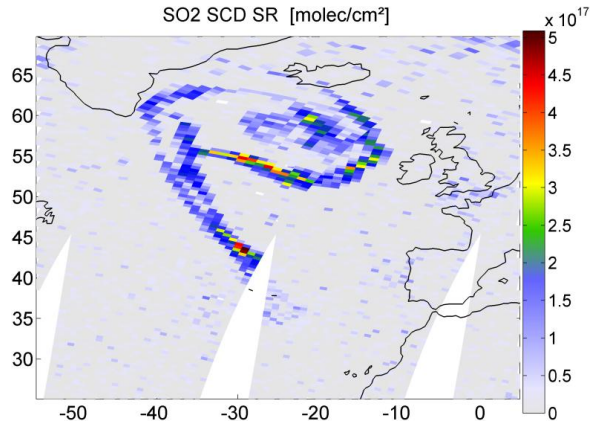
#380 Sarychev 19.06.2009



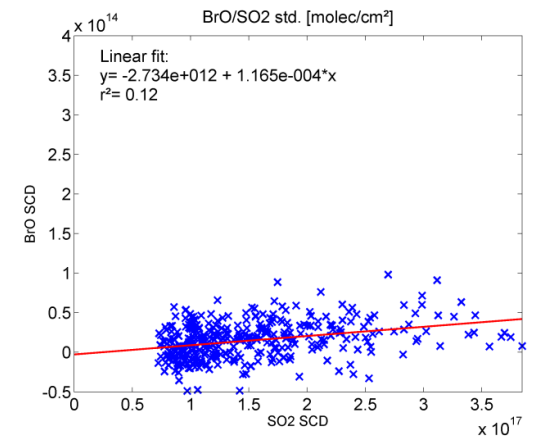
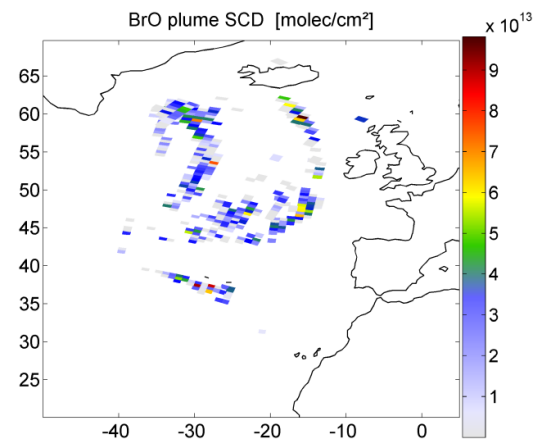
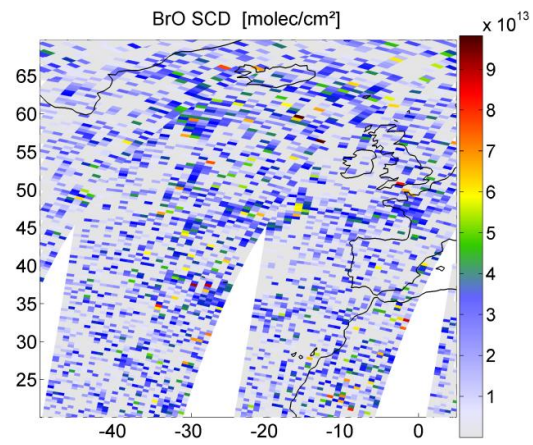
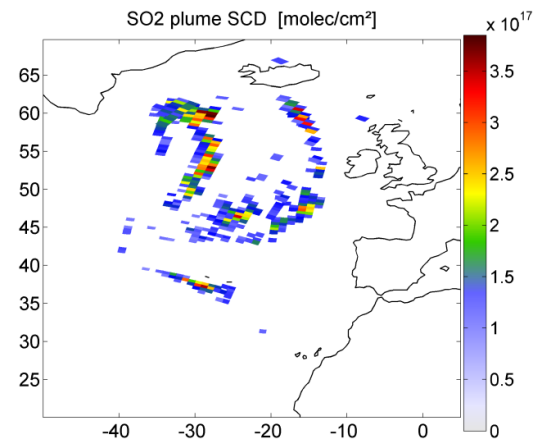
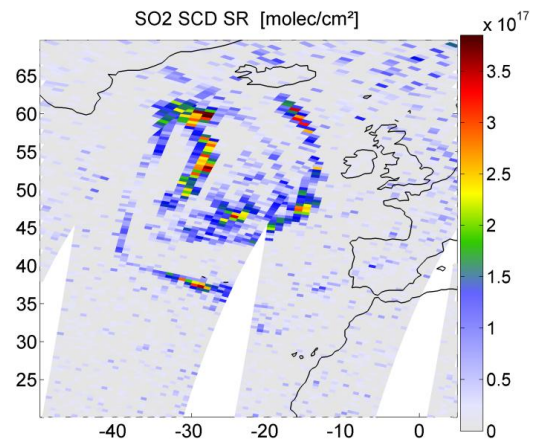
#548 Eyjafjallajökull 27.04.2010



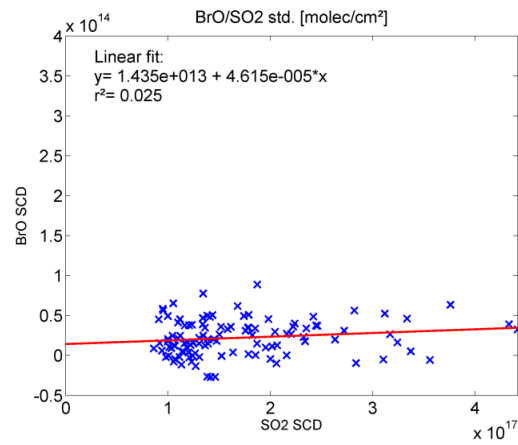
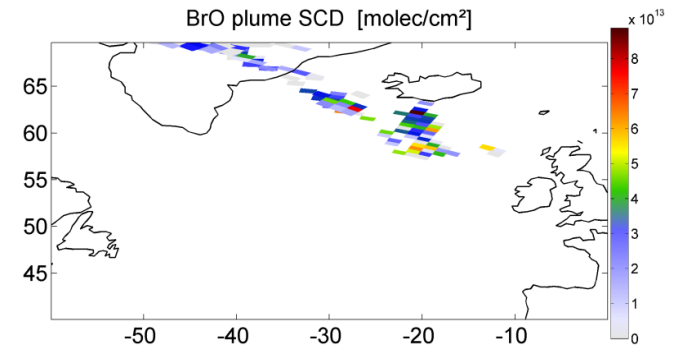
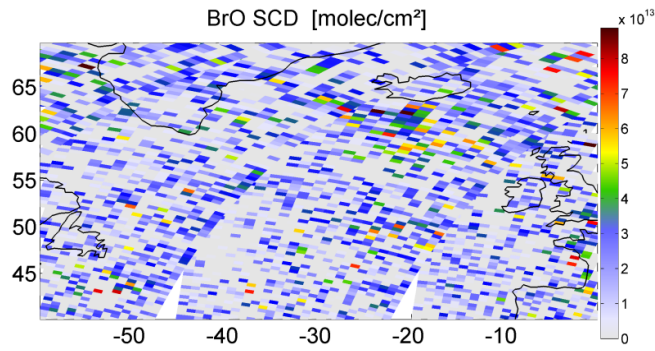
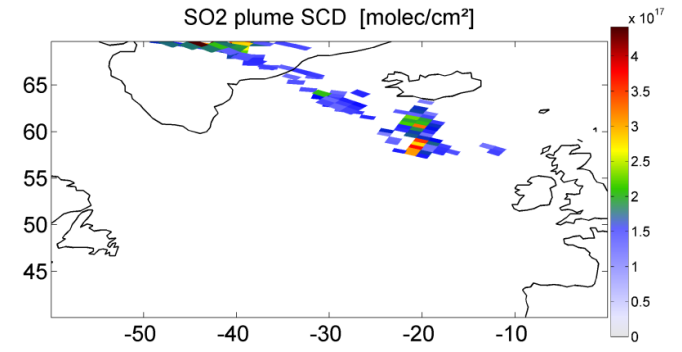
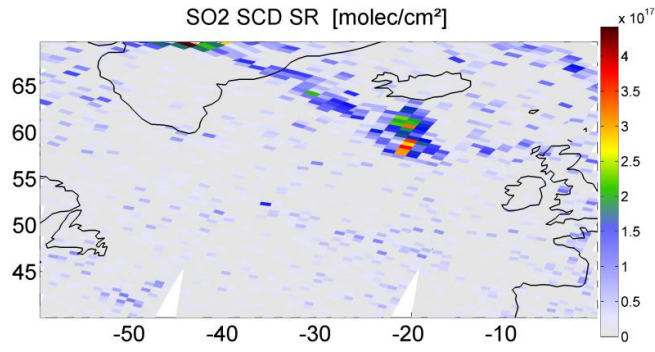
#559 Eyjafjallajökull 09.05.2010



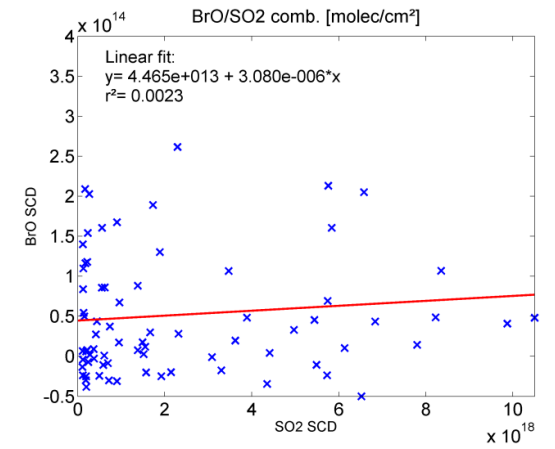
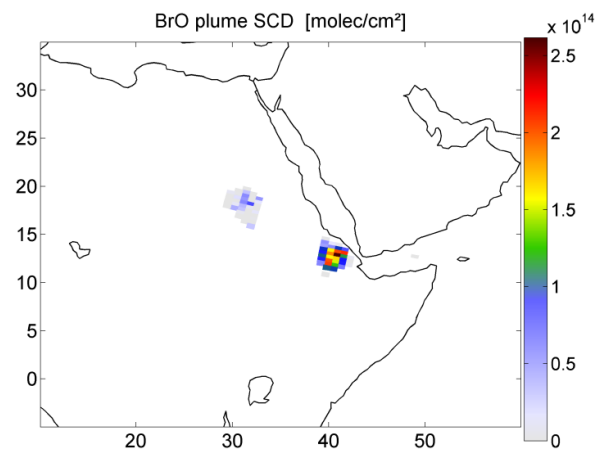
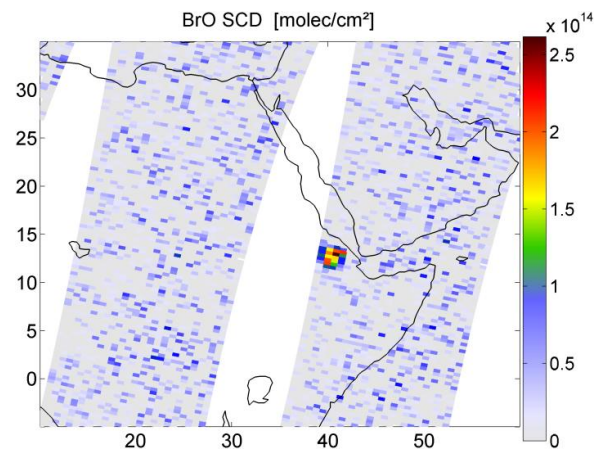
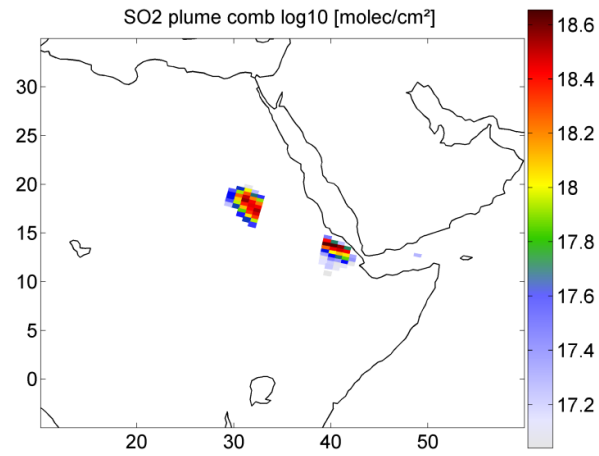
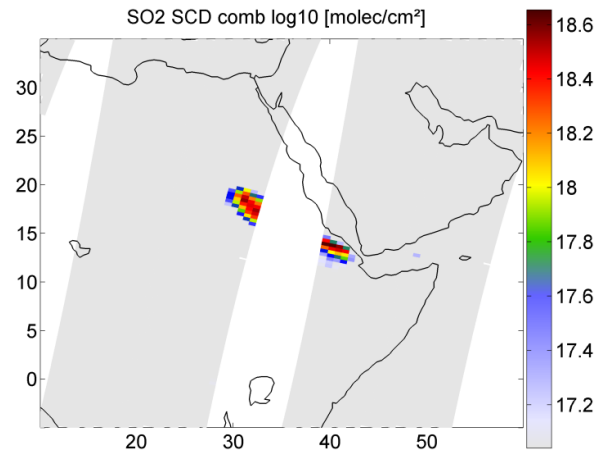
#560 Eyjafjallajökull 10.05.2010



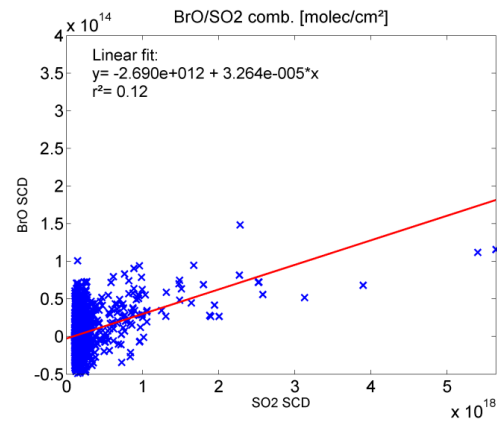
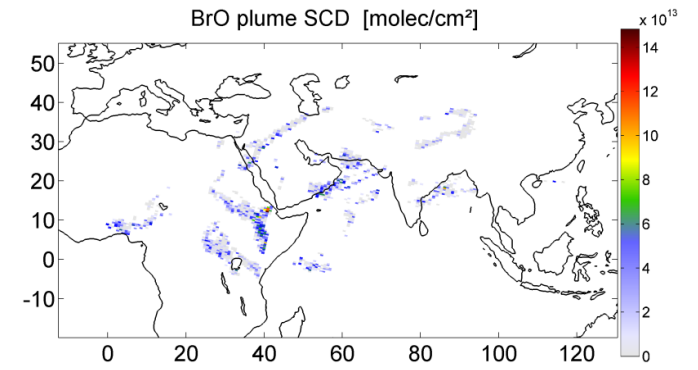
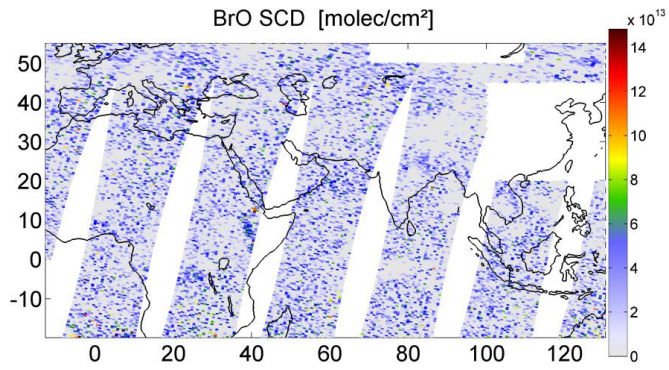
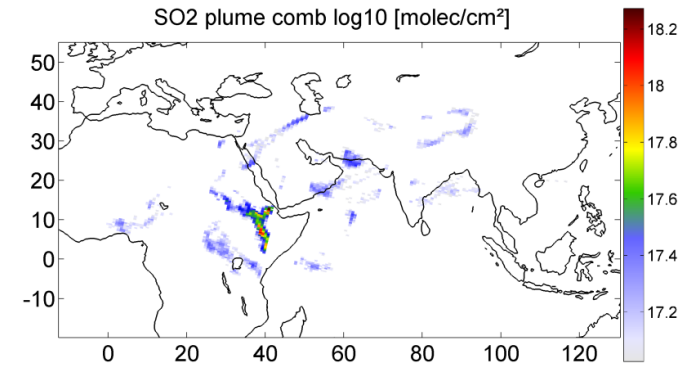
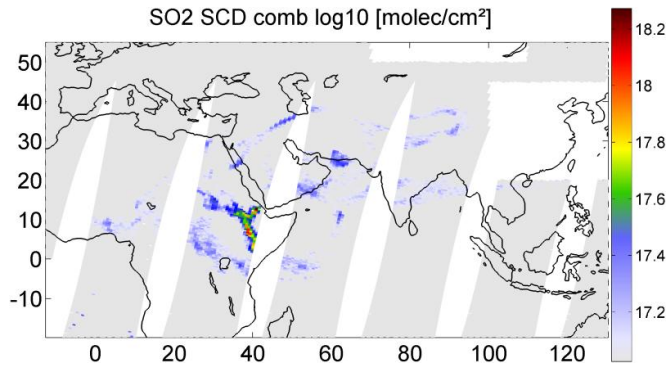
#569 Eyjafjallajökull 15.05.2010



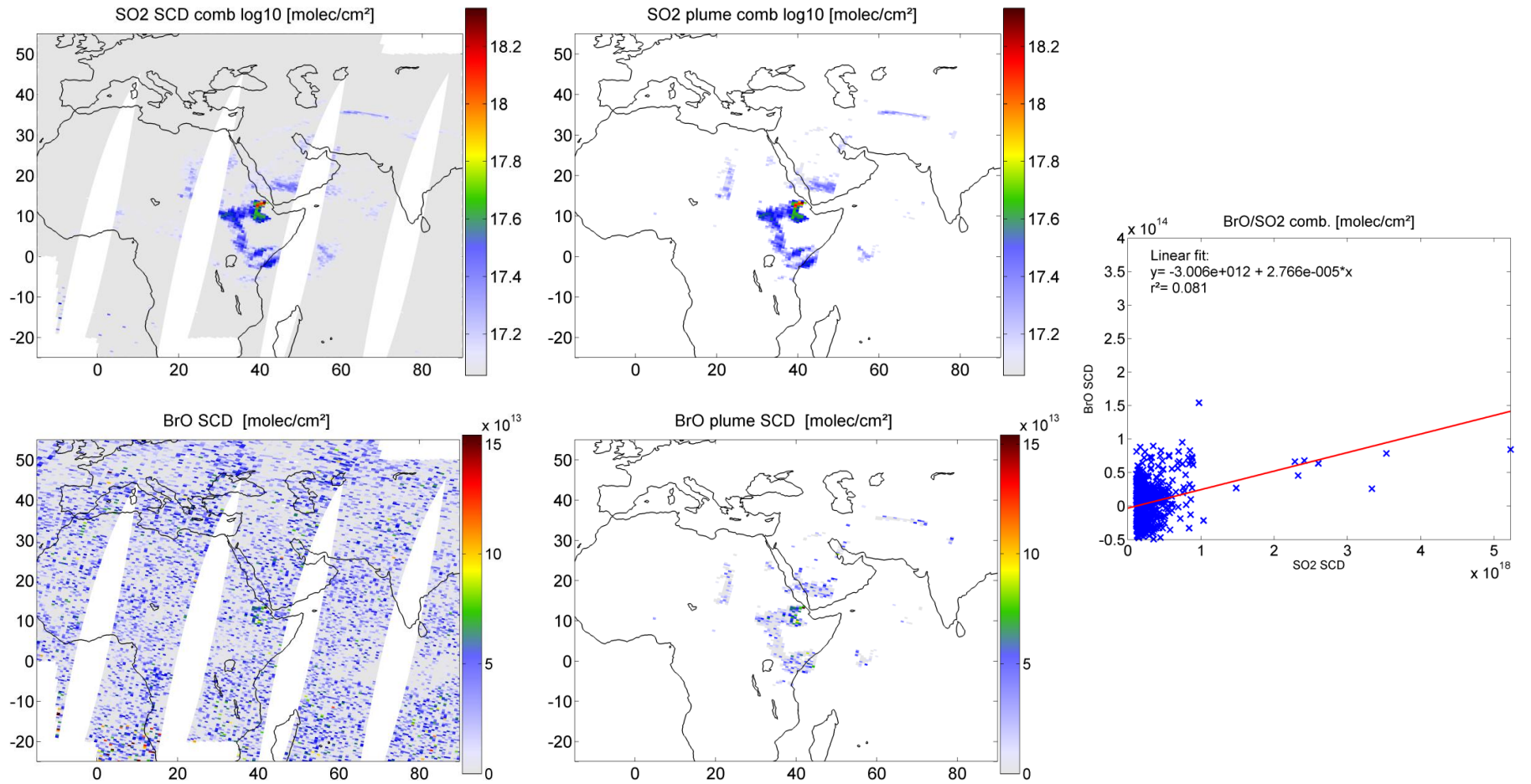
#745 Nabro 13.06.2011



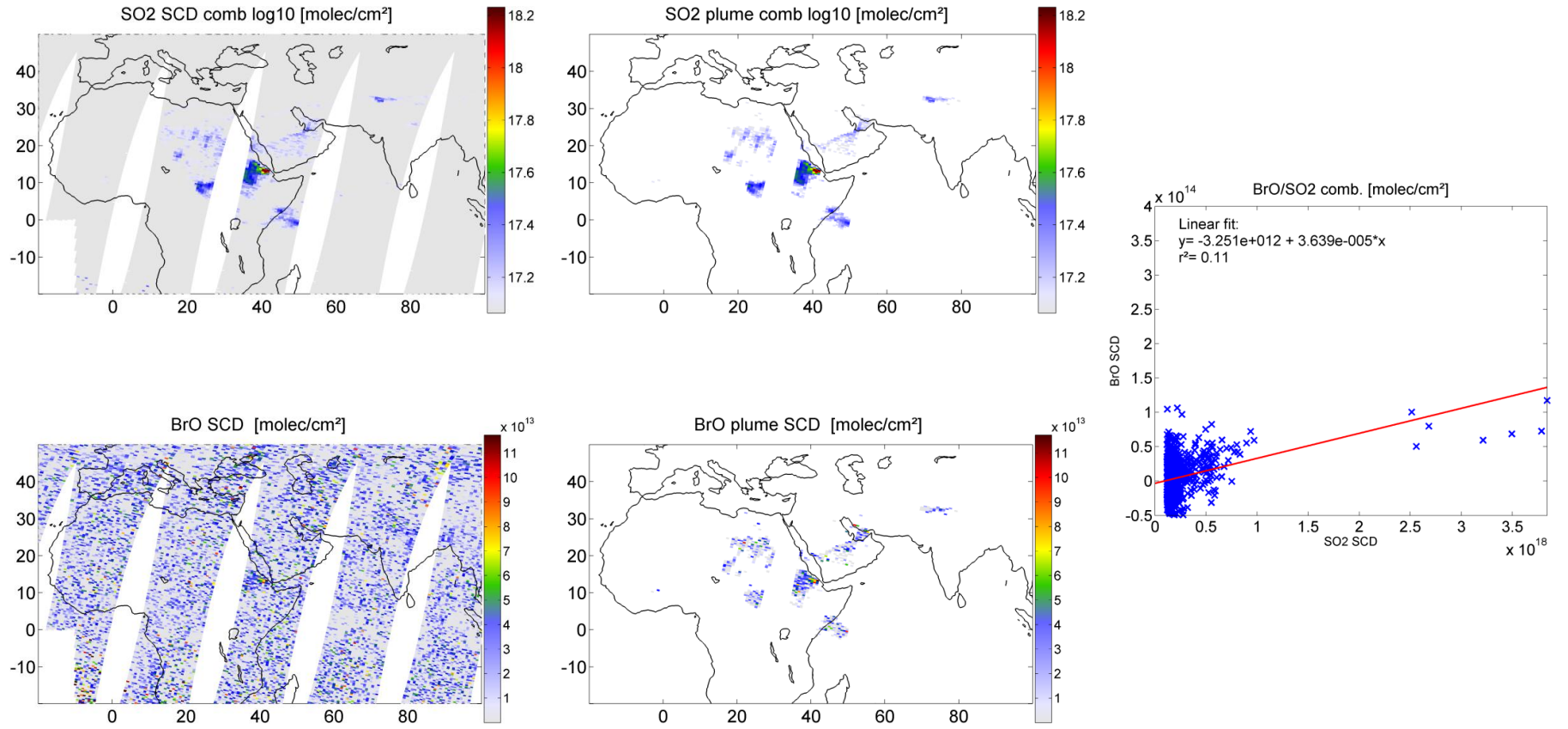
#755 Nabro 20.06.2011



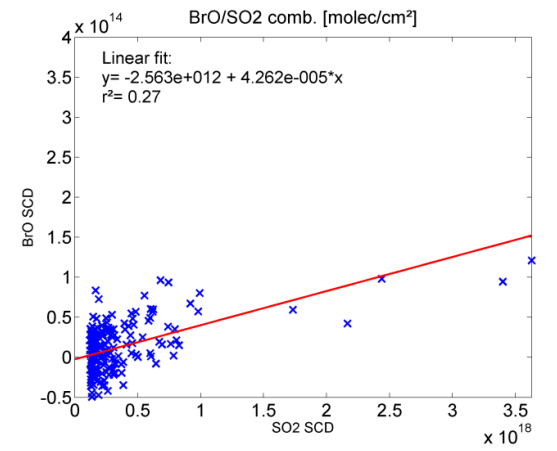
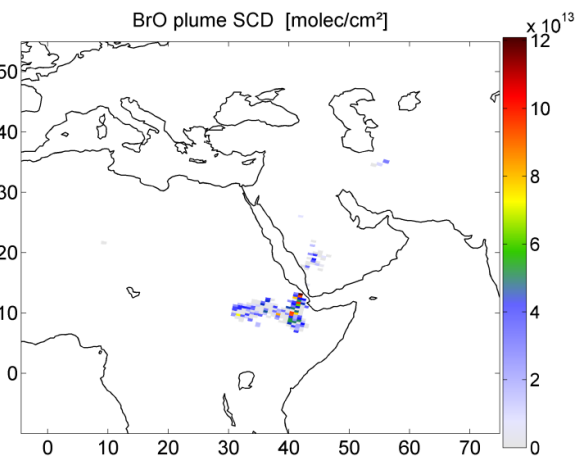
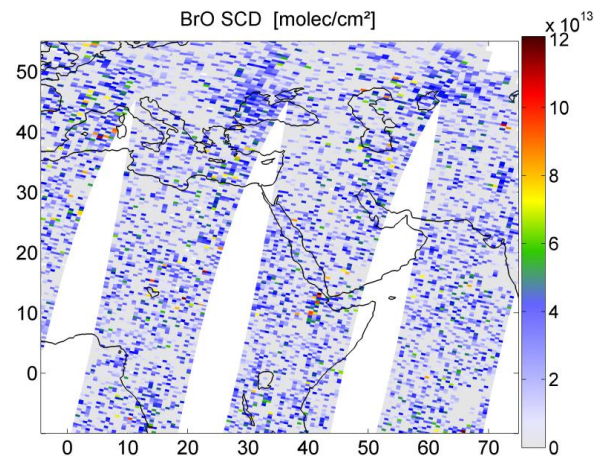
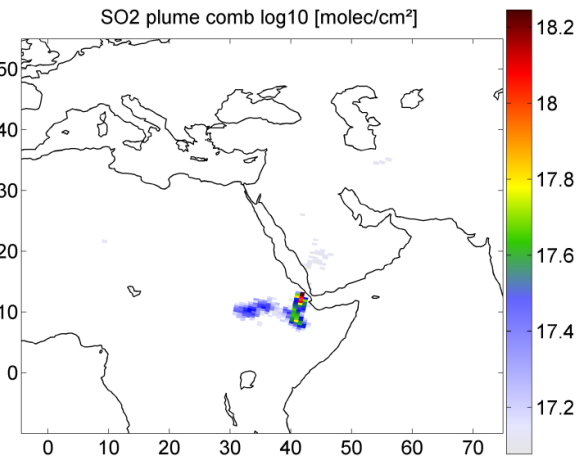
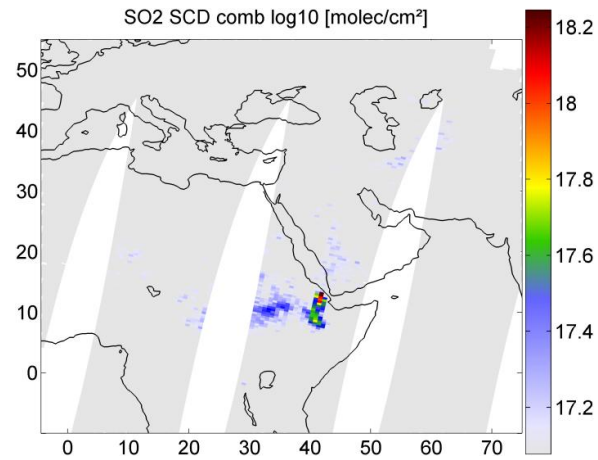
#758 Nabro 21.06.2011



#760 Nabro 22.06.2011



#767 Nabro 26.06.2011





## B. Extracted volcanic plumes January 2007–June 2011

In this appendix, the characteristics for all volcanic SO<sub>2</sub> plumes that had been extracted from the GOME-2 dataset for the time period between January 2007 and June 2011 are presented in tabular form.<sup>1</sup>

The newly developed plume detection algorithm had been able to identify a total of 772 individual volcanic plumes. All plumes were analysed for a possible BrO abundance. For each plume, the following quantities are given:

1. Event number
2. Corresponding volcano
3. Date of observation
4. Maximum BrO SCD in the plume area
5. Maximum SO<sub>2</sub> SCD in the plume area
6. Are the maximum BrO and SO<sub>2</sub> SCD found for the same GOME-2 pixel?
7. Correlation coefficient ( $r^2$ ) from linear fit
8. BrO/SO<sub>2</sub> ratio (slope from linear fit)
9. Ratio of the maximum BrO and SO<sub>2</sub> SCDs
10. Regarded area of observation

As the majority of all plumes showed no evidence for volcanic BrO, the ratio of the maximum BrO and SO<sub>2</sub> SCDs can be used to estimate an upper limit of the mean BrO/SO<sub>2</sub> ratio.

---

<sup>1</sup>This appendix has been accepted for publication as a supplementary part of Hörmann et al. (2012)

#	volcano	date	BrO SCD <sub>max</sub> [molec/cm <sup>2</sup> ]	SO <sub>2</sub> SCD <sub>max</sub> [molec/cm <sup>2</sup> ]	⊕	r <sup>2</sup>	fitted BrO/SO <sub>2</sub>	BrO <sub>max</sub> /SO <sub>2max</sub>	coordinates
1	Tunguahu	20.02.2007	4.4×10 <sup>13</sup>	2.5×10 <sup>17</sup>	no	0.03	3.8×10 <sup>-5</sup>	1.7×10 <sup>-4</sup>	[15 - 20°N, 60 - 92°W]
2	Anatahan	26.02.2007	2.4×10 <sup>13</sup>	1.7×10 <sup>17</sup>	no	0.04	8.2×10 <sup>-5</sup>	1.4×10 <sup>-4</sup>	[0 - 35°N, 130 - 160°E]
3	Anatahan	27.02.2007	3.8×10 <sup>13</sup>	2.0×10 <sup>17</sup>	no	0.08	-9.8×10 <sup>-5</sup>	1.9×10 <sup>-4</sup>	[0 - 35°N, 133 - 165°E]
4	Chikurachki*	07.03.2007	2.9×10 <sup>13</sup>	3.6×10 <sup>17</sup>	no	0.16	8.7×10 <sup>-5</sup>	8.0×10 <sup>-5</sup>	[45 - 64°N, 145 - 180°E]
5	Chikurachki*	07.03.2007	3.9×10 <sup>13</sup>	2.5×10 <sup>17</sup>	no	0.07	7.2×10 <sup>-5</sup>	1.5×10 <sup>-4</sup>	[35 - 65°N, 155 - 190°W]
6	Tunguahu	20.03.2007	4.4×10 <sup>13</sup>	1.7×10 <sup>17</sup>	no	0.00	-1.0×10 <sup>-5</sup>	2.6×10 <sup>-4</sup>	[-10 - 15°N, 74 - 82°W]
7	Ambrym	02.04.2007	3.6×10 <sup>13</sup>	1.9×10 <sup>17</sup>	no	0.21	1.5×10 <sup>-4</sup>	1.8×10 <sup>-4</sup>	[0 - 35°S, 150 - 185°E]
8	Piton de la Fournaise	04.04.2007	5.5×10 <sup>13</sup>	3.2×10 <sup>17</sup>	yes	0.12	6.4×10 <sup>-5</sup>	1.7×10 <sup>-4</sup>	[5 - 40°S, 35 - 70°E]
9	Piton de la Fournaise	05.04.2007	3.5×10 <sup>13</sup>	7.5×10 <sup>17</sup>	no	0.09	2.3×10 <sup>-5</sup>	4.6×10 <sup>-5</sup>	[5 - 40°S, 35 - 75°E]
10†	Piton de la Fournaise	06.04.2007	5.0×10 <sup>13</sup>	5.3×10 <sup>18</sup>	no	0.00	6.8×10 <sup>-7</sup>	9.5×10 <sup>-6</sup>	[0 - 40°S, 35 - 80°E]
11	Ambrym	06.04.2007	4.9×10 <sup>13</sup>	2.8×10 <sup>17</sup>	yes	0.23	1.6×10 <sup>-4</sup>	1.7×10 <sup>-4</sup>	[0 - 35°S, 150 - 183°E]
12†	Piton de la Fournaise	07.04.2007	5.1×10 <sup>13</sup>	2.1×10 <sup>18</sup>	no	0.00	-2.4×10 <sup>-7</sup>	2.3×10 <sup>-5</sup>	[0 - 40°S, 40 - 90°E]
13	Piton de la Fournaise	08.04.2007	5.5×10 <sup>13</sup>	6.2×10 <sup>17</sup>	no	0.01	-1.5×10 <sup>-5</sup>	8.8×10 <sup>-5</sup>	[-40 - 5°N, 30 - 95°E]
14	Ambrym	11.04.2007	3.8×10 <sup>13</sup>	1.9×10 <sup>17</sup>	no	0.00	-2.1×10 <sup>-6</sup>	1.9×10 <sup>-4</sup>	[-35 - 5°N, 39 - 85°E]
15	Piton de la Fournaise	11.04.2007	4.9×10 <sup>13</sup>	1.7×10 <sup>17</sup>	no	0.00	-5.6×10 <sup>-6</sup>	2.7×10 <sup>-4</sup>	[0 - 35°S, 150 - 184°E]
16	Etna	12.04.2007	4.6×10 <sup>13</sup>	2.0×10 <sup>17</sup>	no	0.14	1.5×10 <sup>-4</sup>	2.2×10 <sup>-4</sup>	[10 - 45°N, 10 - 44°E]
17	Nyiragongo	14.04.2007	2.5×10 <sup>13</sup>	2.0×10 <sup>17</sup>	no	0.29	-1.3×10 <sup>-4</sup>	1.2×10 <sup>-4</sup>	[-20 - 15°N, 10 - 45°E]
18	Chikurachki*	16.04.2007	3.4×10 <sup>13</sup>	2.1×10 <sup>17</sup>	yes	0.15	1.9×10 <sup>-4</sup>	1.5×10 <sup>-4</sup>	[35 - 70°N, 140 - 175°E]
19	Nevado del Huila	18.04.2007	4.3×10 <sup>13</sup>	9.0×10 <sup>17</sup>	no	0.01	4.9×10 <sup>-6</sup>	4.8×10 <sup>-5</sup>	[-10 - 20°N, 73 - 82°W]
20	Etna	30.04.2007	3.5×10 <sup>13</sup>	5.2×10 <sup>17</sup>	yes	0.27	6.9×10 <sup>-5</sup>	6.7×10 <sup>-5</sup>	[20 - 55°N, 5 - 40°E]
21	Ambrym	01.05.2007	5.0×10 <sup>13</sup>	2.4×10 <sup>17</sup>	no	0.05	1.0×10 <sup>-4</sup>	2.0×10 <sup>-4</sup>	[0 - 35°S, 150 - 185°E]
22	Bezymianny*	11./12.05.2007	1.3×10 <sup>14</sup>	3.1×10 <sup>17</sup>	no	0.62	4.4×10 <sup>-4</sup>	4.1×10 <sup>-4</sup>	[40 - 70°N, 145 - 180°E]
23	Bezymianny*	12.05.2007	3.3×10 <sup>13</sup>	1.1×10 <sup>17</sup>	no	0.05	1.3×10 <sup>-4</sup>	2.8×10 <sup>-4</sup>	[40 - 70°N, 165 - 200°W]
24	Kliuchevskoi	14.05.2007	2.3×10 <sup>13</sup>	1.4×10 <sup>17</sup>	no	0.00	1.8×10 <sup>-5</sup>	1.6×10 <sup>-4</sup>	[40 - 70°N, 140 - 175°E]
25	Kliuchevskoi	17.05.2007	3.1×10 <sup>13</sup>	2.6×10 <sup>17</sup>	no	0.00	-3.5×10 <sup>-6</sup>	1.1×10 <sup>-4</sup>	[45 - 70°N, 130 - 165°E]
26	Kliuchevskoi	18./19.05.2007	3.5×10 <sup>13</sup>	1.9×10 <sup>17</sup>	no	0.12	-1.0×10 <sup>-4</sup>	1.8×10 <sup>-4</sup>	[40 - 70°N, 145 - 180°E]
27	Kliuchevskoi	19./20.05.2007	4.6×10 <sup>13</sup>	2.6×10 <sup>17</sup>	yes	0.29	1.6×10 <sup>-4</sup>	1.7×10 <sup>-4</sup>	[40 - 70°N, 145 - 180°E]
28	Kliuchevskoi	20./21.05.2007	5.1×10 <sup>13</sup>	1.9×10 <sup>17</sup>	no	0.40	2.7×10 <sup>-4</sup>	2.6×10 <sup>-4</sup>	[40 - 70°N, 145 - 180°E]
29	Kliuchevskoi	21./22.05.2007	6.2×10 <sup>13</sup>	2.1×10 <sup>17</sup>	no	0.02	5.8×10 <sup>-5</sup>	2.8×10 <sup>-4</sup>	[40 - 70°N, 175 - 210°W]
30	Kliuchevskoi	22./23.05.2007	2.9×10 <sup>13</sup>	2.2×10 <sup>17</sup>	no	0.03	3.7×10 <sup>-5</sup>	1.3×10 <sup>-4</sup>	[35 - 70°N, 145 - 180°E]
31	Kliuchevskoi	23./24.05.2007	2.6×10 <sup>13</sup>	2.1×10 <sup>17</sup>	no	0.00	-6.1×10 <sup>-6</sup>	1.2×10 <sup>-4</sup>	[35 - 70°N, 145 - 180°E]
32	Kliuchevskoi	24.05.2007	4.0×10 <sup>13</sup>	2.7×10 <sup>17</sup>	no	0.06	6.9×10 <sup>-5</sup>	1.4×10 <sup>-4</sup>	[35 - 70°N, 145 - 180°E]
33	Kliuchevskoi	25.05.2007	3.9×10 <sup>13</sup>	1.8×10 <sup>17</sup>	no	0.26	2.2×10 <sup>-4</sup>	2.1×10 <sup>-4</sup>	[40 - 70°N, 145 - 180°E]
34	Kliuchevskoi	26.05.2007	2.9×10 <sup>13</sup>	2.5×10 <sup>17</sup>	no	0.09	7.7×10 <sup>-5</sup>	1.1×10 <sup>-4</sup>	[35 - 70°N, 140 - 175°E]
35	Kliuchevskoi	29.05.2007	3.4×10 <sup>13</sup>	2.2×10 <sup>17</sup>	no	0.06	8.1×10 <sup>-5</sup>	1.5×10 <sup>-4</sup>	[35 - 70°N, 135 - 175°E]
36	Kliuchevskoi	30./31.05.2007	3.4×10 <sup>13</sup>	2.3×10 <sup>17</sup>	no	0.00	1.5×10 <sup>-5</sup>	1.4×10 <sup>-4</sup>	[30 - 70°N, 135 - 180°E]
37	Kliuchevskoi	03.06.2007	3.6×10 <sup>13</sup>	2.6×10 <sup>17</sup>	no	0.01	3.0×10 <sup>-5</sup>	1.3×10 <sup>-4</sup>	[35 - 70°N, 145 - 180°E]
38	Ambrym	18.06.2007	6.2×10 <sup>13</sup>	2.0×10 <sup>17</sup>	no	0.03	8.9×10 <sup>-5</sup>	3.0×10 <sup>-4</sup>	[0 - 35°S, 150 - 185°E]
39	Popocatepetl	19.06.2007	2.8×10 <sup>13</sup>	2.4×10 <sup>17</sup>	no	0.01	-2.0×10 <sup>-5</sup>	1.1×10 <sup>-4</sup>	[0 - 35°N, 85 - 115°W]
40	Kliuchevskoi	19./20.06.2007	4.1×10 <sup>13</sup>	2.4×10 <sup>17</sup>	no	0.19	1.0×10 <sup>-4</sup>	1.6×10 <sup>-4</sup>	[40 - 70°N, 140 - 175°E]
41	Kliuchevskoi	20./21.06.2007	3.4×10 <sup>13</sup>	2.5×10 <sup>17</sup>	no	0.08	7.1×10 <sup>-5</sup>	1.3×10 <sup>-4</sup>	[35 - 70°N, 135 - 175°E]
42	Kliuchevskoi	21./22.06.2007	4.0×10 <sup>13</sup>	3.4×10 <sup>17</sup>	no	0.00	9.8×10 <sup>-6</sup>	1.1×10 <sup>-4</sup>	[35 - 70°N, 140 - 180°E]
43	Kliuchevskoi	22./23.06.2007	4.9×10 <sup>13</sup>	1.5×10 <sup>17</sup>	no	0.03	1.0×10 <sup>-4</sup>	3.3×10 <sup>-4</sup>	[40 - 70°N, 140 - 175°E]
44	Kliuchevskoi	28./29.06.2007	4.8×10 <sup>13</sup>	4.8×10 <sup>17</sup>	no	0.15	6.7×10 <sup>-5</sup>	1.0×10 <sup>-4</sup>	[35 - 70°N, 140 - 180°E]
45	Kliuchevskoi	01./02.07.2007	6.4×10 <sup>13</sup>	1.4×10 <sup>17</sup>	no	0.09	1.7×10 <sup>-4</sup>	4.4×10 <sup>-4</sup>	[40 - 70°N, 145 - 180°E]
46	Ambrym	02.07.2007	2.7×10 <sup>13</sup>	3.8×10 <sup>17</sup>	yes	0.06	4.0×10 <sup>-5</sup>	7.0×10 <sup>-5</sup>	[0 - 35°S, 150 - 183°E]
47	Kliuchevskoi	03./04.07.2007	3.2×10 <sup>13</sup>	1.7×10 <sup>17</sup>	no	0.02	4.6×10 <sup>-5</sup>	1.8×10 <sup>-4</sup>	[35 - 70°N, 145 - 180°E]
48	Ambrym	16.07.2007	5.3×10 <sup>13</sup>	2.6×10 <sup>17</sup>	yes	0.38	2.1×10 <sup>-4</sup>	2.0×10 <sup>-4</sup>	[0 - 35°S, 150 - 181°E]
49	Ambrym	22.07.2007	6.0×10 <sup>13</sup>	1.7×10 <sup>17</sup>	no	0.08	1.6×10 <sup>-4</sup>	3.5×10 <sup>-4</sup>	[0 - 35°S, 150 - 185°E]
50	Fuego	09.08.2007	3.2×10 <sup>13</sup>	1.3×10 <sup>17</sup>	no	0.05	-1.0×10 <sup>-4</sup>	2.4×10 <sup>-4</sup>	[-5 - 35°N, 75 - 110°W]
51‡	Manda Hararo	13.08.2007	3.5×10 <sup>13</sup>	1.1×10 <sup>18</sup>	no	0.05	2.1×10 <sup>-5</sup>	3.3×10 <sup>-5</sup>	[-10 - 30°N, 20 - 50°E]
52	Manda Hararo	14.08.2007	3.2×10 <sup>13</sup>	2.5×10 <sup>17</sup>	no	0.04	-7.1×10 <sup>-5</sup>	1.2×10 <sup>-4</sup>	[-10 - 25°N, 20 - 54°E]
53	Soputan	15.08.2007	4.3×10 <sup>13</sup>	2.1×10 <sup>17</sup>	no	0.04	7.8×10 <sup>-5</sup>	1.9×10 <sup>-4</sup>	[-15 - 20°N, 105 - 135°E]
54	Chikurachki	19.08.2007	2.0×10 <sup>13</sup>	4.8×10 <sup>17</sup>	no	0.02	-5.9×10 <sup>-6</sup>	4.3×10 <sup>-5</sup>	[30 - 65°N, 140 - 175°E]
55	Chikurachki	19.08.2007	2.8×10 <sup>13</sup>	2.3×10 <sup>17</sup>	no	0.05	-4.4×10 <sup>-5</sup>	1.1×10 <sup>-4</sup>	[30 - 65°N, 140 - 190°E]
56	Chikurachki	21.08.2007	2.1×10 <sup>13</sup>	1.9×10 <sup>17</sup>	no	0.10	8.2×10 <sup>-5</sup>	1.1×10 <sup>-4</sup>	[35 - 70°N, 145 - 180°E]
57	Chikurachki	31.08.2007	3.2×10 <sup>13</sup>	1.4×10 <sup>17</sup>	no	0.01	4.4×10 <sup>-5</sup>	2.2×10 <sup>-4</sup>	[35 - 70°N, 150 - 185°E]
58	Chikurachki	04.09.2007	2.8×10 <sup>13</sup>	3.7×10 <sup>17</sup>	no	0.21	8.6×10 <sup>-5</sup>	7.6×10 <sup>-5</sup>	[35 - 70°N, 155 - 190°E]
59	Etna	05.09.2007	4.8×10 <sup>13</sup>	4.4×10 <sup>17</sup>	no	0.19	7.5×10 <sup>-5</sup>	1.0×10 <sup>-4</sup>	[20 - 55°N, 5 - 40°E]
60	Etna	06.09.2007	4.1×10 <sup>13</sup>	1.6×10 <sup>17</sup>	no	0.15	2.3×10 <sup>-4</sup>	2.4×10 <sup>-4</sup>	[35 - 70°N, 10 - 45°E]
61†	Jebel at Tair	01.10.2007	5.7×10 <sup>13</sup>	1.0×10 <sup>18</sup>	no	0.02	1.3×10 <sup>-5</sup>	5.2×10 <sup>-5</sup>	[-5 - 40°N, 16 - 55°E]
62	Jebel at Tair	02.10.2007	5.5×10 <sup>13</sup>	8.0×10 <sup>17</sup>	no	0.01	5.6×10 <sup>-6</sup>	6.8×10 <sup>-5</sup>	[0 - 45°N, 25 - 64°E]
63	Jebel at Tair	03.10.2007	5.6×10 <sup>13</sup>	5.6×10 <sup>17</sup>	no	0.03	3.3×10 <sup>-5</sup>	1.0×10 <sup>-4</sup>	[5 - 50°N, 15 - 75°E]
64	Jebel at Tair	04.10.2007	5.3×10 <sup>13</sup>	1.5×10 <sup>17</sup>	no	0.05	-2.2×10 <sup>-4</sup>	3.5×10 <sup>-4</sup>	[20 - 50°N, 70 - 104°E]
65	Jebel at Tair	04.10.2007	4.1×10 <sup>13</sup>	3.9×10 <sup>17</sup>	yes	0.00	-1.6×10 <sup>-5</sup>	1.0×10 <sup>-4</sup>	[10 - 50°N, 45 - 80°E]
66	Jebel at Tair	05.10.2007	4.8×10 <sup>13</sup>	2.7×10 <sup>17</sup>	no	0.05	6.7×10 <sup>-5</sup>	1.7×10 <sup>-4</sup>	[15 - 55°N, 60 - 105°E]
67	Soputan	26.10.2007	4.5×10 <sup>13</sup>	3.0×10 <sup>17</sup>	no	0.00	2.0×10 <sup>-5</sup>	1.5×10 <sup>-4</sup>	[-20 - 20°N, 100 - 133°E]
68‡	Etna	24.11.2007	1.4×10 <sup>14</sup>	1.1×10 <sup>18</sup>	yes	0.61	1.0×10 <sup>-4</sup>	1.2×10 <sup>-4</sup>	[20 - 49°N, 0 - 35°E]
69	Etna	25.11.2007	8.0×10 <sup>13</sup>	3.1×10 <sup>17</sup>	no	0.02	6.1×10 <sup>-5</sup>	2.5×10 <sup>-4</sup>	[15 - 49°N, 10 - 50°E]
70	Bagana	10.12.2007	3.3×10 <sup>13</sup>	3.6×10 <sup>17</sup>	no	0.00	9.6×10 <sup>-6</sup>	9.2×10 <sup>-5</sup>	[-25 - 10°N, 135 - 168°E]
71	Bagana	11.12.2007	3.9×10 <sup>13</sup>	1.7×10 <sup>17</sup>	no	0.07	2.2×10 <sup>-4</sup>	2.2×10 <sup>-4</sup>	[-25 - 10°N, 135 - 170°E]
72	Bagana	30.12.2007	4.2×10 <sup>13</sup>	4.2×10 <sup>17</sup>	yes	0.19	1.0×10 <sup>-4</sup>	9.9×10 <sup>-5</sup>	[-25 - 10°N, 140 - 171°E]
73	Tungurahua	06.02.2008	3.8×10 <sup>13</sup>	1.6×10 <sup>17</sup>	no	0.00	-3.2×10 <sup>-6</sup>	2.4×10 <sup>-4</sup>	[-20 - 15°N, 65 - 95°W]
74	Anatahan	05.03.2008	3.6×10 <sup>13</sup>	1.7×10 <sup>17</sup>	no	0.04	-9.2×10 <sup>-5</sup>	2.0×10 <sup>-4</sup>	[0 - 35°N, 132 - 164°E]
75	Anatahan	05.03.2008	2.7×10 <sup>13</sup>	3.4×10 <sup>17</sup>	no	0.14	9.2×10 <sup>-5</sup>	7.9×10 <sup>-5</sup>	[0 - 35°N, 130 - 165°E]

⊕ location of SO<sub>2</sub> SCD<sub>max</sub> is the same as for BrO SCD<sub>max</sub> † combined SO<sub>2</sub> product in case of high SO<sub>2</sub> SCDs ≥ 1 × 10<sup>18</sup> molec/cm<sup>2</sup> ‡ SO<sub>2</sub> SCDs ≥ 1 × 10<sup>18</sup> molec/cm<sup>2</sup>, but no plume pixel found in the SO<sub>2</sub> AR

\* corresponding volcano cannot be clearly identified

#	volcano	date	BrO SCD <sub>max</sub> [molec/cm <sup>2</sup> ]	SO <sub>2</sub> SCD <sub>max</sub> [molec/cm <sup>2</sup> ]	⊕	r <sup>2</sup>	fitted BrO/SO <sub>2</sub>	BrO <sub>max</sub> /SO <sub>2max</sub>	coordinates
76	Anatahan	14.03.2008	3.9 × 10 <sup>13</sup>	2.0 × 10 <sup>17</sup>	no	0.05	1.0 × 10 <sup>-4</sup>	1.9 × 10 <sup>-4</sup>	[0 - 35°N, 128 - 160°E]
77	Kīlauea	24.03.2008	3.3 × 10 <sup>13</sup>	1.4 × 10 <sup>17</sup>	yes	0.16	2.1 × 10 <sup>-4</sup>	2.3 × 10 <sup>-4</sup>	[0 - 35°N, 142 - 175°W]
78	Anatahan	24.03.2008	3.8 × 10 <sup>13</sup>	3.5 × 10 <sup>17</sup>	yes	0.03	4.9 × 10 <sup>-5</sup>	1.0 × 10 <sup>-4</sup>	[0 - 35°N, 130 - 165°E]
79	Kīlauea	25.03.2008	3.9 × 10 <sup>13</sup>	1.9 × 10 <sup>17</sup>	no	0.02	6.6 × 10 <sup>-5</sup>	2.0 × 10 <sup>-4</sup>	[0 - 35°N, 140 - 175°W]
80	Kīlauea	29.03.2008	4.8 × 10 <sup>13</sup>	2.2 × 10 <sup>17</sup>	no	0.00	8.1 × 10 <sup>-6</sup>	2.1 × 10 <sup>-4</sup>	[0 - 35°N, 141 - 175°W]
81	Kīlauea	04.04.2008	3.4 × 10 <sup>13</sup>	3.3 × 10 <sup>17</sup>	no	0.00	-7.5 × 10 <sup>-6</sup>	1.0 × 10 <sup>-4</sup>	[0 - 35°N, 135 - 170°W]
82	Kīlauea	05.04.2008	1.6 × 10 <sup>13</sup>	2.0 × 10 <sup>17</sup>	no	0.13	-1.0 × 10 <sup>-4</sup>	8.2 × 10 <sup>-5</sup>	[0 - 35°N, 140 - 175°W]
83	Kīlauea	12.04.2008	4.6 × 10 <sup>13</sup>	2.0 × 10 <sup>17</sup>	no	0.01	-5.0 × 10 <sup>-5</sup>	2.2 × 10 <sup>-4</sup>	[0 - 35°N, 144 - 175°W]
84	Kīlauea	13.04.2008	2.8 × 10 <sup>13</sup>	1.8 × 10 <sup>17</sup>	no	0.05	-1.2 × 10 <sup>-4</sup>	1.5 × 10 <sup>-4</sup>	[0 - 35°N, 140 - 175°W]
85	Kīlauea	18.04.2008	4.5 × 10 <sup>13</sup>	2.1 × 10 <sup>17</sup>	no	0.01	3.6 × 10 <sup>-5</sup>	2.1 × 10 <sup>-4</sup>	[0 - 35°N, 140 - 175°W]
86	Kīlauea	19.04.2008	3.5 × 10 <sup>13</sup>	1.3 × 10 <sup>17</sup>	no	0.03	-1.1 × 10 <sup>-4</sup>	2.6 × 10 <sup>-4</sup>	[0 - 35°N, 140 - 172°W]
87	Kīlauea	22.04.2008	6.7 × 10 <sup>13</sup>	1.6 × 10 <sup>17</sup>	no	0.01	6.2 × 10 <sup>-5</sup>	4.1 × 10 <sup>-4</sup>	[0 - 35°N, 142 - 175°W]
88	Kīlauea	26.04.2008	3.1 × 10 <sup>13</sup>	3.8 × 10 <sup>17</sup>	no	0.00	3.0 × 10 <sup>-6</sup>	8.2 × 10 <sup>-5</sup>	[0 - 35°N, 140 - 175°W]
89	Kīlauea	27.04.2008	4.4 × 10 <sup>13</sup>	3.2 × 10 <sup>17</sup>	no	0.01	-2.8 × 10 <sup>-5</sup>	1.3 × 10 <sup>-4</sup>	[0 - 40°N, 140 - 180°W]
90	Kīlauea	02.05.2008	4.1 × 10 <sup>13</sup>	2.3 × 10 <sup>17</sup>	no	0.01	-2.9 × 10 <sup>-5</sup>	1.7 × 10 <sup>-4</sup>	[0 - 35°N, 141 - 175°W]
91	Kīlauea	03.05.2008	3.5 × 10 <sup>13</sup>	3.0 × 10 <sup>17</sup>	no	0.18	1.3 × 10 <sup>-4</sup>	1.1 × 10 <sup>-4</sup>	[0 - 35°N, 140 - 175°W]
92	Kīlauea	07.05.2008	5.1 × 10 <sup>13</sup>	1.9 × 10 <sup>17</sup>	no	0.14	1.8 × 10 <sup>-4</sup>	2.6 × 10 <sup>-4</sup>	[0 - 35°N, 140 - 175°W]
93	Kīlauea	08.05.2008	4.9 × 10 <sup>13</sup>	1.6 × 10 <sup>17</sup>	no	0.12	3.0 × 10 <sup>-4</sup>	2.9 × 10 <sup>-4</sup>	[0 - 35°N, 140 - 174°W]
94†	Etna	11.05.2008	2.3 × 10 <sup>14</sup>	1.5 × 10 <sup>18</sup>	yes	0.60	9.8 × 10 <sup>-5</sup>	1.4 × 10 <sup>-4</sup>	[20 - 55°N, 5 - 45°E]
95	Kīlauea	11.05.2008	5.4 × 10 <sup>13</sup>	1.8 × 10 <sup>17</sup>	no	0.04	1.1 × 10 <sup>-4</sup>	2.9 × 10 <sup>-4</sup>	[0 - 35°N, 144 - 175°W]
96	Kīlauea	12.05.2008	6.1 × 10 <sup>13</sup>	4.0 × 10 <sup>17</sup>	no	0.07	6.4 × 10 <sup>-5</sup>	1.5 × 10 <sup>-4</sup>	[15 - 55°N, 25 - 69°E]
97	Etna	14.05.2008	2.4 × 10 <sup>14</sup>	8.2 × 10 <sup>17</sup>	yes	0.70	2.5 × 10 <sup>-4</sup>	2.9 × 10 <sup>-4</sup>	[20 - 60°N, -5 - 35°E]
98	Kīlauea	14.05.2008	1.6 × 10 <sup>13</sup>	1.8 × 10 <sup>17</sup>	no	0.03	-3.2 × 10 <sup>-5</sup>	8.8 × 10 <sup>-5</sup>	[0 - 35°N, 140 - 175°W]
99	Etna	15.05.2008	6.1 × 10 <sup>13</sup>	1.9 × 10 <sup>17</sup>	no	0.01	6.9 × 10 <sup>-5</sup>	3.1 × 10 <sup>-4</sup>	[20 - 55°N, 0 - 35°E]
100	Kīlauea	16.05.2008	3.3 × 10 <sup>13</sup>	6.1 × 10 <sup>17</sup>	no	0.00	1.5 × 10 <sup>-5</sup>	5.4 × 10 <sup>-5</sup>	[0 - 35°N, 143 - 175°W]
101	Kīlauea	17.05.2008	3.9 × 10 <sup>13</sup>	3.8 × 10 <sup>17</sup>	no	0.00	6.0 × 10 <sup>-6</sup>	1.0 × 10 <sup>-4</sup>	[0 - 40°N, 140 - 180°W]
102	Kīlauea	22.05.2008	4.3 × 10 <sup>13</sup>	2.2 × 10 <sup>17</sup>	no	0.00	-1.8 × 10 <sup>-5</sup>	1.9 × 10 <sup>-4</sup>	[0 - 35°N, 140 - 175°W]
103	Kīlauea	26.05.2008	5.3 × 10 <sup>13</sup>	1.9 × 10 <sup>17</sup>	no	0.04	-1.4 × 10 <sup>-4</sup>	2.8 × 10 <sup>-4</sup>	[0 - 35°N, 141 - 175°W]
104	Cerro Azul	30.05.2008	5.1 × 10 <sup>13</sup>	6.5 × 10 <sup>17</sup>	no	0.08	3.6 × 10 <sup>-5</sup>	7.8 × 10 <sup>-5</sup>	[-20 - 20°N, 75 - 110°W]
105	Kīlauea	30.05.2008	5.4 × 10 <sup>13</sup>	1.3 × 10 <sup>17</sup>	no	0.00	-3.2 × 10 <sup>-5</sup>	3.9 × 10 <sup>-4</sup>	[0 - 35°N, 150 - 175°W]
106	Cerro Azul	31.05.2008	5.9 × 10 <sup>13</sup>	4.7 × 10 <sup>17</sup>	no	0.00	8.6 × 10 <sup>-6</sup>	1.2 × 10 <sup>-4</sup>	[-20 - 20°N, 75 - 109°W]
107	Kīlauea	31.05.2008	4.1 × 10 <sup>13</sup>	1.8 × 10 <sup>17</sup>	no	0.02	-6.8 × 10 <sup>-5</sup>	2.1 × 10 <sup>-4</sup>	[0 - 35°N, 140 - 175°W]
108	Cerro Azul	04.06.2008	3.3 × 10 <sup>13</sup>	4.1 × 10 <sup>17</sup>	yes	0.02	-5.9 × 10 <sup>-6</sup>	7.9 × 10 <sup>-5</sup>	[-20 - 15°N, 75 - 110°W]
109	Kīlauea	04.06.2008	4.9 × 10 <sup>13</sup>	1.7 × 10 <sup>17</sup>	no	0.14	2.3 × 10 <sup>-4</sup>	2.8 × 10 <sup>-4</sup>	[0 - 35°N, 145 - 175°W]
110	Cerro Azul	05.06.2008	3.2 × 10 <sup>13</sup>	2.4 × 10 <sup>17</sup>	no	0.01	-3.5 × 10 <sup>-5</sup>	1.3 × 10 <sup>-4</sup>	[-20 - 15°N, 75 - 108°W]
111	Kīlauea	05.06.2008	5.5 × 10 <sup>13</sup>	1.5 × 10 <sup>17</sup>	no	0.00	4.3 × 10 <sup>-5</sup>	3.6 × 10 <sup>-4</sup>	[0 - 35°N, 140 - 175°W]
112	Cerro Azul	06.06.2008	2.6 × 10 <sup>13</sup>	2.4 × 10 <sup>17</sup>	no	0.01	-1.3 × 10 <sup>-5</sup>	1.0 × 10 <sup>-4</sup>	[-20 - 15°N, 70 - 103°W]
113	Soputan	07.06.2008	6.0 × 10 <sup>13</sup>	3.6 × 10 <sup>17</sup>	no	0.01	3.9 × 10 <sup>-5</sup>	1.6 × 10 <sup>-4</sup>	[-25 - 9°N, 119 - 129°E]
114	Cerro Azul	08.06.2008	3.6 × 10 <sup>13</sup>	4.7 × 10 <sup>17</sup>	no	0.01	1.3 × 10 <sup>-5</sup>	7.7 × 10 <sup>-5</sup>	[-20 - 15°N, 78 - 110°W]
115	Cerro Azul	09.06.2008	4.5 × 10 <sup>13</sup>	1.9 × 10 <sup>17</sup>	yes	0.01	3.0 × 10 <sup>-5</sup>	2.2 × 10 <sup>-4</sup>	[-20 - 15°N, 75 - 110°W]
116	Kīlauea	11.06.2008	3.6 × 10 <sup>13</sup>	2.1 × 10 <sup>17</sup>	no	0.01	3.5 × 10 <sup>-5</sup>	1.7 × 10 <sup>-4</sup>	[0 - 35°N, 140 - 173°W]
117	Popocatepetl	12.06.2008	3.6 × 10 <sup>13</sup>	2.5 × 10 <sup>17</sup>	yes	0.03	4.1 × 10 <sup>-5</sup>	1.4 × 10 <sup>-4</sup>	[0 - 35°N, 80 - 115°W]
118	Kīlauea	14.06.2008	3.5 × 10 <sup>13</sup>	2.4 × 10 <sup>17</sup>	no	0.02	-4.7 × 10 <sup>-5</sup>	1.4 × 10 <sup>-4</sup>	[0 - 35°N, 143 - 175°W]
119	Popocatepetl	15.06.2008	3.6 × 10 <sup>13</sup>	2.7 × 10 <sup>17</sup>	yes	0.02	3.8 × 10 <sup>-5</sup>	1.3 × 10 <sup>-4</sup>	[0 - 35°N, 80 - 115°W]
120	Kīlauea	19.06.2008	2.1 × 10 <sup>13</sup>	2.0 × 10 <sup>17</sup>	no	0.09	-1.1 × 10 <sup>-4</sup>	1.0 × 10 <sup>-4</sup>	[0 - 35°N, 142 - 175°W]
121	Kīlauea	30.06.2008	1.3 × 10 <sup>13</sup>	2.4 × 10 <sup>17</sup>	no	0.04	4.5 × 10 <sup>-5</sup>	5.6 × 10 <sup>-5</sup>	[0 - 35°N, 140 - 175°W]
122	Kīlauea	03.07.2008	4.7 × 10 <sup>13</sup>	2.2 × 10 <sup>17</sup>	no	0.09	1.8 × 10 <sup>-4</sup>	2.1 × 10 <sup>-4</sup>	[0 - 35°N, 145 - 180°W]
123	Kīlauea	04.07.2008	6.3 × 10 <sup>13</sup>	2.9 × 10 <sup>17</sup>	no	0.07	1.0 × 10 <sup>-4</sup>	2.1 × 10 <sup>-4</sup>	[0 - 35°N, 140 - 175°W]
124	Kīlauea	05.07.2008	3.7 × 10 <sup>13</sup>	1.5 × 10 <sup>17</sup>	no	0.00	-9.8 × 10 <sup>-6</sup>	2.3 × 10 <sup>-4</sup>	[0 - 35°N, 140 - 174°W]
125	Kīlauea	08.07.2008	3.8 × 10 <sup>13</sup>	2.9 × 10 <sup>17</sup>	no	0.21	1.3 × 10 <sup>-4</sup>	1.3 × 10 <sup>-4</sup>	[0 - 35°N, 144 - 175°W]
126	Kīlauea	10.07.2008	4.1 × 10 <sup>13</sup>	2.5 × 10 <sup>17</sup>	no	0.03	6.7 × 10 <sup>-5</sup>	1.6 × 10 <sup>-4</sup>	[0 - 35°N, 140 - 173°W]
127	Kīlauea	11.07.2008	2.7 × 10 <sup>13</sup>	2.2 × 10 <sup>17</sup>	no	0.03	-6.3 × 10 <sup>-5</sup>	1.2 × 10 <sup>-4</sup>	[0 - 35°N, 140 - 175°W]
128†	Okmok	13.07.2008	3.4 × 10 <sup>13</sup>	4.1 × 10 <sup>18</sup>	no	0.01	2.1 × 10 <sup>-6</sup>	8.2 × 10 <sup>-6</sup>	[30 - 70°N, 140 - 185°W]
129	Kīlauea	13.07.2008	4.9 × 10 <sup>13</sup>	2.9 × 10 <sup>17</sup>	no	0.00	-5.4 × 10 <sup>-6</sup>	1.7 × 10 <sup>-4</sup>	[0 - 35°N, 143 - 175°W]
130†	Okmok	14.07.2008	3.0 × 10 <sup>13</sup>	1.8 × 10 <sup>18</sup>	no	0.01	4.1 × 10 <sup>-6</sup>	1.6 × 10 <sup>-5</sup>	[25 - 70°N, 130 - 180°W]
131	Kīlauea	14.07.2008	7.3 × 10 <sup>13</sup>	3.3 × 10 <sup>17</sup>	yes	0.15	1.1 × 10 <sup>-4</sup>	2.2 × 10 <sup>-4</sup>	[0 - 35°N, 140 - 175°W]
132†	Okmok	15.07.2008	5.1 × 10 <sup>13</sup>	1.9 × 10 <sup>18</sup>	no	0.00	1.6 × 10 <sup>-6</sup>	2.6 × 10 <sup>-5</sup>	[20 - 65°N, 130 - 180°W]
133	Kīlauea	15.07.2008	3.6 × 10 <sup>13</sup>	3.5 × 10 <sup>17</sup>	yes	0.08	7.3 × 10 <sup>-5</sup>	1.0 × 10 <sup>-4</sup>	[0 - 35°N, 140 - 172°W]
134	Okmok	16.07.2008	5.4 × 10 <sup>13</sup>	9.6 × 10 <sup>17</sup>	no	0.00	1.2 × 10 <sup>-6</sup>	5.6 × 10 <sup>-5</sup>	[20 - 65°N, 120 - 175°W]
135	Okmok	17.07.2008	6.6 × 10 <sup>13</sup>	7.6 × 10 <sup>17</sup>	no	0.00	-1.1 × 10 <sup>-6</sup>	8.6 × 10 <sup>-5</sup>	[20 - 65°N, 95 - 170°W]
136	Kīlauea	17.07.2008	4.8 × 10 <sup>13</sup>	1.8 × 10 <sup>17</sup>	no	0.00	4.5 × 10 <sup>-5</sup>	2.6 × 10 <sup>-4</sup>	[0 - 35°N, 140 - 180°W]
137	Okmok	18.07.2008	6.6 × 10 <sup>13</sup>	9.0 × 10 <sup>17</sup>	no	0.03	3.2 × 10 <sup>-5</sup>	7.3 × 10 <sup>-5</sup>	[25 - 70°N, 65 - 155°W]
138	Kīlauea	18.07.2008	5.8 × 10 <sup>13</sup>	2.1 × 10 <sup>17</sup>	no	0.01	6.2 × 10 <sup>-5</sup>	2.7 × 10 <sup>-4</sup>	[0 - 35°N, 142 - 175°W]
139	Okmok	19.07.2008	4.8 × 10 <sup>13</sup>	2.2 × 10 <sup>17</sup>	no	0.00	-2.8 × 10 <sup>-5</sup>	2.1 × 10 <sup>-4</sup>	[30 - 70°N, 30 - 95°W]
140	Kīlauea	19.07.2008	5.1 × 10 <sup>13</sup>	3.3 × 10 <sup>17</sup>	no	0.04	-6.2 × 10 <sup>-5</sup>	1.5 × 10 <sup>-4</sup>	[20 - 65°N, 90 - 150°W]
141	Okmok	19.07.2008	4.2 × 10 <sup>13</sup>	2.1 × 10 <sup>17</sup>	no	0.09	-1.4 × 10 <sup>-4</sup>	2.0 × 10 <sup>-4</sup>	[0 - 35°N, 140 - 175°W]
142	Okmok	20.07.2008	3.0 × 10 <sup>13</sup>	1.3 × 10 <sup>17</sup>	no	0.02	1.4 × 10 <sup>-4</sup>	2.2 × 10 <sup>-4</sup>	[45 - 70°N, 20 - 55°W]
143	Okmok	20.07.2008	5.0 × 10 <sup>13</sup>	1.5 × 10 <sup>17</sup>	no	0.01	8.0 × 10 <sup>-5</sup>	3.2 × 10 <sup>-4</sup>	[20 - 55°N, 130 - 165°W]
144	Okmok	20.07.2008	5.7 × 10 <sup>13</sup>	4.2 × 10 <sup>17</sup>	no	0.06	7.8 × 10 <sup>-5</sup>	1.3 × 10 <sup>-4</sup>	[30 - 65°N, 60 - 110°W]
145	Kīlauea	20.07.2008	6.9 × 10 <sup>13</sup>	3.2 × 10 <sup>17</sup>	no	0.22	1.4 × 10 <sup>-4</sup>	2.1 × 10 <sup>-4</sup>	[0 - 35°N, 140 - 171°W]
146	Okmok	20.07.2008	3.0 × 10 <sup>13</sup>	1.3 × 10 <sup>17</sup>	no	0.02	1.4 × 10 <sup>-4</sup>	2.2 × 10 <sup>-4</sup>	[45 - 70°N, 20 - 55°W]
147	Okmok	21.07.2008	6.7 × 10 <sup>13</sup>	1.7 × 10 <sup>17</sup>	no	0.02	-1.1 × 10 <sup>-4</sup>	3.9 × 10 <sup>-4</sup>	[35 - 70°N, 35 - 75°W]
148	Okmok	22.07.2008	4.0 × 10 <sup>13</sup>	1.7 × 10 <sup>17</sup>	no	0.00	3.0 × 10 <sup>-5</sup>	2.3 × 10 <sup>-4</sup>	[35 - 70°N, 135 - 170°W]
149	Kīlauea	22.07.2008	3.8 × 10 <sup>13</sup>	2.0 × 10 <sup>17</sup>	no	0.06	1.0 × 10 <sup>-4</sup>	1.8 × 10 <sup>-4</sup>	[0 - 35°N, 140 - 175°W]
150	Karymsky	27.07.2008	3.1 × 10 <sup>13</sup>	1.6 × 10 <sup>17</sup>	no	0.17	1.8 × 10 <sup>-4</sup>	1.9 × 10 <sup>-4</sup>	[35 - 70°N, 140 - 175°E]

⊕ location of SO<sub>2</sub> SCD<sub>max</sub> is the same as for BrO SCD<sub>max</sub> † combined SO<sub>2</sub> product in case of high SO<sub>2</sub> SCDs ≥ 1 × 10<sup>18</sup> molec/cm<sup>2</sup> ‡ SO<sub>2</sub> SCDs ≥ 1 × 10<sup>18</sup> molec/cm<sup>2</sup>, but no plume pixel found in the SO<sub>2</sub> AR

\* corresponding volcano cannot be clearly identified

#	volcano	date	BrO SCD <sub>max</sub> [molec/cm <sup>2</sup> ]	SO <sub>2</sub> SCD <sub>max</sub> [molec/cm <sup>2</sup> ]	⊕	r <sup>2</sup>	fitted BrO/SO <sub>2</sub>	BrO <sub>max</sub> /SO <sub>2,max</sub>	coordinates
151	Karymsky	27.07.2008	5.1 × 10 <sup>13</sup>	2.3 × 10 <sup>17</sup>	no	0.06	1.1 × 10 <sup>-4</sup>	2.1 × 10 <sup>-4</sup>	[30 - 65°N, 140 - 175°E]
152	Tungurahua	28.07.2008	4.9 × 10 <sup>13</sup>	2.5 × 10 <sup>17</sup>	no	0.11	7.4 × 10 <sup>-5</sup>	1.9 × 10 <sup>-4</sup>	[-15 - 20°N, 69 - 100°W]
153	Kīlauea	28.07.2008	4.4 × 10 <sup>13</sup>	2.0 × 10 <sup>17</sup>	no	0.07	-1.0 × 10 <sup>-4</sup>	2.1 × 10 <sup>-4</sup>	[0 - 35°N, 140 - 175°W]
154	Kīlauea	29.07.2008	5.5 × 10 <sup>13</sup>	2.8 × 10 <sup>17</sup>	no	0.03	8.6 × 10 <sup>-5</sup>	1.9 × 10 <sup>-4</sup>	[0 - 35°N, 140 - 175°W]
155	Karymsky	01.08.2008	3.4 × 10 <sup>13</sup>	1.4 × 10 <sup>17</sup>	no	0.01	6.7 × 10 <sup>-5</sup>	2.4 × 10 <sup>-4</sup>	[30 - 65°N, 135 - 170°E]
156	Karymsky	01.08.2008	2.6 × 10 <sup>13</sup>	1.8 × 10 <sup>17</sup>	no	0.02	6.7 × 10 <sup>-5</sup>	1.4 × 10 <sup>-4</sup>	[25 - 65°N, 140 - 175°E]
157	Kīlauea	02.08.2008	3.2 × 10 <sup>13</sup>	2.4 × 10 <sup>17</sup>	no	0.03	6.7 × 10 <sup>-5</sup>	1.3 × 10 <sup>-4</sup>	[0 - 35°N, 140 - 175°W]
158	Kīlauea	03.08.2008	4.2 × 10 <sup>13</sup>	2.9 × 10 <sup>17</sup>	yes	0.06	5.9 × 10 <sup>-5</sup>	1.4 × 10 <sup>-4</sup>	[0 - 35°N, 140 - 174°W]
159	Kīlauea	06.08.2008	5.0 × 10 <sup>13</sup>	2.4 × 10 <sup>17</sup>	no	0.01	5.2 × 10 <sup>-5</sup>	2.0 × 10 <sup>-4</sup>	[0 - 35°N, 144 - 175°W]
160†	Kasatochi	08.08.2008	3.6 × 10 <sup>14</sup>	3.9 × 10 <sup>19</sup>	no	0.22	8.6 × 10 <sup>-6</sup>	9.2 × 10 <sup>-6</sup>	[30 - 70°N, 145 - 195°W]
161	Kīlauea	08.08.2008	3.6 × 10 <sup>13</sup>	2.0 × 10 <sup>17</sup>	no	0.19	-1.6 × 10 <sup>-4</sup>	1.8 × 10 <sup>-4</sup>	[0 - 35°N, 140 - 173°W]
162†	Kasatochi	09.08.2008	4.5 × 10 <sup>14</sup>	2.6 × 10 <sup>19</sup>	no	0.24	1.9 × 10 <sup>-5</sup>	1.7 × 10 <sup>-5</sup>	[25 - 70°N, 135 - 190°W]
163†	Kasatochi	10.08.2008	4.3 × 10 <sup>14</sup>	1.9 × 10 <sup>19</sup>	no	0.41	2.4 × 10 <sup>-5</sup>	2.2 × 10 <sup>-5</sup>	[25 - 70°N, 110 - 185°W]
164†	Kasatochi	11.08.2008	3.7 × 10 <sup>14</sup>	1.9 × 10 <sup>19</sup>	no	0.50	4.2 × 10 <sup>-5</sup>	1.9 × 10 <sup>-5</sup>	[20 - 70°N, 60 - 180°W]
165†	Kasatochi	12.08.2008	3.0 × 10 <sup>14</sup>	1.6 × 10 <sup>19</sup>	no	0.21	2.4 × 10 <sup>-5</sup>	1.9 × 10 <sup>-5</sup>	[20 - 70°N, 50 - 175°W]
166	Kīlauea	12.08.2008	6.2 × 10 <sup>13</sup>	1.3 × 10 <sup>17</sup>	no	0.01	9.5 × 10 <sup>-5</sup>	4.6 × 10 <sup>-4</sup>	[0 - 35°N, 140 - 175°W]
167†	Kasatochi	13.08.2008	1.3 × 10 <sup>14</sup>	1.5 × 10 <sup>19</sup>	no	0.14	1.2 × 10 <sup>-5</sup>	9.0 × 10 <sup>-6</sup>	[25 - 70°N, 20 - 175°W]
168	Kīlauea	13.08.2008	2.2 × 10 <sup>13</sup>	1.5 × 10 <sup>17</sup>	no	0.00	5.2 × 10 <sup>-5</sup>	1.5 × 10 <sup>-4</sup>	[0 - 35°N, 140 - 172°W]
169†	Kasatochi	14.08.2008	1.1 × 10 <sup>14</sup>	6.9 × 10 <sup>18</sup>	no	0.00	1.8 × 10 <sup>-6</sup>	1.7 × 10 <sup>-5</sup>	[20 - 70°N, -200 - 15°E]
170†	Kasatochi	15.08.2008	9.4 × 10 <sup>13</sup>	4.9 × 10 <sup>18</sup>	no	0.01	6.0 × 10 <sup>-6</sup>	1.9 × 10 <sup>-5</sup>	[20 - 70°N, -225 - 40°E]
171	Kīlauea	15.08.2008	6.5 × 10 <sup>13</sup>	2.3 × 10 <sup>17</sup>	no	0.02	5.7 × 10 <sup>-5</sup>	2.8 × 10 <sup>-4</sup>	[0 - 35°N, 140 - 180°W]
172†	Kasatochi	16.08.2008	2.9 × 10 <sup>14</sup>	3.0 × 10 <sup>18</sup>	no	0.00	5.3 × 10 <sup>-6</sup>	9.7 × 10 <sup>-5</sup>	[20 - 70°N, -170 - 50°E]
173	Kīlauea	16.08.2008	4.2 × 10 <sup>13</sup>	2.1 × 10 <sup>17</sup>	no	0.12	1.5 × 10 <sup>-4</sup>	1.9 × 10 <sup>-4</sup>	[0 - 35°N, 142 - 175°W]
174	Kasatochi	16.08.2008	5.9 × 10 <sup>13</sup>	1.7 × 10 <sup>17</sup>	no	0.00	-5.1 × 10 <sup>-5</sup>	3.3 × 10 <sup>-4</sup>	[40 - 70°N, 35 - 80°E]
175†	Kasatochi	17.08.2008	2.2 × 10 <sup>15</sup>	3.1 × 10 <sup>18</sup>	no	0.00	1.6 × 10 <sup>-5</sup>	6.9 × 10 <sup>-4</sup>	[20 - 70°N, -150 - 80°E]
176	Kasatochi	17.08.2008	5.9 × 10 <sup>13</sup>	3.1 × 10 <sup>17</sup>	no	0.06	9.2 × 10 <sup>-5</sup>	1.8 × 10 <sup>-4</sup>	[35 - 70°N, 147 - 175°E]
177†	Kasatochi	18.08.2008	8.5 × 10 <sup>13</sup>	1.6 × 10 <sup>18</sup>	no	0.03	2.8 × 10 <sup>-5</sup>	5.0 × 10 <sup>-5</sup>	[25 - 70°N, -135 - 35°E]
178	Kasatochi	18.08.2008	8.7 × 10 <sup>13</sup>	9.7 × 10 <sup>17</sup>	no	0.04	3.5 × 10 <sup>-5</sup>	9.0 × 10 <sup>-5</sup>	[20 - 70°N, -45 - 100°E]
179	Kasatochi	18.08.2008	6.7 × 10 <sup>13</sup>	3.1 × 10 <sup>17</sup>	no	0.08	8.6 × 10 <sup>-5</sup>	2.1 × 10 <sup>-4</sup>	[35 - 70°N, 144 - 185°E]
180	Kasatochi	19.08.2008	4.7 × 10 <sup>13</sup>	1.4 × 10 <sup>17</sup>	no	0.03	-1.5 × 10 <sup>-4</sup>	3.2 × 10 <sup>-4</sup>	[25 - 60°N, 65 - 105°E]
181	Kasatochi	19.08.2008	5.5 × 10 <sup>13</sup>	7.5 × 10 <sup>17</sup>	no	0.04	3.1 × 10 <sup>-5</sup>	7.3 × 10 <sup>-5</sup>	[25 - 70°N, 10 - 77°W]
182	Kasatochi	19.08.2008	8.2 × 10 <sup>13</sup>	2.5 × 10 <sup>17</sup>	no	0.06	1.5 × 10 <sup>-4</sup>	3.2 × 10 <sup>-4</sup>	[35 - 70°N, 158 - 190°E]
183	Kasatochi	20.08.2008	6.7 × 10 <sup>13</sup>	7.6 × 10 <sup>17</sup>	no	0.01	-2.7 × 10 <sup>-5</sup>	8.7 × 10 <sup>-5</sup>	[25 - 70°N, 55 - 125°W]
184	Kasatochi	20.08.2008	7.6 × 10 <sup>13</sup>	8.3 × 10 <sup>17</sup>	no	0.00	8.4 × 10 <sup>-6</sup>	9.1 × 10 <sup>-5</sup>	[35 - 70°N, -15 - 80°E]
185	Kasatochi	20.08.2008	6.0 × 10 <sup>13</sup>	6.7 × 10 <sup>17</sup>	no	0.03	3.4 × 10 <sup>-5</sup>	9.0 × 10 <sup>-5</sup>	[15 - 70°N, 0 - 60°W]
186	Kasatochi	20.08.2008	5.0 × 10 <sup>13</sup>	2.8 × 10 <sup>17</sup>	no	0.28	1.6 × 10 <sup>-4</sup>	1.7 × 10 <sup>-4</sup>	[35 - 70°N, 160 - 180°W]
187	Kasatochi	23.08.2008	7.3 × 10 <sup>13</sup>	4.5 × 10 <sup>17</sup>	no	0.00	-1.5 × 10 <sup>-5</sup>	1.6 × 10 <sup>-4</sup>	[35 - 70°N, 95 - 140°E]
188	Kasatochi	23.08.2008	7.9 × 10 <sup>13</sup>	4.2 × 10 <sup>17</sup>	no	0.00	-7.1 × 10 <sup>-7</sup>	1.8 × 10 <sup>-4</sup>	[30 - 70°N, 10 - 75°E]
189	Kasatochi	23.08.2008	4.2 × 10 <sup>13</sup>	1.9 × 10 <sup>17</sup>	no	0.00	-2.6 × 10 <sup>-5</sup>	2.1 × 10 <sup>-4</sup>	[35 - 70°N, 30 - 65°W]
190	Kasatochi	23.08.2008	8.9 × 10 <sup>13</sup>	2.6 × 10 <sup>17</sup>	no	0.01	6.3 × 10 <sup>-5</sup>	3.4 × 10 <sup>-4</sup>	[15 - 70°N, 60 - 115°W]
191	Kasatochi	24.08.2008	6.7 × 10 <sup>13</sup>	2.7 × 10 <sup>17</sup>	no	0.00	8.0 × 10 <sup>-6</sup>	2.4 × 10 <sup>-4</sup>	[15 - 70°N, 55 - 150°W]
192	Kasatochi	24.08.2008	5.7 × 10 <sup>13</sup>	3.5 × 10 <sup>17</sup>	no	0.01	-3.3 × 10 <sup>-5</sup>	1.6 × 10 <sup>-4</sup>	[35 - 70°N, 95 - 140°E]
193	Kasatochi	24.08.2008	4.8 × 10 <sup>13</sup>	3.2 × 10 <sup>17</sup>	no	0.00	-5.6 × 10 <sup>-6</sup>	1.4 × 10 <sup>-4</sup>	[35 - 70°N, 25 - 80°E]
194	Kasatochi	24.08.2008	3.4 × 10 <sup>13</sup>	1.6 × 10 <sup>17</sup>	no	0.00	-2.3 × 10 <sup>-5</sup>	2.0 × 10 <sup>-4</sup>	[30 - 65°N, 20 - 55°W]
195	Kasatochi	24./25.08.2008	4.0 × 10 <sup>13</sup>	2.1 × 10 <sup>17</sup>	no	0.01	-6.4 × 10 <sup>-5</sup>	1.8 × 10 <sup>-4</sup>	[45 - 70°N, 170 - 210°W]
196	Kasatochi	25.08.2008	6.5 × 10 <sup>13</sup>	1.8 × 10 <sup>17</sup>	no	0.02	1.0 × 10 <sup>-4</sup>	3.6 × 10 <sup>-4</sup>	[15 - 55°N, 80 - 125°W]
197	Kasatochi	26.08.2008	3.0 × 10 <sup>13</sup>	1.4 × 10 <sup>17</sup>	no	0.00	-2.6 × 10 <sup>-5</sup>	2.0 × 10 <sup>-4</sup>	[50 - 70°N, 115 - 150°E]
198	Kīlauea	25.08.2008	4.4 × 10 <sup>13</sup>	2.6 × 10 <sup>17</sup>	no	0.00	-2.9 × 10 <sup>-5</sup>	1.7 × 10 <sup>-4</sup>	[0 - 35°N, 140 - 175°W]
199	Kasatochi	25.08.2008	5.2 × 10 <sup>13</sup>	2.2 × 10 <sup>17</sup>	no	0.03	1.0 × 10 <sup>-4</sup>	2.3 × 10 <sup>-4</sup>	[40 - 70°N, 40 - 140°W]
200	Kasatochi	25.08.2008	5.9 × 10 <sup>13</sup>	1.4 × 10 <sup>17</sup>	no	0.02	1.8 × 10 <sup>-4</sup>	4.2 × 10 <sup>-4</sup>	[35 - 70°N, 100 - 145°E]
201	Kasatochi	25.08.2008	4.5 × 10 <sup>13</sup>	2.7 × 10 <sup>17</sup>	no	0.05	-6.4 × 10 <sup>-5</sup>	1.6 × 10 <sup>-4</sup>	[50 - 70°N, 15 - 70°E]
202	Kasatochi	26.08.2008	2.9 × 10 <sup>13</sup>	3.0 × 10 <sup>17</sup>	no	0.00	4.2 × 10 <sup>-6</sup>	9.8 × 10 <sup>-5</sup>	[50 - 70°N, 35 - 70°E]
203	Kasatochi	26.08.2008	5.4 × 10 <sup>13</sup>	2.5 × 10 <sup>17</sup>	no	0.01	4.6 × 10 <sup>-5</sup>	2.1 × 10 <sup>-4</sup>	[40 - 70°N, 25 - 80°W]
204	Kasatochi	26.08.2008	3.6 × 10 <sup>13</sup>	1.8 × 10 <sup>17</sup>	no	0.02	-9.6 × 10 <sup>-5</sup>	1.9 × 10 <sup>-4</sup>	[15 - 55°N, 90 - 125°W]
205	Kīlauea	26.08.2008	4.4 × 10 <sup>13</sup>	4.2 × 10 <sup>17</sup>	no	0.01	2.5 × 10 <sup>-5</sup>	1.0 × 10 <sup>-4</sup>	[0 - 35°N, 141 - 175°W]
206	Kasatochi	26.08.2008	4.9 × 10 <sup>13</sup>	2.3 × 10 <sup>17</sup>	no	0.00	5.8 × 10 <sup>-6</sup>	2.0 × 10 <sup>-4</sup>	[25 - 60°N, 160 - 200°W]
207	Kasatochi	26./27.08.2008	2.9 × 10 <sup>13</sup>	1.2 × 10 <sup>17</sup>	no	0.01	-4.6 × 10 <sup>-5</sup>	2.3 × 10 <sup>-4</sup>	[35 - 70°N, 135 - 170°E]
208	Kasatochi	27.08.2008	8.1 × 10 <sup>13</sup>	2.4 × 10 <sup>17</sup>	no	0.00	-4.4 × 10 <sup>-5</sup>	3.3 × 10 <sup>-4</sup>	[30 - 70°N, 125 - 185°W]
209	Kasatochi	27.08.2008	3.8 × 10 <sup>13</sup>	1.1 × 10 <sup>17</sup>	no	0.03	-2.2 × 10 <sup>-4</sup>	3.3 × 10 <sup>-4</sup>	[45 - 70°N, 15 - 55°W]
210	Kasatochi	27.08.2008	4.0 × 10 <sup>13</sup>	2.4 × 10 <sup>17</sup>	no	0.02	3.9 × 10 <sup>-5</sup>	1.6 × 10 <sup>-4</sup>	[40 - 70°N, 40 - 75°W]
211	Kasatochi	27.08.2008	3.3 × 10 <sup>13</sup>	1.5 × 10 <sup>17</sup>	no	0.00	-1.4 × 10 <sup>-5</sup>	2.2 × 10 <sup>-4</sup>	[15 - 55°N, 90 - 125°W]
212	Kīlauea	27.08.2008	3.9 × 10 <sup>13</sup>	1.9 × 10 <sup>17</sup>	no	0.00	3.5 × 10 <sup>-6</sup>	2.0 × 10 <sup>-4</sup>	[0 - 35°N, 140 - 175°W]
213	Kasatochi	27.08.2008	5.1 × 10 <sup>13</sup>	3.7 × 10 <sup>17</sup>	no	0.18	8.4 × 10 <sup>-5</sup>	1.3 × 10 <sup>-4</sup>	[50 - 70°N, 45 - 70°E]
214	Kasatochi	28.08.2008	5.0 × 10 <sup>13</sup>	1.6 × 10 <sup>17</sup>	no	0.00	-9.0 × 10 <sup>-5</sup>	3.1 × 10 <sup>-4</sup>	[40 - 70°N, 95 - 130°W]
215	Kasatochi	28.08.2008	6.4 × 10 <sup>13</sup>	1.3 × 10 <sup>17</sup>	no	0.00	4.6 × 10 <sup>-5</sup>	4.7 × 10 <sup>-4</sup>	[40 - 70°N, 115 - 150°W]
216	Kīlauea	28.08.2008	3.9 × 10 <sup>13</sup>	3.7 × 10 <sup>17</sup>	yes	0.31	9.1 × 10 <sup>-5</sup>	1.0 × 10 <sup>-4</sup>	[0 - 35°N, 140 - 175°W]
217	Kasatochi	28.08.2008	6.9 × 10 <sup>13</sup>	1.8 × 10 <sup>17</sup>	no	0.05	2.1 × 10 <sup>-4</sup>	3.7 × 10 <sup>-4</sup>	[25 - 60°N, 155 - 190°E]
218	Kasatochi	29.08.2008	4.4 × 10 <sup>13</sup>	1.8 × 10 <sup>17</sup>	no	0.01	4.5 × 10 <sup>-5</sup>	2.4 × 10 <sup>-4</sup>	[45 - 70°N, 100 - 135°E]
219	Kasatochi	30.08.2008	3.9 × 10 <sup>13</sup>	1.7 × 10 <sup>17</sup>	no	0.06	1.6 × 10 <sup>-4</sup>	2.3 × 10 <sup>-4</sup>	[45 - 70°N, 115 - 155°E]
220	Kīlauea	30.08.2008	4.1 × 10 <sup>13</sup>	2.6 × 10 <sup>17</sup>	no	0.04	6.0 × 10 <sup>-5</sup>	1.5 × 10 <sup>-4</sup>	[0 - 35°N, 145 - 180°W]
221	Kasatochi	30./31.08.2008	4.1 × 10 <sup>13</sup>	2.5 × 10 <sup>17</sup>	no	0.03	-7.5 × 10 <sup>-5</sup>	1.6 × 10 <sup>-4</sup>	[50 - 70°N, 120 - 160°E]
222	Kīlauea	31.08.2008	5.9 × 10 <sup>13</sup>	3.1 × 10 <sup>17</sup>	no	0.03	6.5 × 10 <sup>-5</sup>	1.8 × 10 <sup>-4</sup>	[0 - 35°N, 140 - 175°W]
223	Kasatochi	31.08/01.09.2008	4.7 × 10 <sup>13</sup>	2.6 × 10 <sup>17</sup>	no	0.00	-2.6 × 10 <sup>-5</sup>	1.8 × 10 <sup>-4</sup>	[35 - 70°N, 170 - 210°W]
224	Kasatochi	01.09.2008	6.4 × 10 <sup>13</sup>	1.7 × 10 <sup>17</sup>	no	0.03	1.7 × 10 <sup>-4</sup>	3.6 × 10 <sup>-4</sup>	[30 - 70°N, 145 - 190°W]
225	Kasatochi	02.09.2008	3.3 × 10 <sup>13</sup>	1.3 × 10 <sup>17</sup>	no	0.00	-4.3 × 10 <sup>-5</sup>	2.4 × 10 <sup>-4</sup>	[40 - 70°N, 156 - 195°W]

⊕ location of SO<sub>2</sub> SCD<sub>max</sub> is the same as for BrO SCD<sub>max</sub> † combined SO<sub>2</sub> product in case of high SO<sub>2</sub> SCDs ≥ 1 × 10<sup>18</sup> molec/cm<sup>2</sup> ‡ SO<sub>2</sub> SCDs ≥ 1 × 10<sup>18</sup> molec/cm<sup>2</sup>, but no plume pixel found in the SO<sub>2</sub> AR

\* corresponding volcano cannot be clearly identified

#	volcano	date	BrO SCD <sub>max</sub> [molec/cm <sup>2</sup> ]	SO <sub>2</sub> SCD <sub>max</sub> [molec/cm <sup>2</sup> ]	⊕	r <sup>2</sup>	fitted BrO/SO <sub>2</sub>	BrO <sub>max</sub> /SO <sub>2,max</sub>	coordinates
226	Kasatochi	03.09.2008	4.3 × 10 <sup>13</sup>	1.8 × 10 <sup>17</sup>	no	0.01	-3.6 × 10 <sup>-5</sup>	2.3 × 10 <sup>-4</sup>	[30 - 65°N, 155 - 195°W]
227	Kīlauea	04.09.2008	6.2 × 10 <sup>13</sup>	2.4 × 10 <sup>17</sup>	no	0.04	1.1 × 10 <sup>-4</sup>	2.6 × 10 <sup>-4</sup>	[0 - 35°N, 144 - 180°W]
228	Kasatochi	05.09.2008	5.8 × 10 <sup>13</sup>	1.6 × 10 <sup>17</sup>	no	0.06	-2.0 × 10 <sup>-4</sup>	3.5 × 10 <sup>-4</sup>	[45 - 70°N, 120 - 155°W]
229	Kīlauea	05.09.2008	5.6 × 10 <sup>13</sup>	3.2 × 10 <sup>17</sup>	yes	0.20	1.0 × 10 <sup>-4</sup>	1.7 × 10 <sup>-4</sup>	[0 - 35°N, 140 - 175°W]
230	Kīlauea	06.09.2008	3.9 × 10 <sup>13</sup>	1.8 × 10 <sup>17</sup>	no	0.02	-4.2 × 10 <sup>-5</sup>	2.1 × 10 <sup>-4</sup>	[0 - 35°N, 140 - 173°W]
231	Kīlauea	09.09.2008	5.2 × 10 <sup>13</sup>	3.1 × 10 <sup>17</sup>	no	0.03	6.1 × 10 <sup>-5</sup>	1.6 × 10 <sup>-4</sup>	[0 - 35°N, 143 - 175°W]
232	Kīlauea	10.09.2008	5.2 × 10 <sup>13</sup>	3.1 × 10 <sup>17</sup>	no	0.02	3.9 × 10 <sup>-5</sup>	1.6 × 10 <sup>-4</sup>	[0 - 35°N, 142 - 175°W]
233	Kīlauea	11.09.2008	1.9 × 10 <sup>13</sup>	1.9 × 10 <sup>17</sup>	no	0.03	4.4 × 10 <sup>-5</sup>	1.0 × 10 <sup>-4</sup>	[0 - 35°N, 140 - 172°W]
234	Kīlauea	14.09.2008	4.3 × 10 <sup>13</sup>	4.9 × 10 <sup>17</sup>	no	0.00	-2.4 × 10 <sup>-6</sup>	8.7 × 10 <sup>-5</sup>	[0 - 35°N, 142 - 175°W]
235	Kīlauea	15.09.2008	5.5 × 10 <sup>13</sup>	2.8 × 10 <sup>17</sup>	no	0.00	5.7 × 10 <sup>-6</sup>	1.9 × 10 <sup>-4</sup>	[0 - 35°N, 140 - 175°W]
236	Kīlauea	18.09.2008	4.2 × 10 <sup>13</sup>	1.4 × 10 <sup>17</sup>	no	0.04	1.3 × 10 <sup>-4</sup>	2.9 × 10 <sup>-4</sup>	[0 - 35°N, 140 - 175°W]
237	Kīlauea	19.09.2008	3.6 × 10 <sup>13</sup>	4.5 × 10 <sup>17</sup>	no	0.05	-5.3 × 10 <sup>-5</sup>	8.0 × 10 <sup>-5</sup>	[0 - 35°N, 142 - 180°W]
238	Kīlauea	23.09.2008	5.3 × 10 <sup>13</sup>	1.4 × 10 <sup>17</sup>	no	0.00	2.3 × 10 <sup>-5</sup>	3.5 × 10 <sup>-4</sup>	[0 - 35°N, 146 - 180°W]
239	Kīlauea	29.09.2008	6.0 × 10 <sup>13</sup>	2.9 × 10 <sup>17</sup>	no	0.00	9.9 × 10 <sup>-6</sup>	2.0 × 10 <sup>-4</sup>	[0 - 35°N, 140 - 175°W]
240	Kīlauea	30.09.2008	5.4 × 10 <sup>13</sup>	2.0 × 10 <sup>17</sup>	no	0.04	9.8 × 10 <sup>-5</sup>	2.6 × 10 <sup>-4</sup>	[0 - 35°N, 140 - 174°W]
241	Kīlauea	03.10.2008	4.4 × 10 <sup>13</sup>	2.1 × 10 <sup>17</sup>	no	0.03	7.5 × 10 <sup>-5</sup>	2.0 × 10 <sup>-4</sup>	[0 - 35°N, 144 - 175°W]
242	Kīlauea	08.10.2008	4.5 × 10 <sup>13</sup>	1.8 × 10 <sup>17</sup>	no	0.00	-1.8 × 10 <sup>-5</sup>	2.4 × 10 <sup>-4</sup>	[-15 - 20°N, 95 - 132°E]
243	Kīlauea	08.10.2008	4.5 × 10 <sup>13</sup>	2.1 × 10 <sup>17</sup>	no	0.06	1.3 × 10 <sup>-4</sup>	2.0 × 10 <sup>-4</sup>	[0 - 35°N, 143 - 175°W]
244	Kīlauea	10.10.2008	2.0 × 10 <sup>13</sup>	2.0 × 10 <sup>17</sup>	no	0.00	5.5 × 10 <sup>-6</sup>	1.0 × 10 <sup>-4</sup>	[0 - 35°N, 140 - 172°W]
245	Kīlauea	13.10.2008	5.7 × 10 <sup>13</sup>	3.2 × 10 <sup>17</sup>	no	0.01	-3.1 × 10 <sup>-5</sup>	1.7 × 10 <sup>-4</sup>	[0 - 35°N, 142 - 175°W]
246	Kīlauea	27.10.2008	5.4 × 10 <sup>13</sup>	4.2 × 10 <sup>17</sup>	no	0.00	1.3 × 10 <sup>-5</sup>	1.2 × 10 <sup>-4</sup>	[0 - 35°N, 145 - 175°W]
247	Nevedo del Huila	28.10.2008	4.7 × 10 <sup>13</sup>	2.9 × 10 <sup>17</sup>	no	0.05	7.8 × 10 <sup>-5</sup>	1.6 × 10 <sup>-4</sup>	[-15 - 20°N, 66 - 95°W]
248	Nevedo del Huila	29.10.2008	3.3 × 10 <sup>13</sup>	3.2 × 10 <sup>17</sup>	no	0.00	-3.6 × 10 <sup>-6</sup>	1.0 × 10 <sup>-4</sup>	[-15 - 20°N, 62 - 100°W]
249†	Dalaffilla	04.11.2008	1.7 × 10 <sup>14</sup>	4.3 × 10 <sup>18</sup>	no	0.01	1.4 × 10 <sup>-5</sup>	3.9 × 10 <sup>-5</sup>	[0 - 40°N, 30 - 70°E]
250†	Dalaffilla	05.11.2008	1.2 × 10 <sup>14</sup>	1.6 × 10 <sup>18</sup>	no	0.05	3.1 × 10 <sup>-5</sup>	7.4 × 10 <sup>-5</sup>	[-5 - 50°N, 25 - 100°E]
251†	Dalaffilla	06.11.2008	9.1 × 10 <sup>13</sup>	1.4 × 10 <sup>18</sup>	no	0.06	2.9 × 10 <sup>-5</sup>	6.3 × 10 <sup>-5</sup>	[5 - 50°N, 46 - 110°E]
252	Dalaffilla	06.11.2008	6.4 × 10 <sup>13</sup>	1.3 × 10 <sup>17</sup>	no	0.02	1.9 × 10 <sup>-4</sup>	4.9 × 10 <sup>-4</sup>	[0 - 35°N, 25 - 60°E]
253	Dalaffilla	07.11.2008	5.5 × 10 <sup>13</sup>	7.8 × 10 <sup>17</sup>	no	0.05	3.0 × 10 <sup>-5</sup>	7.0 × 10 <sup>-5</sup>	[5 - 45°N, 60 - 115°E]
254	Dalaffilla	07.11.2008	6.1 × 10 <sup>13</sup>	2.5 × 10 <sup>17</sup>	no	0.05	-8.7 × 10 <sup>-5</sup>	2.4 × 10 <sup>-4</sup>	[10 - 50°N, 140 - 175°E]
255	Dalaffilla	08.11.2008	7.2 × 10 <sup>13</sup>	3.0 × 10 <sup>17</sup>	no	0.01	3.0 × 10 <sup>-5</sup>	2.3 × 10 <sup>-4</sup>	[-5 - 40°N, 60 - 120°E]
256	Dalaffilla	08.11.2008	5.7 × 10 <sup>13</sup>	2.4 × 10 <sup>17</sup>	no	0.01	6.1 × 10 <sup>-5</sup>	2.4 × 10 <sup>-4</sup>	[0 - 50°N, 140 - 177°E]
257	Dalaffilla	09.11.2008	5.1 × 10 <sup>13</sup>	1.6 × 10 <sup>17</sup>	no	0.01	4.3 × 10 <sup>-5</sup>	3.1 × 10 <sup>-4</sup>	[-5 - 35°N, 150 - 190°E]
258	Dalaffilla	10.11.2008	5.0 × 10 <sup>13</sup>	1.8 × 10 <sup>17</sup>	no	0.02	1.2 × 10 <sup>-4</sup>	2.8 × 10 <sup>-4</sup>	[-5 - 35°N, 50 - 100°E]
259	Dalaffilla	10.11.2008	7.2 × 10 <sup>13</sup>	1.7 × 10 <sup>17</sup>	no	0.00	1.4 × 10 <sup>-5</sup>	4.2 × 10 <sup>-4</sup>	[-5 - 30°N, 147 - 186°E]
260	Galeras	11.11.2008	6.6 × 10 <sup>13</sup>	2.3 × 10 <sup>17</sup>	no	0.05	1.4 × 10 <sup>-4</sup>	2.8 × 10 <sup>-4</sup>	[-20 - 20°N, 65 - 100°W]
261	Nevedo del Huila	13.11.2008	4.3 × 10 <sup>13</sup>	2.4 × 10 <sup>17</sup>	no	0.21	-1.6 × 10 <sup>-4</sup>	1.7 × 10 <sup>-4</sup>	[-15 - 20°N, 60 - 95°W]
262	Ambrym	15.11.2008	3.3 × 10 <sup>13</sup>	2.3 × 10 <sup>17</sup>	no	0.01	4.0 × 10 <sup>-5</sup>	1.4 × 10 <sup>-4</sup>	[0 - 35°S, 150 - 185°E]
263	Kīlauea	16.11.2008	6.7 × 10 <sup>13</sup>	2.2 × 10 <sup>17</sup>	no	0.00	-5.9 × 10 <sup>-5</sup>	3.0 × 10 <sup>-4</sup>	[0 - 35°N, 141 - 175°W]
264	Nevedo del Huila	22.11.2008	4.3 × 10 <sup>13</sup>	2.8 × 10 <sup>17</sup>	no	0.00	2.3 × 10 <sup>-5</sup>	1.5 × 10 <sup>-4</sup>	[-15 - 20°N, 63 - 95°W]
265	Kīlauea	02.12.2008	1.5 × 10 <sup>13</sup>	2.5 × 10 <sup>17</sup>	no	0.31	-1.7 × 10 <sup>-4</sup>	5.9 × 10 <sup>-5</sup>	[5 - 40°N, 140 - 172°W]
266	Ambrym	06.12.2008	2.1 × 10 <sup>13</sup>	1.9 × 10 <sup>17</sup>	no	0.25	1.2 × 10 <sup>-4</sup>	1.1 × 10 <sup>-4</sup>	[0 - 35°S, 150 - 185°E]
267	Ambrym	14.12.2008	5.5 × 10 <sup>13</sup>	2.2 × 10 <sup>17</sup>	no	0.00	1.8 × 10 <sup>-5</sup>	2.4 × 10 <sup>-4</sup>	[0 - 35°S, 150 - 185°E]
268	Tungurahua	25.12.2008	2.3 × 10 <sup>13</sup>	2.7 × 10 <sup>17</sup>	no	0.04	-3.5 × 10 <sup>-5</sup>	8.8 × 10 <sup>-5</sup>	[-20 - 15°N, 68 - 95°W]
269	Tungurahua	26.12.2008	3.9 × 10 <sup>13</sup>	1.7 × 10 <sup>17</sup>	no	0.01	4.5 × 10 <sup>-5</sup>	2.2 × 10 <sup>-4</sup>	[-20 - 15°N, 70 - 95°W]
270	Ambrym	29.12.2008	1.4 × 10 <sup>13</sup>	3.0 × 10 <sup>17</sup>	no	0.00	-3.4 × 10 <sup>-5</sup>	4.5 × 10 <sup>-5</sup>	[0 - 35°S, 150 - 182°E]
271	Ambrym	30.12.2008	3.2 × 10 <sup>13</sup>	2.3 × 10 <sup>17</sup>	no	0.12	1.4 × 10 <sup>-4</sup>	1.3 × 10 <sup>-4</sup>	[0 - 35°S, 150 - 185°E]
272	Tungurahua	20.01.2009	2.1 × 10 <sup>13</sup>	1.7 × 10 <sup>17</sup>	no	0.26	-1.5 × 10 <sup>-4</sup>	1.1 × 10 <sup>-4</sup>	[-20 - 15°N, 66 - 95°W]
273	Ambrym	22.01.2009	4.3 × 10 <sup>13</sup>	2.9 × 10 <sup>17</sup>	no	0.01	2.1 × 10 <sup>-5</sup>	1.5 × 10 <sup>-4</sup>	[0 - 35°S, 150 - 181°E]
274	Ambrym	11.02.2009	3.7 × 10 <sup>13</sup>	2.4 × 10 <sup>17</sup>	no	0.01	3.3 × 10 <sup>-5</sup>	1.5 × 10 <sup>-4</sup>	[0 - 35°S, 150 - 185°E]
275	Ambrym	06.03.2009	5.4 × 10 <sup>13</sup>	3.7 × 10 <sup>17</sup>	no	0.00	5.7 × 10 <sup>-6</sup>	1.4 × 10 <sup>-4</sup>	[0 - 35°S, 150 - 185°E]
276	Ambrym	07.03.2009	4.2 × 10 <sup>13</sup>	2.6 × 10 <sup>17</sup>	no	0.09	8.7 × 10 <sup>-5</sup>	1.6 × 10 <sup>-4</sup>	[-35 - 5°N, 150 - 185°E]
277	Ambrym	11.03.2009	4.2 × 10 <sup>13</sup>	3.2 × 10 <sup>17</sup>	no	0.10	1.0 × 10 <sup>-4</sup>	1.3 × 10 <sup>-4</sup>	[0 - 35°S, 150 - 185°E]
278†	Mt. Redoubt	23.03.2009	1.7 × 10 <sup>14</sup>	4.4 × 10 <sup>18</sup>	no	0.47	4.4 × 10 <sup>-5</sup>	3.8 × 10 <sup>-5</sup>	[45 - 70°N, 115 - 170°W]
279‡	Mt. Redoubt	24.03.2009	1.1 × 10 <sup>14</sup>	1.0 × 10 <sup>18</sup>	no	0.50	1.0 × 10 <sup>-4</sup>	1.0 × 10 <sup>-4</sup>	[45 - 70°N, 115 - 142°W]
280‡	Mt. Redoubt	25.03.2009	1.2 × 10 <sup>14</sup>	1.0 × 10 <sup>18</sup>	no	0.25	8.2 × 10 <sup>-5</sup>	1.2 × 10 <sup>-4</sup>	[30 - 70°N, 100 - 140°W]
281	Mt. Redoubt	26.03.2009	9.3 × 10 <sup>13</sup>	7.2 × 10 <sup>17</sup>	no	0.31	1.4 × 10 <sup>-4</sup>	1.2 × 10 <sup>-4</sup>	[20 - 70°N, 85 - 130°W]
282†	Mt. Redoubt	26.03.2009	1.9 × 10 <sup>14</sup>	5.8 × 10 <sup>18</sup>	yes	0.90	3.5 × 10 <sup>-5</sup>	3.3 × 10 <sup>-5</sup>	[40 - 70°N, 135 - 170°W]
283	Ambrym	26.03.2009	5.2 × 10 <sup>13</sup>	2.3 × 10 <sup>17</sup>	no	0.07	8.5 × 10 <sup>-5</sup>	2.2 × 10 <sup>-4</sup>	[0 - 35°S, 150 - 182°E]
284‡	Mt. Redoubt	27.03.2009	7.9 × 10 <sup>13</sup>	1.0 × 10 <sup>18</sup>	no	0.01	1.7 × 10 <sup>-5</sup>	7.6 × 10 <sup>-5</sup>	[20 - 70°N, 70 - 125°W]
285†	Mt. Redoubt	27.03.2009	8.0 × 10 <sup>13</sup>	3.1 × 10 <sup>18</sup>	no	0.17	2.7 × 10 <sup>-5</sup>	2.5 × 10 <sup>-5</sup>	[45 - 70°N, 115 - 170°W]
286	Mt. Redoubt	28.03.2009	7.8 × 10 <sup>13</sup>	6.8 × 10 <sup>17</sup>	no	0.07	6.7 × 10 <sup>-5</sup>	1.1 × 10 <sup>-4</sup>	[20 - 70°N, 40 - 110°W]
287‡	Mt. Redoubt	28.03.2009	9.3 × 10 <sup>13</sup>	1.1 × 10 <sup>18</sup>	no	0.02	2.1 × 10 <sup>-5</sup>	8.2 × 10 <sup>-5</sup>	[45 - 70°N, 100 - 165°W]
288	Mt. Redoubt	29.03.2009	1.0 × 10 <sup>14</sup>	5.4 × 10 <sup>17</sup>	no	0.06	7.7 × 10 <sup>-5</sup>	1.9 × 10 <sup>-4</sup>	[25 - 70°N, 95 - 140°W]
289	Mt. Redoubt	29.03.2009	5.0 × 10 <sup>13</sup>	2.4 × 10 <sup>17</sup>	no	0.04	1.1 × 10 <sup>-4</sup>	2.0 × 10 <sup>-4</sup>	[15 - 70°N, 25 - 70°W]
290	Mt. Redoubt	30.03.2009	9.2 × 10 <sup>13</sup>	3.3 × 10 <sup>17</sup>	no	0.00	5.5 × 10 <sup>-5</sup>	2.7 × 10 <sup>-4</sup>	[20 - 70°N, 80 - 125°W]
291	Mt. Redoubt	30.03.2009	1.0 × 10 <sup>14</sup>	3.9 × 10 <sup>17</sup>	yes	0.56	2.9 × 10 <sup>-4</sup>	2.5 × 10 <sup>-4</sup>	[45 - 70°N, 135 - 170°W]
292	Mt. Redoubt	31.03.2009	4.5 × 10 <sup>13</sup>	1.2 × 10 <sup>17</sup>	no	0.01	1.7 × 10 <sup>-4</sup>	3.5 × 10 <sup>-4</sup>	[35 - 70°N, 80 - 115°W]
293	Mt. Redoubt	31.03.2009	1.5 × 10 <sup>13</sup>	2.1 × 10 <sup>17</sup>	no	0.08	1.1 × 10 <sup>-4</sup>	7.2 × 10 <sup>-5</sup>	[50 - 70°N, 150 - 185°W]
294	Ambrym	31.03.2009	6.7 × 10 <sup>13</sup>	4.7 × 10 <sup>17</sup>	no	0.30	1.6 × 10 <sup>-4</sup>	1.4 × 10 <sup>-4</sup>	[0 - 35°S, 150 - 183°E]
295	Ambrym	01.04.2009	4.7 × 10 <sup>13</sup>	2.2 × 10 <sup>17</sup>	no	0.06	1.0 × 10 <sup>-4</sup>	2.0 × 10 <sup>-4</sup>	[0 - 35°S, 150 - 185°E]
296	Mt. Redoubt	03.04.2009	5.2 × 10 <sup>13</sup>	2.4 × 10 <sup>17</sup>	no	0.00	-2.3 × 10 <sup>-5</sup>	2.1 × 10 <sup>-4</sup>	[45 - 70°N, 20 - 55°E]
297†	Mt. Redoubt	04.04.2009	6.2 × 10 <sup>13</sup>	1.8 × 10 <sup>18</sup>	no	0.00	-2.6 × 10 <sup>-6</sup>	3.3 × 10 <sup>-5</sup>	[35 - 70°N, 125 - 170°W]
298	Mt. Redoubt	05.04.2009	6.5 × 10 <sup>13</sup>	2.9 × 10 <sup>17</sup>	no	0.00	6.4 × 10 <sup>-6</sup>	2.2 × 10 <sup>-4</sup>	[15 - 70°N, 115 - 155°W]
299	Mt. Redoubt	06.04.2009	7.1 × 10 <sup>13</sup>	4.2 × 10 <sup>17</sup>	no	0.00	-1.0 × 10 <sup>-5</sup>	1.6 × 10 <sup>-4</sup>	[15 - 70°N, 85 - 170°W]
300	Rabaul	06.04.2009	6.8 × 10 <sup>13</sup>	1.5 × 10 <sup>17</sup>	no	0.38	5.3 × 10 <sup>-4</sup>	4.5 × 10 <sup>-4</sup>	[-20 - 15°N, 135 - 167°E]

⊕ location of SO<sub>2</sub> SCD<sub>max</sub> is the same as for BrO SCD<sub>max</sub> † combined SO<sub>2</sub> product in case of high SO<sub>2</sub> SCDs ≥ 1 × 10<sup>18</sup> molec/cm<sup>2</sup> ‡ SO<sub>2</sub> SCDs ≥ 1 × 10<sup>18</sup> molec/cm<sup>2</sup>, but no plume pixel found in the SO<sub>2</sub> AR

\* corresponding volcano cannot be clearly identified

#	volcano	date	BrO SCD <sub>max</sub> [molec/cm <sup>2</sup> ]	SO <sub>2</sub> SCD <sub>max</sub> [molec/cm <sup>2</sup> ]	⊕	r <sup>2</sup>	fitted BrO/SO <sub>2</sub>	BrO <sub>max</sub> /SO <sub>2max</sub>	coordinates
301	Mt. Redoubt	07.04.2009	4.2×10 <sup>13</sup>	2.3×10 <sup>17</sup>	no	0.00	1.5×10 <sup>-5</sup>	1.7×10 <sup>-4</sup>	[45 - 70°N, 70 - 105°W]
302	Mt. Redoubt	07.04.2009	3.0×10 <sup>13</sup>	1.3×10 <sup>17</sup>	no	0.04	1.9×10 <sup>-4</sup>	2.1×10 <sup>-4</sup>	[20 - 55°N, 70 - 105°W]
303	Mt. Redoubt	07.04.2009	6.7×10 <sup>13</sup>	2.1×10 <sup>17</sup>	no	0.06	1.5×10 <sup>-4</sup>	3.2×10 <sup>-4</sup>	[20 - 60°N, 105 - 145°W]
304	Mt. Redoubt	07.04.2009	7.7×10 <sup>13</sup>	5.3×10 <sup>17</sup>	no	0.15	1.4×10 <sup>-4</sup>	1.4×10 <sup>-4</sup>	[45 - 70°N, 130 - 170°W]
305	Mt. Redoubt	08.04.2009	7.1×10 <sup>13</sup>	2.9×10 <sup>17</sup>	no	0.19	1.8×10 <sup>-4</sup>	2.3×10 <sup>-4</sup>	[40 - 70°N, 125 - 170°W]
306	Mt. Redoubt	09.04.2009	8.5×10 <sup>13</sup>	3.3×10 <sup>17</sup>	no	0.41	3.0×10 <sup>-4</sup>	2.5×10 <sup>-4</sup>	[40 - 70°N, 115 - 170°W]
307	Mt. Redoubt	10.04.2009	6.0×10 <sup>13</sup>	1.6×10 <sup>17</sup>	no	0.00	-8.7×10 <sup>-6</sup>	3.7×10 <sup>-4</sup>	[50 - 70°N, 125 - 160°W]
308	Mt. Redoubt	11.04.2009	8.8×10 <sup>13</sup>	3.2×10 <sup>17</sup>	no	0.23	2.5×10 <sup>-4</sup>	2.7×10 <sup>-4</sup>	[45 - 70°N, 135 - 175°W]
309	Fernandina	12.04.2009	6.4×10 <sup>13</sup>	5.8×10 <sup>17</sup>	no	0.00	9.0×10 <sup>-6</sup>	1.1×10 <sup>-4</sup>	[-20 - 15°N, 85 - 115°W]
310	Mt. Redoubt	12.04.2009	9.5×10 <sup>13</sup>	4.7×10 <sup>17</sup>	no	0.14	1.7×10 <sup>-4</sup>	2.0×10 <sup>-4</sup>	[45 - 70°N, 135 - 185°W]
311	Fernandina	13.04.2009	6.8×10 <sup>13</sup>	7.9×10 <sup>17</sup>	no	0.01	1.2×10 <sup>-5</sup>	8.7×10 <sup>-5</sup>	[-20 - 20°N, 79 - 118°W]
312	Mt. Redoubt	13.04.2009	9.2×10 <sup>13</sup>	3.0×10 <sup>17</sup>	no	0.33	2.7×10 <sup>-4</sup>	3.0×10 <sup>-4</sup>	[45 - 70°N, 135 - 170°W]
313	Fernandina	14.04.2009	7.7×10 <sup>13</sup>	8.8×10 <sup>17</sup>	no	0.02	8.6×10 <sup>-6</sup>	8.7×10 <sup>-5</sup>	[-20 - 20°N, 75 - 114°W]
314	Fernandina	15.04.2009	1.1×10 <sup>14</sup>	4.1×10 <sup>17</sup>	no	0.02	2.6×10 <sup>-5</sup>	2.8×10 <sup>-4</sup>	[-20 - 15°N, 76 - 109°W]
315	Fernandina	15.04.2009	5.0×10 <sup>13</sup>	4.4×10 <sup>17</sup>	no	0.01	-1.8×10 <sup>-5</sup>	1.1×10 <sup>-4</sup>	[-20 - 20°N, 95 - 130°W]
316	Fernandina	16.04.2009	5.7×10 <sup>13</sup>	3.9×10 <sup>17</sup>	no	0.00	1.4×10 <sup>-5</sup>	1.4×10 <sup>-4</sup>	[-20 - 20°N, 89 - 135°W]
317	Mt. Redoubt	16.04.2009	1.4×10 <sup>14</sup>	5.1×10 <sup>17</sup>	yes	0.49	2.6×10 <sup>-4</sup>	2.7×10 <sup>-4</sup>	[35 - 70°N, 140 - 180°W]
318	Fernandina	17.04.2009	6.3×10 <sup>13</sup>	4.9×10 <sup>17</sup>	no	0.01	2.4×10 <sup>-5</sup>	1.2×10 <sup>-4</sup>	[-20 - 20°N, 83 - 120°W]
319	Fernandina	17.04.2009	4.7×10 <sup>13</sup>	2.6×10 <sup>17</sup>	no	0.01	4.4×10 <sup>-5</sup>	1.7×10 <sup>-4</sup>	[-20 - 15°N, 110 - 140°W]
320	Mt. Redoubt	17.04.2009	7.7×10 <sup>13</sup>	3.1×10 <sup>17</sup>	no	0.25	3.9×10 <sup>-4</sup>	2.4×10 <sup>-4</sup>	[35 - 70°N, 135 - 175°W]
321	Fernandina	18.04.2009	6.7×10 <sup>13</sup>	3.9×10 <sup>17</sup>	no	0.01	3.3×10 <sup>-5</sup>	1.7×10 <sup>-4</sup>	[-20 - 20°N, 83 - 120°W]
322	Mt. Redoubt	18.04.2009	1.1×10 <sup>14</sup>	4.8×10 <sup>17</sup>	no	0.62	2.2×10 <sup>-4</sup>	2.4×10 <sup>-4</sup>	[35 - 70°N, 135 - 170°W]
323	Fernandina	19.04.2009	4.7×10 <sup>13</sup>	4.8×10 <sup>17</sup>	no	0.00	1.7×10 <sup>-5</sup>	9.6×10 <sup>-5</sup>	[-20 - 15°N, 75 - 113°W]
324	Mt. Redoubt	19.04.2009	6.7×10 <sup>13</sup>	3.3×10 <sup>17</sup>	no	0.33	2.1×10 <sup>-4</sup>	2.0×10 <sup>-4</sup>	[50 - 70°N, 140 - 175°W]
325	Fernandina	20.04.2009	5.8×10 <sup>13</sup>	3.1×10 <sup>17</sup>	no	0.00	3.2×10 <sup>-6</sup>	1.8×10 <sup>-4</sup>	[-20 - 20°N, 75 - 108°W]
326	Mt. Redoubt	20.04.2009	9.1×10 <sup>13</sup>	4.2×10 <sup>17</sup>	no	0.17	2.2×10 <sup>-4</sup>	2.1×10 <sup>-4</sup>	[40 - 70°N, 135 - 170°W]
327	Mt. Redoubt	21.04.2009	6.5×10 <sup>13</sup>	2.2×10 <sup>17</sup>	yes	0.27	3.9×10 <sup>-4</sup>	2.8×10 <sup>-4</sup>	[40 - 70°N, 135 - 170°W]
328	Fernandina	23.04.2009	7.4×10 <sup>13</sup>	8.0×10 <sup>17</sup>	no	0.00	6.3×10 <sup>-6</sup>	9.2×10 <sup>-5</sup>	[-20 - 15°N, 78 - 117°W]
329	Mt. Redoubt	23.04.2009	3.5×10 <sup>13</sup>	1.6×10 <sup>17</sup>	no	0.08	-1.3×10 <sup>-4</sup>	2.1×10 <sup>-4</sup>	[35 - 70°N, 130 - 165°W]
330	Koryaksky	24.04.2009	3.6×10 <sup>13</sup>	2.4×10 <sup>17</sup>	no	0.02	3.5×10 <sup>-5</sup>	1.4×10 <sup>-4</sup>	[35 - 70°N, 140 - 175°E]
331	Fernandina	24.04.2009	5.8×10 <sup>13</sup>	5.8×10 <sup>17</sup>	no	0.03	4.5×10 <sup>-5</sup>	1.0×10 <sup>-4</sup>	[-20 - 15°N, 75 - 112°W]
332	Fernandina	25.04.2009	6.1×10 <sup>13</sup>	4.0×10 <sup>17</sup>	no	0.00	1.5×10 <sup>-5</sup>	1.5×10 <sup>-4</sup>	[-20 - 20°N, 75 - 107°W]
333	Mt. Redoubt	25.04.2009	6.6×10 <sup>13</sup>	2.0×10 <sup>17</sup>	no	0.30	4.1×10 <sup>-4</sup>	3.3×10 <sup>-4</sup>	[45 - 70°N, 125 - 160°W]
334	Fernandina	26.04.2009	4.8×10 <sup>13</sup>	2.0×10 <sup>17</sup>	no	0.01	6.8×10 <sup>-5</sup>	2.3×10 <sup>-4</sup>	[-20 - 20°N, 87 - 120°W]
335	Fernandina	27.04.2009	7.1×10 <sup>13</sup>	3.8×10 <sup>17</sup>	no	0.00	2.9×10 <sup>-5</sup>	1.8×10 <sup>-4</sup>	[-20 - 20°N, 75 - 120°W]
336	Mt. Redoubt	27.04.2009	4.6×10 <sup>13</sup>	1.5×10 <sup>17</sup>	no	0.12	1.3×10 <sup>-4</sup>	3.0×10 <sup>-4</sup>	[45 - 70°N, 135 - 170°W]
337	Fernandina	28.04.2009	5.8×10 <sup>13</sup>	3.2×10 <sup>17</sup>	no	0.02	4.2×10 <sup>-5</sup>	1.7×10 <sup>-4</sup>	[-20 - 15°N, 78 - 115°W]
338	Mt. Redoubt	28.04.2009	7.3×10 <sup>13</sup>	1.8×10 <sup>17</sup>	no	0.11	2.4×10 <sup>-4</sup>	3.9×10 <sup>-4</sup>	[45 - 70°N, 135 - 170°W]
339	Fernandina	29.04.2009	5.2×10 <sup>13</sup>	1.9×10 <sup>17</sup>	no	0.00	3.7×10 <sup>-5</sup>	2.6×10 <sup>-4</sup>	[-20 - 15°N, 75 - 111°W]
340	Mt. Redoubt	29.04.2009	4.4×10 <sup>13</sup>	2.6×10 <sup>17</sup>	no	0.16	2.0×10 <sup>-4</sup>	1.6×10 <sup>-4</sup>	[50 - 70°N, 125 - 160°W]
341	Kilauea	30.04.2009	2.5×10 <sup>13</sup>	2.9×10 <sup>17</sup>	no	0.02	-4.5×10 <sup>-5</sup>	8.7×10 <sup>-5</sup>	[0 - 35°N, 140 - 175°W]
342	Mt. Redoubt	04.05.2009	7.4×10 <sup>13</sup>	2.5×10 <sup>17</sup>	no	0.02	1.1×10 <sup>-4</sup>	2.9×10 <sup>-4</sup>	[40 - 70°N, 140 - 175°W]
343	Kilauea	04.05.2009	3.5×10 <sup>13</sup>	3.2×10 <sup>17</sup>	no	0.02	4.2×10 <sup>-5</sup>	1.0×10 <sup>-4</sup>	[0 - 35°N, 142 - 175°W]
344	Mt. Redoubt	05.05.2009	8.2×10 <sup>13</sup>	3.0×10 <sup>17</sup>	no	0.37	2.6×10 <sup>-4</sup>	2.7×10 <sup>-4</sup>	[35 - 70°N, 140 - 175°W]
345	Mt. Redoubt	06.05.2009	9.6×10 <sup>13</sup>	2.4×10 <sup>17</sup>	no	0.09	1.2×10 <sup>-4</sup>	3.9×10 <sup>-4</sup>	[30 - 70°N, 120 - 170°W]
346	Mt. Redoubt	07.05.2009	5.3×10 <sup>13</sup>	2.4×10 <sup>17</sup>	no	0.05	8.2×10 <sup>-5</sup>	2.1×10 <sup>-4</sup>	[30 - 65°N, 120 - 155°W]
347	Mt. Redoubt	08.05.2009	4.7×10 <sup>13</sup>	8.2×10 <sup>17</sup>	no	0.01	1.2×10 <sup>-4</sup>	5.7×10 <sup>-5</sup>	[30 - 65°N, 110 - 145°W]
348	Mt. Redoubt	08.05.2009	5.9×10 <sup>13</sup>	2.6×10 <sup>17</sup>	yes	0.03	9.8×10 <sup>-5</sup>	2.2×10 <sup>-4</sup>	[40 - 70°N, 135 - 170°W]
349	Mt. Redoubt	09.05.2009	4.3×10 <sup>13</sup>	1.7×10 <sup>17</sup>	no	0.01	3.6×10 <sup>-5</sup>	2.4×10 <sup>-4</sup>	[25 - 60°N, 110 - 145°W]
350	Mt. Redoubt	10.05.2009	4.6×10 <sup>13</sup>	2.6×10 <sup>17</sup>	yes	0.17	2.0×10 <sup>-4</sup>	1.7×10 <sup>-4</sup>	[30 - 70°N, 130 - 165°W]
351	Mt. Redoubt	11.05.2009	5.5×10 <sup>13</sup>	2.8×10 <sup>17</sup>	no	0.27	2.3×10 <sup>-4</sup>	1.9×10 <sup>-4</sup>	[30 - 70°N, 130 - 165°W]
352	Koryaksky	11.05.2009	3.0×10 <sup>13</sup>	1.6×10 <sup>17</sup>	no	0.01	4.6×10 <sup>-5</sup>	1.8×10 <sup>-4</sup>	[35 - 70°N, 175 - 210°W]
353	Mt. Redoubt	12.05.2009	6.8×10 <sup>13</sup>	2.4×10 <sup>17</sup>	no	0.04	1.2×10 <sup>-4</sup>	2.7×10 <sup>-4</sup>	[35 - 70°N, 130 - 170°W]
354	Koryaksky	13.05.2009	5.4×10 <sup>13</sup>	1.7×10 <sup>17</sup>	no	0.00	3.3×10 <sup>-5</sup>	3.0×10 <sup>-4</sup>	[35 - 70°N, 140 - 175°E]
355	Mt. Redoubt	13.05.2009	3.7×10 <sup>13</sup>	2.2×10 <sup>17</sup>	no	0.01	3.0×10 <sup>-5</sup>	1.6×10 <sup>-4</sup>	[35 - 70°N, 140 - 180°W]
356	Mt. Redoubt	14.05.2009	5.8×10 <sup>13</sup>	2.7×10 <sup>17</sup>	no	0.06	9.9×10 <sup>-5</sup>	2.1×10 <sup>-4</sup>	[40 - 70°N, 135 - 170°W]
357	Mt. Redoubt	15.05.2009	7.5×10 <sup>13</sup>	3.4×10 <sup>17</sup>	yes	0.11	1.1×10 <sup>-4</sup>	2.1×10 <sup>-4</sup>	[35 - 70°N, 130 - 175°W]
358	Mt. Redoubt	16.05.2009	4.0×10 <sup>13</sup>	1.5×10 <sup>17</sup>	no	0.05	1.2×10 <sup>-4</sup>	2.5×10 <sup>-4</sup>	[25 - 65°N, 145 - 180°W]
359	Mt. Redoubt	19.05.2009	5.0×10 <sup>13</sup>	3.2×10 <sup>17</sup>	no	0.10	1.2×10 <sup>-4</sup>	1.5×10 <sup>-4</sup>	[45 - 70°N, 135 - 175°W]
360	Mt. Redoubt	20.05.2009	6.7×10 <sup>13</sup>	1.9×10 <sup>17</sup>	no	0.17	2.6×10 <sup>-4</sup>	3.4×10 <sup>-4</sup>	[45 - 70°N, 140 - 175°W]
361	Mt. Redoubt	26.05.2009	5.3×10 <sup>13</sup>	1.3×10 <sup>17</sup>	no	0.31	-6.9×10 <sup>-4</sup>	3.9×10 <sup>-4</sup>	[40 - 70°N, 135 - 170°W]
362	Mt. Redoubt	27.05.2009	4.8×10 <sup>13</sup>	2.3×10 <sup>17</sup>	no	0.17	1.3×10 <sup>-4</sup>	2.1×10 <sup>-4</sup>	[45 - 70°N, 130 - 170°W]
363	Mt. Redoubt	29.05.2009	9.1×10 <sup>13</sup>	3.8×10 <sup>17</sup>	yes	0.56	2.4×10 <sup>-4</sup>	2.4×10 <sup>-4</sup>	[45 - 70°N, 135 - 170°W]
364	Karymsky	03.06.2009	2.1×10 <sup>13</sup>	1.5×10 <sup>17</sup>	yes	0.13	1.1×10 <sup>-4</sup>	1.3×10 <sup>-4</sup>	[30 - 65°N, 155 - 190°E]
365	Mt. Redoubt	06.06.2009	3.5×10 <sup>13</sup>	1.6×10 <sup>17</sup>	no	0.18	2.2×10 <sup>-4</sup>	2.2×10 <sup>-4</sup>	[45 - 70°N, 135 - 170°W]
366	Galeras	08.06.2009	4.3×10 <sup>13</sup>	1.9×10 <sup>17</sup>	no	0.22	-1.9×10 <sup>-4</sup>	2.2×10 <sup>-4</sup>	[-15 - 20°N, 64 - 95°W]
367	Mt. Redoubt	10.06.2009	3.7×10 <sup>13</sup>	1.7×10 <sup>17</sup>	no	0.01	4.0×10 <sup>-5</sup>	2.1×10 <sup>-4</sup>	[40 - 70°N, 130 - 165°W]
368	Mt. Redoubt	12.06.2009	5.5×10 <sup>13</sup>	4.3×10 <sup>17</sup>	no	0.00	2.2×10 <sup>-5</sup>	1.2×10 <sup>-4</sup>	[25 - 70°N, 135 - 190°W]
369†	Sarychev	12./13.06.2009	1.2×10 <sup>14</sup>	1.7×10 <sup>18</sup>	no	0.02	2.2×10 <sup>-5</sup>	7.0×10 <sup>-5</sup>	[30 - 65°N, 130 - 175°E]
370†	Sarychev	13./14.06.2009	1.0×10 <sup>14</sup>	3.9×10 <sup>18</sup>	no	0.01	4.6×10 <sup>-6</sup>	2.1×10 <sup>-5</sup>	[25 - 70°N, 115 - 235°W]
371	Sarychev	14.06.2009	6.7×10 <sup>13</sup>	1.9×10 <sup>17</sup>	no	0.02	9.3×10 <sup>-5</sup>	3.4×10 <sup>-4</sup>	[20 - 55°N, 100 - 135°W]
372†	Sarychev	14./15.06.2009	7.0×10 <sup>13</sup>	2.5×10 <sup>19</sup>	no	0.01	2.5×10 <sup>-7</sup>	2.7×10 <sup>-6</sup>	[25 - 65°N, 135 - 235°W]
373	Sarychev	15.06.2009	5.4×10 <sup>13</sup>	1.9×10 <sup>17</sup>	no	0.11	1.8×10 <sup>-4</sup>	2.8×10 <sup>-4</sup>	[25 - 60°N, 110 - 145°W]
374	Sarychev	15.06.2009	5.3×10 <sup>13</sup>	9.4×10 <sup>17</sup>	no	0.00	5.2×10 <sup>-6</sup>	5.7×10 <sup>-5</sup>	[25 - 70°N, 135 - 190°W]
375†	Sarychev	15./16.06.2009	1.9×10 <sup>14</sup>	2.3×10 <sup>19</sup>	no	0.01	3.9×10 <sup>-6</sup>	8.2×10 <sup>-6</sup>	[25 - 70°N, 120 - 180°E]

⊕ location of SO<sub>2</sub> SCD<sub>max</sub> is the same as for BrO SCD<sub>max</sub> † combined SO<sub>2</sub> product in case of high SO<sub>2</sub> SCDs ≥ 1 × 10<sup>18</sup> molec/cm<sup>2</sup> ‡ SO<sub>2</sub> SCDs ≥ 1 × 10<sup>18</sup> molec/cm<sup>2</sup>, but no plume pixel found in the SO<sub>2</sub> AR

\* corresponding volcano cannot be clearly identified

#	volcano	date	BrO SCD <sub>max</sub> [molec/cm <sup>2</sup> ]	SO <sub>2</sub> SCD <sub>max</sub> [molec/cm <sup>2</sup> ]	⊕	r <sup>2</sup>	fitted BrO/SO <sub>2</sub>	BrO <sub>max</sub> /SO <sub>2</sub> max	coordinates
376	Sarychev	16.06.2009	6.7×10 <sup>13</sup>	1.6×10 <sup>17</sup>	no	0.04	1.1×10 <sup>-4</sup>	4.0×10 <sup>-4</sup>	[10 - 45°N, 100 - 135°W]
377†	Sarychev	16./17.06.2009	1.4×10 <sup>14</sup>	1.6×10 <sup>19</sup>	no	0.01	4.0×10 <sup>-6</sup>	8.7×10 <sup>-6</sup>	[20 - 70°N, 135 - 250°W]
378†	Sarychev	17./18.06.2009	1.6×10 <sup>14</sup>	1.1×10 <sup>19</sup>	no	0.01	5.8×10 <sup>-6</sup>	1.4×10 <sup>-5</sup>	[20 - 70°N, 115 - 250°W]
379†	Sarychev	18./19.06.2009	9.1×10 <sup>13</sup>	4.7×10 <sup>18</sup>	no	0.01	4.1×10 <sup>-6</sup>	1.9×10 <sup>-5</sup>	[25 - 70°N, 100 - 231°W]
380†	Sarychev	19.06.2009	1.4×10 <sup>14</sup>	2.3×10 <sup>18</sup>	no	0.02	8.7×10 <sup>-6</sup>	6.3×10 <sup>-5</sup>	[45 - 70°N, 110 - 135°E]
381†	Sarychev	19.06.2009	8.6×10 <sup>13</sup>	4.6×10 <sup>18</sup>	no	0.01	2.1×10 <sup>-6</sup>	1.8×10 <sup>-5</sup>	[25 - 70°N, 116 - 155°W]
382†	Sarychev	20.06.2009	8.1×10 <sup>13</sup>	2.3×10 <sup>18</sup>	no	0.00	-3.7×10 <sup>-8</sup>	3.4×10 <sup>-5</sup>	[35 - 70°N, 100 - 160°E]
383†	Sarychev	20./21.06.2009	8.7×10 <sup>13</sup>	4.7×10 <sup>18</sup>	no	0.00	1.8×10 <sup>-6</sup>	1.8×10 <sup>-5</sup>	[15 - 70°N, 85 - 260°W]
384†	Sarychev	21./22.06.2009	8.2×10 <sup>13</sup>	3.5×10 <sup>18</sup>	no	0.00	-2.5×10 <sup>-6</sup>	2.2×10 <sup>-5</sup>	[20 - 70°N, 65 - 230°W]
385†	Sarychev	22./23.06.2009	8.5×10 <sup>13</sup>	3.2×10 <sup>18</sup>	no	0.01	-3.9×10 <sup>-6</sup>	2.6×10 <sup>-5</sup>	[20 - 70°N, 50 - 225°W]
386†	Sarychev	23.06.2009	8.7×10 <sup>13</sup>	3.3×10 <sup>18</sup>	no	0.00	-1.5×10 <sup>-6</sup>	2.6×10 <sup>-5</sup>	[15 - 70°N, -180 - -30°E]
387†	Sarychev	23./24.06.2009	8.5×10 <sup>13</sup>	3.3×10 <sup>18</sup>	no	0.00	3.7×10 <sup>-6</sup>	2.5×10 <sup>-5</sup>	[15 - 70°N, 30 - 235°W]
388†	Sarychev	24.06.2009	8.3×10 <sup>13</sup>	2.4×10 <sup>18</sup>	no	0.02	2.2×10 <sup>-5</sup>	3.3×10 <sup>-5</sup>	[20 - 70°N, -180 - -10°E]
389†	Sarychev	24.06.2009	8.1×10 <sup>13</sup>	2.5×10 <sup>18</sup>	no	0.01	1.6×10 <sup>-5</sup>	3.2×10 <sup>-5</sup>	[20 - 70°N, 10 - 189°W]
390†	Sarychev	25.06.2009	7.4×10 <sup>13</sup>	2.8×10 <sup>18</sup>	no	0.00	3.6×10 <sup>-8</sup>	2.6×10 <sup>-5</sup>	[5 - 70°N, 5 - 210°W]
391	Sarychev	26.06.2009	5.5×10 <sup>13</sup>	5.4×10 <sup>17</sup>	no	0.01	2.0×10 <sup>-5</sup>	1.0×10 <sup>-4</sup>	[15 - 70°N, 0 - 50°W]
392†	Sarychev	26.06.2009	5.7×10 <sup>13</sup>	3.5×10 <sup>18</sup>	no	0.01	7.5×10 <sup>-6</sup>	1.6×10 <sup>-5</sup>	[45 - 70°N, 40 - 105°W]
393†	Sarychev	26.06.2009	6.7×10 <sup>13</sup>	3.0×10 <sup>18</sup>	no	0.00	1.8×10 <sup>-6</sup>	2.2×10 <sup>-5</sup>	[20 - 70°N, 125 - 195°W]
394	Kīlauea	26.06.2009	4.4×10 <sup>13</sup>	1.7×10 <sup>17</sup>	no	0.14	-2.6×10 <sup>-4</sup>	2.4×10 <sup>-4</sup>	[0 - 35°N, 143 - 175°W]
395	Sarychev	27.06.2009	7.3×10 <sup>13</sup>	2.7×10 <sup>17</sup>	no	0.00	8.8×10 <sup>-6</sup>	2.7×10 <sup>-4</sup>	[10 - 70°N, -65 - 5°E]
396	Sarychev	27.06.2009	5.1×10 <sup>13</sup>	2.3×10 <sup>17</sup>	no	0.08	1.3×10 <sup>-4</sup>	2.2×10 <sup>-4</sup>	[50 - 70°N, 100 - 135°W]
397†	Sarychev	27.06.2009	5.5×10 <sup>13</sup>	2.9×10 <sup>18</sup>	no	0.02	7.8×10 <sup>-6</sup>	1.8×10 <sup>-5</sup>	[20 - 70°N, 125 - 200°W]
398	Sarychev	28.06.2009	9.7×10 <sup>13</sup>	2.3×10 <sup>17</sup>	no	0.00	7.2×10 <sup>-7</sup>	4.1×10 <sup>-4</sup>	[30 - 70°N, 0 - 55°W]
399†	Sarychev	28.06.2009	6.2×10 <sup>13</sup>	2.5×10 <sup>18</sup>	no	0.02	8.8×10 <sup>-6</sup>	2.4×10 <sup>-5</sup>	[20 - 70°N, 90 - 195°W]
400	Sarychev	29.06.2009	5.5×10 <sup>13</sup>	2.1×10 <sup>17</sup>	no	0.00	1.3×10 <sup>-5</sup>	2.5×10 <sup>-4</sup>	[30 - 70°N, -45 - 5°E]
401	Sarychev	29.06.2009	2.7×10 <sup>13</sup>	1.7×10 <sup>17</sup>	no	0.09	-2.1×10 <sup>-4</sup>	1.5×10 <sup>-4</sup>	[50 - 70°N, 65 - 105°W]
402†	Sarychev	29.06.2009	5.8×10 <sup>13</sup>	2.3×10 <sup>18</sup>	no	0.01	7.8×10 <sup>-6</sup>	2.5×10 <sup>-5</sup>	[30 - 70°N, 130 - 190°W]
403	Sarychev	30.06.2009	5.2×10 <sup>13</sup>	1.9×10 <sup>17</sup>	no	0.02	-7.1×10 <sup>-5</sup>	2.6×10 <sup>-4</sup>	[30 - 70°N, -50 - 10°E]
404	Mando Hararo	30.06.2009	6.1×10 <sup>13</sup>	7.0×10 <sup>17</sup>	no	0.05	3.9×10 <sup>-5</sup>	8.7×10 <sup>-5</sup>	[-10 - 30°N, 20 - 54°E]
405	Sarychev	30.06.2009	5.1×10 <sup>13</sup>	1.9×10 <sup>17</sup>	no	0.02	-6.8×10 <sup>-5</sup>	2.6×10 <sup>-4</sup>	[30 - 70°N, 5 - 10°E]
406†	Sarychev	30.06.2009	5.8×10 <sup>13</sup>	1.9×10 <sup>18</sup>	no	0.00	-5.0×10 <sup>-6</sup>	3.0×10 <sup>-5</sup>	[35 - 70°N, 130 - 190°W]
407	Sarychev	01.07.2009	5.0×10 <sup>13</sup>	2.0×10 <sup>17</sup>	no	0.00	-5.1×10 <sup>-6</sup>	2.4×10 <sup>-4</sup>	[50 - 70°N, 0 - 35°E]
408	Sarychev	01.07.2009	4.4×10 <sup>13</sup>	1.1×10 <sup>17</sup>	no	0.01	1.4×10 <sup>-4</sup>	3.9×10 <sup>-4</sup>	[30 - 65°N, 5 - 40°W]
409	Sarychev	01.07.2009	2.5×10 <sup>13</sup>	2.6×10 <sup>17</sup>	no	0.00	1.9×10 <sup>-6</sup>	9.5×10 <sup>-5</sup>	[50 - 70°N, 65 - 105°W]
410	Sarychev	01.07.2009	4.4×10 <sup>13</sup>	2.6×10 <sup>17</sup>	no	0.10	-9.0×10 <sup>-5</sup>	1.6×10 <sup>-4</sup>	[50 - 70°N, 65 - 105°W]
411	Sarychev	01.07.2009	7.4×10 <sup>13</sup>	1.7×10 <sup>17</sup>	no	0.00	-8.3×10 <sup>-5</sup>	4.3×10 <sup>-4</sup>	[40 - 70°N, 95 - 130°W]
412†	Sarychev	01.07.2009	6.6×10 <sup>13</sup>	2.1×10 <sup>18</sup>	no	0.00	-4.3×10 <sup>-6</sup>	3.0×10 <sup>-5</sup>	[35 - 70°N, 125 - 195°W]
413	Sarychev	02.07.2009	3.8×10 <sup>13</sup>	1.9×10 <sup>17</sup>	no	0.00	3.9×10 <sup>-5</sup>	2.0×10 <sup>-4</sup>	[45 - 70°N, 15 - 50°E]
414	Sarychev	02.07.2009	6.7×10 <sup>13</sup>	1.4×10 <sup>17</sup>	no	0.20	-9.0×10 <sup>-4</sup>	4.7×10 <sup>-4</sup>	[50 - 70°N, 75 - 110°W]
415	Sarychev	02./03.07.2009	8.2×10 <sup>13</sup>	9.4×10 <sup>17</sup>	no	0.00	4.1×10 <sup>-6</sup>	8.7×10 <sup>-5</sup>	[35 - 70°N, 130 - 205°W]
416	Sarychev	02./03.07.2009	4.2×10 <sup>13</sup>	3.7×10 <sup>17</sup>	no	0.06	7.8×10 <sup>-5</sup>	1.1×10 <sup>-4</sup>	[30 - 65°N, 130 - 165°E]
417	Sarychev	02./03.07.2009	3.1×10 <sup>13</sup>	1.5×10 <sup>17</sup>	no	0.01	7.2×10 <sup>-5</sup>	1.9×10 <sup>-4</sup>	[45 - 70°N, -60 - -10°E]
418	Sarychev	03.07.2009	3.4×10 <sup>13</sup>	2.6×10 <sup>17</sup>	no	0.06	-1.2×10 <sup>-4</sup>	1.3×10 <sup>-4</sup>	[35 - 70°N, 30 - 70°E]
419	Sarychev	03.07.2009	2.9×10 <sup>13</sup>	1.4×10 <sup>17</sup>	no	0.04	1.7×10 <sup>-4</sup>	2.1×10 <sup>-4</sup>	[45 - 70°N, 10 - 60°W]
420	Sarychev	03.07.2009	7.0×10 <sup>13</sup>	2.7×10 <sup>17</sup>	no	0.00	-1.7×10 <sup>-5</sup>	2.5×10 <sup>-4</sup>	[50 - 70°N, 55 - 100°W]
421	Sarychev	03.07.2009	6.4×10 <sup>13</sup>	2.8×10 <sup>17</sup>	no	0.01	5.3×10 <sup>-5</sup>	2.2×10 <sup>-4</sup>	[30 - 70°N, 125 - 190°W]
422	Sarychev	03./04.07.2009	4.5×10 <sup>13</sup>	3.8×10 <sup>17</sup>	yes	0.15	8.6×10 <sup>-5</sup>	1.1×10 <sup>-4</sup>	[30 - 70°N, 130 - 170°E]
423	Sarychev	04.07.2009	5.4×10 <sup>13</sup>	2.0×10 <sup>17</sup>	no	0.03	-9.2×10 <sup>-5</sup>	2.6×10 <sup>-4</sup>	[30 - 70°N, 45 - 85°E]
424	Sarychev	04.07.2009	7.0×10 <sup>13</sup>	5.8×10 <sup>17</sup>	no	0.01	4.0×10 <sup>-5</sup>	1.2×10 <sup>-4</sup>	[25 - 70°N, 120 - 185°W]
425	Sarychev	04./05.07.2009	5.8×10 <sup>13</sup>	2.1×10 <sup>17</sup>	no	0.01	3.0×10 <sup>-5</sup>	2.6×10 <sup>-4</sup>	[30 - 70°N, 135 - 180°E]
426	Sarychev	05.07.2009	6.5×10 <sup>13</sup>	1.6×10 <sup>17</sup>	no	0.05	1.8×10 <sup>-4</sup>	4.0×10 <sup>-4</sup>	[45 - 70°N, 25 - 65°W]
427	Sarychev	05./06.07.2009	4.5×10 <sup>13</sup>	3.1×10 <sup>17</sup>	no	0.02	4.7×10 <sup>-5</sup>	1.4×10 <sup>-4</sup>	[30 - 70°N, 170 - 220°W]
428	Sarychev	06.07.2009	4.9×10 <sup>13</sup>	2.7×10 <sup>17</sup>	no	0.07	8.0×10 <sup>-5</sup>	1.8×10 <sup>-4</sup>	[50 - 70°N, 135 - 170°W]
429	Sarychev	06.07.2009	3.3×10 <sup>13</sup>	3.8×10 <sup>17</sup>	no	0.03	3.7×10 <sup>-5</sup>	8.7×10 <sup>-5</sup>	[30 - 65°N, 160 - 195°W]
430	Sarychev	06./07.07.2009	4.5×10 <sup>13</sup>	4.7×10 <sup>17</sup>	yes	0.01	1.7×10 <sup>-5</sup>	9.5×10 <sup>-5</sup>	[35 - 70°N, 130 - 180°E]
431	Sarychev	07.07.2009	5.3×10 <sup>13</sup>	3.1×10 <sup>17</sup>	no	0.01	1.8×10 <sup>-5</sup>	1.6×10 <sup>-4</sup>	[45 - 70°N, 125 - 160°W]
432	Sarychev	07./08.07.2009	5.1×10 <sup>13</sup>	5.7×10 <sup>17</sup>	no	0.00	1.5×10 <sup>-5</sup>	8.8×10 <sup>-5</sup>	[45 - 70°N, 125 - 170°E]
433	Sarychev	08.07.2009	4.4×10 <sup>13</sup>	5.7×10 <sup>17</sup>	no	0.05	-1.1×10 <sup>-4</sup>	7.7×10 <sup>-5</sup>	[40 - 70°N, 125 - 160°W]
434	Sarychev	08.07.2009	2.7×10 <sup>13</sup>	3.0×10 <sup>17</sup>	no	0.00	9.2×10 <sup>-6</sup>	9.1×10 <sup>-5</sup>	[35 - 70°N, 150 - 185°W]
435	Sarychev	09.07.2009	5.6×10 <sup>13</sup>	4.4×10 <sup>17</sup>	no	0.02	-6.1×10 <sup>-5</sup>	1.2×10 <sup>-4</sup>	[40 - 70°N, 125 - 170°E]
436	Sarychev	09.07.2009	4.3×10 <sup>13</sup>	2.1×10 <sup>17</sup>	no	0.11	1.2×10 <sup>-4</sup>	2.0×10 <sup>-4</sup>	[40 - 70°N, 125 - 170°W]
437	Sarychev	09.07.2009	3.3×10 <sup>13</sup>	1.9×10 <sup>17</sup>	no	0.00	1.3×10 <sup>-5</sup>	1.7×10 <sup>-4</sup>	[40 - 70°N, 155 - 190°W]
438	Sarychev	09./10.07.2009	5.9×10 <sup>13</sup>	3.4×10 <sup>17</sup>	no	0.00	5.3×10 <sup>-6</sup>	1.7×10 <sup>-4</sup>	[35 - 70°N, 120 - 175°E]
439	Sarychev	10.07.2009	5.2×10 <sup>13</sup>	2.3×10 <sup>17</sup>	no	0.10	-1.7×10 <sup>-4</sup>	2.2×10 <sup>-4</sup>	[40 - 70°N, 125 - 170°W]
440	Sarychev	12.07.2009	6.0×10 <sup>13</sup>	2.8×10 <sup>17</sup>	no	0.00	3.6×10 <sup>-5</sup>	2.1×10 <sup>-4</sup>	[45 - 70°N, 105 - 145°E]
441	Sarychev	12.07.2009	1.8×10 <sup>13</sup>	1.7×10 <sup>17</sup>	yes	0.36	2.9×10 <sup>-4</sup>	1.0×10 <sup>-4</sup>	[50 - 70°N, -25 - 10°E]
442	Sarychev	12.07.2009	4.1×10 <sup>13</sup>	1.5×10 <sup>17</sup>	no	0.06	1.5×10 <sup>-4</sup>	2.7×10 <sup>-4</sup>	[35 - 70°N, 125 - 160°W]
443	Sarychev	13.07.2009	5.8×10 <sup>13</sup>	2.2×10 <sup>17</sup>	no	0.00	-1.5×10 <sup>-5</sup>	2.5×10 <sup>-4</sup>	[40 - 70°N, 105 - 170°E]
444	Sarychev	13.07.2009	1.3×10 <sup>13</sup>	1.5×10 <sup>17</sup>	no	0.01	-5.5×10 <sup>-5</sup>	8.4×10 <sup>-5</sup>	[35 - 70°N, 130 - 165°W]
445	Sarychev	14.07.2009	5.4×10 <sup>13</sup>	2.0×10 <sup>17</sup>	no	0.04	8.4×10 <sup>-5</sup>	2.7×10 <sup>-4</sup>	[35 - 70°N, 135 - 170°E]
446	Sarychev	14.07.2009	5.6×10 <sup>13</sup>	1.5×10 <sup>17</sup>	no	0.02	-1.5×10 <sup>-4</sup>	3.5×10 <sup>-4</sup>	[40 - 70°N, 105 - 150°E]
447	Sarychev	14.07.2009	5.1×10 <sup>13</sup>	1.9×10 <sup>17</sup>	no	0.00	-1.6×10 <sup>-6</sup>	2.6×10 <sup>-4</sup>	[35 - 70°N, 130 - 165°W]
448	Sarychev	15.07.2009	4.6×10 <sup>13</sup>	2.6×10 <sup>17</sup>	no	0.03	-1.1×10 <sup>-4</sup>	1.7×10 <sup>-4</sup>	[35 - 70°N, 140 - 175°E]
449	Sarychev	15.07.2009	6.1×10 <sup>13</sup>	1.4×10 <sup>17</sup>	no	0.00	2.0×10 <sup>-5</sup>	4.3×10 <sup>-4</sup>	[40 - 70°N, 120 - 155°E]
450	Sarychev	15.07.2009	3.0×10 <sup>13</sup>	1.2×10 <sup>17</sup>	no	0.09	1.8×10 <sup>-4</sup>	2.4×10 <sup>-4</sup>	[35 - 70°N, 130 - 165°W]

⊕ location of SO<sub>2</sub> SCD<sub>max</sub> is the same as for BrO SCD<sub>max</sub> † combined SO<sub>2</sub> product in case of high SO<sub>2</sub> SCDs ≥ 1×10<sup>18</sup> molec/cm<sup>2</sup> ‡ SO<sub>2</sub> SCDs ≥ 1×10<sup>18</sup> molec/cm<sup>2</sup>, but no plume pixel found in the SO<sub>2</sub> AR  
 \* corresponding volcano cannot be clearly identified

#	volcano	date	BrO SCD <sub>max</sub> [molec/cm <sup>2</sup> ]	SO <sub>2</sub> SCD <sub>max</sub> [molec/cm <sup>2</sup> ]	⊕	r <sup>2</sup>	fitted BrO/SO <sub>2</sub>	BrO <sub>max</sub> /SO <sub>2max</sub>	coordinates
451	Sarychev	15.07.2009	2.3 × 10 <sup>13</sup>	1.7 × 10 <sup>17</sup>	no	0.00	2.5 × 10 <sup>-5</sup>	1.3 × 10 <sup>-4</sup>	[35 - 70°N, 150 - 185°E]
452	Sarychev	17.07.2009	3.5 × 10 <sup>13</sup>	1.5 × 10 <sup>17</sup>	no	0.00	-1.5 × 10 <sup>-5</sup>	2.3 × 10 <sup>-4</sup>	[40 - 70°N, 160 - 195°W]
453	Sarychev	21.07.2009	3.5 × 10 <sup>13</sup>	1.4 × 10 <sup>17</sup>	no	0.03	-1.2 × 10 <sup>-4</sup>	2.5 × 10 <sup>-4</sup>	[45 - 70°N, 155 - 190°E]
454	Kilauea	18.08.2009	3.6 × 10 <sup>13</sup>	2.0 × 10 <sup>17</sup>	yes	0.10	1.4 × 10 <sup>-4</sup>	1.7 × 10 <sup>-4</sup>	[0 - 35°N, 144 - 175°W]
455	Koryaksky	19.08.2009	3.2 × 10 <sup>13</sup>	2.1 × 10 <sup>17</sup>	no	0.11	-1.2 × 10 <sup>-4</sup>	1.4 × 10 <sup>-4</sup>	[30 - 65°N, 135 - 170°E]
456	Koryaksky	20.08.2009	4.9 × 10 <sup>13</sup>	1.6 × 10 <sup>17</sup>	yes	0.09	1.8 × 10 <sup>-4</sup>	3.1 × 10 <sup>-4</sup>	[35 - 70°N, 155 - 190°E]
457	Ambrym	12.09.2009	4.5 × 10 <sup>13</sup>	2.5 × 10 <sup>17</sup>	no	0.03	5.4 × 10 <sup>-5</sup>	1.8 × 10 <sup>-4</sup>	[0 - 35°S, 150 - 185°E]
458	Langila	28.09.2009	4.8 × 10 <sup>13</sup>	2.9 × 10 <sup>17</sup>	no	0.11	-1.1 × 10 <sup>-4</sup>	1.6 × 10 <sup>-4</sup>	[-25 - 10°N, 132 - 165°E]
459	Ambrym	05.10.2009	5.8 × 10 <sup>13</sup>	1.7 × 10 <sup>17</sup>	no	0.02	9.9 × 10 <sup>-5</sup>	3.3 × 10 <sup>-4</sup>	[0 - 35°S, 150 - 181°E]
460	Nevado del Huila	17.10.2009	4.8 × 10 <sup>13</sup>	3.9 × 10 <sup>17</sup>	no	0.04	-3.0 × 10 <sup>-5</sup>	1.2 × 10 <sup>-4</sup>	[-15 - 20°N, 62 - 95°W]
461	Nevado del Huila	18.10.2009	3.3 × 10 <sup>13</sup>	2.5 × 10 <sup>17</sup>	yes	0.35	2.3 × 10 <sup>-4</sup>	1.3 × 10 <sup>-4</sup>	[-15 - 20°N, 62 - 95°W]
462	Nevado del Huila	21.10.2009	5.6 × 10 <sup>13</sup>	2.1 × 10 <sup>17</sup>	no	0.04	9.9 × 10 <sup>-5</sup>	2.6 × 10 <sup>-4</sup>	[-15 - 20°N, 65 - 95°W]
463	Nevado del Huila	24.10.2009	9.8 × 10 <sup>12</sup>	3.2 × 10 <sup>17</sup>	no	0.27	-9.2 × 10 <sup>-5</sup>	3.0 × 10 <sup>-5</sup>	[-12 - 20°N, 60 - 89°W]
464	Nevado del Huila	28.10.2009	4.8 × 10 <sup>13</sup>	2.4 × 10 <sup>17</sup>	no	0.01	3.9 × 10 <sup>-5</sup>	2.0 × 10 <sup>-4</sup>	[-15 - 20°N, 60 - 86°W]
465	Nevado del Huila	31.10.2009	7.5 × 10 <sup>13</sup>	5.0 × 10 <sup>17</sup>	no	0.37	1.1 × 10 <sup>-4</sup>	1.5 × 10 <sup>-4</sup>	[-15 - 20°N, 64 - 95°W]
466	Nevado del Huila	01.11.2009	2.0 × 10 <sup>13</sup>	2.0 × 10 <sup>17</sup>	no	0.02	-2.7 × 10 <sup>-5</sup>	9.7 × 10 <sup>-5</sup>	[-15 - 20°N, 59 - 90°W]
467	Ambrym	03.11.2009	6.8 × 10 <sup>13</sup>	1.5 × 10 <sup>17</sup>	no	0.00	-3.6 × 10 <sup>-5</sup>	4.3 × 10 <sup>-4</sup>	[0 - 35°S, 150 - 181°E]
468	Nevado del Huila	06.11.2009	5.8 × 10 <sup>13</sup>	2.3 × 10 <sup>17</sup>	no	0.23	2.3 × 10 <sup>-4</sup>	2.5 × 10 <sup>-4</sup>	[-25 - 20°N, 60 - 95°W]
469	Nevado del Huila	10.11.2009	4.3 × 10 <sup>13</sup>	3.5 × 10 <sup>17</sup>	yes	0.11	1.0 × 10 <sup>-4</sup>	1.2 × 10 <sup>-4</sup>	[-15 - 20°N, 62 - 95°W]
470	Nevado del Huila	11.11.2009	7.8 × 10 <sup>13</sup>	5.9 × 10 <sup>17</sup>	no	0.38	1.1 × 10 <sup>-4</sup>	1.3 × 10 <sup>-4</sup>	[-10 - 20°N, 71 - 80°W]
471	Nevado del Huila	12.11.2009	2.6 × 10 <sup>13</sup>	2.3 × 10 <sup>17</sup>	no	0.41	-1.9 × 10 <sup>-4</sup>	1.1 × 10 <sup>-4</sup>	[-11 - 20°N, 60 - 91°W]
472	Ambrym	13.11.2009	4.8 × 10 <sup>13</sup>	1.6 × 10 <sup>17</sup>	no	0.02	5.0 × 10 <sup>-5</sup>	2.9 × 10 <sup>-4</sup>	[0 - 35°S, 150 - 182°E]
473	Nevado del Huila	14.11.2009	5.6 × 10 <sup>13</sup>	1.8 × 10 <sup>17</sup>	no	0.07	2.4 × 10 <sup>-4</sup>	2.9 × 10 <sup>-4</sup>	[-15 - 20°N, 65 - 95°W]
474	Nevado del Huila	15.11.2009	3.0 × 10 <sup>13</sup>	1.1 × 10 <sup>17</sup>	yes	0.03	4.6 × 10 <sup>-5</sup>	1.3 × 10 <sup>-4</sup>	[-15 - 20°N, 60 - 95°W]
475	Nevado del Huila	16.11.2009	7.8 × 10 <sup>13</sup>	4.7 × 10 <sup>17</sup>	no	0.09	6.8 × 10 <sup>-5</sup>	1.6 × 10 <sup>-4</sup>	[-15 - 20°N, 62 - 95°W]
476	Nevado del Huila	20.11.2009	7.2 × 10 <sup>13</sup>	6.1 × 10 <sup>17</sup>	yes	0.54	1.1 × 10 <sup>-4</sup>	1.1 × 10 <sup>-4</sup>	[-15 - 20°N, 61 - 95°W]
477	Nevado del Huila	21.11.2009	5.4 × 10 <sup>13</sup>	4.0 × 10 <sup>17</sup>	no	0.03	4.7 × 10 <sup>-5</sup>	1.3 × 10 <sup>-4</sup>	[-15 - 20°N, 61 - 94°W]
478	Nevado del Huila	24.11.2009	6.4 × 10 <sup>13</sup>	3.2 × 10 <sup>17</sup>	no	0.22	1.3 × 10 <sup>-4</sup>	1.9 × 10 <sup>-4</sup>	[-15 - 20°N, 65 - 95°W]
479	Nevado del Huila	29.11.2009	4.1 × 10 <sup>13</sup>	3.0 × 10 <sup>17</sup>	no	0.06	7.5 × 10 <sup>-5</sup>	1.3 × 10 <sup>-4</sup>	[-15 - 20°N, 64 - 95°W]
480	Nevado del Huila	01.12.2009	4.0 × 10 <sup>13</sup>	2.8 × 10 <sup>17</sup>	no	0.31	1.5 × 10 <sup>-4</sup>	1.4 × 10 <sup>-4</sup>	[-15 - 20°N, 60 - 93°W]
481	Ambrym	02.12.2009	8.3 × 10 <sup>13</sup>	2.0 × 10 <sup>17</sup>	no	0.02	-8.0 × 10 <sup>-5</sup>	4.0 × 10 <sup>-4</sup>	[0 - 35°S, 150 - 181°E]
482	Nevado del Huila	04.12.2009	6.5 × 10 <sup>13</sup>	2.4 × 10 <sup>17</sup>	no	0.03	1.0 × 10 <sup>-4</sup>	2.7 × 10 <sup>-4</sup>	[-15 - 20°N, 63 - 95°W]
483	Nevado del Huila	09.12.2009	5.9 × 10 <sup>13</sup>	2.1 × 10 <sup>17</sup>	no	0.00	-5.2 × 10 <sup>-6</sup>	2.7 × 10 <sup>-4</sup>	[-15 - 20°N, 62 - 95°W]
484†	Nyamuragira	03.01.2010	7.0 × 10 <sup>13</sup>	4.3 × 10 <sup>18</sup>	no	0.03	4.9 × 10 <sup>-6</sup>	1.6 × 10 <sup>-5</sup>	[-20 - 20°N, 10 - 43°E]
485	Nyamuragira	04.01.2010	5.5 × 10 <sup>13</sup>	8.2 × 10 <sup>17</sup>	no	0.09	2.9 × 10 <sup>-5</sup>	6.7 × 10 <sup>-5</sup>	[-20 - 15°N, 8 - 45°E]
486	Nyamuragira	06.01.2010	1.6 × 10 <sup>13</sup>	1.8 × 10 <sup>17</sup>	no	0.00	2.8 × 10 <sup>-5</sup>	9.2 × 10 <sup>-5</sup>	[-25 - 15°N, 0 - 40°E]
487	Nyamuragira	07.01.2010	6.7 × 10 <sup>13</sup>	9.7 × 10 <sup>17</sup>	no	0.05	3.6 × 10 <sup>-5</sup>	6.9 × 10 <sup>-5</sup>	[-25 - 20°N, 5 - 39°E]
488	Nyamuragira	08.01.2010	7.9 × 10 <sup>13</sup>	2.7 × 10 <sup>17</sup>	no	0.00	-1.2 × 10 <sup>-5</sup>	2.8 × 10 <sup>-4</sup>	[-20 - 15°N, 19 - 29°E]
489†	Nyamuragira	09.01.2010	6.7 × 10 <sup>13</sup>	3.6 × 10 <sup>18</sup>	no	0.03	1.1 × 10 <sup>-5</sup>	1.8 × 10 <sup>-5</sup>	[-25 - 15°N, 8 - 45°E]
490	Nyamuragira	10.01.2010	3.4 × 10 <sup>13</sup>	8.9 × 10 <sup>17</sup>	no	0.06	1.4 × 10 <sup>-5</sup>	3.8 × 10 <sup>-5</sup>	[-20 - 15°N, 15 - 45°E]
491	Ambrym	10.01.2010	7.0 × 10 <sup>13</sup>	3.7 × 10 <sup>17</sup>	no	0.04	7.6 × 10 <sup>-5</sup>	1.9 × 10 <sup>-4</sup>	[0 - 35°S, 150 - 182°E]
492	Nyamuragira	11.01.2010	6.6 × 10 <sup>13</sup>	2.4 × 10 <sup>17</sup>	no	0.00	-5.4 × 10 <sup>-6</sup>	2.7 × 10 <sup>-4</sup>	[-20 - 20°N, 5 - 40°E]
493	Ambrym	11.01.2010	7.7 × 10 <sup>13</sup>	2.9 × 10 <sup>17</sup>	no	0.06	9.4 × 10 <sup>-5</sup>	2.6 × 10 <sup>-4</sup>	[0 - 35°S, 150 - 185°E]
494	Nyamuragira	12.01.2010	7.0 × 10 <sup>13</sup>	5.4 × 10 <sup>17</sup>	no	0.01	-2.6 × 10 <sup>-5</sup>	1.2 × 10 <sup>-4</sup>	[-20 - 20°N, 5 - 40°E]
495†	Nyamuragira	13.01.2010	4.3 × 10 <sup>13</sup>	2.5 × 10 <sup>18</sup>	no	0.01	2.2 × 10 <sup>-6</sup>	1.7 × 10 <sup>-5</sup>	[-20 - 20°N, 10 - 45°E]
496†	Nyamuragira	14.01.2010	4.5 × 10 <sup>13</sup>	1.4 × 10 <sup>18</sup>	no	0.01	4.6 × 10 <sup>-6</sup>	3.0 × 10 <sup>-5</sup>	[-20 - 20°N, 10 - 45°E]
497	Ambrym	14.01.2010	5.2 × 10 <sup>13</sup>	3.3 × 10 <sup>17</sup>	no	0.02	6.9 × 10 <sup>-5</sup>	2.2 × 10 <sup>-4</sup>	[0 - 35°S, 150 - 185°E]
498	Nyamuragira	15.01.2010	4.6 × 10 <sup>13</sup>	2.6 × 10 <sup>17</sup>	yes	0.25	1.9 × 10 <sup>-4</sup>	1.7 × 10 <sup>-4</sup>	[-20 - 15°N, 15 - 45°E]
499	Kilauea	15.01.2010	4.3 × 10 <sup>13</sup>	2.0 × 10 <sup>17</sup>	no	0.01	-1.0 × 10 <sup>-4</sup>	2.1 × 10 <sup>-4</sup>	[0 - 35°N, 143 - 175°W]
500	Ambrym	15.01.2010	6.4 × 10 <sup>13</sup>	5.0 × 10 <sup>17</sup>	no	0.08	7.8 × 10 <sup>-5</sup>	1.2 × 10 <sup>-4</sup>	[-35 - 5°N, 150 - 184°E]
501	Nyamuragira	16.01.2010	6.1 × 10 <sup>13</sup>	1.5 × 10 <sup>17</sup>	no	0.02	1.7 × 10 <sup>-4</sup>	3.9 × 10 <sup>-4</sup>	[-20 - 20°N, 5 - 35°E]
502	Ambrym	16.01.2010	6.3 × 10 <sup>13</sup>	3.4 × 10 <sup>17</sup>	no	0.00	2.0 × 10 <sup>-6</sup>	1.8 × 10 <sup>-4</sup>	[-35 - 5°N, 150 - 185°E]
503	Nyamuragira	17.01.2010	5.3 × 10 <sup>13</sup>	3.9 × 10 <sup>17</sup>	no	0.06	6.5 × 10 <sup>-5</sup>	1.3 × 10 <sup>-4</sup>	[-20 - 15°N, 10 - 40°E]
504	Ambrym	17.01.2010	5.8 × 10 <sup>13</sup>	2.0 × 10 <sup>17</sup>	no	0.01	5.2 × 10 <sup>-5</sup>	2.9 × 10 <sup>-4</sup>	[-35 - 5°N, 150 - 185°E]
505	Nyamuragira	18.01.2010	5.8 × 10 <sup>13</sup>	3.4 × 10 <sup>17</sup>	no	0.01	-3.2 × 10 <sup>-5</sup>	1.7 × 10 <sup>-4</sup>	[-20 - 15°N, 10 - 45°E]
506	Nyamuragira	19.01.2010	3.9 × 10 <sup>13</sup>	3.9 × 10 <sup>17</sup>	no	0.01	2.0 × 10 <sup>-5</sup>	1.0 × 10 <sup>-4</sup>	[-20 - 15°N, 11 - 45°E]
507	Ambrym	19.01.2010	5.1 × 10 <sup>13</sup>	2.3 × 10 <sup>17</sup>	no	0.00	2.1 × 10 <sup>-5</sup>	2.2 × 10 <sup>-4</sup>	[0 - 35°S, 145 - 179°E]
508	Ambrym	20.01.2010	7.7 × 10 <sup>13</sup>	3.6 × 10 <sup>17</sup>	no	0.04	1.0 × 10 <sup>-4</sup>	2.1 × 10 <sup>-4</sup>	[0 - 35°S, 150 - 184°E]
509	Nyamuragira	21.01.2010	3.9 × 10 <sup>13</sup>	1.3 × 10 <sup>17</sup>	no	0.03	1.1 × 10 <sup>-4</sup>	2.9 × 10 <sup>-4</sup>	[-20 - 15°N, 5 - 35°E]
510	Tungurahua	21.01.2010	3.6 × 10 <sup>13</sup>	2.3 × 10 <sup>17</sup>	no	0.10	-1.1 × 10 <sup>-4</sup>	1.5 × 10 <sup>-4</sup>	[-20 - 15°N, 65 - 95°W]
511	Ambrym	21.01.2010	4.0 × 10 <sup>13</sup>	4.6 × 10 <sup>17</sup>	no	0.03	5.4 × 10 <sup>-5</sup>	8.6 × 10 <sup>-5</sup>	[-20 - 35°S, 150 - 185°E]
512	Nyamuragira	22.01.2010	4.2 × 10 <sup>13</sup>	2.8 × 10 <sup>17</sup>	no	0.01	2.4 × 10 <sup>-5</sup>	1.5 × 10 <sup>-4</sup>	[-20 - 15°N, 10 - 40°E]
513	Ambrym	22.01.2010	2.4 × 10 <sup>13</sup>	2.6 × 10 <sup>17</sup>	no	0.00	2.8 × 10 <sup>-6</sup>	9.4 × 10 <sup>-5</sup>	[0 - 35°S, 150 - 185°E]
514	Nyamuragira	23.01.2010	6.2 × 10 <sup>13</sup>	3.7 × 10 <sup>17</sup>	no	0.02	3.3 × 10 <sup>-5</sup>	1.6 × 10 <sup>-4</sup>	[-20 - 15°N, 10 - 45°E]
515	Nyamuragira	24.01.2010	4.6 × 10 <sup>13</sup>	4.9 × 10 <sup>17</sup>	no	0.01	-2.0 × 10 <sup>-5</sup>	9.3 × 10 <sup>-5</sup>	[-20 - 15°N, 12 - 45°E]
516	Ambrym	24.01.2010	4.3 × 10 <sup>13</sup>	1.6 × 10 <sup>17</sup>	no	0.03	9.3 × 10 <sup>-5</sup>	2.6 × 10 <sup>-4</sup>	[-30 - 5°N, 145 - 181°E]
517	Tungurahua	26.01.2010	6.0 × 10 <sup>13</sup>	2.3 × 10 <sup>17</sup>	no	0.00	2.8 × 10 <sup>-7</sup>	2.5 × 10 <sup>-4</sup>	[-20 - 15°N, 65 - 95°W]
518	Nyamuragira	27.01.2010	5.7 × 10 <sup>13</sup>	4.6 × 10 <sup>17</sup>	no	0.09	5.7 × 10 <sup>-5</sup>	1.2 × 10 <sup>-4</sup>	[-20 - 15°N, 10 - 41°E]
519	Ambrym	03.02.2010	4.4 × 10 <sup>13</sup>	3.8 × 10 <sup>17</sup>	no	0.20	1.0 × 10 <sup>-4</sup>	1.1 × 10 <sup>-4</sup>	[0 - 35°S, 150 - 181°E]
520	Ambrym	04.02.2010	5.4 × 10 <sup>13</sup>	4.7 × 10 <sup>17</sup>	no	0.00	-1.4 × 10 <sup>-5</sup>	1.1 × 10 <sup>-4</sup>	[-35 - 5°N, 150 - 188°E]
521	Ambrym	05.02.2010	3.3 × 10 <sup>13</sup>	2.6 × 10 <sup>17</sup>	no	0.05	7.8 × 10 <sup>-5</sup>	1.2 × 10 <sup>-4</sup>	[0 - 35°S, 152 - 185°E]
522	Ambrym	07.02.2010	4.5 × 10 <sup>13</sup>	1.7 × 10 <sup>17</sup>	no	0.09	1.9 × 10 <sup>-4</sup>	2.5 × 10 <sup>-4</sup>	[0 - 35°S, 150 - 185°E]
523	Soufriere Hills	12.02.2010	5.8 × 10 <sup>13</sup>	4.0 × 10 <sup>17</sup>	no	0.00	-1.0 × 10 <sup>-5</sup>	1.4 × 10 <sup>-4</sup>	[-5 - 35°N, 30 - 80°W]
524	Soufriere Hills	13.02.2010	7.7 × 10 <sup>13</sup>	2.1 × 10 <sup>17</sup>	no	0.03	-2.3 × 10 <sup>-4</sup>	3.5 × 10 <sup>-4</sup>	[0 - 30°N, 35 - 70°W]
525	Soufriere Hills	14.02.2010	6.9 × 10 <sup>13</sup>	1.8 × 10 <sup>17</sup>	no	0.00	-3.1 × 10 <sup>-5</sup>	3.7 × 10 <sup>-4</sup>	[0 - 30°N, 38 - 70°W]

⊕ location of SO<sub>2</sub> SCD<sub>max</sub> is the same as for BrO SCD<sub>max</sub> † combined SO<sub>2</sub> product in case of high SO<sub>2</sub> SCDs ≥ 1 × 10<sup>18</sup> molec/cm<sup>2</sup> ‡ SO<sub>2</sub> SCDs ≥ 1 × 10<sup>18</sup> molec/cm<sup>2</sup>, but no plume pixel found in the SO<sub>2</sub> AR

\* corresponding volcano cannot be clearly identified

#	volcano	date	BrO SCD <sub>max</sub> [molec/cm <sup>2</sup> ]	SO <sub>2</sub> SCD <sub>max</sub> [molec/cm <sup>2</sup> ]	⊕	r <sup>2</sup>	fitted BrO/SO <sub>2</sub>	BrO <sub>max</sub> /SO <sub>2max</sub>	coordinates
526	Kīlauea	18.02.2010	3.3 × 10 <sup>13</sup>	1.9 × 10 <sup>17</sup>	no	0.03	7.9 × 10 <sup>-5</sup>	1.6 × 10 <sup>-4</sup>	[0 - 35°N, 142 - 175°W]
527	Ambrym	04.03.2010	4.2 × 10 <sup>13</sup>	2.2 × 10 <sup>17</sup>	no	0.05	1.1 × 10 <sup>-4</sup>	1.8 × 10 <sup>-4</sup>	[0 - 35°S, 150 - 182°E]
528	Ambrym	06.03.2010	2.9 × 10 <sup>13</sup>	2.1 × 10 <sup>17</sup>	no	0.01	3.7 × 10 <sup>-5</sup>	1.3 × 10 <sup>-4</sup>	[0 - 35°S, 152 - 185°E]
529	Turrialba*	09.03.2010	7.2 × 10 <sup>13</sup>	2.3 × 10 <sup>17</sup>	yes	0.33	3.0 × 10 <sup>-4</sup>	3.1 × 10 <sup>-4</sup>	[-10 - 25°N, 70 - 100°W]
530	Kīlauea	19.03.2010	3.1 × 10 <sup>13</sup>	1.6 × 10 <sup>17</sup>	no	0.00	2.5 × 10 <sup>-5</sup>	1.8 × 10 <sup>-4</sup>	[0 - 35°N, 142 - 175°W]
531	Kīlauea	20.03.2010	6.5 × 10 <sup>13</sup>	1.5 × 10 <sup>17</sup>	no	0.01	-1.1 × 10 <sup>-4</sup>	4.2 × 10 <sup>-4</sup>	[0 - 35°N, 140 - 175°W]
532	Ambrym	23.03.2010	4.1 × 10 <sup>13</sup>	2.2 × 10 <sup>17</sup>	no	0.00	3.9 × 10 <sup>-5</sup>	1.8 × 10 <sup>-4</sup>	[0 - 35°S, 150 - 185°E]
533	Ambrym	24.03.2010	5.7 × 10 <sup>13</sup>	2.9 × 10 <sup>17</sup>	no	0.01	-2.0 × 10 <sup>-5</sup>	1.9 × 10 <sup>-4</sup>	[0 - 35°S, 150 - 185°E]
534	Ambrym	04.04.2010	5.7 × 10 <sup>13</sup>	1.6 × 10 <sup>17</sup>	no	0.07	1.8 × 10 <sup>-4</sup>	3.4 × 10 <sup>-4</sup>	[0 - 35°S, 152 - 185°E]
535	Ambrym	08.04.2010	6.7 × 10 <sup>13</sup>	3.0 × 10 <sup>17</sup>	no	0.70	3.3 × 10 <sup>-4</sup>	2.2 × 10 <sup>-4</sup>	[0 - 35°S, 150 - 185°E]
536	Ambrym	09.04.2010	4.9 × 10 <sup>13</sup>	2.2 × 10 <sup>17</sup>	no	0.06	1.3 × 10 <sup>-4</sup>	2.2 × 10 <sup>-4</sup>	[-30 - 5°N, 154 - 185°E]
537	Ambrym	12.04.2010	8.0 × 10 <sup>13</sup>	4.7 × 10 <sup>17</sup>	no	0.02	5.8 × 10 <sup>-5</sup>	1.7 × 10 <sup>-4</sup>	[0 - 35°S, 150 - 185°E]
538	Ambrym	13.04.2010	7.7 × 10 <sup>13</sup>	2.5 × 10 <sup>17</sup>	no	0.01	4.5 × 10 <sup>-5</sup>	3.0 × 10 <sup>-4</sup>	[0 - 35°S, 150 - 185°E]
539	Ambrym	19.04.2010	7.0 × 10 <sup>13</sup>	3.1 × 10 <sup>17</sup>	yes	0.38	2.2 × 10 <sup>-4</sup>	2.2 × 10 <sup>-4</sup>	[-30 - 5°N, 150 - 185°E]
540	Eyjafjallajökull	22.04.2010	9.0 × 10 <sup>13</sup>	3.8 × 10 <sup>17</sup>	no	0.11	2.1 × 10 <sup>-4</sup>	2.3 × 10 <sup>-4</sup>	[45 - 70°N, 0 - 35°W]
541	Eyjafjallajökull	23.04.2010	1.6 × 10 <sup>14</sup>	3.7 × 10 <sup>17</sup>	yes	0.65	5.1 × 10 <sup>-4</sup>	4.3 × 10 <sup>-4</sup>	[45 - 70°N, 0 - 35°W]
542	Ambrym	23.04.2010	5.9 × 10 <sup>13</sup>	4.2 × 10 <sup>17</sup>	no	0.07	9.6 × 10 <sup>-5</sup>	1.3 × 10 <sup>-4</sup>	[-35 - 5°N, 150 - 185°E]
543	Ambrym	24.04.2010	1.2 × 10 <sup>14</sup>	2.7 × 10 <sup>17</sup>	no	0.30	4.3 × 10 <sup>-4</sup>	4.6 × 10 <sup>-4</sup>	[45 - 70°N, 0 - 35°W]
544	Eyjafjallajökull	24.04.2010	5.3 × 10 <sup>13</sup>	1.6 × 10 <sup>17</sup>	no	0.01	-6.6 × 10 <sup>-5</sup>	3.2 × 10 <sup>-4</sup>	[-35 - 5°N, 155 - 190°E]
545	Eyjafjallajökull	25.04.2010	1.3 × 10 <sup>14</sup>	4.6 × 10 <sup>17</sup>	no	0.75	3.3 × 10 <sup>-4</sup>	2.9 × 10 <sup>-4</sup>	[45 - 70°N, 0 - 35°W]
546	Eyjafjallajökull	26.04.2010	8.8 × 10 <sup>13</sup>	4.2 × 10 <sup>17</sup>	yes	0.58	2.5 × 10 <sup>-4</sup>	2.0 × 10 <sup>-4</sup>	[45 - 70°N, 0 - 35°W]
547	Ambrym	26.04.2010	5.8 × 10 <sup>13</sup>	2.8 × 10 <sup>17</sup>	no	0.21	2.1 × 10 <sup>-4</sup>	2.0 × 10 <sup>-4</sup>	[-30 - 5°N, 150 - 182°E]
548	Eyjafjallajökull	27.04.2010	1.1 × 10 <sup>14</sup>	3.1 × 10 <sup>17</sup>	no	0.07	9.4 × 10 <sup>-5</sup>	3.5 × 10 <sup>-4</sup>	[45 - 70°N, 0 - 40°W]
549	Eyjafjallajökull	28.04.2010	6.4 × 10 <sup>13</sup>	2.5 × 10 <sup>17</sup>	no	0.30	2.8 × 10 <sup>-4</sup>	2.5 × 10 <sup>-4</sup>	[45 - 70°N, 0 - 35°W]
550	Eyjafjallajökull	29.04.2010	1.3 × 10 <sup>14</sup>	6.1 × 10 <sup>17</sup>	yes	0.54	1.9 × 10 <sup>-4</sup>	2.1 × 10 <sup>-4</sup>	[40 - 70°N, 0 - 45°W]
551	Eyjafjallajökull	30.04.2010	1.4 × 10 <sup>14</sup>	4.2 × 10 <sup>17</sup>	yes	0.50	2.9 × 10 <sup>-4</sup>	3.3 × 10 <sup>-4</sup>	[40 - 70°N, -40 - 5°E]
552	Eyjafjallajökull	01.05.2010	4.9 × 10 <sup>13</sup>	1.8 × 10 <sup>17</sup>	no	0.13	3.8 × 10 <sup>-4</sup>	2.6 × 10 <sup>-4</sup>	[40 - 70°N, 0 - 35°W]
553	Eyjafjallajökull	03.05.2010	4.4 × 10 <sup>13</sup>	1.4 × 10 <sup>17</sup>	no	0.01	5.5 × 10 <sup>-5</sup>	3.0 × 10 <sup>-4</sup>	[35 - 70°N, -30 - 5°E]
554	Eyjafjallajökull	04.05.2010	4.3 × 10 <sup>13</sup>	2.2 × 10 <sup>17</sup>	yes	0.17	2.4 × 10 <sup>-4</sup>	1.9 × 10 <sup>-4</sup>	[35 - 70°N, -30 - 15°E]
555	Eyjafjallajökull	05.05.2010	1.7 × 10 <sup>14</sup>	7.2 × 10 <sup>17</sup>	no	0.34	1.3 × 10 <sup>-4</sup>	2.4 × 10 <sup>-4</sup>	[35 - 70°N, -35 - 15°E]
556	Eyjafjallajökull	06.05.2010	9.3 × 10 <sup>13</sup>	4.6 × 10 <sup>17</sup>	no	0.06	7.3 × 10 <sup>-5</sup>	2.0 × 10 <sup>-4</sup>	[25 - 70°N, -35 - 10°E]
557	Eyjafjallajökull	07.05.2010	1.0 × 10 <sup>14</sup>	5.5 × 10 <sup>17</sup>	no	0.29	1.5 × 10 <sup>-4</sup>	1.9 × 10 <sup>-4</sup>	[20 - 70°N, -45 - 10°E]
558	Eyjafjallajökull	08.05.2010	9.5 × 10 <sup>13</sup>	5.7 × 10 <sup>17</sup>	no	0.26	1.5 × 10 <sup>-4</sup>	1.6 × 10 <sup>-4</sup>	[25 - 70°N, 0 - 50°W]
559	Eyjafjallajökull	09.05.2010	1.0 × 10 <sup>14</sup>	5.0 × 10 <sup>17</sup>	no	0.14	1.3 × 10 <sup>-4</sup>	2.1 × 10 <sup>-4</sup>	[25 - 70°N, -55 - 5°E]
560	Eyjafjallajökull	10.05.2010	9.8 × 10 <sup>13</sup>	3.8 × 10 <sup>17</sup>	no	0.12	1.1 × 10 <sup>-4</sup>	2.5 × 10 <sup>-4</sup>	[20 - 70°N, -45 - 5°E]
561	Eyjafjallajökull	11.05.2010	8.2 × 10 <sup>13</sup>	4.2 × 10 <sup>17</sup>	no	0.05	8.7 × 10 <sup>-5</sup>	1.9 × 10 <sup>-4</sup>	[15 - 70°N, -55 - 10°E]
562	Kīlauea	11.05.2010	4.0 × 10 <sup>13</sup>	2.5 × 10 <sup>17</sup>	no	0.06	1.2 × 10 <sup>-4</sup>	1.6 × 10 <sup>-4</sup>	[0 - 35°N, 143 - 175°W]
563	Ambrym	11.05.2010	8.6 × 10 <sup>13</sup>	6.4 × 10 <sup>17</sup>	yes	0.59	1.6 × 10 <sup>-4</sup>	1.3 × 10 <sup>-4</sup>	[0 - 35°S, 150 - 190°E]
564	Eyjafjallajökull	12.05.2010	7.5 × 10 <sup>13</sup>	4.6 × 10 <sup>17</sup>	no	0.03	9.6 × 10 <sup>-5</sup>	1.6 × 10 <sup>-4</sup>	[20 - 70°N, -55 - 10°E]
565	Ambrym	12.05.2010	6.0 × 10 <sup>13</sup>	2.9 × 10 <sup>17</sup>	no	0.03	-8.3 × 10 <sup>-5</sup>	2.0 × 10 <sup>-4</sup>	[0 - 35°S, 150 - 185°E]
566	Eyjafjallajökull	13.05.2010	1.3 × 10 <sup>14</sup>	2.8 × 10 <sup>17</sup>	no	0.17	2.6 × 10 <sup>-4</sup>	4.7 × 10 <sup>-4</sup>	[45 - 70°N, -35 - 190°E]
567	Eyjafjallajökull	13.05.2010	3.4 × 10 <sup>13</sup>	1.0 × 10 <sup>17</sup>	no	0.33	-1.2 × 10 <sup>-3</sup>	3.1 × 10 <sup>-4</sup>	[20 - 55°N, 5 - 40°W]
568	Eyjafjallajökull	14.05.2010	1.3 × 10 <sup>14</sup>	8.4 × 10 <sup>17</sup>	no	0.42	1.4 × 10 <sup>-4</sup>	1.6 × 10 <sup>-4</sup>	[35 - 70°N, -50 - 15°E]
569	Eyjafjallajökull	15.05.2010	8.8 × 10 <sup>13</sup>	4.4 × 10 <sup>17</sup>	no	0.02	4.6 × 10 <sup>-5</sup>	2.0 × 10 <sup>-4</sup>	[40 - 70°N, 0 - 60°W]
570	Eyjafjallajökull	16.05.2010	1.2 × 10 <sup>14</sup>	3.5 × 10 <sup>17</sup>	no	0.32	3.1 × 10 <sup>-4</sup>	3.5 × 10 <sup>-4</sup>	[35 - 70°N, -35 - 20°E]
571	Eyjafjallajökull	16.05.2010	2.6 × 10 <sup>13</sup>	2.7 × 10 <sup>17</sup>	no	0.09	-1.0 × 10 <sup>-4</sup>	9.6 × 10 <sup>-5</sup>	[50 - 70°N, 25 - 60°W]
572	Eyjafjallajökull	17.05.2010	1.5 × 10 <sup>14</sup>	7.3 × 10 <sup>17</sup>	no	0.42	2.6 × 10 <sup>-4</sup>	2.0 × 10 <sup>-4</sup>	[35 - 70°N, -55 - 20°E]
573	Eyjafjallajökull	18.05.2010	6.5 × 10 <sup>13</sup>	1.3 × 10 <sup>17</sup>	no	0.00	-8.3 × 10 <sup>-5</sup>	4.8 × 10 <sup>-4</sup>	[30 - 65°N, -10 - 30°E]
574	Eyjafjallajökull	19.05.2010	9.1 × 10 <sup>13</sup>	1.9 × 10 <sup>17</sup>	no	0.07	2.6 × 10 <sup>-4</sup>	4.7 × 10 <sup>-4</sup>	[50 - 70°N, 0 - 35°W]
575	Eyjafjallajökull	20.05.2010	8.5 × 10 <sup>13</sup>	1.9 × 10 <sup>17</sup>	no	0.16	3.7 × 10 <sup>-4</sup>	4.4 × 10 <sup>-4</sup>	[50 - 70°N, -35 - 15°E]
576	Ambrym	26.05.2010	6.0 × 10 <sup>13</sup>	2.0 × 10 <sup>17</sup>	no	0.15	4.7 × 10 <sup>-4</sup>	2.9 × 10 <sup>-4</sup>	[0 - 35°S, 155 - 186°E]
577	Ambrym	27.05.2010	6.0 × 10 <sup>13</sup>	2.3 × 10 <sup>17</sup>	no	0.17	3.8 × 10 <sup>-4</sup>	2.5 × 10 <sup>-4</sup>	[0 - 35°S, 151 - 185°E]
578†	Pacaya	28.05.2010	2.5 × 10 <sup>13</sup>	1.3 × 10 <sup>18</sup>	no	0.04	1.2 × 10 <sup>-5</sup>	1.9 × 10 <sup>-5</sup>	[-5 - 35°N, 79 - 115°W]
579	Pacaya	29.05.2010	6.5 × 10 <sup>13</sup>	5.7 × 10 <sup>17</sup>	no	0.00	1.3 × 10 <sup>-5</sup>	1.1 × 10 <sup>-4</sup>	[-10 - 35°N, 70 - 115°W]
580	Pacaya	30.05.2010	7.2 × 10 <sup>13</sup>	3.4 × 10 <sup>17</sup>	no	0.06	7.0 × 10 <sup>-5</sup>	2.0 × 10 <sup>-4</sup>	[-5 - 35°N, 75 - 115°W]
581	Pacaya	31.05.2010	8.5 × 10 <sup>13</sup>	3.7 × 10 <sup>17</sup>	no	0.03	9.1 × 10 <sup>-5</sup>	2.3 × 10 <sup>-4</sup>	[0 - 35°N, 89 - 120°W]
582	Bezymianny*	31.05/01.06.2010	6.0 × 10 <sup>13</sup>	2.5 × 10 <sup>17</sup>	no	0.17	2.0 × 10 <sup>-4</sup>	2.3 × 10 <sup>-4</sup>	[40 - 70°N, 140 - 180°E]
583	Pacaya	01.06.2010	5.7 × 10 <sup>13</sup>	1.7 × 10 <sup>17</sup>	no	0.00	3.6 × 10 <sup>-5</sup>	3.3 × 10 <sup>-4</sup>	[0 - 35°N, 85 - 123°W]
584	Bezymianny*	09.06.2010	3.8 × 10 <sup>13</sup>	1.8 × 10 <sup>17</sup>	no	0.00	-1.4 × 10 <sup>-4</sup>	2.1 × 10 <sup>-4</sup>	[35 - 70°N, 145 - 180°E]
585	Ambrym	09.06.2010	7.0 × 10 <sup>13</sup>	1.6 × 10 <sup>17</sup>	no	0.10	3.7 × 10 <sup>-4</sup>	4.2 × 10 <sup>-4</sup>	[0 - 35°S, 150 - 183°E]
586	Ambrym	19.06.2010	7.2 × 10 <sup>13</sup>	1.7 × 10 <sup>17</sup>	no	0.01	2.0 × 10 <sup>-4</sup>	4.2 × 10 <sup>-4</sup>	[0 - 35°S, 150 - 185°E]
587	Kliuchevskoi*	23.06.2010	6.2 × 10 <sup>13</sup>	2.5 × 10 <sup>17</sup>	no	0.10	1.3 × 10 <sup>-4</sup>	2.4 × 10 <sup>-4</sup>	[35 - 70°N, 145 - 180°E]
588	Kīlauea	28.06.2010	7.5 × 10 <sup>13</sup>	1.6 × 10 <sup>17</sup>	no	0.02	-1.6 × 10 <sup>-4</sup>	4.4 × 10 <sup>-4</sup>	[0 - 35°N, 145 - 175°W]
589	Ambrym	28.06.2010	6.5 × 10 <sup>13</sup>	3.0 × 10 <sup>17</sup>	no	0.32	2.5 × 10 <sup>-4</sup>	2.1 × 10 <sup>-4</sup>	[0 - 35°S, 151 - 182°E]
590	Gorely*	11./12.07.2010	4.2 × 10 <sup>13</sup>	1.4 × 10 <sup>17</sup>	no	0.04	3.0 × 10 <sup>-4</sup>	2.9 × 10 <sup>-4</sup>	[35 - 70°N, 140 - 175°E]
591	Rabaul	23.07.2010	3.6 × 10 <sup>13</sup>	2.1 × 10 <sup>17</sup>	no	0.03	-9.3 × 10 <sup>-5</sup>	1.7 × 10 <sup>-4</sup>	[-20 - 15°N, 130 - 164°E]
592	Ambrym	15.08.2010	5.6 × 10 <sup>13</sup>	2.6 × 10 <sup>17</sup>	no	0.13	1.7 × 10 <sup>-4</sup>	2.1 × 10 <sup>-4</sup>	[0 - 35°S, 150 - 185°E]
593	Kliuchevskoi	30.08.2010	3.8 × 10 <sup>13</sup>	2.0 × 10 <sup>17</sup>	no	0.20	2.0 × 10 <sup>-4</sup>	1.8 × 10 <sup>-4</sup>	[35 - 70°N, 145 - 180°E]
594	Kliuchevskoi	02./03.09.2010	3.7 × 10 <sup>13</sup>	2.4 × 10 <sup>17</sup>	no	0.01	6.8 × 10 <sup>-5</sup>	1.5 × 10 <sup>-4</sup>	[40 - 70°N, 145 - 180°E]
595	Ambrym	13.09.2010	4.5 × 10 <sup>13</sup>	2.5 × 10 <sup>17</sup>	no	0.07	-9.1 × 10 <sup>-5</sup>	1.7 × 10 <sup>-4</sup>	[0 - 35°S, 150 - 185°E]
596	Ambrym	14.09.2010	6.2 × 10 <sup>13</sup>	1.8 × 10 <sup>17</sup>	no	0.01	4.8 × 10 <sup>-5</sup>	3.3 × 10 <sup>-4</sup>	[0 - 35°S, 150 - 185°E]
597	Ambrym	13.10.2010	6.2 × 10 <sup>13</sup>	2.9 × 10 <sup>17</sup>	no	0.34	1.9 × 10 <sup>-4</sup>	2.0 × 10 <sup>-4</sup>	[0 - 35°S, 150 - 185°E]
598	Ambrym	17.10.2010	7.8 × 10 <sup>13</sup>	4.3 × 10 <sup>17</sup>	yes	0.01	2.7 × 10 <sup>-5</sup>	1.8 × 10 <sup>-4</sup>	[-35 - 5°N, 150 - 182°E]
599	Ambrym	18.10.2010	6.1 × 10 <sup>13</sup>	1.8 × 10 <sup>17</sup>	no	0.03	1.4 × 10 <sup>-4</sup>	3.2 × 10 <sup>-4</sup>	[-30 - 5°N, 147 - 180°E]
600	Ambrym	27.10.2010	6.0 × 10 <sup>13</sup>	2.3 × 10 <sup>17</sup>	no	0.16	2.1 × 10 <sup>-4</sup>	2.5 × 10 <sup>-4</sup>	[-35 - 5°N, 150 - 183°E]

⊕ location of SO<sub>2</sub> SCD<sub>max</sub> is the same as for BrO SCD<sub>max</sub> † combined SO<sub>2</sub> product in case of high SO<sub>2</sub> SCDs ≥ 1 × 10<sup>18</sup> molec/cm<sup>2</sup> ‡ SO<sub>2</sub> SCDs ≥ 1 × 10<sup>18</sup> molec/cm<sup>2</sup>, but no plume pixel found in the SO<sub>2</sub> AR

\* corresponding volcano cannot be clearly identified

#	volcano	date	BrO SCD <sub>max</sub> [molec/cm <sup>2</sup> ]	SO <sub>2</sub> SCD <sub>max</sub> [molec/cm <sup>2</sup> ]	⊕	r <sup>2</sup>	fitted BrO/SO <sub>2</sub>	BrO <sub>max</sub> /SO <sub>2max</sub>	coordinates
601	Shiveluch	28.10.2010	5.5 × 10 <sup>13</sup>	5.9 × 10 <sup>17</sup>	no	0.00	-6.8 × 10 <sup>-6</sup>	9.3 × 10 <sup>-5</sup>	[35 - 56°N, 155 - 190°W]
602	Ambrym	01.11.2010	4.6 × 10 <sup>13</sup>	3.1 × 10 <sup>17</sup>	no	0.06	-1.0 × 10 <sup>-4</sup>	1.4 × 10 <sup>-4</sup>	[0 - 35°S, 150 - 190°E]
603	Ambrym	02.11.2010	6.8 × 10 <sup>13</sup>	3.9 × 10 <sup>17</sup>	no	0.19	2.0 × 10 <sup>-4</sup>	1.7 × 10 <sup>-4</sup>	[0 - 35°S, 150 - 189°E]
604	Ambrym	03.11.2010	6.4 × 10 <sup>13</sup>	4.0 × 10 <sup>17</sup>	no	0.09	5.9 × 10 <sup>-5</sup>	1.5 × 10 <sup>-4</sup>	[0 - 35°S, 153 - 185°E]
605 <sup>†</sup>	Merapi	04.11.2010	6.4 × 10 <sup>13</sup>	1.4 × 10 <sup>18</sup>	no	0.20	4.9 × 10 <sup>-5</sup>	4.4 × 10 <sup>-5</sup>	[-25 - 10°N, 85 - 120°E]
606 <sup>†</sup>	Merapi	05.11.2010	7.1 × 10 <sup>13</sup>	8.9 × 10 <sup>18</sup>	no	0.02	4.9 × 10 <sup>-6</sup>	8.0 × 10 <sup>-6</sup>	[-30 - 15°N, 80 - 125°E]
607	Ambrym	05.11.2010	6.4 × 10 <sup>13</sup>	3.3 × 10 <sup>17</sup>	no	0.11	1.3 × 10 <sup>-4</sup>	1.9 × 10 <sup>-4</sup>	[0 - 35°S, 150 - 185°E]
608 <sup>†</sup>	Merapi	06.11.2010	5.9 × 10 <sup>13</sup>	1.7 × 10 <sup>18</sup>	no	0.00	7.9 × 10 <sup>-6</sup>	3.3 × 10 <sup>-5</sup>	[-40 - 15°N, 70 - 130°E]
609	Merapi	07.11.2010	1.0 × 10 <sup>14</sup>	8.6 × 10 <sup>17</sup>	no	0.00	-4.1 × 10 <sup>-6</sup>	1.2 × 10 <sup>-4</sup>	[-45 - 15°N, 75 - 130°E]
610	Merapi	08.11.2010	7.2 × 10 <sup>13</sup>	4.9 × 10 <sup>17</sup>	no	0.01	2.2 × 10 <sup>-5</sup>	1.4 × 10 <sup>-4</sup>	[-45 - 10°N, 70 - 135°E]
611	Merapi	09.11.2010	8.4 × 10 <sup>13</sup>	8.6 × 10 <sup>17</sup>	no	0.01	3.9 × 10 <sup>-5</sup>	9.7 × 10 <sup>-5</sup>	[-45 - 15°N, 65 - 140°E]
612	Merapi	10.11.2010	7.4 × 10 <sup>13</sup>	4.5 × 10 <sup>17</sup>	no	0.01	4.8 × 10 <sup>-5</sup>	1.6 × 10 <sup>-4</sup>	[-35 - 10°N, 55 - 126°E]
613	Ambrym	10.11.2010	6.1 × 10 <sup>13</sup>	2.3 × 10 <sup>17</sup>	yes	0.32	2.8 × 10 <sup>-4</sup>	2.5 × 10 <sup>-4</sup>	[0 - 35°S, 150 - 185°E]
614	Merapi	11.11.2010	6.5 × 10 <sup>13</sup>	3.3 × 10 <sup>17</sup>	no	0.00	3.9 × 10 <sup>-5</sup>	1.9 × 10 <sup>-4</sup>	[-35 - 10°N, 70 - 130°E]
615	Merapi	12.11.2010	7.7 × 10 <sup>13</sup>	2.4 × 10 <sup>17</sup>	no	0.01	6.5 × 10 <sup>-5</sup>	3.1 × 10 <sup>-4</sup>	[-40 - 10°N, 72 - 125°E]
616	Merapi	13.11.2010	3.0 × 10 <sup>13</sup>	1.0 × 10 <sup>17</sup>	no	0.04	-4.6 × 10 <sup>-4</sup>	2.9 × 10 <sup>-4</sup>	[0 - 35°S, 80 - 114°E]
617	Ambrym	16.11.2010	7.2 × 10 <sup>13</sup>	2.9 × 10 <sup>17</sup>	no	0.14	1.9 × 10 <sup>-4</sup>	2.4 × 10 <sup>-4</sup>	[0 - 35°S, 150 - 185°E]
618	Ambrym	19.11.2010	4.5 × 10 <sup>13</sup>	2.1 × 10 <sup>17</sup>	no	0.01	-8.2 × 10 <sup>-5</sup>	2.1 × 10 <sup>-4</sup>	[0 - 35°S, 150 - 176°E]
619	Tungurahua	27.11.2010	3.2 × 10 <sup>13</sup>	1.9 × 10 <sup>17</sup>	no	0.00	-2.5 × 10 <sup>-5</sup>	1.6 × 10 <sup>-4</sup>	[-20 - 15°N, 69 - 100°W]
620	Tungurahua	28.11.2010	2.4 × 10 <sup>13</sup>	1.9 × 10 <sup>17</sup>	no	0.00	4.1 × 10 <sup>-5</sup>	1.2 × 10 <sup>-4</sup>	[-20 - 15°N, 65 - 95°W]
621	Merapi	30.11.2010	5.5 × 10 <sup>13</sup>	2.6 × 10 <sup>17</sup>	yes	0.25	1.9 × 10 <sup>-4</sup>	2.0 × 10 <sup>-4</sup>	[-25 - 10°N, 65 - 129°E]
622	Ambrym	30.11.2010	7.6 × 10 <sup>13</sup>	2.4 × 10 <sup>17</sup>	no	0.26	3.0 × 10 <sup>-4</sup>	3.1 × 10 <sup>-4</sup>	[0 - 35°S, 150 - 183°E]
623	Tungurahua	01.12.2010	3.8 × 10 <sup>13</sup>	3.4 × 10 <sup>17</sup>	no	0.00	-2.0 × 10 <sup>-5</sup>	1.1 × 10 <sup>-4</sup>	[-20 - 15°N, 66 - 95°W]
624	Ambrym	01.12.2010	4.6 × 10 <sup>13</sup>	3.6 × 10 <sup>17</sup>	no	0.22	1.0 × 10 <sup>-4</sup>	1.2 × 10 <sup>-4</sup>	[0 - 35°S, 150 - 185°E]
625	Tungurahua	02.12.2010	4.6 × 10 <sup>13</sup>	2.1 × 10 <sup>17</sup>	no	0.00	-5.4 × 10 <sup>-5</sup>	2.1 × 10 <sup>-4</sup>	[-20 - 15°N, 68 - 95°W]
626	Ambrym	02.12.2010	3.8 × 10 <sup>13</sup>	1.4 × 10 <sup>17</sup>	no	0.37	3.0 × 10 <sup>-4</sup>	2.6 × 10 <sup>-4</sup>	[0 - 35°S, 153 - 185°E]
627	Tungurahua	03.12.2010	4.9 × 10 <sup>13</sup>	1.9 × 10 <sup>17</sup>	no	0.00	4.3 × 10 <sup>-5</sup>	2.4 × 10 <sup>-4</sup>	[-20 - 15°N, 65 - 95°W]
628	Pacaya*	07.12.2010	5.2 × 10 <sup>13</sup>	1.5 × 10 <sup>17</sup>	no	0.27	-9.7 × 10 <sup>-4</sup>	3.3 × 10 <sup>-4</sup>	[0 - 35°N, 81 - 115°W]
629	Ambrym	11.12.2010	4.2 × 10 <sup>13</sup>	2.0 × 10 <sup>17</sup>	no	0.05	8.5 × 10 <sup>-5</sup>	2.1 × 10 <sup>-4</sup>	[0 - 35°S, 150 - 185°E]
630	Shiveluch*	14.12.2010	5.1 × 10 <sup>13</sup>	6.2 × 10 <sup>17</sup>	no	0.00	6.8 × 10 <sup>-6</sup>	8.2 × 10 <sup>-5</sup>	[25 - 45°N, 135 - 170°W]
631	Ambrym	14.12.2010	6.8 × 10 <sup>13</sup>	1.7 × 10 <sup>17</sup>	no	0.01	9.3 × 10 <sup>-5</sup>	3.9 × 10 <sup>-4</sup>	[0 - 35°S, 150 - 181°E]
632	Shiveluch*	15.12.2010	1.8 × 10 <sup>14</sup>	3.9 × 10 <sup>17</sup>	no	0.04	-1.6 × 10 <sup>-4</sup>	4.5 × 10 <sup>-4</sup>	[25 - 45°N, 105 - 140°W]
633	Tengger Caldera	16.12.2010	5.9 × 10 <sup>13</sup>	2.1 × 10 <sup>17</sup>	no	0.00	2.0 × 10 <sup>-5</sup>	2.7 × 10 <sup>-4</sup>	[-25 - 10°N, 100 - 135°E]
634	Shiveluch*	16.12.2010	2.9 × 10 <sup>13</sup>	3.5 × 10 <sup>17</sup>	no	0.13	-1.2 × 10 <sup>-4</sup>	8.1 × 10 <sup>-5</sup>	[25 - 45°N, 70 - 105°W]
635	Tengger Caldera	21.12.2010	2.2 × 10 <sup>13</sup>	1.8 × 10 <sup>17</sup>	no	0.07	-8.5 × 10 <sup>-5</sup>	1.1 × 10 <sup>-4</sup>	[-25 - 10°N, 99 - 130°E]
636	Tengger Caldera	23.12.2010	5.9 × 10 <sup>13</sup>	1.5 × 10 <sup>17</sup>	no	0.02	1.2 × 10 <sup>-4</sup>	3.7 × 10 <sup>-4</sup>	[-25 - 15°N, 95 - 125°E]
637	Tengger Caldera	24.12.2010	8.9 × 10 <sup>13</sup>	1.5 × 10 <sup>17</sup>	no	0.03	2.5 × 10 <sup>-4</sup>	5.8 × 10 <sup>-4</sup>	[-25 - 10°N, 95 - 128°E]
638	Ambrym	24.12.2010	5.5 × 10 <sup>13</sup>	2.9 × 10 <sup>17</sup>	no	0.05	-1.1 × 10 <sup>-4</sup>	1.8 × 10 <sup>-4</sup>	[0 - 35°S, 150 - 182°E]
639	Ambrym	25.12.2010	3.0 × 10 <sup>13</sup>	1.8 × 10 <sup>17</sup>	yes	0.01	2.2 × 10 <sup>-5</sup>	1.6 × 10 <sup>-4</sup>	[0 - 35°S, 150 - 185°E]
640	Ambrym	26.12.2010	3.9 × 10 <sup>13</sup>	1.7 × 10 <sup>17</sup>	yes	0.09	1.7 × 10 <sup>-4</sup>	2.2 × 10 <sup>-4</sup>	[0 - 35°S, 153 - 185°E]
641	Ambrym	27.12.2010	9.0 × 10 <sup>13</sup>	1.8 × 10 <sup>17</sup>	no	0.18	3.7 × 10 <sup>-4</sup>	4.7 × 10 <sup>-4</sup>	[-30 - 5°N, 145 - 180°E]
642	Ambrym	28.12.2010	5.7 × 10 <sup>13</sup>	1.9 × 10 <sup>17</sup>	no	0.01	6.3 × 10 <sup>-5</sup>	2.8 × 10 <sup>-4</sup>	[0 - 35°S, 145 - 178°E]
643	Ambrym	02.01.2011	5.6 × 10 <sup>13</sup>	2.7 × 10 <sup>17</sup>	no	0.18	1.4 × 10 <sup>-4</sup>	2.1 × 10 <sup>-4</sup>	[0 - 35°S, 150 - 185°E]
644	Tengger Caldera*	03.01.2011	5.9 × 10 <sup>13</sup>	2.8 × 10 <sup>17</sup>	no	0.16	1.3 × 10 <sup>-4</sup>	2.1 × 10 <sup>-4</sup>	[-25 - 10°N, 95 - 130°E]
645	Ambrym	03.01.2011	4.2 × 10 <sup>13</sup>	3.3 × 10 <sup>17</sup>	no	0.24	1.2 × 10 <sup>-4</sup>	1.2 × 10 <sup>-4</sup>	[0 - 35°S, 150 - 190°E]
646	Ambrym	04.01.2011	4.7 × 10 <sup>13</sup>	2.0 × 10 <sup>17</sup>	no	0.05	1.2 × 10 <sup>-4</sup>	2.3 × 10 <sup>-4</sup>	[0 - 35°S, 150 - 189°E]
647	Ambrym	18.01.2011	9.8 × 10 <sup>13</sup>	4.8 × 10 <sup>17</sup>	no	0.36	2.1 × 10 <sup>-4</sup>	2.0 × 10 <sup>-4</sup>	[0 - 35°S, 150 - 185°E]
648	Ambrym	19.01.2011	5.3 × 10 <sup>13</sup>	1.8 × 10 <sup>17</sup>	no	0.02	-7.7 × 10 <sup>-5</sup>	2.8 × 10 <sup>-4</sup>	[-30 - 5°N, 153 - 185°E]
649	Sakura-jima*	27.01.2011	4.4 × 10 <sup>13</sup>	2.7 × 10 <sup>17</sup>	no	0.04	-1.2 × 10 <sup>-4</sup>	1.5 × 10 <sup>-4</sup>	[10 - 45°N, 125 - 164°E]
650	Ambrym	27.01.2011	4.6 × 10 <sup>13</sup>	2.8 × 10 <sup>17</sup>	no	0.40	2.0 × 10 <sup>-4</sup>	1.6 × 10 <sup>-4</sup>	[0 - 35°S, 150 - 183°E]
651	Tengger Caldera	28.01.2011	7.4 × 10 <sup>13</sup>	2.3 × 10 <sup>17</sup>	no	0.01	9.2 × 10 <sup>-5</sup>	3.1 × 10 <sup>-4</sup>	[-25 - 10°N, 95 - 135°E]
652	Ambrym	28.01.2011	5.8 × 10 <sup>13</sup>	1.9 × 10 <sup>17</sup>	no	0.00	-3.0 × 10 <sup>-5</sup>	3.0 × 10 <sup>-4</sup>	[-35 - 5°N, 150 - 185°E]
653	Tengger Caldera	29.01.2011	2.7 × 10 <sup>13</sup>	4.8 × 10 <sup>17</sup>	no	0.05	2.3 × 10 <sup>-5</sup>	5.6 × 10 <sup>-5</sup>	[-25 - 10°N, 95 - 130°E]
654	Tengger Caldera	31.01.2011	9.4 × 10 <sup>13</sup>	1.7 × 10 <sup>17</sup>	no	0.16	-3.2 × 10 <sup>-4</sup>	5.4 × 10 <sup>-4</sup>	[-25 - 10°N, 95 - 125°E]
655	Etna	31.01.2011	3.3 × 10 <sup>13</sup>	2.3 × 10 <sup>17</sup>	no	0.00	-2.1 × 10 <sup>-5</sup>	1.4 × 10 <sup>-4</sup>	[25 - 51°N, 5 - 40°E]
656	Tengger Caldera	03.02.2011	1.1 × 10 <sup>13</sup>	2.5 × 10 <sup>17</sup>	no	0.02	-2.9 × 10 <sup>-5</sup>	4.7 × 10 <sup>-5</sup>	[-25 - 10°N, 95 - 130°E]
657	Tengger Caldera	05.02.2011	4.3 × 10 <sup>13</sup>	1.3 × 10 <sup>17</sup>	no	0.15	-3.3 × 10 <sup>-4</sup>	3.1 × 10 <sup>-4</sup>	[-25 - 10°N, 95 - 126°E]
658	Ambrym	10.02.2011	8.2 × 10 <sup>13</sup>	2.7 × 10 <sup>17</sup>	no	0.03	1.2 × 10 <sup>-4</sup>	2.9 × 10 <sup>-4</sup>	[-35 - 5°N, 145 - 181°E]
659	Tengger Caldera	11.02.2011	6.7 × 10 <sup>13</sup>	1.7 × 10 <sup>17</sup>	no	0.00	2.2 × 10 <sup>-5</sup>	3.8 × 10 <sup>-4</sup>	[-25 - 10°N, 100 - 132°E]
660	Ambrym	11.02.2011	9.6 × 10 <sup>13</sup>	2.8 × 10 <sup>17</sup>	no	0.01	-4.9 × 10 <sup>-5</sup>	3.3 × 10 <sup>-4</sup>	[-35 - 5°N, 150 - 185°E]
661	Ambrym	15.02.2011	7.4 × 10 <sup>13</sup>	4.3 × 10 <sup>17</sup>	no	0.10	7.1 × 10 <sup>-5</sup>	1.7 × 10 <sup>-4</sup>	[0 - 35°S, 150 - 182°E]
662	Ambrym	06.03.2011	4.9 × 10 <sup>13</sup>	3.2 × 10 <sup>17</sup>	no	0.15	9.1 × 10 <sup>-5</sup>	1.5 × 10 <sup>-4</sup>	[0 - 35°S, 150 - 185°E]
663	Tengger Caldera	11.03.2011	4.7 × 10 <sup>13</sup>	3.0 × 10 <sup>17</sup>	no	0.05	5.8 × 10 <sup>-5</sup>	1.5 × 10 <sup>-4</sup>	[-25 - 10°N, 95 - 127°E]
664	Shiveluch*	13/14.03.2011	1.6 × 10 <sup>14</sup>	2.8 × 10 <sup>17</sup>	no	0.38	8.3 × 10 <sup>-4</sup>	5.7 × 10 <sup>-4</sup>	[40 - 67°N, 135 - 170°E]
665	Shiveluch*	15.03.2011	1.0 × 10 <sup>14</sup>	3.7 × 10 <sup>17</sup>	no	0.49	4.7 × 10 <sup>-4</sup>	2.7 × 10 <sup>-4</sup>	[35 - 68°N, 135 - 170°E]
666	Shiveluch*	16.03.2011	7.0 × 10 <sup>13</sup>	2.4 × 10 <sup>17</sup>	no	0.01	1.7 × 10 <sup>-4</sup>	2.8 × 10 <sup>-4</sup>	[35 - 68°N, 130 - 180°E]
667	Shiveluch*	16/17.03.2011	8.1 × 10 <sup>13</sup>	2.9 × 10 <sup>17</sup>	no	0.37	4.1 × 10 <sup>-4</sup>	2.7 × 10 <sup>-4</sup>	[40 - 68°N, 140 - 175°E]
668	Shiveluch*	21.03.2011	3.9 × 10 <sup>13</sup>	3.2 × 10 <sup>17</sup>	yes	0.81	3.0 × 10 <sup>-4</sup>	1.2 × 10 <sup>-4</sup>	[40 - 70°N, 145 - 180°E]
669	Ambrym	21.03.2011	8.2 × 10 <sup>13</sup>	2.3 × 10 <sup>17</sup>	no	0.20	3.1 × 10 <sup>-4</sup>	3.5 × 10 <sup>-4</sup>	[0 - 35°S, 150 - 182°E]
670	Shiveluch*	23/24.03.2011	8.9 × 10 <sup>13</sup>	2.6 × 10 <sup>17</sup>	no	0.02	-1.1 × 10 <sup>-4</sup>	3.3 × 10 <sup>-4</sup>	[40 - 70°N, 145 - 180°E]
671	Ambrym	25.03.2011	4.9 × 10 <sup>13</sup>	3.3 × 10 <sup>17</sup>	no	0.00	-8.6 × 10 <sup>-6</sup>	1.4 × 10 <sup>-4</sup>	[-35 - 5°N, 150 - 185°E]
672	Shiveluch*	26.03.2011	8.5 × 10 <sup>13</sup>	3.5 × 10 <sup>17</sup>	yes	0.62	4.1 × 10 <sup>-4</sup>	2.4 × 10 <sup>-4</sup>	[35 - 70°N, 145 - 180°E]
673	Ambrym	27.03.2011	4.9 × 10 <sup>13</sup>	2.7 × 10 <sup>17</sup>	no	0.07	1.4 × 10 <sup>-4</sup>	1.8 × 10 <sup>-4</sup>	[-35 - 5°N, 150 - 185°E]
674	Shiveluch*	28/29.03.2011	6.5 × 10 <sup>13</sup>	3.0 × 10 <sup>17</sup>	no	0.04	-1.0 × 10 <sup>-4</sup>	2.1 × 10 <sup>-4</sup>	[40 - 70°N, 145 - 180°E]
675	Kliuchevskoi*	29/30.03.2011	1.3 × 10 <sup>14</sup>	6.0 × 10 <sup>17</sup>	yes	0.79	2.6 × 10 <sup>-4</sup>	2.1 × 10 <sup>-4</sup>	[40 - 70°N, 145 - 180°E]

⊕ location of SO<sub>2</sub> SCD<sub>max</sub> is the same as for BrO SCD<sub>max</sub> † combined SO<sub>2</sub> product in case of high SO<sub>2</sub> SCDs ≥ 1 × 10<sup>18</sup> molec/cm<sup>2</sup> ‡ SO<sub>2</sub> SCDs ≥ 1 × 10<sup>18</sup> molec/cm<sup>2</sup>, but no plume pixel found in the SO<sub>2</sub> AR

\* corresponding volcano cannot be clearly identified

#	volcano	date	BrO SCD <sub>max</sub> [molec/cm <sup>2</sup> ]	SO <sub>2</sub> SCD <sub>max</sub> [molec/cm <sup>2</sup> ]	⊕	r <sup>2</sup>	fitted BrO/SO <sub>2</sub>	BrO <sub>max</sub> /SO <sub>2,max</sub>	coordinates
676	Ambrym	06.04.2011	5.4 × 10 <sup>13</sup>	1.7 × 10 <sup>17</sup>	no	0.09	1.8 × 10 <sup>-4</sup>	3.1 × 10 <sup>-4</sup>	[0 - 35°S, 155 - 190°E]
677	Etna	11.04.2011	7.1 × 10 <sup>13</sup>	3.0 × 10 <sup>17</sup>	no	0.12	1.6 × 10 <sup>-4</sup>	2.3 × 10 <sup>-4</sup>	[15 - 50°N, 10 - 45°E]
678	Ambrym	11.04.2011	4.0 × 10 <sup>13</sup>	2.5 × 10 <sup>17</sup>	no	0.01	4.7 × 10 <sup>-5</sup>	1.6 × 10 <sup>-4</sup>	[0 - 35°S, 151 - 185°E]
679	Shiveluch*	19.04.2011	5.3 × 10 <sup>13</sup>	1.5 × 10 <sup>17</sup>	no	0.03	2.4 × 10 <sup>-4</sup>	3.5 × 10 <sup>-4</sup>	[35 - 70°N, 135 - 170°E]
680	Ambrym	19.04.2011	7.7 × 10 <sup>13</sup>	3.2 × 10 <sup>17</sup>	no	0.18	2.4 × 10 <sup>-4</sup>	2.4 × 10 <sup>-4</sup>	[0 - 35°S, 150 - 182°E]
681	Shiveluch*	21./22.04.2011	5.1 × 10 <sup>13</sup>	1.8 × 10 <sup>17</sup>	yes	0.30	6.1 × 10 <sup>-4</sup>	2.7 × 10 <sup>-4</sup>	[35 - 70°N, 135 - 170°E]
682	Tungurahua	22.04.2011	3.5 × 10 <sup>13</sup>	4.1 × 10 <sup>17</sup>	no	0.18	1.3 × 10 <sup>-4</sup>	8.5 × 10 <sup>-5</sup>	[-20 - 15°N, 65 - 95°W]
683	Kizimen*	22./23.04.2011	9.1 × 10 <sup>13</sup>	5.3 × 10 <sup>17</sup>	no	0.38	1.8 × 10 <sup>-4</sup>	1.7 × 10 <sup>-4</sup>	[35 - 70°N, 140 - 180°E]
684	Shiveluch*	23./24.04.2011	7.9 × 10 <sup>13</sup>	3.3 × 10 <sup>17</sup>	yes	0.49	2.7 × 10 <sup>-4</sup>	2.3 × 10 <sup>-4</sup>	[35 - 70°N, 170 - 205°W]
685	Tungurahua	25.04.2011	5.2 × 10 <sup>13</sup>	7.1 × 10 <sup>17</sup>	no	0.03	3.5 × 10 <sup>-5</sup>	7.2 × 10 <sup>-5</sup>	[-20 - 15°N, 67 - 100°W]
686	Tungurahua	26.04.2011	5.8 × 10 <sup>13</sup>	3.6 × 10 <sup>17</sup>	no	0.01	4.5 × 10 <sup>-5</sup>	1.5 × 10 <sup>-4</sup>	[-20 - 15°N, 68 - 100°W]
687	Shiveluch*	26.04.2011	7.6 × 10 <sup>13</sup>	2.9 × 10 <sup>17</sup>	no	0.30	2.1 × 10 <sup>-4</sup>	2.5 × 10 <sup>-4</sup>	[35 - 70°N, 145 - 180°E]
688	Tungurahua	27.04.2011	2.0 × 10 <sup>14</sup>	4.3 × 10 <sup>17</sup>	no	0.00	3.6 × 10 <sup>-5</sup>	4.7 × 10 <sup>-4</sup>	[-20 - 15°N, 65 - 95°W]
689	Shiveluch*	27./28.04.2011	5.6 × 10 <sup>13</sup>	2.7 × 10 <sup>17</sup>	no	0.00	-1.6 × 10 <sup>-6</sup>	2.0 × 10 <sup>-4</sup>	[35 - 70°N, 175 - 215°W]
690	Shiveluch*	28.04.2011	7.3 × 10 <sup>13</sup>	3.2 × 10 <sup>17</sup>	no	0.07	7.9 × 10 <sup>-5</sup>	2.2 × 10 <sup>-4</sup>	[40 - 70°N, 145 - 180°E]
691	Shiveluch*	29.04.2011	4.7 × 10 <sup>13</sup>	1.9 × 10 <sup>17</sup>	no	0.04	1.1 × 10 <sup>-4</sup>	2.4 × 10 <sup>-4</sup>	[40 - 70°N, 150 - 185°E]
692	Tungurahua	30.04.2011	4.5 × 10 <sup>13</sup>	5.1 × 10 <sup>17</sup>	no	0.10	7.6 × 10 <sup>-5</sup>	8.9 × 10 <sup>-5</sup>	[-20 - 15°N, 65 - 95°W]
693	Tungurahua	01.05.2011	6.8 × 10 <sup>13</sup>	3.9 × 10 <sup>17</sup>	no	0.03	5.1 × 10 <sup>-5</sup>	1.7 × 10 <sup>-4</sup>	[-20 - 15°N, 67 - 95°W]
694	Shiveluch*	01./02.05.2011	7.4 × 10 <sup>13</sup>	3.5 × 10 <sup>17</sup>	no	0.24	1.4 × 10 <sup>-4</sup>	2.0 × 10 <sup>-4</sup>	[35 - 70°N, 140 - 180°E]
695	Tungurahua	02.05.2011	7.5 × 10 <sup>13</sup>	2.5 × 10 <sup>17</sup>	no	0.01	-3.4 × 10 <sup>-5</sup>	2.9 × 10 <sup>-4</sup>	[-20 - 15°N, 65 - 87°W]
696	Kizimen*	03.05.2011	6.6 × 10 <sup>13</sup>	3.7 × 10 <sup>17</sup>	yes	0.46	2.1 × 10 <sup>-4</sup>	1.7 × 10 <sup>-4</sup>	[40 - 70°N, 145 - 175°E]
697	Kizimen*	03./04.05.2011	6.8 × 10 <sup>13</sup>	3.0 × 10 <sup>17</sup>	no	0.01	6.0 × 10 <sup>-5</sup>	2.2 × 10 <sup>-4</sup>	[35 - 70°N, 140 - 180°E]
698	Ambrym	04.05.2011	5.3 × 10 <sup>13</sup>	1.9 × 10 <sup>17</sup>	no	0.00	-1.1 × 10 <sup>-5</sup>	2.7 × 10 <sup>-4</sup>	[0 - 35°S, 150 - 185°E]
699	Kizimen*	05./06.05.2011	6.4 × 10 <sup>13</sup>	2.0 × 10 <sup>17</sup>	no	0.11	3.8 × 10 <sup>-4</sup>	3.1 × 10 <sup>-4</sup>	[35 - 70°N, 145 - 180°E]
700	Kizimen*	08./09.05.2011	8.8 × 10 <sup>13</sup>	3.3 × 10 <sup>17</sup>	no	0.56	3.0 × 10 <sup>-4</sup>	2.6 × 10 <sup>-4</sup>	[40 - 70°N, 140 - 180°E]
701	Etna	12.05.2011	7.0 × 10 <sup>13</sup>	3.2 × 10 <sup>17</sup>	no	0.01	2.3 × 10 <sup>-5</sup>	2.2 × 10 <sup>-4</sup>	[15 - 50°N, 0 - 33°E]
702	Shiveluch*	13.05.2011	5.9 × 10 <sup>13</sup>	2.2 × 10 <sup>17</sup>	no	0.07	3.6 × 10 <sup>-5</sup>	2.6 × 10 <sup>-4</sup>	[35 - 70°N, 145 - 180°E]
703	Shiveluch*	18.05.2011	7.3 × 10 <sup>13</sup>	2.5 × 10 <sup>17</sup>	no	0.12	1.4 × 10 <sup>-4</sup>	2.8 × 10 <sup>-4</sup>	[35 - 70°N, 140 - 175°E]
704	Shiveluch*	19.05.2011	6.5 × 10 <sup>13</sup>	2.9 × 10 <sup>17</sup>	yes	0.42	3.1 × 10 <sup>-4</sup>	2.2 × 10 <sup>-4</sup>	[35 - 70°N, 145 - 180°E]
705‡	Shiveluch*	20./21.05.2011	4.3 × 10 <sup>13</sup>	9.9 × 10 <sup>17</sup>	no	0.01	2.4 × 10 <sup>-6</sup>	4.3 × 10 <sup>-5</sup>	[35 - 70°N, 125 - 175°E]
706	Karymsky	21./22.05.2011	8.0 × 10 <sup>13</sup>	3.7 × 10 <sup>17</sup>	no	0.44	2.1 × 10 <sup>-4</sup>	2.1 × 10 <sup>-4</sup>	[35 - 70°N, 140 - 175°E]
707†	Grímsvötn	22.05.2011	5.6 × 10 <sup>13</sup>	2.2 × 10 <sup>19</sup>	no	0.00	1.7 × 10 <sup>-7</sup>	2.5 × 10 <sup>-6</sup>	[45 - 70°N, -40 - 5°E]
708	Karymsky	23.05.2011	4.4 × 10 <sup>13</sup>	1.5 × 10 <sup>17</sup>	no	0.01	5.1 × 10 <sup>-5</sup>	2.7 × 10 <sup>-4</sup>	[30 - 70°N, 140 - 175°E]
709	Grímsvötn	24.05.2011	4.2 × 10 <sup>13</sup>	5.1 × 10 <sup>17</sup>	no	0.00	3.4 × 10 <sup>-6</sup>	8.2 × 10 <sup>-5</sup>	[45 - 70°N, 45 - 80°E]
710	Karymsky	24./25.05.2011	8.6 × 10 <sup>13</sup>	3.7 × 10 <sup>17</sup>	yes	0.32	2.8 × 10 <sup>-4</sup>	2.2 × 10 <sup>-4</sup>	[30 - 70°N, 175 - 215°W]
711†	Grímsvötn	25.05.2011	6.9 × 10 <sup>13</sup>	5.6 × 10 <sup>18</sup>	no	0.04	2.3 × 10 <sup>-6</sup>	1.2 × 10 <sup>-5</sup>	[35 - 70°N, -110 - -35°E]
712	Grímsvötn	25.05.2011	5.6 × 10 <sup>13</sup>	3.5 × 10 <sup>17</sup>	no	0.02	-4.5 × 10 <sup>-5</sup>	1.5 × 10 <sup>-4</sup>	[30 - 70°N, 45 - 90°E]
713	Grímsvötn	26.05.2011	7.5 × 10 <sup>13</sup>	2.5 × 10 <sup>17</sup>	no	0.20	2.5 × 10 <sup>-4</sup>	3.0 × 10 <sup>-4</sup>	[30 - 65°N, 50 - 95°E]
714†	Grímsvötn	26.05.2011	6.1 × 10 <sup>13</sup>	3.9 × 10 <sup>18</sup>	no	0.00	2.5 × 10 <sup>-6</sup>	1.5 × 10 <sup>-5</sup>	[40 - 70°N, 20 - 100°W]
715†	Grímsvötn	27.05.2011	7.1 × 10 <sup>13</sup>	2.7 × 10 <sup>18</sup>	no	0.00	4.2 × 10 <sup>-6</sup>	2.5 × 10 <sup>-5</sup>	[40 - 70°N, 0 - 95°W]
716	Kliuchevskoi*	28./29.05.2011	5.9 × 10 <sup>13</sup>	1.4 × 10 <sup>17</sup>	no	0.13	5.7 × 10 <sup>-4</sup>	4.1 × 10 <sup>-4</sup>	[35 - 70°N, 140 - 175°E]
717†	Grímsvötn	29.05.2011	7.7 × 10 <sup>13</sup>	2.2 × 10 <sup>18</sup>	no	0.01	1.0 × 10 <sup>-5</sup>	3.3 × 10 <sup>-5</sup>	[35 - 70°N, -75 - 35°E]
718	Grímsvötn	30.05.2011	8.0 × 10 <sup>13</sup>	9.8 × 10 <sup>17</sup>	no	0.02	2.6 × 10 <sup>-5</sup>	8.1 × 10 <sup>-5</sup>	[35 - 70°N, -65 - 20°E]
719	Grímsvötn	31.05.2011	4.3 × 10 <sup>13</sup>	2.3 × 10 <sup>17</sup>	no	0.01	4.2 × 10 <sup>-5</sup>	1.8 × 10 <sup>-4</sup>	[45 - 70°N, 35 - 70°E]
720†	Grímsvötn	31.05.2011	1.0 × 10 <sup>14</sup>	2.5 × 10 <sup>18</sup>	no	0.01	1.3 × 10 <sup>-5</sup>	4.1 × 10 <sup>-5</sup>	[30 - 70°N, -25 - 25°E]
721	Grímsvötn	31.05.2011	3.4 × 10 <sup>13</sup>	3.3 × 10 <sup>17</sup>	no	0.01	-3.5 × 10 <sup>-5</sup>	1.0 × 10 <sup>-4</sup>	[50 - 70°N, 15 - 60°W]
722	Grímsvötn	01.06.2011	8.4 × 10 <sup>13</sup>	3.0 × 10 <sup>17</sup>	no	0.05	9.0 × 10 <sup>-5</sup>	2.7 × 10 <sup>-4</sup>	[25 - 60°N, -15 - 25°E]
723	Grímsvötn	01.06.2011	3.0 × 10 <sup>13</sup>	2.7 × 10 <sup>17</sup>	no	0.00	-1.8 × 10 <sup>-5</sup>	1.1 × 10 <sup>-4</sup>	[50 - 70°N, 20 - 55°W]
724	Grímsvötn	02.06.2011	6.7 × 10 <sup>13</sup>	2.2 × 10 <sup>17</sup>	no	0.02	1.0 × 10 <sup>-4</sup>	2.9 × 10 <sup>-4</sup>	[20 - 60°N, -15 - 25°E]
725	Grímsvötn	02.06.2011	8.1 × 10 <sup>13</sup>	3.5 × 10 <sup>17</sup>	no	0.00	1.5 × 10 <sup>-5</sup>	2.3 × 10 <sup>-4</sup>	[45 - 70°N, 150 - 155°W]
726	Grímsvötn	02.06.2011	6.3 × 10 <sup>13</sup>	4.6 × 10 <sup>17</sup>	no	0.00	-1.3 × 10 <sup>-5</sup>	1.3 × 10 <sup>-4</sup>	[50 - 70°N, 120 - 160°W]
727	Grímsvötn	03.06.2011	1.0 × 10 <sup>14</sup>	2.5 × 10 <sup>17</sup>	no	0.01	-5.6 × 10 <sup>-5</sup>	4.2 × 10 <sup>-4</sup>	[50 - 70°N, 0 - 40°W]
728	Grímsvötn	03.06.2011	5.1 × 10 <sup>13</sup>	1.4 × 10 <sup>17</sup>	no	0.03	-1.7 × 10 <sup>-4</sup>	3.5 × 10 <sup>-4</sup>	[20 - 60°N, -20 - 24°E]
729	Grímsvötn	04.06.2011	7.1 × 10 <sup>13</sup>	1.6 × 10 <sup>17</sup>	no	0.05	2.6 × 10 <sup>-4</sup>	4.4 × 10 <sup>-4</sup>	[20 - 55°N, -15 - 20°E]
730	Grímsvötn	04.06.2011	6.0 × 10 <sup>13</sup>	2.9 × 10 <sup>17</sup>	no	0.02	6.9 × 10 <sup>-5</sup>	2.0 × 10 <sup>-4</sup>	[35 - 70°N, 85 - 140°W]
731	Grímsvötn	05.06.2011	5.9 × 10 <sup>13</sup>	1.4 × 10 <sup>17</sup>	no	0.03	1.8 × 10 <sup>-4</sup>	4.1 × 10 <sup>-4</sup>	[25 - 60°N, -10 - 25°E]
732	Grímsvötn	05.06.2011	7.1 × 10 <sup>13</sup>	4.5 × 10 <sup>17</sup>	no	0.00	-6.7 × 10 <sup>-6</sup>	1.5 × 10 <sup>-4</sup>	[50 - 70°N, 0 - 40°W]
733	Grímsvötn	05.06.2011	8.0 × 10 <sup>13</sup>	2.4 × 10 <sup>17</sup>	no	0.03	1.2 × 10 <sup>-4</sup>	3.2 × 10 <sup>-4</sup>	[35 - 70°N, 65 - 105°W]
734	Grímsvötn	05.06.2011	4.6 × 10 <sup>13</sup>	1.7 × 10 <sup>17</sup>	no	0.08	3.3 × 10 <sup>-4</sup>	2.7 × 10 <sup>-4</sup>	[45 - 70°N, 100 - 140°W]
735	Grímsvötn	06.06.2011	8.9 × 10 <sup>13</sup>	4.2 × 10 <sup>17</sup>	no	0.01	-5.0 × 10 <sup>-5</sup>	2.1 × 10 <sup>-4</sup>	[40 - 70°N, -40 - 10°E]
736	Grímsvötn	06.06.2011	5.5 × 10 <sup>13</sup>	1.9 × 10 <sup>17</sup>	no	0.01	1.0 × 10 <sup>-4</sup>	2.7 × 10 <sup>-4</sup>	[40 - 70°N, 50 - 95°W]
737	Grímsvötn	06.06.2011	9.6 × 10 <sup>13</sup>	1.5 × 10 <sup>17</sup>	no	0.00	-7.6 × 10 <sup>-5</sup>	6.0 × 10 <sup>-4</sup>	[40 - 70°N, 100 - 135°W]
738	Grímsvötn	07.06.2011	7.8 × 10 <sup>13</sup>	2.9 × 10 <sup>17</sup>	no	0.00	1.8 × 10 <sup>-5</sup>	2.6 × 10 <sup>-4</sup>	[35 - 70°N, -40 - 10°E]
739	Grímsvötn	07.06.2011	4.8 × 10 <sup>13</sup>	1.3 × 10 <sup>17</sup>	no	0.01	1.4 × 10 <sup>-4</sup>	3.5 × 10 <sup>-4</sup>	[45 - 70°N, 95 - 130°W]
740	Shiveluch*	07.06.2011	6.8 × 10 <sup>13</sup>	1.6 × 10 <sup>17</sup>	yes	0.63	4.7 × 10 <sup>-4</sup>	4.0 × 10 <sup>-4</sup>	[40 - 70°N, 145 - 180°E]
741	Grímsvötn	10.06.2011	4.1 × 10 <sup>13</sup>	1.5 × 10 <sup>17</sup>	no	0.18	4.4 × 10 <sup>-4</sup>	2.6 × 10 <sup>-4</sup>	[40 - 70°N, 0 - 35°W]
742	Shiveluch*	11.06.2011	3.8 × 10 <sup>13</sup>	2.3 × 10 <sup>17</sup>	no	0.12	1.2 × 10 <sup>-4</sup>	1.6 × 10 <sup>-4</sup>	[35 - 70°N, 140 - 175°E]
743	Shiveluch*	11.06.2011	4.0 × 10 <sup>13</sup>	2.8 × 10 <sup>17</sup>	yes	0.57	2.4 × 10 <sup>-4</sup>	1.4 × 10 <sup>-4</sup>	[35 - 70°N, 145 - 180°E]
744	Shiveluch*	12./13.06.2011	6.7 × 10 <sup>13</sup>	2.4 × 10 <sup>17</sup>	no	0.00	4.1 × 10 <sup>-5</sup>	2.7 × 10 <sup>-4</sup>	[35 - 70°N, 170 - 215°W]
745†	Nabro	13.06.2011	2.6 × 10 <sup>14</sup>	1.0 × 10 <sup>19</sup>	no	0.00	3.0 × 10 <sup>-6</sup>	2.4 × 10 <sup>-5</sup>	[-5 - 35°N, 10 - 60°E]
746	Shiveluch*	13.06.2011	3.2 × 10 <sup>13</sup>	1.6 × 10 <sup>17</sup>	no	0.15	2.7 × 10 <sup>-4</sup>	1.9 × 10 <sup>-4</sup>	[35 - 70°N, 142 - 180°E]
747†	Nabro	14.06.2011	1.1 × 10 <sup>14</sup>	3.2 × 10 <sup>18</sup>	no	0.00	2.0 × 10 <sup>-6</sup>	3.6 × 10 <sup>-5</sup>	[0 - 50°N, 16 - 40°E]
748†	Nabro	15.06.2011	2.6 × 10 <sup>14</sup>	2.2 × 10 <sup>19</sup>	no	0.27	1.8 × 10 <sup>-5</sup>	1.1 × 10 <sup>-5</sup>	[-10 - 65°N, 5 - 95°E]
749†	Nabro	16.06.2011	1.8 × 10 <sup>14</sup>	1.2 × 10 <sup>19</sup>	no	0.29	2.0 × 10 <sup>-5</sup>	1.4 × 10 <sup>-5</sup>	[-15 - 60°N, 0 - 110°E]
750	Ambrym	16.06.2011	9.3 × 10 <sup>13</sup>	3.6 × 10 <sup>17</sup>	yes	0.57	3.1 × 10 <sup>-4</sup>	2.5 × 10 <sup>-4</sup>	[0 - 35°S, 150 - 182°E]

⊕ location of SO<sub>2</sub> SCD<sub>max</sub> is the same as for BrO SCD<sub>max</sub> † combined SO<sub>2</sub> product in case of high SO<sub>2</sub> SCDs ≥ 1 × 10<sup>18</sup> molec/cm<sup>2</sup> ‡ SO<sub>2</sub> SCDs ≥ 1 × 10<sup>18</sup> molec/cm<sup>2</sup>, but no plume pixel found in the SO<sub>2</sub> AR

\* corresponding volcano cannot be clearly identified

#	volcano	date	BrO SCD <sub>max</sub> [molec/cm <sup>2</sup> ]	SO <sub>2</sub> SCD <sub>max</sub> [molec/cm <sup>2</sup> ]	⊕	r <sup>2</sup>	fitted BrO/SO <sub>2</sub>	BrO <sub>max</sub> /SO <sub>2</sub> max	coordinates
751 <sup>†</sup>	Nabro	17.06.2011	9.1 × 10 <sup>13</sup>	3.8 × 10 <sup>18</sup>	no	0.10	3.0 × 10 <sup>-5</sup>	2.3 × 10 <sup>-5</sup>	[-15 - 65°N, 0 - 125°E]
752	Kīlauea	17.06.2011	4.0 × 10 <sup>13</sup>	1.9 × 10 <sup>17</sup>	no	0.01	3.2 × 10 <sup>-5</sup>	2.0 × 10 <sup>-4</sup>	[0 - 35°N, 140 - 175°W]
753 <sup>†</sup>	Nabro	18.06.2011	1.1 × 10 <sup>14</sup>	5.6 × 10 <sup>18</sup>	no	0.03	2.6 × 10 <sup>-5</sup>	2.1 × 10 <sup>-5</sup>	[-20 - 70°N, 0 - 135°E]
754 <sup>†</sup>	Nabro	19.06.2011	8.6 × 10 <sup>13</sup>	1.7 × 10 <sup>18</sup>	no	0.01	2.1 × 10 <sup>-5</sup>	4.9 × 10 <sup>-5</sup>	[-20 - 65°N, -10 - 140°E]
755 <sup>†</sup>	Nabro	20.06.2011	1.4 × 10 <sup>14</sup>	5.6 × 10 <sup>18</sup>	no	0.12	3.2 × 10 <sup>-5</sup>	2.6 × 10 <sup>-5</sup>	[-20 - 55°N, -13 - 130°E]
756	Nabro	21.06.2011	2.5 × 10 <sup>13</sup>	2.0 × 10 <sup>17</sup>	no	0.05	-8.2 × 10 <sup>-5</sup>	1.2 × 10 <sup>-4</sup>	[20 - 60°N, 130 - 160°E]
757	Nabro	21.06.2011	3.5 × 10 <sup>13</sup>	1.7 × 10 <sup>17</sup>	no	0.02	9.1 × 10 <sup>-5</sup>	1.9 × 10 <sup>-4</sup>	[10 - 50°N, 75 - 110°E]
758 <sup>†</sup>	Nabro	21.06.2011	1.5 × 10 <sup>14</sup>	5.2 × 10 <sup>18</sup>	no	0.08	2.7 × 10 <sup>-5</sup>	2.9 × 10 <sup>-5</sup>	[-25 - 55°N, -15 - 90°E]
759	Nabro	21.06.2011	5.3 × 10 <sup>13</sup>	2.0 × 10 <sup>17</sup>	no	0.02	-7.4 × 10 <sup>-5</sup>	2.6 × 10 <sup>-4</sup>	[20 - 55°N, 130 - 180°E]
760 <sup>†</sup>	Nabro	22.06.2011	1.1 × 10 <sup>14</sup>	3.8 × 10 <sup>18</sup>	yes	0.11	3.6 × 10 <sup>-5</sup>	3.0 × 10 <sup>-5</sup>	[-20 - 50°N, -20 - 100°E]
761	Nabro	22.06.2011	5.1 × 10 <sup>13</sup>	1.8 × 10 <sup>17</sup>	no	0.04	1.4 × 10 <sup>-4</sup>	2.7 × 10 <sup>-4</sup>	[15 - 55°N, 140 - 185°E]
762	Nabro	23.06.2011	4.9 × 10 <sup>13</sup>	2.2 × 10 <sup>17</sup>	no	0.03	1.0 × 10 <sup>-4</sup>	2.1 × 10 <sup>-4</sup>	[15 - 50°N, 55 - 95°E]
763 <sup>†</sup>	Nabro	23.06.2011	1.1 × 10 <sup>14</sup>	1.7 × 10 <sup>18</sup>	no	0.03	3.3 × 10 <sup>-5</sup>	6.5 × 10 <sup>-5</sup>	[-20 - 55°N, -10 - 70°E]
764	Nabro	23.06.2011	5.2 × 10 <sup>13</sup>	1.4 × 10 <sup>17</sup>	no	0.01	9.3 × 10 <sup>-5</sup>	3.6 × 10 <sup>-4</sup>	[15 - 50°N, 150 - 182°E]
765	Nabro	24.06.2011	1.0 × 10 <sup>14</sup>	7.6 × 10 <sup>17</sup>	no	0.03	3.8 × 10 <sup>-5</sup>	1.4 × 10 <sup>-4</sup>	[-20 - 60°N, -10 - 60°E]
766 <sup>†</sup>	Nabro	25.06.2011	8.1 × 10 <sup>13</sup>	1.3 × 10 <sup>18</sup>	no	0.06	3.5 × 10 <sup>-5</sup>	6.0 × 10 <sup>-5</sup>	[-15 - 60°N, -10 - 70°E]
767 <sup>†</sup>	Nabro	26.06.2011	1.2 × 10 <sup>14</sup>	3.6 × 10 <sup>18</sup>	yes	0.27	4.2 × 10 <sup>-5</sup>	3.3 × 10 <sup>-5</sup>	[-10 - 55°N, -4 - 75°E]
768	Nabro	27.06.2011	1.5 × 10 <sup>13</sup>	9.8 × 10 <sup>16</sup>	no	0.05	-2.0 × 10 <sup>-4</sup>	1.5 × 10 <sup>-4</sup>	[20 - 50°N, 70 - 105°E]
769 <sup>†</sup>	Nabro	27.06.2011	1.0 × 10 <sup>14</sup>	2.6 × 10 <sup>18</sup>	yes	0.14	3.0 × 10 <sup>-5</sup>	3.8 × 10 <sup>-5</sup>	[-15 - 35°N, -15 - 60°E]
770	Nabro	28.06.2011	4.3 × 10 <sup>13</sup>	1.0 × 10 <sup>17</sup>	yes	0.60	1.9 × 10 <sup>-3</sup>	4.1 × 10 <sup>-4</sup>	[-10 - 25°N, 15 - 44°E]
771 <sup>†</sup>	Nabro	29.06.2011	9.9 × 10 <sup>13</sup>	1.6 × 10 <sup>18</sup>	yes	0.20	5.7 × 10 <sup>-5</sup>	6.2 × 10 <sup>-5</sup>	[-15 - 35°N, 10 - 51°E]
772	Nabro	30.06.2011	6.1 × 10 <sup>13</sup>	4.0 × 10 <sup>17</sup>	no	0.00	4.8 × 10 <sup>-6</sup>	1.5 × 10 <sup>-4</sup>	[-10 - 30°N, 14 - 55°E]

⊕ location of SO<sub>2</sub> SCD<sub>max</sub> is the same as for BrO SCD<sub>max</sub>    † combined SO<sub>2</sub> product in case of high SO<sub>2</sub> SCDs ≥ 1 × 10<sup>18</sup> molec/cm<sup>2</sup>    ‡ SO<sub>2</sub> SCDs ≥ 1 × 10<sup>18</sup> molec/cm<sup>2</sup>, but no plume pixel found in the SO<sub>2</sub> AR

\* corresponding volcano cannot be clearly identified

## Bibliography

- Afe, O. T., Richter, A., Sierk, B., Wittrock, F., and Burrows, J. P.: BrO emission from volcanoes: A survey using GOME and SCIAMACHY measurements, *Geophys. Res. Lett.*, 31, 4 PP., doi:200410.1029/2004GL020994, 2004.
- Aiuppa, A., Federico, C., Franco, A., Giudice, G., Gurrieri, S., Inguaggiato, S., Liuzzo, M., McGonigle, A. J. S., and Valenza, M.: Emission of bromine and iodine from Mount Etna volcano, *Geochem. Geophys. Geos.*, 6, Q08 008, doi:10.1029/2005GC000965, 2005.
- Aiuppa, A., Franco, A., von Glasow, R., Allen, A. G., D'Alessandro, W., Mather, T. A., Pyle, D. M., and Valenza, M.: The tropospheric processing of acidic gases and hydrogen sulphide in volcanic gas plumes as inferred from field and model investigations, *Atmos. Chem. Phys.*, 7, 1441–1450, doi:10.5194/acp-7-1441-2007, 2007.
- Andreae, M., Annegarn, H., Barrie, L., Feichter, J., Hegg, D., Jayaraman, A., Leaitch, R., Murphy, D., Nganga, J., and Pitari, G.: Aerosols, their Direct and Indirect Effects, Chapter 5 in IPCC Third Assessment Report - Climate Change 2001, pp. P. 289–348, doi:199810.1029/98GL52359, 1991.
- Baker, A. K., Rauthe-Schöch, A., Schuck, T. J., Brenninkmeijer, C. A. M., Velthoven, P. F. J. v., Wisher, A., and Oram, D. E.: Investigation of chlorine radical chemistry in the Eyjafjallajökull volcanic plume using observed depletions in non-methane hydrocarbons, *Geophys. Res. Lett.*, 38, doi:10.1029/2011GL047571, 2011a.
- Baker, A. K., Schuck, T. J., Slemr, F., van Velthoven, P., Zahn, A., and Brenninkmeijer, C. A. M.: Characterization of non-methane hydrocarbons in Asian summer monsoon outflow observed by the CARIBIC aircraft, *Atmos. Chem. Phys.*, 11, 503–518, doi:10.5194/acp-11-503-2011, 2011b.
- Bani, P., Oppenheimer, C., Tsanev, V., Carn, S., Cronin, S., Crimp, R., Calkins, J., Charley, D., Lardy, M., and Roberts, T.: Surge in sulphur and halogen degassing from Ambrym volcano, Vanuatu, *B. Volcanol.*, 71, 1159–1168, doi:10.1007/s00445-009-0293-7, 2009.
- Barrie, L. A., Bottenheim, J. W., Schnell, R. C., Crutzen, P. J., and Rasmussen, R. A.: Ozone destruction and photochemical reactions at polar sunrise in the lower Arctic atmosphere, Published online: 14 July 1988; doi:10.1038/334138a0, 334, 138–141, doi:10.1038/334138a0, 1988.

- Beek, R. d., Vountas, M., Rozanov, V. V., Richter, A., and Burrows, J. P.: The ring effect in the cloudy atmosphere, *Geophys. Res. Lett.*, 28, 721–724, doi:10.1029/2000GL012240, 2001.
- Beirle, S., Platt, U., Glasow, R. v., Wenig, M., and Wagner, T.: Estimate of nitrogen oxide emissions from shipping by satellite remote sensing, *Geophys. Res. Lett.*, 31, L18 102, doi:10.1029/2004GL020312, 2004.
- Beirle, S., Boersma, K. F., Platt, U., Lawrence, M. G., and Wagner, T.: Megacity Emissions and Lifetimes of Nitrogen Oxides Probed from Space, *Science*, 333, 1737–1739, doi:10.1126/science.1207824, 2011.
- Berg, N., Mellqvist, J., Jalkanen, J.-P., and Balzani, J.: Ship emissions of SO<sub>2</sub> and NO<sub>2</sub>: DOAS measurements from airborne platforms, *Atmos. Meas. Tech.*, 5, 1085–1098, doi:10.5194/amt-5-1085-2012, 2012.
- Biondo, S. and Marten, J.: History of flue-gas desulfurization systems since 1850. research, development, and demonstration, *J. Air Pollut. Control Assoc.*, 27, 948–961, 1977.
- Bluth, G. J. S., Doiron, S. D., Schnetzler, C. C., Krueger, A. J., and Walter, L. S.: Global tracking of the SO<sub>2</sub> clouds from the June, 1991 Mount Pinatubo eruptions, *Geophys. Res. Lett.*, 19, P. 151, doi:199210.1029/91GL02792, 1992.
- Bobrowski, N. and Giuffrida, G.: Bromine monoxide/sulphur dioxide ratios in relation to volcanological observations at Mt. Etna 2006–2009, *Solid Earth Discuss.*, 4, 475–505, doi:10.5194/sed-4-475-2012, 2012.
- Bobrowski, N. and Platt, U.: SO<sub>2</sub>/BrO ratios studied in five volcanic plumes, *J. Volcanol. Geoth. Res.*, 166, 147–160, doi:10.1016/j.jvolgeores.2007.07.003, 2007.
- Bobrowski, N., Hönninger, G., Galle, B., and Platt, U.: Detection of bromine monoxide in a volcanic plume, *Nature*, 423, 273–276, doi:10.1038/nature01625, 2003.
- Bobrowski, N., von Glasow, R., Aiuppa, A., Inguaggiato, S., Louban, I., Ibrahim, O. W., and Platt, U.: Reactive halogen chemistry in volcanic plumes, *J. Geophys. Res.*, 112, 17 PP., doi:200710.1029/2006JD007206, 2007.
- Bobrowski, N., Kern, C., Platt, U., Hörmann, C., and Wagner, T.: Novel SO<sub>2</sub> spectral evaluation scheme using the 360–390 nm wavelength range, *Atmos. Meas. Tech.*, 3, 879–891, doi:10.5194/amt-3-879-2010, 2010.
- Bogumil, K., Orphal, J., Homann, T., Voigt, S., Spietz, P., Fleischmann, O., Vogel, A., Hartmann, M., Kromminga, H., Bovensmann, H., Frerick, J., and Burrows, J.: Measurements of molecular absorption spectra with the SCIAMACHY pre-flight model: instrument characterization and reference data for atmospheric remote-sensing in the 230–2380 nm region, *J. Photoch. Photobio. A*, 157, 167–184, doi:doi:10.1016/S1010-6030(03)00062-5, 2003.

- Boichu, M., Oppenheimer, C., Roberts, T. J., Tsanev, V., and Kyle, P. R.: On bromine, nitrogen oxides and ozone depletion in the tropospheric plume of Erebus volcano (Antarctica), *Atmos. Environ.*, 45, 3856–3866, doi:10.1016/j.atmosenv.2011.03.027, 2011.
- Bonaccorso, A., Bonforte, A., Calvari, S., Negro, C. D., Grazia, G. D., Ganci, G., Neri, M., Vicari, A., and Boschi, E.: The initial phases of the 2008–2009 Mount Etna eruption: A multidisciplinary approach for hazard assessment, *J. Geophys. Res.*, 116, B03 203, doi:10.1029/2010JB007906, 2011.
- Bovensmann, H., Burrows, J. P., Buchwitz, M., Frerick, J., Noël, S., Rozanov, V. V., Chance, K. V., and Goede, A. P. H.: SCIAMACHY: Mission Objectives and Measurement Modes, *J. Atmos. Sci.*, 56, 127–150, doi:10.1175/1520-0469(1999)056<0127:SMOAMM>2.0.CO;2, 1999.
- Bramstedt, K., Richter, A., van Roozendaal, M., and de Smedt, I.: Comparisons of SCIAMACHY Sulfur Dioxide Observations, vol. 562, p. 11, available online at: <http://envisat.esa.int/workshops/acve2/papers/ESC02KB.pdf>, 2004.
- Brenninkmeijer, C. A. M., Crutzen, P., Boumard, F., Dauer, T., Dix, B., Ebinghaus, R., Filippi, D., Fischer, H., Franke, H., Frieß, U., Heintzenberg, J., Helleis, F., Hermann, M., Kock, H. H., Koepfel, C., Lelieveld, J., Leuenberger, M., Martinsson, B. G., Miemczyk, S., Moret, H. P., Nguyen, H. N., Nyfeler, P., Oram, D., O’Sullivan, D., Penkett, S., Platt, U., Pucek, M., Ramonet, M., Randa, B., Reichelt, M., Rhee, T. S., Rohwer, J., Rosenfeld, K., Scharffe, D., Schlager, H., Schumann, U., Slemr, F., Sprung, D., Stock, P., Thaler, R., Valentino, F., van Velthoven, P., Waibel, A., Wandel, A., Waschitschek, K., Wiedensohler, A., Xueref-Remy, I., Zahn, A., Zech, U., and Ziereis, H.: Civil Aircraft for the regular investigation of the atmosphere based on an instrumented container: The new CARIBIC system, *Atmos. Chem. Phys.*, 7, 4953–4976, doi:10.5194/acp-7-4953-2007, 2007.
- Burton, M., Caltabiano, T., Murè, F., Salerno, G., and Randazzo, D.: SO<sub>2</sub> flux from Stromboli during the 2007 eruption: Results from the FLAME network and traverse measurements, *J. Volcanol. Geoth. Res.*, 182, 214–220, doi:10.1016/j.jvolgeores.2008.11.025, 2009.
- Burton, M. R., Oppenheimer, C., Horrocks, L. A., and Francis, P. W.: Remote sensing of CO<sub>2</sub> and H<sub>2</sub>O emission rates from Masaya volcano, Nicaragua, *Geology*, 28, 915–918, doi:10.1130/0091-7613(2000)28<915:RSOAH>2.0.CO;2, 2000.
- Burton, M. R., Oppenheimer, C., Horrocks, L. A., and Francis, P. W.: Diurnal changes in volcanic plume chemistry observed by lunar and solar occultation spectroscopy, *Geophys. Res. Lett.*, 28, P. 843, doi:200110.1029/2000GL008499, 2001.
- Cageao, J. F., Blavier, J. P., McGuire, Y., Jiang, V., Nemtchinov, F. P., Mills, S. P., and Sander, R. P.: High-Resolution Fourier-Transform Ultraviolet-Visible Spectrometer for the Measurement of Atmospheric Trace Species: Application to OH, *Appl. Opt.*, 40, 2024, 2001.

- Calabrese, S., Aiuppa, A., Allard, P., Bagnato, E., Bellomo, S., Brusca, L., D'Alessandro, W., and Parello, F.: Atmospheric sources and sinks of volcanogenic elements in a basaltic volcano (Etna, Italy), *Geochim. Cosmochim. Ac.*, 75, 7401–7425, doi:10.1016/j.gca.2011.09.040, 2011.
- Callies, J., Corpaccioli, E., Eisinger, M., Hahne, A., and Lefevre, A.: GOME-2 - MetOp's Second Generation Sensor for Operational ozone Monitoring, *ESA Bulletin*, 102, 2000.
- Campion, R., Salerno, G. G., Coheur, P.-F., Hurtmans, D., Clarisse, L., Kazahaya, K., Burton, M., Caltabiano, T., Clerbaux, C., and Bernard, A.: Measuring volcanic degassing of SO<sub>2</sub> in the lower troposphere with ASTER band ratios, *J. Volcanol. Geoth. Res.*, 194, 42–54, doi:10.1016/j.jvolgeores.2010.04.010, 2010.
- Cantrell, C. A.: Technical Note: Review of methods for linear least-squares fitting of data and application to atmospheric chemistry problems, *Atmos. Chem. Phys.*, 8, 5477–5487, doi:10.5194/acp-8-5477-2008, 2008.
- Carn, S., Krueger, A., Arellano, S., Krotkov, N., and Yang, K.: Daily monitoring of Ecuadorian volcanic degassing from space, *J. Volcanol. Geoth. Res.*, 176, 141–150, doi:10.1016/j.jvolgeores.2008.01.029, 2008.
- Carn, S. A., Strow, L. L., Souza-Machado, S. d., Edmonds, Y., and Hannon, S.: Quantifying tropospheric volcanic emissions with AIRS: The 2002 eruption of Mt. Etna (Italy), *Geophys. Res. Lett.*, 32, 5 PP., doi:200510.1029/2004GL021034, 2005.
- Carn, S. A., Krueger, A. J., Krotkov, N. A., Yang, K., and Levelt, P. F.: Sulfur dioxide emissions from Peruvian copper smelters detected by the Ozone Monitoring Instrument, *Geophys. Res. Lett.*, 34, 5 PP., doi:200710.1029/2006GL029020, 2007.
- Carn, S. A., Krueger, A. J., Krotkov, N. A., Yang, K., and Evans, K.: Tracking volcanic sulfur dioxide clouds for aviation hazard mitigation, *Nat. Hazards*, 51, doi:10.1007/s11069-008-9228-4, 2009a.
- Carn, S. A., Pallister, J. S., Lara, L., Ewert, J. W., Watt, S., Prata, A. J., Thomas, R. J., and Villarosa, G.: The Unexpected Awakening of Chaitén Volcano, Chile, *Eos, Transactions American Geophysical Union*, 90, 205, doi:10.1029/2009EO240001, 2009b.
- Carroll, M. A., Sanders, R. W., Solomon, S., and Schmeltekopf, A. L.: Visible and near-ultraviolet spectroscopy at McMurdo Station, Antarctica: 6. Observations of BrO, *J. Geophys. Res.*, 94, 16 633–16 638, doi:10.1029/JD094iD14p16633, 1989.
- Chahine, M. T. and Center, G. S. F.: AIRS/AMSU/HSB: the Atmospheric Infrared Sounder, with its companion Advanced Microwave Sounding Unit and Humidity Sounder for Brazil : providing new insights into earth's weather and climate, National Aeronautics and Space Administration, Goddard Space Flight Center, 2000.

- Chance, K. V. and Spurr, R. J. D.: Ring effect studies: Rayleigh scattering, including molecular parameters for rotational Raman scattering, and the Fraunhofer spectrum, *Appl. Opt.*, 36, 5224–5230, doi:10.1364/AO.36.005224, 1997.
- Clarisse, L., Coheur, P. F., Prata, A. J., Hurtmans, D., Razavi, A., Phulpin, T., Hadji-Lazaro, J., and Clerbaux, C.: Tracking and quantifying volcanic SO<sub>2</sub> with IASI, the September 2007 eruption at Jebel at Tair, *Atmos. Chem. Phys.*, 8, 7723–7734, doi:10.5194/acp-8-7723-2008, 2008.
- Clarisse, L., Hurtmans, D., Prata, A. J., Karagulian, F., Clerbaux, C., De Mazière, M., and Coheur, P.-F.: Retrieving radius, concentration, optical depth, and mass of different types of aerosols from high-resolution infrared nadir spectra, *Appl. Opt.*, 49, 3713, doi:10.1364/AO.49.003713, 2010a.
- Clarisse, L., Prata, F., Lacour, J.-L., Hurtmans, D., Clerbaux, C., and Coheur, P.-F.: A correlation method for volcanic ash detection using hyperspectral infrared measurements, *Geophys. Res. Lett.*, 37, L19 806, doi:10.1029/2010GL044828, 2010b.
- Clarisse, L., Coheur, P.-F., Chefdeville, S., Lacour, J.-L., Hurtmans, D., and Clerbaux, C.: Infrared satellite observations of hydrogen sulfide in the volcanic plume of the August 2008 Kasatochi eruption, *Geophys. Res. Lett.*, 38, L10 804, doi:10.1029/2011GL047402, 2011.
- Clerbaux, C., Coheur, P.-F., Clarisse, L., Hadji-Lazaro, J., Hurtmans, D., Turquety, S., Bowman, K., Worden, H., and Carn, S. A.: Measurements of SO<sub>2</sub> profiles in volcanic plumes from the NASA Tropospheric Emission Spectrometer (TES), *Geophys. Res. Lett.*, 35, L22 807, doi:10.1029/2008GL035566, 2008.
- Daag, A. S., Tubianosa, B. S., Newhall, C. G., Tuñgol, N. M., Javier, D., Dolan, M. T., Reyes, P. J. D., Arboleda, R. A., Martinez, M. L., and Regalado, T. M.: Monitoring Sulfur Dioxide Emission at Mount Pinatubo, in: *Fire and Mud: Eruptions and Lahars of Mount Pinatubo, Philippines*, pp. 409 – 434, Newhall, C. G. and Punongbayan, R. S. (eds), Univ. Wash. Press, Seattle, 1996a.
- Daag, A. S., Tubianosa, B. S., Newhall, C. G., Tuñgol, N. M., Javier, D., Dolan, M. T., Reyes, P. J. D., Arboleda, R. A., Martinez, M. M. L., and Regalado, M. T. M.: Monitoring sulfur dioxide emission at Mount Pinatubo, in *Fire and Mud: Eruptions and Lahars of Mount Pinatubo, Philippines*, Univ. of Wash. Press, Seattle, pp. 409–414, available online at <http://pubs.usgs.gov/pinatubo/daag1/index.html>, 1996b.
- D’Alessandro, W., Bellomo, S., Bonfanti, P., Brusca, L., and Longo, M.: Salinity variations in the water resources fed by the Etnean volcanic aquifers (Sicily, Italy): natural vs. anthropogenic causes, *Environ. Model. Asses.*, 173, 431–446, doi:10.1007/s10661-010-1397-4, 2011.
- Davidson, R. and MacKinnon, J. G.: *Estimation and Inference in Econometrics*, Oxford University Press, p. 78–79, 1993.

- Davis, A. B. and Marshak, A.: Solar radiation transport in the cloudy atmosphere: a 3D perspective on observations and climate impacts, *Rep. Prog. Phys.*, **73**, 026 801, doi:10.1088/0034-4885/73/2/026801, 2010.
- De Smedt, I., Van Roozendael, M., and Jacobs, T.: Technical Note: Optimization of DOAS settings for BrO fitting from SCIAMACHY nadir spectra - Comparison with GOME BrO retrievals, Belgian Institute for Space Aeronomy (IASB-BIRA), Brussels, Belgium, 2004.
- Delmelle, P.: Environmental impacts of tropospheric volcanic gas plumes, Geological Society, London, Special Publications, **213**, 381–399, doi:10.1144/GSL.SP.2003.213.01.23, 2003.
- Delmelle, P., Stix, J., Bourque, C. P.-A., Baxter, P. J., Garcia-Alvarez, J., and Barquero, J.: Dry Deposition and Heavy Acid Loading in the Vicinity of Masaya Volcano, a Major Sulfur and Chlorine Source in Nicaragua, *Environ. Sci. Technol.*, **35**, 1289–1293, doi:10.1021/es000153m, 2001.
- Deutschmann, T., Beirle, S., Frieß, U., Grzegorski, M., Kern, C., Kritzen, L., Platt, U., Prados-Román, C., Pukite, J., Wagner, T., Werner, B., and Pfeilsticker, K.: The Monte Carlo atmospheric radiative transfer model McArtim: Introduction and validation of Jacobians and 3D features, *J. Quant. Spectrosc. Ra.*, **112**, 1119–1137, doi:10.1016/j.jqsrt.2010.12.009, 2011.
- Dikty, S. and Richter, A.: GOME-2 on MetOp-A Support for Analysis of GOME-2 In-Orbit Degradation and Impacts on Level 2 Data Products, final report, October 2011, URL [http://www.eumetsat.int/groups/ops/documents/document/pdf\\_gome2\\_degrade\\_final\\_rep.pdf](http://www.eumetsat.int/groups/ops/documents/document/pdf_gome2_degrade_final_rep.pdf), last access on 12 September 2012, 2011.
- Dix, B., Brenninkmeijer, C. A. M., Frieß, U., Wagner, T., and Platt, U.: Airborne multi-axis DOAS measurements of atmospheric trace gases on CARIBIC long-distance flights, *Atmos. Meas. Tech.*, **2**, 639–652, doi:10.5194/amt-2-639-2009, 2009.
- Doutriaux-Boucher, M. and Dubuisson, P.: Detection of volcanic SO<sub>2</sub> by spaceborne infrared radiometers, *Atmos. Res.*, **92**, 69–79, doi:10.1016/j.atmosres.2008.08.009, 2009.
- Draxler, R. R. and Rolph, G. D.: HYSPLIT (HYbrid Single-Particle Lagrangian Integrated Trajectory) model access via NOAA ARL READY Website, URL <http://ready.arl.noaa.gov/HYSPLIT.php>, last access on 12 September 2012, 2012.
- Edner, H., Ragnarson, P., Svanberg, S., Wallinder, E., Ferrara, R., Cioni, R., Raco, B., and Taddeucci, G.: Total fluxes of sulfur dioxide from the Italian volcanoes Etna, Stromboli, and Vulcano measured by differential absorption lidar and passive differential optical absorption spectroscopy, *J. Geophys. Res.*, **99**, 18 827–18,838, doi:10.1029/94JD01515, 1994.

- Eskes, H. J. and Boersma, K. F.: Averaging kernels for DOAS total-column satellite retrievals, *Atmos. Chem. Phys.*, **3**, 1285–1291, doi:10.5194/acp-3-1285-2003, 2003.
- EUMETSAT: GOME-2 Product Guide, available at: <http://oiswww.eumetsat.org/WEBOPS/eps-pg/GOME-2/GOME2-PG-index.htm>; last access on 12 September 2012, 2005.
- Fan, S. and Jacob, D. J.: Surface ozone depletion in Arctic spring sustained by bromine reactions on aerosols, *Nature*, **359**, 522–524, doi:10.1038/359522a0, 1992.
- Farquhar, J., Bao, H., and Thiemens, M.: Atmospheric influence of Earth’s earliest sulfur cycle, *Science*, **289**, 756–758, doi:10.1126/science.289.5480.756, 2000.
- Fayt, C. and Van Roozendaal, M.: WinDOAS 2.1 Software User Manual, Belgian Institute for Space Aeronomy - BIRA/IASB, <http://uv-vis.aeronomie.be/software/WinDOAS/WinDOAS-SUM-210b.pdf>, 2001.
- Fioletov, V. E., McLinden, C., Krotkov, N., Moran, M. D., and Yang, K.: Poster: Estimation of SO<sub>2</sub> emissions using OMI satellite retrievals, Environmental Canada, available online at <http://www.geiacenter.org/workshops/current/presentations/P5%20-%20Fioletov.pdf>, 2011a.
- Fioletov, V. E., McLinden, C. A., Krotkov, N., Moran, M. D., and Yang, K.: Estimation of SO<sub>2</sub> emissions using OMI retrievals, *Geophys. Res. Lett.*, **38**, 5 PP., doi:201110.1029/2011GL049402, 2011b.
- Francis, P., Maciejewski, A., Oppenheimer, C., Chaffin, C., and Caltabiano, T.: SO<sub>2</sub>:HCl ratios in the plumes from Mt. Etna and Vulcano determined by Fourier Transform Spectroscopy, *Geophys. Res. Lett.*, **22**, P. 1717, doi:199510.1029/95GL01657, 1995.
- Franklin, B.: Meteorological imaginations and conjectures, *Lit. Philos. Soc. Manchester*, **2**, 373–377, available online at [http://www.mangeogsoc.org.uk/pdfs/payne\\_10\\_2.pdf](http://www.mangeogsoc.org.uk/pdfs/payne_10_2.pdf), 1784.
- Friedlingstein, P., Houghton, R. A., Marland, G., Hackler, J., Boden, T. A., Conway, T. J., Canadell, J. G., Raupach, M. R., Ciais, P., and Quéré, C. L.: Update on CO<sub>2</sub> emissions, *Nat. Geosci.*, **3**, 811–812, doi:10.1038/ngeo1022, 2010.
- Frieß U., Monks, P. S., Remedios, J. J., Rozanov, A., Sinreich, R., Wagner, T., and Platt, U.: MAX-DOAS O<sub>4</sub> measurements: A new technique to derive information on atmospheric aerosols: 2. Modeling studies, *J. Geophys. Res.*, **111**, D14 203, doi: 10.1029/2005JD006618, 2006.
- Galle, B., Oppenheimer, C., Geyer, A., McGonigle, A. J., Edmonds, M., and Horrocks, L.: A miniaturised ultraviolet spectrometer for remote sensing of SO<sub>2</sub> fluxes: a new tool for volcano surveillance, *J. Volcanol. Geoth. Res.*, **119**, 241–254, doi:10.1016/S0377-0273(02)00356-6, 2003.

- Galle, B., Bobrowski, N., Carn, S., Johansson, M., Kasereka, M., Oppenheimer, C., Yalire, M., and Zhang, Y.: Gas Emissions from Nyiragongo Volcano D.R. of Congo, measured by UV Mini-DOAS Spectroscopy, EGU meeting, <http://linkcrypt.ws/dir/ea0rbz1v81094oe>, last access on 12 September 2012, 2005.
- Galle, B., Johansson, M., Rivera, C., Zhang, Y., Kihlman, M., Kern, C., Lehmann, T., Platt, U., Arellano, S., and Hidalgo, S.: Network for Observation of Volcanic and Atmospheric Change (NOVAC) – A global network for volcanic gas monitoring: Network layout and instrument description, *J. Geophys. Res.*, 115, D05304, doi:10.1029/2009JD011823, 2010.
- Galle, B., Delgado, H., Garzon, G., Vogel, L., and Platt, U.: NOVAC: Network for Observation of Volcanic and Atmospheric Change, Final Report, European Union, 2011.
- Gangale, G., Prata, A. J., and Clarisse, L.: The infrared spectral signature of volcanic ash determined from high-spectral resolution satellite measurements, *Remote Sens. Environ.*, pp. 414–425, doi:10.1016/j.rse.2009.09.007, 2009.
- Gerlach, T.: Volcanic versus anthropogenic carbon dioxide, *Eos, Transactions American Geophysical Union*, 92, 201–202, 2012.
- Gerlach, T. M.: Volcanic sources of tropospheric ozone-depleting trace gases, *Geochem. Geophys. Geosy.*, 5, 16 PP., doi:200410.1029/2004GC000747, 2004.
- Gottwald, M. and Bovensmann, H.: *SCIAMACHY - Exploring the Changing Earth's Atmosphere*, Springer Netherlands, 1st edition. edn., 2010.
- Graaf, M. d., Stammes, P., Torres, O., and Koелеmeijer, R. B. A.: Absorbing Aerosol Index: Sensitivity analysis, application to GOME and comparison with TOMS, *J. Geophys. Res.*, 110, 19 PP., doi:200510.1029/2004JD005178, 2005.
- Graf, H., Feichter, J., and Langmann, B.: Volcanic sulfur emissions: Estimates of source strength and its contribution to the global sulfate distribution, *J. Geophys. Res.*, 102, PP. 10,727–10,738, doi:199710.1029/96JD03265, 1997.
- Grainger, J. F. and Ring, J.: Anomalous Fraunhofer Line Profiles, Published online: 24 February 1962; | doi:10.1038/193762a0, 193, 762–762, doi:10.1038/193762a0, 1962.
- Greenblatt, G. D., Orlando, J. J., Burkholder, J. B., and Ravishankara, A. R.: Absorption Measurements of Oxygen Between 330 and 1140 nm, *J. Geophys. Res.*, 95, PP. 18,577–18,582, doi:199010.1029/JD095iD11p18577, 1997.
- Grutter, M., Basaldud, R., Rivera, C., Harig, R., Junkerman, W., Caetano, E., and Delgado-Granados, H.: SO<sub>2</sub> emissions from Popocatepetl volcano: emission rates and plume imaging using optical remote sensing techniques, *Atmos. Chem. Phys.*, 8, 6655–6663, doi:10.5194/acp-8-6655-2008, 2008.

- Gür, B., Spietz, P., Orphal, J., and Burrows, J. P.: Absorption Spectra Measurements with the GOME-2 FMs using the IUP/IFE-UBs Calibration Apparatus for Trace Gas Absorption Spectroscopy VATGAS, Final Report, University of Bremen, October 2005, 2005.
- Halmer, M., Schmincke, H.-U., and Graf, H.-F.: The annual volcanic gas input into the atmosphere, in particular into the stratosphere: a global data set for the past 100 years, *J. Volcanol. Geoth. Res.*, 115, 511–528, doi:10.1016/S0377-0273(01)00318-3, 2002.
- Herman, J. R., Bhartia, P. K., Torres, O., Hsu, C., Seftor, C., and Celarier, E.: Global distribution of UV-absorbing aerosols from Nimbus 7/TOMS data, *J. Geophys. Res.*, 102, PP. 16,911–16,922, doi:199710.1029/96JD03680, 1997.
- Heue, K.-P.: Airborne Multi AXes DOAS instrument and measurements of two dimensional trace gas distribution, Ph.D. thesis, University of Heidelberg, 2005.
- Heue, K.-P., Brenninkmeijer, C. A. M., Wagner, T., Mies, K., Dix, B., Frieß, U., Martinsson, B. G., Slemr, F., and van Velthoven, P. F. J.: Observations of the 2008 Kasatochi volcanic SO<sub>2</sub> plume by CARIBIC aircraft DOAS and the GOME-2 satellite, *Atmos. Chem. Phys.*, 10, 4699–4713, doi:10.5194/acp-10-4699-2010, 2010.
- Heue, K.-P., Brenninkmeijer, C. A. M., Baker, A. K., Rauthe-Schöch, A., Walter, D., Wagner, T., Hörmann, C., Sihler, H., Dix, B., Frieß U., Platt, U., Martinsson, B. G., van Velthoven, P. F. J., Zahn, A., and Ebinghaus, R.: SO<sub>2</sub> and BrO observation in the plume of the Eyjafjallajökull volcano 2010: CARIBIC and GOME-2 retrievals, *Atmos. Chem. Phys.*, 11, 2973–2989, doi:10.5194/acp-11-2973-2011, 2011.
- Hoff, R. M.: Differential SO<sub>2</sub> column measurements of the Mt. Pinatubo volcanic plume, *Geophys. Res. Lett.*, 19, P. 175, doi:199210.1029/91GL02793, 1992.
- Holasek, R. E., Self, S., and Woods, A. W.: Satellite observations and interpretation of the 1991 Mount Pinatubo eruption plumes, *J. Geophys. Res.*, 101, 27 635–27,655, doi:10.1029/96JB01179, 1996.
- Hörmann, C., Sihler, H., Bobrowski, N., Beirle, S., Penning de Vries, M., Platt, U., and Wagner, T.: Systematic investigation of bromine monoxide in volcanic plumes from space by using the GOME-2 instrument, *Atmos. Chem. Phys. Dis.*, 12, 29 325–29 389, doi:10.5194/acpd-12-29325-2012, 2012.
- Horrocks, L., Burton, M., Francis, P., and Oppenheimer, C.: Stable gas plume composition measured by OP-FTIR spectroscopy at Masaya Volcano, Nicaragua, 1998–1999, *Geophys. Res. Lett.*, 26, P. 3497, doi:199910.1029/1999GL008383, 1999.
- Johansson, M., Galle, B., Zhang, Y., Rivera, C., Chen, D., and Wyser, K.: The dual-beam mini-DOAS technique - measurements of volcanic gas emission, plume height and plume speed with a single instrument, *B. Volcanol.*, 71, doi:10.1007/s00445-008-0260-8, 2009.

- Karagulian, F., Clarisse, L., Clerbaux, C., Prata, A. J., Hurtmans, D., and Coheur, P. F.: Detection of volcanic SO<sub>2</sub>, ash, and H<sub>2</sub>SO<sub>4</sub> using the Infrared Atmospheric Sounding Interferometer (IASI), *J. Geophys. Res.*, 115, D00L02, doi:10.1029/2009JD012786, 2010.
- Keene, W. C., Khalil, M. A. K., Iii, D. J. E., McCulloch, A., Graedel, T. E., Lobert, J. M., Aucott, M. L., Gong, S. L., Harper, D. B., Kleiman, G., Midgley, P., Moore, R. M., Seuzaret, C., Sturges, W. T., Benkovitz, C. M., Koropalov, V., Barrie, L. A., and Li, Y. F.: Composite global emissions of reactive chlorine from anthropogenic and natural sources: Reactive Chlorine Emissions Inventory, *J. Geophys. Res.*, 104, 8429–8440, doi:10.1029/1998JD100084, 1999.
- Kelly, P. J., Kern, C., Roberts, T. J., Lopez, T., Werner, C., and Aiuppa, A.: Rapid chemical evolution of tropospheric volcanic emissions from Redoubt Volcano, Alaska, based on observations of ozone and halogen-containing gases, *J. Volcanol. Geoth. Res.*, doi:10.1016/j.jvolgeores.2012.04.023, 2012.
- Kerminen, V.-M., Niemi, J. V., Timonen, H., Aurela, M., Frey, A., Carbone, S., Saarikoski, S., Teinilä, K., Hakkarainen, J., Tamminen, J., Vira, J., Prank, M., Sofiev, M., and Hillamo, R.: Characterization of a volcanic ash episode in southern Finland caused by the Grimsvötn eruption in Iceland in May 2011, *Atmos. Chem. Phys.*, 11, 12 227–12 239, doi:10.5194/acp-11-12227-2011, 2011.
- Kern, C.: Spectroscopic measurements of volcanic gas emissions in the ultra-violet wavelength region, Ph.D. thesis, Combined Faculties for the Natural Sciences and for Mathematics, University of Heidelberg, 2009.
- Kern, C.: Comment on: *Enhancement of the volcanogenic "bromine explosion" via reactive nitrogen chemistry (Kilauea volcano, Hawaii)* by G. G. Salerno et al., *Atmos. Chem. Phys. Discuss.*, 10, C2767–C2778, doi:10.5194/acpd-10-10313-2010, available online at <http://www.atmos-chem-phys-discuss.net/10/C2766/2010/acpd-10-C2766-2010.pdf>, 2010.
- Kern, C., Vogel, L., Rivera, C., Herrera, M., Platt, U., and Sihler, H.: Halogen oxide measurements at Masaya Volcano, Nicaragua using active long path differential optical absorption spectroscopy, *B. Volcanol.*, 71, 659–670, doi:10.1007/s00445-008-0252-8, 2008.
- Kern, C., Deutschmann, T., Vogel, L., Wöhrbach, M., Wagner, T., and Platt, U.: Radiative transfer corrections for accurate spectroscopic measurements of volcanic gas emissions, *B. Volcanol.*, 72, doi:10.1007/s00445-009-0313-7, 2010.
- Kern, C., Deutschmann, T., Werner, C. A., Sutton, A. J., Elias, T., and Kelly, P.: Improving the accuracy of SO<sub>2</sub> column densities and emission rates obtained from upward-looking UV-spectroscopic measurements of volcanic plumes by taking realistic radiative transfer into account, *J. Geophys. Res.*, doi:10.1029/2012JD017936, 2012.

- Khokhar, M. F., Platt, U., and Wagner, T.: Temporal trends of anthropogenic SO<sub>2</sub> emitted by non-ferrous metal smelters in Peru and Russia estimated from Satellite observations, *Atmos. Chem. Phys. Dis.*, 8, 17 393–17 422, doi:10.5194/acpd-8-17393-2008, 2008.
- Khokhar, M. F. A.: Retrieval and interpretation of tropospheric SO<sub>2</sub> from UV-vis satellite instruments, Ph.D. thesis, University of Leipzig, 2006.
- Kious, W. J., Kious, J. W., Tilling, R. I., and S.), G. S. U.: *This Dynamic Earth: The Story of Plate Tectonics*, New York University Press, 1996.
- Kodera, K.: Influence of volcanic eruptions on the troposphere through stratospheric dynamical processes in the northern hemisphere winter, *J. Geophys. Res.*, 99, 1273–1282, doi:10.1029/93JD02731, 1994.
- Kraus, S.: DOASIS: DOAS Intelligent System, University of Heidelberg, Heidelberg, copyright 2004 Stefan Kraus, in cooperation with Hoffmann Messtechnik GmbH, 2004.
- Kromminga, H., Orphal, J., Spietz, P., Voigt, S., and Burrows, J.: New measurements of OClO absorption cross-sections in the 325–435 nm region and their temperature dependence between 213 and 293 K, *J. Photoch. Photobio. A*, 157, 149–160, doi:10.1016/S1010-6030(03)00071-6, 2003.
- Krotkov, N., Carn, S., Krueger, A., Bhartia, P., and Yang, K.: Band residual difference algorithm for retrieval of SO<sub>2</sub> from the aura ozone monitoring instrument (OMI), *IEEE T. Geosci. Remote*, 44, 1259 – 1266, doi:10.1109/TGRS.2005.861932, 2006.
- Krueger, K., Kutterolf, S., Hansteen, T. H., Appel, K., Freundt, A., Peréz, W., and Wehrmann, H.: The combined bromine and chlorine release from large volcanic eruptions: A threat to stratospheric ozone, in: *Poster at AGU Chapman Conference on Volcanism and the Atmosphere*, 10–15 June 2012, Selfoss, Iceland, 2012.
- Kühl, S., Wilms-Grabe, W., Frankenberg, C., Grzegorski, M., Platt, U., and Wagner, T.: Comparison of OClO nadir measurements from SCIAMACHY and GOME, *Adv. Space Res.*, 37, 2247–2253, doi:10.1016/j.asr.2005.06.061, 2006.
- Kurosu, T. P., Change, K., and Volkamer, R.: Measurements of Tropospheric BrO, HCHO and CHO–CHO from the Ozone Monitoring Instrument on EOS Aura, in: *Oral presentation at the ATMOS conference 2006*, 8–12 May 2006, Frascati, Italy, available online at [http://earth.esa.int/workshops/atmos2006/participants/254/pres\\_254\\_kurosu.pdf](http://earth.esa.int/workshops/atmos2006/participants/254/pres_254_kurosu.pdf), 2006.
- Kurucz, R. L., Furenlid, I., Brault, J., and Testerman, L.: *Solar flux atlas from 296 to 1300 nm*, National Solar Observatory Atlas, Sunspot, New Mexico: National Solar Observatory, 1984, 1984.
- Lambert, G., Le Cloarec, M.-F., and Pennisi, M.: Volcanic output of SO<sub>2</sub> and trace metals: A new approach, *Geochim. Cosmochim. Ac.*, 52, 39–42, doi:10.1016/0016-7037(88)90054-3, 1988.

- Le Guern, F.: Les débits de CO<sub>2</sub> et de SO<sub>2</sub> volcaniques dans l'atmosphère, *Bulletin Volcanologique*, 45, 197–202, doi:10.1007/BF02597730, 1982.
- Lee, C., Kim, Y. J., Tanimoto, H., Bobrowski, N., Platt, U., Mori, T., Yamamoto, K., and Hong, C. S.: High ClO and ozone depletion observed in the plume of Sakurajima volcano, Japan, *Geophys. Res. Lett.*, 32, L21 809, doi:10.1029/2005GL023785, 2005.
- Lee, C., Kim, Y. J., Lee, H., and Choi, B. C.: MAX-DOAS Measurements of ClO, SO<sub>2</sub> and NO<sub>2</sub> in the Mid-Latitude Coastal Boundary Layer and a Power Plant Plume, in: *Advanced Environmental Monitoring*, edited by Kim, Y. J. and Platt, U., pp. 37–49, Springer Netherlands, Dordrecht, 2008.
- Lee, C., Martin, R. V., Donkelaar, A. v., O'Byrne, G., Krotkov, N., Richter, A., Huey, L. G., and Holloway, J. S.: Retrieval of vertical columns of sulfur dioxide from SCIAMACHY and OMI: Air mass factor algorithm development, validation, and error analysis, *J. Geophys. Res.*, 114, D22 303, doi:10.1029/2009JD012123, 2009.
- Lee, C., Martin, R. V., van Donkelaar, A., Lee, H., Dickerson, R. R., Hains, J. C., Krotkov, N., Richter, A., Vinnikov, K., and Schwab, J. J.: SO<sub>2</sub> emissions and lifetimes: Estimates from inverse modeling using in situ and global, space-based (SCIAMACHY and OMI) observations, *J. Geophys. Res.*, 116, D063 404, doi:10.1029/2010JD014758, 2011.
- Levelt, P., van den Oord, G., Dobber, M., Mälkki, A., Visser, H., Vries, J. d., Stammes, P., Lundell, J., and Saari, H.: The ozone monitoring instrument, *IEEE T. Geosci. Remote*, 44, 1093 – 1101, doi:10.1109/TGRS.2006.872333, 2006.
- Levin, B. W., Rybin, A. V., Vasilenko, N. F., Prytkov, A. S., Chibisova, M. V., Kogan, M. G., Steblov, G. M., and Frolov, D. I.: Monitoring of the eruption of the Sarychev Peak Volcano in Matua Island in 2009 (central Kurile islands), *Dokl. Earth Sci.*, 435, 1507–1510, doi:10.1134/S1028334X10110218, 2010.
- Li, C., Zhang, Q., Krotkov, N. A., Streets, D. G., He, K., Tsay, S.-C., and Gleason, J. F.: Recent large reduction in sulfur dioxide emissions from Chinese power plants observed by the Ozone Monitoring Instrument, *Geophys. Res. Lett.*, 37, L08 807, doi:10.1029/2010GL042594, 2010.
- Louban, I., Bobrowski, N., Rouwet, D., Inguaggiato, S., and Platt, U.: Imaging DOAS for volcanological applications, *B. Volcanol.*, 71, 753–765, doi:10.1007/s00445-008-0262-6, 2009.
- Martin, R., Watt, S., Pyle, D., Mather, T., Matthews, N., Georg, R., Day, J., Fairhead, T., Witt, M., and Quayle, B.: Environmental effects of ashfall in Argentina from the 2008 Chaitén volcanic eruption, *J. Volcanol. Geoth. Res.*, 184, 462–472, doi:10.1016/j.jvolgeores.2009.04.010, 2009.
- Martin-Del Pozzo, A. L.: Precursors to eruptions of Popocatépetl Volcano, México, *Geofis. Int.*, 51, 87–107, 2012.

- Martínez-Alonso, S., Deeter, M. N., Worden, H. M., Clerbaux, C., Mao, D., and Gille, J. C.: First satellite identification of volcanic carbon monoxide, *Geophys. Res. Lett.*, 39, L21 809, doi:10.1029/2012GL053275, 2012.
- McConnell, J. C., Henderson, G. S., Barrie, L., Bottenheim, J., Niki, H., Langford, C. H., and Templeton, E. M. J.: Photochemical bromine production implicated in Arctic boundary-layer ozone depletion, *Nature*, 355, 150–152, doi:10.1038/355150a0, 1992.
- McCormick, M. P., Thomason, L. W., and Trepte, C. R.: Atmospheric effects of the Mt Pinatubo eruption, *Nature*, Published online: 02 February 1995; | doi:10.1038/373399a0, 373, 399–404, doi:10.1038/373399a0, 1995.
- McGonigle, A. J. S. and Oppenheimer, C.: Optical sensing of volcanic gas and aerosol emissions, Geological Society, London, Special Publications, 213, 149–168, doi:10.1144/GSL.SP.2003.213.01.09, 2003.
- McGonigle, A. J. S., Oppenheimer, C., Galle, B., Mather, T. A., and Pyle, D. M.: Walking traverse and scanning DOAS measurements of volcanic gas emission rates, *Geophys. Res. Lett.*, 29, 1985, doi:10.1029/2002GL015827, 2002.
- McGonigle, A. J. S., Aiuppa, A., Giudice, G., Tamburello, G., Hodson, A. J., and Gurrieri, S.: Unmanned aerial vehicle measurements of volcanic carbon dioxide fluxes, *Geophys. Res. Lett.*, 35, 4 PP., doi:200810.1029/2007GL032508, 2008.
- Meller, R. and Moortgat, G. K.: Temperature dependence of the absorption cross sections of formaldehyde between 223 and 323 K in the wavelength range 225–375 nm, *J. Geophys. Res.*, 105, 7089–7101, doi:10.1029/1999JD901074, 2000.
- Mie, G.: Beiträge zur Optik trüber Medien, speziell kolloidaler Metallösungen, *Ann. Phys.–Berlin*, 330, 377–445, doi:10.1002/andp.19083300302, 1908.
- Millán, M.: Remote sensing of air pollutants. A study of some atmospheric scattering effects, *Atmos. Environ.* (1967), 14, 1241–1253, doi:10.1016/0004-6981(80)90226-7, 1980.
- Mori, T. and Notsu, K.: Remote CO, COS, CO<sub>2</sub>, SO<sub>2</sub>, HCl detection and temperature estimation of volcanic gas, *Geophys. Res. Lett.*, 24, P. 2047, doi:199710.1029/97GL52058, 1997.
- Mori, T., Hirabayashi, J., Kazahaya, K., Mori, T., Ohwasa, M., Miyashita, M., Iino, H., and Nakahori, Y.: Compact Ultraviolet Spectrometer System for monitoring volcanic SO<sub>2</sub> emission: validation and preliminary observation, *Bull. Volcanol. Soc. Japan*, 52, 105–112, 2007.
- Munro, R., Eisinger, M., Anderson, C., Callies, J., Carpaccioli, E., Lang, R., Lefevre, A., Livschitz, Y., and Albinana, A. P.: GOME-2 on MetOp, The 2006 EUMETSAT Meteorological Satellite Conference, Helsinki, Finland, 2006.

- Neal, C. A., McGimsey, R. G., Dixon, J. P., Cameron, C. E., Nuzhaev, A. A., and Chibisova, M.: 2008 Volcanic activity in Alaska, Kamchatka, and the Kurile Islands: Summary of events and response of the Alaska Volcano Observatory: U.S. Geological Survey Scientific Investigations Report 2010-5243, URL <http://pubs.usgs.gov/sir/2010/5243>, last access on 12 September 2012, 2011.
- Nguyen, H. N., Gudmundsson, A., and Martinsson, B. G.: Design and Calibration of a Multi-Channel Aerosol Sampler for Tropopause Region Studies from the CARIBIC Platform, *Aerosol Sci. Tech.*, 40, 649–655, doi:10.1080/02786820600767807, 2006.
- Nowlan, C. R., Liu, X., Chance, K., Cai, Z., Kurosu, T. P., Lee, C., and Martin, R. V.: Retrievals of sulfur dioxide from the Global Ozone Monitoring Experiment 2 (GOME-2) using an optimal estimation approach: Algorithm and initial validation, *J. Geophys. Res.*, 116, D18 301, doi:10.1029/2011JD015808, 2011.
- Oppenheimer, C.: Climatic, environmental and human consequences of the largest known historic eruption: Tambora volcano (Indonesia) 1815, *Prog. Phys. Geog.*, 27, 230–259, doi:10.1191/0309133303pp379ra, 2003.
- Oppenheimer, C., Francis, P., Burton, M., Maciejewski, A., and Boardman, L.: Remote measurement of volcanic gases by Fourier transform infrared spectroscopy, *Appl. Phys. B - Lasers O.*, 67, 505–515, doi:10.1007/s003400050536, 1998.
- Oppenheimer, C., Pyle, D. M., and Barclay, D. J.: *Volcanic Degassing: Special Publication*, Geological Society, 2003.
- Oppenheimer, C., Tsanev, V., Braban, C., Cox, R., Adams, J., Aiuppa, A., Bobrowski, N., Delmelle, P., Barclay, J., and Mcgonigle, A.: BrO formation in volcanic plumes, *Geochim. Cosmochim. Ac.*, 70, 2935–2941, doi:10.1016/j.gca.2006.04.001, 2006.
- Oppenheimer, C., Kyle, P., Eisele, F., Crawford, J., Huey, G., Tanner, D., Kim, S., Mauldin, L., Blake, D., Beyersdorf, A., Buhr, M., and Davis, D.: Atmospheric chemistry of an Antarctic volcanic plume, *J. Geophys. Res.*, 115, 15 PP., doi:201010.1029/2009JD011910, 2010.
- Palmer, P. I., Jacob, D. J., Chance, K., Martin, R. V., Spurr, R. J. D., Kurosu, T. P., Bey, I., Yantosca, R., Fiore, A., and Li, Q.: Air mass factor formulation for spectroscopic measurements from satellites: Application to formaldehyde retrievals from the Global Ozone Monitoring Experiment, *J. Geophys. Res.*, 106, 14 539–14,550, doi:10.1029/2000JD900772, 2001.
- Penning de Vries, M. and Wagner, T.: Modelled and measured effects of clouds on UV Aerosol Indices on a local, regional, and global scale, *Atmos. Chem. Phys.*, 11, 12 715–12 735, doi:10.5194/acp-11-12715-2011, 2011.
- Penning de Vries, M. J. M., Beirle, S., and Wagner, T.: UV Aerosol Indices from SCIAMACHY: introducing the SCattering Index (SCI), *Atmos. Chem. Phys.*, 9, 9555–9567, doi:10.5194/acp-9-9555-2009, 2009.

- Perlwitz, J. and Graf, H.-F.: The Statistical Connection between Tropospheric and Stratospheric Circulation of the Northern Hemisphere in Winter, *J. Climate*, 8, 2281–2295, doi:10.1175/1520-0442(1995)008<2281:TSCBTA>2.0.CO;2, 1995.
- Perner, D., Ehhalt, D. H., Pätz, H. W., Platt, U., Röth, E. P., and Volz, A.: OH Radicals in the lower troposphere, *Geophys. Res. Lett.*, 3, 466–468, doi:10.1029/GL003i008p00466, 1976.
- Pieri, D. and Abrams, M.: ASTER watches the world’s volcanoes: a new paradigm for volcanological observations from orbit, *J. Volcanol. Geoth. Res.*, 135, 13–28, doi:10.1016/j.jvolgeores.2003.12.018, 2004.
- Platt, U. and Lehrer, E.: Arctic Tropospheric Ozone Chemistry, ARCTOC, Final Report of the EU-Project No. EV5V-CT93-0318, Heidelberg, 1996.
- Platt, U. and Stutz, J.: *Differential Optical Absorption Spectroscopy: Principles And Applications*, Springer, 2008.
- Platt, U., Perner, D., and Pätz, H. W.: Simultaneous measurement of atmospheric CH<sub>2</sub>O, O<sub>3</sub>, and NO<sub>2</sub> by differential optical absorption, *J. Geophys. Res.*, 84, 6329–6335, doi:10.1029/JC084iC10p06329, 1979.
- Pollack, J. B., Toon, O. B., Sagan, C., Summers, A., Baldwin, B., and Camp, W. V.: Volcanic explosions and climatic change: A theoretical assessment, *J. Geophys. Res.*, 81, 1071–1083, doi:10.1029/JC081i006p01071, 1976.
- Prata, A. J.: Infrared radiative transfer calculations for volcanic ash clouds, *Geophys. Res. Lett.*, 16, 1293–1296, doi:10.1029/GL016i011p01293, 1989.
- Prata, A. J. and Bernardo, C.: Retrieval of volcanic SO<sub>2</sub> column abundance from Atmospheric Infrared Sounder data, *J. Geophys. Res.*, 112, D20 204, doi:10.1029/2006JD007955, 2007.
- Prata, A. J. and Prata, A. T.: Eyjafjallajökull volcanic ash concentrations determined using Spin Enhanced Visible and Infrared Imager measurements, *J. Geophys. Res.*, 117, D00U23, doi:10.1029/2011JD016800, 2012.
- Prata, A. J., Rose, W. I., Self, S., and O’Brien, D. M.: Global, long-term sulphur dioxide measurements from TOVS data: A new tool for studying explosive volcanism and climate, *Geoph. Monog. Series*, 139, 75–92, doi:10.1029/139GM05, 2003.
- Prata, A. J., Carn, S. A., Stohl, A., and Kerkmann, J.: Long range transport and fate of a stratospheric volcanic cloud from Soufrière Hills volcano, Montserrat, *Atmos. Chem. Phys.*, 7, 5093–5103, doi:10.5194/acp-7-5093-2007, 2007.
- Puķite, J., Kūhl, S., Deutschmann, T., Platt, U., and Wagner, T.: Extending differential optical absorption spectroscopy for limb measurements in the UV, *Atmos. Meas. Tech.*, 3, 631–653, doi:10.5194/amt-3-631-2010, 2010.

- Pugnaghi, S., Gangale, G., Corradini, S., and Buongiorno, M.: Mt. Etna sulfur dioxide flux monitoring using ASTER-TIR data and atmospheric observations, *J. Volcanol. Geoth. Res.*, 152, 74–90, doi:10.1016/j.jvolgeores.2005.10.004, 2006.
- Punongbayan, R. S. and Newhall, C. G.: Early warning for the 1991 eruptions of Pinatubo volcano - a success story, available online at: <http://cidbimena.desastres.hn/pdf/eng/doc15271/doc15271.htm>, 1999.
- Pyle, D. and Mather, T.: Halogens in igneous processes and their fluxes to the atmosphere and oceans from volcanic activity: A review, *Chem. Geol.*, 263, 110–121, doi:10.1016/j.chemgeo.2008.11.013, 2009.
- Pyle, D. M. and Mather, T. A.: The regional influence of volcanic emissions from Popocatepétl, Mexico: Discussion of "Measurement of aerosol particles, gases and flux radiation in the Pico de Orizaba National Park, and its relationship to air pollution transport", Márquez et al., 2005, *Atmos. Environ.*, 39, 3877–3890, *Atmos. Environ.*, 39, 6475–6478, doi:10.1016/j.atmosenv.2005.07.022, 2005.
- Rampino, M. R. and Self, S.: Historic eruptions of Tambora (1815), Krakatau (1883), and Agung (1963), their stratospheric aerosols, and climatic impact, *Quaternary Res.*, 18, 127–143, doi:10.1016/0033-5894(82)90065-5, 1982.
- Ramsey, M. S., Realmuto, V. J., Hulley, G. C., and Hook, S. J.: HypsIRI Thermal Infrared (TIR) Band Study Report, NASA Jet Propulsion Laboratory, California Institute of Technology, Pasadena, California, available online at: [http://hyspiri.jpl.nasa.gov/downloads/reports\\_whitepapers/HyspIRI\\_TIR\\_Band\\_Report\\_gchv1\\_VJRv1\\_pmbv1\\_MSrv2\\_1.pdf](http://hyspiri.jpl.nasa.gov/downloads/reports_whitepapers/HyspIRI_TIR_Band_Report_gchv1_VJRv1_pmbv1_MSrv2_1.pdf), 2012.
- Read, W. G., Froidevaux, L., and Waters, J. W.: Microwave limb sounder measurement of stratospheric SO<sub>2</sub> from the Mt. Pinatubo Volcano, *Geophys. Res. Lett.*, 20, 1299–1302, doi:10.1029/93GL00831, 1993.
- Realmuto, V. J., Abrams, M. J., Buongiorno, M. F., and Pieri, D. C.: The use of multispectral thermal infrared image data to estimate the sulfur dioxide flux from volcanoes: A case study from Mount Etna, Sicily, July 29, 1986, *J. Geophys. Res.*, 99, 481–488, doi:10.1029/93JB02062, 1994.
- Richter, A.: Algorithm Theoretical Basis Document for the GOME-2 Rapid Volcanic SO<sub>2</sub> product, first draft, October 2009, URL [http://www.doas-bremen.de/so2\\_alerts/gome2\\_so2\\_atbd\\_091005.pdf](http://www.doas-bremen.de/so2_alerts/gome2_so2_atbd_091005.pdf), last access on 12 September 2012, 2009.
- Richter, A. and Burrows, J.: Tropospheric NO<sub>2</sub> from GOME measurements, *Adv. Space Res.*, 29, 1673–1683, doi:10.1016/S0273-1177(02)00100-X, 2002.
- Richter, A. and Wagner, T.: The Use of UV, Visible and Near IR Solar Back Scattered Radiation to Determine Trace Gases, in: *The Remote Sensing of Tropospheric Composition from Space*, edited by Burrows, J. P., Borrell, P., Platt, U., Guzzi, R., Platt, U., and Lanzerotti, L. J., *Physics of Earth and Space Environments*, pp. 67–121, Springer Berlin Heidelberg, 2011.

- Richter, A., Wittrock, F., Ladstätter-Weissenmayer, A., and Burrows, J.: GOME measurements of stratospheric and tropospheric BrO, *Adv. Space Res.*, 29, 1667–1672, doi:10.1016/S0273-1177(02)00123-0, 2002.
- Richter, A., Wittrock, F., and Burrows, J. P.: SO<sub>2</sub> measurements with SCIAMACHY, available online at: [http://earth.esa.int/workshops/atmos2006/participants/804/paper\\_richter\\_esa\\_06.pdf](http://earth.esa.int/workshops/atmos2006/participants/804/paper_richter_esa_06.pdf), 2006.
- Richter, A., Wittrock, F., Schönhardt, A., and Burrows, J.: Quantifying volcanic SO<sub>2</sub> emissions using GOME-2 measurements, Poster at the EGU General Assembly 2009, 7679, XY247, URL [http://www.iup.uni-bremen.de/doas/posters/egu\\_2009\\_richter.pdf](http://www.iup.uni-bremen.de/doas/posters/egu_2009_richter.pdf), last access on 12 September 2012, 2009.
- Rivera, C., Sosa, G., Wöhrnschimmel, H., de Foy, B., Johansson, M., and Galle, B.: Tula industrial complex (Mexico) emissions of SO<sub>2</sub> and NO<sub>2</sub> during the MCMA 2006 field campaign using a mobile mini-DOAS system, *Atmos. Chem. Phys.*, 9, 6351–6361, doi:10.5194/acp-9-6351-2009, 2009.
- Rix, M., Valks, P., Hao, N., Loyola, D., Schlager, H., Huntrieser, H., Flemming, J., Koehler, U., Schumann, U., and Inness, A.: Volcanic SO<sub>2</sub>, BrO and plume height estimations using GOME-2 satellite measurements during the eruption of Eyjafjallajökull in May 2010, *J. Geophys. Res.*, 117, doi:10.1029/2011JD016718, 2012.
- Robock, A.: Volcanic eruptions and climate, *Rev. Geophys.*, 38, 191–219, doi:10.1029/1998RG000054, 2000.
- Rolph, G. D.: Real-time Environmental Applications and Display sYstem (READY) Website, URL <http://ready.arl.noaa.gov>, last access on 12 September 2012, 2012.
- SACS: Support to Aviation Control Service, URL <http://sacs.aeronomie.be>, last access on 12 September 2012, 2012.
- Salerno, G. G., Oppenheimer, C., Tsanev, V. I., Sutton, A. J., Roberts, T. J., and Elias, T.: Enhancement of the volcanogenic "bromine explosio" via reactive nitrogen chemistry (Kilauea volcano, Hawaii), *Atmos. Chem. Phys. Dis.*, 10, 10 313–10 334, doi:10.5194/acpd-10-10313-2010, 2010.
- Schäfer, R. and Metzger, B.: Was macht eigentlich das Waldsterben?, in: *Umweltgeschichte und Umweltzukunft - Zur gesellschaftlichen Relevanz einer jungen Disziplin*, pp. 201 – 228, Masius, P. and Sparenberg, O. and Sprenger, J., Universitätsverlag Göttingen, 2009.
- Schmincke, H.-U.: *Volcanism*, 1st ed. 2004. Corr. 2nd printing, 324 p., ISBN 978-3-540-43650-8, Springer, 2005.
- Schuck, T. J., Brenninkmeijer, C. A. M., Slemr, F., Xueref-Remy, I., and Zahn, A.: Greenhouse gas analysis of air samples collected onboard the CARIBIC passenger aircraft, *Atmos. Meas. Tech.*, 2, 449–464, doi:10.5194/amt-2-449-2009, 2009.

- Schumann, U., Weinzierl, B., Reitebuch, O., Schlager, H., Minikin, A., Forster, C., Baumann, R., Sailer, T., Graf, K., Mannstein, H., Voigt, C., Rahm, S., Simmet, R., Scheibe, M., Lichtenstern, M., Stock, P., Rüba, H., Schäuble, D., Tafferner, A., Rautenhaus, M., Gerz, T., Ziereis, H., Krautstrunk, M., Mallaun, C., Gayet, J.-F., Lieke, K., Kandler, K., Ebert, M., Weinbruch, S., Stohl, A., Gasteiger, J., Groß S., Freudenthaler, V., Wiegner, M., Ansmann, A., Tesche, M., Olafsson, H., and Sturm, K.: Airborne observations of the Eyjafjalla volcano ash cloud over Europe during air space closure in April and May 2010, *Atmos. Chem. Phys.*, 11, 2245–2279, doi:10.5194/acp-11-2245-2011, 2011.
- Seinfeld, J. H. and Pandis, S. N.: *Atmospheric Chemistry and Physics: From Air Pollution to Climate Change*, Wiley-Interscience, 1 edn., 1997.
- Seitz, K., Buxmann, J., Pöhler, D., Sommer, T., Tschritter, J., Neary, T., O’Dowd, C., and Platt, U.: The spatial distribution of the reactive iodine species IO from simultaneous active and passive DOAS observations, *Atmos. Chem. Phys.*, 10, 2117–2128, doi:10.5194/acp-10-2117-2010, 2010.
- Siebert, L., Simkin, T., and Kimberly, P.: *Volcanoes of the World: Third Edition*, University of California Press, 3 edn., 2011.
- Sihler, H.: *Halogen Activation in the Polar Troposphere*, Ph.D. thesis, Combined Faculties for the Natural Sciences and for Mathematics, University of Heidelberg, 2012.
- Sihler, H., Platt, U., Beirle, S., Marbach, T., Kühl, S., Dörner, S., Verschaeve, J., Frieß, U., Pöhler, D., Vogel, L., Sander, R., and Wagner, T.: Tropospheric BrO column densities in the Arctic derived from satellite: retrieval and comparison to ground-based measurements, *Atmos. Meas. Tech.*, 5, 2779–2807, doi:10.5194/amt-5-2779-2012, 2012.
- Simarski, L. T.: *Volcanism and Climate Change: American Geophysical Union Special Report*, May 1992, outgrowth of AGU Chapman Conference on climate, volcanism and global change, Hilo, Hawaii, convened by Self, S. and Turco, R. P., 1992.
- Simpson, W. R., von Glasow, R., Riedel, K., Anderson, P., Ariya, P., Bottenheim, J., Burrows, J., Carpenter, L. J., Frieß, U., Goodsite, M. E., Heard, D., Hutterli, M., Jacobi, H., Kaleschke, L., Neff, B., Plane, J., Platt, U., Richter, A., Roscoe, H., Sander, R., Shepson, P., Sodeau, J., Steffen, A., Wagner, T., and Wolff, E.: Halogens and their role in polar boundary-layer ozone depletion, *Atmos. Chem. Phys.*, 7, 4375–4418, 2007.
- Smithsonian: *Global Volcanism Program, Smithsonian/USGS Weekly Volcanic Activity Reports 2007-2011*, URL <http://volcano.si.edu/reports/usgs/>, last access on 12 September 2012, 2007-2011.
- Solomon, S.: Stratospheric ozone depletion: A review of concepts and history, *Rev. Geophys.*, 37, 275–316, doi:10.1029/1999RG900008, 1999.

- Solomon, S., Schmeltekopf, A. L., and Sanders, R. W.: On the interpretation of zenith sky absorption measurements, *J. Geophys. Res.*, 92, 8311–8319, doi:10.1029/JD092iD07p08311, 1987.
- Stoiber, R. E. and Jepsen, A.: Sulfur Dioxide Contributions to the Atmosphere by Volcanoes, *Science*, 182, 577–578, doi:10.1126/science.182.4112.577, 1973.
- Streets, D. and Waldhoff, S.: Present and future emissions of air pollutants in China: SO<sub>2</sub>, NO<sub>x</sub>, and CO, *Atmos. Environ.*, 34, 363–374, doi:10.1016/S1352-2310(99)00167-3, 2000.
- Strutt, J. W.: On the Transmission of Light through an Atmosphere containing Small Particles in Suspension, and on the Origin of the Blue of the Sky, in: *Scientific Papers*, vol. 4 of *Cambridge Library Collection - Mathematics*, Cambridge University Press, reprinted in 2009, 1899.
- Stutz, J., Pikelnaya, O., Hurlock, S. C., Trick, S., Pechtl, S., and Glasow, R. v.: Daytime OIO in the Gulf of Maine, *Geophys. Res. Lett.*, 34, L22 816, doi:10.1029/2007GL031332, 2007.
- Symonds, R., Gerlach, T., and Reed, M.: Magmatic gas scrubbing: implications for volcano monitoring, *J. Volcanol. Geoth. Res.*, 108, 303–341, doi:10.1016/S0377-0273(00)00292-4, 2001.
- Symonds, R. B., Rose, W. I., and Reed, M. H.: Contribution of Cl- and F-bearing gases to the atmosphere by volcanoes, Published online: 04 August 1988, 334, 415–418, doi:10.1038/334415a0, 1988.
- Tazieff, H. and Sabroux, J.: Forecasting volcanic events, no. 1 in *Dev. Volcano.*, Elsevier, Amsterdam ; New York :, 1983.
- Textor, C., Graf, H., and Timmreck, C.: Emissions from volcanoes, in: *Emissions of Atmospheric Trace Compounds*, vol. 18, pp. 269 – 303, Kluwer Academic Publ., Dordrecht, editor: Granier, C.; editor: Artaxo, P.; editor: Reeves, C. E., 2004.
- Theys, N., Roozendael, M. V., Dils, B., Hendrick, F., Hao, N., and Mazière, M. D.: First satellite detection of volcanic bromine monoxide emission after the Kasatochi eruption, *Geophys. Res. Lett.*, 36, 4 PP., doi:200910.1029/2008GL036552, 2009.
- Theys, N., Van Roozendael, M., Hendrick, F., Yang, X., De Smedt, I., Richter, A., Begoin, M., Errera, Q., Johnston, P. V., Kreher, K., and De Mazière, M.: Global observations of tropospheric BrO columns using GOME-2 satellite data, *Atmos. Chem. Phys.*, 11, 1791–1811, 2011.
- Thomas, H. E. and Prata, A. J.: Sulphur dioxide as a volcanic ash proxy during the April–May 2010 eruption of Eyjafjallajökull Volcano, Iceland, *Atmos. Chem. Phys.*, 11, 6871–6880, doi:10.5194/acp-11-6871-2011, 2011.

- Thomas, H. E. and Watson, I. M.: Observations of volcanic emissions from space: current and future perspectives, *Nat. Hazards*, 54, 323–354, doi:10.1007/s11069-009-9471-3, 2009.
- Thompson, D. W. J. and Wallace, J. M.: The Arctic oscillation signature in the wintertime geopotential height and temperature fields, *Geophys. Res. Lett.*, 25, 1297–1300, doi:10.1029/98GL00950, 1998.
- Thordarson, T. and Self, S.: Atmospheric and environmental effects of the 1783–1784 Laki eruption: A review and reassessment, *J. Geophys. Res.*, 108, 4011, doi:10.1029/2001JD002042, 2003.
- Tilling, R. I.: Eruptions of Mount St. Helens: past, present, and future, Dept. of the Interior, U.S. Geological Survey, 1984.
- Tilling, R. I. and Lipman, P. W.: Lessons in reducing volcano risk, *Nature*, Published online: 22 July 1993, 364, 277–280, doi:10.1038/364277a0, 1993.
- Torres, O., Bhartia, P. K., Herman, J. R., Ahmad, Z., and Gleason, J.: Derivation of aerosol properties from satellite measurements of backscattered ultraviolet radiation: Theoretical basis, *J. Geophys. Res.*, 103, PP. 17,099–17,110, doi:199810.1029/98JD00900, 1998.
- Twomey, S.: The Influence of Pollution on the Shortwave Albedo of Clouds, *J. Atmos. Sci.*, 34, 1149–1152, doi:10.1175/1520-0469(1977)034(1149:TIOPOT)2.0.CO;2, 1977.
- Urai, M.: Sulfur dioxide flux estimation at Oyama volcano in Miyake-Jima, Japan, using advanced spaceborne thermal emission and reflection radiometer (ASTER), pp. 14–19, doi:10.1117/12.455102, URL <http://dx.doi.org/10.1117/12.455102>, 2002.
- USGS: United States Geological Survey (USGS) website, URL <http://www.usgs.gov>, last access on 12 September 2012, 2012.
- van Hoek, M.: Possibilities to avoid row anomaly rows, Koninklijk Nederlands Meteorologisch Instituut, KNMI, De Bilt, available online at: [http://www.knmi.com/bibliotheek/knmipubDIV/TN-OMIE/tnomieknmi963\\_possibilities\\_to\\_avoid\\_row\\_anomaly\\_rows.pdf](http://www.knmi.com/bibliotheek/knmipubDIV/TN-OMIE/tnomieknmi963_possibilities_to_avoid_row_anomaly_rows.pdf), 2010.
- Van Roozendael, M., Loyola, D., Spurr, R., Balis, D., Lambert, J.-C., Livschitz, Y., Valks, P., Ruppert, T., Kenter, P., Fayt, C., and Zehner, C.: Ten years of GOME/ERS-2 total ozone data—The new GOME data processor (GDP) version 4: 1. Algorithm description, *J. Geophys. Res.*, 111, 21 PP., doi:200610.1029/2005JD006375, 2006a.
- Van Roozendael, M., Theys, N., and De Smedt, I.: SCIAMACHY BrO total column Product Specification Document, rev. 1, 30 January 2006, URL [http://bro.aeronomie.be/Documents/BIRA\\_SCIA\\_BrO\\_PSD\\_v1r1.pdf](http://bro.aeronomie.be/Documents/BIRA_SCIA_BrO_PSD_v1r1.pdf), the data is freely

available at <http://bro.aeronomie.be/level2.php>, last access on 12 September 2012, 2006b.

- Vandaele, A., Hermans, C., Simon, P., Carleer, M., Colin, R., Fally, S., Mérienne, M., Jenouvrier, A., and Coquart, B.: Measurements of the NO<sub>2</sub> absorption cross-section from 42 000 cm<sup>-1</sup> to 10 000 cm<sup>-1</sup> (238–1000 nm) at 220 K and 294 K, *J. Quant. Spectrosc. Ra.*, 59, 171–184, doi:10.1016/S0022-4073(97)00168-4, 1998.
- Vandaele, A. C., Hermans, C., Fally, S., Carleer, M., Colin, R., Mérienne, M., Jenouvrier, A., and Coquart, B.: High-resolution Fourier transform measurement of the NO<sub>2</sub> visible and near-infrared absorption cross sections: Temperature and pressure effects, *J. Geophys. Res.*, 107, 12 PP., doi:200210.1029/2001JD000971, 2002.
- Villasenor, R., Magdaleno, M., Quintanar, A., Gallardo, J., López, M., Jurado, R., Miranda, A., Aguilar, M., Melgarejo, L., Palmerín, E., Vallejo, C., and Barchet, W.: An air quality emission inventory of offshore operations for the exploration and production of petroleum by the Mexican oil industry, *Atmos. Environ.*, 37, 3713–3729, doi:10.1016/S1352-2310(03)00445-X, 2003.
- Vogel, L.: Volcanic plumes: Evaluation of spectroscopic measurements, early detection, and bromine chemistry, Ph.D. thesis, Combined Faculties for the Natural Sciences and for Mathematics, University of Heidelberg, 2012.
- Vogel, L., Galle, B., Kern, C., Delgado Granados, H., Conde, V., Norman, P., Arelano, S., Landgren, O., Lübcke, P., Alvarez Nieves, J. M., Cárdenas Gonzáles, L., and Platt, U.: Early in-flight detection of SO<sub>2</sub> via Differential Optical Absorption Spectroscopy: a feasible aviation safety measure to prevent potential encounters with volcanic plumes, *Atmos. Meas. Tech.*, 4, 1785–1804, 2011.
- von Glasow, R.: Atmospheric chemistry in volcanic plumes, *Proc. Natl.Acad. Sci.*, 107, 6594–6599, doi:10.1073/pnas.0913164107, 2010.
- von Glasow, R. and Crutzen, P.: Tropospheric Halogen Chemistry, in: *Treatise on Geochemistry*, pp. 1–67, Elsevier, 2003.
- von Glasow, R., Bobrowski, N., and Kern, C.: The effects of volcanic eruptions on atmospheric chemistry, *Chem. Geol.*, 263, 131–142, doi:10.1016/j.chemgeo.2008.08.020, 2009.
- Vountas, M., Rozanov, V. V., and Burrows, J. P.: Ring effect: Impact of rotational Raman scattering on radiative transfer in Earth's atmosphere, *J. Quant. Spectrosc. Ra.*, 60, 943–961, doi:10.1016/S0022-4073(97)00186-6, 1998.
- Wagner, T.: Satellite Observations of Atmospheric Halogen Oxides, Ph.D. thesis, Combined Faculties for the Natural Sciences and for Mathematics, University of Heidelberg, 1999.
- Wagner, T. and Platt, U.: Satellite mapping of enhanced BrO concentrations in the troposphere, *Nature*, 395, 486–490, doi:10.1038/26723, 1998.

- Wagner, T., Dix, B., Friedeburg, C. v., Frieß, U., Sanghavi, S., Sinreich, R., and Platt, U.: MAX-DOAS O<sub>4</sub> measurements: A new technique to derive information on atmospheric aerosols – Principles and information content, *J. Geophys. Res.*, 109, D22 205, doi:10.1029/2004JD004904, 2004.
- Wagner, T., Beirle, S., and Deutschmann, T.: Three-dimensional simulation of the Ring effect in observations of scattered sun light using Monte Carlo radiative transfer models, *Atmos. Meas. Tech.*, 2, 113–124, doi:10.5194/amt-2-113-2009, 2009.
- Walter, D., Heue, K.-P., Rauthe-Schöch, A., Brenninkmeijer, C. a. M., Lamsal, L. N., Krotkov, N. A., and Platt, U.: Flux calculation using CARIBIC DOAS aircraft measurements: SO<sub>2</sub> emission of Norilsk, *J. Geophys. Res.*, 117, D11 305, doi:10.1029/2011JD017335, 2012.
- Wang, P. and van der A, R. J.: FRESKO Product Specification Document, Koninklijk Nederlands Meteorologisch Instituut, De Bilt, Netherlands, tEM/PSD2/003, Issue: 3.0, 2011.
- Watson, I., Realmuto, V., Rose, W., Prata, A., Bluth, G., Gu, Y., Bader, C., and Yu, T.: Thermal infrared remote sensing of volcanic emissions using the moderate resolution imaging spectroradiometer, *J. Volcanol. Geoth. Res.*, 135, 75–89, doi:10.1016/j.jvolgeores.2003.12.017, 2004.
- Weibring, P., Edner, H., Svanberg, S., Cecchi, G., Pantani, L., Ferrara, R., and Caltabiano, T.: Monitoring of volcanic sulphur dioxide emissions using differential absorption lidar (DIAL), differential optical absorption spectroscopy (DOAS), and correlation spectroscopy (COSPEC), *Appl. Phys. B - Lasers O.*, 67, 419–426, doi:10.1007/s003400050525, 1998.
- Wen, S. and Rose, W. I.: Retrieval of sizes and total masses of particles in volcanic clouds using AVHRR bands 4 and 5, *J. Geophys. Res.*, 99, 5421–5431, doi:10.1029/93JD03340, 1994.
- Wendisch, M. and Yang, P.: *Theory of Atmospheric Radiative Transfer: A Comprehensive Introduction*, Wiley & Sons., 2012.
- Wennberg, P.: Atmospheric chemistry: Bromine explosion, *Nature*, 397, 299–301, doi:10.1038/16805, 1999.
- Wilmouth, D. M., Hanisco, T. F., Donahue, N. M., and Anderson, J. G.: Fourier Transform Ultraviolet Spectroscopy of the A<sup>2</sup>Π<sub>3/2</sub> ← X<sup>2</sup>Π<sub>3/2</sub> Transition of BrO, *J. Phys. Chem. A*, 103, 8935–8945, doi:10.1021/jp991651o, 1999.
- Winer, A. and Biermann, H.: Long pathlength differential optical absorption spectroscopy (DOAS) measurements of gaseous HONO, NO<sub>2</sub> and HCNO in the California South Coast Air Basin, *Research on Chemical Intermediates*, 20, 423–445, doi:10.1163/156856794X00405, 1994.

- World Meteorological Organization: WMO statement on the status of the global climate in 2011, available online at: [http://www.wmo.int/pages/prog/wcp/wcdmp/documents/1085\\_en.pdf](http://www.wmo.int/pages/prog/wcp/wcdmp/documents/1085_en.pdf), 2012.
- Xu, X., Chen, C., Qi, H., He, R., You, C., and Xiang, G.: Development of coal combustion pollution control for SO<sub>2</sub> and NO<sub>x</sub> in China, *Fuel Processing Technology*, 62, 153–160, doi:10.1016/S0378-3820(99)00116-2, 2000.
- Yang, K., Krotkov, N. A., Krueger, A. J., Carn, S. A., Bhartia, P. K., and Levelt, P. F.: Retrieval of large volcanic SO<sub>2</sub> columns from the Aura Ozone Monitoring Instrument: Comparison and limitations, *J. Geophys. Res.*, 112, D24S43, doi:10.1029/2007JD008825, 2007.
- Yang, K., Liu, X., Krotkov, N. A., Krueger, A. J., and Carn, S. A.: Estimating the altitude of volcanic sulfur dioxide plumes from space borne hyper-spectral UV measurements, *Geophys. Res. Lett.*, 36, 6 PP., doi:200910.1029/2009GL038025, 2009.
- Zelenski, M. and Taran, Y.: Volcanic emissions of molecular chlorine, *Geochim. Cosmochim. Ac.*, 87, 210–226, doi:10.1016/j.gca.2012.03.034, 2012.
- Zhang, X., van Geffen, J., Liao, H., Zhang, P., and Lou, S.: Spatiotemporal variations of tropospheric SO<sub>2</sub> over China by SCIAMACHY observations during 2004–2009, *Atmos. Environ.*, 60, 238–246, doi:10.1016/j.atmosenv.2012.06.009, 2012.



# Danksagungen

Zahlreiche Menschen haben in den letzten Jahren zur Entstehung dieser Doktorarbeit beigetragen und mir diese schöne Zeit durch ihre Hilfe und Unterstützung erst ermöglicht. Zunächst gilt es mich bei allen Mitgliedern meiner beiden Arbeitsgruppen am Institut für Umweltphysik in Heidelberg und am Max Planck Institut für Chemie in Mainz zu bedanken, die mich herzlich in ihre schon fast familiäre Gemeinschaft aufgenommen haben. Durch sie habe ich mich immer wohl gefühlt. Vielen Dank für die letzten Jahre!

Darüber hinaus gebührt mein Dank insbesondere:

- Meinem Doktorvater Prof. Ulrich Platt vom IUP Heidelberg und Prof. Thomas Wagner vom MPIC in Mainz, die mir diese Arbeit an unterschiedlichen Instituten erst möglich gemacht haben und damit die einmalige Möglichkeit gaben, verschiedene Perspektiven desselben Themas zu erleben. Beide hatten zudem immer ein offenes Ohr für mich und haben durch ihre Ideen und Motivation dafür gesorgt, dass mir nicht irgendwann die Puste ausgegangen ist. Diese Unterstützung ist nicht selbstverständlich und ich weiß dies sehr zu schätzen. Danke!
- Prof. Bernd Jähne, der die Erstellung des Zweitgutachtens dieser Arbeit übernommen hat.
- Den Leitern der Max Planck International Research School, Elmar Uherek und Agnes Heinemann für ihre Unterstützung.
- Den Mitgliedern meines PAC Komitees, neben Ulrich Platt und Thomas Wagner auch noch Steffen Beirle und Thierry Marbach.
- Allen, die mir beim Korrekturlesen dieser Arbeit sehr geholfen haben: Marloes, Holger, Steffen B., Steffen D., Julia, Nicole, Leif, Peter, Fabienne. Euch allen vielen Dank für die Mühe und die nützlichen und konstruktiven Anmerkungen. Vielleicht kann ich mich bei dem ein oder anderen irgendwann mit demselben Fleiß revangieren.
- Allen, die mich an verschiedene Vulkane in der Welt begleitet haben, insbesondere Nicole, Leif, Christoph, Roland und Sebastian. Es waren spannende Messkampagnen und ich bin dankbar für die Möglichkeit fremde Länder und Kulturen erlebt zu haben, die ich sonst wahrscheinlich nie zu Gesicht bekommen hätte. Diese Reisen wären für sich schon toll gewesen, aber richtig Spaß hat es erst mit euch zusammen gemacht. Hoffentlich werden weitere tolle gemeinsame Erlebnisse folgen.

- Marloes, meiner liebsten Zimmerkollegin, die mir immer bereitwillig geholfen und mich trotz eigener Arbeit immer unterstützt und motiviert hat.
- Holger, der wie ich an beiden Instituten in HD und Mainz zuhause war. Von Beginn an konnte ich auf ihn, seine Ratschläge und kreativen Ideen zählen.
- Conny und Rüdiger, die immer den Überblick bewahrt haben und mir tatkräftig bei technischen Fragen zur Seite standen.
- Nicole, die mit ihrer Leidenschaft für Vulkane auch mich immer wieder motiviert und mitgerissen hat. Wer würde nicht gerne sein Leben am Fuss des Ätna verbringen und jährlich den hauseigenen Wein ernten.
- Leif, mit dem man immer eine spaßige Zeit verbringen kann, egal ob am Vulkan, während langer Konferenzabende oder auch einfach mal zwischendurch. Hab dich eigentlich nie schlecht gelaunt erlebt, bewahr dir das!
- Meinen Zimmerkollegen in Heidelberg, die insbesondere in den letzten Monaten mit mir die Zusammenschreib-Phase geteilt haben, Felix, Nils und Tim.
- Meinen Freunden in HD, teilweise noch im Studium, mitten in der Doktorarbeit oder auch schon im harten Berufsalltag: Krishna, Tillmann, Mario, Gabi, Markus, Diana, Max, Simone, Fabienne, Marlen, Lea, Ulf.
- Natürlich meiner Familie, insbesondere meinen Eltern. Ohne ihre Unterstützung und das Vertrauen wäre als das nicht machbar gewesen. Danke für diese Chance!
- Sylvie, die immer für mich da war, motiviert und ertragen hat, auch wenn ich zu manchen Zeiten vielleicht nicht immer ohne Weiteres zu ertragen war. Danke!